

20000 814175

12

ADA150673

DTIC
ELECTE
F 527 83

DTIC 84/00

85 02 21 021

SECURITY CLASSIFICATION OF THIS PAGE (When Data Entered)

DD FORM 1 JAN 73 1473

UNCLASSIFIED

SECURITY CLASSIFICATION OF THIS PAGE (When Data Entered)

AERO-HYDROACOUSTICS FOR SHIPS

Accession For	
NTIS GRA&I	<input checked="checked" type="checkbox"/>
DTIC TAB	<input type="checkbox"/>
Unannounced	<input type="checkbox"/>
Justification	
By _____	
Distribution/	
Availability Codes	
Dist	Avail and/or Special
A-1	



AERO-HYDROACOUSTICS FOR SHIPS

BY

WILLIAM K. BLAKE

**Research Physicist
Ship Acoustics Department**

**DAVID TAYLOR NAVAL SHIP RESEARCH
AND DEVELOPMENT CENTER**

VOLUME II

Chapters 7 to 10

JUNE 1984

FOREWORD

This book is a comprehensive and unified treatment of the mechanisms of flow-generated sound that occurs on ships and in marine machinery. Often the control of these mechanisms involves the essentials of both fluid mechanics and structural dynamics.

Dynamical properties of various types of flow and of various structural elements that are typical of ship application are thus examined in detail beginning with the fundamentals of each physical source. Organization of the book provides for the treatment of elementary sources of flow noise and the principles of random vibration in Volume 1. Normal mode analysis is the cornerstone of the methods used there to describe the behavior of flow induced vibration. Naval applications that involve turbulent boundary layer and lifting surface flows are discussed in Volume 2. Aerodynamic noise sources, in so far as they occur anogously in underwater acoustics, are examined in detail for low Mach number marine application.

PREFACE

The requirements for reduced levels of shipboard sound and vibration have become increasingly demanding as each technological advancement in ship systems leads to a more sophisticated design goal. It is now clear that many traditional means of control that invoke the obstruction of transmission paths and the mechanical isolation of sound sources have now been fully exploited and in many instances are proving inadequate. This is particularly true in cases involving fluid flow. Modern technology now requires noise and vibration control that is fully integrated with the design of hydraulic machinery, propulsion equipment, and turbo machinery, to name only a few. It is often the case that the physical fundamentals of design also involve parameters which are essentially common to noise and vibration production and that very useful performance and acoustic tradeoffs may be conducted in design if only the noise-producing fundamentals are recognized by the designer. These tradeoffs may even be conducted as early as the preliminary design stage. These tradeoffs are as feasible in the private sector as they are in the Navy. In fact in almost every aspect of noise and vibration control which is important to the Navy, there is a parallel development of understanding in some other application. The purpose of this book is thus to provide an integrated description of the fundamentals of fluid-dynamically generated sound and vibration which is founded on the combined principles of acoustics, classical fluid mechanics, and vibration.

It is the aim of this book to set down the fundamentals of sound generation by different classes of fluid motions and flow-body interactions. Since the generation of sound is intimately connected with the creation of turbulence and other manifestations of flow unsteadiness, it is important to understand both acoustics and the appropriate elements of unsteady fluid mechanics. Thus a great deal of attention has been placed on the essentials of various turbulent flows, hydrodynamics of cavitation, boundary layer theory, and lifting surface theory. The purpose is to develop understanding and perspective on the part of the reader; for this reason, theoretical relationships that are derived are copiously illustrated with experimental data. This is often done through the use of dimensionless forms which give generalized presentations to support and extend the theory. In most cases that involve experimental results not collected by the author, this has required a

complete reworking of the data into a form that is consistent with the philosophy of the book. Fluid dynamic sources so treated include such classes of flows as flow tones, jet noise, cavitation, vortex shedding sounds, all forms of subsonic lifting surface noise, and sources which occur in axial flow machinery. Since in underwater acoustics, vibration often plays a dominant role, there is a chapter on the fundamentals of random vibration as it relates to flow-excited structures.

The scope of the book is broad, and all topics could not be covered completely. So, each chapter includes an extensive reference list. The lists are not exhaustive, but are reasonably complete.

The book is written for scientists and engineers who are not experts in fluid mechanics or acoustics; however, a knowledge of the fundamentals of each, particularly fluid mechanics, would be helpful. The treatment of structural vibration and structural acoustics is relatively cursory because there are already rather good monographs on those subjects that are available, as referenced. Although much of the mathematical treatment used is rather sophisticated, the analyses have been concentrated and kept identifiably separate from physical discussions whenever possible. This is so that readers desiring a more descriptive approach may also be served by the book.

The book has evolved from the author's own research experiences, as well as from the literature of both the aeroacoustics and hydroacoustics communities. The author is indebted to his colleagues at the Center and, in particular, to those in the Hydroacoustics Branch of the Ship Acoustics Department for their continuing interest in the project. Many people contributed to the preparation of the various chapters. Special thanks go to Professor Patrick Leehey of MIT whose graduate course on flow noise provided me with both instruction and inspiration, and to Drs. Alan Powell and Maurice Sevik who provided continuing understanding, stimulation, and encouragement as the work progressed. The work could not have been undertaken at all without the help of S. Blazek and A. R. Paladino of the Naval Sea Systems Command who sponsored much of the writing. Technical consultations with current and past colleagues at the Center on as many aspects of the work as possible were necessary to give the work depth and perspective; thanks are extended to G. Franz, J. T. C. Shen, G. Maidanik, M. Strasberg, F. C. DeMetz, as well as to T. Brooks of NASA, and R. Schlinker of UTRC. From time to time I imposed on a variety of experts to review selected chapters for content; gratitude is extended to

M. Casarella, D. Crighton, M. Howe, R. E. A. Arndt, R. Armstrong, F. B. Peterson, A. Kilcullen, D. Feit, M. C. Junger, F. E. Geib, R. Henders, R. A. Cumming, W. B. Morgan, L. J. Maga, and R. E. Biancardi. Thanks are also due to D. Paladino and J. Gershfeld who read all or part of the manuscript and located many of the inconsistencies and errors.

The creation of camera-ready copy was made possible by a team of B. Devaney, B. Hay, J. Seidenstricker, and M. Gotthardt of DTNSRDC. C. Naas (also of DTNSRDC) and K. Simon (of Forte, Inc.) did the exceptionally difficult job of editing. T. Gilleland and R. Schmidt of the Center's Publications Department coordinated the typing and artwork.

Finally, the main debts are owed to my wife Donna who initially suggested the project and whose enduring gifts of love, support, and patience made possible its completion and to our daughters Kristen and Helen for their cheerfulness as they virtually grew up with the book around them.

W. K. Blake

Bethesda, MD

June 1984

CONTENTS

	Page
EPREFACE	vii
LIST OF RECURRING SYMBOLS	xvii

VOLUME I

PART 1 - INTRODUCTION

1.1 THE DISCIPLINES OF FLOW NOISE	1
1.2 DIMENSIONAL ANALYSIS.	3
1.3 SIMILITUDE IN AERO-HYDROACOUSTIC MODEL TESTING.	12
1.4 REPRESENTATIONS OF SOUND LEVELS	16
1.4.1 Sound Level Definition	16
1.4.2 Sound Pressure Spectra	18
1.4.3 Combination of Levels.	23
1.4.4 Use of Dimensionless Spectrum Levels	24

PART 2 - GENERAL THEORIES OF FLOW-INDUCED NOISE

2.1 FUNDAMENTALS OF LINEAR ACOUSTICS THEORY	34
2.1.1 The Wave Equation.	34
2.1.2 Characteristics of Multipole Radiation	42
2.2 SOMMERFELD'S RADIATION CONDITION.	51
2.3 Lighthill's THEORY OF AERODYNAMIC NOISE	52
2.3.1 The Wave Equation.	52
2.3.2 Kirchhoff's Integral Equation and the Retarded Potential	56
2.3.3 Acoustic Radiation from Free Turbulence.	61
2.4 EFFECTS OF SURFACES ON FLOW-INDUCED NOISE	67
2.4.1 Curle's Development of Lighthill's Wave Equation	67
2.4.2 Illustration I: Radiation from a Heaving Sphere	71
2.4.3 Illustration II: Radiation from a Concentrated Hydrodynamic Force: The Force Dipole	73
2.4.4 Powell's Reflection Theorem.	74
2.5 POWELL'S THEORY OF VORTEX SOUND	80
2.5.1 General Implications	80
2.5.2 Derivation of the Wave Equation with Vortical Sources.	81
2.5.3 The Physical Significance of the Vorticity Source.	83
2.5.4 The Effect of Solid Boundaries	90
2.6 REPRESENTATIONS IN THE FREQUENCY DOMAIN	91
2.6.1 Helmholtz Integral Equation.	92
2.6.2 Generalized Transforms and Stochastic Variables.	96
2.7 APPENDIX - DIPOLE RADIATION FROM THE HEAVING SPHERE: EXACT AND ASYMPTOTIC SOLUTIONS.	107
2.7.1 Asymptotic Formulas.	107
2.7.2 Exact Solutions.	111
2.8 REFERENCES.	113

CHAPTER 3 - JETS, WHISTLES, AND OTHER SHEAR-FLOW NOISES

3.1	INTRODUCTION.	116
3.2	SHEAR FLOW INSTABILITIES AND THE GENERATION OF VORTICITY.	117
3.3	FREE SHEAR LAYER AND CAVITY RESONANCE	125
3.4	SELF-EXCITATION OF LAMINAR JETS	135
3.4.1	Dimensionless Frequencies of Tonal Disturbances.	135
3.4.2	Hole, Ring, and Edge Tones	142
3.5	A SUMMARY OF STATISTICAL DESCRIPTIONS OF TURBULENCE	150
3.5.1	General Comments	150
3.5.2	Correlation Functions of Random Variables.	151
3.5.3	Frequency and Wave Number Spectra.	155
3.6	FUNDAMENTALS OF NOISE FROM SUBSONIC TURBULENT JETS.	160
3.6.1	Formal Analytical Relationships for Source Convection.	160
3.6.2	Measured Characteristics of Jet Noise.	166
3.6.3	Some Qualities of Jet Noise Deduced from Flow Structure.	173
3.7	NOISE FROM UNSTEADY MASS INJECTION.	197
3.7.1	Sound From Efflux Inhomogeneities.	198
3.7.2	Inhomogeneities in the Free Turbulent Field.	205
3.8	APPENDIX A - MEASUREMENT OF CROSS SPECTRAL DENSITIES WITH FILTERED SIGNALS.	208
3.9	REFERENCES.	219

CHAPTER 4 - TWO-PHASE FLOW NOISE

4.1	INTRODUCTION.	229
4.1.1	General Concepts	229
4.1.2	The Cavitation Index and Cavitation Similitude	233
4.2	BASIC EQUATIONS OF BUBBLE DYNAMICS.	238
4.2.1	Linear Bubble Motions.	238
4.2.2	Sound Propagation in Bubbly Liquids.	248
4.2.3	Theoretical Cavitation Thresholds; Non-Linear Oscillations Spherical Bubbles.	259
4.2.4	Effects of Gas Content and Nuclei Distribution	272
4.2.5	The Collapse of Cavitation Bubbles	283
4.3	HYDRODYNAMIC CAVITATION INCEPTION	302
4.3.1	General Equilibrium Theory	302
4.3.2	Examples of Cavitation Inception in Turbulent Flows.	316
4.4	HYDRODYNAMIC CAVITATION NOISE	334
4.4.1	Theoretical Spectrum of Single-Bubble Cavitation Noise	334
4.4.2	Simple Rules of Similitude	344
4.4.3	Examples of Hydrodynamically-Induced Cavitation Noise.	353
4.4.4	Propeller Cavitation	365
4.4.5	Stochastic Models of Bubble Cavitation Noise	381
4.5	SOUNDS FROM OTHER BUBBLE MOTIONS.	397
4.5.1	Sound Pulses from Formation and Splitting.	397
4.5.2	Bubbles Excited by a Pressure Field: Speed Dependence.	404
4.5.3	Measurements of Bubble Noise	407
4.5.4	Hydromechanics of Bubble Formation	411

4.6	APPENDIX A - DERIVATION OF APPROXIMATE SPECTRAL FUNCTIONS	424
4.7	APPENDIX B - PHYSICAL PROPERTIES OF AIR AND WATER	427
4.8	APPENDIX C - NOMOGRAPHS FOR COMPUTING PROPELLER PARAMETERS.	428
4.9	REFERENCES.	431

CHAPTER 5 - GENERATION OF AEOLIAN TONES BY RIGID CYLINDERS

5.1	INTRODUCTION: GENERAL DESCRIPTION OF VORTEX FLOW, LIFT FLUCTUATION, AND SOUND	448
5.2	MECHANICS OF VORTEX FORMATION BEHIND CIRCULAR CYLINDERS	450
5.2.1	General Description of Wake Structure and Vortex Generation	450
5.2.2	Wave-Mechanical Analysis of Vortex Production.	453
5.2.3	Secondary Disturbances in the Vortex Formation Zone.	462
5.3	MEASURED FLOW-INDUCED FORCES AND THEIR FREQUENCIES.	462
5.3.1	Mean Drag and Vortex Shedding Frequencies.	462
5.3.2	Oscillatory Lift and Drag on Circular Cylinders.	472
5.3.3	Representations of Axial Phase-Uniformity: Correlation Lengths.	476
5.4	ENVIRONMENTAL INFLUENCES ON VORTEX SHEDDING	481
5.5	ESTIMATIONS OF WAKE-INDUCED FORCES IN TWO-DIMENSIONAL FLOW.	486
5.6	FORMULATION OF THE ACOUSTIC PROBLEM FOR COMPACT SURFACES.	497
5.6.1	General Equations.	497
5.6.2	Importance of Quadrupole Radiation	500
5.6.3	Radiation from a Rigid Cylinder in a Cross-Flow.	502
5.6.4	Review of Measured Acoustic Intensities.	506
5.7	RADIATION FROM ROTATING RODS.	511
5.8	OTHER TOPICS IN VORTEX-INDUCED NOISE.	517
5.8.1	Cylinders with Non Circular Cross Sections	519
5.8.2	Unsteadiness in Tube Bundles	521
5.8.3	Methods of Reducing Vortex-Induced Forces.	526
5.9	REFERENCES.	529

CHAPTER 6 - STOCHASTIC THEORY OF FLOW-INDUCED VIBRATION AND NOISE

6.1	INTRODUCTION.	537
6.2	RESPONSE OF SINGLE-DEGREE-OF-FREEDOM SYSTEMS TO TEMPORALLY RANDOM EXCITATION	539
6.3	GENERAL FEATURES OF STRUCTURES DRIVEN BY RANDOMLY-DISTRIBUTED PRESSURE FIELDS	545
6.3.1	Modal Velocities and Excitation Functions.	545
6.3.2	Vibration of Effectively Infinite Surfaces; The Infinite Plate	549
6.3.3	Random Excitation of Single Mode Oscillators	552
6.3.4	Response Estimates for Structures of Many Modes.	556
6.4	MODAL SHAPE FUNCTIONS FOR SIMPLE STRUCTURES	565
6.5	ESSENTIAL FEATURES OF STRUCTURAL RADIATION.	571
6.5.1	Analysis of a Simply Supported Panel	571
6.5.2	Fluid Impedance of a Simply Supported Panel.	576
6.5.3	Radiated Acoustic Power.	579
6.5.4	Radiation Efficiencies of Simple Structures.	584

	<u>Page</u>
6.5.5 Relationships for Estimating Total Acoustic Power.	587
6.5.6 Added Masses of Simple Structures.	593
6.6 RADIATION FROM STRUCTURES IN HEAVY FLUIDS	594
6.6.1 Radiation From Essentially Infinite Point-Driven Plates.	594
6.6.2 Elements of Fluid Loading Without Modal Coupling	596
6.7 EXAMPLE I: RADIATION FROM A RECTANGULAR PANEL DRIVEN BY A TONAL LOCAL FORCE	599
6.7.1 Determination of Mode Order.	600
6.7.2 Acoustic Classification of Mode Order.	602
6.7.3 Response Amplitude of the Panel.	604
6.7.4 Location in Space of the Maximum Sound Pressure Level.	604
6.7.5 Magnitude of the Far Field Pressure.	606
6.8 EXAMPLE II: RADIATION FROM A RECTANGULAR PANEL DRIVEN BY A BROADBAND FORCE	610
6.9 REFERENCES.	619
INDEX (Repeated from Volume II)	622a

VOLUME II

CHAPTER 7 - TURBULENT-BOUNDARY-LAYER STRUCTURE AND SURFACE PRESSURE

7.1 INTRODUCTION.	623
7.2 EQUILIBRIUM TURBULENT BOUNDARY LAYERS.	625
7.2.1 General Relationships and Dimensionless Representations.	625
7.2.2 Dimensionless Representations of the Mean Velocity Profile	632
7.2.3 Prediction of the Wall-Shear Coefficient and Boundary- Layer Length Scales.	641
7.2.4 Turbulence Intensities and Statistical Correlations.	648
7.2.5 Description of Turbulence in the Frequency Domain	660
7.2.6 Modern Views of Boundary-Layer Structure	673
7.3 ANALYTICAL DESCRIPTIONS OF THE WALL PRESSURE FIELD.	683
7.3.1 General Relationships.	683
7.3.2 Overall Considerations of the Wave Number Spectrum	694
7.3.3 Features of Turbulence Structure Affecting the Wave Number Spectrum of Wall Pressure	702
7.3.4 Characteristics of the Frequency Spectrum of Wall Pressure	708
7.3.5 Kinematic Modeling of Turbulence Using Wave Mechanics Analogies.	712
7.3.6 Low Wave Number Spectrum and Unsteady Local Convection	717
7.3.7 Recent Modeling of $\phi_p(\vec{k}, \omega)$	723
7.4 PRESSURE FLUCTUATIONS BENEATH EQUILIBRIUM WALL LAYERS.	729
7.4.1 Intensity and Frequency Dependence of Wall Pressures	729
7.4.2 Spatial Characteristics and Convection of Wall Pressures	737
7.4.3 Description in the Wave Number Domain.	747
7.4.4 Measured Pressures at Low Wave Numbers Using Spatial Filtering Techniques	752
7.4.5 Particularities of Rough-Wall Boundary-Layer Pressures	770
7.4.6 Effects of Transducer Size and Shape: The Response Function	772

	Page
7.4.7 Transduction of Boundary-Layer Pressure Through Rubber Blankets.	779
7.4.8 Pressure Fluctuations in Turbulent Pipe Flow	783
7.5 TURBULENT FLOW OVER CURVED SURFACES	785
7.5.1 Transition to Turbulence	785
7.5.2 Adverse and Favorable Static Pressure Gradients in Fully Developed Turbulence	799
7.5.3 Pressure Fluctuations Beneath Separated Turbulent Flow	806
7.5.4 Thick Axisymmetric Turbulent Boundary Layers: The Circular Cylinder.	807
7.6 REFERENCES.	813
 CHAPTER 8 — BOUNDARY-LAYER-INDUCED VIBRATION AND NOISE —	
8.1 INTRODUCTION.	832
8.2 FLOW-EXCITED STRUCTURAL VIBRATION	833
8.2.1 General Method	833
8.2.2 Effects of Hydrodynamic Coincidence on Single-Mode Response.	838
8.2.3 Empirical Confirmation	846
8.2.4 Average Response of Many Modes	849
8.3 SOUND FROM FLOW-INDUCED VIBRATION	856
8.4 GENERAL RULES FOR HYDROACOUSTIC SIMILARITY AND NOISE CONTROL, <i>and</i>	861
8.5 HISTORICAL NOTES ON MODELING $\phi_p(k, \omega)$	868
8.6 DIRECT RADIATION FROM TURBULENT BOUNDARY LAYERS.	870
8.6.1 Qualitative Analysis of Direct Radiation	871
8.6.2 Recent Analyses of Direct Radiation.	875
8.7 REFERENCES.	892
 CHAPTER 9 — THE HYDROACOUSTICS OF NON-CAVITATING LIFTING SURFACES —	
9.1 INTRODUCTION.	898
9.2 FUNDAMENTALS OF LIFTING-SURFACE NOISE	899
9.2.1 Classifications of Flow Disturbances	899
9.2.2 Characteristic Length and Time Scales for Acoustic and Aerodynamic Classifications.	901
9.2.3 Low and High Frequency Limits of Theory.	908
9.3 NOISE FROM INFLOW UNSTEADINESS.	924
9.3.1 Elements of Unsteady Airfoil Theory.	924
9.3.2 Oscillatory Lift Spectra from Ingested Turbulence.	936
9.3.3 Surface Pressures Resulting From Unsteady Loads.	943
9.3.4 Observations of Noise From Inflow Inhomogeneities.	946
9.4 VISCOUS EFFECTS: (BOUNDARY-LAYER AND VORTEX-WAKE DEVELOPMENT)	953
9.4.1 Boundary-Layer Growth on Lifting Surfaces.	955
9.4.2 Conditions for Vortex Formation at Trailing Edges of Rigid Surfaces	959
9.4.3 Suppression of Vortex Shedding With Changes in Edge Geometry.	965
9.4.4 Alternative Definitions of Strouhal Numbers.	969
9.5 SELF-INDUCED SURFACE PRESSURE FLUCTUATIONS.	978
9.5.1 Tonal Surface Pressures From Vortex Shedding: Theory.	979
9.5.2 Measured Pressures From Vortex Shedding.	988

	Page
9.5.3 Pressures From Turbulent Separation	993
9.5.4 Spanwise Correlation Lengths	998
9.5.5 The Flow-Induced Forces at Trailing Edges.	1000
9.6 SOUND FROM TRAILING-EDGE FLOW	1001
9.6.1 Summary.	1001
9.6.2 Acoustic Tones From Vortex Shedding.	1003
9.6.3 Sound From Aeroacoustic Scattering	1011
9.7 FLOW-INDUCED VIBRATION AND SINGING, <i>and</i>	1037
9.7.1 Linear Flow Excitation of Lifting Surfaces	1038
9.7.2 Vibration Induced by Vortex Shedding From Cylinders and Airfoils	1046
9.8 ILLUSTRATION: ESTIMATION OF RADIATED NOISE FROM A HYDROFOIL, <i>and</i>	1068
9.8.1 Noise From Inflow Turbulence	1070
9.8.2 Trailing-Edge Noise.	1071
9.8.3 Acoustic Tones from Vortex Shedding.	1072
9.8.4 Enhancement From Surface Vibration	1073
9.8.5 Relative Sound Levels from Surface Motion and Pressures.	1076
9.9 REFERENCES.	1082
 CHAPTER 10 - NOISE FROM AXIAL FLOW MACHINERY - -	
10.1 INTRODUCTION.	1096
10.2 ELEMENTARY ACOUSTICS OF ROTATING MACHINERY,	1097
10.2.1 Sources of Noise.	1097
10.2.2 The Tonal Spectrum of Compressor Noise.	1100
10.2.3 Elementary Considerations for the Control of Interaction Noise	1104
10.3 DESIGN PARAMETERS OF ROTORS AS LIFTING SURFACES,	1110
10.3.1 Similitude of Turbomachines	1111
10.3.2 Propeller Blades as Lifting Surfaces.	1115
10.4 THEORETICAL FREE-FIELD ACOUSTICS OF ROTORS.	1124
10.4.1 Fundamental Analysis.	1124
10.4.2 Interaction Tones from Rotating Blade Forces.	1131
10.5 SELF-NOISE FROM ROTATING MACHINERY,	1142
10.5.1 Sounds From Steady Loading: Gutter Sound.	1142
10.5.2 Laminar Flow Surfaces	1145
10.5.3 Turbulent Trailing-Edge Noise	1149
10.5.4 Broadband Noise Related to Loading.	1152
10.5.5 Propeller Singing	1158
10.5.6 Thickness Noise	1159
10.6 INTERACTION NOISE IN AXIAL FLOW MACHINES, <i>and</i>	1160
10.6.1 Deterministic Unsteady Loading.	1160
10.6.2 Turbulent Inflows	1181
10.7 ROTATING MACHINERY IN ENCLOSURES/ <i>ducts</i>	1193
10.7.1 Elementary Duct Acoustics	1193
10.7.2 Propagating Modes of a Ducted Rotor	1196
10.8 REFERENCES.	1202
INDEX	1213

LIST OF RECURRING SYMBOLS

R	Aspect ratio
A_p	Area of a panel, or hydrofoil
b	Shear layer length scale (Chapter 3)
B	No. of blades in a rotor or propeller
C	Blade chord
C_D, C_L, C_f, C_p	Drag, lift, friction, and pressure coefficients, respectively
c	Wave speed, subscripted: 0 - acoustic b - flexural bending m - membrane (Chapter 6) m - mixture (Chapters 3 and 4) l - longitudinal g - group (Chapter 6), gas (Chapter 4)
D	Drag
D	Diameter (jet, propeller, rotor in Chapters 3, 4, 9)
d	Cylinder diameter, cross section
$E(x)$	Expected value of $x(=\bar{x})$
f	Frequency
$F_i(t)$	Force, or force per unit area, in i direction
F_r	Froude number
$G(\vec{x}, \vec{y}), G(\vec{x}, \vec{y}, \omega)$	Green functions
h	Thickness of plate, hydrofoil, propeller blade
$H_n(\xi)$	Cylindrical Hankel function, n^{th} order
I	Acoustic intensity
J	Propeller advance coefficient
$J_n(\xi)$	Bessel's function, first kind, n^{th} order
k, k_i	Wave number: i, i^{th} direction; k_{13} , in the 1, 3 plane

k_g	Geometric roughness height
k_s	Equivalent hydrodynamic sand roughness height
k_o	Acoustic wave number ω/c_o
k_n, k_{mn}	Wave numbers of n-th or m, n. modes
k_p	Plate bending wave number, $k_p = \omega/C_b$
k_T, k_q	Thrust and torque coefficients for propellers and rotors, Equations (9-4), (9-5)
K	Cavitation index $(P_\infty - P_v)/q_\infty$
L	Lift or lift per unit area
L_1, L_3	Length across the stream, span
L_i	Geometric length in i-th direction
l_o	Length scale used to denote a characteristic of fluid motion
l_c, l_f	Spanwise correlation length, eddy formation length
M	Mass
m_s	Structural plating mass per unit area
m_m, m_{mn}	Fluid added mass per unit area for m or mn vibration mode
M_c, M_T, M	Mach numbers: convection (c), tip (T)
n_s	Shaft speed, revolutions per second
$n(k), n(\omega)$	Mode number densities
\vec{n}, n_i	Unit normal vector
$n(R)$	Bubble distribution density number of bubbles per fluid volume per radius increment
N	Number of bubbles per unit fluid volume
p	Fluctuating pressure; occasionally subscripted for clarity: a or rad - acoustic, b - boundary layer, h - hydrodynamic
P	Average pressure
P_∞	Upstream pressure

$P, P(\omega, \Delta\omega)$	Power, total and in bandwidth $\Delta\omega$, respectively
P_i	Rotor pitch
\dot{q}	Rate of mass injection per unit volume
q_∞, q_T	Dynamic pressures based on U_∞ and U_T
Q	Torque
Re_L	Reynolds number based on any given length scale L , and velocity scale, U_∞ ($U_\infty L/\nu$)
R	Radius; used in Chapter 4 for general bubble radius, Chapter 10 for propeller radius coordinate
R_b	Bubble radius
R_T, R_H	Rotor Tip and Hub Radii, respectively
R_{pp}	Correlation function of pressure, normalized
R_{ij}	Correlation function of velocity fluctuations u_i and u_j , normalized
r	Acoustic range, occasionally subscripted to clarify special source point-field point identification
\vec{r}, r_i	Correlation point separation — the distribution from r is clear in the text
S	Strouhal number $f_s l/U$ where l and U depend on the shedding body
$S_{mn}(\vec{k})$	Modal spectrum function
S_e, S_{2D}	One- and two-dimensional Sears functions
$S_p(r, \omega)$	Spectrum function used in Chapter 4 for cavitation noise
t	time
T_{ij}	Lighthill's stress tensor (page 54)
U	Average velocity, advance, U_a free stream, U_∞ convection, U_c tip, U_T hydrodynamic friction, $U_T = \sqrt{\tau_w/\rho_o}$ shedding, $U_s = U_\infty \sqrt{1 - C_{pb}}$

\vec{u}, u_i	fluctuating velocities
T	Average time
$\bar{T}, T(t)$	Thrust, steady and unsteady
V	Vane number in Chapter 10
v	Volume fluctuation
$v(t)$	Transverse velocity of vibrating plate, beam, hydrofoil
W_e	Weber number in Chapter 4
\vec{x}, x_i	Acoustic field point coordinate
\vec{y}, y_i	Acoustic source point coordinate
y_f	Cross-wake shear layer thickness at point of maximum streamwise velocity fluctuation in wake

GREEK SYMBOLS:

α	Complex wave number, used in stability analyses and as dummy variable
β	Volumetric concentration (Chapters 3 and 4); fluid loading factor $\rho_o c_o / \rho_p h \omega$ (Chapters 1, 6, 7, 8)
Γ	Vortex circulation
γ	Adiabatic gas constant (Chapter 4), rotor blade angle (Chapter 10)
δ	Boundary layer or shear-layer thickness, also $\delta(.99)$ and $\delta(.995)$
$\delta(x)$	Dirac delta function, $\int \delta(x) dx = 1$
δ^*	Boundary (shear) layer displacement thickness
$\eta_t, \eta_{rad}, \eta_m, \eta_v, \eta_h$	Loss factors: t, total; rad, radiation; m, mechanical; v, viscous; h, hydrodynamic
η_i, η_p	Powering efficiencies: i, ideal; p, propeller
θ	Angular coordinate
θ_t	Integral time scale of turbulence
ϕ	Angular coordinate

$\phi_v(\omega)$	Auto-spectral density of $V(t)$, subscripted: p for $p(t)$; i for $u_i(t)$, f for $F(t)$
$\phi_v(\vec{y}, \omega)$	Auto-spectral density of $V(f)$ with dependence on location y emphasized, other subscripts as above
$\phi_{pp}(\vec{k}, \omega)$	Wave number, frequency spectrum of pressures
$\phi_m(\omega - \vec{U}_c \cdot \vec{k})$	moving axis spectrum
$\phi_i(k_j)$	Wave number spectrum of velocity fluctuation u_i
$\phi_{ij}(\vec{r}, \omega)$	Cross-spectral density between $u_i(\vec{y}, t)$ and $u_j(\vec{y} + \vec{r}, t)$
κ	von Karman constant (Chapter 7), radius of gyration of vibrating plate, beam, hydrofoil (Chapters 6, 8, 9)
$\vec{\kappa}, \kappa_{13}$	dummy wave number variables
λ	Wavelength (also turbulent microscale in Chapters 4 and 7, when subscripted with i, j , or t)
Λ	Integral correlation length; for spatial separations in i direction, Λ_i
μ	Viscosity
ν	Kinematic viscosity, ν_e eddy viscosity
ν_p	Poisson's ratio
$\pi(\omega)$	Power spectral density
ρ	Density: ρ_c , average fluid; ρ_g , gas; ρ_m , mixture; ρ_p , plate material
σ_{mn}	Radiation efficiency of mn mode, also σ_{rad}
τ	Time delay, correlation
τ_w	Wall shear
τ_{ij}	Viscous shear stress tensor, p. 53
$\phi(\vec{y}), \phi(y_i)$	Potential functions
$\psi_{mn}(\vec{y}), \psi_m(\vec{y})$	Mode shape functions
$\psi(\vec{y})$	Stream function
ω	Circular frequency, $\omega = 2\pi f$
$\vec{\omega}, \omega_i$	Vorticity vector, component
Ω	Shaft rate

CHAPTER 7

TURBULENT-BOUNDARY-LAYER STRUCTURE AND SURFACE PRESSURE

7.1 INTRODUCTION

This chapter presents the underlying fluid mechanics of the broad and important range of hydroacoustical problems related to the behavior of the turbulent boundary layer. The geometry of a developing turbulent boundary layer is shown in Figure 7.1. The region of turbulent flow is (crudely speaking at least) confined to some distance, say δ , from the boundary (δ is determined by the relative velocity, the kinematic viscosity of the fluid, and the streamwise extent y_1 of the wetted surface) in which there is a gradient of fluid motion that is ultimately responsible for the maintenance of a largely disordered field of vorticity. The turbulent motion contained in this boundary-layer region induces fluctuating pressures on the boundary. The structure of the boundary layer and its fluctuating wall pressures as well as the potential for wall vibration by, and direct acoustic radiation from, turbulent boundary layers are discussed in this and the following chapter.

This chapter approaches the subject of boundary-layer structure from two directions. The first is practical; it is recognized that estimations of sound and vibration induced by turbulent boundary layers must be based on empirical information

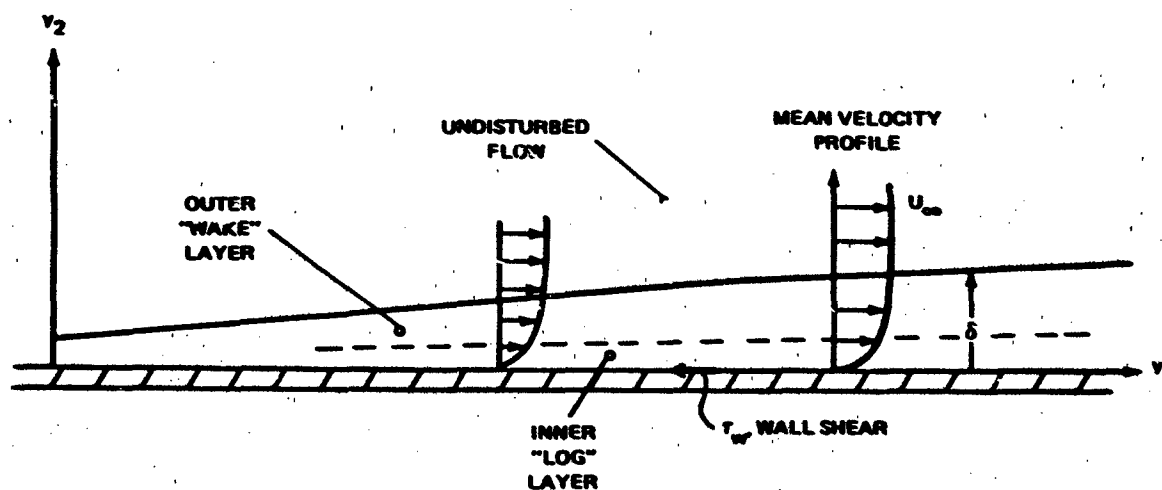


Figure 7.1 - Schematic of a Developing Turbulent Boundary Layer
Showing Overall Thickness δ , Wall Shear τ_w ,
and the Growing Inner and Outer Layers

and that laws of similitude must be established for both the flow and the structure. The latter is discussed in Chapter 6; this chapter deals with the parameters for establishing force, length, and time scales with which we may describe those qualities of wall pressure fluctuations which permit a coupling of the boundary layer with its surrounding acoustic medium and its contiguous surface.

The second direction is theoretical: It is recognized that a considerable level of effort has been expended over the years in relating the statistical scales of wall pressure to the boundary-layer turbulence structure. This theoretical effort has been made for two fundamental reasons. First, such analyses support the selection of scaling parameters; second, the analyses provide a basis for extrapolating measurements in one regime of space and time to another regime that may apply to some new problem. Although these theoretical models are incomplete and not without their inconsistencies, they are summarized in Section 7.3.

It was shown in Chapter 6 that the flexural motion of surfaces is describable in terms of the resultant force induced by moving fluid on the surface. This force must be described in terms of a mean-square flow-induced pressure and its correlation area. In order to predict or to scale the flow-induced vibration, it is necessary to describe these unsteady flow forces in terms of the pressure, time, and length scales characteristic of the turbulent boundary layer. Thus in this chapter we examine the general similarity laws that govern the time-averaged behavior of turbulent boundary layers in order to identify these scaling parameters. The distributions of Reynolds stresses and the statistical descriptions of fluctuating velocities and wall pressures of turbulent boundary layers are discussed in a format that illustrates important dimensionless representations of these quantities. The representations are the result of the interrelationships between the pressure and velocity fields suggested by various integral forms of the equations of motion.

Without doubt, the most extensive body of literature on any aspect of the subject is concerned with fully developed boundary layers on flat smooth and rough surfaces at zero angle of incidence. This is because these boundary layers, called "self-preserving" or "equilibrium," are characterized by a mean velocity profile $U(y_1, y_2)$ (the coordinate in the direction of the flow is y_1 and that normal to the surface is y_2) such that at all locations y_1 the dependence of U on y_2 changes only by a velocity scale and a length scale. This is an easily quantifiable class of

boundary layers that includes those subjected to a particular type of streamwise static pressure gradient. Unfortunately, there are in practice many other classes of flows that involve laminar to turbulent boundary-layer transition, adjustment of the flow to abrupt changes in wall roughness, severe adverse pressure gradients leading to flow separation. These boundary layers are not self-preserving and therefore cannot be simply quantified in functions with two variables. Thus these cases, although practical, are not often examined in a laboratory environment. In the course of the discussion some general rules for estimating the behavior of the more practical types of boundary-layer flow are presented.

This chapter is organized according to the general theme that noise-producing characteristics of the boundary layer may be quantified using scale factors that evolve from considerations of boundary-layer structure. Thus we first consider the similarity concepts for mean motion, followed by discussions of the time-averaged statistical properties of the turbulent velocities. Recent hypotheses concerning the nature of the boundary layer structure and turbulence production are examined. Analytical expressions that formally, yet approximately, relate the wall pressure fluctuations to the turbulence structure adjacent to the wall are derived to disclose pertinent scaling variables and important statistical measurement quantities. We then examine the experimentally determined characteristics of the wall pressure fluctuations beneath planar turbulent boundary layers and some characteristics of boundary layers on curved surfaces, including laminar to turbulence transition, adverse and favorable pressure gradients, and pressures in separated flow.

7.2 EQUILIBRIUM TURBULENT BOUNDARY LAYERS

7.2.1 General Relationships and Dimensionless Representations

This subject has been covered in a wide variety of texts devoted to the subject, e.g., those of Schlichting,¹ Hinze,² Townsend,³ Cebeci and Smith,⁶ Cebeci and Bradshaw,⁵ and White.²³⁹ Rotta⁶ and Clauser⁷ have written extensive review articles dealing with various effects of wall roughness and pressure gradients on the mean motion. In this section we examine certain dimensionless representations that appear to describe the general turbulent motion; for full background, consult references 1-8. The present treatment highlights the fundamental structure that establishes both scaling relations and flow modeling, which are used in later sections.

To form a basis on which to examine the turbulent boundary layer, we first examine some important aspects that arise from the manipulation of the equation

of continuity (Equation (2.1)) and the momentum equation (Equation (2.36)) for incompressible flow. These relationships will be applied to a turbulence field with a mean shear velocity $U_i(y_i)$, which is, in general flow geometries, dependent on three-space coordinates. The flow field is composed of both mean and turbulent disturbances; i.e., we replace the u 's in Equation (2.1) and (2.36) by

$$u_i' = U_i(y_i) + u_i$$

where the statistical properties outlined in Section 3.5 apply to the random variable u_i . Another step is to time-average quantities as they would be measured at a point in the flow. This manipulation gives $\overline{u_i'} = U_i(y_i)$ and, for continuity,

$$\frac{\partial U_i(y_i)}{\partial y_i} = 0$$

and momentum,

$$\frac{\partial U_i U_j}{\partial y_j} + \frac{\partial \overline{u_i u_j}}{\partial y_j} = -\frac{1}{\rho_0} \frac{\partial P}{\partial y_i} + \nu \frac{\partial^2 U_i}{\partial y_j^2} \quad (7.1)$$

If the boundary layer is two dimensional, i.e., $\partial/\partial y_3 = 0$, expressing that there are no transverse gradients of the mean motion, more or less as pictured in Figure 7.1, then the mean velocity can be approximated as $U_i = U_1$ and Equation (7.1) becomes, to a first approximation, in the 1 direction,

$$U_2 \frac{\partial U_1}{\partial y_2} + U_1 \frac{\partial U_1}{\partial y_2} + \frac{\partial \overline{u_1 u_1}}{\partial y_j} = -\frac{1}{\rho_0} \frac{\partial P}{\partial y_1} + \nu \frac{\partial^2 U_1}{\partial y_j^2}, \quad j = 1, 2 \quad (7.2)$$

The small mean vertical velocity, $U_2(y_2)$, due to boundary-layer growth, satisfies

$$\frac{\partial U_1(y_2)}{\partial y_1} + \frac{\partial U_2(y_2)}{\partial y_2} = 0 \quad (7.3)$$

The term $\overline{u_1 u_j}$ is

$$\overline{u_1 u_j} = \overline{u_1^2} + \overline{u_1 u_2} \quad (7.4)$$

where $\overline{u_1 u_2}$ is the turbulent Reynolds stress averaged in time. The lateral Reynolds stress $\overline{u_1 u_3}$ does not contribute to the mean field because of our assumption that $\partial/\partial y_3$ of time-averaged quantities is zero. It is of interest to subtract Equation (7.2) from the complete Equation (2.1) to obtain the equation for the instantaneous turbulence fluctuations:

$$\frac{\partial u_i}{\partial t} + u_j \frac{\partial u_i}{\partial y_j} + \frac{\partial (u_i u_j - \overline{u_i u_j})}{\partial y_j} = - \frac{1}{\rho_0} \frac{\partial p}{\partial y_i} + \nu \nabla^2 u_i, \quad j = 1, 2 \quad (7.5)$$

The term $(u_i u_j - \overline{u_i u_j})$ is recognizable as the Reynolds stress fluctuation, which has a zero time average and constitutes a major contribution to the stress tensor for incompressible turbulent regions.

We can explore some dimensionless parameters by rewriting Equation (7.2) in a revised form for one-dimensional mean flow, neglecting the $U_2(y_2) \ll U_1(y_2)$,

$$\frac{1}{\rho_0} \frac{\partial}{\partial y_1} \left(P + \frac{1}{2} \rho_0 U_1^2 + \rho_0 \overline{u_1^2} \right) = \frac{\partial}{\partial y_2} \left(-u_1 u_2 + \nu \frac{\partial u_1}{\partial y_2} \right) \quad (7.6)$$

where $\left(P + \frac{1}{2} (\rho_0 U_1^2) + \rho_0 \overline{u_1^2} \right)$ is the total stagnation pressure of the flow and on the right-hand side

$$\tau = - \rho_0 \overline{u_1 u_2} + \mu \frac{\partial u_1}{\partial y_2}$$

is called the total stress distribution in the boundary layer. Since, by definition, $\overline{u_1 u_2} = 0$ at $y_2 = 0$, the shear stress at the wall is given by

$$\tau_w = \lim_{y_2 \rightarrow 0} \left[\mu \frac{\partial u_1}{\partial y_2} \right]$$

A velocity scale that is based on the wall shear is defined as

$$U_\tau = \left(\frac{\tau_w}{\rho_o} \right)^{1/2}$$

which is called the "friction velocity" and is expected to be important in determining velocity magnitudes in the boundary layer, at least close to the wall. If the gradient of the stagnation pressure is negative (so-called favorable), say $-a$, then integration of Equation (7.6) yields

$$-\rho_o \overline{u_1 u_2} + \mu \frac{\partial \overline{u_1}}{\partial y_2} = (-a y_2 + \tau_w) \quad (7.7)$$

which shows that the total stress decreases linearly from the value at the wall. Equation (7.1) also gives the gradient of static pressure in the direction normal to the surface $\left(U_2 \ll U_1, \overline{u_i^2}^{1/2} \right)$

$$\frac{1}{\rho_o} \frac{\partial P}{\partial y_2} = - \frac{\partial}{\partial y_2} \left(\overline{u_2^2} \right) - \frac{\partial (\overline{u_1 u_2} + U_1 U_2)}{\partial y_1}$$

This relationship shows that if the boundary layer is rapidly changing, for example, nearing separation, $\partial P / \partial y_2$ is not negligible. For boundary layers for which the streamwise (y_1) gradients are small compared to gradients over the thickness of the layer δ , upon integration from well outside the boundary layer ($y_2 \rightarrow \infty$) to y_2 , the local total pressure is

$$P(y_1, y_2) + \rho_o \overline{u_2^2} = P_\infty(y_1) \quad (7.7a)$$

where P_∞ is the free stream static pressure outside the turbulence at y_1 . The constant stagnation pressure outside the boundary layer where the flow is nonturbulent is

$$P_{\text{stag}} = P_\infty(y_1) + \frac{1}{2} \rho_o U_\infty^2 \quad (7.7b)$$

where $q = 1/2 \rho_0 U_\infty^2$ is the free stream dynamic pressure. Thus, as long as the turbulence is nearly isotropic, $\overline{u_1^2} = \overline{u_2^2}$, the stagnation pressure is nearly constant when streamwise gradients are small and the flow is one dimensional.

We formally define the boundary-layer thickness δ as the distance from the wall for which $U_1 = U_\infty$. Another length scale that governs flow near the wall is ν/U_τ . In general, for equilibrium boundary layers³ one of these length scales, say l_0 , determines the mean velocity distribution in a universal functional form, for example,

$$\frac{U_1 - U_\infty}{U_\tau} = g_u \left(\frac{y}{l_0} \right)$$

When the boundary layer obeys such a similarity form, it is said to be self-preserving.³ It is evident from Equation (7.7) that the local mean velocity should scale on U_τ , but in practice it also increases in proportion to U_∞ because U_τ/U_∞ is generally a slowly varying function of Reynolds number. A dimensionless form of Equation (7.7) may therefore be written

$$\frac{\overline{u_1 u_2}}{U_\tau^2} + \frac{\nu}{(U_\tau l_0)} g_u' \left(\frac{y_2}{l_0} \right) = -\Pi_1 \left(\frac{y_2}{l_0} \right) + 1 \quad (7.8)$$

where the parameter

$$\Pi_1 \left(\frac{y_2}{l_0} \right) = \frac{l_0}{\tau_w} \left| \frac{\partial p_{\text{stag}}}{\partial y_1} \right|$$

is assumed to be independent of y_2 and it is a measure of the streamwise gradient of the stagnation pressure. It follows from Equation (7.8) that the Reynolds stress distribution must also have a dimensionless representation on l_0 , i.e., a viscous Reynolds number $U_\tau l_0 / \nu$ and the parameter Π_1 . Accordingly, we can write the general behavior

$$-\frac{\overline{u_1 u_2}}{U_\tau^2} = h\left(\frac{y_2}{\ell_o}, \frac{U_\tau \ell_o}{v}, \pi_1\right) \quad (7.9)$$

which, in a completely self-preserving flow, reduces to

$$-\frac{\overline{u_1 u_2}}{U_\tau^2} = h\left(\frac{y_2}{\ell_o}\right)$$

The existence of approximate simple dimensionless forms in such cases implies the existence of analogous dimensionless descriptions of the fluctuating characteristics. If we make Equation (7.5) dimensionless on the above variables, we have

$$\frac{\partial u_i'}{\partial t'} + u_j' \frac{\partial u_i'}{\partial y_j'} + \frac{\partial (u_i' u_j' - \overline{u_i' u_j'})}{\partial y_j'} = \frac{\partial p'}{\partial y_i'} + \frac{v}{U_\tau \ell_o} \nabla_{y'}^2 u_i' \quad (7.10)$$

where the dimensionless variables are

$$t' = \frac{t U_\tau}{\ell_o}, \quad \nabla_{y'}^2 = \frac{\ell_o^2}{\partial y_1'^2}$$

$$p' = \frac{p}{\tau_w}, \quad u_i' = \frac{u_i}{U_\tau}$$

This equation implies the existence of dimensionless universal functions, for example, for the pressure, of the type

$$\frac{p}{\tau_w} = P\left(\frac{t U_\tau}{\ell_o}, \frac{y_1}{\ell_o}, \frac{U_\tau \ell_o}{v}, \pi_1\right) \quad (7.11)$$

and similarly for the velocity fluctuations and their products. There may also be a domain of dependence in which disturbances will be determined by the mean velocity:

outside the boundary layer U_∞ . In that case the functional dependence for the fluctuating pressure in the boundary layer should generally include an additional parameter

$$\frac{p}{\tau_w} = P \left(\frac{U_\tau}{l_o}, \frac{y_i}{l_o}, \frac{U_\tau l_o}{\nu}, C_f, \Pi \right) \quad (7.12)$$

where C_f is the mean wall shear coefficient,

$$C_f = 2 \left(\frac{U_\tau}{U_\infty} \right)^2$$

or

$$C_f = \frac{\tau_w}{\frac{1}{2} \rho_o U_\infty^2}$$

The dimensionless equation for the disturbances (Equation (7.10)) can be used to illustrate the use of inner and outer variables in boundary-layer descriptions. It was stated that l_o could be a viscous length scale, $l_o = \nu/U_\tau$, for flow near the wall. If this is the case, then $U_\tau l_o/\nu = 1$ and all terms of the equations that involve viscosity are important. Within $y_2 \leq \nu/U_\tau$ the disturbances are expected to behave as functions of the dimensionless coefficients in Equation (7.11) with the appropriate substitution for l_o . On the other hand, if it is observed that the mean velocity depends on $l_o = \delta$ as a length scale, then the nondimensionalization leads to a Reynolds number $U_\tau \delta/\nu$, which attains large values in turbulent flows. In this case, in Equation (7.10) the viscous terms on the right can be neglected, and there is no apparent clue as to whether U_τ or U_∞ is an appropriate velocity scale. Therefore, for y_i/δ on the order of unity, Equation (7.12) could just as well have been written

$$\frac{p}{\frac{1}{2} \rho_o U_\infty^2} = P \left(\frac{U_\infty}{\delta}, \frac{y_i}{\delta}, C_f, \Pi_1 \right) \quad (7.13)$$

7.2.2 Dimensionless Representations of the Mean Velocity Profile

Returning to Equation (7.6), we see that near enough to the wall where $\overline{u_1 u_2} \ll \nu \partial U_1 / \partial y_2$, we can approximate

$$\frac{\partial U_1}{\partial y_2} = \frac{1}{\nu} \left(\frac{\tau_w}{\rho_o} \right) = \frac{U_\tau^2}{\nu}$$

if the stagnation pressure gradient over y_1 is small enough. In this regard a small gradient means that the stagnation pressure varies negligibly over lengths on the order of ν/U_τ , i.e.,

$$\frac{\partial \left(\frac{p}{\tau_w} \right)}{\partial \left(\frac{y_1 U_\tau}{\nu} \right)} = 0$$

Then

$$\frac{U_1}{U_\tau} = \frac{y_2 U_\tau}{\nu} \quad (7.14)$$

Near the wall, as long as the Reynolds stress is small, i.e., $\overline{u_1 u_2} \ll U_\tau^2$, the mean velocity profile is clearly a simple function of U_τ and ν/U_τ . We call variables U_τ and ν/U_τ "inner" or "viscous" velocity and length scales.

Somewhat farther from the wall the magnitude of $\overline{u_1 u_2}$ becomes on the order of U_τ^2 , in which case $\partial U_1 / \partial y_2$ is also influenced by a distribution of $\overline{u_1 u_2}$. Dimensional reasoning suggests that the mean velocity profile in this part of the boundary layer will depend on y_2 as

$$\frac{U_1}{U_\tau} = f_s \left(\frac{y_2 U_\tau}{\nu} \right) \quad (7.15)$$

for $y_2 U_\tau / \nu$ small enough because of the behavior shown by Equation (7.14) in the region dominated by viscosity. We have also seen that, far from the wall, the behavior

$$\frac{U_1 - U_\infty}{U_\tau} = g\left(\frac{y_2}{\delta}, \Pi_1\right) \quad (7.16)$$

where Π_1 is a parameter that reflects the magnitude of the static pressure gradient, can be expected. In the case of rough walls Equation (7.16) is still expected to hold, but to describe the velocity near the wall Equation (7.15) is replaced by a function

$$\frac{U_1}{U_\tau} = f_r\left(\frac{y_2}{k}\right)$$

where k is a parameter related to the sizes of roughness elements. The length k is an inner variable. It is also expected that combinations of Equations (7.15) and (7.16) should apply in some overlap region.

Figure 7.2 shows the mean velocity profiles measured by a variety of investigators for smooth and rough walls. In the case of smooth walls the variable $y_2^+ = y_2 U_\tau / \nu$ fully describes $U^+ = U/U_\tau$ as long as $y_2^+ < 1000$. At a lower limit of $y_2^+ \approx 10$, Equation (7.14) describes U^+ ; this region of the boundary layer is called the viscous sublayer. In the region $20 < y_2^+ < 1000$ a logarithmic dependence

$$U^+ = A \log y_2^+ + B, \quad 20 < y^+ < 1000 \quad (7.17)$$

takes over. The behavior of velocity profiles over rough walls also follows the behavior of Equation (7.17), but with a different⁹ value of B . We shall return to this point later.

The mean velocity profiles are also represented in Figure 7.3, but this time in the form of Equation (7.16). Using this representation it is clear that the velocity satisfies a velocity defect form

$$\frac{U_\infty - U_1(y_2)}{U_\tau} = A \log \frac{y_2}{\delta} + C, \quad \sim 0.005 < \frac{y_2}{\delta} < \sim 0.2 \quad (7.18)$$

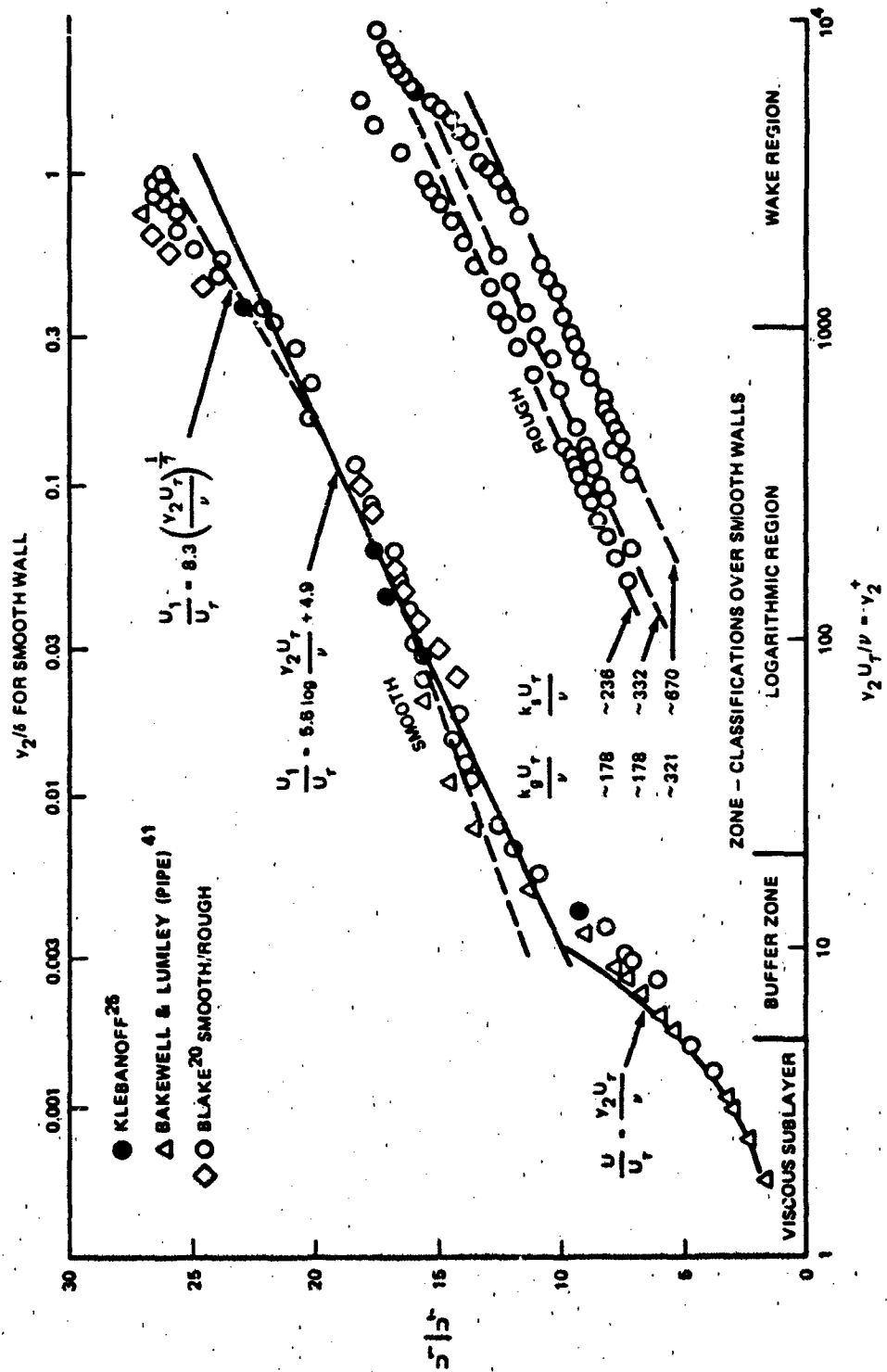


Figure 7.2 - Mean Velocity Normalized on "Inner" (Wall) Variables and the Law of the Wall

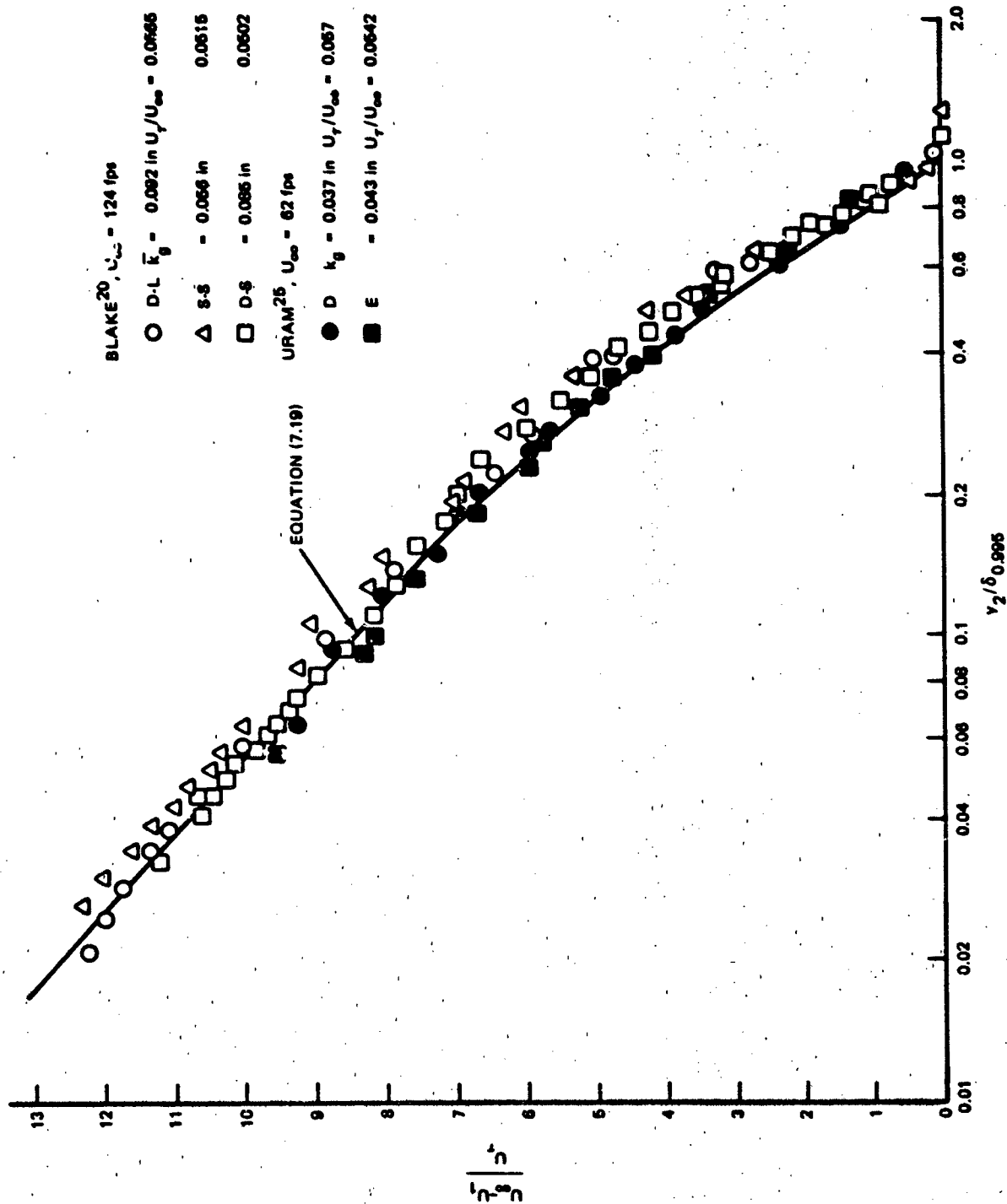


Figure 7.3 - Mean Velocity Profiles Over Rough Walls and the Law of the Wake

and some other functional dependence on y_2/δ is implied by the data for $0.2 < y_2/\delta < 1$. There is no difference between the behaviors of either smooth or rough walls when the mean velocity is expressed as a velocity defect dependent only on y_2/δ . The parameter A is well known, and it is bounded by the limits

$$5.6 \leq A \leq 5.75$$

Simply on the basis of the behavior of the mean velocity profile on the alternatively scaled y_2 , y_2^+ and y_2/δ , four important regions of the boundary layer on smooth walls emerge:

1. viscous sublayer, $0 < y_2^+ < 5$
2. buffer zone, $5 < y_2^+ < 20$
3. logarithmic region, $20 < y_2^+ < 1000$ (approximately $0.004 < y_2/\delta < 0.2$)
4. outer region, $0.2 < y_2/\delta < 1$ approximately.

The buffer zone is so defined because it is a region in which neither Equation (7.14) nor (7.17) applies. The upper limit to the outer region is not well defined, because the turbulent zone has an indefinite boundary whence the approximate limit of $y/\delta = 1$. The outer region has also been called the "wake" region by Coles.¹⁰ He has shown that in this region

$$\frac{U_\infty - U_1}{U_\tau} = A \log \frac{y_2}{\delta} + 1.38 \left[2 - W \left(\frac{y_2}{\delta} \right) \right] \quad (7.19)$$

for flows in which the pressure gradient is negligible. $W(y_2/\delta)$ is Coles' wake function, which he approximates as

$$W \left(\frac{y_2}{\delta} \right) = 1 + \sin \left[\frac{2 \left(\frac{y_2}{\delta} - 1 \right) \pi}{2} \right]$$

Equation (7.19) is shown in Figure 7.3. The wake function is important for all dimensionless distances from the wall $y_2/\delta > 0.2$, and it is, in general, dependent on the magnitude of the pressure gradient.

The logarithmic region of the boundary layer controlled by $y_2^+ = y_2 U_\tau / \nu$ is independent of the pressure gradient except in that the pressure gradient determines

the location of the interface between the logarithmic and wake regions. The effects of pressure gradient are discussed in Section 7.5.2.

There are a number of heuristic^{1,2,8} and dimensional^{7,10} arguments for the existence of a logarithmic region for the mean velocity profile. These arguments are so well described elsewhere that it is not worthwhile to review them here. The important underlying aspect of all these arguments is that it is postulated that there is a region near the wall in which the sizes of the eddies in the flow that contain most of the turbulent kinetic energy are proportional to the distance from the wall. This assumption will be used in describing turbulence quantities in Sections 7.2.5 and 7.3. Mean and turbulent fluid velocities are assumed to be scaled on U_τ (Equation (7.14)) as the only velocity scale. Thus the mean velocity gradient reads

$$\frac{\partial U_1}{\partial y_2} = \frac{1}{\kappa} \frac{U_\tau}{y_2} \quad (7.20)$$

Integration over y_2 yields

$$\frac{U_1}{U_\tau} = \frac{1}{\kappa} \ln \frac{y_2 U_\tau}{\nu} + B \quad (7.21)$$

where B and κ are dimensionless coefficients. The constant κ has been called the von Karman constant and it has been established² at 0.4. The constant A used above is just $1/\kappa \log e$. The constant B is less well established, but it is generally accepted² as between 4.9 and 5.5.

In the case of a rough wall, a parameter dependent on roughness size must be subtracted from Equation (7.21) so that it becomes (using Coles' value of B)

$$\frac{U_1}{U_\tau} = \frac{1}{\kappa} \ln \frac{y_2 U_\tau}{\nu} - B \left(\frac{k_s U_\tau}{\nu} \right) + 5.1 \quad (7.22)$$

where k_s is a length scale dependent on the size, shape, and distribution of the roughness. As seen in Figure 7.2, the constant intercept $B(k_s U_\tau / \nu)$ decreases as the roughness size increases. Taking the difference between Equation (7.22) and

Equation (7.21), we find a shift in the logarithmic profiles, called a "velocity defect",

$$\left(\frac{U_1}{U_\tau}\right)_s - \left(\frac{U_1}{U_\tau}\right)_\tau = \frac{\Delta U_1}{U_\tau} = B \frac{k_s U_\tau}{\nu}$$

which determines B. The above reasoning requires that¹⁰

$$\frac{U_1}{U_\tau} = f\left(\frac{k_s}{y_2}\right) = \frac{1}{\kappa} \ln \frac{k_s}{y_2} + C \quad (7.23)$$

so

$$\frac{\Delta U_1}{U_\tau} = B \left(\frac{k_s U_\tau}{\nu} \right) = \frac{1}{\kappa} \ln \frac{k_s U_\tau}{\nu} + b \quad (7.24)$$

The coefficient established by Nikuradse¹¹ for sand-roughened surfaces is

$$C = 8.5 \quad (7.25)$$

and from comparison of Equations (7.21) through (7.23),

$$b = -3.4 \quad (7.26)$$

k_s is the sand roughness height of Nikuradse's surfaces.

The height k_s should generally be considered as a height parameter that must be derived for each set of experimental data. By accepting Nikuradse's¹¹ result as a standard of comparison, Schlichting¹ derived values of k_s by forcing various data from other rough walls into the form of Equations (7.24) and (7.25). Another approach is not to make such an attempt, but to determine the behavior of $\Delta U/U_\tau$ for each value of $k_g U_\tau/\nu$, where k_g is a geometric roughness size. Figure 7.4 is a summary of roughness effects on the logarithmic profile. The actual roughness size k_g is the geometric size of the roughness. The common characteristic of all

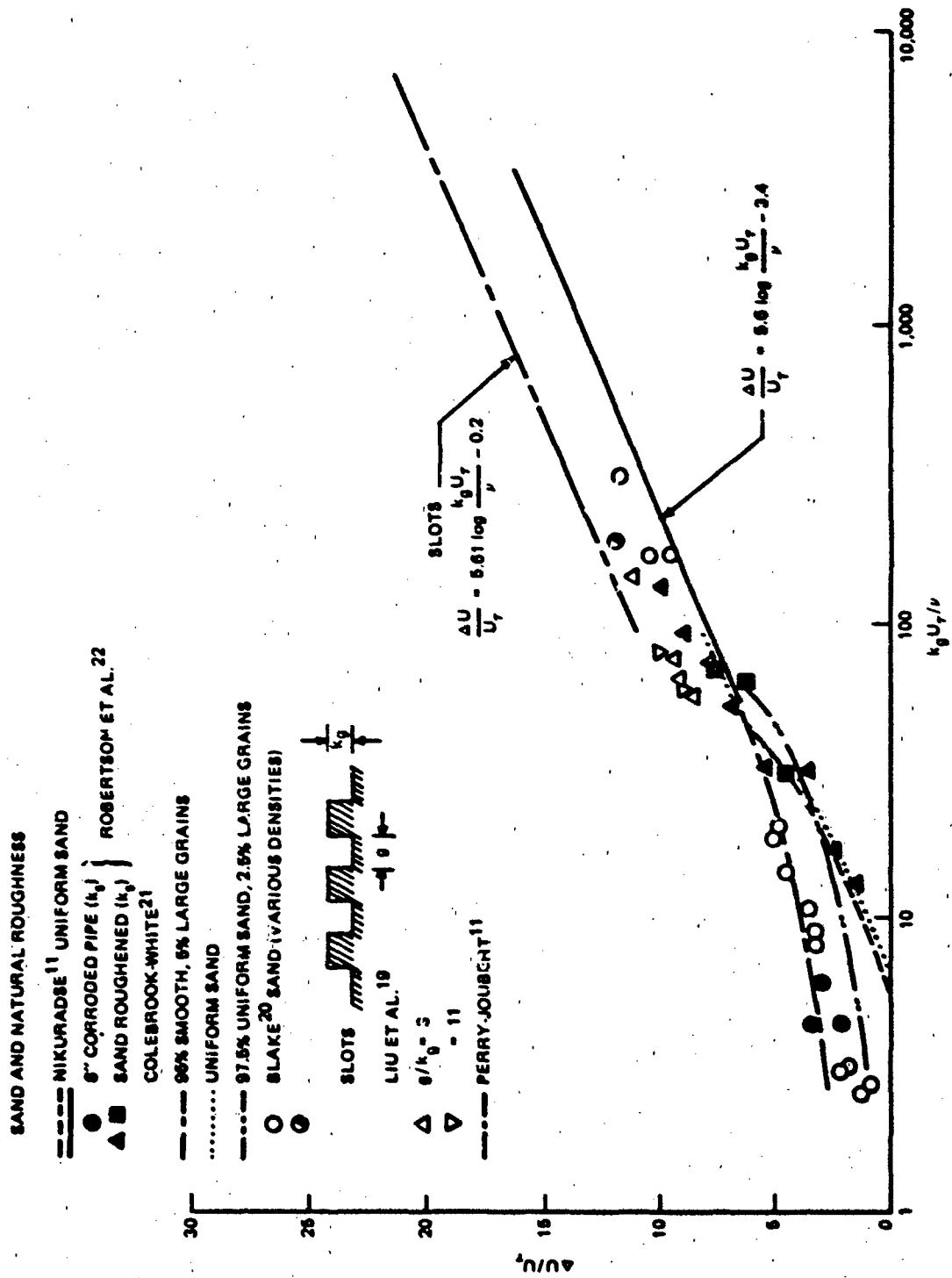


Figure 7.4 - Roughness Defect or Intercept Change for the Logarithmic Region of Rough-Wall Boundary Layers

the rough surfaces shown is that above a critical value of $k_g U_\tau / \nu = k_g^+$ a behavior of the type in Equation (7.24) occurs, but with an intercept b dependent on the geometry of the roughness elements. This common logarithmic behavior therefore makes the definition of an equivalent sand roughness height for rough wall a convenient empirical single parameter with which to quantify the effect of wall roughness on the mean velocity profile. Note also from Figure 7.4 that even for relatively small values of k_g^+ there is a finite value of $\Delta U_1 / U_\tau$. Thus apparently even when a surface is supposed to be "hydraulically smooth," i.e., $k^+ < 4$, there is a roughness effect on the mean velocity profile. This effect occurs with very nonuniformly distributed roughness elements such as corrosion roughness.

Another parameter important for rough walls is the effective datum for y_2 in order that Equation (7.23) is satisfied for large roughnesses. The datum $y_2 = 0$ for the logarithmic profile generally occurs somewhat above the datum of the troughs between the roughness elements, as illustrated in Figure 7.5. Perry and Joubert¹² found $\epsilon/k_g = 0.2$ for two-dimensional slats with a gap-to- k_g height ratio of 3; Perry et al.¹³ found $\epsilon/k_g = 1$ for a gap-to-height ratio of 0.8; Blake¹⁴ found $\epsilon/k_g = 0.5$ for sand-roughened walls. The datum shift is also dependent on the pressure gradient.

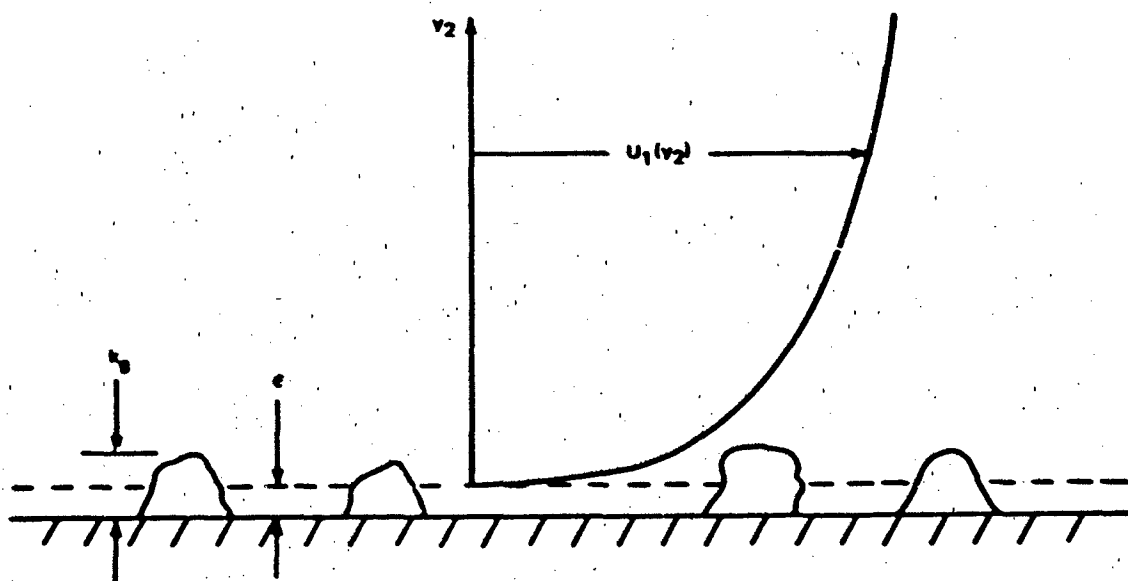


Figure 7.5 - Datum Shift for Boundary Layers Over Rough Walls

In spite of the large number of investigations on rough walls, there is still no adequate scheme for predicting the roughness parameter k_s . We shall see that the geometric roughness size is an important parameter in determining wall pressure fluctuations over rough walls. Root-mean-square height and statistics of separations may be important for sand-grain and other "natural"-type roughness.

7.2.3 Prediction of the Wall-Shear Coefficient and Boundary-Layer Length Scales

The existence of empirical length and velocity scales that collapse mean velocity profiles makes it advantageous to develop schemes for predicting them. Precise computational schemes are outlined by Cebeci and Smith⁴ and by Bradshaw.¹⁵ This is a technical area that has become active since the availability of the high-speed digital computer. A review of available prediction schemes for drag and boundary-layer growth has been prepared by McCarthy.¹⁶

Since the emphasis here is on approximate estimations of noise, it is often sufficient to resort to formulae that approximate flow behavior. These formulae, and all computational schemes for that matter, are based on an integral form of Equations (7.2) and (7.3) as derived by Schlichting¹ following von Karman.¹⁷ Beginning with Equation (7.2) in a form similar to that of Equation (7.6), where the term u_1^2 is neglected in favor of U_1^2 , we have

$$U_1 \frac{\partial U_1}{\partial y_1} + U_2 \frac{\partial U_1}{\partial y_2} + \frac{1}{\rho_o} \frac{\partial P}{\partial y_1} = \frac{\partial \tau}{\partial y_2}$$

Integration over the boundary layer from $0 \leq y_2 \leq \delta$, with the substitution of $P(y_1, y_2) = P_\infty(y_1)$, and the use of Equation (7.7b) gives

$$\frac{\partial}{\partial y_1} \left(\frac{P_\infty(y_1)}{\rho_o} \right) = -U_\infty \frac{\partial U_\infty}{\partial y_1}$$

for the external pressure gradient imposed by the outer potential flow, which will generally vary along the body. The use of Equation (7.3) yields

$$\frac{\tau_w}{\rho_o} = \frac{d}{dy_1} \left(U_\infty^2 \theta \right) + \delta^* U_\infty \frac{dU_\infty}{dy_1} \quad (7.27a)$$

or

$$\frac{\tau_w}{\rho_0 U_\infty^2} = \frac{C_f}{2} = \frac{d\theta}{dy_1} + \frac{\theta}{2} \frac{2+H}{U_\infty^2} \frac{dU_\infty^2}{dy_1} \quad (7.27b)$$

which has been called the von Karman momentum integral equation. In these equations

$$\delta^* = \int_0^\delta \left(1 - \frac{U_1}{U_\infty}\right) dy_2 \quad (7.28)$$

is the displacement thickness,

$$\theta = \int_0^\delta \frac{U_1}{U_\infty} \left(1 - \frac{U_1}{U_\infty}\right) dy_2 \quad (7.29)$$

is the momentum thickness, and

$$H = \frac{\delta^*}{\theta} \quad (7.30)$$

is the shape factor. When we expressed the static pressure gradient in terms of the potential flow outside the boundary layer U_∞ , it was assumed that the static pressure is independent of y_2 . It now remains to show how the various terms in Equations (7.27) can be crudely estimated. From the form of Equations (7.27) it is apparent that the wall-shear coefficient is expected to be a function of the momentum thickness and the origin of the boundary layer. Thus we shall see that both Reynolds numbers

$$R_1 = \frac{y_1 U_\infty}{\nu}$$

and

$$R_\theta = \frac{\theta U_\infty}{\nu}$$

are commonly used in describing boundary layers.

Clauser⁷ has shown interrelationships among some of these functions which result from the existence of the universal velocity defect law (Figure 7.3)

$$\frac{U_{\infty} - U(y_2)}{U_{\tau}} = g\left(\frac{y_2}{\delta}\right) \quad (7.31)$$

He has also shown that even though a universal law for $U(y_2)$ exists, there is no precisely universal law for other properties such as shear or energy, but the lack of universality of these properties cannot generally be measured except under ideal circumstances. Therefore the universal behavior given by Equation (7.31) is hereafter accepted as a signal that a form of approximate universality exists for other turbulence quantities. The existence of the universal form (Equation (7.31)) shows that H is a universal function of C_f

$$H = \left[1 - G\left(\frac{C_f}{2}\right)^{\frac{1}{2}} \right]^{-1} \quad (7.32)$$

where

$$G = \int_0^{\infty} \left(\frac{U_{\infty} - U(y_2)}{U_{\tau}} \right)^2 d\left(\frac{y_2}{\Delta}\right) = 6.8 \quad (7.33)$$

and $\delta^*/\Delta = (C_f/2)^{\frac{1}{2}}$; the factor Δ is defined by

$$\begin{aligned} \frac{\Delta}{\delta} &= \int_0^{\infty} \frac{U_{\infty} - U}{U_{\tau}} d\left(\frac{y_2}{\delta}\right) = \int_0^{\infty} g\left(\frac{y_2}{\delta}\right) d\left(\frac{y_2}{\delta}\right) \\ &= 3.6. \end{aligned}$$

The numerical values apply to flows of small pressure gradient. Figure 7.6, provided by Hama,¹⁸ shows the application of Equation (7.32) for smooth and rough walls. It may be used to determine K from a known or estimated value of C_f .

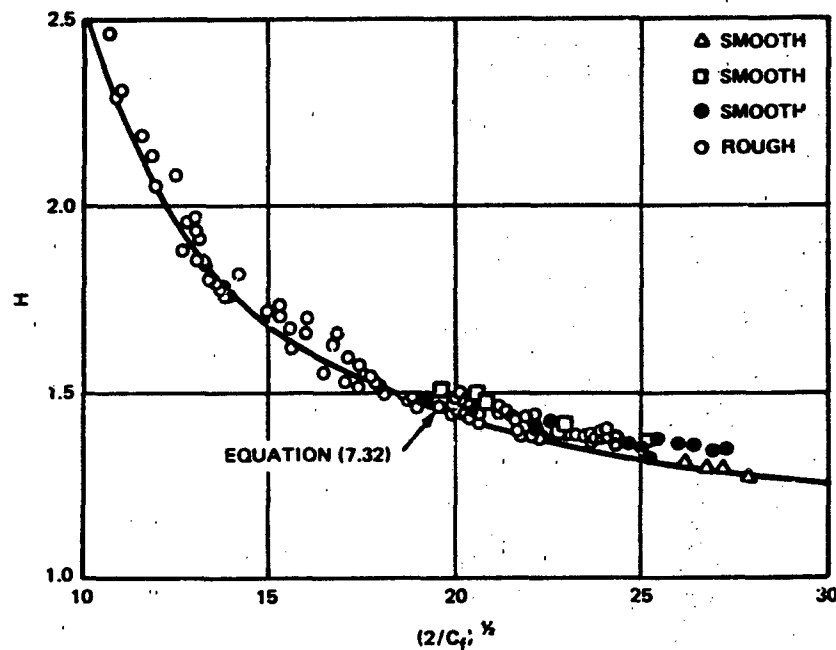


Figure 7.6 - Shape Factor H as a Function of Wall Shear Stress¹⁸

The evaluation of wall-shear coefficients is open to considerable debate, and a large number of relationships have been used. The problem is to relate C_f to the distance downstream of the transition of the turbulent boundary layer, call it y_1 . Various formulae have been derived to apply to different ranges of Reynolds numbers,

$$R_1 = \frac{U_\infty y_1}{\nu}$$

By matching analytic functions to experimental results expressed in the form of Equation (7.31), one can determine a relationship for C_f and θ using Equations (7.28) through (7.33). The simplest formulae to use for smooth walls, however, are based on the assumption¹ that

$$\frac{U_1}{U_\infty} = \left(\frac{y_2}{\delta} \right)^{1/n}$$

This leads to the set of formulae

$$\frac{\delta^*}{\delta} = 1/(n+1) \quad (7.34a)$$

and

$$\frac{\delta^*}{\theta} = H = \frac{n+2}{n} \quad (7.34b)$$

Specifically, when $n = 7$ (see Figure 7.2)

$$\delta^* = \frac{\delta}{8}$$

and

$$\theta = \frac{7\delta}{72}$$

In the same range of Reynolds number¹ for which $n = 7$, it has also been found that

$$C_f \approx 0.0592 (R_1)^{-1/5}, \quad R_1 < 10^8 \quad (7.35)$$

Therefore, with Equation (7.27b) (for $du_\infty/dy_1=0$), we have the useful approximation that

$$\delta = 0.37 y_1 (R_1)^{-1/5} \quad (7.36)$$

Another relationship derived by Schultz-Grunow (see references 11 and 18) based on measured values of $f(y_2/\delta)$ is

$$C_f = 0.370 (\log R_1)^{-2.6}, \quad R_1 < 10^9 \quad (7.37)$$

These equations, with Figure 7.6, allow a determination of approximate values of all parameters δ , δ^* , θ , and C_f . Determine C_f , then find H , find n in Equation (7.34), from n find δ/y_1 and δ^*/y_1 from Equations (7.36) and (7.34).

For rough walls Schlichting¹ presents some useful graphical relationships for the local wall-shear stress in the form of

$$C_f = C_f \left(\frac{U_\infty y_1}{\nu}, \frac{y_1}{k_s} \right)$$

For so-called completely rough walls, indicated by the existence of a velocity profile given by Equation (7.24), the wall-shear coefficient is greater than the value over smooth walls at the same value of R_1 . The rough-wall value, which exceeds the smooth-wall value, can be estimated by a formula giving C_f independent of R_1 .¹

$$C_f = \left(2.87 + 1.58 \log \frac{y_1}{k_s} \right)^{-2.5}, \quad 2 \times 10^2 < \frac{y_1}{k_s} < 10^6 \quad (7.38)$$

This shear coefficient applies at all values of R_1 for which it exceeds smooth-wall coefficients given by Equation (7.35), i.e., it applies for $R_1 > 100 y_1/k_s$. For turbulent flow in this fully rough regime and without pressure gradient, Equation (7.27b) yields

$$\theta = y_1 C_f / 2 \quad (7.39)$$

for use in determining θ from evaluations of Equation (7.38). Table 7.1 gives values of k_s/k_g for a large number of rough surfaces. This table, compiled from data in Figure 7.4, should allow a rough computation for most circumstances. To use Figure 7.4, the geometric roughness size is the variable on the abscissa. To determine k_s/k_g , simply note the horizontal shift necessary to line up points with Nikuradse's equation; H is determined from Figure 7.6.

The length factor δ , although of theoretical importance as an outer length parameter, is of less practical value than δ^* because the outer extremity of a turbulent boundary is ill defined by its nature. Thus alternative ways have been proposed to define δ as a point for which

$$U_1(\delta_{0.99}) = 0.99 U_\infty$$

TABLE 7.1
SELECTED VALUES* OF k_s/k_g

Type 3-DML	Reference	k_s/k_g	k_g^+
Triangular protrusions	24	3.48	2000-4000
Merchant Ship hull-corrosion	23 ⁺	0.3	~70
Sand	20	~1.5	170-330
Sand-lined pipe	22	1.0 ~1.3	10-130
Corroded pipe	22	0.25-1	2.5-20
Sand-lined pipe	21	0.1	29-540
5% $g/k_g = 0.35$ cm			
95% smooth			
Sand uniform size	19	1.37	2.6-65
2-DML			
Triangular grooves with $2k_g$ pitch	24	1.5	99-1200
Slots - $g/k_g = 3$	19	2.2	60-147
Slots - $g/k_g = 11$	19	3	60-80

*See also reference 1.

+This value extracted by the author from data presented.

or

$$U_1(\delta_{0.995}) = 0.995 U_\infty$$

The boundary-layer displacement thickness (Equation (7.28)), has also found widespread acceptance as a length scale. Because it is an integrated parameter, it is much less susceptible to subjective decisions on whether to take 0.99 or 0.995 as a definition of the boundary-layer limit. Measured turbulence quantities will be seen nondimensionalized on δ or δ^* almost interchangeably.

7.2.4 Turbulence Intensities and Statistical Correlations

The turbulence intensities and the statistical properties are considered important here because they will be used as a basis for arguments of similarity of pressure fluctuations. Specifically, a picture of turbulence structure is developed that is used in Section 7.3. The characteristics that are most important in this regard are:

1. Turbulence intensities and Reynolds stresses as well as their dimensionless forms for smooth and rough walls,
2. length and time scales of turbulence quantities in a frame or reference moving at the average translation speed of the fluid,
3. length scales of turbulence quantities in the frame of reference fixed with the surface,
4. nondimensionalizing variables for use in expressing time and space macro- and microscales.

The turbulence intensities on smooth and rough walls have been measured extensively by a large number of investigators. However, there are no fully consistent sets of statistical measurements made in the same facility in which all important properties have been measured on smooth and rough walls; thus it is necessary to piece together the results of a number of independent investigations. A few principal investigations have been selected because they cover a wide range of statistics on a limited range of roughness configurations, or they cover a few representative measurements made on a large number of wall types. In many cases, originally presented results are renormalized to present them in a common framework with other results. As well as could be determined, all measurement programs

considered here had mean velocity profiles that satisfied the similarity form of Equation (7.31) shown in Figure 7.3.

Turbulence intensities for the longitudinal and vertical components over smooth walls are presented as a function

$$\frac{(\overline{u_i^2})^{1/2}}{U_\tau} = f_i\left(\frac{y_2}{\delta}, \frac{U_\infty \theta}{\nu}\right) \quad (7.40)$$

in Figure 7.7. Vertical intensities have been obtained by both Klebanoff²⁵ and Blake.²⁰ Except in the outer region, the intensities are in reasonably good agreement. Close to the wall Klebanoff²⁵ shows the streamwise component to increase; the limit $\overline{u_1^2}^{1/2}/U_\tau = 3$ appears to apply. Results by Bull²⁶ (Mach number 0.5) and Wooldridge and Willmarth^{27,28} (Mach number 0.2) have been included because they were simultaneously obtained with wall-pressure fluctuation measurements. Bull's results were obtained at a number of streamwise locations (approximately $5 \times 10^6 < R_1 < 30 \times 10^6$), and they satisfied the above similarity form with the variables U_τ and δ . Thus it appears that the functional dependence shown in Figure 7.7 is only an approximate similarity representation of the streamwise fluctuations on smooth walls. Measurements of the vertical (u_2) fluctuation reach a maximum of $\overline{u_2^2}^{1/2} = U_\tau$ which is nearly invariant through $0.015 < y_2/\delta < 0.3$.

Dimensionless intensities of all three turbulence components for rough walls are compared to Klebanoff's results over a smooth wall in Figure 7.8a. Here, the results of Yeh and Nickerson²⁹ (over sand roughness, $k_g = 0.25$ in) and of Corrsin and Kistler³⁰ (over a wavy wall with $5/64$ in wave height and $1/3$ in wavelength) show that, except for the u_1 -component, the wall-shear nondimensionalization appears to correlate the results from various sources. The normalized streamwise intensities of Yeh and Nickerson are larger than the others, but a look at the relative values of U_τ/U_∞ will confirm that u_1 apparently increases more in proportion with U_τ than with U_∞ .

The measured intensities show considerable anisotropy for regions of the boundary layer inside $y_2/\delta = 0.7$. Figure 7.8b shows additional results for u_1 and u_2 fluctuations compiled from results of Blake^{14,20} and Uram.²³ The results used here are for Uram's plates B and D which have cylinder heights of 0.11 in (B) and 0.037 in (D); the element distribution resembled a face-centered pattern with

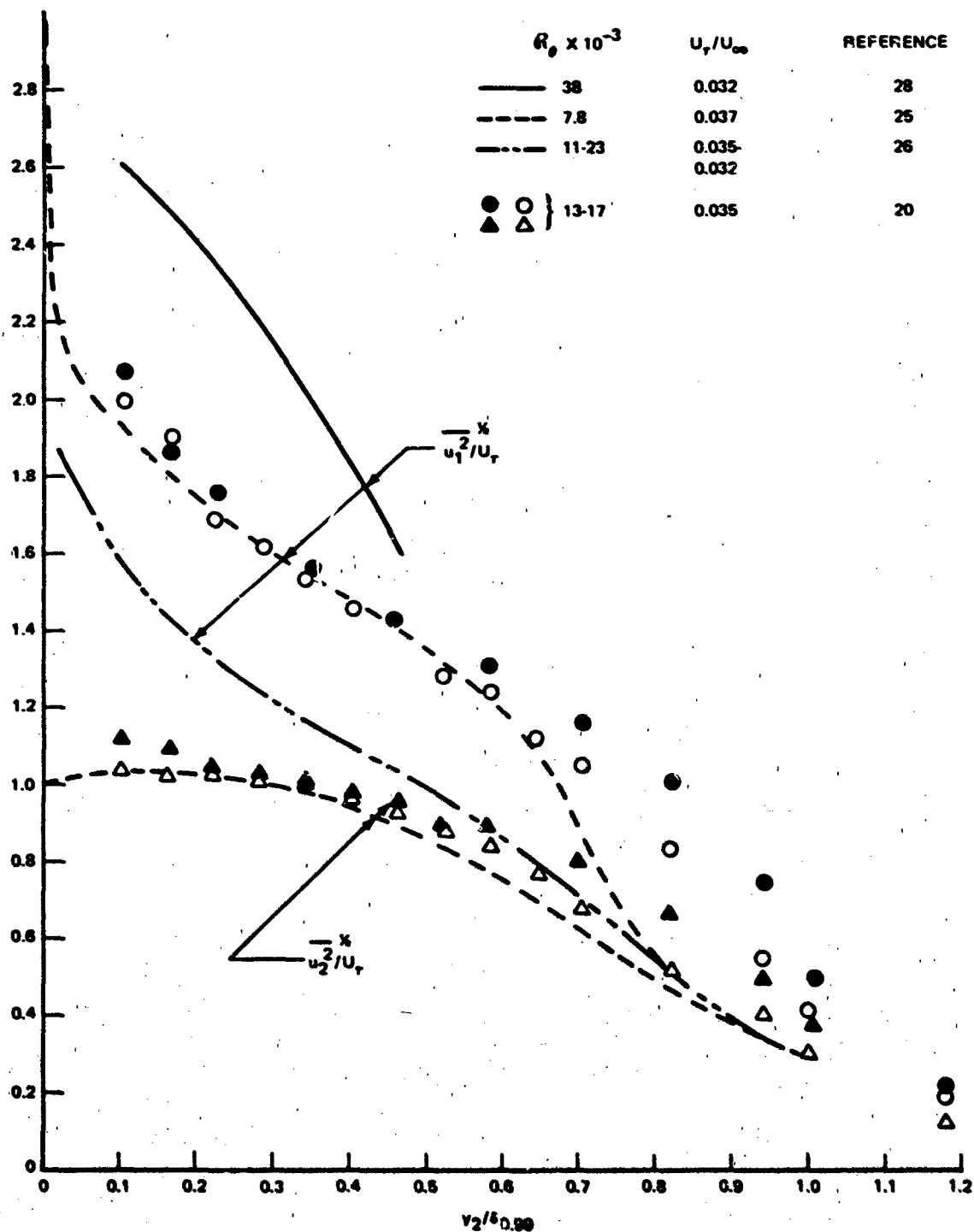


Figure 7.7 - Turbulence Intensities in Boundary Layers for Which Wall Pressure Fluctuations Have Also Been Measured

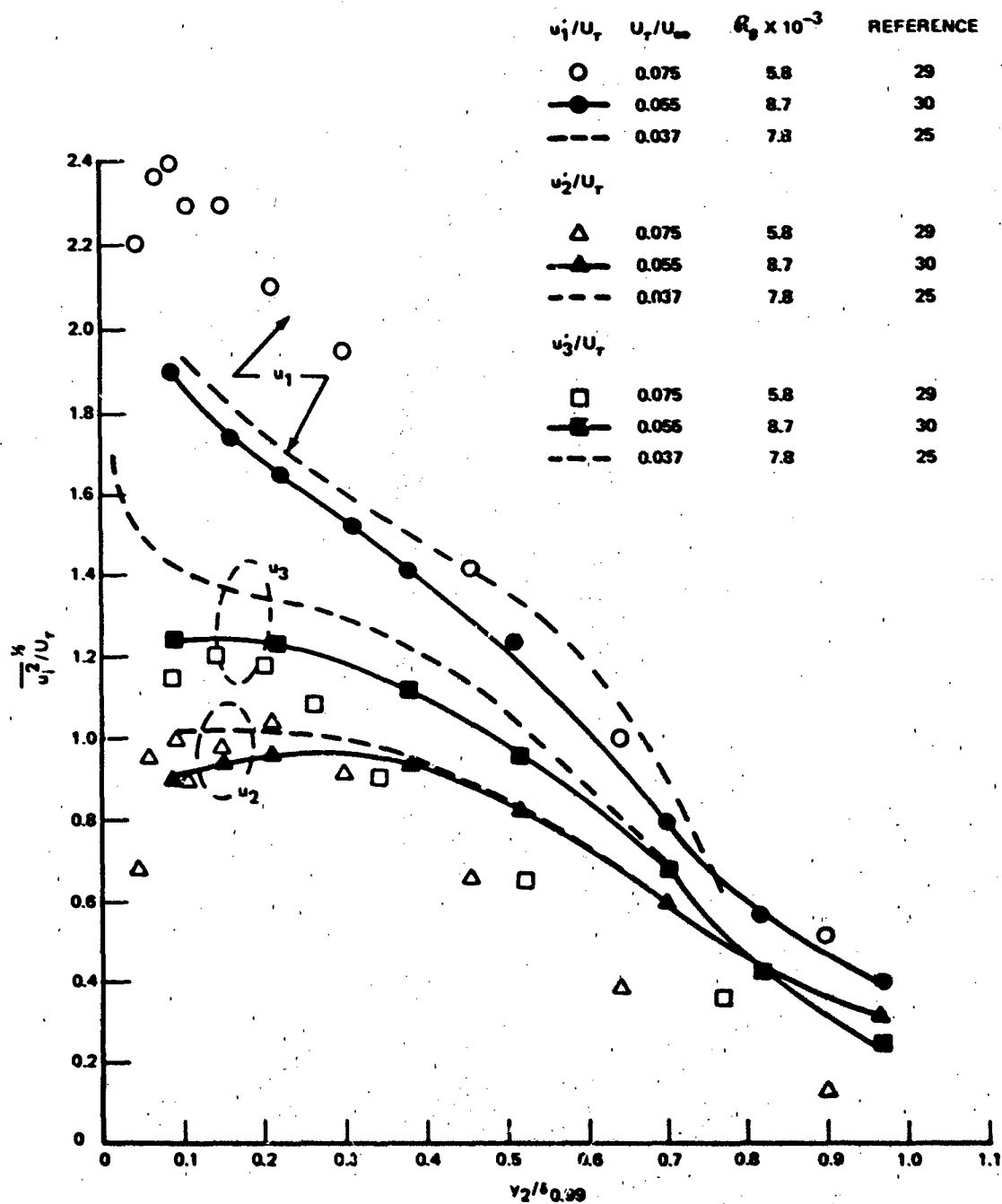


Figure 7.8a - Three Turbulence Components Over Smooth and Rough Walls Normalized on U_r

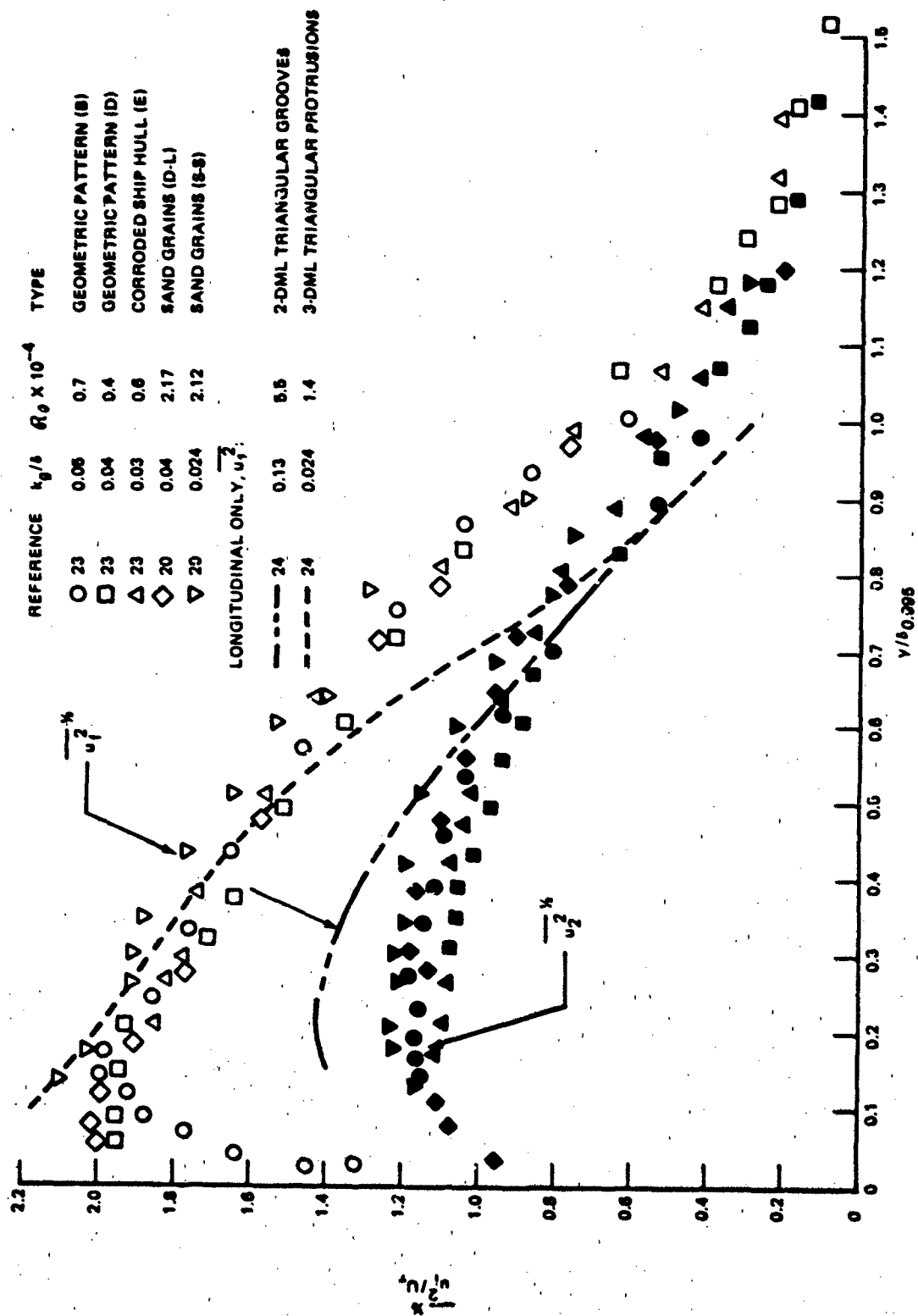


Figure 7.8b - Turbulence Intensities Over Various Rough Walls with Geometric and Natural Roughness Patterns

streamwise distances between rows of 0.219 in (B) and 0.163 in (D) and distances between elements in a row of 0.438 in (B) and 0.188 in (D). Peg diameters were 0.125 in (B) and 0.15 in (D). The third set of results is for the plate with natural roughness (E) for which an average roughness height k_g was 0.043 in. Here again, U_τ appears to be the governing parameter in determining turbulence intensities over rough walls. All results suggest that the intensities decrease as the wall is approached for $y_2/\delta < 0.1$. The results of Arndt and Ippen²⁴ support the general behavior of u_1^2/U_τ^2 , except when k_g/δ approaches 0.1.

The turbulent Reynolds stresses increase in approximate proportion U_τ^2 , as shown by the collection of data from Klebanoff²⁵ and Blake¹⁴ in Figure 7.9. However, over rough walls, as also shown by Antonia and Luxton,³¹ $-u_1 u_2/U_\tau^2$ as well as u_1^2/U_τ^2 diminishes as the wall is approached for $y_2/\delta < 0.1$. For the results of Blake,¹⁴ $k_g/\delta = 0.04$, this effect occurs within distances from the wall on the order of $3 k_g$. The lines were determined by integrating Equations (7.2) and (7.3) using experimental data and the assumption that $\partial P/\partial y_1 = 0$.

The collection of experimental results indicates that dimensionless representations for turbulence quantities in the form implied by Equation (7.13) and leading to Equation (7.40) are acceptable. The dependence on $U_\tau \theta/\nu$ in the latter equation implies an unspecified dependence on C_f which the results do not disclose, but which is suggested as weak. Another important effect that has been overlooked here is the influence of upstream history,¹⁵ which is especially important for developing boundary layers.

It will be shown in the next and later sections that the turbulent boundary-layer pressure and induced noise and vibration are integrally related to the space-time covariances of the turbulent velocities and their products. Historically there has been interest in these covariances because they indicate how the turbulence is related from point to point and time to time. Knowledge of these relationships on a statistical basis may be interpreted in terms of the motion of eddies of different effective sizes. These interpretations then lead to speculations about energy transfer and a variety of other transport phenomena in the turbulent boundary layer.

The most extensive measurement programs following Taylor's pioneering work^{32,33} have been those of Favre and his co-workers³⁴⁻³⁷ and Grant,³⁸ with complementary measurements by Tritton³⁹ and Blackwelder and Kovaszny.⁴⁰

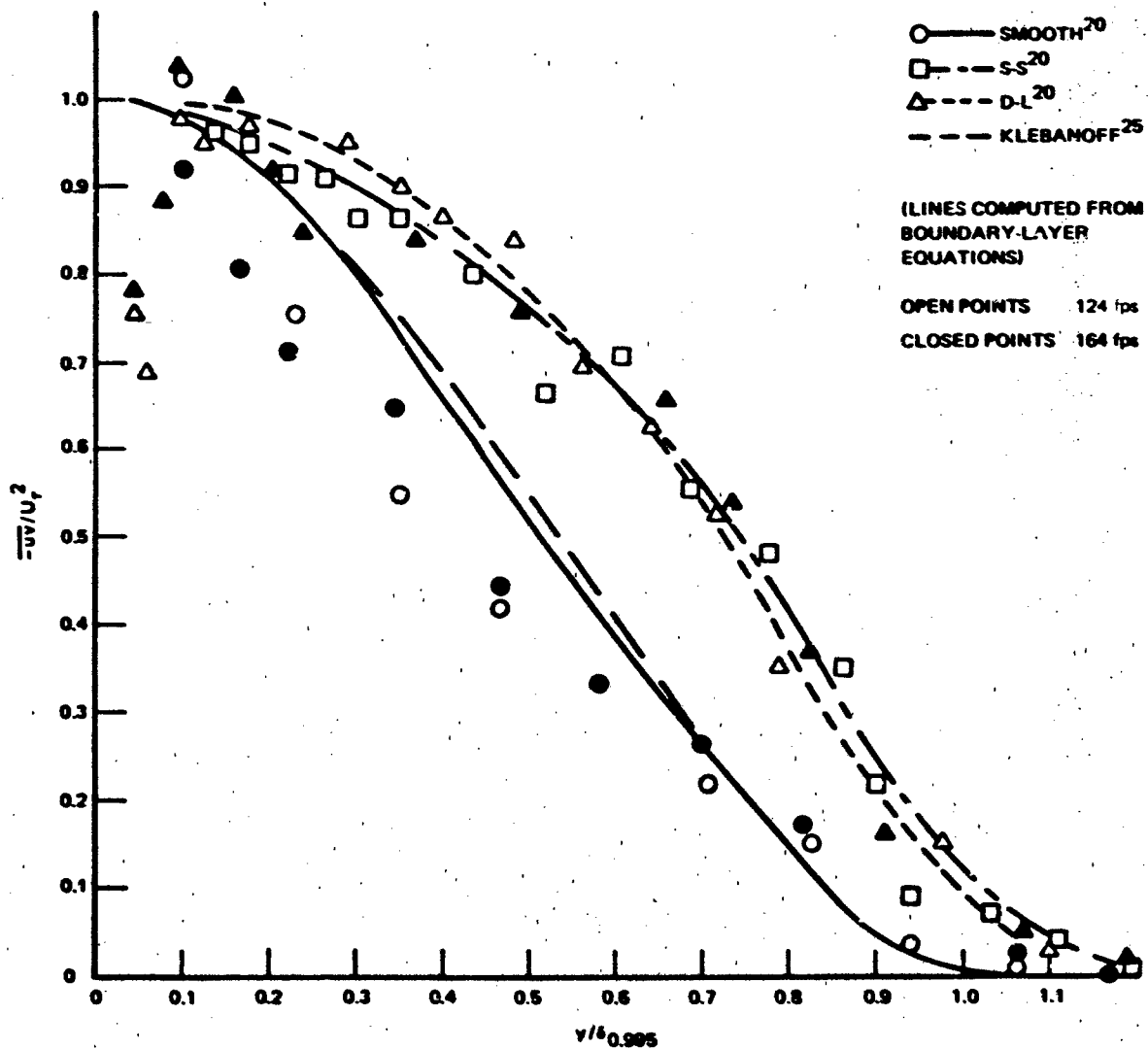


Figure 7.9 - Profile of Turbulent Reynolds Stresses,
Smooth and Rough Walls

The correlation of velocity fluctuations at space-time combinations (\vec{y}, t) and $(\vec{y} + \vec{r}, t + \tau)$ are presented as in Chapter 3, where we defined

$$R_{ij}(\vec{r}, \tau) = \frac{\overline{u_i(\vec{y}, t) u_j(\vec{y} + \vec{r}, t + \tau)}}{\left[\overline{u_i^2(\vec{y}, t)} \overline{u_j^2(\vec{y} + \vec{r}, t + \tau)} \right]^{1/2}} \quad (7.41)$$

The vinculum denotes a time average. The directions and coordinates are the same as those used in Chapter 3; i.e., the 1 direction is aligned with the flow, 2 normal to the flow direction and to the surface, and 3 is parallel to the surface and normal to the flow.

Figure 7.10 shows some space-time correlations $R_{11}(r_1, 0, 0, \tau)$, $R_{22}(r_1, 0, 0, \tau)$, and $R_{12}(r_1, 0, 0, \tau)$ that were obtained by Blackwelder and Kovaszny. ³⁸ These correlations were measured at various positions y_2 in a wind tunnel boundary layer. Time delay has been nondimensionalized as $\tau U_1 / \delta$ and separations as r_1 / δ . These correlation functions display properties similar to those discussed in Section 3.5.2 for jet turbulence; the functions show convection of disturbances that lose their identities as they are convected. The convection velocity U_c is approximately equal to the local mean velocity in the boundary layer; i.e., $U_c = U_1(y_2)$. As Figure 7.10 shows, the correlation $R_{11}(r_1, 0, 0, \tau_m)$ decreases to 0.2 in distance $r_1 = 20\delta$ at $y_2 / \delta = 0.45$, while $R_{22}(r_1, 0, 0, \tau_m)$ decreases to 0.2 in distance $r_1 = 10\delta$. Since the moving axis correlation therefore decays with increasing r_1 , the convection of an eddy packet is hardly frozen. Furthermore, the individual correlation functions at constant r_1 / δ have a broader peak near $\tau = \tau_m$ than for the autocorrelation ($r_1 = 0$) near $\tau = 0$. This behavior has been interpreted in the following way. At small values of r_1 eddies of all sizes, large and small, contribute to the form of the correlation function. Now by Taylor's hypothesis ^{32,33} (Chapter 3), the space and time variations can be interchanged so that the fact that a certain decorrelation is observed in $\Delta \tau_m U_1 / \delta$ implies a similar decorrelation in a corresponding $\Delta r_1 / \delta$. A broadening of $R(r_1, \tau)$, with increasing r_1 , shows that the correlation extends over larger regions as the eddy field moving downstream loses the identity of smaller-scale disturbances. Figure 7.10 shows that the rate of decorrelation is more pronounced for the u_2 fluctuations, and close to the wall turbulence identity is lost in shorter distances.

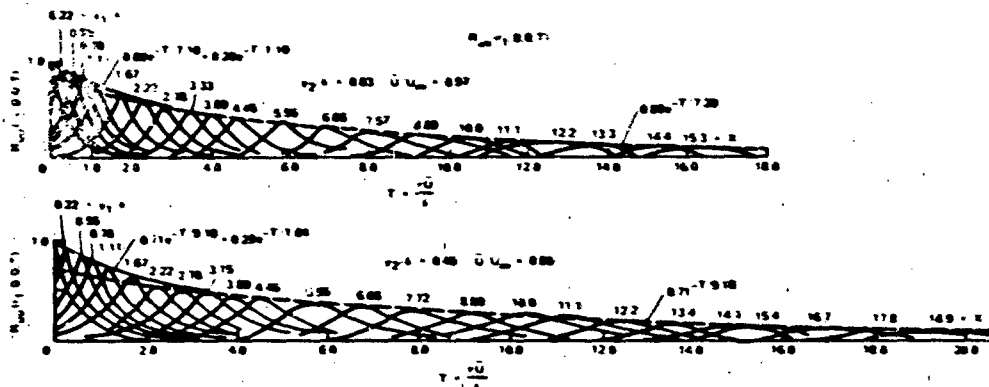


Figure 7.10a - Space-Time Autocorrelations of u , $R_{uu}(r_1, 0, 0, T)$. The Envelopes Represent the Autocorrelations in the Convected Eulerian Frame

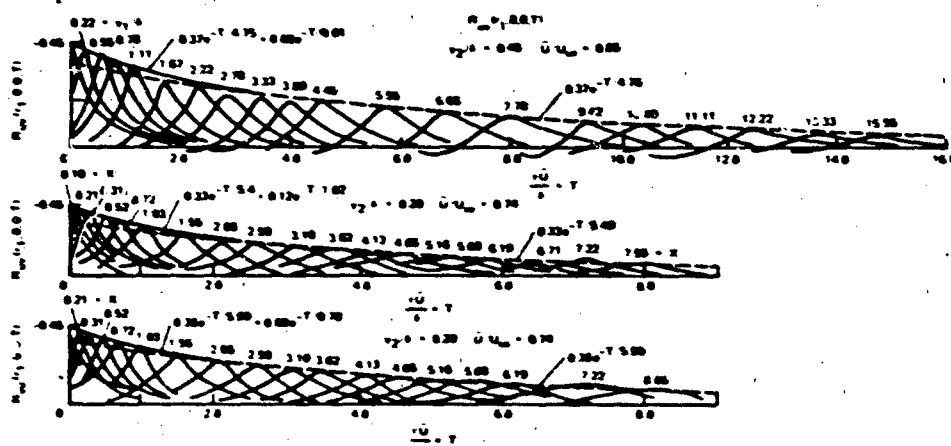


Figure 7.10b - Space-Time Cross Correlations of u and v , $R_{uv}(r_1, 0, 0, T)$ and $R_{vu}(r_1, 0, 0, T)$. The Envelopes Represent the Cross Correlations in a Convected Eulerian Frame

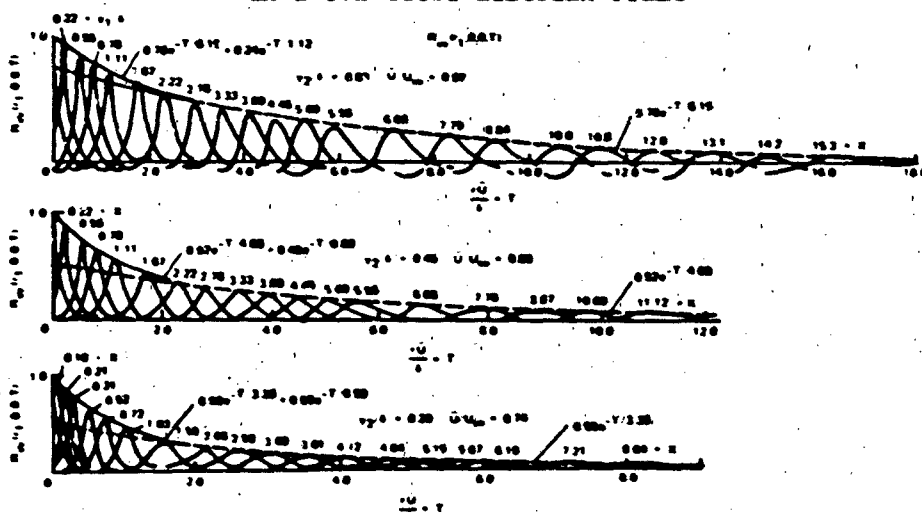


Figure 7.10c - Space-Time Autocorrelations of v , $R_{vv}(r_1, 0, 0, T)$. The Envelopes Represent the Autocorrelations in a Convected Eulerian Frame

Figure 7.10 - Space-Time Correlations of uu' , uv' , and vv' Over Smooth Walls⁴⁰

Spatial correlations at zero time delay indicate the instantaneous spatial extent of the eddies. Some measurements by Grant for three coordinates are shown in Figure 7.11. These correlations show that disturbances are correlated more in r_1 than in r_2 and r_3 when the reference probe is close to the wall. Farther from the wall, $y_2 = 0.6\delta$, differences among the various correlation functions diminish, indicating a trend toward isotropy. Near the wall, $y_2 < 0.06\delta$, the correlations indicate that the correlated u_1 disturbances are extended in the r_1 direction relative to the r_2, r_3 directions. The $R_{22}(\vec{r}, 0)$ correlations conform to this picture, but the correlation extent in r_1 is less than it is for the u_1 disturbances. Reference to Figure 7.2 shows that, for the subject value of y_2 , these differences in correlation behavior have been observed in the wake and logarithmic regions. More recent measurements by Tritton³⁹ ($R_\theta = 2200$) extend and confirm Grant's correlations. Correlations with the r_2 separations are not symmetric about $r_2 = 0$ because of anisotropy brought on by the effect of the wall. This can be seen from information in Figure 7.12, which was extracted from correlation results presented by Favre.³⁶ Although r_1 was not maintained constant, the anisotropy is clearly evident.

Correlations in and near the viscous sublayer have been measured by Bakewell and Lumley⁴¹ at a relatively small Reynolds number. They interpreted these measurements to disclose the existence of a paired eddy structure near the wall which is elongated in the r_1 direction. The lateral extent of the vortex pair, with nearly equal and opposite vorticity vectors directed along r_1 , was on the order of $r_3 U_\tau / \nu = 100$, with a vertical scale of $r_2 U_\tau / \nu = 100$. Along the same line of investigation, more recent correlations of Gupta, Laufer, and Kaplan,⁴² ($R_\theta = 3300$) using signal conditioning techniques support Bakewell and Lumley's observations. Their results disclose the existence of a structure nearly periodic in the spanwise direction with a wavelength of $\lambda_3 U_\tau / \nu = 100$. The organized behavior of these eddies persists for relatively short periods of time; thus for averaging times T longer than $TU_\tau / \delta = 70$ the statistical identity of the pattern was not apparent. This spatial pattern of large eddies is now widely accepted; Townsend³ had earlier postulated that the eddies are as cones lying on the wall with their axes in the r_1 direction and apices upstream. Townsend's geometry is consistent with observed spatial correlations of velocity fluctuations. There is therefore an elongated structure in the boundary layer extending from the sublayer region into the logarithmic region that is responsible for the overall spatial character of the turbulence field and that is altered as it is convected downstream so that larger scales persist.

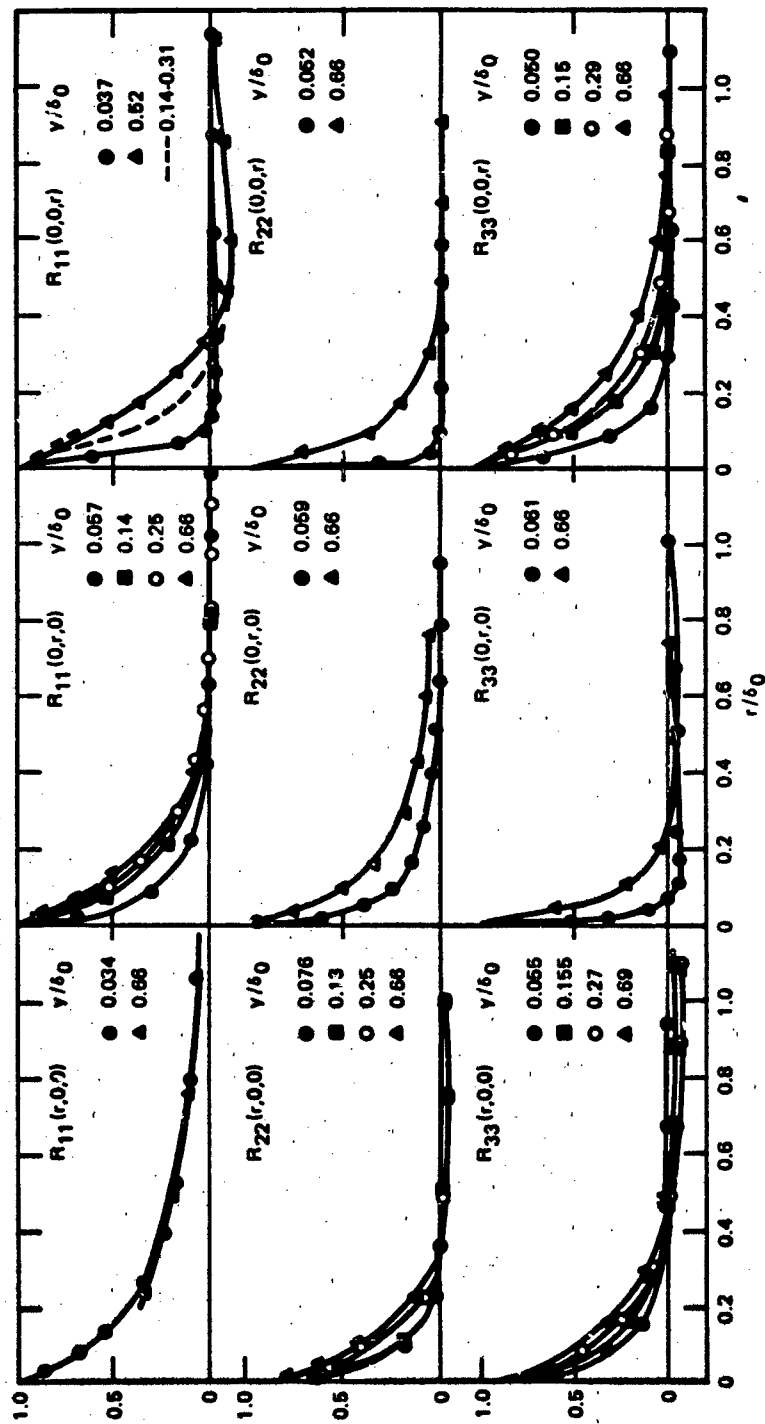


Figure 7.11 - Nine Spatial Correlations in Turbulent Boundary Layer,
 $\delta_0 = 1.4\delta$. From Grant ³³

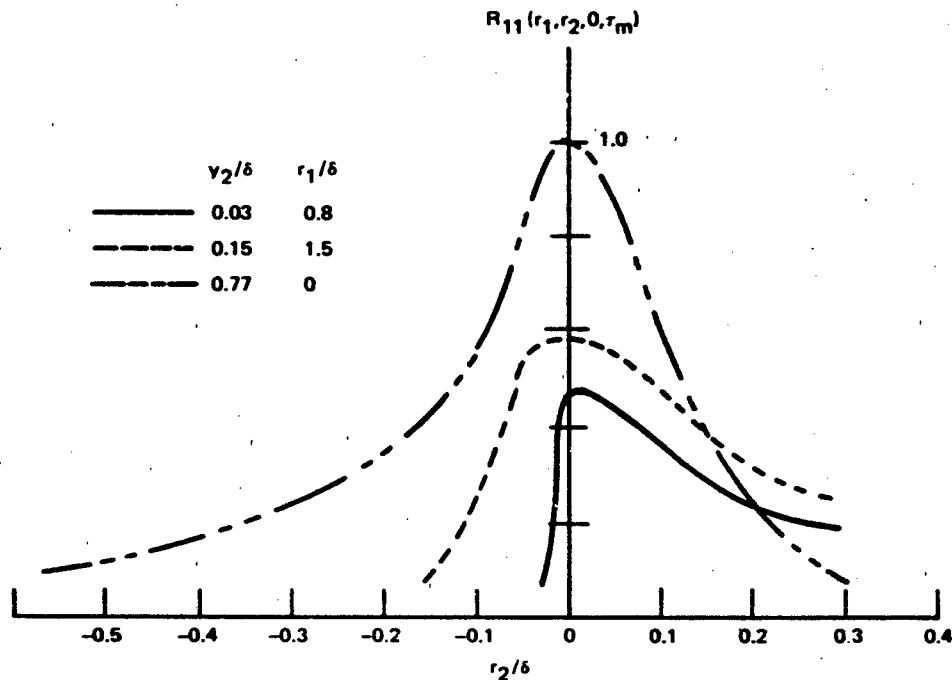


Figure 7.12 - Streamwise Velocity Correlations
with Vertical Separations. From Favre³⁶

The correlation functions of the turbulence have been shown to satisfy the inequalities well known in other fields (see Section 3.5.3):

$$\begin{aligned}
 R_{ij}(0,0) &\geq R_{ij}(r_1,\tau) \geq R_{ij}(\vec{r},\tau) \\
 R_{ij}(0,0) &\geq R_{ij}\left(r_1, \tau - \frac{r_1}{U_c}\right) > R_{ij}(r_1,\tau) \\
 R_{ij}(0,\tau) &\geq R_{ij}(r_1,\tau)
 \end{aligned}
 \tag{7.42}$$

The space-time correlation with streamwise separation can therefore be profitably written in various alternative forms in which the space variable is chosen to move with the turbulence field. Accordingly, as in Section 3.6.33, the correlation function will be approximated as

$$\overline{R}_{ij}(r_1 - U_c \tau, \tau) = R_{ij}(r_1 - U_c \tau) R_M(\tau)$$

to emphasize moving axis correlation. $R_{ij}(r_1 - U_c \tau)$ is the spatial correlation translated to a new origin $r_1 = U_c \tau$, and $R_M(\tau)$ is the moving axis correlation introduced earlier.

7.2.5 Description of Turbulence in the Frequency Domain

The cross-correlation function and cross-spectral density are Fourier-transform pairs as defined by the relationships in Section 3.5.3. In the discussion below the frequency spectrum of the turbulence at a point is normalized as

$$\left(\overline{u_i^2} \overline{u_j^2} \right)^{1/2} = \int_{-\infty}^{\infty} \phi_{ij}(0, \omega, y_2) d\omega \quad (7.43)$$

where, as a generalization of Section 3.6.3.3,

$$\phi_{ij}(0, \omega, y_2) = \lim_{\vec{r} \rightarrow 0} \phi_{ij}(\vec{r}, \omega, y_2)$$

and,

$$\phi_{ij}(\vec{r}, \omega, y_2) = \frac{1}{2\pi} \int_{-\infty}^{\infty} e^{i\omega\tau} \left[\overline{u_i^2} \overline{u_j^2} \right]^{1/2} R_{ij}(\vec{r}, \tau) d\tau \quad (7.44)$$

is the cross-spectral density corresponding to the space-time correlation of the $u_i u_j$ velocities. We assume spatial homogeneity of the turbulence statistics in the plane of the wall.

By Equation (7.43), the level of the spectrum can be nondimensionalized by either the turbulence intensity or the friction velocity squared, U_τ^2 . The time scale must be a combination of the local mean streamwise velocity in the boundary layer, by virtue of Taylor's hypothesis, and a pertinent length scale. In the inner (logarithmic) region of the boundary layer, $y_2/\delta < 0.3$, as shown in Figure 7.2, Bradshaw⁴³ has suggested that since y_2 is the length scale for mean motion it is also an appropriate scale for the inactive convected turbulent motion.

Figures 7.13 and 7.14 show a variety of turbulence spectra nondimensionalized in the form

$$\frac{\phi_{ij}(0, \omega, y_2) U(y_2)}{U_\tau^2 y_2} = f_{ij} \left(\frac{\omega y_2}{U(y_2)} \right)$$

for both zero and adverse pressure gradients over smooth and rough walls. At large dimensionless frequencies, $\omega y_2 / U(y_2) > 1$, the spectral densities all seem to be roughly expressible in the form

$$\phi_{ij}(0, \omega, y_2) = U_\tau^2 \left(\frac{y_2}{U(y_2)} \right) f_{ij} \left(\frac{\omega y_2}{U(y_2)} \right) \quad (7.45)$$

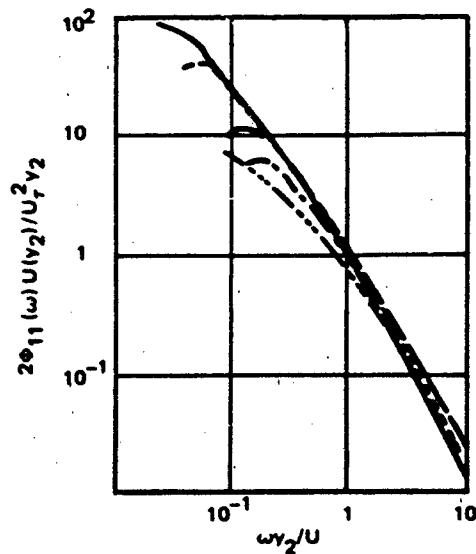
where $f_{ij}(\Omega)$ is a dimensionless function of frequency. At lower frequencies, spectra at different values of y/δ do not behave in this manner.

The viscous sublayer has been found by Einstein and Li⁴⁴ to consist of oscillatory motions, and Bakewell and Lumley⁴¹ have found that within the region $y^+ < 10$ the frequency spectrum of the (u_1) velocity fluctuations behaves as

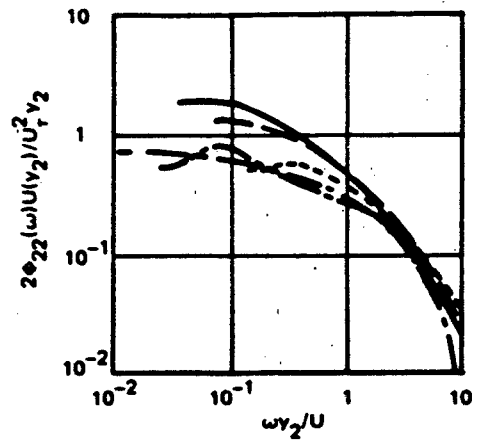
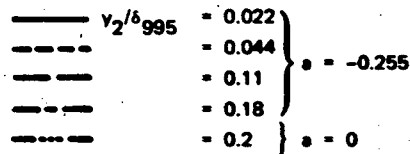
$$\begin{aligned} \frac{\phi_{11} \left(\frac{\omega v}{U_\tau^2} \right)}{U_\tau^2} \left[\left(y_2^+ \right)^2 \left(\frac{\omega v}{U_\tau^2} \right) \right]^{-1} &= f \left(\frac{\omega v}{U_\tau^2} \right) \\ &\approx 7 \left(\frac{\omega v}{U_\tau^2} \right), \quad \frac{\omega v}{U_\tau^2} < 3 \times 10^{-2} \end{aligned}$$

This relationship arises from the fact that, although the disturbances have a stochastic time dependence, say $f(t)$, they have a deterministic y_2 dependence, i.e., the dimensionless (on U_τ) fluctuating velocity behaves as

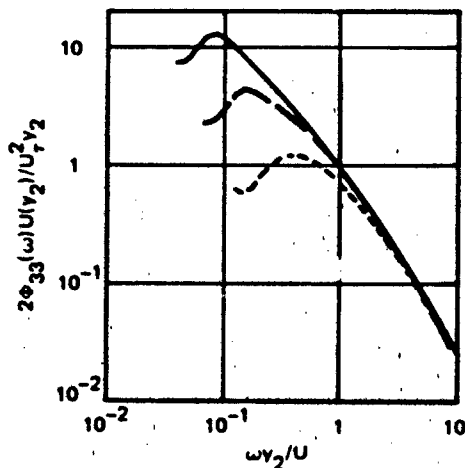
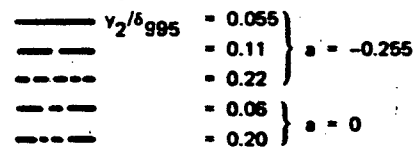
$$u_1^+ (y_2^+, t^+) = y_2^+ f \left(\frac{t U_\tau^2}{v} \right)$$



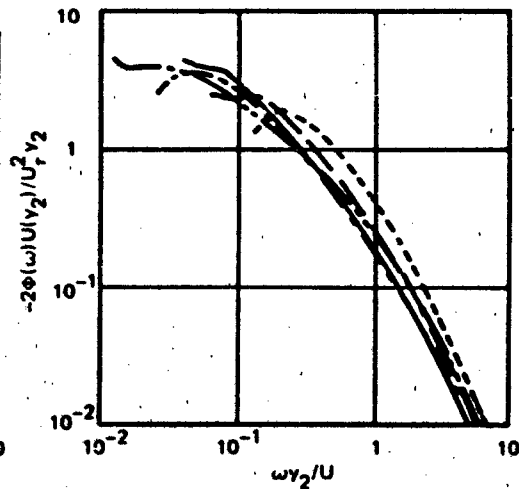
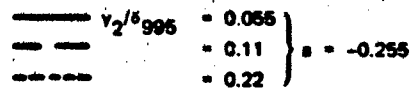
INNER-LAYER FREQUENCY SPECTRA
AT $y_1 = 83$ IN, u COMPONENT



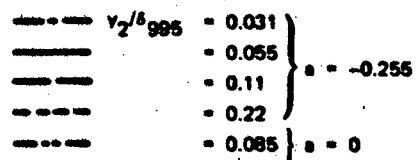
INNER-LAYER FREQUENCY SPECTRA
AT $y_1 = 83$ IN, v COMPONENT



INNER-LAYER FREQUENCY SPECTRA
AT $x = 83$ IN, w COMPONENT



INNER-LAYER FREQUENCY SPECTRA
AT $x = 83$ IN, uv



ADVERSE AND ZERO PRESSURE GRADIENT, $U_1 \propto y_1^2$, $R_\theta \approx 9020$

Figure 7.13 - Frequency Spectra of Turbulence Quantities in the Inner ("Log") Layer Normalized on y_2 . From Bradshaw⁴³

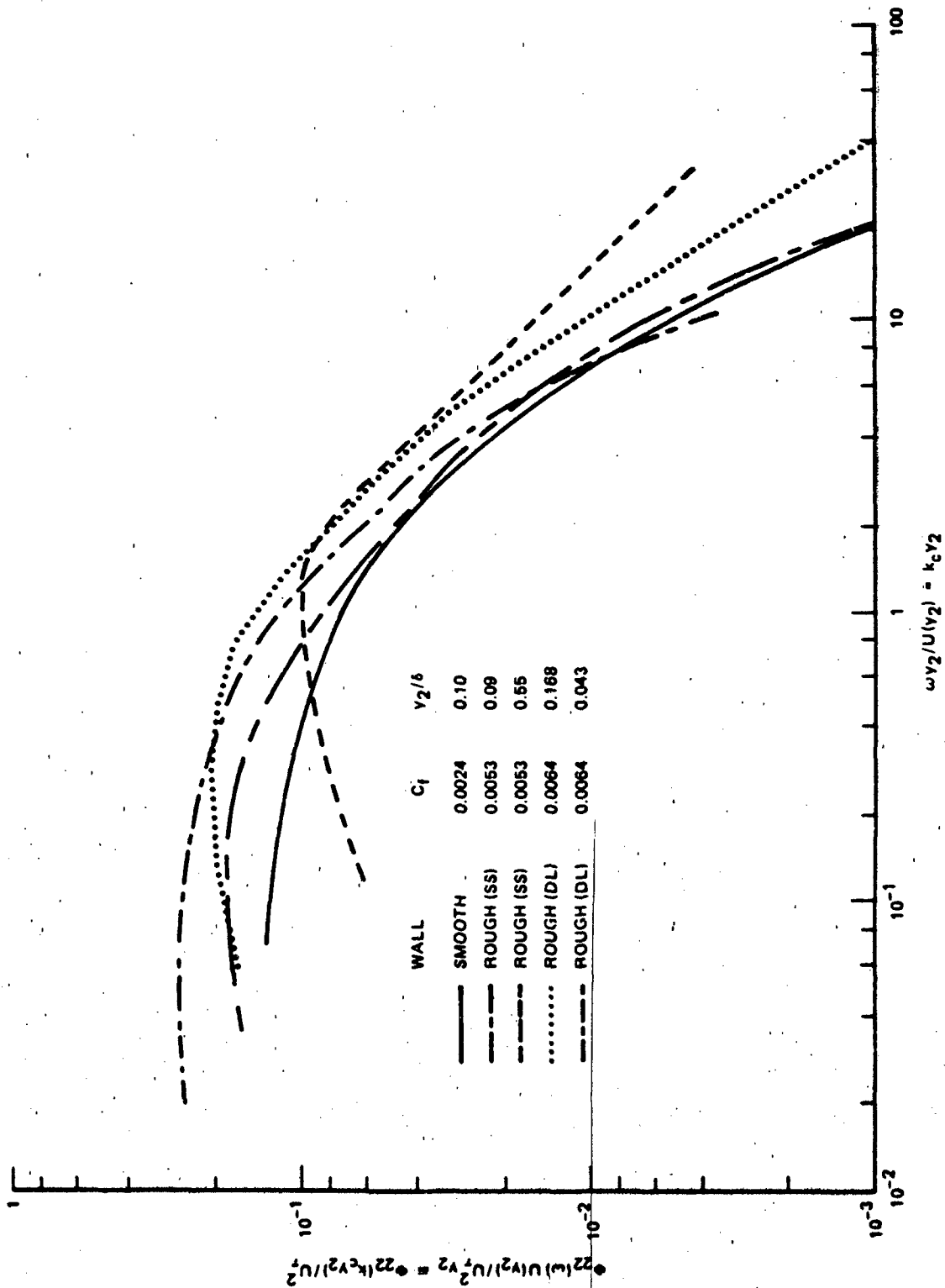


Figure 7.14 - Spectral Densities of u_2 Turbulence Intensities Over Smooth and Rough Walls in the Inner Layer. Adopted from Blake²⁰

Temporally stochastic velocity fluctuations were also observed in the sublayer by Eckelmann,⁴⁵ who confirmed the proportionality of u_1^+ and y_2^+ and further established a limit on the vertical velocity of $(\overline{u_2^2})_{\max} = U_\tau^2$.

Cross-spectral densities with probe separations in the streamwise direction, $\vec{r} = r_1, 0, 0$, have been measured by Favre.³⁶ Some of these measurements are shown in Figure 7.15 in the same dimensionless form as that used in Figure 3.22 (Section 3.6.3.3), and they have the same interpretation regarding eddy decay. $U_c(\omega)$ is the convection velocity of the disturbance at the frequency of measurement. The variable $\omega r_1 / U_c(\omega)$ is actually the phase α_1 of the cross-spectral density function determined electronically in the measurement. The phase has been given a convection interpretation by extending Taylor's hypothesis to apply to filtered disturbances. For each dimensionless frequency at a particular value of y_2/δ , the cross-spectrum amplitude appears as a unique function of the phase. The decrease in $\phi_{11}(r_1, \omega, y_2) / \phi_{11}(0, \omega, y_2)$ with increasing phase becomes less dramatic at larger distances from the wall. Also, the convection velocities given in Figure 7.16 as functions of $U(y_2)$ and $\omega\delta/U_c$ show that very close to the wall U_c is actually greater than $U(y_2)$. In the outer region U_c is less than the local velocity.

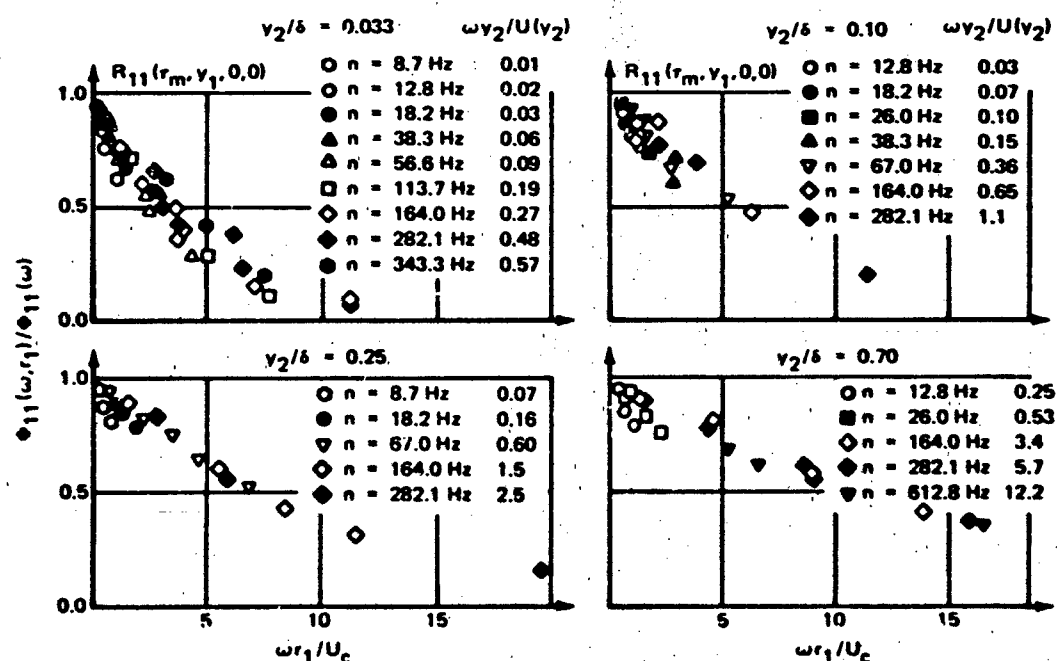


Figure 7.15 - Space-Time Correlation Coefficient with Optimum Delay Along the Motion. $R_0 = 8700$. From Favre³⁶

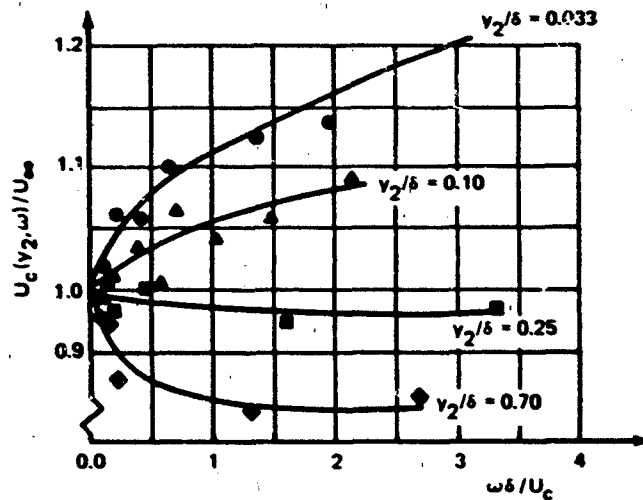


Figure 7.16 - Convection Phase Speed for Longitudinal Turbulence Component $\delta/\delta^* = 4.77$. From Favre³⁶

It is possible to fit the data of Figure 7.15 with an exponential of the form

$$\frac{\phi_{11}(\omega, r_1)}{\phi_{11}(\omega)} = A \left(\frac{\omega r_1}{U_c} \right) = \exp \left[-\gamma_1 \left| \frac{\omega r_1}{U_c} \right| \right] \quad (7.46)$$

where the coefficients γ_1 increase as the wall is approached, as shown in Figure 7.17a. If we approximate this dependence as

$$\gamma_1 = a_1 \left(\frac{\delta}{y_2} \right)^{1/2}, \quad a_1 = 0.044$$

and the convection velocity as

$$U_c = U(y_2)$$

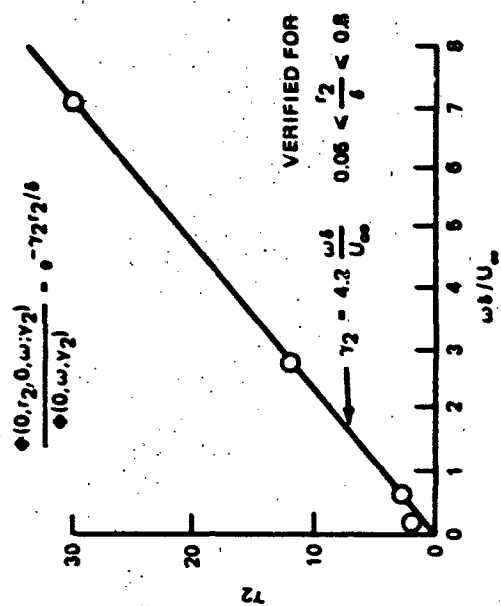


Figure 7.17b

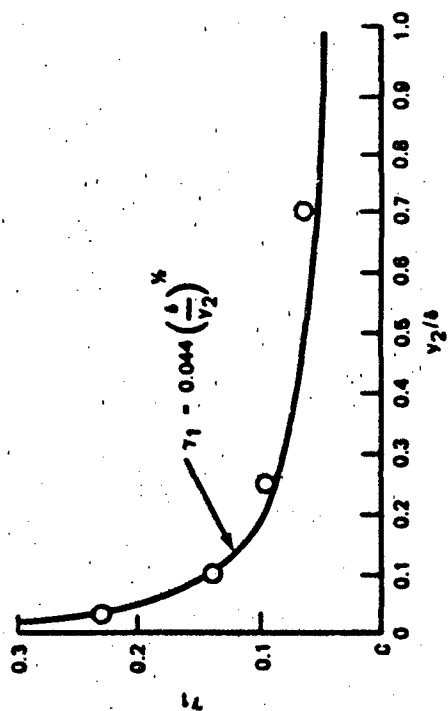


Figure 7.17a

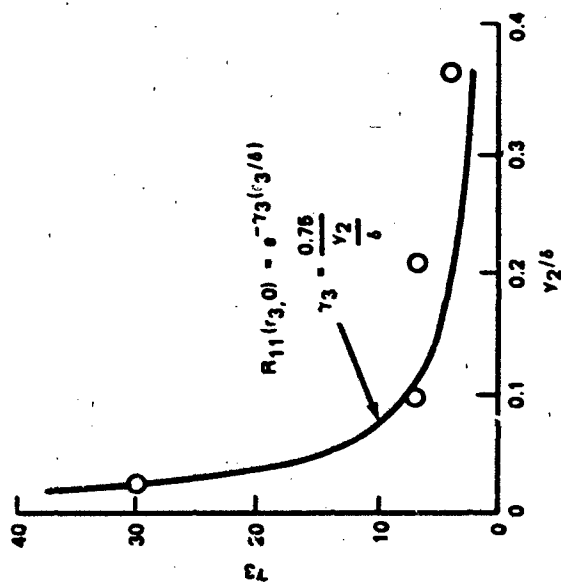


Figure 7.17c

Figure 7.17 - Exponential Correlation Factors, γ_1 , γ_2 , γ_3 , for Turbulent Velocity Fluctuations (see Equation (7.48))

then Equation (7.46) takes the form

$$A\left(\frac{\omega r_1}{U(y_2)}\right) = \exp \left[-a_1 \left(\frac{\delta}{y_2}\right)^{\frac{1}{2}} \left(\frac{\omega y_2}{U(y_2)}\right) \left|\frac{r_1}{y_2}\right| \right] \quad (7.47)$$

This function simply says that decorrelation in the plane of the wall occurs in streamwise distances that are nearly comparable with the distance y_2 of the plane from the wall. Assuming that the eddy dimension is also proportional to its distance from the wall, this function can be interpreted to show that eddy life times are commensurate with eddy sizes. Recall also the arguments in Section 7.2 leading to the logarithmic profile (Equations (7.20) and (7.21)). Other empirical results can be similarly summarized by a set of analytical functions written in the approximate form (invoking Equation (7.45)) which separates each of the temporal and spatial coordinate dependencies:

$$\begin{aligned} \phi_{11}(\vec{r}, \omega, y_2) = U^2 \left(\frac{y_2}{U(y_2)}\right) & \left[\frac{\phi_{11}\left(\frac{\omega y_2}{U(y_2)}\right)}{U(y_2)} \right] \exp(i\omega r_1/U(y_2)) \\ & \cdot e^{-\gamma_1 \left[\left(\frac{\omega y_2}{U(y_2)}\right) \left|\frac{r_1}{y_2}\right| \right]} e^{-\gamma_2 \left| \frac{\omega r_2}{U_\infty} \right|} e^{-\gamma_3 \left| \frac{r_3}{y_2} \right| \left(1 - \left| \frac{r_3}{y_2} \right| \right)} \end{aligned} \quad (7.48)$$

for $\omega y_2/U(y_2) > 0.5$, $y_2/\delta < 0.3$. The broadband correlations of Grant and Tritton (Figure 7.17) gives γ_3 , and the narrowband correlations of Favre, et al.³⁶ give γ_2 , as shown in Figure 7.17b and c. Similar relationships for the other $\phi_{ij}(\vec{r}, \omega, y_2)$ are expected to hold, but with slightly different values for the coefficients γ_i , as indicated by the space-time correlations.

Using the Fourier transform relationships of Section 3.5.3, a wave number spectral density in the 1.3 plane of the fluctuating velocities can be found from the above formula for the spatial cross-spectral density, i.e.,

$$\phi_{11}(\vec{k}, \omega, y_2) = \phi_{11}(k_1 y_2) y_2 \cdot \frac{1}{\pi} \left[\frac{\gamma_3 y_2}{\gamma_3^2 + (k_3 y_2)^2} - \frac{2y_2^3 (\gamma_3^2 - k_3^2 y_2^2)}{[\gamma_3^2 + (k_3 y_2)^2]^2} \right] \cdot \frac{1}{\pi} \frac{\gamma_1 \omega}{(k_1 U_c - \omega)^2 + (\gamma_1 \omega)^2} \quad (7.49)$$

which has the separable form of Equation (3.105)

$$\phi_{11}(\vec{k}, \omega, y_2) = y_2^3 U_c^{-1} \phi_{11}(k_1 y_2) \phi_3(k_3 y_2) \phi_m\left(k_1 y_2 - \frac{\omega y_2}{U_c}\right)$$

This relationship shows a maximum at $k_1 = \omega/U_c$ whose wave number bandwidth is $\Delta k_1 = 2\gamma_1 \omega/U_c$; the third function on the right, which is the moving axis spectrum, is responsible for this behavior. The sharpness of this maximum often allows us to interchange between k_1 and ω/U_c . Accordingly, $\phi_{11}(\vec{k}, \omega, y_2)$ may be rewritten in the equivalent form of Equation (3.93)

$$\phi_{11}(\vec{k}, \omega, y_2) = \frac{1}{u_1^2} \cdot \left[\frac{\phi_{11}(k_1 y_2)}{u_1^2} \right] \cdot \phi_3(k_3 y_2) y_2 \cdot \phi_m(\omega - U_c k_1) \quad (7.50)$$

where $\phi_{11}(k_1 y_2)/u_1^2$, $\phi_3(k_3 y_2)$ and $\phi_m(\omega - U_c k_1)$ correspond to the identified functions above. Correlation between planes y_2 and y_2' has been expressed by

$$R_{11}(y_2 - y_2') = \exp \left[-\gamma_2 \left| \frac{\omega r_2}{U_c} \right| \right]$$

which, due to the interchangeability of k_1 and ω/U_c , may also be written

$$R_{11}(r_2) = \exp \left[-\gamma_2 |k_1 r_2| \right] \quad (7.51)$$

The correlation "thickness" of such planes parallel to the wall is therefore

$$\Lambda_2(k_1) = \int_0^{\delta} e^{-\gamma_2 k_1 r_1} dr_1$$

$$= (\gamma_2 k_1)^{-1}$$

as long as $k_1 > \delta^{-1}$. The turbulence at high wave numbers, $k_1 > \delta^{-1}$, may therefore be regarded as existing in layers of thickness $(\gamma_2 k_1)^{-1}$. Since $\phi_{11}(k_1 y_2)$ and $\phi_3(k_3 y_2)$ indicate that $|k|$ scales on y_2 , higher wave number turbulence effectively exists at smaller heights from the wall and in strata of decreasing thickness. This is entirely consistent with the hypothesis of Bradshaw⁴³ discussed earlier (see Equation (7.45)), and we will find it useful in estimating the behavior of the wall pressure spectrum in Section 7.3.

The more conventional measures of eddy length and time scales^{2-4,7} introduced in Equations (3.90) are also useful in describing boundary-layer turbulence. In addition, there is often reported an integral correlation area

$$A_{ij} = \iint_0^{\infty} R(\vec{r}, 0) dr_i dr_j \quad (7.52)$$

in the ij plane and a correlation volume already introduced (Chapter 3, Equation (3.107)). By implementation of Equations (3.90b) and (3.90c), the integral time scale and streamwise length scale for the convected eddy structure are related by Taylor's hypothesis:

$$\Lambda_1 = U_c \theta_\tau$$

There is also a microscale for the turbulent field recognized^{2,3,46,47} as representative of the smallest energy-containing eddy. Therefore we look to the shape of the correlation function near $r_i = 0$ or $\tau = 0$. A Taylor's series expansion of $R(r)$ near $r = 0$ has as its first two terms

$$R(r) = 1 + \frac{1}{2} \frac{\partial^2 R(0)}{\partial r^2} r^2$$

Since $\partial^2 R(0)/\partial r^2$ is negative, $R(r)$ is a parabola

$$R(r) = 1 - \frac{r^2}{\lambda^2}$$

where

$$\frac{1}{\lambda^2} = -\frac{1}{2} \frac{\partial^2 R(0)}{\partial r^2} \quad (7.53)$$

and λ is called the microscale, or dissipation length. The longitudinal microscale can be determined from the autospectrum and letting $k_c = \omega/U_c$. Then

$$\frac{1}{\lambda_1^2} = \int_0^\infty \frac{k_c^2 \phi_{ij}(k_c)}{\left(\overline{u_i^2 u_j^2}\right)^{1/2}} dk_c \quad (7.54)$$

Thus, knowing the frequency spectrum for the $u_i u_j$ product at a fixed point in the flow, we can determine the streamwise scales without the availability of spatial correlations if the assumption of nearly frozen convection is valid. For length scales in the 2 and 3 directions, two-point correlations are of course necessary.

Figure 7.18 shows a collection of streamwise microscales for u_1 fluctuations over smooth and rough walls. The microscale appears to be a fraction of the displacement thickness throughout much of the boundary layer for all degrees of wall roughness. In the logarithmic region of the boundary layer, $y_2 < \delta^*$, $\lambda_1 = 1/3 \delta^*$. All λ_1 have been obtained using Equation (7.54); λ_2 have been determined from Equation (7.53). Turbulence integral scales from a variety of sources^{14,23,25,48} are summarized in Figure 7.19. Here Λ_1 was determined from u_1 disturbances using the frequency spectrum and Equations (3.90), while Λ_2 and Λ_3 were obtained from u_1 correlation functions using Equation (3.90a). The precision in determining Λ_1 is poor because the limiting spectrum level as frequency approaches zero is uncertain.

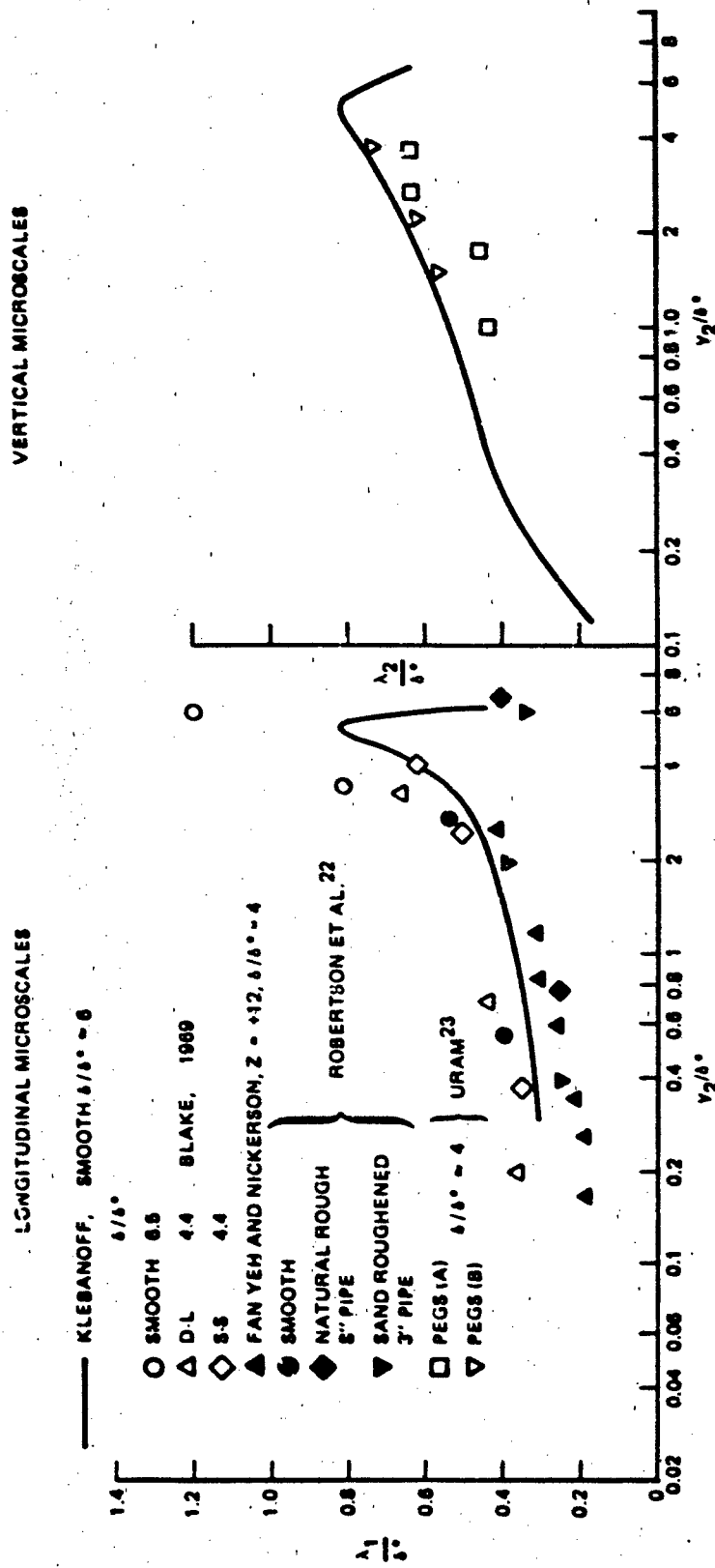


Figure 7.18 - Turbulent Microscales, Smooth and Rough Walls¹⁴

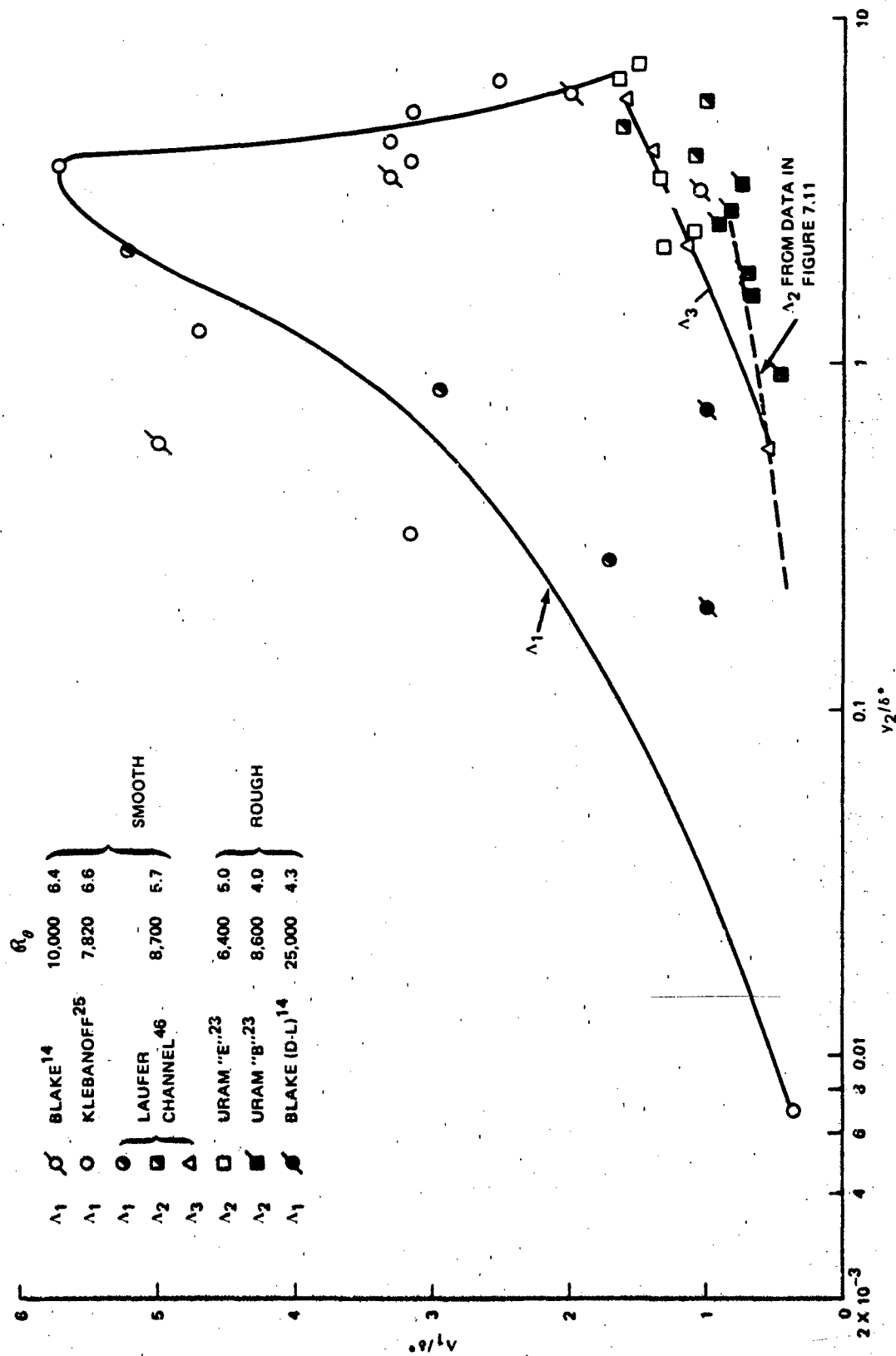


Figure 7.19 - Integral Turbulence Scales Obtained from U_1 Fluctuations Over Smooth and Rough Walls, Solid Lines Drawn as Visual Aids Only

The most striking feature of the summary is that Λ_1 far exceeds Λ_2 and Λ_3 in the vicinity of $3 < y_2/\delta^* < \delta/\delta^*$ over smooth walls, while over rough walls all Λ_i appear to be of the comparable magnitude. Only one measurement of Λ_3 is shown: that of Laufer obtained in a smooth-walled channel flow. This value is most likely too large because the range of r_3 over which measurements were obtained did not extend into the region of $R_{11}(r_3) < 0$. As shown in Figure 7.11, for r_3 sufficiently large this correlation function has a region of negative values that tends to reduce the integral length scale, especially in the outer region of the boundary layer. The vertical integral scale increases with y_2 , as illustrated by the y_2/δ^* dependence of Λ_2/δ^* , which was determined (assuming $\delta/\delta^* \approx 6$) from Grant's correlation $R_{11}(0, r_2, 0)$, shown in Figure 7.13. Uram's and Laufer's integral scales are within a factor of 2 of those deduced from Grant's measurements. There has been little other attention paid to the integral scales of boundary-layer turbulence.

7.2.6 Modern Views of Boundary-Layer Structure

The preceding discussion dealt with statistical descriptions of the turbulent boundary layer. These descriptions have led to approximate dimensionless representations of temporal mean and root-mean-square quantities based on the gross energetics of the boundary layer. Apart from quantifying the average statistics of the energy-containing eddies of the turbulence in the boundary layer and the dependence of such properties on the gross features of the boundary layer such as the wall-shear stress and the boundary layer thickness, these properties disclose relatively little about the physics of turbulence dynamics that lead to the maintenance of the boundary layer and especially to the generation of wall pressures. It is suggested later that a connection between the wall pressure and the turbulent motion may exist, but it is probably obscured by the gross energetics. Turbulence production is controlled by the Reynolds shear stresses, $\overline{u_1 u_2}$, but wall pressures are determined by various gradients of the Reynolds stress tensor.

To illustrate these notions, we note that near the wall,^{1-6,15} say $y_2/\delta < 0.3$, turbulence production manifested by Reynolds stresses nearly balances dissipation D , i.e.,

$$\frac{\overline{-u_1 u_2}}{U_\tau^2} \frac{\partial \left(\frac{U}{U_\tau} \right)}{\partial \left(\frac{y_2}{\delta} \right)} \approx \frac{D\delta}{U_\tau^3} \quad (7.55)$$

For any flow, the dissipation of turbulent energy is given by²

$$D = \nu \overline{\frac{\partial u_i}{\partial x_j} \frac{\partial u_i}{\partial x_j}} = \nu \overline{\omega_k \omega_k}$$

where $\vec{\omega}$ is a vorticity vector, and

$$D = 15 \nu \left(\overline{\frac{\partial u}{\partial x}} \right)^2$$

for locally isotropic flow.

It will be shown (Section 7.3) that the wall-pressure fluctuations are the result of the weighted integral of the fluctuating stress tensor, over the thickness of the boundary layer; the source term for wall pressures can be rewritten here as (see also Equation (7.82))

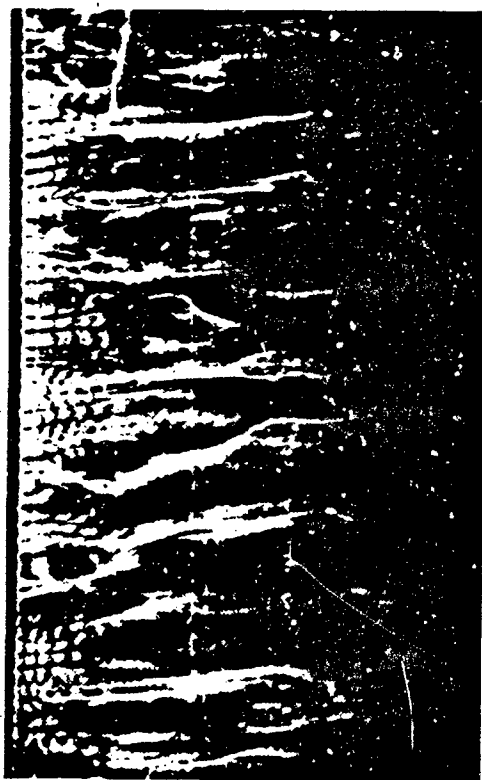
$$\frac{1}{\rho_0} \frac{\partial^2 (T_{ij} - \bar{T}_{ij})}{\partial y_i \partial y_j} = 2 \frac{\partial u_1}{\partial y_2} \frac{\partial u_2}{\partial y_1} + \frac{\partial^2 (u_1 u_j - \bar{u}_1 \bar{u}_j)}{\partial y_i \partial y_i} \quad (7.56)$$

The second term that arises from the fluctuating vorticity in the fluid includes an important contribution from the $u_1 u_2$ product, while the first represents an interaction of the mean shear with the turbulent fluctuations. It is the $u_1 u_2$ component of pressure sources shown above that links the pressure fluctuations with the instantaneous production represented by the left side of Equation (7.55). The motion that dominates the production of turbulence has been called the "active" motion in the boundary layer, while the terms determined by the overall kinetic energy of the turbulence have been called the "inactive" motion in the boundary layer. Hinze² shows that the ratio of the turbulence stress to the total turbulent velocity, $-\overline{u_1 u_2}/q$, is approximately 0.15 throughout the boundary layer. Thus the turbulence contribution responsible for production constitutes only 15% of the mean-square⁴⁶ of the total motion (i.e., of the irrotational or inactive motion) that determines the total local intensity. Note that Phillips⁴⁶ has shown that $\overline{u_1 u_2}$ is identically zero when the flow is irrotational. The pressure fluctuations, on the other hand, are contributed to by the spatial gradients of these same Reynolds stresses, so that we must infer the existence of some contribution to the pressures

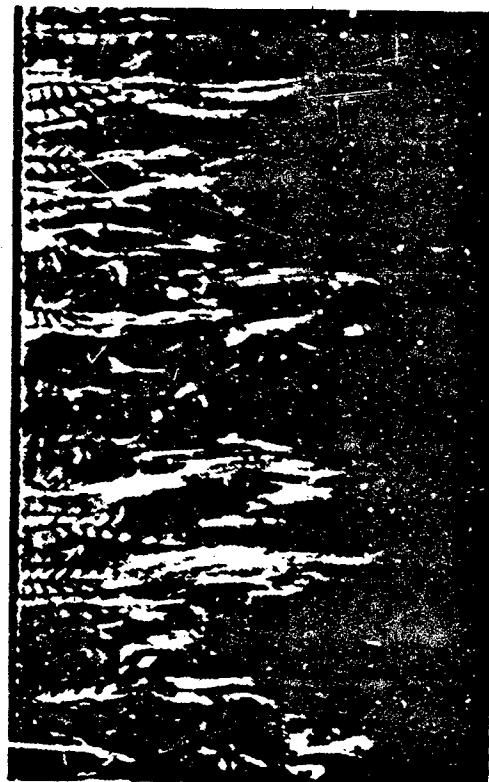
from this active (or turbulence-producing) motion. Furthermore, it is now known that organized intermittent structures in the boundary layer exist; these, it turns out, do not contribute to the local intensity over long periods of time. These correlated structures dominate the mechanics of the Reynolds stresses and therefore quite possibly are related to low wave number pressures because of their well-defined spatial characteristics. As we shall see, this spatially coherent boundary-layer motion accounts for nearly all the Reynolds shear stress but relatively little convected turbulent energy. A study of structures related to only 15% of the total kinetic energy requires special experimental techniques that involve both visualization and conditional electronic sampling. As tempting as the following ideas may appear, there has been little substantive work to establish the existence or nonexistence of a link between pressure fluctuations and the production of turbulence.

The remainder of this subsection is devoted to a brief description of the work in turbulence structure conducted over the last decade or so. This work may also be interpreted to offer some kinematic basis for the importance of the spatial and temporal structure of the $u_1 u_2$ Reynolds stresses and of the local vertical convection considered in the spectrum modeling of Section 7.3. An excellent review has been prepared by Willmarth and Bogar.⁴⁹

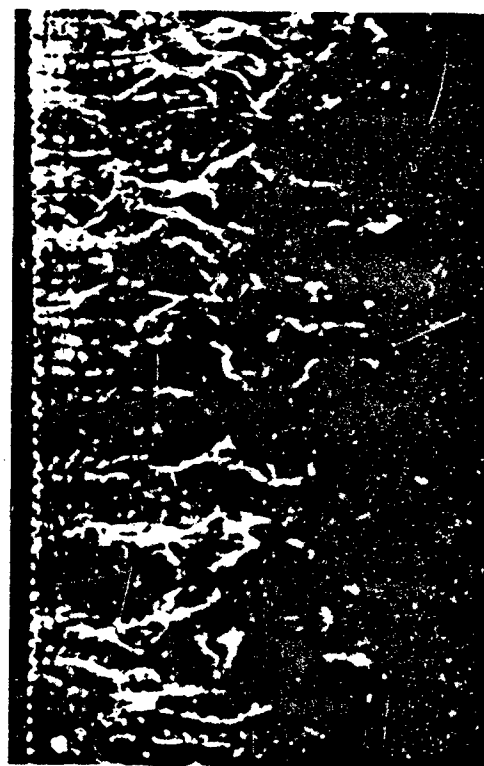
Townsend⁴⁷ first postulated the existence of a streamwise vortex structure. Later flow visualizations of Kline and his associates⁵⁰⁻⁵² (at $R_0=666$) showed that elongated streamwise vortices existed throughout the viscous sublayer, say within $y^+ = 15$. These disturbances were spatially well organized, as shown in Figure 7.20, but temporally unstable, ejecting from the wall region into the bulk of the boundary layer. In the description given by Kline et al.,⁵² when hydrogen bubbles or dye are injected into the boundary layer from an electrolysis wire on the wall, the tracer maintains a trajectory in which it rises slowly away from the wall as it is convected downstream. When it reaches a height of roughly $y^+ = 8$ to 12, it begins oscillations that increase in intensity as the fluid moves farther from the wall. At y^+ on the order of 10 to 30 these oscillations are abruptly terminated as the fluid streak moves briskly from the wall. As it moves farther, the streak becomes controlled and a portion of it breaks off from the main and is convected downstream.



$y^+ = 4.5$



$y^+ = 9.6$



$y^+ = 38$



$y^+ = 507$

Figure 7.20 - Photographs of the Structure of a Flat Plate Turbulent Boundary Layer. Visualization Provided by Pulsed Hydrogen Bubble Tracers with the Electrolysis Wire

Positioned at the Indicated Values of y^+ . From Kline et al. 52

These observations contradict, to some degree, observations made earlier in laminar boundary layers as they undergo transition to turbulence. In that case injected dye streaks remained transverse to the flow direction until they developed a three-dimensional kink,⁵³ resembling locally a "U" pointed upstream and nearly in the plane of the wall. Progressive deformation of this originally sinuous vortex resulted in a streamwise-oriented vortex structure that eventually culminated in fully developed turbulence. In the case of the turbulent boundary layer, the dye streaks did not originate in a transverse orientation and the subsequent breakdown was not preceded by the generation of well-defined Tollmien-Schlichting waves followed by Emmons spots, as is so well known in transition boundary layers (see Section 7.5.1 and the reviews by Hinze² and Mollo-Christensen⁵⁴).

Nearly concurrent with the flow visualization measurements of Kline and associates were the sublayer measurements of Bakewell and Lumley at low Reynolds number ($R_\theta = 450$) which were interpreted to disclose a well-structured and disturbance-filled sublayer. These were discussed in Section 7.2.5. At about the same time Tu and Willmarth^{55,56} published their space-time correlations of wall pressure with the various velocity components u_1 , u_2 , and u_3 . The iso-correlation lines of pu_1 in the y_1, y_3 plane were elongated in the y_1 direction and generally confined to the region $y_2 < 2\delta^*$. As illustrated in Figure 7.21, iso-correlation lines in the y_2, y_3 plane were nearly circular and centered within $y_2 \leq \delta^*$. The absolute value of the correlation coefficients did not exceed 0.15, indicating a very weak relationship between the wall pressure at a point on the surface and any local turbulent fluctuation. The correlations of pu_3 shown in Figure 7.21 were interpreted to show that the wall pressures are influenced by a swept vortex structure whose axis was nearly parallel to the flow direction. Another observation of Willmarth and Tu⁵⁶ ($R_\theta = 4 \times 10^4$) is that the moving axis correlation of

$$R_{pu_2} \left(r_1, r_2 = y_2, r_3 = 0, \tau = \frac{r_1}{U(y_2)} \right)$$

is odd about $r_1 = 0$, with the correlation function being negative with r_1 negative. This observation suggests that a locally adverse (increasing with y_1) gradient of instantaneous pressure is connected with a motion of fluid away from the wall.

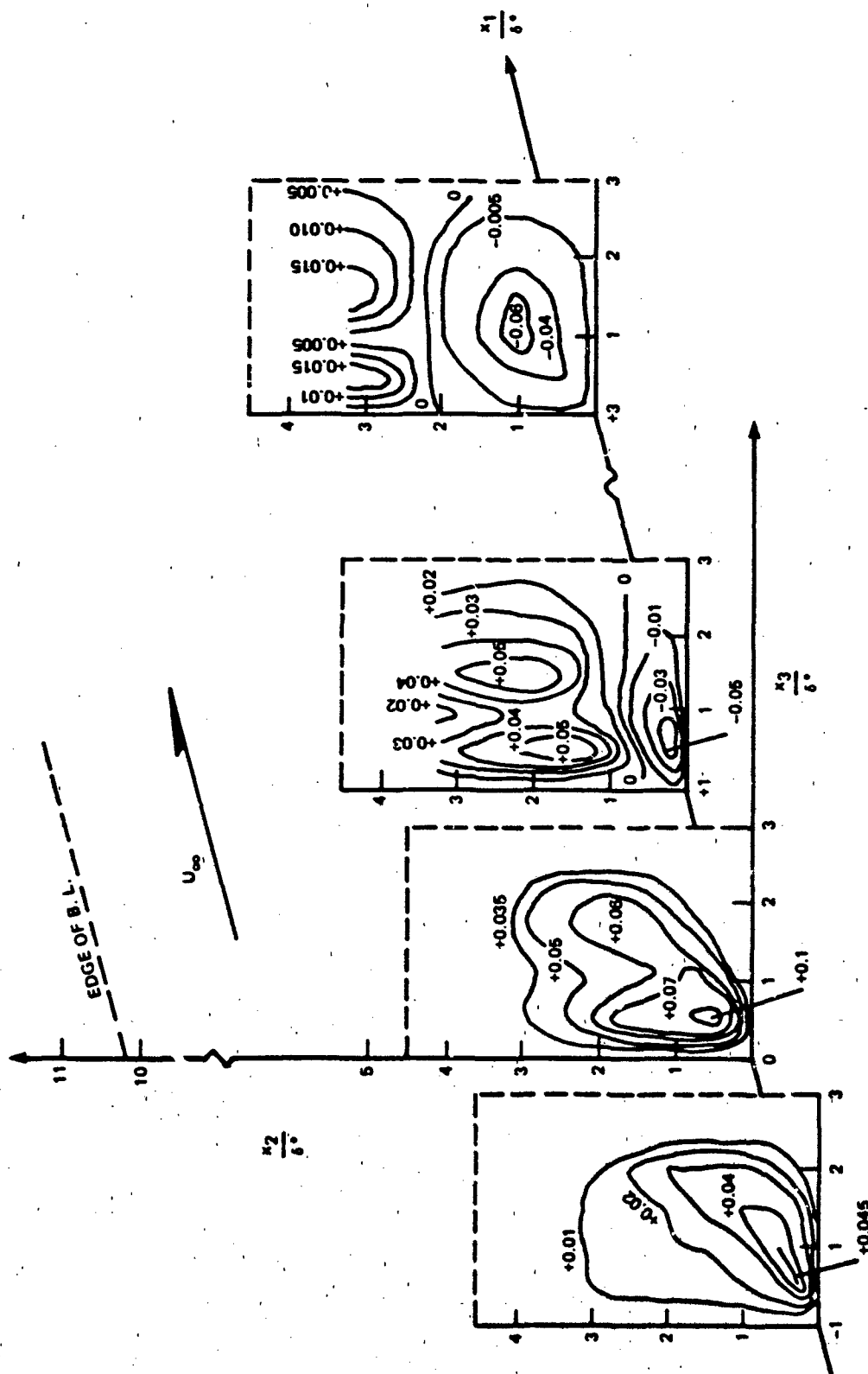


Figure 7.21 - Three-Dimensional Diagram of Contours of $R_{pu_3} = \text{Constant}$ Showing the Development of Large-Scale "Average" Vortex Structure Responsible for Wall Pressure^{55,56}

The intermittent bursting observed by Kline et al.^{50,52,57,58} was further investigated electronically in order to develop a measure of a mean burst frequency duration. It has now been reasonably well established^{59,60} that the burst period T_B may be nondimensionalized on outer variables δ and U_∞ so that

$$\frac{T_B U_\infty}{\delta} \approx 5 \text{ for } 500 < R_\theta < 10^4$$

(Note that a point extracted by Rao et al.⁶⁰ from Lu and Willmarth⁶¹ has been subsequently shown to be erroneously interpreted.⁶²) Intermittent turbulent activity was also observed by Rao et al. ($R_\theta \approx 620$) (within the limitations that their counting procedures provided) to be identifiable with the same period almost throughout the boundary layer. In this regard, Kovasznay et al.⁶³ ($R_\theta \approx 2750$) found, using velocity cross correlations, an intermittent structure occupying the region $y > 0.5\delta$ which also oriented streamwise with an aspect ratio of 2 to 1. This structure, although intermittent, is random, with a convection velocity $U_c = 0.9U_\infty$. The leading edge of these turbulent patches moves slightly faster than the trailing boundary of the patches. The outer nonturbulent flow moves over these turbulent patches somewhat as flow over a corrugated washboard. The turbulent flow within these intermittent regions was also found⁴⁰ to provide approximately 80% of the $\overline{u_1 u_2}$ Reynolds stress and 50% of the total local turbulent kinetic energy in these regions. A connection between the near-wall dynamics and the large-scale turbulent motion in the wake-like region of the turbulent boundary layer is generally regarded as likely.

The flow visualizations of Corino and Brodkey⁶⁴ ($R_\theta = 1000$) and Grass⁶⁵ (smooth and rough free-surface channel flow) show that the occurrence of an event near the wall has an associated local deflection of the instantaneous streamwise velocity $u_1(y_2, t)$ profile that propagates outward from the wall. Corino and Brodkey identify a sequence of events that involves the ejection process. In the vicinity of $y^+ = 20$ a local deceleration of fluid occurred which is on the order of $0.5 U_1(y_2)$ (where $U_1(y_2)$ is the long time average), and it occupied a vertical extent of $\Delta y_2^+ = 15$. This process was followed with an introduction from above of higher-velocity fluid overtaking the relatively slow-moving patch. This resulted in a local inflection in the instantaneous profile $u_1(y_2, t)$ because of the temporary stratification of slow- and fast-moving fluids. Before the slower-moving fluid could be accelerated

all the way to the wall, its interface with the faster fluid was a sharp shear layer. This shear layer was unstable, erupting violently, ejecting slow-moving ($U(y_2, t) - \bar{U}_1(y_2) < 0$) fluid out into the boundary layer. This process occupied Δy_1^+ of only 20 to 40; it originated at distances from the wall $5 < y_2^+ < 15$ regardless of Reynolds number. The correspondence between these visualizations and those of Kline et al.^{51,52} is provided by the fact that the bursting in Kline's case (viewed from above and through the boundary layer) was preceded by oscillations near $y_2^+ = 10$, with ejections occurring between $y_2^+ = 10$ to 30. We note in passing that similar observations of the instantaneous character of $U_1(y_2, t)$ had been made as early as 1932 by Fage and Townend.⁶⁶ More recent and novel visualizations of Offen and Kline⁵⁷ were made using simultaneous emissions by hydrogen bubbles from a small wire, wall-slot dye injection, and dye injection from a pitot tube. This combination facilitated the coordinated identification of structures in two orthogonal planes as well as the observation of local entrainment of fluid moving from upstream by the wall structure. Figure 7.22a shows the salient features of the observations of Offen and Kline. Oscillations of wall dye in the y_1, y_2 plane were simultaneously associated with zones of high shear in $U_1(y_2, t)$ (I and II). In this zone a region of high vorticity oriented in the y_1 or y_3 direction soon developed (II). Ejections of wall dye into the boundary layer occurred after the formation of the vortices at the point at which the vortex passed closest to the wall (III). Just prior to the development of high shear regions, fluid sweeps toward the wall from the logarithmic region (IV), while just downstream of the bursting location another sweep was developing at the head of the vortex formed by the ejection (IV). This observation led to Offen and Kline's conclusion that the interaction between the sublayer and logarithmic region is provided by the burst, which generates the sweep that, in turn, precedes another burst. The burst period scales on outer variables because the rate of ejection or bursting is determined by the motion of vortices in the logarithmic region.

Turbulence events near the wall have been related to a locally adverse fluctuating wall pressure gradient by Burton⁶⁷ ($R_\theta \approx 4000$). Signal conditioning was used to gate the sampling of wall pressure fluctuations with the occurrence of a decrease of U_1 corresponding to a retardation at $y_2^+ = 15$. No pressure disturbance was observed to be associated with a sweep. Offen and Kline⁵⁸ had also postulated a connection between a locally adverse fluctuating wall pressure gradient and the occurrence of a shear layer and the local separation near the wall.

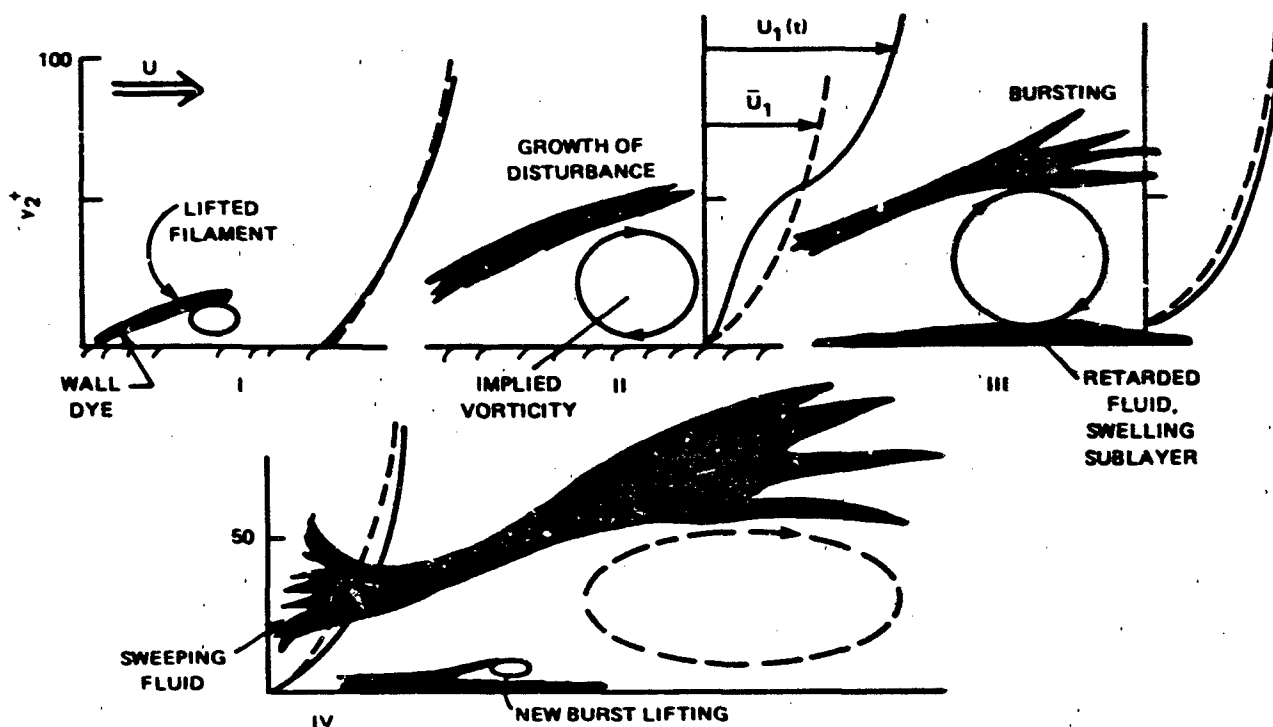


Figure 7.22a - Sequence of Inner-Couter Flow Interactions

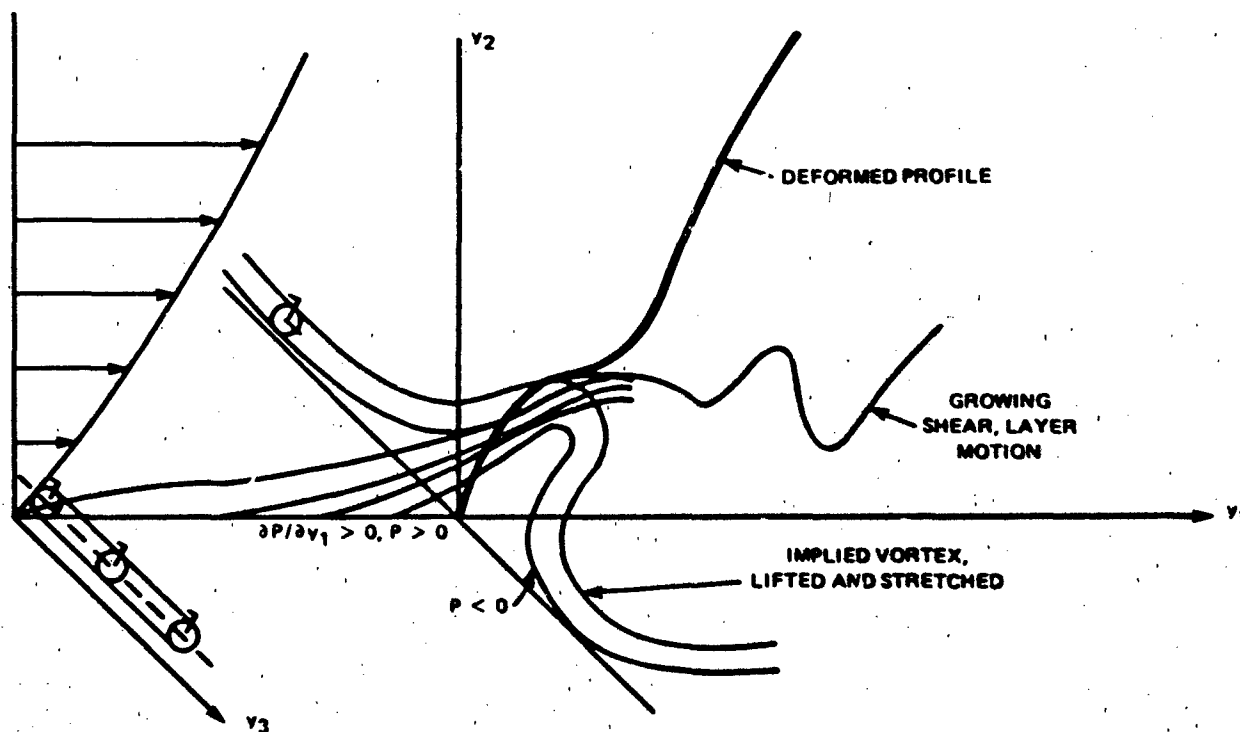


Figure 7.22b - Vortex Representation of Wall Layer

Figure 7.22 - Vortex Structure and Bursting Events Leading to Boundary-Layer Turbulence Production

Figure 7.22b shows a schematic of the previously described vortex representation consistent with the viewpoint illustrated in Figure 7.22a. The implied vorticity generated by the bursting fluid is shown as the apex of a "U" vortex, which, by continuity of vorticity, must be connected to a transversely oriented vortex in the sublayer. The correlation measurements of Tu and Willmarth imply relatively high local pressures inside the "U" or in the region of the slow-moving streak and relatively low pressures where the streamwise vortex intersects the wall. The adverse gradient implied by the existence of sweeps toward the wall is consistent with Tu and Willmarth's and Burton's correlation results.

A relationship between u_1 and u_2 fluctuations has already been implied; a sweeping motion $u_1 > 0$ is correlated with a movement of fluid near the wall, $u_2 < 0$. Conversely, the bursting involves the ejection, $u_2 > 0$, of low-speed fluid, $u_1 < 0$. Quantitative relationships between extrema in the total velocities (as opposed to fluctuations $u_i = U_i - \bar{U}_i$) U_1 and U_2 have been drawn by a number of investigators.^{61,65,68-72}

The theoretical connection between these events and the energetics of turbulence is seen by reference to Equation (7.55). The instantaneous production is afforded by $-u_1 u_2 > 0$, while instantaneous dissipation occurs when large gradients of velocity occur. Thus, near the wall, where both large products of $(-u_1 u_2)$ and large local shear du_1/dy_2 occur, both dissipation and production are important. A quantitative experimental connection between the bursting process and the maintenance of boundary layer turbulence was made by Kim et al.⁶⁸ and Wallace et al.⁷¹ (see also the discussion by Mollo-Christensen⁵⁴). Signal conditioning has been used to isolate the various classes of Reynolds stress contributions by Willmarth and Lu,⁶⁹ Brodkey et al.,⁷² and Lu and Willmarth.⁶¹

The measurements of Willmarth and Lu⁶⁹ and Lu and Willmarth⁶¹ at high Reynolds number showed a variety of u_1, u_2 combinations that were categorized into quadrants depending on the sign combination of the velocity fluctuations. For either both positive (first quadrant) or both negative (third quadrant) $\overline{u_1 u_2}$ was positive and comparable. The contribution of each of these two quadrants was on the order (0.2) of $(-\overline{u_1 u_2})$ throughout the boundary layer, where

$$\overline{u_1 u_2} = \sum_i (u_1 u_2)_i$$

and $i = 1, 2, 3, 4$ identifies the quadrant. $\overline{u_1 u_2}$ is as always the total Reynolds shear stress. On the other hand, Willmarth and Lu found that throughout the boundary layer for the burst $(u_1 u_2)_2 / \overline{u_1 u_2} = 0.77$ and for the sweep $(u_1 u_2)_4 / \overline{u_1 u_2} = 0.55$, which shows that the burst event slightly dominates the total $\overline{u_1 u_2}$. The implication of these two magnitudes is that the production of turbulence is controlled by the burst event.

There is no known quantitative relationship between the wall pressure fluctuations and the results of conditionally sampled Eulerian measurements and these Lagrangian visualizations besides that measured by Burton⁶⁷ and suggested by others, e.g., Offen and Kline.^{57,58} Furthermore, as shown by the pressure-velocity correlations of Tu and Willmarth⁵⁵ and Willmarth and Tu,⁵⁶ a locally negative wall pressure fluctuation can be connected to the base at the wall of the stretched U-shaped vortex that results from the bursting event, and a locally positive wall pressure fluctuation occurs at the center of the U vortex (which had been a region of low momentum just downstream of a sweep event). Thus some kind of connection between wall pressure fluctuations and large turbulent structures is indicated, but the nature of the connection and how this relationship controls variation of various parts of the wave number frequency spectrum remains to be seen. It was stated at the beginning of this section that these organized structures were not clearly evident from even two-point correlations of velocity fluctuations (except in a crude sense) and not evident at all in conventional single-point time-averaged intensity measurements. It was only through the combined use of carefully conducted visualization and signal-conditioning measurements that these structures became apparent. The same holds true for wall pressure fluctuations. In using local point pressure signals and signal conditioning of $u_1(y_2^+ = 15)$, Burton⁶⁷ was able to observe only a relatively small quantitative connection between the production structure and wall pressure. Spatial filtering of the wall pressure signal in addition to temporal signal conditioning may be required.

3 ANALYTICAL DESCRIPTIONS OF THE WALL PRESSURE FIELD

3.1 General Relationships

Various analytical relationships between the fluctuating wall pressure and the velocity field in the adjacent boundary layer have been proposed. These formulations result from three basic points of view. The earliest and most prevalent line

of reasoning⁷³⁻⁸⁹ essentially begins with Equation (2.52) or its analog for incompressible flow. The acoustic wave equation, or the Poisson equation if strictly incompressible flow is assumed, is manipulated into an integral equation similar to Equation (2.57) using the methods of Chapter 2. The resulting expression is then subjected to various simplifying assumptions that generally conform to existing experimental observations and intuitive reasoning. A second approach^{90,91} examines the wave mechanical properties of disturbances that may be sustained by the streamwise velocity profile in the boundary layer. These analyses yield eigenmode solutions for velocity fluctuations that are kinematically related to the pressure fluctuations through the equations of motion. Analytical predictions of wave phase speeds and spatial decay rates conform very well to observed statistics of the turbulent velocity and pressure fields. In this analysis the equations of motion are rearranged so that linear first-order velocity fluctuations are driven by the nonlinear second-order fluctuations. The method focuses on a series of wave harmonic velocity fluctuations as solutions to the equations. The resulting pressures are then found. The influence of slight fluid compressibility is examined⁹² in what may be called a third method. Here a solution for the pressure fluctuations was found as an expansion of powers of (small) Mach number. This approach emphasized the importance of disturbances that induce long-scale (low wave number in the streamwise direction) pressure fluctuations that can create acoustic radiation.

The implementation of the acoustic approximation (Equation (2.6)) in Equation (2.52) yields the relationship

$$\frac{1}{c_o^2} \frac{\partial^2 p}{\partial t^2} - \nabla^2 p = \frac{\partial^2 \rho_o (u_i u_j - \overline{u_i u_j})}{\partial y_i \partial y_j} \quad (7.57)$$

for the fluctuating pressure p which has zero time average, $\bar{p} = 0$. We have approximated the source term in the turbulent field to include only incompressible Reynolds stresses but still represent both acoustic and hydrodynamic contributions to the pressure. If the boundary layer is assumed to exist on a rigid, flat surface, as illustrated in Figure 7.23, then Equations (2.45), (2.48), and (2.55) give, by the same methods of imaging that provided Equation (2.80) (noting that $\partial r / \partial y_2 = -\partial r' / \partial y_2'$),

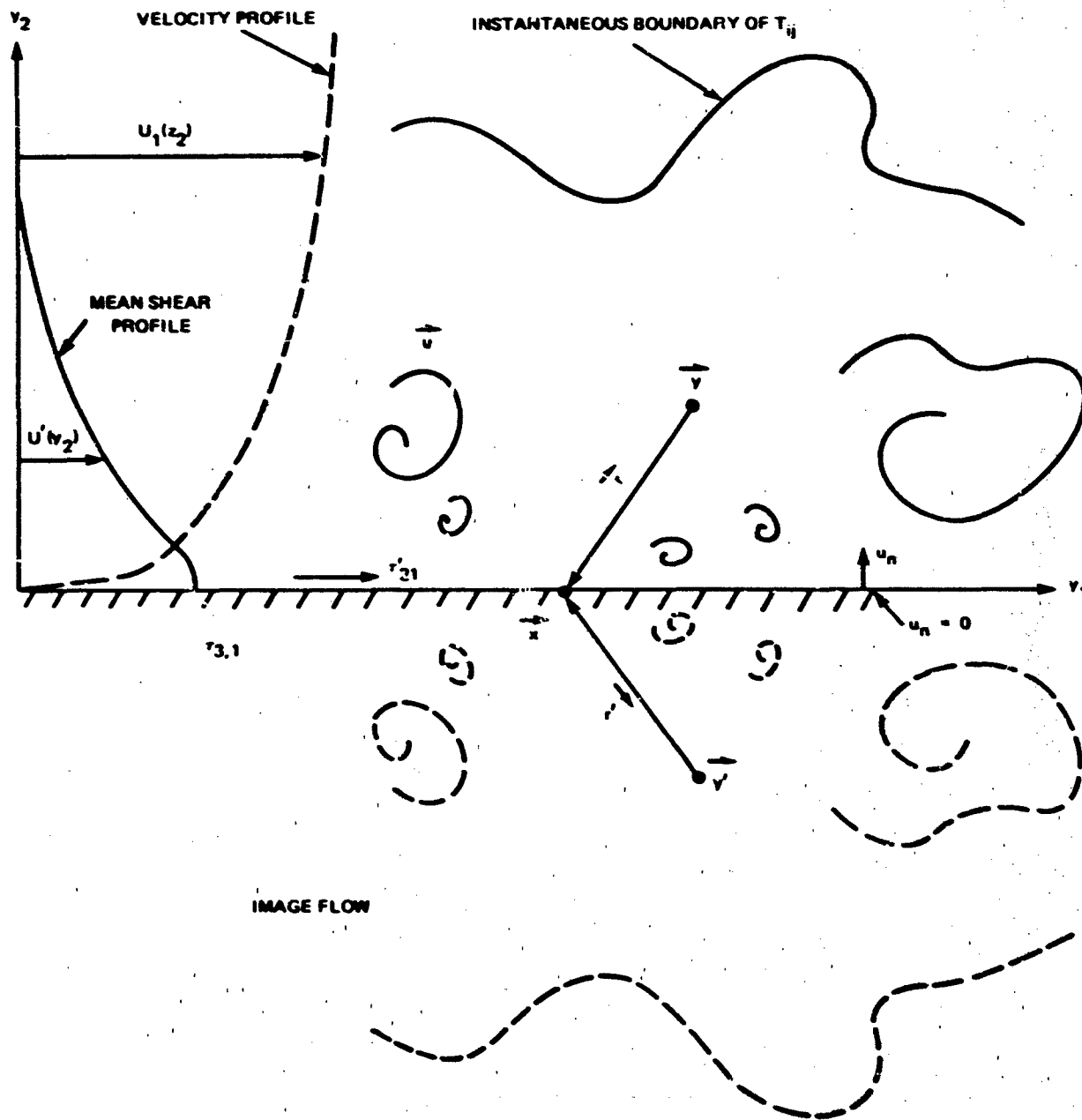


Figure 7.23 - Illustration of the Turbulent Field Adjacent to a Flat and Rigid Boundary

$$p(\vec{x}, t) = \frac{1}{2\pi} \iiint_V \frac{\partial^2 \rho_0 (u_i u_j - \overline{u_i u_j})}{\partial y_i \partial y_j} \frac{d(V(\vec{y}))}{r} - \frac{1}{2\pi} \int_S \frac{\partial \tau'_{i2}}{\partial y_i} \frac{dS(\vec{y})}{r} \quad (i \neq 2) \quad (7.58)$$

The surface integral is over the entire plane $y_2 = 0$ as well as a control surface, which may be assumed to be a hemispherical "dome" at a large distance from the wall location \vec{x} . The τ'_{ij} denotes the viscous part of the stress tensor as represented in Equation (2.48). Note that in Powell's treatment of the radiated sound in Section 2.4.4 the viscous stresses were assumed to be zero.

A solution of the equation 7.58 is greatly simplified if it can be shown that that contribution from τ'_{i2} can be neglected. Below we examine order-of-magnitude arguments which support this neglect in both this problem as well as Powell's (see pp 74-79). The surface shear stress-gradients may be expanded

$$\frac{\partial \tau'_{i2}}{\partial y_i} = \frac{\partial \tau'_{i2}}{\partial y_1} + \frac{\partial \tau'_{i2}}{\partial y_3} \quad (7.59)$$

and on the rigid surface, $y_2 = 0$

$$-\frac{1}{\rho_0} \frac{\partial p}{\partial y_2} + \frac{1}{\rho_0} \frac{\partial \tau'_{i2}}{\partial y_2} = \rho_0 \frac{\partial u_2}{\partial t} = 0 \quad (7.60)$$

where τ'_{i2} is the shear stress at the wall (neglecting bulk viscosity)

$$\begin{aligned} \tau'_{i2} &= \mu \left(\frac{\partial u_i}{\partial y_2} + \frac{\partial u_2}{\partial y_i} \right) \Big|_{y_2=0} \quad i \neq 2 \\ &= \mu \frac{\partial u_i}{\partial y_2} \Big|_{y_2=0} \quad i \neq 2 \end{aligned} \quad (7.61)$$

The integrand in the surface integral is equal to the normal gradient of the fluctuating pressure and the gradient of the fluctuating wall-shear stress in the wall plane. The surface integral has been shown by Kraichnan⁷³ and Burton⁶⁷ to be a negligible contribution to the wall pressure. At the wall, $u_1 = 0$; therefore, by Equations (7.60) and (7.61), the normal derivative of the fluctuating pressure is

$$\frac{1}{\rho_0} \frac{\partial p}{\partial y_2} = \nu \frac{\partial^2 u_2}{\partial y_2^2} \quad (7.62)$$

From the continuity equation

$$\frac{\partial u_2}{\partial y_2} = - \frac{\partial u_1}{\partial y_1} - \frac{\partial u_3}{\partial y_3}$$

and therefore

$$\frac{\partial^2 u_2}{\partial y_2^2} = - \frac{\partial}{\partial y_2} \left(\frac{\partial u_1}{\partial y_1} + \frac{\partial u_3}{\partial y_3} \right) = - \frac{\partial}{\partial y_1} \frac{\partial u_1}{\partial y_2} - \frac{\partial}{\partial y_3} \left(\frac{\partial u_3}{\partial y_2} \right) \quad (7.63)$$

Very near the wall, measurements show the order of $(u_1^2)^{1/2} \approx 0.2 U_1$ so that approximately

$$\left(\frac{\partial u_1}{\partial x_2} \right)^2 \approx 0.2 \frac{\partial U_1}{\partial x_2} \quad (7.64)$$

Also, it is reasoned by Kraichnan that $\partial u_1 / \partial x_1 \approx \partial u_3 / \partial x_3$. Thus an upper bound on $\partial u_2 / \partial y_2$ may be obtained by considering the contribution of u_1 alone. Equation (7.64) is rewritten

$$\left(\frac{\partial u_1}{\partial x_2} \right)^2 \approx 0.2 \frac{\tau_w}{\mu} \quad (7.65)$$

If ℓ is a length scale of the turbulence and we approximate $\partial/\partial x_1$ as ℓ^{-1} , then, by Equation (7.63),

$$\lim_{y_2 \rightarrow 0} \left(\frac{\partial^2 u_2}{\partial y_2^2} \right) \approx 0.2 \frac{\tau_w}{\mu \ell}$$

and, by Equation (7.62),

$$\overline{\left(\frac{\partial p}{\partial y_2} \right)^2}^{1/2} \approx 0.2 \frac{\tau_w}{\ell} \quad (7.66)$$

$$y_2 = 0$$

In the body of the turbulence field, however, the root mean square of the normal gradient of the pressure is on the order

$$\begin{aligned} \overline{\left(\frac{\partial p}{\partial y_2} \right)^2}^{1/2} &= \rho_o \frac{u_2^2}{\ell} = \rho_o \frac{U^2}{\ell} \\ &= \frac{\tau_w}{\ell} \end{aligned} \quad (7.67)$$

The upper bound of Equation (7.66) compared to the approximation of Equation (7.67) led Kraichnan to deduce that $\partial p/\partial y_2$ at $y_2 = 0$ is at least rather small relative to its value in the flow; therefore he assumed

$$\left(\frac{\partial p}{\partial y_2} \right)_{y_2 = 0} = 0$$

An alternative line of reasoning by Burton⁶⁷ relies on measured values of fluctuating wall shear stress and its spatial macroscale. By Equation (7.60) on $y_2 = 0$

$$\frac{\partial p}{\partial y_2} = \frac{\partial \tau_{12}}{\partial y_2}$$

Burton assumed that $\tau_{i2} = \tau_{12} + \tau_{32} \approx 2\tau_w^2$ so that

$$\left(\frac{\partial p}{\partial y_2} \right)^2 \bigg|_{y_2=0} \approx 2 \frac{\tau_w^2}{\Lambda_\tau^2}$$

where τ_w^2 is the root-mean-square wall shear and Λ_τ is an integral length scale of the fluctuating wall shear in the plane of the plate. The mean square of the surface integral in Equation (7.58) can be approximated by

$$\overline{p_{\text{surf}}^2} \approx A_c \left(\frac{\partial \tau_{i2}}{\partial y_i} \right)^2 \approx \frac{A_c}{\Lambda_\tau^2} \tau_w^2$$

where A_c is the correlation area of the wall-shear fluctuations. Burton's measurements show that $\tau_w^2 \approx 0.004 \overline{p_{\text{surf}}^2}$; thus, if $A_c \approx \Lambda_\tau^2$, then

$$\begin{array}{l} \overline{p_{\text{surf}}^2} \\ \text{integral} \\ \text{contribution} \end{array} \approx 0.004 \begin{array}{l} (\overline{p^2})_{\text{total}} \\ \text{wall} \\ \text{pressure} \end{array} \quad (7.68)$$

indicating that the contribution of the surface integral to the root mean square is only on the order of 6%. This is in contrast, however, to the larger share suggested in Section 7.3.7.

These arguments show convincing evidence that the surface integral in Equation (7.58) may be neglected compared to the volume integral, at least where the non-acoustic, near-field fluctuating wall pressures are concerned. We proceed in a manner analogous to the development used in Section 3.6.1, except that we deal with near-field rather than far-field pressures and ignore source convection.

Thus we have fluctuating pressure in the fluid on or above a rigid planar wall given by

$$p(\vec{x}, t) = \frac{1}{2\pi} \iiint_V \left[\frac{\partial^2 \rho_0 (u_i u_j - \overline{u_i u_j})}{\partial y_i \partial y_j} \right] \frac{dV(\vec{y})}{r} \quad (7.69)$$

where the brackets denote the retardation, as the starting point for most of the analyses.^{73-85,86,87} In analyzing wall pressures, Lilley⁷⁶ and Ffowcs-Williams⁷⁷ replaced Equation (7.69) by its three-dimensional Fourier transform using the definition

$$\tilde{p}(\vec{k}, \omega) = \frac{1}{(2\pi)^3} \iiint_{-\infty}^{\infty} e^{-i(\vec{k} \cdot \vec{X} - \omega t)} p(\vec{X}, t) d\vec{X} dt \quad (7.70)$$

where \vec{k} is the wave vector in the plane of the surface, $\vec{k} = (k_1, k_3)$, $\vec{X} = X_1, X_3$. Operating Equation (7.70) on Equation (7.69) and letting

$$\begin{aligned} T_{ij}(\vec{y}, t - \frac{|\vec{r}|}{c_0}) &= T_{ij}(\vec{y}, t) \\ &= \int_{-\infty}^{\infty} \tilde{T}_{ij}(\vec{y}, \omega) e^{-i\omega(t - |\vec{r}|/c_0)} d\omega \end{aligned} \quad (7.71)$$

where

$$\begin{aligned} r^2 &= (x_1 - y_1)^2 + y_2^2 + (x_3 - y_3)^2 \\ &= |\vec{x} - \vec{y}|^2 \end{aligned}$$

we obtain, invoking Equation (2.123),

$$\tilde{p}(\vec{k}, \omega) = \frac{1}{(2\pi)^2} \iiint_V dV(\vec{y}) \frac{\partial^2 T_{ij}(\vec{y}, \omega)}{\partial y_i \partial y_j} \iint_{-\infty}^{\infty} d\vec{X} \frac{e^{-i\vec{k} \cdot \vec{X} + i k_0 |\vec{r}|}}{r} d\omega \quad (7.72)$$

Since

$$\frac{1}{2\pi} \iint_{-\infty}^{\infty} \frac{e^{+i k_0 r}}{r} e^{+i \vec{k} \cdot \vec{X}} d\vec{X} = \frac{+i \exp \left[+i y_2 (k_0^2 - k^2)^{1/2} \right]}{(k_0^2 - k^2)^{1/2}} e^{+i \vec{k} \cdot \vec{y}} \quad (7.73)$$

with the convention $(-1)^{\frac{1}{2}} = i$ for $y_2 > 0$, Equation (7.72) becomes

$$\tilde{p}(\vec{k}, \omega) = \frac{+i}{(2\pi)^2} \iiint \frac{\partial^2 \tilde{T}_{ij}(\vec{y}, \omega)}{\partial y_i \partial y_j} \frac{e^{+iy_2(k_o^2 - k^2)^{\frac{1}{2}}}}{(k_o^2 - k^2)^{\frac{1}{2}}} e^{-i\vec{k} \cdot \vec{y}} dV(\vec{y}) \quad (7.74)$$

Integration by parts over the infinite volume gives

$$\begin{aligned} \tilde{p}(\vec{k}, \omega) = & \frac{1}{(2\pi)^2} \iiint \tilde{T}_{ij}(\vec{y}, \omega) \left[(k_o^2 - k^2)^{\frac{1}{2}} \delta_{i2} + k_i \right] \left[(k_o^2 - k^2)^{\frac{1}{2}} \delta_{j2} + k_j \right] \\ & \cdot \frac{e^{+iy_2(k_o^2 - k^2)^{\frac{1}{2}}}}{(k_o^2 - k^2)^{\frac{1}{2}}} e^{-i\vec{k} \cdot \vec{y}} dV(\vec{y}) \quad i, j = 1, 3 \text{ on } k \end{aligned} \quad (7.75)$$

Equation (7.75), first obtained by Ffowcs Williams,⁷⁷ is particularly valuable for our purposes because it can be used to illustrate the most important physical aspects of the generation of surface pressures of various length scales and frequencies by adjacent turbulent boundary flow.

We can rewrite Equation (7.75) in terms of the Fourier transform of the source density:

$$\tilde{T}_{ij}(y_2, \vec{k}, \omega) = \frac{1}{(2\pi)^2} \iint_{-\infty}^{\infty} \tilde{T}_{ij}(\vec{y}, \omega) e^{-i\vec{k} \cdot \vec{y}} dy_1 dy_3 \quad (7.76)$$

so that the wave number transform of the pressure is

$$\begin{aligned} \tilde{p}(\vec{k}, \omega) = & i \int_0^{\infty} \tilde{T}_{ij}(y_2, \vec{k}, \omega) \left[(k_o^2 - k^2)^{\frac{1}{2}} \delta_{i2} + k_i \right] \left[(k_o^2 - k^2)^{\frac{1}{2}} \delta_{j2} + k_j \right] \\ & \cdot \frac{e^{+iy_2(k_o^2 - k^2)^{\frac{1}{2}}}}{(k_o^2 - k^2)^{\frac{1}{2}}} dy_2 \end{aligned} \quad (7.77)$$

The wave number frequency spectrum of the wall pressure fluctuations homogeneous in the 1,3 plane is quadratically related to the modulus of $\tilde{p}(\vec{k}, \omega)$ by Equation (3.45), i.e.,

$$\phi_p(\vec{k}, \omega) \delta(\vec{k} - \vec{k}') \delta(\omega - \omega') = \langle p(\vec{k}, \omega) p(\vec{k}', \omega) \rangle \quad (7.78)$$

where the brackets denote an ensemble average.

Using the relationships of Section 3.5.3, the above relationships can be used to find either the cross-correlation function of the wall pressure, related to the spectral density (Equation (7.78)), by

$$\overline{p^2} R_{pp}(\vec{r}, \tau) = \iiint_{-\infty}^{\infty} e^{i(\vec{k} \cdot \vec{r} - \omega \tau)} \phi_p(\vec{k}, \omega) d\vec{k} d\omega \quad (7.79)$$

or the spatial cross-spectral density of the wall pressure, which is

$$\phi_p(\vec{r}, \omega) = \iint_{-\infty}^{\infty} e^{i\vec{k} \cdot \vec{r}} \phi_p(\vec{k}, \omega) d\vec{k} \quad (7.80)$$

or

$$\phi_p(\vec{r}, \omega) = \frac{1}{2\pi} \int_{-\infty}^{\infty} e^{i\omega \tau} \overline{p^2} R_{pp}(\vec{r}, \tau) d\tau \quad (7.81)$$

Thus, hypothetically, we can determine any of the spectral functions by simple manipulations of Equation (7.77) or (7.84) as long as the source function $\tilde{W}_{ij}(y_2, \vec{k}, \omega)$ is known. As we shall see later, the use of Equation (7.77) or (7.84) for prediction is, in fact, severely limited by our inadequate knowledge of the source term; however, we will examine the possible relationships between the spectral characteristics of the source and the wave number spectrum of the wall pressure.

An important component due only to the presence of a mean velocity profile, du_1/dy_2 , is called the mean-shear-turbulence interaction, and it depends on a

quantity $U_1(y_2) u_2(y_2)$. For a planar incompressible boundary layer, this is seen by expanding the source function given in Equation (7.69), which reduces to

$$\frac{\partial^2 (u_1 u_j - \overline{u_1 u_j})}{\partial y_1 \partial y_j} = 2 \frac{\partial U_1}{\partial y_2} \frac{\partial u_2}{\partial y_1} + \frac{\partial^2 (u_1 u_j - \overline{u_1 u_j})}{\partial y_1 \partial y_j} \quad (7.82)$$

then the term

$$\frac{\partial^2 U_1 u_2}{\partial y_1 \partial y_2} = \frac{\partial^2 U_1 u_1}{\partial y_1 \partial y_2} + \frac{\partial^2 U_1 u_3}{\partial y_1 \partial y_3}$$

is expanded using the divergence theorem for incompressible flow to remove terms like $\partial u_1 / \partial y_2$ and $\partial u_3 / \partial y_3$. When dealing with this source in applications of incompressible flow, it is best to derive an alternative to Equation (7.77) even though that equation is formally correct for both compressible or incompressible flow. Letting

$$\tilde{u}_2(y_2, \vec{k}, \omega) = \frac{1}{(2\pi)^2} \iint_{S_{1,3}} \tilde{u}_2(\vec{y}, \omega) e^{-i\vec{k} \cdot \vec{y}} dy_1 dy_3 \quad (7.83)$$

we find $\tilde{p}(\vec{k}, \omega)$ from the mean-shear interaction to be given by

$$\tilde{p}_{MS}(\vec{k}, \omega) = i \int \frac{\partial U_1}{\partial y_2} \frac{k_1 \tilde{u}_2(y_2, \vec{k}, \omega)}{(k_o^2 - k^2)^{1/2}} e^{i y_2 (k_o^2 - k^2)^{1/2}} dy_2, \quad k > k_o \quad (7.84)$$

and the second term (which has been called⁷³ the turbulence-turbulence contribution) is still given directly by the initial result (Equation 7.77).

The wall pressures resulting from the nonlinear turbulence-turbulence terms* are not examined explicitly in this text. This contribution has received some

*Responsible for "shear noise" in the modeling of jet noise by Ribner (see Chapter 3).

attention in the past^{73,80} and again recently.^{86,87} It is generally regarded to be of secondary (though not necessarily trivial) importance to the boundary layer pressures, but a precise value is still unknown. Kraichnan estimated the importance of the nonlinear terms by assuming the turbulence statistics to be Gaussian and expanding the fourth-order statistics into a series of terms that included second-order statistics. Subsequent order-of-magnitude evaluations of the terms involved led to the conclusion that

$$\frac{\overline{P_{MS}^2}}{\overline{P_{TT}^2}} \approx \frac{4}{15 C_f} \gg 1$$

In more recent modeling, Chase⁸⁶ found evidence indicating a ratio that is more nearly 2.5, while Meecham and Travis⁸⁷ calculated a value

$$\frac{\overline{P_{MS}^2}}{\overline{P_{TT}^2}} \approx 10$$

for a turbulence model based on a Gaussian-isotropic hypothesis.

7.3.2 Overall Considerations of the Wave Number Spectrum

The wave number frequency spectrum of the terms in the stress tensor is peaked at a wave number $k_1 \delta = \omega \delta / U_c$, due to the convected nature of the turbulence (see Section 7.2.5). The establishment of more specific wave number frequency behavior particularly for the range $k_1 \delta \ll \omega \delta / U_c$ is the subject of rather extensive and complex analysis,^{73-76,80-82,85,86,243,244} especially if interest is in the pressure contributions due to low wave number turbulence fluctuations that exclude the energy-containing eddies. Here we consider some important generalities of the wave number spectrum reserving for the next section some simplified analytical quantification.

We first note that in Equations (7.77) and (7.84) an important relationship exists between the wave number of pressure k and the wave number of sound $k_o = \omega / C_o$

that influences the transmission of disturbances to the wall. The exponential involving $(k_o^2 - k^2)^{1/2}$ takes on the behavior ($y_2 > 0$)

$$e^{+iy_2 (k_o^2 - k^2)^{1/2}} = e^{+iy_2 k_o} \quad k \ll k_o$$

$$= e^{-y_2 k} \quad k \gg k_o$$

thus for subsonic wave numbers ($k > k_o$), pressure disturbances of a given wave number decay with increasing distance from the source. For sonic and supersonic wave numbers ($k' < k_o$), however, the disturbance is transducted without exponential attenuation. For $k = k_o$ there is an apparent singularity in the spectrum. For wave numbers between the limits $k_o < k < \delta^{-1}$ subsonic disturbances are transducted through the boundary layer with only slight attenuation. Thus at these values of wave number the contributions to the wall pressure come from throughout the turbulent boundary layer; for $k \gg \delta^{-1}$ the pressures are the result of a complex source distribution arising from eddy motions.

We consider three distinct regions of wave number, illustrated in Figure 7.24, noting that for $k < 0$ (k_o) we must deal with the complete source function (Equation (7.77)) because the incompressibility approximation leading to Equation (7.83) is invalid.

a. For $k \leq k_o$, Equation (7.77) yields a propagating pressure,

$$\hat{p}(\vec{k}, \omega) = i \int_0^\infty \hat{\gamma}_{ij}(y_2, \vec{k}, \omega) \cdot k_o e^{+iy_2 k_o} dy_2 \quad (7.85)$$

so that the wave number spectrum of wall pressure is

$$\Phi_{pp}(\vec{k}, \omega) = \bar{\Phi}_{ij}(\vec{k}, \omega) \rho_o^2 k_o^2 \delta^2 U_\tau^4, \quad k_1 < k_o \quad (7.86a)$$

$$= \bar{\Phi}_{ij}(\vec{k}, \omega) \rho_o^2 U_\tau^4 M^2 \left(\frac{\omega \delta}{U_c} \right)^2 \quad (7.86b)$$

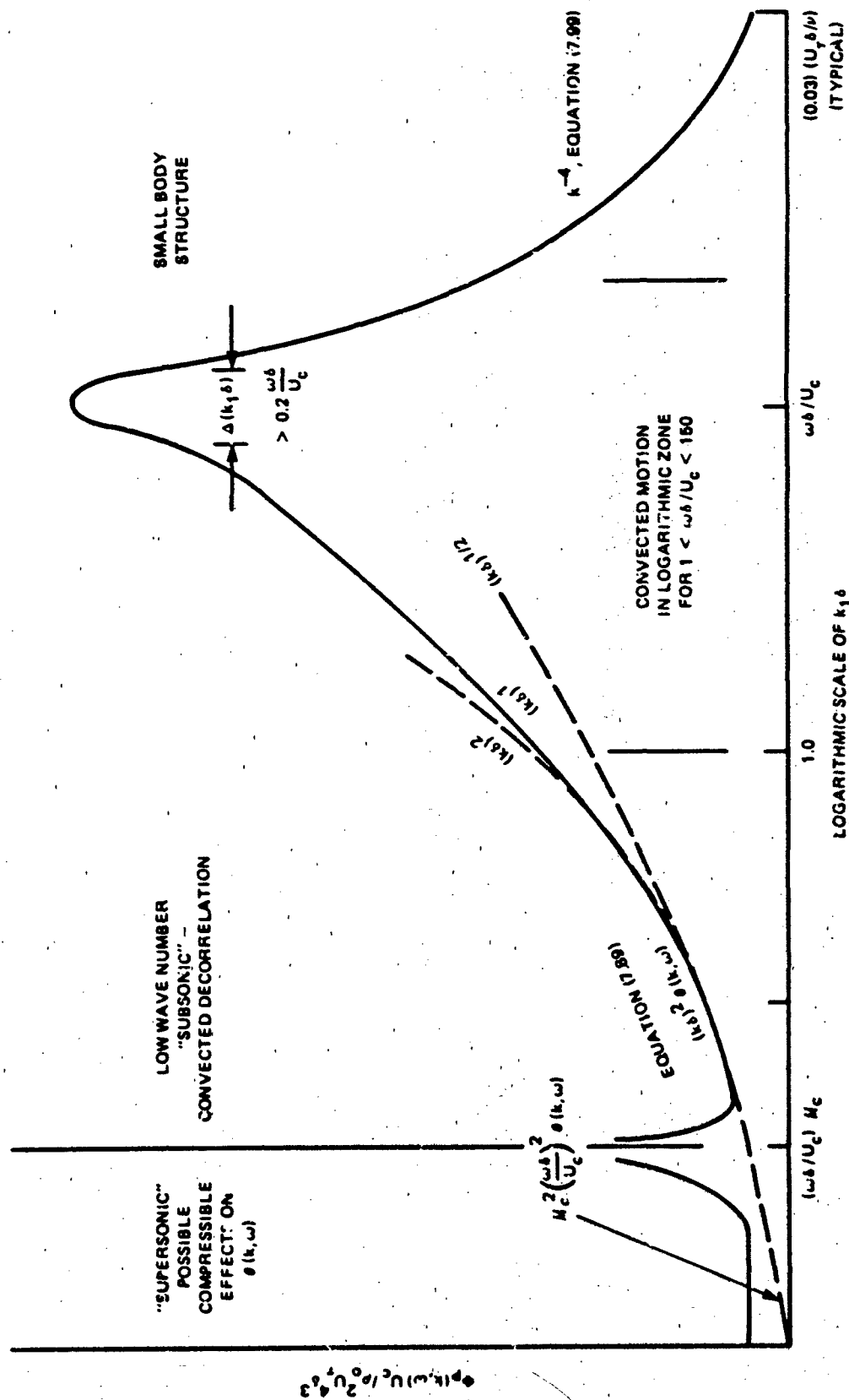


Figure 7.24 - Wave Number Spectrum of Boundary-Layer Pressure Theoretically Determined Using Velocity Correlations in the Appropriate Wave Number Ranges, $k_1 = (k_1, 0)$

a velocity magnitude is assumed for now to scale on the friction velocity U_τ in accordance with properties discussed in Section 7.2. The dimensionless spectrum function $\bar{\phi}_{ij}$ represents an average over y_2, y_2' of the general spectrum, which is formally defined by

$$\begin{aligned} \bar{\phi}_{ijkl}(y_2, y_2', \vec{k}, \omega) &= \left[\bar{\tau}_{ij}(y_2, \vec{k}, \omega) \bar{\tau}_{ij}(y_2', \vec{k}', \omega') \right] / U_\tau^4 \\ &\quad \left[\delta(\vec{k} - \vec{k}') \delta(\omega - \omega') \right]^{-1} \overline{(u_i u_j)} \overline{(u_k u_l)}^{-1} \\ &= \frac{1}{(2\pi)^3} \iiint R_{ijkl}(y_2, y_2', \vec{r}_s, \tau) e^{-i(\vec{k} \cdot \vec{r}_s - \omega \tau)} d\vec{r}_s d\tau \quad (7.87) \end{aligned}$$

it certainly no measurement of it has been made. Essentially, it should have qualitatively similar properties to the source function considered for turbulent flows (Section 3.6.3).

If $\phi_{ij}(\vec{k}, \omega)$ scales on δ and U_c as a dimensionless quantity, then $\phi_{ij} = \phi_{ij}(\vec{k}, \omega) U_c / \delta^3$, and similarly for the spectrum $\phi_p(\vec{k}, \omega)^*$. The wave number spectrum of the pressure is thus seen to be independent of $k = (k_1^2 + k_2^2)^{1/2}$ at low k and to increase quadratically with frequency depending on the behavior of $\phi_{ij}(\vec{k}, \omega)$. In this "super-sonic" range the effect of Mach number is important.

The special case of $k = k_0$ arises because of the formal singularity in the $(k_1^2 + k_2^2)^{-1/2}$ of Equation (7.77). Methods of removing this singularity are discussed in Section 8.5.2. In one method Bergeron⁹² and later Ffowcs Williams²⁴⁰ noted that the singularity is partly the result of having assumed the existence of strictly infinite and homogeneous flow on a rigid plane. Appropriately accounting for the fact that the surface is finite of length L , it is shown that the spectrum level at $k = k_0$ is $(\omega L / C_0)$ times the spectrum level at $k = 0$ (see Equation (8.47)). Other physical limitations on the spectrum level at $k = k_0$ include dissipation and surface compliance (see Section 8.5.2).

*There is no firm position to be taken on the dependence of the wave number spectrum on boundary layer thickness although it shall be used throughout this chapter as a flow length scale. Recent theoretical work by Chase,⁸⁶ in fact postulates that k itself is the dominant length scale.

b. In the range $k_0 < k \ll \delta^{-1}$, Equation (7.77) yields

$$\tilde{p}(\vec{k}, \omega) = i \int_0^\infty \tilde{T}_{ij}(y_2, k, \omega) k e^{-ky_2} dy_2 \quad (7.88)$$

so that as long as $\tilde{T}_{ij}(y_2, k, \omega)$ effectively vanishes outside $y_2 = \delta$,

$$\phi_{pp}(\vec{k}, \omega) = \bar{\phi}_{ij}(\vec{k}, \omega) \rho_0^2 U_c^2 k^2 \delta^2 \quad (7.89)$$

This function shows a quadratic dependence on $k\delta$ that is altered only by possible k dependence of the unknown source spectrum $\bar{\phi}$. Equations (7.86) and (7.89) show that the cross-over frequency above which compressible effects are expected to become significant at a given wave number is

$$\left(\frac{\omega\delta}{U_c}\right)^2 = (k\delta)^2 M_c^{-2}$$

where U_c is the mean convection velocity of the pressures and $M_c = U_c/C_0$.

c. The high wave number range of $\delta^{-1} < k < \infty$ includes the region dominated by turbulence convection, i.e., $k_1 = \omega/U_c$. The source function has a fairly sharp maximum at $k_1 = \omega/U_c$, as illustrated in Figure 7.25. The details of this behavior can be elucidated by referring to the properties of the convected turbulent field. This is seen most clearly in the dominant mean-shear-turbulence interaction, although it could also be seen by working with the turbulence-turbulence interaction. Combining Equations (7.78) and (7.83) in the limit of $k \gg k_0$, we have

$$\phi_{pMS}(\vec{k}, \omega) = 4\rho_0^2 \left(\frac{k_1}{k}\right)^2 \int_0^\infty dy_2 \int_0^\infty dy_2' \left(\frac{\overline{u_2^2} \overline{u_2'^2}}{2}\right)^{1/2} U_1'(y_2) U_1'(y_2') \\ \cdot R_2(y_2' - y_2) \left[\frac{\phi_{22}(\vec{k}, \omega, y_2)}{\left(\frac{\overline{u_2^2} \overline{u_2'^2}}{2}\right)^{1/2}} \right] e^{-k(y_2 + y_2')} \quad (7.90)$$

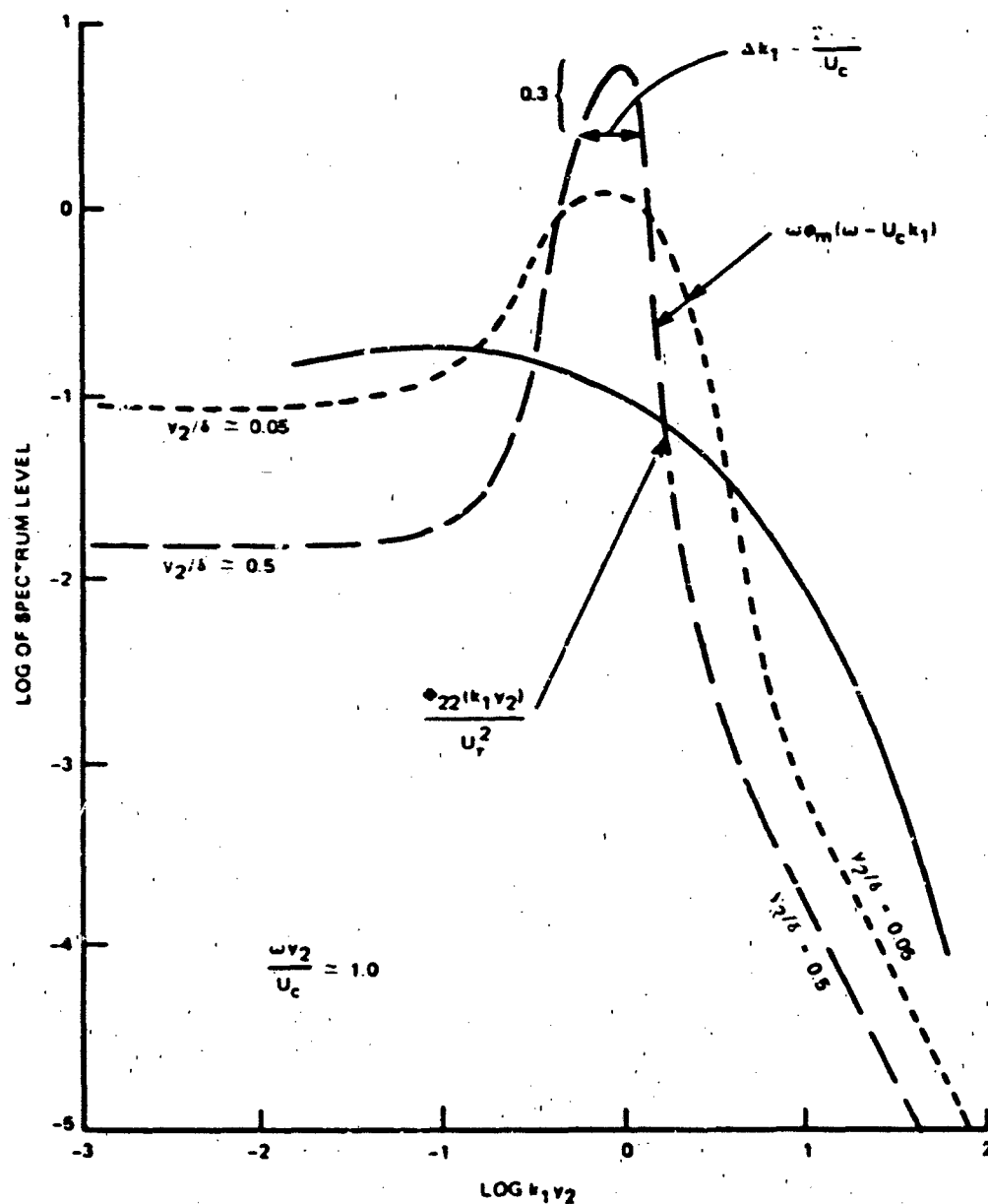


Figure 7.25. Wave Number Frequency Spectra of Velocity Fluctuations, u_2 , Illustrated for the Functions in Equation (7.49) and Using Experimental Data of Figures 7.14 and 7.17; v_1 Depends on v_2 as Shown in Figure 7.17

which is quite similar to relationships derived by Lilley⁷⁶ and Chase.⁸⁶ Abbreviated notation for the profiles of mean-square velocities

$$\overline{u_2^2}(y_2) = \overline{u_2'^2}$$

and

$$\overline{u_2^2}(y_2') = \overline{u_2'^2}$$

have been introduced.

The functions $\left(\overline{u_2^2} \overline{u_2'^2}\right)^{1/2}$ and $U_1(y_2) U(y_2')$ express the intensity of turbulence sources across the boundary layers, $R_2(y_2' - y_2)$ expresses the correlation of eddies at levels y_2 and y_2' (see, for example, the discussion of Equation (7.50)), and $\phi_{22}(\vec{k}, \omega)$ (e.g., Equation (7.48)) expresses the wave number frequency content of those eddies. At high enough wave numbers, $k > \delta^{-1}$, we may consider that $R_{22}(y_2' - y_2)$ nearly vanishes for $\delta \gg y_2' - y_2 > \Lambda_2$ so that the turbulence field is regarded as stratified in layers Λ_2 thick. In each layer the velocity fluctuations have the wave number decomposition suggested by Equation (7.49) and illustrated in Figure 7.25. Specifically, the turbulence in each strata is assumed to be convected at a speed $U_c = \omega/k_1$, as suggested by the measurements and Bradshaw's⁴³ proposition that velocity fluctuations of wave number k_1 are situated at distances from the wall y_2 such that $k_1 y_2 = \text{constant}$ is maintained. These notions result in the view that the pressures are imposed on the wall by the convected turbulence in such a manner that $\phi_p(\vec{k}, \omega)$ also has its maximum values near $k_1 = \omega/\bar{U}_c$, $k_3 = 0$ where \bar{U}_c is an average convection velocity of the turbulent pressures. The shape of the spectrum is essentially a result of the combined effects of the turbulence strata. Figure 7.25 shows that the dimensionless spectrum of the pressure sources broadens near convective wave numbers as the wall is approached. In evaluating Equation (7.90), this density function must be weighted by a magnitude function (Figure 7.26) that is strongly peaked near the wall. The pressure spectrum (Figure 7.24) reflects the resultant convective behavior of the pressure sources.

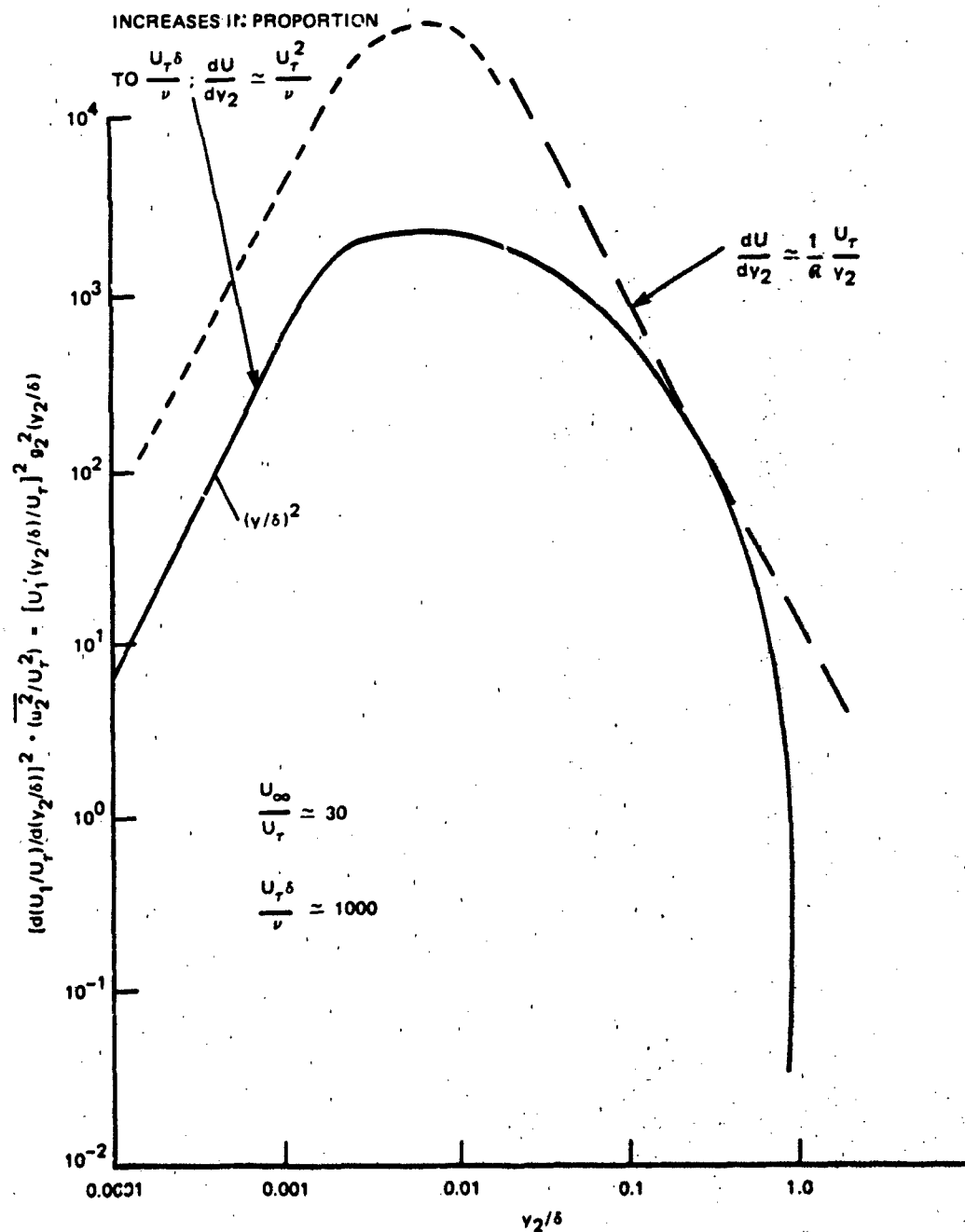


Figure 7.26 - Source Distribution Function for Mean Shear Turbulence Component of Wall Pressure on Smooth Walls (see Equation (7.104))

7.3.3 Features of Turbulence Structure Affecting the Wave Number Spectrum of Wall Pressure

Quantitative evaluation of Equation (7.90) is predicated on an effective model of the wave number spectrum of the turbulence and the correlation function in planes parallel to the wall. One such model has already been given as Equation (7.49), in which the functions in r_2 , k_1 , and k_3 are separable, although alternate expressions have been proposed by Chase^{85,86} following upon the work of Kronauer and co-workers,⁹³⁻⁹⁵ who do not separate the functional behavior in r_2 , k_1 , k_3 . That work is referred to later in this section. Lilley⁷⁴⁻⁷⁶ also used a separable model and expressed the correlation function of r_2 alternatively as^{74,76} $\exp [-(r_2/\ell_2)^2]$ and $\exp [-(r_2/\ell_2)]$.⁷⁵ There are certain advantages to the nonseparable representation,^{85,86} since it permits a more general dependence on wave number and wave direction that is prohibited when the separable models are used. However, separability permits a certain degree of analytical simplicity and should also effectively portray the convected turbulence sources.

Another point to be brought out with regard to the spatial statistics is indicated by the $(k_1/k)^2 = \cos^2 \theta$ dependence shown in Equation (7.90). Even if the spectrum $\phi_{22}(\vec{k}, \omega)$ has no preference in the k_1, k_3 plane, the spectrum of the pressure fluctuations will be enhanced in the k_1 direction relative to the k_3 direction. This means that spatial correlations will reflect smaller scales in the r_1 direction than in the r_3 direction. Figure 7.27 illustrates this behavior. The iso-correlations of the turbulent velocities are either circular or elliptic in the r_1 direction, but those for the pressure are elongated along r_3 .

The separable source function suggested by Equation (7.49) is rewritten

$$\phi_{22}(\vec{k}, \omega, y_2) = y_2^2 \phi_{22}(\vec{k}y_2) \phi_m(\omega - U_c k_1) \quad (7.91)$$

which may be further separated

$$\phi_{22}(\vec{k}, \omega, y_2) = y_2^2 \phi_{22}(k_1 y_2) \phi_3(k_3 y_2) \phi_m(\omega - U_c k_1) \quad (7.92)$$

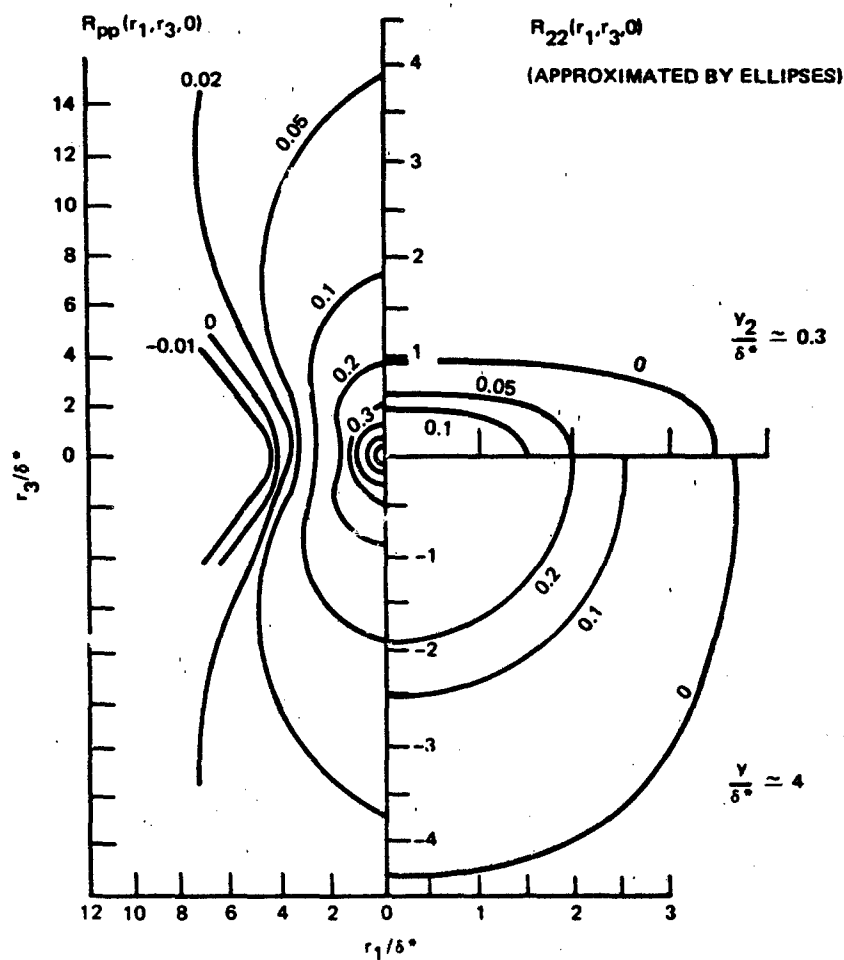


Figure 7.27 - Iso-Correlation Contours of Wall Pressure R_{pp} (From Bull²⁶) and Vertical Velocity Fluctuations R_{22} Above Smooth Walls (From Grant³⁸).

and the correlation function can be written in the approximate form

$$R_2(y_2 - y_2') \approx \Lambda_2 \delta(y_2 - y_2') \quad (7.93)$$

where the integral scale is approximately proportional to the mean distance from the wall,

$$\Lambda_2 \approx y_2 \quad (7.94)$$

The alternative form to Equation (7.92) follows from interpretations of measurements of Morrison and Kronauer,^{93,94} who determined a lateral wave number spectrum by transforming the cross-spectral density with lateral separations

$$\int_{-\infty}^{\infty} \omega \phi_{uu}(k_1, k_3, \omega; y_2) dk_1 = \int_0^{2\pi} \omega \phi_{uu}(\omega, r_1=0, r_3; y_2) e^{ik_3 r_3} dr_3$$

They interpreted their measurements to indicate a superposition of geometrically similar wave-like disturbances giving a general behavior of the spectrum function

$$\phi_{uu}(k_1, k_3, \omega; y_2) = U_\tau^2 g^2\left(\frac{y_2}{\delta}\right) y_2^2 \phi_T(ky_2) A(k_1, k_3) \phi_m(\omega - U_c k_1)$$

where $U_\tau g(y_2/\delta)$ describes the profile of velocity intensities across the boundary layer (e.g., Figures 7.7 to 7.9); $\phi_T(ky_2)$ is a dimensionless turbulence spectral density. It is regarded that the energy density is determined by the wave number magnitude $(k_1^2 + k_3^2)^{1/2} = k$ and that the distribution of energy is uniquely determined by y_2 . Therefore, just as in Equation (7.92), small y_2 implies a concentration energy to higher wave numbers. The function $A(k_1, k_3)$ is a wave direction function independent of y_2 . Chase^{85,86} has suggested that a similar relation exists for the vertical velocity fluctuations, which he writes as

$$\phi_{22}(k_1, k_3, \omega; y_2) = U_\tau^2 g^2\left(\frac{y_2}{\delta}\right) \frac{f_1(ky_2) A(k_1, k_3)}{k^2} \phi_m(\omega - k_1 U_c) \quad (7.95)$$

where the moving axis spectrum is the one in Equation (7.92). The distinction between Equations (7.92) and (7.95) therefore lies only in the different hypothesis of geometric similarity of the constituent waves. In the first case waves of the form

$$v = \hat{v}(y_2) a_1(k_1 y_2) a_2(k_3 y_2) e^{i(k_1 y_1 + k_3 y_3)}$$

are implied, while in the second case waves of the form

$$v = \hat{v}(ky) b(\alpha) e^{i(k_1 y_1 + k_3 y_3)}$$

where $\tan \alpha = k_3/k_1$, are implied; a_1 , a_2 , and b are dimensionless functions of their arguments. The function $f_1(ky_2)$, elucidated by Morrison and Kronauer, has a broad peak at $ky_2 \approx 0.6$, with a width of $\Delta(ky_2) \approx 2.5$. When $k\delta > 1$ it will be useful to use the approximation

$$f_1(ky_2) = 2.5 \delta(ky_2 - 0.6) \quad (7.96)$$

to bring out the peaked nature of this function. This result is consistent with Bradshaw's hypothesis of $k_1 y_2$ similarity in the logarithmic region of the wall layer. Evidently $f_1(ky_2)$ (Equation (7.96)) is consistent with the $(k_1 y_2) \phi_{22}(k_1 y_2)$ (Equation (7.92)), which also has a broad peak centered on $k_1 y_2 \approx 0(1)$ (see Figures 7.13, 7.14, and 7.25). If we adopt Equation (7.94) with Equations (7.92) and (7.93), we find the wave number spectrum to be approximated by the dimensionless form

$$\frac{\phi_p(\vec{k}, \omega)}{\rho_0^2 U_\tau^4 \delta^2} = a \cdot \left(\frac{k_1}{k}\right)^2 \cdot A\left(\frac{k_1}{k}\right) \int_0^\infty d\left(\frac{y_2}{\delta}\right) e^{-2ky_2} \cdot \frac{\left[U'_1\left(\frac{y_2}{\delta}\right)\right]^2}{U_\tau^2} \cdot g_2^2\left(\frac{y_2}{\delta}\right) \cdot \left(\frac{y_2}{\delta}\right)^3 \cdot \frac{f_1(ky_2)}{k^2 y_2^2} \phi_m(\omega - U_c k_1)$$

in which the factor a represents a collection of the numerical coefficients. The function $(U'_1(y_2/\delta)/U_\tau)^2 g_2^2(y_2/\delta)$ represents the convective source density at various strata of the boundary layer which is shown in Figure 7.26 to be peaked in the buffer zone. This figure was constructed from Equation (7.14) and measured profiles shown in Figures 7.7 and 7.8. The g_2 vanishes as $y_2 \rightarrow 0$, and $U'(y_2)$ vanishes as $y_2 \rightarrow \delta$, setting limits on the overall source function. When $k\delta \gg 1$, the approximation, Equation (7.95), holds so that we may further approximate (for $k \gg \delta^{-1}$)

$$\frac{\phi_p(\vec{k}, \omega)}{\frac{MS}{\rho_o U_\tau^4 \delta^2}} \sim b \left(\frac{k_1}{k}\right)^2 A\left(\frac{k_1}{k}\right) \frac{\phi_m\left(\frac{\omega \delta}{U\left(\frac{0.6}{k}\right)} - k_1 \delta\right)}{(k\delta)^2} g_2^2\left(\frac{0.6}{k\delta}\right) \quad (7.97)$$

where b is another numerical coefficient that includes the von Karman constant (κ from $U'(y_2)$) and additional coefficients; as long as $0.4 > y_2/\delta > 0.05$, the dimensionless intensity function $g_2^2(y_2/\delta)$ is effectively unity. The lower limit on y_2 corresponds to $0.6/k\delta = 0.05$ or $k\delta = 10$; thus Equation (7.92) depends on wave number roughly as

$$\frac{\phi_p(\vec{k}, \omega)}{\frac{MS}{\rho_o U_\tau^4 \delta^2}} \sim b \left(\frac{k_1}{k}\right)^2 A\left(\frac{k_1}{k}\right) \frac{\phi_m\left(\frac{\omega \delta}{U\left(\frac{0.6}{k\delta}\right)} - k_1 \delta\right)}{(k\delta)^2} \text{ in the range } 1 < k\delta < 10 \quad (7.98)$$

where $U(0.6/k\delta)$ is the mean velocity at $y_2 = 0.6/k$ ($U_c \approx U \approx 0.6 U_\infty$). Therefore, in this wave number range, the moving-axis spectrum of the velocity fluctuations has a direct influence on the imposed pressure fluctuations. The bandwidths of the peaks $\Delta k_1 \delta$ in Figures 7.24 and 7.25 are essentially equal.

Equation (7.98) allows us to complete the sketched spectrum in Figure 7.24 when use is made of the moving-axis spectrum in Equation (7.48). Near $k_1 = \omega/U_c$ the peak will be of the same order as that shown in Figure 7.25 because of the variable source level at different values of $(k_1 \delta)$. At wave numbers well above $k_1 \delta = \omega \delta / U$ (Equation (7.98)) the moving axis spectrum of Equation (7.48) gives

$$\frac{\omega \phi_p(\vec{k}, \omega)}{\frac{MS}{\rho_o U_\tau^4 \delta^2}} \sim b \left(\frac{k_1}{k}\right)^2 A\left(\frac{k_1}{k}\right) \frac{\gamma_1}{\pi} \left(\frac{\omega \delta}{U}\right)^2 \frac{1}{(k_1 \delta)^4}; \quad \text{for } k_1 \delta < 10 \quad (7.99)$$

When $y_2/\delta < 20 \nu/U_\tau \delta$, accordingly when $k_1 \delta > 30 \times 10^{-3} U_\tau \delta \nu > 10$, $g_2^2(y_2/\delta) = (y_2/\delta)^2$, and therefore

$$\frac{\omega \phi_p(\vec{k}, \omega)}{\rho_o U_\tau^4 \delta^2} = c \left(\frac{k_1}{k}\right)^2 A\left(\frac{k_1}{k}\right) \frac{\gamma_1}{\pi} \left(\frac{\omega \delta}{U}\right)^2 \frac{1}{(k_1 \delta)^6}; \quad \text{for } k_1 \delta > 30 \times 10^{-3} U_\tau \delta / \nu > \omega \delta / U \quad (7.100)$$

In the alternate limits of $k\delta \ll 1$ it is necessary to examine theoretically the kinematics of the boundary layer because (especially when $k_1 \ll \omega/U_c$) the measured statistics of the boundary layer are not able to elucidate this wave number region. Essentially, the moving axis spectrum shown in Figure 7.25, as indicated by measurements of convected turbulence, is incorrect in the range $k_1 \ll \omega/U_c$, and certain kinematic arguments (e.g., those used by Chase⁸⁶) are required to extrapolate to this region. It was shown by Chase⁸⁶ that the velocity spectrum can be written as k_1^2 times a wave number spectrum of a stream function. Therefore, if the stream function spectrum is to remain finite as $k_1 \rightarrow 0$, the strongest dependence of $\phi_{22}(\vec{k}, \omega; y_2)$ on k_1 that can be tolerated is k_1^2 , i.e.,

$$\phi_{22}(\vec{k}, \omega; y_2) = k_1^2 \phi_{\phi\phi}(\vec{k}, \omega; y_2)$$

which implies a spectrum function⁸⁶ of the dimensional form

$$\phi_{22}(\vec{k}, \omega; y_2) = U_\tau^2 g_2^2 \left(\frac{y_2}{\delta} \right) y_2^2 k_1^2 y_2^2 \phi_{\phi\phi}(\vec{k}y_2, \omega; y_2) \quad (7.101)$$

for which $\phi_{\phi\phi}(\vec{k}, \omega; y_2)$

$$\begin{aligned} \lim_{k \rightarrow 0} \phi_{\phi\phi}(\vec{k}, \omega; y_2) &= \text{constant with dimension of time} \\ &= \phi_{\phi\phi}(\omega) \end{aligned}$$

Accordingly, Equation (7.90) suggests the limiting form of the wall pressure spectrum at very low wave numbers, i.e.,

$$\phi_{pp}(\vec{k}, \omega) = \tau_w^2 \delta^2 (k_1 \delta)^2 \bar{\phi}_{\phi\phi}(\omega) \quad k_1 \delta \ll 1 \quad (7.102)$$

where $\bar{\phi}_{\phi\phi}(\omega)$ is the average over the boundary layer of $\phi_{\phi\phi}(\omega)$ and the boundary layer thickness has been retained as the length scale although it could be argued that alternate choices might be v/U_τ or U_∞/ω .

7.3.4 Characteristics of the Frequency Spectrum of Wall Pressure

As in the last section, functional behavior is derived, and no attempt is made to assess quantitative levels. General characteristics of the frequency spectrum of the wall pressures at a point are now deduced by integrating $\phi_p(\vec{k}, \omega)$ over all (k_1, k_3) (Equation (7.80) for $\vec{r}=0$). The result is shown in Figure 7.28. This frequency spectrum would be measured by a transducer of infinitesimal size fixed in a wall beneath the boundary layer. Since we are interested in integrated effects, we may invoke Taylor's hypothesis and replace the moving axis spectrum in Equation (7.96) by the delta function approximation. Accordingly, letting $dk_1 dk_3 = k dk d\theta$, $(k_1/k) = \cos \theta$ and $A(k_1, k_3) = A(\theta)$

$$\begin{aligned} \frac{\phi_p(\omega)}{\rho_o^2 U_\tau^4} &= a_1 \cdot \int_0^\pi \cos^2 \theta A(\theta) d\theta \cdot \int_0^\infty \int_0^\infty d\xi e^{-2k\delta\xi} \xi g(\xi) \\ &\dots \frac{f_1(k\delta\xi)}{(k\delta)^2} \delta(\omega - U_c k_1) (k\delta) d(k\delta) \end{aligned} \quad (7.103)$$

where

$$g(\xi) = g\left(\frac{y_2}{\delta}\right) = \left[\frac{U'\left(\frac{y_2}{\delta}\right)}{U_\tau} \right]^2 g_2\left(\frac{y_2}{\delta}\right) \quad (7.104)$$

is the source function shown in Figure 7.26. Formally carrying out the integrations,

$$\frac{\phi_p(\omega)}{\rho_o^2 U_\tau^4} \frac{U_c}{\delta} = a_2 \left(\frac{\omega\delta}{U_c} \right)^{-1} \int_0^\infty \xi e^{-2\Omega\xi} g(\xi) f_1(\Omega\xi) d\xi \quad (7.105)$$

where $\Omega = \omega\delta/U_c$ is expected to be unity or greater. The source function has the approximate functional limits

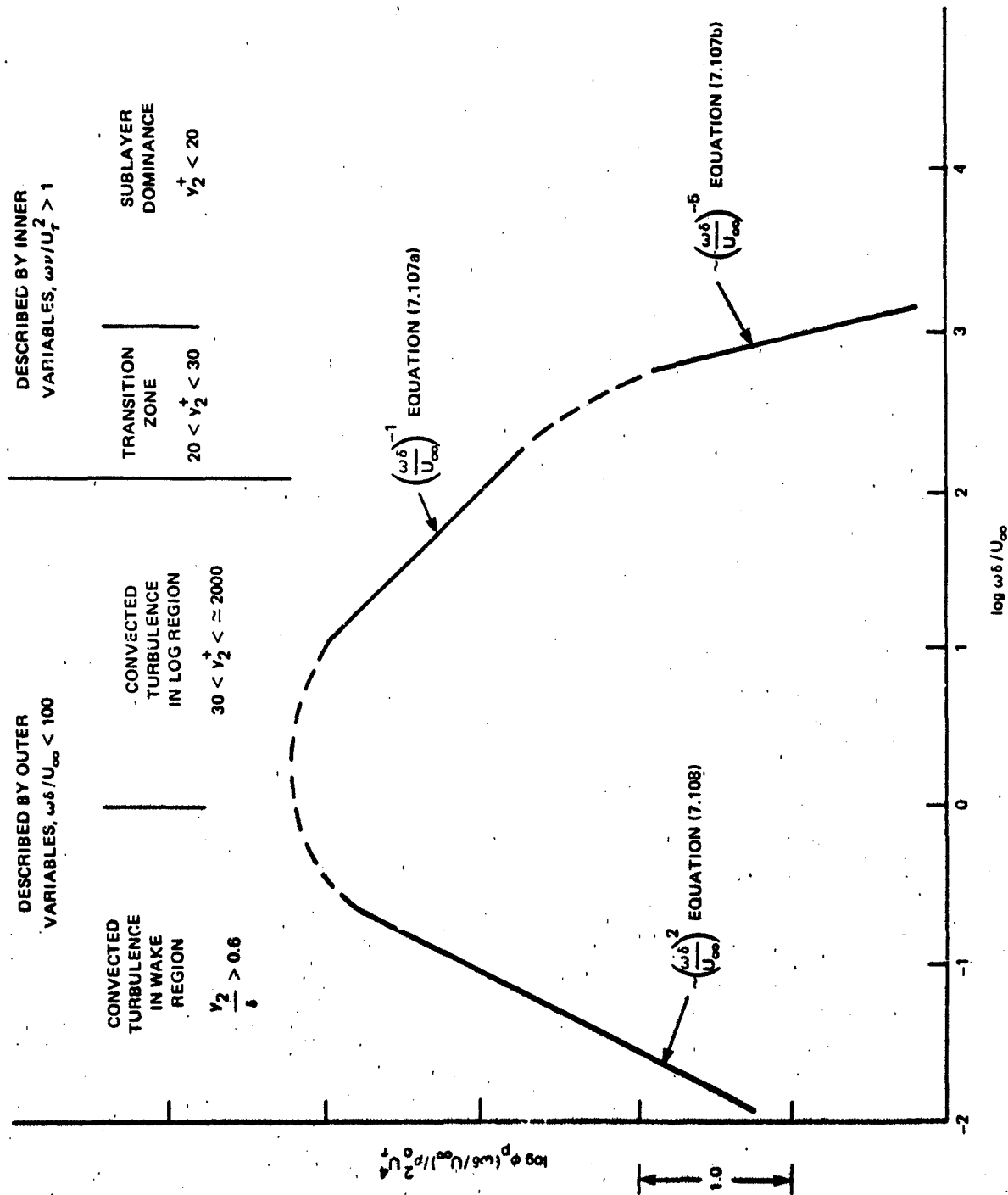


Figure 7.28 - Frequency Spectrum of Wall Pressure Fluctuations at a Point.
Wave Number Integral of $\phi(\vec{k}, \omega)$ is Dominated by Convected Disturbances

$$g(\xi) \approx \xi^2 \quad 0 < \xi < \approx \frac{20}{\left(\frac{U_\tau \delta}{\nu}\right)}$$

$$g(\xi) \approx \frac{1}{\xi^2} \quad 1 > \xi > \frac{20}{\left(\frac{U_\tau \delta}{\nu}\right)}$$

$$\approx 0 \quad \xi > 1$$

Now, as long as $\Omega > 2$, the delta function approximation for $f_1(\Omega\xi)$ (Equation (7.96)), will hold since the integration will extend over the peak of $f_1(\Omega\xi)$. Therefore Equation (7.105) becomes

$$\frac{\phi_p(\omega)}{\rho_o^2 U_\tau^4} \frac{U_c}{\delta} \sim a_3 \left(\frac{\omega\delta}{U_c}\right)^{-1} \left[\frac{g\left(\frac{0.6}{\Omega}\right)}{\Omega^2} \right] \frac{\omega\delta}{U_c} \quad \Omega > 2 \quad (7.106)$$

The above limits on $g(\xi)$ suggest the frequency dependence

$$\frac{\phi_p(\omega)}{\rho_o^2 U_\tau^4} \frac{U_c}{\delta} \sim \left(\frac{\omega\delta}{U_c}\right)^{-1}, \quad U_c \approx 0.6 \text{ to } 0.7 U_\infty, \quad 2 < \frac{\omega\delta}{U_c} < \frac{U_\tau \delta}{20\nu} \quad (7.107a)$$

and at very high frequencies

$$\frac{\phi_p(\omega)}{\rho_o^2 U_\tau^4} \left(\frac{U_\tau^2}{\nu}\right) \sim \left(\frac{\omega\nu}{U_\tau^2}\right)^{-5}, \quad U_c \approx 0.4 \text{ to } 0.6 U_\infty, \quad \frac{\omega\delta}{U_c} > \frac{U_\tau \delta}{20\nu} \quad (7.107b)$$

or $\omega\nu/U_\tau^2 > 60$, for example. The first behavior pertains to pressures exerted by eddies convected in the logarithmic region, and the second behavior pertains to pressures exerted in the buffer and sublayer regions where the amplitude of velocity fluctuations increases nearly linearly with distance from the wall² and the mean velocity gradient is nearly constant. These pressures are strongly influenced by viscosity whence there exists an upper bound on frequency that is dependent on $U_\tau \delta/\nu$. An alternative upper limit on the frequency could be stated as

$$\frac{\omega v}{U_\tau^2} > \frac{U_c}{U_\tau} = \left[30 \left(\frac{C_f}{2} \right)^{\frac{1}{2}} \right]^{-1} \approx 1$$

since $U_c \approx 0.6 U_\infty$ and $U_\infty/U_\tau \approx 30$, generally.

The limits on convection velocity shown above are crudely determined by the average velocity in the logarithmic region ($0.8 U_\infty > U > 0.6 U_\infty$) and in the buffer zone ($0.6 U_\infty > U > 0.4 U_\infty$), respectively. Measurements of convection velocities at these high frequencies $\omega \delta / U_c > U_\tau \delta / 20 \nu$ are lacking.

At frequencies low enough that $\omega \delta / U_c \ll 1$, the steps leading to Equation (7.105) are not valid, and the full equation must be reexamined. Equation (7.90) may be rearranged to give

$$\frac{\phi_p(\omega)}{\rho_0^2 U_\tau^4} = \int_{-\infty}^{\infty} dk_1 \int_{-\infty}^{\infty} dk_3 \int_{-\infty}^{\infty} dy_2 \cdot \left(\frac{k_1}{k} \right) e^{-2ky_2} \left(\frac{1}{y_2} \right) \\ \cdot y_2 \left[\frac{y_2^2 \phi_{22}(ky_2) \phi_m(\omega - U_c k_1)}{u_2^2} \right]$$

where the integration of the correlation function over y_2' yielded y_2 , and the equation preceding Equation (7.92) has been used. The delta function approximation on $\phi_m(\omega - U_c k_1)$ may still be used, giving (with $U'(y_2) \approx \kappa U_\tau / y_2$)

$$\frac{\phi_p(\omega)}{\rho_0^2 U_\tau^4} \approx 4 \frac{\delta}{U_c} \left(\frac{\omega \delta}{U_c} \right)^2 \kappa^2 \int_{-\infty}^{\infty} dk_3 \delta \int_0^1 d \left(\frac{y_2}{\delta} \right) \cdot \left(\frac{y_2}{\delta} \right) \\ \cdot \frac{\exp \left\{ -2y_2 \left[\left(\frac{\omega \delta}{U_c} \right)^2 + (k_3 \delta)^2 \right]^{\frac{1}{2}} \right\}}{\left[\left(\frac{\omega \delta}{U_c} \right)^2 + (k_3 \delta)^2 \right]} \left[\frac{\phi_{22} \left\{ \left[\left(\frac{\omega \delta}{U_c} \right)^2 + (k_3 \delta)^2 \right]^{\frac{1}{2}} \left(\frac{y_2}{\delta} \right) \right\}}{u_2^2} \right]$$

Now, since $\omega\delta/U_c \ll 1$, the delta function approximation is invoked on $f(ky_2) = f(k_3y_2)$ to complete the k_3y_2 integration, giving an autospectrum of wall pressure that has the frequency dependence

$$\frac{\phi_p(\omega)}{\rho_0^2 U_c^4} \frac{U_c}{\delta} = \left(\frac{\omega\delta}{U_c} \right)^2, \text{ for } U_c \approx 0.8 U_\infty \frac{\omega\delta}{U_c} \ll 1 \quad (7.108)$$

This result has been obtained by Lilly and Hodgson⁷⁴ and by Chase,⁸⁶ although Chase has suggested that, in the limit, as $\omega\delta/U_c \rightarrow 0$ this quadratic behavior tails off and the spectrum approaches a constant value.

7.3.5 Kinematic Modeling of Turbulence Using Wave Mechanics Analogies

In this section the analytical representations of the wave vector spectrum $\phi_{22}(\omega, \vec{k}, y_2, y_2')$ are examined. As before, $\vec{k} = (k_1, k_3)$, and y_2 and y_2' are different elevations from the wall. A key issue to be settled is a description of the dependence of the energy density on wave number and wave direction. Stated in terms of the preceding discussion, a justification of the forms $\phi_1(k_1y_2) \cdot \phi_3(k_3y_2)$ or $\phi(ky_2) A(k_1, k_3)$ is required. A second issue, especially with regard to the low wave number spectrum ($k \ll \omega/U_c$), is the behavior of the moving-axis spectrum at low wave numbers. These two issues are related to some extent because the low wave number asymptote of the spectrum must be consistent with the well-known behavior at $k_1 = \omega/U_c$.

One of the earliest wave mechanical descriptions is that of Landahl.^{90,91} The velocity fluctuations can be (formally, at least) decomposed into wave vector components by Fourier transforming $u_2(\vec{y}, t)$; i.e.,

$$\bar{u}_2(\vec{k}, \omega, y_2) = \frac{1}{2\pi} \iiint_{-\infty}^{\infty} e^{-i(\vec{k} \cdot \vec{y} - \omega t)} u_2(\vec{y}, t) dy_1 dy_3 d\omega \quad (7.109)$$

Therefore each component propagates according to the characteristic

$$u_2(\vec{k}, \omega; \vec{y}, t) = \bar{u}_2(\vec{k}, \omega, y_2) e^{i(\vec{k} \cdot \vec{y} - \omega t)}$$

We are dealing with small-amplitude disturbances; Landahl^{90,91} has proposed expanding the wave amplitude as a summation over modes of the Orr-Sommerfeld equation. Letting the stream function of the fluctuating velocity be $\phi(\vec{k}, y_2)$, then

$$\bar{u}_2(\vec{k}, \omega, y_2) = -ik_1 \phi(\vec{k}, y_2)$$

and, extending the methods of Chapter 3, Landahl found an inhomogeneous Orr-Sommerfeld equation for $\phi(\vec{k}, y_2)$, (see Equation 3.4)

$$\begin{aligned} (U_1 - C) (\phi'' - k^2 \phi) - U_1'' \phi + \frac{iv}{k} (\phi^{iv} - 2k^2 \phi'' + k^4 \phi) \\ = \tilde{q} (k_1 k)^{-1} \end{aligned} \quad (7.110)$$

where \tilde{q} is the Fourier transform (in k_1, k_3, ω) of

$$q = v^2 \left(\frac{\partial T_{21}}{\partial y_j} \right)_{j \neq 2} - \frac{\partial}{\partial y_2} \left(\frac{\partial^2 T_{ij}}{\partial y_1 \partial y_j} \right) \quad (7.111)$$

This manipulation separates the linear, first-order functions on the left-hand side from the nonlinear, second-order quantities, which are essentially the turbulent stresses. Special solutions to this equation are sought in terms of the eigenmodes $\hat{\phi}$ of the homogeneous adjoint equation^{96,97}.

$$(U_1 - C) \left(\hat{\phi}_n'' - k^2 \hat{\phi}_n \right) + 2U_1' \hat{\phi}_n' + \frac{iv}{k_1} \left(\hat{\phi}_n^{iv} - 2k^2 \hat{\phi}_n'' + k^4 \hat{\phi}_n \right) = 0 \quad (7.112)$$

so that

$$\phi(\vec{k}, y_2) = \sum \hat{A}_n \hat{\phi}_n(y_2) \quad (7.113)$$

where the amplitude coefficient is given by

$$\hat{A}_n(\vec{k}, y_2) = \frac{1}{\omega(k - \alpha_n)} \int_0^\infty \tilde{q}(\vec{k}, \omega; y_2) \hat{\phi}_n(y_2) dy_2 \quad (7.114)$$

and, for spatially varying wave amplitudes,

$$\alpha_n = (\alpha_n)_r + i(\alpha_n)_i$$

is the complex wave number of the wave $\hat{\phi}_n(y_2)$. For the turbulent boundary layer, $(\alpha_n)_i$ are positive, indicating the existence of damped waves traveling at speed $C = \omega/(\alpha_n)_r$. Once the potential is known, all the velocity fluctuations and, ultimately, as we have already seen, the pressure fluctuations can be found by integration across the boundary layer. The analysis successfully predicted the convection velocities and normalized cross-spectral densities,

$$\frac{|\phi_{pp}(\vec{r}, \omega)|}{\phi_p(\omega)}$$

observed for the wall pressures. The breadth Δk_1 in the wave number spectrum $\phi_p(\vec{k}, \omega)$ near $k_1 = \omega/U_c$ is determined by the value of α_1 . Accordingly, the decay of $|\phi_{pp}(r_1, \omega)|$ with increasing r_1 reflects the overall damping of the turbulence structure.

Further analysis of wave-like structure in the boundary layer was conducted using similar methodology by Schubert and Corcos⁹⁸; calculated magnitudes of velocity fluctuations agreed well with those measured by Klebanoff,²⁵ Hussain and Reynolds⁹⁹⁻¹⁰¹ (excited by a vibrating ribbon), and Davis,^{102,103} who measured and calculated disturbances induced in the boundary layer by a wavy wall.^{102,103} As noted in Chapter 3, solutions of the Orr-Sommerfeld equation are applicable to turbulent flows only when the wavelength of the eigenmode $2\pi/\alpha_n$ is much larger than the scale of the surrounding turbulence. In such cases, the effect of the turbulence has been modeled using an eddy-viscosity model^{99,102,103} where the effective viscosity for a Reynolds stress $\overline{u_1 u_2}$ is

$$v_e = \overline{u_1 u_2} \langle U_1' \rangle^{-1}$$

The Orr-Sommerfeld equation and Landahl's⁹⁰ methodology has also been used^{104,105} to predict the existence of unstable small wavelength waves in locally defected velocity profiles. These waves ultimately¹⁰⁶ result in the formation of three-dimensional "bursts" of turbulence observed in transitional flows¹⁰⁷ (Section 7.2.6).

The wave-like motions predicted by Landahl suggest a wave number spectrum of the form

$$\phi_{22}(\vec{k}, \omega; y_2) = k_1^2 \phi_{\phi\phi}(\vec{k}, \omega; y_2) \quad (7.115)$$

where $\phi_{\phi\phi}(\vec{k}, \omega; y_2)$ is the spectrum of the velocity stream function. By Equation (7.113) this has a general form that supports the separation of the intensity function $g(y_2)$ in Equations (7-92) and (7-94), i.e.,

$$\phi_{\phi\phi}(\vec{k}, \omega; y_2) = g(y_2) \psi(\vec{k}, \omega)$$

where $\psi(\vec{k}, \omega)$ is not necessarily completely separable because the source function $\tilde{q}(\vec{k}, \omega; y_2)$ may not be. As described by Landahl, the dominant wave behavior that is controlled by the poles $k = \alpha_n$ of Equation (7.114) does have separate longitudinal and lateral dependence.

The approach of Morrison and Kronauer,⁹³ also based on the wave theory, was proposed subsequent to Landahl's analysis and proposes a somewhat different factorability. The disturbance waves are assumed to be oriented in directions \hat{z} parallel to the plane of the wall and with wave fronts that make an angle α to the transverse (y_3) direction. The wave speed \hat{c} is presumed to be a function of y , and it has a trace magnitude in the streamwise y_1 direction of

$$c_1 = \frac{\hat{c}}{\sin \alpha}$$

and in the transverse y_3 direction of

$$c_3 = \frac{\hat{c}}{\cos \alpha}$$

The wave function, or stream function, is presumed to have the form

$$\phi(\hat{k}; y_2, \hat{z}, t) = \phi(y_2, \hat{k}) e^{i\hat{k}(\hat{z} - \hat{c}t)} \quad (7.116)$$

where \hat{k} lies in the 1,3 plane and $k = |\hat{k}|$. The normal velocity fluctuation u_2 is given by

$$\begin{aligned} u_2 &= -\partial \phi(\hat{k}; y_2, \hat{z}, t) / \partial \hat{z} \\ &= -i\hat{k} \phi(\hat{k}; y_2, \hat{z}, t) \end{aligned}$$

The functions $\phi(y_2, \hat{k})$ are assumed to have the form

$$k\phi(y_2, \hat{k}) = b_1(\alpha) h_1(ky_2) \quad (7.117)$$

where $b_1(\alpha)$ is not a function of y_2 . When Equations (7.116) and (7.117) are substituted into the momentum and continuity equation, the resulting equation resembles the Orr-Sommerfeld equation; however, instead of the $U_1 - C$ that appears in Equation (7.111), the difference between U_1 and the trace velocity C_1 is obtained; i.e., the appropriate leading term is

$$\left(U_1 - \frac{c}{\sin \alpha} \right) \left[\phi''(y_2, \hat{k}) - k^2 \phi(y_2, \hat{k}) \right] - U_1'' \phi(y_2, \hat{k}) = \text{viscous and nonlinear terms}$$

where $\phi(y_2, \hat{k})$ is given by Equation (7.116) and the primes denote differentiation with respect to y_2 . In the logarithmic region governed by Equation (7.21), $U'' = -(\kappa y_2^2)^{-1}$, so that geometrically similar solutions will be dependent only on the product κy_2 , and $\phi(k, y_2) = \phi(\kappa y_2)$ only if

$$\frac{C}{\sin \alpha} = B - \frac{1}{\kappa} \ln \kappa k$$

where B and κ appear in Equation (7.21). Then

$$\frac{C}{\sin \alpha} - U_1 = -\frac{1}{\kappa} \ln(mky_2)$$

and at the critical layer, $y_2 = y_0$, defined by $U_1 = C/\sin \alpha$, the wave number is given by

$$ky_2 = \text{constant}$$

This means that the wave number of all geometrically similar waves that satisfy Equation (7.118) scale on y_2 . The wave direction must also be independent of y_2 .

The condition for geometrically similar wave solutions requiring $ky_2 = \text{constant}$ in the logarithmic region could also have followed from Equation (7.109); the feature that appears to be unique to the Kronauer-Morrison representation is the constancy of the function $b(\alpha)$ with respect to y_2 . That is, whole families of waves may have the same orientation α at all levels y_2 , but a y_2 -dependent energy density.

7.3.6 Low Wave Number Spectrum and Unsteady Local Convection

It will be shown in Chapter 8 that boundary-layer-induced vibration and sound are often the result of nonzero spectral magnitudes of wall pressure at wave numbers significantly less than $k_1 = \omega/U_c$. This has already been shown (Section 3.6.3.3) for subsonic turbulent jet noise where the Reynolds stresses in the jet couple to the external acoustic medium at wave numbers much less than ω/U_c . We have seen that these low wave number disturbances are traceable to the existence of space-time (moving-axis) decorrelation in a frame of reference moving with the turbulence field. This decorrelation accounts for the finite values of the moving-axis spectrum when $k_1 \ll \omega/U_c$. We now inquire into the kinematic effects of unsteady convection of turbulence in causing moving-axis decorrelation and therefore, by implication, low wave number pressures.

These effects were first recognized by Lin,¹⁰⁸ who showed that the validity of Taylor's hypothesis in interpreting space-time correlations for a given eddy wave number k_1 is limited to situations with separations $r > 2\pi/k_1$ and time delays $\tau > 2\pi/k_1 U_c$. Dynamic constraints are that the turbulence level is low,

$$\frac{u^2}{U^2} \ll 1$$

and that the mean flow shear is small in the sense that

$$\frac{k_1 U}{2\pi} \gg \frac{dU}{dy_2}$$

This last condition (also derived by Lumley¹⁰⁹) can be interpreted in terms of a logarithmic profile as

$$k_1 y_2 \gg 2.5 \frac{U_\tau}{\bar{U}(y_2)}$$

At the edge of the sublayer the mean velocity is small, $U(y_2)/U_\tau \approx 10$, so that this condition is most limiting there, and it is effectively restated $k_1 y_2 \gg 0.25$ for $y_2^+ > 20$. Other conditions for the validity of Taylor's hypothesis, also defined by Lumley,¹⁰⁹ have to do with the curvature of the energy spectrum. Fisher and Davies¹¹⁰ illustrated that various wave number components are convected at various velocities and that convection is not at all steady.

The dynamics of a nonfrozen turbulence field can be envisioned, following Fisher and Davies,¹¹⁰ as due to a superposition of eddies of various sizes, each having an influence on the translation of another. High wave number patterns are considered to be locally convected by the velocity field of lower wave number eddies. Thus for each eddy component we postulate a stochastic convection velocity with a mean U_c . Consistent with this viewpoint, we again express the instantaneous velocity fluctuation as a linear superposition of generalized wave number components,

$$u_1(\vec{y}, t) = \iiint e^{+i\vec{k} \cdot (\vec{y} - \vec{U}(t))} u(\vec{k}) d^3\vec{k}$$

where $\vec{k} = k_1, k_2, k_3 (k_1, k_2)$. The space-time cross correlation of the velocities at space-time points (\vec{y}, t) and $(\vec{y} + \vec{r}, t + \tau)$ is written as an ensemble average (see Chapter 3)

$$\langle u_i(\vec{y}+\vec{r}, t+\tau) u_j(\vec{y}, t) \rangle$$

$$= \iiint_{-\infty}^{\infty} \langle e^{+i\vec{k}' \cdot (\vec{y}+\vec{r}-U(t+\tau))} e^{-i\vec{k} \cdot (\vec{y}+\vec{U}t)} \rangle$$

$$\langle u_i(\vec{k}') u_j^*(\vec{k}) \rangle d^3\vec{k}' d^3\vec{k}$$

$$= \overline{u_i u_j} \iiint_{-\infty}^{\infty} \langle e^{+i\vec{k} \cdot (\vec{r}-\vec{U}\tau)} \rangle \phi_{ij}(\vec{k}) d^3\vec{k} \quad (7.118)$$

The assumption has been made that the convection velocity and the energy intensity are statistically independent variables; the method has been used by Lumley.¹⁰⁹ This statistical independence requires that the space and time scales of \vec{U} are larger than κ^{-1} or $(U_c \kappa)^{-1}$; i.e., the energy of the convected field is not affected by motions induced by the larger-scale convecting field.¹⁰⁹ The three-dimensional convection velocity \vec{U} has a mean component U_c that shows up in the measurements. We write

$$\vec{U} = U_c + \vec{v}$$

where \vec{v} is the three-dimensional unsteadiness of convection. The average of \vec{v} is zero, and the probability distribution of \vec{v} is $P(\vec{v})$. In addition, we note that the ensemble average of the phase is

$$\begin{aligned} & \langle e^{+i\vec{k}' \cdot (\vec{r}-\vec{U}\tau)} \rangle \\ &= e^{+i\vec{k} \cdot (\vec{r}-\vec{U}_c \tau)} \langle e^{+i\vec{k} \cdot \vec{v}\tau} \rangle \\ &= e^{+i(\vec{k} \cdot \vec{r} - \vec{U}_c k_1 \tau)} \langle e^{+i\vec{k} \cdot \vec{v}\tau} \rangle \end{aligned} \quad (7.119)$$

and that by definition

$$\langle e^{+i\vec{k} \cdot \vec{v}\tau} \rangle = \iiint e^{+i\vec{k} \cdot \vec{v}\tau} P(\vec{v}) d^3(\vec{v}) \quad (7.120)$$

Substituting Equations (7.119) and (7.120) into Equation (7.118) and invoking the relationship between $R_{ij}(\vec{r}, \tau)$ and $\phi_{ij}(\vec{k}, \omega)$ (Section 3.5.3), we obtain the wave number frequency spectrum for the turbulent field as

$$\phi_{ij}(\vec{k}, \omega) = \phi_{ij}(\vec{k}) \iiint P(\vec{k} \cdot \vec{v}) \delta(U_c k_1 - \omega + \vec{k} \cdot \vec{v}) d^3(\vec{v}) \quad (7.121)$$

This spectrum form has been used by Chase,^{85,111} and it provides a more physically rational representation of the turbulent sources than the more convenient forms used earlier. Equation (7.121) is of the form that separates the moving axis spectrum,

$$\phi_{ij}(\vec{k}, \omega) = \phi_{ij}(\vec{k}) \phi_m(\omega - U_c k_1) \quad (7.122)$$

which was introduced in Equations (3.93), (7.49), and (7.50). The moving axis spectrum accounts for the decorrelation of turbulence in a moving reference frame and therefore can be explained on the basis of a distribution of unsteady convection velocities.

There is a physical basis for this unsteady convection found in the flow-visualization studies described in Section 7.2.6. There visualizations show clearly that unilateral convection is made nonexistent except in an average sense because of turbulent ejection and mixing, especially in the logarithmic region of the boundary layer. These dynamics perhaps involve even larger regions and may extend to the wake region, as suggested by the similarity in time scales of outer intermittency and Reynolds stress ejection, as discussed earlier.

Chase⁸⁵ has suggested that this local convection can contribute to the existence of wall pressure disturbances at low wave numbers, $k_1 \ll \omega/U_c$. Subsequently,⁸⁶ however, he has suggested that unsteady convection is not the only mechanism and possibly it may not be sufficient for the generation of substantial low wave number

pressure. The integrand in Equation (7.121) contains important contributions at all frequencies that satisfy

$$\omega = U_c k_1 + \vec{k} \cdot \vec{v}$$

At wave number $k_1 U_c \ll \omega$, we still have, on the average, a frequency of occurrence of

$$\omega = \langle (\vec{k} \cdot \vec{v})^2 \rangle^{1/2}$$

where, in general,³⁵

$$\begin{aligned} \langle (\vec{k} \cdot \vec{v})^2 \rangle &= k_1^2 \langle v_1^2 \rangle + k_2^2 \langle v_2^2 \rangle + k_3^2 \langle v_3^2 \rangle \\ &+ 2 \left[k_1 k_2 \langle v_1 v_2 \rangle + k_1 k_3 \langle v_1 v_3 \rangle + k_2 k_3 \langle v_2 v_3 \rangle \right] \end{aligned}$$

Thus, if $\langle v_1^2 \rangle / U_c^2 \ll 1$, the frequencies are determined by local convection through terms of the form, say, $\omega \approx k_2 \langle v_2^2 \rangle^{1/2}$. Since $\langle v_2^2 \rangle$ is essentially the mean-square turbulence velocity normal to the wall, these disturbances have a high trace velocity in the plane of the wall. Accordingly, they have a long wavelength parallel to the wall, but they may have a short wavelength and a low velocity normal to the wall. The postulation of this velocity field pattern is supported by the well-known existence of velocity disturbances with small cross-stream (y_2) stream-wise length scales.

The assumption is made that $P(\vec{v})$ is one dimensional, i.e., equal probabilities for velocities in all directions. Assuming a Gaussian distribution for the velocity fluctuation, we let

$$P(V) = \frac{1}{2\pi \left[\overline{(v^2)}^{1/2} \right]^3} \exp \left[-\frac{1}{2} \frac{v^2}{\overline{(v^2)}} \right] \quad (7.123)$$

so that $P(\vec{V}) = (4\pi)^{-1} P(V)$ and $d\vec{V} = 4\pi V^2 dV$. The forms of Equations (7.121) and (7.123) imply the existence of a source spectrum, written by Chase in the form

$$\Phi_{ij}(\vec{k}, \omega) = \Phi_{ij}(\vec{k}) \left\{ \frac{1}{(2\pi)^{\frac{1}{2}}} \cdot \frac{1}{\omega_k} \exp \left[-\frac{1}{2} \frac{(\omega - U_c k_1)^2}{\omega_k^2} \right] \right\} \quad (7.124)$$

where the term in curly brackets is the moving axis spectrum and where

$$\omega_k^2 = k_1^2 \langle V_1^2 \rangle + k_2^2 \langle V_2^2 \rangle + k_3^2 \langle V_3^2 \rangle + 2k_1 k_2 \langle V_1 V_2 \rangle$$

Equation (7.124) results from the fact that $\vec{k} \cdot \vec{V} = \omega - U_c k_1$ in Equation (7.121), and a measure of $V/\langle V^2 \rangle^{\frac{1}{2}}$ is $k \cdot V/\langle (k \cdot V)^2 \rangle^{\frac{1}{2}}$.

In order to utilize the spectrum given by Equation (7.124) in the pressure spectrum of Equation (7.90), the inverse transform must be taken to replace

$$R_2(y_2' - y_2) \Phi_{22}(\vec{k}, \omega)$$

by, for example,⁸⁵

$$\int_{-\infty}^{\infty} e^{i(y_2 - y_2')} k_2 \Phi_{22}(\vec{k}, \omega) dk_2$$

To use this function to predict turbulent boundary layer pressure it is still necessary to specify a functional dependence of the three-dimensional spectrum function $\Phi_{22}(\vec{k})$ that appears in Equation (7.124). However, the nonvanishing behavior of $\Phi_m(\omega - U_c k_1)$ at $\omega \gg U_c k_1$ has been given some basis in the kinematics of the boundary layer turbulence. In the methods used by Chase,^{85,86} trial functions for $\Phi_{22}(\vec{k})$ are introduced into the integrals and the integrals are evaluated. In selecting these functions the wave number dependence is always selected to appear, with y_2 being the only physical length scale. Adjustable coefficients always appear in the trial functions, and these are evaluated by matching the theory with available autospectra and spatial correlation functions controlled by wave numbers near $k_1 = \omega/U_c$.

7.3.7 Recent Modeling of $\Phi_p(\vec{k}, \omega)$

A recent modeling⁸⁶ of wall pressure spectra accounts for both the linear mean shear and the nonlinear turbulence-turbulence interaction terms. The resulting spectrum form is

$$\frac{\Phi_p(\vec{k}, \omega) U_\infty}{\tau_w^2} = \frac{U_\infty}{U_\tau} \left(C_M k_1^2 K_M^{-5} + C_T k^2 K_T^{-5} \right) \quad (7.125)$$

where

$$K_{M/T}^2 = \frac{(\omega - U_c k_1)^2}{h_M^2 U_\tau^2} + k^2 + (b_{M/T} \delta)^{-2}$$

and the subscripts M or T refer to either the mean shear or turbulence interactions. The modeling provides for a spectrum form for the wall-normal velocity fluctuations of the form

$$\Phi_{22}(\xi, \vec{\kappa}, \omega) = k^2 \overline{u^2}(\xi) U_\tau A\left(\frac{k_1}{k_3}\right) \xi^6 F\left(\kappa_+, \xi, \frac{k_2}{\kappa_+}\right)$$

for use in evaluating the mean-shear contribution, where ξ represents a geometric mean wall distance $\xi = (y_2 y_2')^{1/2}$ and $\overline{u^2}(\xi)$ is derived from

$$\left[\overline{u^2}(y_2) \overline{u^2}(y_2') \right]^{1/2} = \overline{u^2}(\xi) \exp \left[-\frac{(y_2 + y_2')}{\delta_M} \right]$$

which is an intensity function that approximates the distribution of root mean square velocity across the boundary layer. The wave numbers are

$$\kappa_+ = \sqrt{k^2 + k_2^2} + \frac{(\omega - U_c k_1)^2}{h_M^2 U_\tau^2}$$

and

$$\vec{\kappa} = k_1, k_2, k_3 = \vec{k}, k_2$$

Similar representations are used for the turbulence interactions. The functional form for κ_+ is determined from the assumption that the space-time correlation can be expressed as $(\vec{r}=r_1, r_3)$

$$R_{22}(\vec{r}, \tau) \approx R_{22} \left[\left(|r|^2 + h_M^2 U_\tau^2 \tau^2 \right)^{1/2}, 0 \right]$$

where h_M is a scale factor. Note that this presumption does not provide for a separable correlation model of the form given by Equation (3.100).

The coefficients in Equation (7.125) may be derived from the measured spectrum functions consistent with Equation (7.108a) and the cross spectrum defined above Equation (3.102);

$$\frac{\phi_p(\omega)}{\tau_w^2 \delta^*} \approx \frac{2\pi}{3} h(C_M + C_T) (1+r_T) \left(\frac{\omega \delta^*}{U_\infty} \right)^{-1} \quad (7.126a)$$

$$\frac{\phi_p(r_1, 0, \omega)}{\phi_p(\omega)} = \left(1 - \frac{\mu \left| \frac{\omega r_1}{U_c} \right|}{1+r_T} \right) \exp \left(-\mu \left| \frac{\omega r_1}{U_c} \right| \right) \quad (7.126b)$$

and

$$\frac{\phi_p(0, r_3, \omega)}{\phi_p(\omega)} = \left(1 + \frac{1-r_T}{1+r_T} \left| \frac{\omega r_3}{U_c} \right| \right) \exp \left(-\omega \left| \frac{r_3}{U_c} \right| \right) \quad (7.127a)$$

The parameter r_T represents the fraction of mean square wall pressure that is due to the turbulence-turbulence interactions ($r_T < 1$) and

$$r_T = \frac{C_T h_T^2}{C_T h_T^2 + C_M h_M^2} \quad (7.127b)$$

The h_M and h_T are taken from the space-time correlations, but since the linear and nonlinear contributions cannot be separated, it is assumed that $h_M = h_T = h$. In the model, parameter h is related to μ by

$$\mu = \frac{h U_\tau}{U_c}$$

and the spectrum $\phi_p(\omega)$ has a maximum at frequency ω_{\max} so that when $C_T \ll C_M$ and $r_\tau \ll 1$

$$b_M = (2)^{\frac{1}{2}} \frac{U_c}{\omega_{\max} \delta}$$

Differences between b_M and b_T may be discerned from space-time correlations or from the limit as $\omega \rightarrow 0$ of $\phi_p(\omega)$. In either case values of these parameters are only weakly indicated by measurements, and Chase's best estimates⁸⁶ are $b_M = 0.756$ and $b_T = 0.378$. Precise definition of these parameters does not have a significant influence on $\phi_p(k, \omega)$, however, since the term $(b\delta)^{-1}$ in Equation 7.125 is negligible for practical values of k and when $\omega\delta/U_\infty > 1$.

The parameters C_M , C_T , r_τ , and h therefore control the magnitude of the wave number frequency spectrum, and these parameters are easily determined from measurements via Equations (7.126 and 7.127). In Section 7.4.4 values of these parameters are given for various wall types.

Asymptotic terms of the spectrum functions are*

$$\frac{\phi\left(k_1 \gg \frac{\omega}{U_c}, 0, \omega\right)}{\tau_w^2 \frac{(\delta^*)^3}{U_\infty}} = \left(\frac{U_\infty}{U_\tau}\right) (k_1 \delta^*)^{-3} \left(\frac{U_c}{h U_\tau}\right)^{-5} (C_M + C_T)$$

$$\frac{\phi\left(k_1 = \frac{\omega}{U_c}, 0, \omega\right)}{\tau_w^2 \frac{(\delta^*)^3}{U_\infty}} = \frac{U_\infty}{U_\tau} \left(\frac{\omega \delta^*}{U_c}\right)^{-3} (C_M + C_T)$$

Note that in these and the above expressions δ^ appears even though it may be cancelled from both sides of the equations. This retention of δ^* permits some qualitative relationship to the parameters of Section 7.2.

and

$$\frac{\phi \left(k_1 \ll \frac{\omega}{U_c}, 0, \omega \right)}{\tau_w^2 \frac{(\delta^*)^3}{U_\infty}} = \left(\frac{U_\tau}{U_\infty} \right)^4 (k_1 \delta^*)^2 \left(\frac{\omega \delta^*}{U_\infty} \right)^{-5} h^5 (C_M + C_T)$$

These equations are bounded by viscous effects of the kind noted in Equation 7.101; however, Chase's criterion is

$$b \left[\left(k_1^2 + k_3^2 \right) + \frac{(\omega - U_c k_1)^2}{h^2 U_\tau^2} \right]^{\frac{1}{2}} \frac{v}{U_\tau} > 1$$

Realistically, this means for fixed ω/U_c one must have k_1 such that

$$b \frac{U_c k_1}{U_\tau h} \frac{v}{U_\tau} > 1$$

for viscous effects to be important. The condition corresponding to Equation 7.101 is therefore

$$k_1 \delta > \frac{h}{b} \frac{U_\tau}{U_c} \frac{U_\tau \delta}{v}$$

$$\approx 0.04 \frac{U_\tau \delta}{v} > \frac{\omega \delta}{U_c}$$

for smooth walls. This limiting condition is nearly identical to that given earlier and it is based on a similar argument.

Table 7.2 lists three sets of parameters from measurement programs that were discussed in Section 7.2. Wall pressures measured in these programs are discussed in Section 7.5. Figure 7.29 shows Equation 7.125 for each set of parameters. The most sensitive parameter is μ (or h), which is determined from the two-point cross-spectral density of wall pressure with longitudinally separated transducers.

TABLE 7.2
PARAMETERS FOR USE IN EQUATIONS (7.126) AND (7.127)

	Smooth ²⁰	Smooth ²⁶	Rough ²⁰
$C_M + C_T$	0.071	0.12	0.066
r_T	0.38	0.38	0.38
h	4.6	3.0	5.0
b_M	0.44	0.76	0.76
b_T	0.22	0.38	0.22
$\frac{U_\tau}{U_\infty}$	0.037	0.035	0.05
$\frac{U_c}{U_\infty}$	0.7	0.60	0.50
μ	0.24	0.18	0.50

For rough walls the decay of correlation is much more pronounced than for smooth walls, as shown in Section 7.5. Unless $\omega\delta^*/U_\infty < 0.04$ the factors $(b_1 \delta)^{-1}$ remain insignificant so that the ratio

$$\frac{\phi(k_1, 0, \omega)}{\phi\left(k_c = \frac{\omega}{U_c}, 0, \omega\right)}$$

is a function of $k_1/(\omega/U_c)$ and U_τ/U_∞ and h . Figure 7.29 therefore portrays a reasonably general relationship among the various wave number regions for each wall.

The validity of Equation 7.125 is limited by the knowledge of the dynamical properties of the wall pressure sources in the range of $k_1 \delta$ of order unity. To date, all turbulence measurements are restricted to the region of $\vec{k} = (\omega/U_c, 0)$. A second question pertains to an identification of what spatial scales enter; the model presumes a scale based on distance from the wall. The third question to be resolved is how the source region falls off at given k_1, k_3 as $y_2 > \delta$. The model

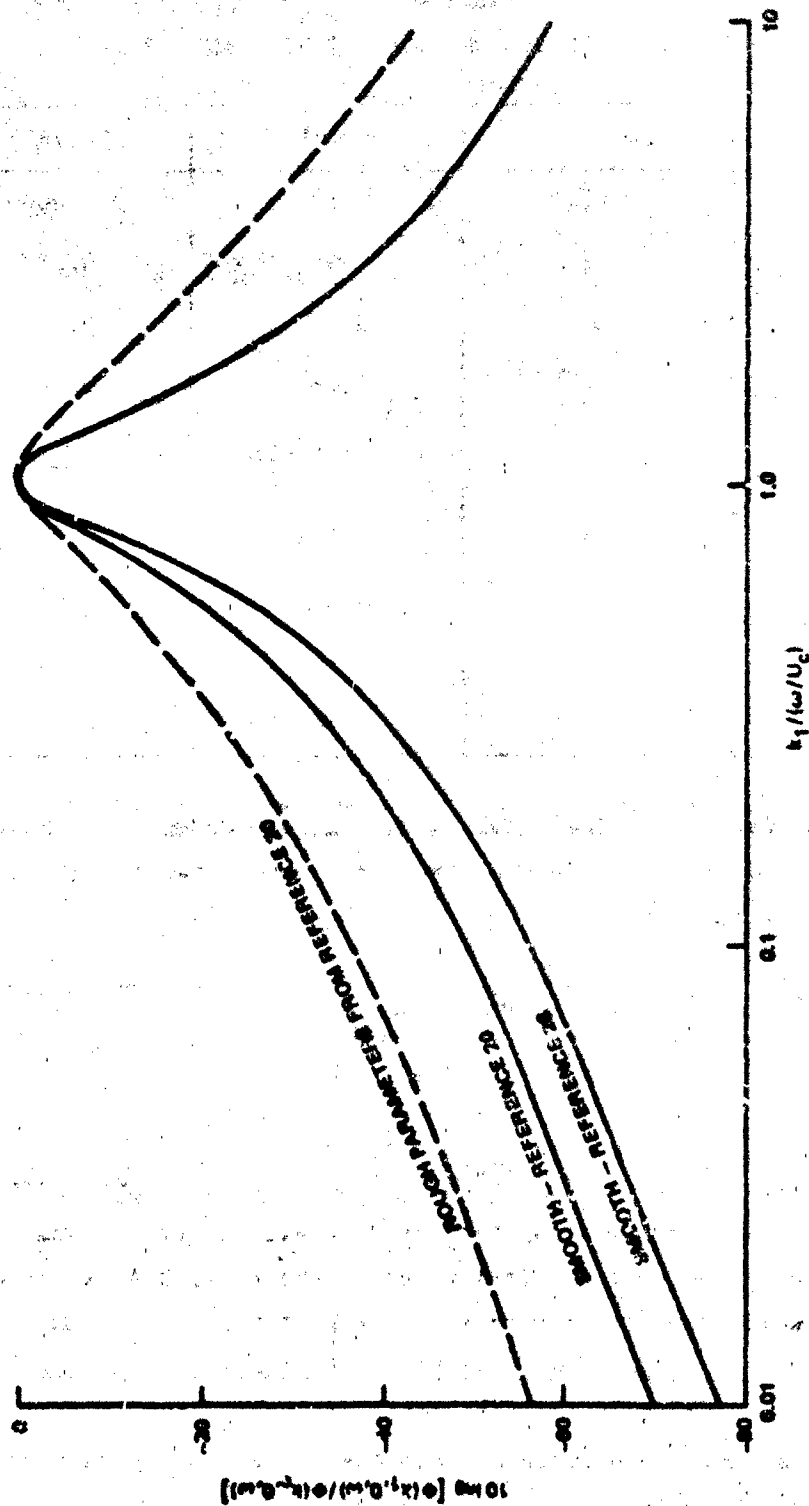


Figure 7.29 - Theoretical Spectrum Forms Derived by Chase⁸⁶ and Fitted to Parameters Determined in References 20 and 26. These Curves Apply to Purely Incompressible Motion, for the Range of k_1 Shown, $M_c < 0.01$

presumes that this fall off is rapid enough that the entire source zone is confined to $y_2 < \delta$. The dependence on k_1 for $\delta^{-1} < k_1 < \omega/U_c$ could be altered by the asymptotic nature of the sources in the vicinity $y_2 \geq \delta$.

Following Chase's model, Equation (7.125), Ffowcs Williams²⁴⁰ attempted to unify the analytical difficulties in modeling the wave number spectrum by suitable expansions in wave number. Essentially at low wave number $k \ll \delta^{-1}$ he confirmed that the second derivative nature of the source spectrum (see Equation (7.74)) leads to expressions which are quadratic in either Mach number (Equation (7.86b)) or k (Equation (7.89)), while at wave numbers significantly larger than δ^{-1} the Corcos form of the spectrum (see Equation (7.133)) follows from turbulence modeling of the form introduced earlier as Equation (7.48) or (7.92). At the acoustic wave number $k = k_0$ the evaluation of the pressure spectrum given in the form of say, Equation (7.77) is not possible due to the singular behavior at $k = k_0$. This difficulty of singularity can be elucidated by dealing with the compressible form of Equation (7.69), i.e., Equation (2.57) and noting that $P = (\rho - \rho_0)c_0^2$, and that the infinite, plane, and rigid surface specularly reflects the pressure. With the field point x on the surface and integration over $|y| \sim \delta$ to $|y| \rightarrow \infty$ an expression for the space time correlation of wall pressure between points separated a distance r is given by

$$(4\pi)^2 \overline{p^2} R_{pp}(\vec{r}, \tau) = \int_{V_1} \int_{V_2} \left\langle \left(\sigma\left(\vec{y}, t - \frac{|\vec{x}-\vec{y}|}{c_0}\right) \sigma\left(\vec{y}', t + \tau - \frac{|\vec{x}+\vec{r}-\vec{y}'|}{c_0}\right) \right) \right\rangle \\ \times \frac{dV_1 dV_2}{|\vec{x}-\vec{y}| |\vec{x}+\vec{r}-\vec{y}'|}$$

where $\vec{y}' - \vec{y} = \vec{\xi}$ is a field separation variable where $\sigma(\vec{y}, t)$ represents the sum of the source density above the surface and its image in the surface (see p. 77 and p. 685). Now, under the assumption that the contribution to the wall pressure is the net from the entire volume extending from $|\vec{x}-\vec{y}| \sim \delta$ to $|\vec{x}-\vec{y}| \rightarrow \infty$ the above integral can be recast into the approximate form (using same far field approximation for $|\vec{x}-\vec{y}|$ that led to Equations such as (2.36) and (2.75))

$$\overline{p^2} R_{pp}(\vec{r}, \tau) = \frac{1}{(4\pi)^2} \int_{v_1} \int_{v_2} \left\langle \sigma \left(\vec{y}, t - \frac{y}{c_0} + \frac{\vec{y} \cdot \vec{x}}{yc_0} \right) \times \right.$$

$$\left. \sigma \left(\vec{y} + \vec{\xi}, t + \tau - \left(\frac{y}{c_0} - \frac{(\vec{y} + \vec{\xi}) \cdot (\vec{x} + \vec{r})}{yc_0} \right) \right) \right\rangle \frac{dV(\vec{y}) dV(\vec{y}')}{y^2}$$

Now, each elemental source volume in cylindrical co-ordinates is $dV = y_{13} dy_{13} d\theta dy_2$ with range $0 \leq y_2 < \infty$, $\delta < y_{13} < \infty$, and $0 \leq \theta \leq 2\pi$. Furthermore since $\vec{y}' = \vec{y} + \vec{\xi}$ then, as before, (e.g., Equation (5.48)) we have $dV_1 = (y_{13} dy_{13} d\theta dy_2)$ and

$$dV_1 dV_2 = (y_{13} dy_{13} d\theta dy_2) (d^2 \xi_{13} d\xi_2)$$

and we will abbreviate $y_{13} = y$ and $dy_{13} = dy$. Thus the correlation function is

$$\overline{p^2} R_{pp}(\vec{r}, \tau) = \frac{1}{(4\pi)^2} \int_{\theta=0}^{2\pi} \int_{y=\delta}^{\infty} \int \overline{\sigma^2}(\vec{y}) R_{\sigma\sigma} \left(\vec{\xi}, \tau - \frac{\vec{y} \cdot (\vec{r} - \vec{\xi})}{yc_0} \right)$$

$$\times \frac{dy}{y} d\theta dy_2 d\xi_2 d^2 \xi_{13}$$

where $\sigma^2 R_{\sigma\sigma}$ is a \vec{y} -independent correlation function for a homogeneous turbulent field in the plane of the surface in the spirit of Equation (3.51). Integration over the boundary layer disk in the plane of the surface $\delta < y < R$ yields

$$\overline{p^2} R_{pp}(\vec{r}, \tau) \sim \int_0^\infty dy_2 \int_0^{2\pi} d\theta \int_{-\infty}^\infty d\xi \overline{\sigma^2}(y_2) R_{\sigma\sigma}\left(y_2, \vec{\xi}, \tau - \frac{\vec{r}_y \cdot \vec{\xi}_y}{c_0}\right) \ln \frac{R}{\delta}$$

This function is logarithmically singular as $R \gg \delta$, i.e., as the size of the surface is made large compared with the boundary layer thickness. Note the separation variables r_y and ξ_y just denote the magnitudes r and ξ in the plane of the surface in the direction of \vec{y} . The same methods that led to Equation (3.61) may be used to obtain.

$$\phi_{pp}(\vec{k}, \omega) \sim \int_0^\infty dy_2 \int_0^\infty d\xi_2 \int_0^{2\pi} d\theta \phi_{\sigma\sigma}(y_2, \xi_2, \vec{k}, \omega)$$

$$\delta(k - k_0 \cos \theta) \ln R/\delta$$

which Ffowcs Williams reduced to the notation of Equations (7.86a) and (7.89)

$$\phi_{pp}(\vec{k}, \omega) \sim \rho_0^2 U_\tau^4 k_0^4 \delta^4 \ln \frac{R}{\delta} \overline{\phi}_{ijkl}(\vec{k}, \omega) \delta(k - k_0)$$

At low wave numbers the only contributor to the sources σ are those lying in the plane of the surface and all others which involve derivatives d/dy_2 integrate over y_2 to zero (since $u_i u_j = 0$ both on the rigid surface and far from the surface). Thus the only part of the source spectrum that contributes is

$$\phi_{\sigma\sigma}(\vec{k}, \omega) = \rho_0^2 U_\tau^4 k^4 \bar{\phi}_{\alpha\beta\gamma\delta}(\vec{k}, \omega)$$

where the indices denote Reynolds stresses lying the plane of the surface.

The entire wave number spectrum for $0 < k < \infty$ is a linear combination of functions each of which apply to the appropriate range of wave number, say, $0 < k < k_0$, $k = k_0$, $k > k_0$. Assuming a common function for the turbulence source spectrum such as Equation (3.105) all the ranges of low wave number, $k \ll \omega/U_c$, may thus be covered by

$$\phi_{pp}(\vec{k}, \omega) = \tau_w^2 \delta^2 \phi(k_1, k_3, \omega) \delta/U_\infty$$

$$\times \left\{ a_0 (U_c k / \omega)^2 + a_1 M^2 + a_2 M^4 \ln \frac{R}{\delta} \delta \left(\frac{k U_c}{\omega} - M_c \right) \right\}$$

which includes Equations (7.89) and (7.86a) and where the numerical coefficients a_0 , a_1 and a_2 are still unknown and the spectrum function $\phi(k_1, k_3, \omega)$ is presumed to be controlled by the purely hydrodynamic turbulence behavior in the boundary layer.

Finally, an emerging approach to field modeling has been proposed by Ffowcs Williams and Pursehouse²⁴¹ who attempt to account for the intrinsically unstable nature of the instantaneous shear flow (e.g., see Figure 7.22) in the boundary layer. This is done by approximating the velocity gradient with a vortex sheet so that the fluid responds both acoustically (linearly) and hydrodynamically via the induced shear layer instabilities. Thus it is a model in which the turbulence sources and the sound field are coupled and the implication is that the sound field cannot be calculated on the basis of an assumed independent source field as in the basis of Lighthill's theory.

7.4 PRESSURE FLUCTUATIONS BENEATH EQUILIBRIUM WALL LAYERS

As in the case of the turbulent velocities, the wall pressures are stochastic in space and time so that both single and multiple sensors are used to determine spatial scales and local intensities. In the case of wall pressure measurements, the sizes of transducers limit the precision of some types of measurements. This problem was more severe in the early stages of research, before miniature sensor technology reached its current state. However, the influence of finite sensor size is, even today, a more severe limitation on wall pressure measurements than on velocity fluctuations, and the effects will be examined. Also, since it is of interest to utilize flush-mounted hydrophones in some oceanographic sensor applications, the behavior of rubber blankets in shielding transducers from boundary-layer pressure is discussed.

7.4.1 Intensity and Frequency Dependence of Wall Pressures

As a practical matter, our discussions can be profitably separated to discuss measured results published before and after 1962. In 1962 and 1963 Willmarth and Wooldridge^{27,28} and Bull^{112,113} (republished as reference 26) published work that is classical as far as depth and completeness are concerned. Before 1962, measurement programs were relatively crude because results were prone to contamination from acoustic background noise and wall vibration in the case of measurements performed with piezoelectric transducers, and miniature transducer technology was just becoming available. The advantage of these transducers is their greater pressure sensitivity, which is required in the aerodynamic environment. Another limitation in the early research was the capability to compute cross-correlation and cross-spectral densities of transducer outputs. The amount of time and care required to provide precise statistical measures of turbulence quantities (and pressures and velocities, for that matter) is not well appreciated by new-comers to the field who have at their disposal modern (hybridized digital and analog) fast Fourier transform and correlation apparatus. Today it takes only a few seconds to compute a complete cross-correlation function that probably took hours to compute twenty years ago.

The earliest measurements are those reported by Willmarth,¹¹⁴ who provided a frequency spectrum and root-mean-square pressure. The interested reader should consult Willmarth's account of the early work in this field.¹¹⁵ Space-time correlations were obtained by Willmarth¹¹⁶ with the motivation that the spatial correlation scale was needed to account for the aerodynamic excitation of aircraft fuselages and the wind generation of water waves. Other early attempts at measuring the frequency spectrum are those of Mull and Algranti¹¹⁷ on an aeroplane wing at Mach numbers 0.3 to 0.8 and Tack et al.,¹¹⁸ who also measured space-time correlations and cross-spectral densities from which convection velocities and moving axis time scales could be determined. Harrison¹¹⁹ had earlier published the first cross-spectral densities, finding convection velocities for the pressures of approximately $0.8 U_\infty$. The main shortcoming of all these early measurements was, as mentioned above, restricted electronic frequency response, spatial averaging by the sensor, and limitation by facility noise and vibration. In some aerodynamic measurements an effort was made to increase the spatial resolution of the microphones by placing a cap perforated with a small pin hole. Because of the air volume between the microphone and the hole, the response was limited by a Helmholtz resonance. More recently, Blake^{20,120} reported measurements with a pinhole microphone for which this resonance frequency was 17,000 Hz.

The autospectral density of wall pressure fluctuations is shown in the dimensionless form

$$\frac{\phi_p(\omega) U_\infty}{q_\infty^2 \delta^*} \text{ versus } \frac{\omega \delta^*}{U_\infty}$$

in Figure 7.30. Results from a number of sources are in substantial agreement; for each result are shown the friction velocity and the ratio of the microphone diameter to the boundary-layer displacement thickness d/δ^* . In all cases U_τ/U_∞ is nearly the same, but the relative microphone size differs by a factor of 3. The effects of spatial averaging become important (see Section 7.4.5) when roughly $\omega d/U_\infty \approx 1.2$. This frequency occurs at $\omega \delta^*/U_\infty = 3, 4, \text{ and } 12$ for the values $d/\delta^* = 0.4, 0.3, \text{ and } 0.1$, respectively. As shown in Figure 7.30, the effect of the transducer on the high-frequency part of the pressure spectrum is impressive.

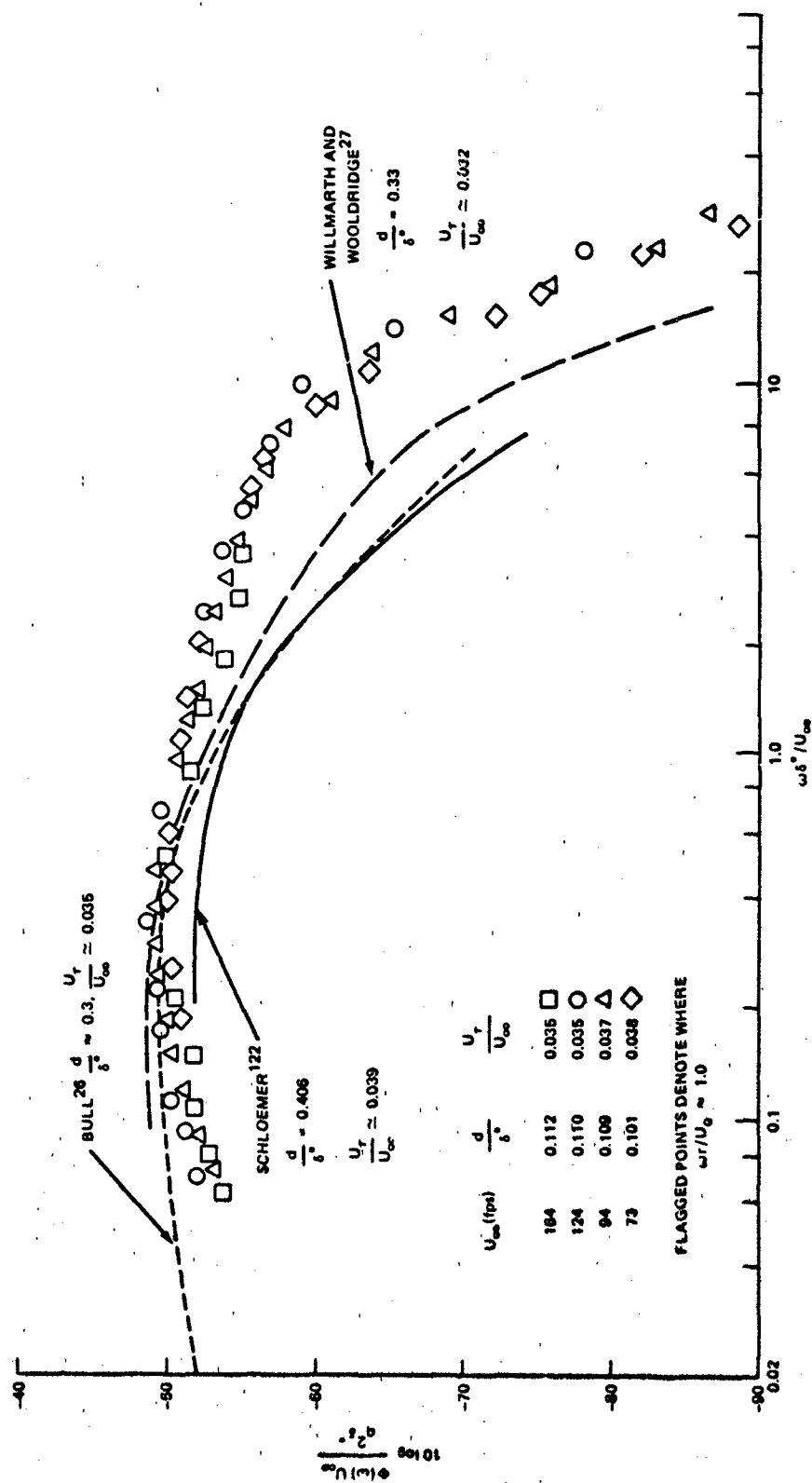


Figure 7.30 - Wall Pressure Spectra, Smooth Wall. From Blake ²⁰

At frequencies less than $\omega\delta/U_\infty < 1$, the wall pressure spectrum increases with increasing frequency, and there is an intermediate range of frequency for which $\omega^{-0.7}$ dependence is observed. This range extends to $\omega\delta^*/U_\infty \approx 10$ (or $\omega\delta/U_\infty \approx 100$), beyond which a more pronounced reduction with frequency is observed. This behavior is in agreement with the trends shown in Figure 7.28. The reduction in spectrum level at low frequencies that is predicted by the theory and observed by Bull and Blake has not been characteristic of all measurements. Quite often the background noise and vibration of the facility contaminate at frequencies less than $\omega\delta^*/U_\infty = 0.1$. The measurements by Bull extend to $\omega\delta^*/U_\infty = 0.02$ without the influence of facility background noise. Measurements by Hodgeson¹²² at low frequency on a glider wing showed a flat spectrum down to $\omega\delta^*/U_\infty = 0.1$. In this experimental program he established that earlier measurements¹²³ had been influenced by the presence of an adverse pressure gradient in the boundary layer and that a strong increase in pressure with frequency at low frequencies observed then was due to that gradient (see also Section 7.5.3). Evidence of an increase in the spectrum level as frequency decreases has also been provided by Serafini,¹²⁴ who reported low-frequency pressure fluctuations to $\omega\delta^*/U_\infty = 0.002$. The Mach number was held constant at 0.6 while the measurement point was changed in the wind tunnel to increase δ^* from 0.047 in. to 0.321 in. The dimensionless spectral densities in the frequency range $0.05 < \omega\delta^*/U_\infty < 0.5$, increased as dimensionless frequency was reduced as $(\omega\delta^*/U_\infty)^{-1}$. This behavior was probably not due to acoustic noise in the facility because Serafini nondimensionalized the measurements on q_∞ and δ^* to a spread of less than $\pm 20\%$ for the full range of parameters. It is possible, but not certain, that upstream history influenced these very-low-frequency wall pressures as has been shown recently by Blake and Maga¹²⁵ on the side of a smooth strut on which leading-edge separation occurred. At a distance of more than 20δ from the separation zone, they showed the spectrum of the pressures to be enhanced for $0.02 < \omega\delta^*/U_\infty < 1$ for various angles of attack of the airfoil. It should be noted that the free stream turbulence intensities, $\overline{u_1^2}/U_\infty^2$, were for Schloemer, 0.0012; Willmarth and Wooldridge, 0.0006; Bull, 0.00025; Blake, < 0.001 ; and Serafini, somewhat larger, 0.01 to 0.02. One questions whether the higher turbulence intensity in Serafini's facility could have caused enhanced low-frequency pressure fluctuations.

We now consider the physical aspects of the wall pressure and the relationship between the measured and theoretical spectra. To compare the measured spectra in Figure 7.30 to the sketch in Figure 7.28, note that δ/δ^* is approximately 10, and $20 \log C_f$ lies between the extremes of -52 and -51 for the results of reference 20. Thus nondimensionalizing on τ_w^2 or q_∞^2 are nearly equivalent in this figure. Pressure spectral densities for smooth and rough walls are nondimensionalized on τ_w^2 in Figure 7.31. For $\omega\delta^*/U_\infty < 3$, this nondimensionalization on outer variables appears to characterize the pressure spectrum. The smooth wall spectra show that for $\omega\delta^*/U_\infty$ between 0.4 and 8.0 there is a dependence of nearly $\omega^{-0.7}$, while at higher frequencies the spectrum decreases roughly as ω^{-5} . These frequency dependencies are quite similar to the predicted behavior illustrated in Figure 7.28. The frequency marking the change in dependency was also suggested to occur above $\omega\delta/U_\infty = 100$, and this point is roughly matched by $\omega\delta^*/U_\infty = 10$. The maximum in the spectrum was also predicted near $\omega\delta^*/U_\infty = 0.2$ to 0.3 ($\omega\delta/U_\infty = 2$), which is confirmed by the measurements. Inner-variable scaling was predicted to become important for $\omega\delta^*/U_\infty > 10$ to 15 ($\omega\delta/U_\infty = 100$) because eddies convected near the sublayer determine these contributions. Figure 7.32 is a comparison of measurements from references 20, 126, and 127 re-normalized in inner variables. As the Reynolds number increases, the spectrum level below $\omega\nu/U_\tau^2 < 0.1$ increases uniformly. At larger dimensionless frequencies (>0.1) the results appear to be well defined, and an upper limit derived by Bull¹²⁸ and based on measurements on a pipe wall appears to be consistent with the data. The discrepancy between the two measurements at high frequencies reduced somewhat by increasing U_τ for Emmerling's measurement by 1.05 and decreasing U_τ for Blake's results by 0.95. This 5% uncertainty in U_τ is very likely, yet the absolute value of high-frequency pressures appears to depend on U_τ as U_τ^8 . Thus comparisons in this range of frequency are sensitive to uncertainties in U_τ . The ω^{-1} power law behavior is approximated in the range $0.1 < \omega\nu/U_\tau^2 < 0.5$ by all investigations.

The root-mean-square wall pressures obtained by various investigators are difficult to compare because each measurement has a limitation at high frequencies due to effects of spatial averaging (see Section 7.4.6). Thus it is preferable to compare autospectra from various sources. However, the spectra in Figure 7.32 suggest that $\overline{p^2}^{1/2}/\tau_w$ should increase slightly with R_θ as proposed by Willmarth.¹¹⁵ Generally accepted values are roughly bounded by

$$2 < \frac{\overline{p^2}^{1/2}}{\tau_w} < 4$$

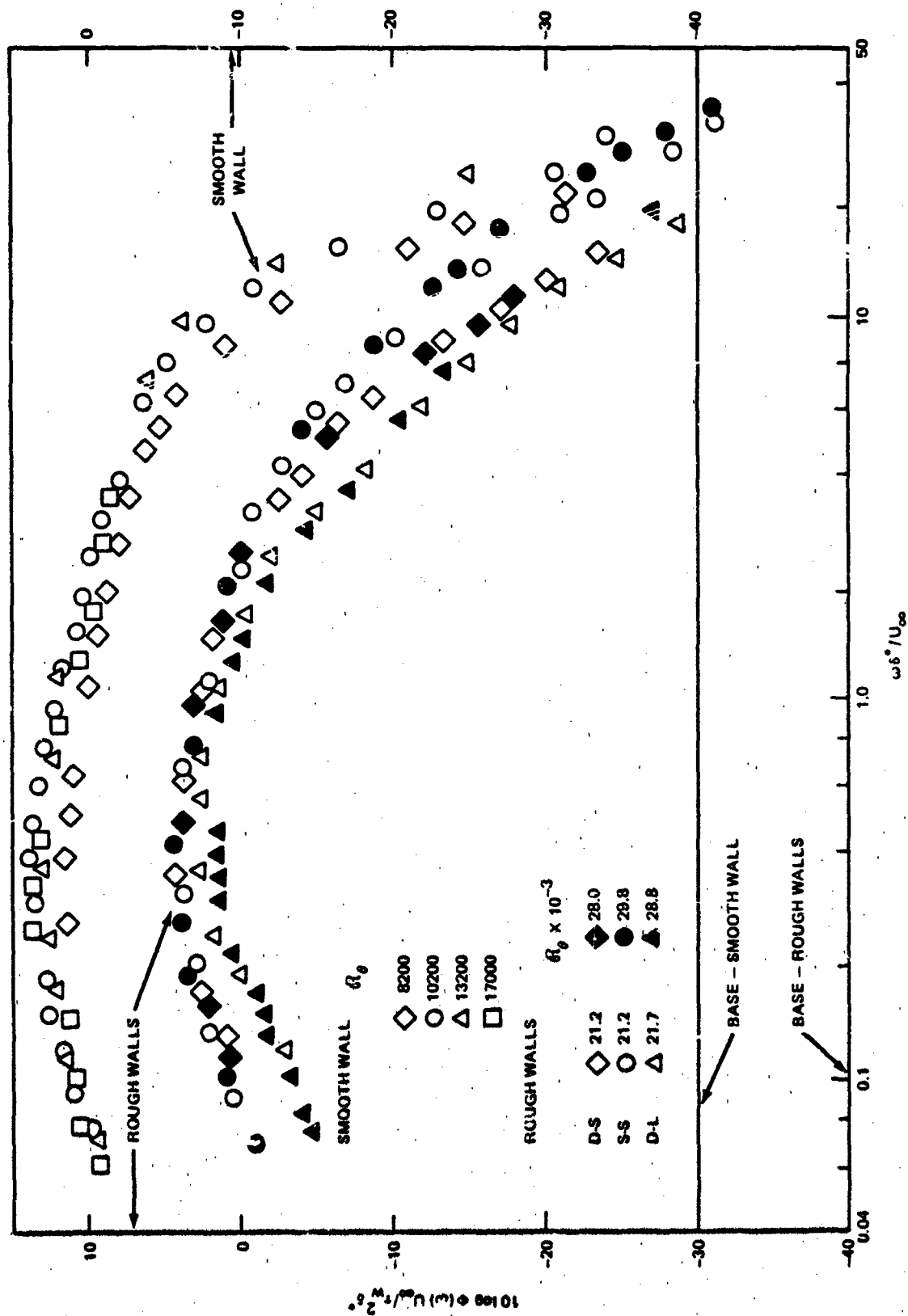


Figure 7.31 - Wall Pressure Spectra, Smooth and Rough Wall Comparison. From Blake²⁰

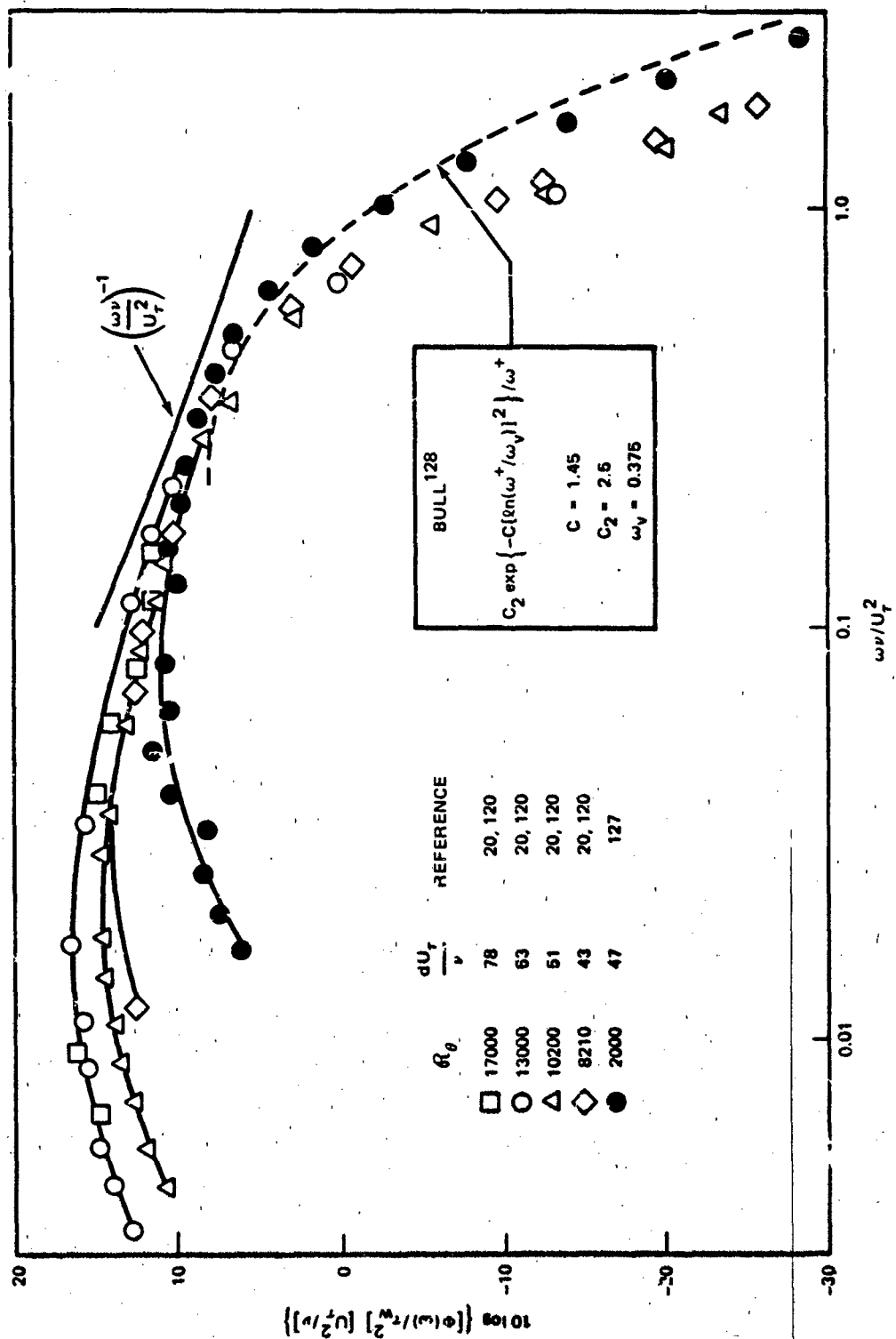


Figure 7.32 - Spectrum of Wall Pressure Fluctuations at a Point
Nondimensionalized on Viscous Scales

depending on the source of the experimental data, as shown in Figure 7.33. Another summary of older data has been given by Bull²⁶; the line attributed to him in Figure 7.33 is from his measurements. The more recent data obtained for $d/\delta^* \leq 0.2$ show generally larger root-mean-square values that increase slowly with R_θ , in agreement with Bull's results. Measured values on rough walls have no identifiable influence of spatial averaging, but they depend on roughness.

The wall shear appears to approximately determine the level of the pressure spectral density as predicted from the theory as it appears to also set the levels of the velocity fluctuations. Furthermore, the low-frequency pressures and (as we shall see presently) the overall length scale of boundary layer pressure, is established by δ^* (or nearly equivalently δ).

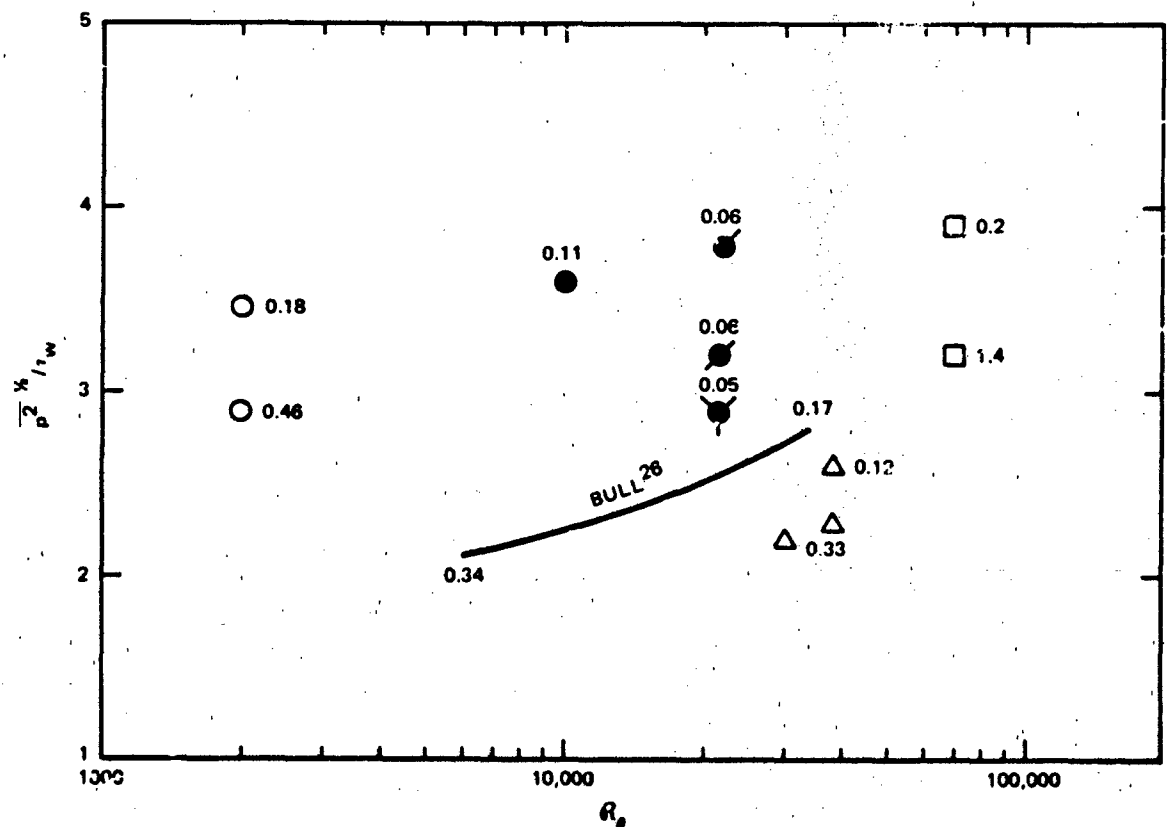


Figure 7.33 - Variation of Root-Mean-Square Pressure with R_θ .

Emmerling¹²⁷ ○; Serafini¹²⁴ □; Blake,²⁰ Smooth ●, Rough SS ●
 DS/DL ●; Willmarth.^{27,115} Numbers Denote Values
 of d/δ^* ; Data Pertain to grad $P = 0$

7.4.2 Spatial Characteristics and Convection of Wall Pressures

The experimental method of determining the spatial scales of turbulent wall pressure is the same as that used in turbulent velocity measurement. Following Equation (7.41) we define the space-time correlation of wall pressure fluctuations as

$$R_{pp}(\vec{r}, \tau) = \frac{\overline{p(\vec{y}, t) p(\vec{y} + \vec{r}, t + \tau)}}{\left[\overline{p^2(\vec{y}, t)} \overline{p^2(\vec{y} + \vec{r}, t + \tau)} \right]^{1/2}} \quad (7.128)$$

where $p(\vec{y}, t)$ is the fluctuating wall pressure, the vinculum denotes a time average, and, of course, \vec{y} and $\vec{y} + \vec{r}$ are in the plane (1,3) of the wall. In equilibrium boundary layers with nearly vanishing static pressure gradient, the pressure fluctuations are statistically spatially homogeneous,⁵¹ so that without loss of generality we may replace

$$\left[\overline{p^2(\vec{y}, t)} \overline{p^2(\vec{y} + \vec{r}, t + \tau)} \right]^{1/2} = \overline{p^2}$$

The first extensive measurements were those of Willmarth and Wooldridge²⁷ who provided the three-dimensional representation shown in Figure 7.34. The space and time coordinates have been made dimensionless on U_∞ and δ^* . The correlation function was obtained with $r_3 = 0$; Figure 7.34 shows $R_{pp}(r_1, 0, \tau)$. The correlation shows the ski-slope characteristic along the $a(r_1, \tau)$ locus which is now familiar in the space-time statistics of turbulence. This behavior is emphasized in Figure 7.35, which shows iso-correlation contours as a function of $\tau U_\infty / \delta^*$ and r_1 / δ^* . The ratio

$$\frac{U_c}{U_\infty} = \frac{r_1}{\tau_m U_\infty}$$

where τ_m is the time delay for maximum correlation at any given value of r_1 , decreases slightly for $r_1 / \delta^* < 5$. As (r_1, τ) are increased along a line defined by nearly constant U_c / U_∞ , the moving axis correlation decreases because of the decaying

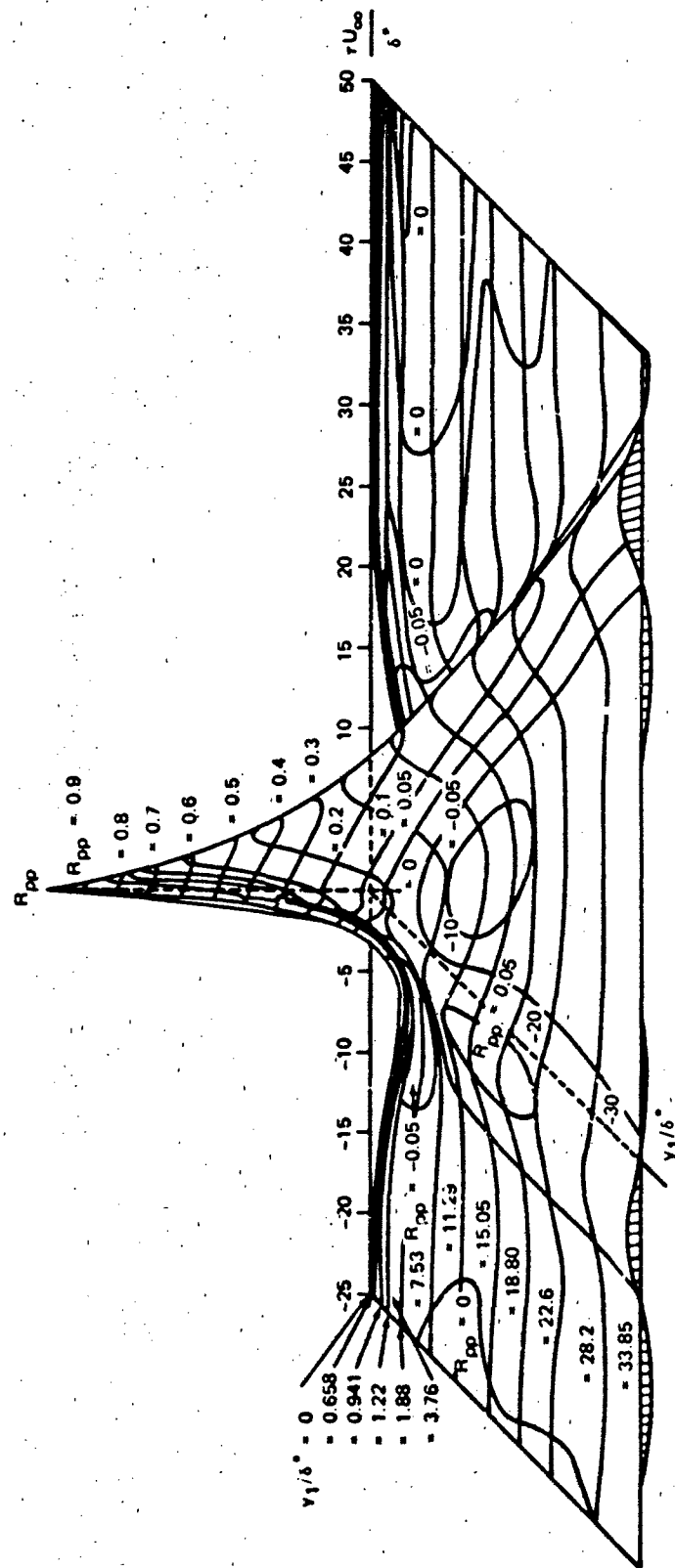


Figure 7.34 - Longitudinal Space-Time Correlation of the Wall Pressure
Displayed in Three Dimensions Using the Data on Smooth Walls.

From Willmarth and Wooldridge²⁷

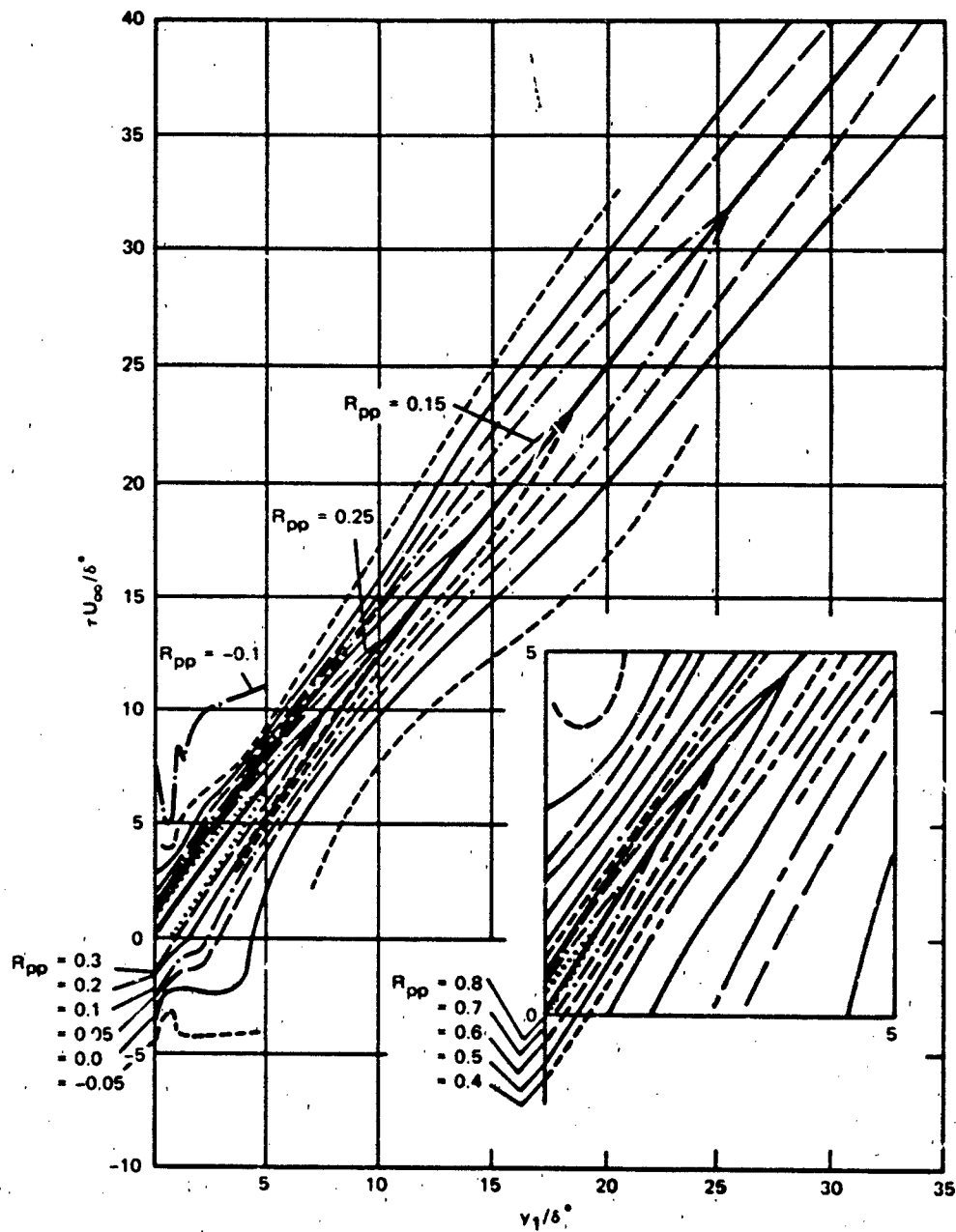


Figure 7.35 - Iso-correlation Contours of Wall Pressure Fluctuations on Smooth Walls with r_1 , τ Variables.

The Heavy Line Denotes the Dominant Eddy Convection for Which the Wall Pressure Decay Rate is Minimum.

From Willmarth and Wooldridge²⁷

influence of the smaller, near-wall, eddy structure. Other iso-correlation contours of

$$R_{pp}(r_1, r_3, 0)$$

are shown in Figure 7.27 from the work of Bull.²⁶ Both the velocities and pressures are shown; each is symmetric about $\vec{r} = 0$. This figure was discussed in connection with our analytical derivations, and it shows that the spatial character of the pressures deviates considerably from isotropy. As shown in Section 7.3.3, the pressure correlations are elongated in the r_3 direction because of convection in the r_1 direction that enhances the importance of the high wave number, or small scale, turbulence structure. That is substantially why the iso-correlations of pressure show a behavior opposite that shown by the turbulent velocities.

Another interesting characteristic of the space-time correlation in Figure 7.34 is the appearance of a secondary ridge along a locus of $r_1 < 0$ and $\tau > 0$. This ridge is actually determined by

$$\frac{U_c}{U_\infty} = \left| \frac{r_1}{\tau_m U_\infty} \right| = M^{-1}$$

where M is the convection Mach number of the flow, and it is attributed to acoustic contamination of the measurement by background noise of the wind tunnel.

The spatial correlation $R_{pp}(r_1, 0, 0)$ in Figure 7.27 shows negative values for $|r_1/\delta^*| > 4$. Historically, this change in sign has very special implications regarding the prediction of acoustic radiation from boundary layers. It will be shown in Chapter 8 that radiated noise in hydroacoustic applications depends on wave number spectrum levels at wave numbers that are very much smaller than reciprocals of the macroscales of the convected turbulence. These spectrum levels have been approximated (see Equation (7.131)) by the integral of the streamwise correlation function over all r_1 . The negative tail on $R_{pp}(r_1, 0, 0)$ tends to nullify the contribution to the integral from the positive values at small r_1 , thus reducing the net spectrum level at small wave number.

The broadband space-time correlations of wall pressure, when expressed in dimensionless form with U_∞ and δ^* , do not appear to be very sensitive to wall roughness. Figure 7.36 shows $R_{pp}(r_1, 0, \tau)$ in a representation like that in Figure 7.10. (For comparisons to that figure, note that $\delta/\delta^* \approx 6$ to 10 for smooth walls and ≈ 4 for the rough wall.) The convection velocity of pressures on the smooth wall is somewhat higher than over the rough wall, reflecting the influence of the velocity defect caused by roughness. The modeling of Section 7.3 indicates that convection velocities of pressures over rough walls should mirror the defect $\Delta U_c/U_\tau = (U_c/U_\tau)_{\text{smooth}} - (U_c/U_\tau)_{\text{rough}}$. At corresponding r_1/δ^* , $\Delta U_c/U_\tau$ was found to range from 9.2 to 10.5 (Figure 7.4 shows the velocity defects for the surfaces in reference 20 to be between 9.5 and 12). Since the moving axis correlation

$$R_{pp}(\tau U_c = r_1, 0, \tau)$$

is not greatly affected by roughness, the lifetime of the broadband disturbances is roughly unaffected by roughness. However, the correlation distance is much reduced because the eddy field velocity is reduced by the factor $\Delta U_c/U_\tau = f(k_g U_\tau/\nu)$.

Large differences in behavior with wall roughness are seen in the cross-spectral densities. We use the representation that was previously found to be useful in describing velocity cross spectra, namely, we nondimensionalize

$$\frac{\psi_p(r_1, 0, \omega)}{\phi_p(\omega)} \text{ versus } \frac{\omega r_1}{U_c}$$

and similarly for the lateral cross-spectrum function, $\phi_p(0, r_3, \omega)$ versus $\omega r_3/U_c$. Figures 7.37 and 7.38 show the cross-spectral density functions and convection velocities. First, we note that the cross-spectral densities of pressures on smooth walls measured by Willmarth and Wooldridge, Bull, and Blake are in substantial agreement and mirror the behavior of the velocity fluctuations. The cross-spectral density, when shown in this representation, depicts a loss of coherence of a disturbance of convected wave number $k_c = \omega/U_c$ in a distance r_1 . A disturbance there is reduced to one-tenth of its initial identity in a distance $r_1 = 18/k_c$ and $r_3 = 3/k_c$ over smooth walls and $r_1 = 7/k_c$ over rough walls. The reduction in the

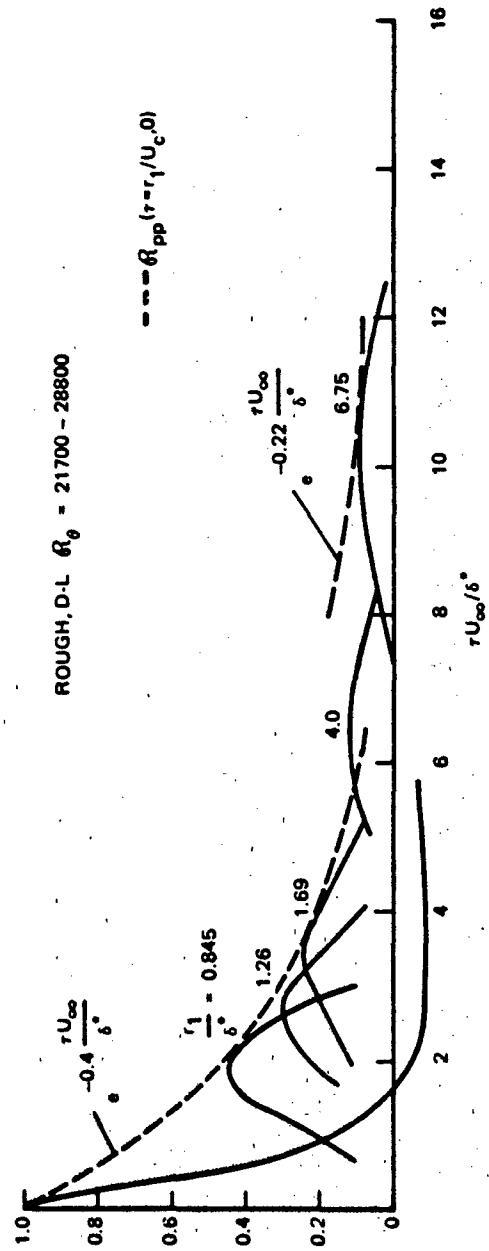
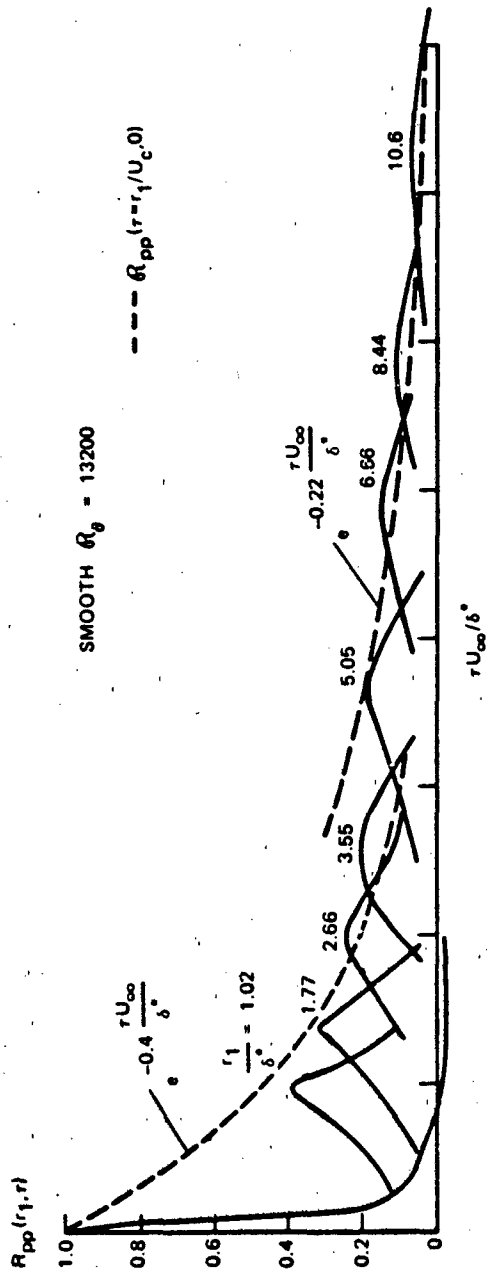


Figure 7.36 - Space-Time Correlations of Wall Pressure on Smooth and Rough Walls.
From Blake²⁰

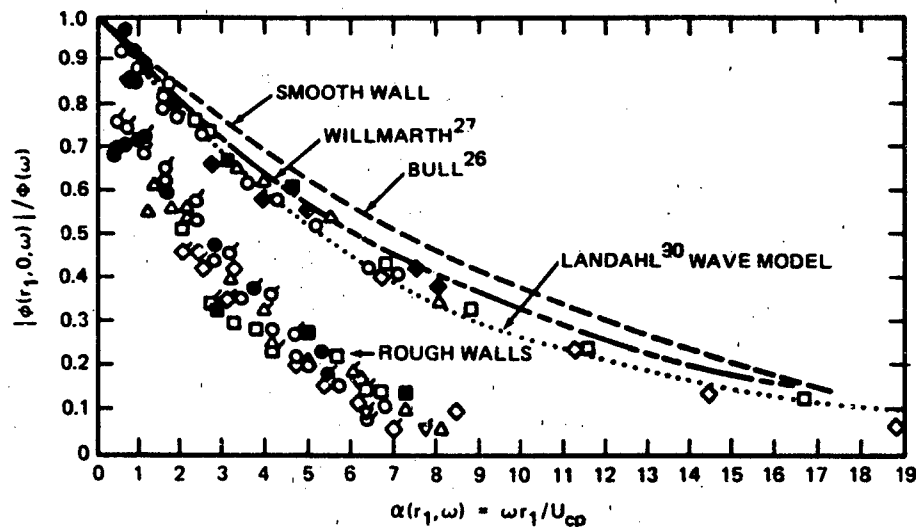


Figure 7.37a - Normalized Longitudinal Cross-Spectral Density for Smooth and Rough Walls. Smooth-Wall Points for r_1/δ^* : \circ , 1.77; \circ , 2.67; Δ , 3.55; \square , 8.41; \diamond , 14.2. (S-S) Rough-Wall Points for r_1/δ^* : \circ , 0.914; Δ , 1.828; \diamond , 4.33; \square , 7.4. (D-L) Rough-Wall Points for r_1/δ^* : σ , 0.845; α , 1.23; σ , 1.69; σ , 4.0; ∇ , 6.75. Open Points; 124 ft/s; Closed Points 164 ft/s.

$$SS: \frac{k U}{\nu} \approx 178, DL: \frac{k U}{\nu} \approx 321^{20}$$

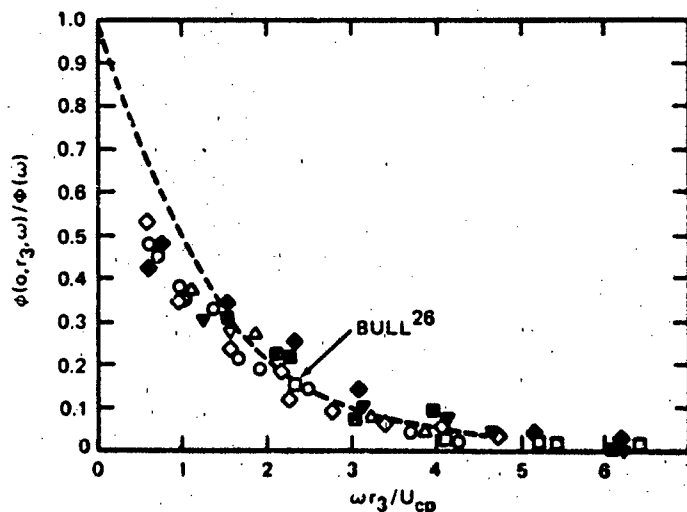


Figure 7.37b - Normalized Lateral Cross-Spectral Density Amplitude for Smooth and Rough Walls. Smooth-Wall Points for r_3/δ^* : \circ , 1.77; Δ , 3.55; \square , 8.41. (S-S) Rough-Wall Points for r_3/δ^* : σ , 0.196; σ , 4.03. (D-L) Rough-Wall Points for r_3/δ^* : \diamond , 0.845; \square , 1.23; ∇ , 1.69. Open Points, 124 ft/s; Closed Points, 164 ft/s²⁰

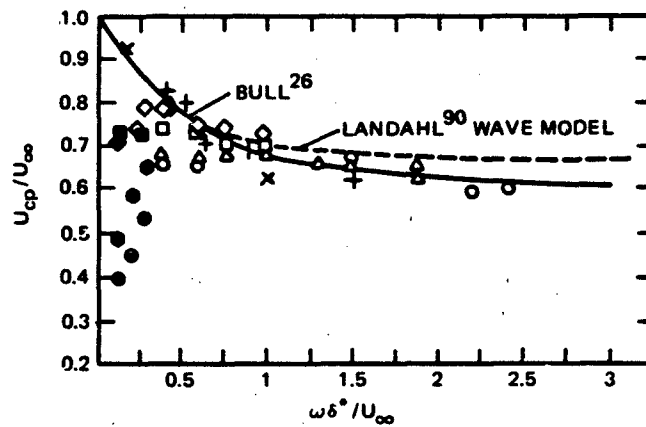


Figure 7.38a - Phase and Group Convection Velocities. Smooth Wall.
 Group Velocities: 126 ft/s, Values of r_1/δ^* : +, 1.77; ●, 8.41;
 ●, 14.2; 164 ft/s: x, 2.67. Phase Velocities: Open Points 126 ft/s;
 Closed Points 164 ft/s. Values of r_1/δ^* : ○, 1.77; ●, 1.78; ▲, 2.67;
 ▲, 3.55; □, ■, 8.41; ◇, ◆, 14.2²⁰

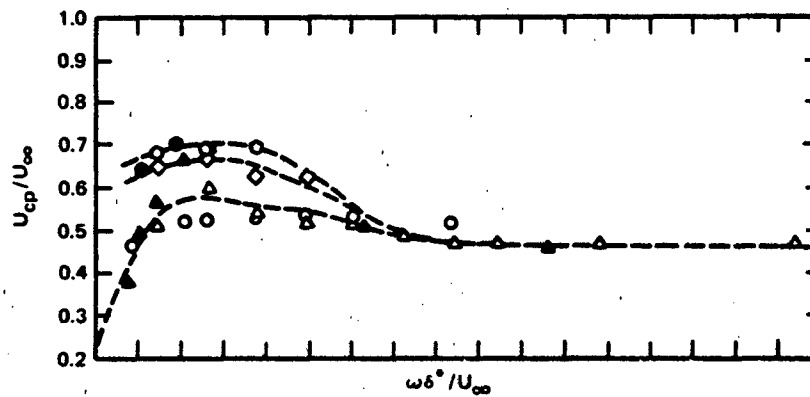


Figure 7.38b - Phase Convection Velocities. Rough Wall (S-S).
 Open Points 124 ft/s Closed Points 164 ft/s. Values of r_1/δ^* :
 ▲, ▲, 0.914; ○, 1.828; ◇, 4.33; ●, ○, 7.4²⁰

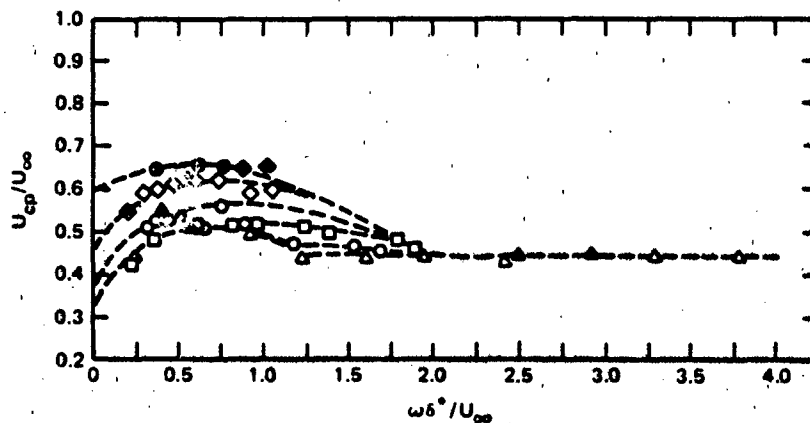


Figure 7.38c - Phase Convection Velocities. Rough Wall (D-L).
 Open Points 124 ft/s; Closed Points 164 ft/s. Values of r_1/δ^* :
 ▲, ▲, 0.845; ○, 1.23; □, 1.69; ○, 2.32; ◆, ◇, 4.0; ●, 6.75²⁰

convection velocity, already attributed to a parallel velocity defect in the mean velocity, is also carried over in the frequency domain. Pressures measured by Priestly¹²⁹ on the ground beneath an atmospheric boundary layer agree with those just discussed.

Before proceeding with discussions of the general implications of the cross-spectral density functions, we note that the results of the various investigations differ in some details. First, the cross-spectrum amplitudes of Blake²⁰ and of Bull²⁶ differ at low frequencies and large separations. Bull's results show a notable decorrelation under these circumstances. The results of Willmarth and Wooldridge²⁷ do not show this decorrelation behavior. However, it should be pointed out that the data sample of Willmarth and Wooldridge is not as extensive as that of Bull. Over rough walls, slight evidence of this decorrelating behavior can be distinguished in the scatter of points, as noted by following the trend of the squares in Figure 7.37a, for example. Another point of disagreement has to do with convection velocities at frequencies $\omega\delta^*/U_\infty < 0.5$. Blake's results show that at a given value of r_1/δ^* , U_c/U_∞ decreases as $\omega\delta^*/U_\infty$ decreases. Bull, on the other hand, shows an opposite behavior; at a given value of r_1/δ^* , U_c/U_∞ increases at lower frequencies. The limit shown by Bull is $U_c/U_\infty = 0.9$ as $\omega \rightarrow 0$. The reason for this and the above discrepancies has not been satisfactorily resolved, although Chase⁸⁶ predicted the trend observed by Blake. Dinkelacker et al.¹³⁰ have reported the observation of low-speed convection ($U_c \approx 2U_\infty$) for eddies convected over short streamwise distances as well as high-speed convection ($U_c \approx 0.8U_\infty$) for eddies convected over large distances.

In case of rough walls, Aupperle and Lambert's¹³¹ results are in substantial agreement with those shown in Figure 7.37a. Their results were obtained over an approximate range of $k_g U_\tau/\nu$ from 120 to 1300, which corresponded to $k_s U_\tau/\nu$ from roughly 600 to 4000, but their roughness elements were not as closely packed as were those of Blake.²⁰ At $k_g U_\tau/\nu = 1300$, Aupperle and Lambert discovered some lack of $\omega r_1/U_c$ similarity, apparently the result of local disturbances in the vicinity of individual roughness elements.

It will be useful to use functional representations of the form of Equation (7.46) for the wall pressures to formulate vibration response in Chapter 3. Corcos^{132,133} was the first to use this type of representation for the cross-spectral densities. For the wall pressures this representation is

$$\phi_p(r_1, 0, \omega) = \phi_p(\omega) e^{-\gamma_1 \left| \frac{\omega r_1}{U_c} \right|} e^{+i\omega r_1 / U_c} \quad (7.129a)$$

and

$$\phi_p(0, r_3, \omega) = \phi_p(\omega) e^{-\gamma_3 \left| \frac{\omega r_3}{U_c} \right|} \quad (7.129b)$$

so that¹³² the complete function is

$$\phi_p(r_1, r_3, \omega) = \phi_p(\omega) e^{-\gamma_1 \left| \frac{\omega r_1}{U_c} \right|} e^{-\gamma_3 \left| \frac{\omega r_3}{U_c} \right|} e^{+i\omega r_1 / U_c} \quad (7.130)$$

where $\gamma_1 = 0.116$ for smooth walls, $\gamma_1 = 0.32$ for the rough walls, and $\gamma_3 = 0.7$ for smooth and rough walls. Compare $\gamma_1 = 0.116$ with the value for turbulence shown in Figure 7.19a for the logarithmic region, i.e., y_2/δ from 0.05 to 0.4. Note that somewhat different functional representatives have been suggested by Chase⁸⁶ to be consistent with his model. See Equations (7.127a) and (7.127b).

Microscales for wall pressures have not been determined, partly because transducers cannot be brought in close enough proximity to generate an osculation parabola,* but more important, because there has been no practical or theoretical necessity to obtain this scale. The integral scales L_1 can be obtained by integrating the spatial correlations (Section 3.6.3.2). It is important to note two crucial limitations. First, if there is significant low-pass filtering, as if by severe spatial cancellation of high-frequency pressures (see Section 7.4.6), $R_{pp}(r_1, 0, 0)$ will show anomalously large negative values for values of r_1 greater than $2\pi U_c / \omega_{co}$, where ω_{co} is the cut-off frequency of the autospectrum. This deficiency arises because Taylor's Hypothesis holds at least approximately. The second limitation arises because at large values of r_1/δ * the background acoustic and vibratory disturbances in the facility will control the correlation.

*See Equation 7.53.

7.4.3 Description in the Wave Number Domain

The relationship between the space-time correlation and the wave number frequency spectrum was established in Section 3.5.3, namely (Equation (3.51)),

$$\phi_p(\vec{k}, \omega) = \frac{1}{(2\pi)^3} \iiint_{-\infty}^{\infty} e^{-i(\vec{k} \cdot \vec{r} - \omega \tau)} \overline{p^2} R_{pp}(\vec{r}, \tau) d^2\vec{r} d\tau \quad (7.131)$$

or

$$\phi_p(\vec{k}, \omega) = \frac{1}{(2\pi)^2} \iint_{-\infty}^{\infty} e^{-i\vec{k} \cdot \vec{r}} \phi_p(\vec{r}, \omega) d^2\vec{r} \quad (7.132)$$

It is necessary to determine values of $\phi_p(\vec{k}, \omega)$ near certain critical wave numbers; the acoustic k_0 , convected $k_c = \omega/U_c$, and corresponding to structural vibration k_p . Each of these is of practical value for predictions of acoustic radiation directly from the boundary layer and for estimations of the flow-induced vibration of extended structures such as naval hulls, aircraft shells, and space vehicles. Examples of these applications are discussed in Chapter 8. In all cases we will require $\phi_p(\vec{k}, \omega)$.

The most simple means of determining $\phi_p(\vec{k}, \omega)$ from experimental data (until 1969, the only means) is to perform the Fourier transform of Equations (7.129) and (7.130). This yields the expression

$$\phi_p(\vec{k}, \omega) = \frac{\phi_p(\omega)}{\pi^2} \frac{\gamma_1 \gamma_3 \left(\frac{\omega \delta^*}{U_c}\right)^2 (\delta^*)^2}{\left[\left(\frac{\gamma_3 \omega \delta^*}{U_c}\right)^2 + (k_3 \delta^*)^2\right] \left[\left(\frac{\gamma_1 \omega \delta^*}{U_c}\right)^2 + \left(k_1 \delta^* - \frac{\omega \delta^*}{U_c}\right)^2\right]} \quad (7.133)$$

Equation (7.133) has the characteristic of locally maximum values near $k_1 = \omega/U_c$, $k_3 = 0$, as illustrated in Figure 7.39. It also has the property that $\phi_p(\vec{k}, \omega) = \phi_p(-\vec{k}, -\omega)$. Since $\gamma_3/\gamma_1 \approx 6$ on smooth walls and $\gamma_3/\gamma_1 = 3$ on rough walls, the shape of $\phi_p(\vec{k}, \omega)$ at constant ω/U_c appears elliptical, as illustrated. Relative to the k_3 dependence, the k_1 dependence over rough walls is somewhat broader. Also shown

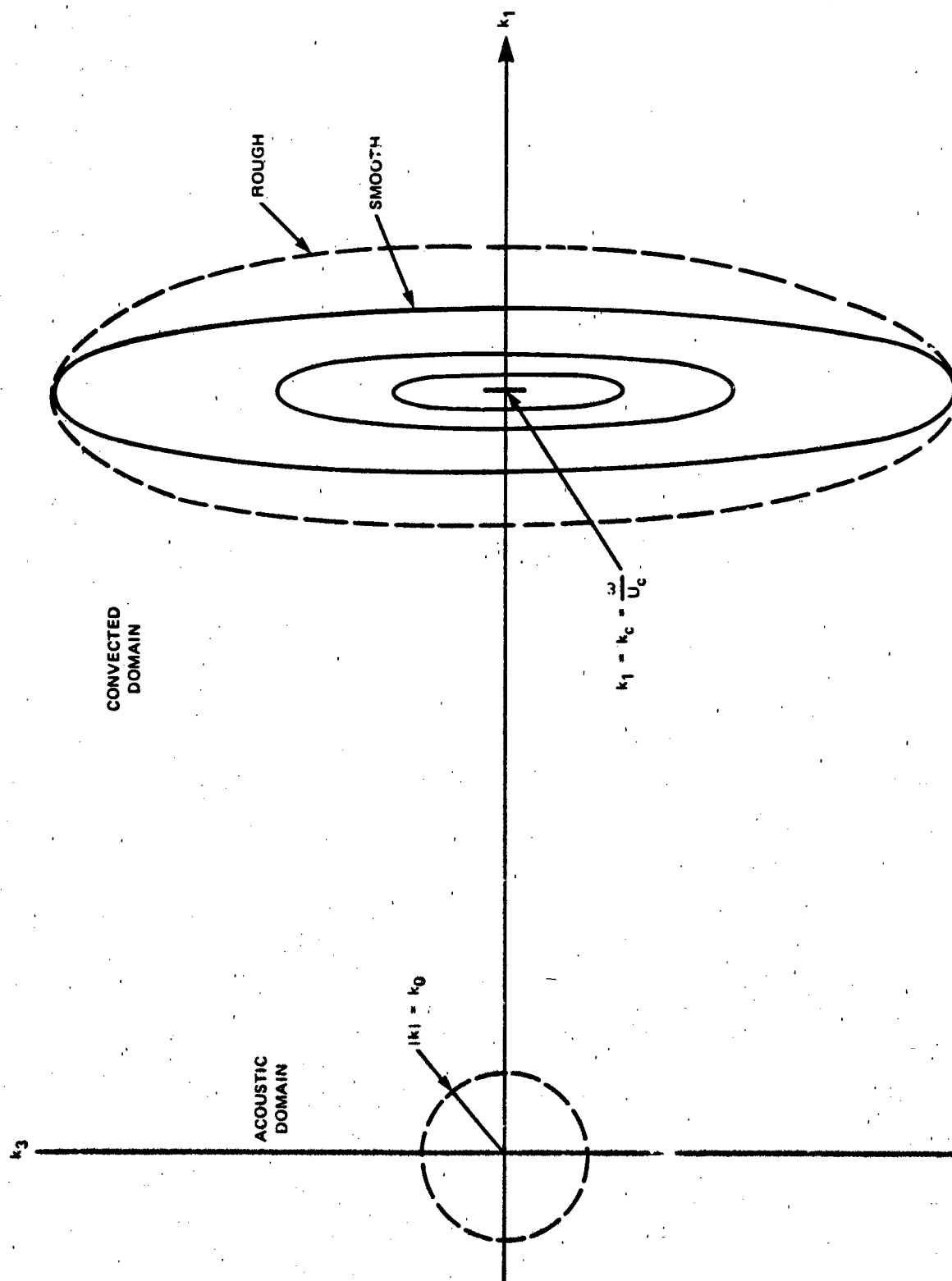


Figure 7.39 - Contours of Constant $\phi(\vec{k}, \omega)$ at a Particular Value of ω and U_c

is a circle of radius $|k| = k_0$ which represents the bound in wave numbers within which acoustic contamination effects are to be expected. The ratio of k_0/k_c depicted in Figure 7.39 is roughly comparable to that which is typical in aerodynamic measurements, i.e., 1.0 to 10. Wills¹³⁴ was the first to determine $\phi_p(\vec{k}, \omega)$ in the vicinity of $\omega/U_c = k_1$ by Fourier transforming $\phi_p(\vec{r}, \omega)$. His results confirm the aspect ratio of the contours in Figure 7.39. Figure 7.40 shows a contour of

$$\phi_p(k_1, \omega) = \int_{-\infty}^{\infty} \phi_p(k_1, k_3, \omega) dk_3$$

that displays the expected locus of $\omega\delta^*/U_\infty$ versus $k_1\delta^*$ for which $\phi_p(k_1, \omega)$ is maximum. This figure is the analog in (k_1, ω) of the correlation function in (r_1, τ) shown in Figures 7.33 and 7.34 and defines a convection velocity bounded by $0.55 < U_c/U_\infty < 0.85$, with the lower bound observed at high frequencies. The spectrum shows an absolute maximum at $\omega\delta^*/U_\infty = 0.2$. Wills' results also confirm that the width of the wave number spectrum near $\omega/U_c = k_1$ is on the order of $\Delta k_1 = 0.2 (\omega/U_c)$ but that it increases as k_1 increases. This behavior is undoubtedly related to the broadening of the turbulence spectrum as the wall is approached (see Figure 7.25).

Equation (7.133) is shown in Figure 7.41 for $\omega\delta^*/U_\infty = 10$ compared with a variety of measurements and other functions described below. The figure represents cuts of constant ω across Wills' spectra. At $k_1\delta^* \gg \omega\delta^*/U_c$, $\phi(k_1, 0, \omega) = (k_1\delta^*)^{-2}$; when $\omega\delta^*/U_\infty \gg k_1\delta^*$, $\phi(k_1, 0, \omega)$ is independent of $k_1\delta^*$. Equation (7.133) gives spectrum levels that are erroneously large in the range $k_1\delta^* \ll \omega\delta^*/U_\infty$, as can be seen by comparing the calculation to the measured points described below.

A number of alternative approximate semiempirical representations of the spectrum $\phi_p(\vec{r}, \omega)$ have been proposed by Chandiramani.¹³⁵⁻¹³⁷ These formulae generally present the wave number spectrum in the form

$$\phi_p(\vec{k}, \omega) = \phi_p(\omega) \phi_{1,3}(k_1, k_3, \omega) \quad (7.134)$$

where

$$\int_{-\infty}^{\infty} \int_{-\infty}^{\infty} \phi_{1,3}(k_1, k_3, \omega) dk_1 dk_3 = 1$$

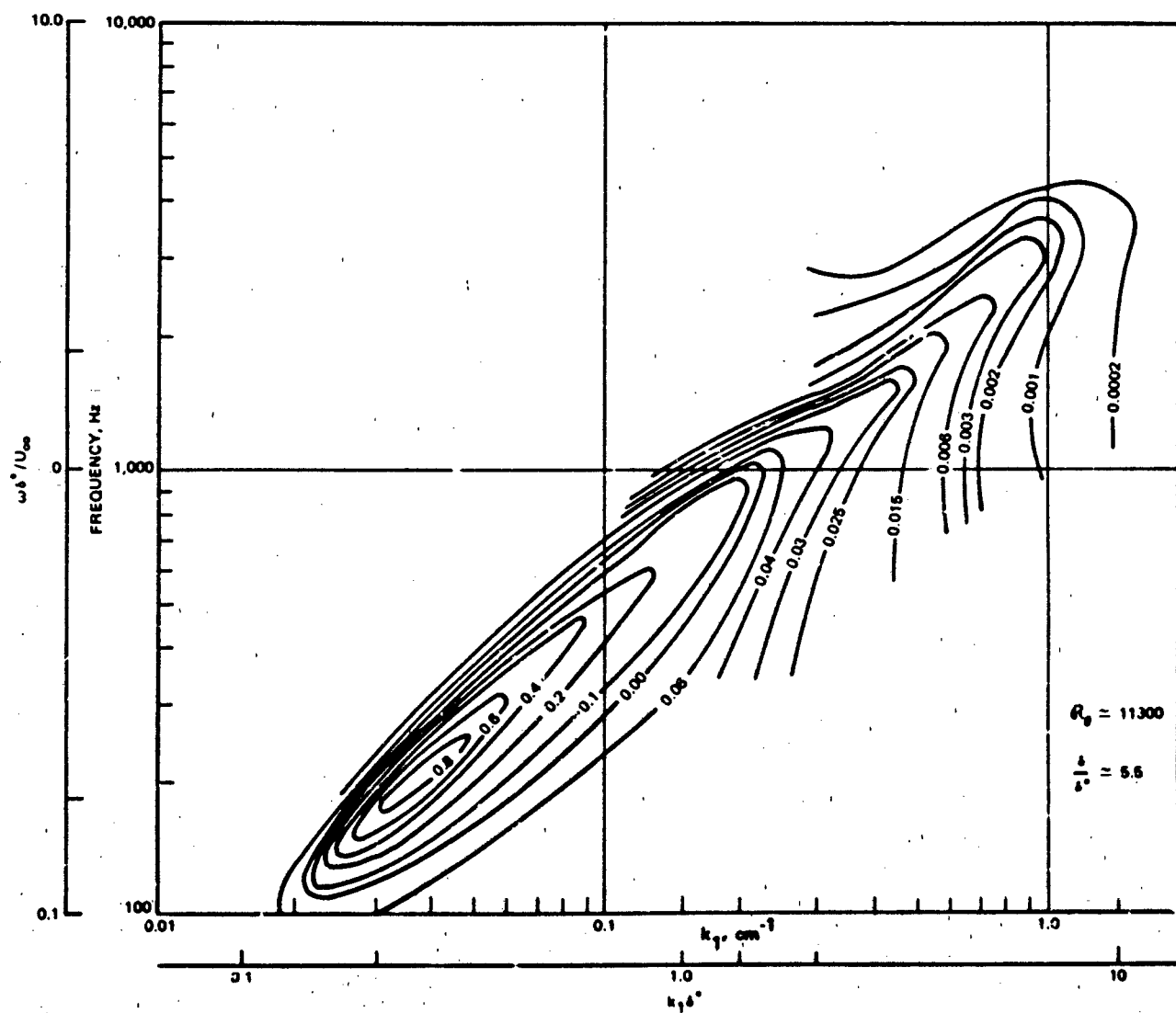


Figure 7.40 - Contour Plot of $\phi(k_1, \omega)$. From Wills¹³⁴

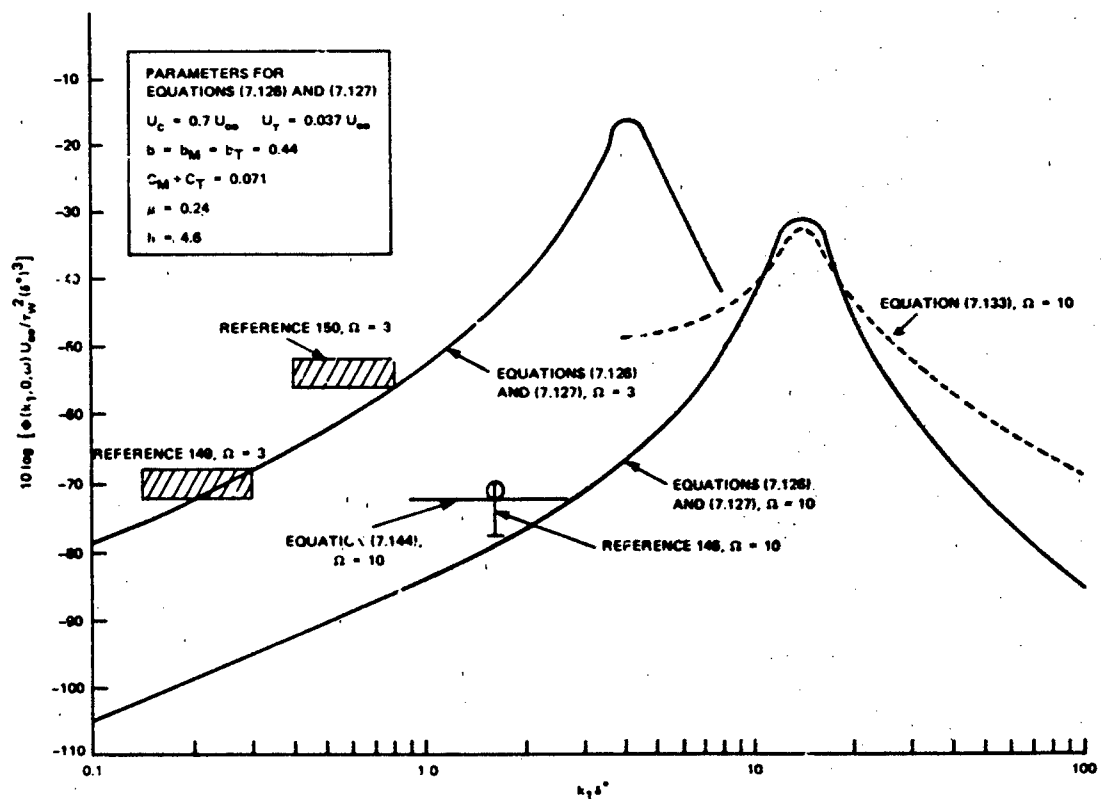


Figure 7.41a - Wall Pressure Spectra in the Purely Hydrodynamic Range of Wave Number, $M_c < 0.01$

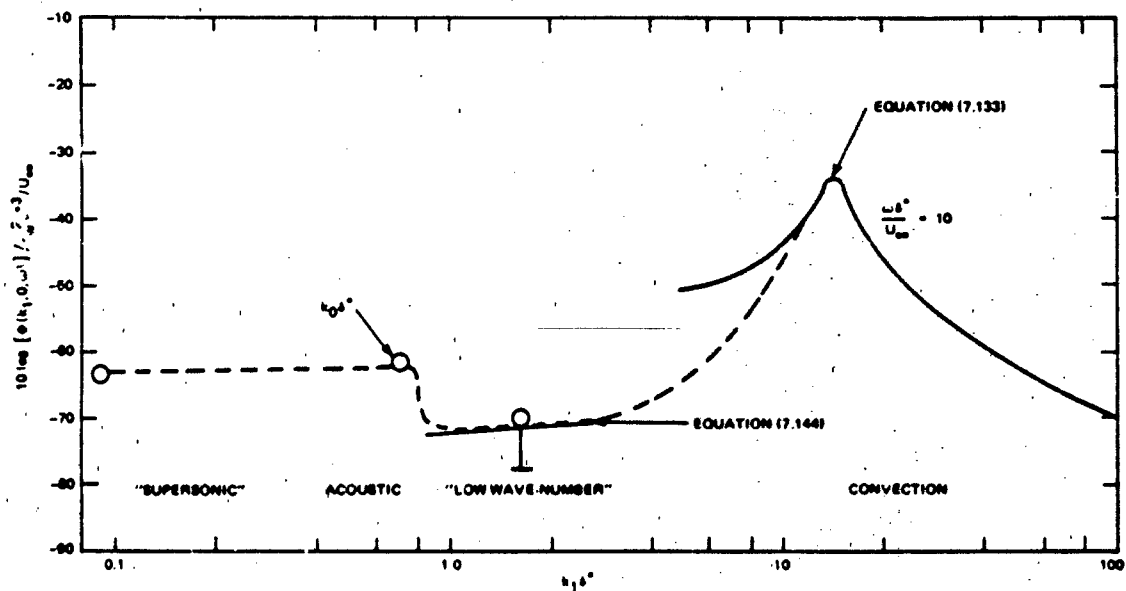


Figure 7.41b - Spectrum for $\omega \delta^+ / U_\infty = 10$ for Extrapolated Measurements of Geib and Farabee at $M_c \approx 0.07$. Dashed Lines Are Inserted as Visual Aids to Indicate a Complete Spectrum

Figure 7.41 - Wave Number Spectra in the Hydrodynamic and Acoustic Regimes of Wave Number, Compared with Available Measurements

Typically, dependencies on the variables were selected to generate a maximum at $k_1 = \omega/U_c$ and the residual k_1, k_3 dependence was introduced in a variety of ways so that the resulting integrals could be determined exactly or at least approximately from measurements of spatial correlation functions. The form commonly used has already been given (Equations (3.105), (7.48) and (7.133)); it is of the form

$$\phi_p(\vec{k}, \omega) = \phi_p(\omega) \phi_1(k_1) \phi_3(k_3) \phi_m\left(k_1 - \frac{\omega}{U_c}\right)$$

in which $\phi_1(k_1)$ is the analog of $R_p(r_1)$, $\phi_3(k_3)$ is the analog of $R_p(r_3)$, and $\phi_m(k_1 - \omega/U_c)$ is derived from the moving axis correlation $R_m(r_1 - U_c \tau, \tau)$. These semi-empirical formulae to some extent preceded the availability of measurements for which $k_1 \ll k_c$, and they have been to some extent superseded by the measured results discussed below. Such analytical methods of approximation are still important for the circumstances for which measurements of cross-spectra are to be approximated by analytical functions which may be used for mathematical modeling.

7.4.4 Measured Pressures at Low Wave Numbers Using Spatial Filtering Techniques

The empirical results for $k_1 < \omega/U_c$ in Figure 7.41 were obtained with special transducer arrays specifically designed to be insensitive to convected disturbances at $k_1 \delta^* = \omega \delta^*/U_c$. At the same time they were receptive to pressures in the range of wave number $k_0 \delta^* < k_1 \delta^* \ll \omega \delta^*/U_c$. The transducer array that was used is called a "wave-vector filter." The concept was devised by Maidanik¹³⁸⁻¹⁴² as a device for measuring low wave number pressures. A schematic is shown in Figure 7.42. An array of transducers is placed in the wall with distances between centers L . The outputs of the transducers are either summed in phase or with alternating (\pm) phase. Such an arrangement can discriminate among disturbances of different length scales. This filtering process is illustrated in Figure 7.43 for the simple case of a four-element array. When the outputs of the elements are alternately phased before being summed, the array response to a disturbance of very long wavelength $\lambda \gg L_A$ is zero because all contributions identically cancel. In the second case, the wavelength of the disturbance is exactly $2L$. By summing the outputs with alternate sign reversal of the elements, the alternate half-waves will reinforce exactly.

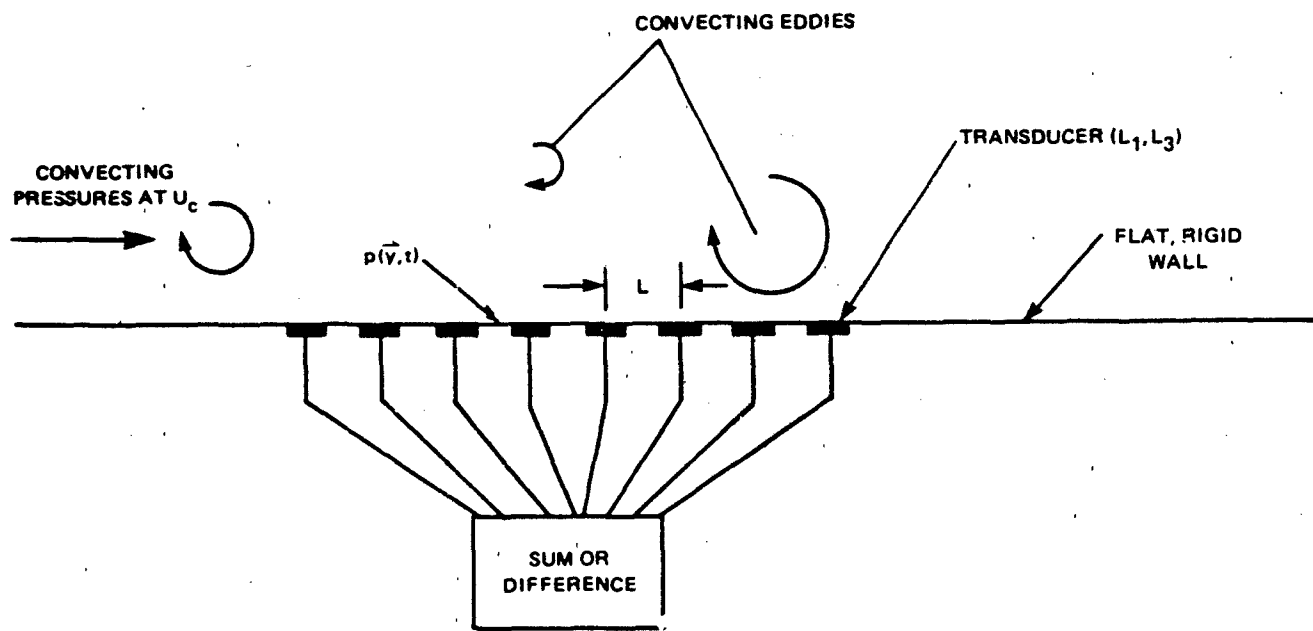


Figure 7.42 - Illustration of Array Used for Spatial Filtering of Wall Pressure Fluctuations

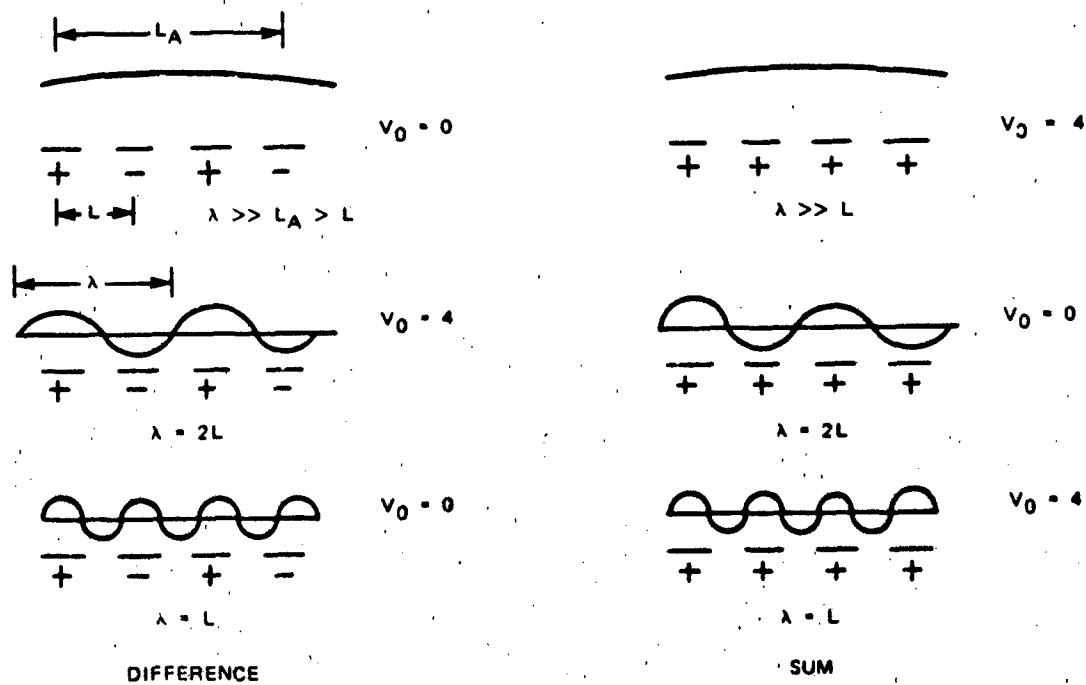


Figure 7.43 - Principle of Wave Vector, or Spatial, Filtering

When the wavelength becomes equal to the spacing, the elements coincide with every positive half-wave. The sum of the alternately phased outputs is then identically zero. The array spacing coincides constructively with all wavelengths for which

$$\lambda = \frac{2L}{2m+1} \quad m = 0, 1 \dots$$

In like manner, the array with common phasing between adjacent elements will respond constructively to disturbances for which

$$\lambda = \frac{L}{m} \quad m = 0, 1, 2 \dots$$

is an exact multiple of the wave length.

A mathematical statement of this result can be derived by writing the pressure $p(\vec{y}, t)$ in terms of its generalized Fourier transform, the inverse of Equation (7.70)

$$p(\vec{y}, t) = \iiint_{-\infty}^{\infty} e^{ik_1(y_1+nL)} e^{-i(\omega t - k_3 y_3)} \tilde{p}(\vec{k}, \omega) d^2 \vec{k} d\omega \quad (7.135)$$

where the coordinate $y_1 + nL$ designates each successive transducer counting from the left; for simplicity it is assumed to lie co-linear with the flow (y_1) direction. The sum of equation outputs from N point transducers is

$$\begin{aligned} p_s(t) &= \frac{1}{N} \sum_{n=0}^{N-1} p(y_1+nL, y_3, t) \\ &= \frac{1}{N} \iiint_{-\infty}^{\infty} e^{i(\vec{k} \cdot \vec{y} - \omega t)} \sum_{n=0}^{N-1} e^{inLk_1} \tilde{p}(\vec{k}, \omega) d^2 \vec{k} d\omega \end{aligned}$$

for the summation mode, and

$$p_d(t) = \iiint_{-\infty}^{\infty} e^{i(\vec{k} \cdot \vec{y} - \omega t)} \frac{1}{N} \sum_{n=0}^{N-1} (-1)^n e^{inLk_1} \tilde{p}(\vec{k}, \omega) d^2 \vec{k} d\omega$$

for the difference mode. We let

$$A_s(k_1) = \frac{1}{N} \sum_{n=0}^{N-1} e^{inLk_1} = \frac{\left[\sin \frac{N}{2} k_1 L \right]}{N \sin \frac{1}{2} k_1 L} e^{i(N-1) \frac{kL}{2}} \quad (7.136a)$$

for the sum mode and

$$A_d(k_1) = \frac{1}{N} \sum_{n=0}^{N-1} (-1)^n e^{ink_1 L} = \frac{\sin \left[\frac{N}{2} (k_1 L - \pi) \right]}{N \sin \frac{1}{2} (k_1 L - \pi)} \quad (7.136b)$$

for the difference mode. These functions have maxima for all values of m defined by

$$k_{1a} L = (2m+1) \pi \text{ difference mode}$$

and

$$k_{1a} L = 2m\pi \text{ sum mode}$$

as shown in Figure 7.44. The wave number bandwidth of the acceptance region is defined by the interval between nulls, which is

$$\Delta k_a L = \frac{2\pi}{N}$$

Another influence on the measurement results from the finite size of the transducer. The output of the transducer is equal to some sensitivity S times the average instantaneous pressure acting on the transducer. Thus the average pressure acting on the transducer for a rectangular transducer of lengths L_1, L_3 is

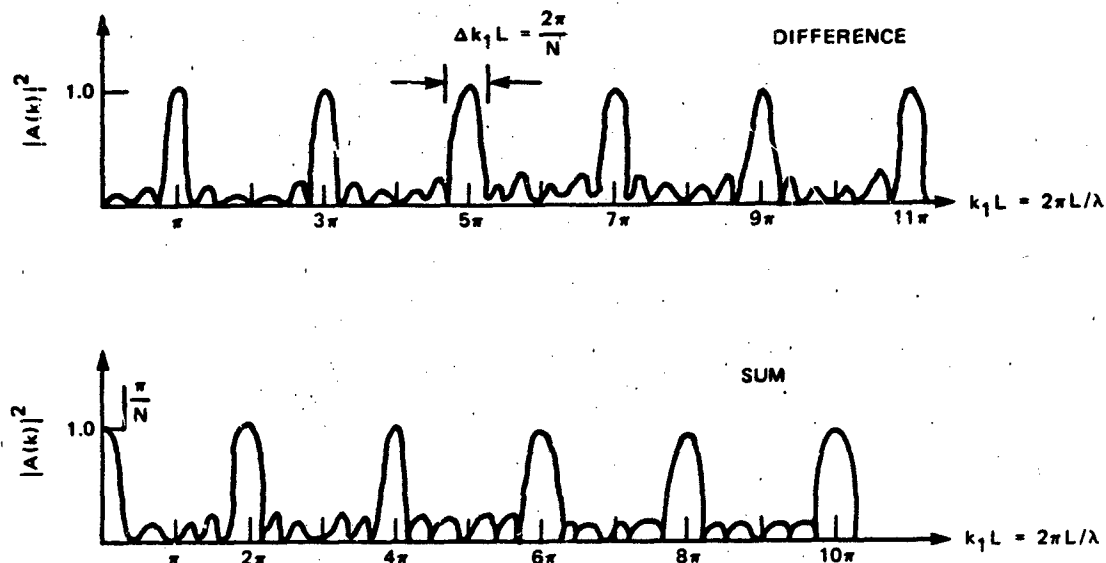


Figure 7.44 - Array Gains of Wave Vector Filters in the Sum and Difference Modes (Equation (7.136))

$$\begin{aligned}
 \overline{p(t)}^L &= \frac{1}{L_1 L_3} \int_{-L_1/2}^{L_1/2} \int_{-L_3/2}^{L_3/2} p(y_1, y_3, t) dy_1 dy_3 \\
 &= \frac{1}{L_1 L_3} \int_{-L_1/2}^{L_1/2} dy_1 \int_{-L_3/2}^{L_3/2} dy_3 \iint_{-\infty}^{\infty} e^{i\vec{k} \cdot \vec{y} - i\omega t} \tilde{p}(\vec{k}, \omega) d^2 \vec{k} d\omega \\
 \overline{p(t)}^L &= \int_{-\infty}^{\infty} \int \frac{\sin k_1 \frac{L_1}{2}}{\frac{k_1 L_1}{2}} \frac{\sin k_3 \frac{L_3}{2}}{\frac{k_3 L_3}{2}} \tilde{p}(\vec{k}, \omega) d^2 \vec{k} d\omega \quad (7.137)
 \end{aligned}$$

We have assumed that the transducer is rectangular in order to supply an example for the analysis; other considerations of spatial averaging are given in the next section. Equation (7.137) is of the form

$$\overline{p(t)}^L = \iiint_{-\infty}^{\infty} S_T(\vec{k}) \hat{p}(\vec{k}, \omega) d^2\vec{k} d\omega$$

where $S_T(\vec{k})$ is the spatial response kernel of the transducer (see Section 7.4.6). In the limit that L_1, L_3 approach zero, the average pressure over L of the pressure on a transducer situated at \vec{y} $\overline{p(\vec{y}, t)}^L$ approaches actual pressure $p(\vec{y}, t)$ because $S(\vec{k})$ becomes unity. Thus, in the realistic case of finite transducers, we write the instantaneous total of the average pressures on transducers in the array as

$$[p(\vec{y}, t)]_{\text{measured}} = \iiint_{-\infty}^{\infty} S_T(\vec{k}) A(\vec{k}) \hat{p}(\vec{k}, \omega) e^{-i\omega t + i\vec{k} \cdot \vec{y}} d^2\vec{k} d\omega \quad (7.138)$$

where \vec{y} is the coordinate of the location of the center of the array. Now in limit of $N = 1$ and $L_1, L_3 \approx 0$, the equation reduces to $p(t)$ being the local pressure at a point on the wall. The mean-square pressure can be found from Equation (7.135) by taking the limit as $T \rightarrow \infty$ of

$$\overline{p^2(t)} = \frac{1}{T} \int_0^T p^2(t) dt$$

to obtain

$$[\overline{p^2}]_{\text{measured}} = \iiint_{-\infty}^{\infty} |S_T(\vec{k})|^2 |A(\vec{k})|^2 \phi_p(\vec{k}, \omega) d^2\vec{k} d\omega \quad (7.139)$$

if the statistical nature of the pressure field on the surfaces of all transducers is identical; i.e., spatially homogeneous. If the signal is filtered in with a filter function $|H(\omega)|^2$ that describes a bandwidth $\Delta\omega$, then the narrowband output is

$$[\overline{p^2(\omega, \Delta\omega)}]_{\text{measured}} = \iint_{-\infty}^{\infty} |H(\omega)|^2 |S_T(\vec{k})|^2 |A(\vec{k})|^2 \phi_p(\vec{k}, \omega) d^2\vec{k} d\omega \quad (7.140)$$

which is the formal expression for the narrowband mean-square pressure from a spatially and temporally filtered pressure disturbance. The frequency spectral density of the array response is just

$$\phi_{p_A}(\omega) = \iint_{-\infty}^{\infty} |S_T(\vec{k})|^2 |A(\vec{k})|^2 \phi_p(\vec{k}, \omega) d^2\vec{k} \quad (7.141)$$

The product $|S_T(\vec{k})|^2 |A(\vec{k})|^2$ is simply a filter function completely analogous to the $|H(\omega)|^2$ of linear temporal filtering. If $|H(\omega)|^2$ is centered on $\omega = \omega_0$ and if $|A(\vec{k})|^2 |S_T(\vec{k})|^2$ can be tailored to have a single acceptance at $\vec{k} = \vec{k}_a$, then the array signal will be sensitive only to pressures of the type $\cos \omega_0 t \cos k_a y$. The array may be aligned with the flow direction; then it receives pressures at $\vec{k} = (k_1, k_3) = (k_a, 0)$ with a bandwidth $\Delta k_a = \Delta k_1 = 2\pi/NL$ and $\Delta k_3 = 2\pi/L_3$. Therefore a highly selective wave number array would consist of a large number of transducers in the flow direction and long in the cross-stream direction. Unfortunately, as shown in Figure 7.43, $A(k_1)$ has a multiplicity of peaks so that a simple $\cos k_a y_1$ interpretation of the filtered signal is not always possible. Therefore the function $|S_T(\vec{k})|^2$ must, if possible, be tailored to minimize the acceptance regions of $A(k_1)$ for large k . For our simple case of the rectangular transducer, $|S_T(\vec{k})|^2$ has diminishing acceptance of wave numbers $k_1 > 1/L_1$ and $k_3 > 1/L_3$, as illustrated in Figure 7.45 for an array of four rectangular sensors in the difference mode. $S_T(k)$ has zeros for $k_3 = m2\pi/L_3$ and $k_1 = n2\pi/L_1$, $m, n \neq 0$. The zero at $k_1 = 2\pi/L_1$ can be made to coincide with $k_1 = 3\pi/L$ if the ratio of transducer length L_1 to separation L is set as

$$\frac{1}{L_1} = \frac{3}{2}$$

As shown in Figure 7.45, the acceptance region at $k_1 L_1 = \pm 3\pi$ has been nullified, and acceptance regions at larger wave numbers have been reduced. Referring again to Figures 7.39, 7.40, and 7.45, we see that the main acceptance region of the space-time filtering ω_0, k_a can be designed to be between the acoustic wave number and the convection wave number, and the relationship between the size of the transducer and the spacing can be set to nullify the second lobe of the spatial

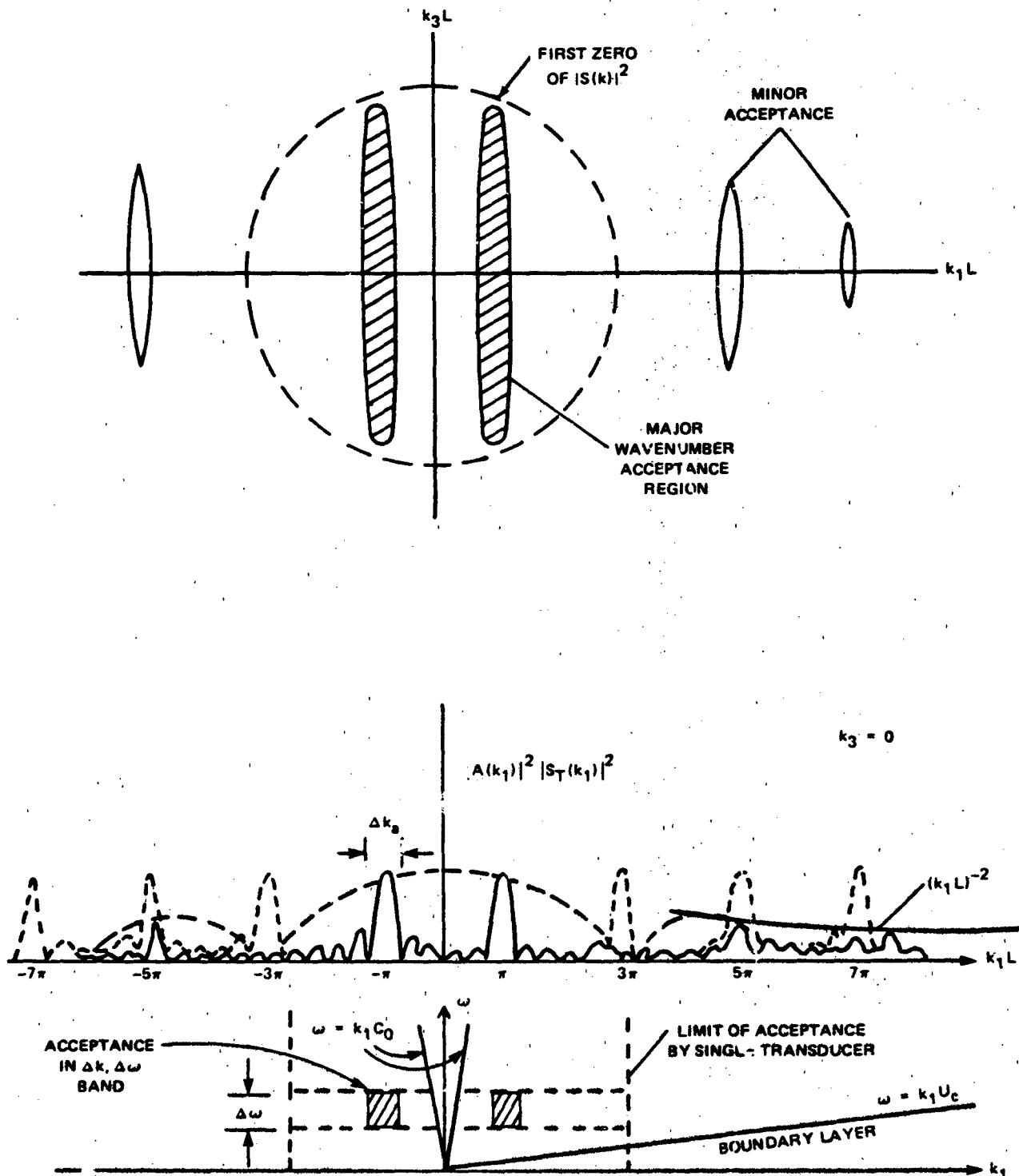


Figure 7.45 - Wave Number Acceptance Regions of an Array of Square Transducers Aligned in the k_1 Direction for the Case $L/L_1 = 3/2$

acceptance region. By increasing the number of elements in the array, the wave number bandwidth can be increased. As a practical matter, it is also advantageous to design the array to be insensitive to wave numbers at k_0 .

The wave number spectrum of the pressure is defined over the complete range $-\infty < k_1 < \infty$, but in the region $k_1 \approx \omega/U_c$, $\phi(\omega, k_1)$ is large, as shown in Figure 7.40. When the array is "tuned" for acceptance in the region $k_1 \ll \omega/U_c$, it receives spectral contributions from lobes at $\vec{k} = \pm \vec{k}_a$. Thus Equation (7.140) expresses the filtered pressure in the wave number frequency bandwidth (for idealized rectangular-shaped filter functions) as

$$\overline{p^2}(\omega, \Delta\omega) = |S_T(\vec{k}_a)|^2 \left[\phi_p(\vec{k}_a, \omega) + \phi_p(-\vec{k}_a, \omega) \right] \cdot 2\Delta\omega \Delta k_a \Delta k_3 \quad (7.142)$$

where $|S_T(\vec{k}_a)|^2$ is the transducer sensitivity function at the acceptance wave number k_a of the filter, but $|S_T(\vec{k}_a)|^2 \approx 1$ for an appropriately designed array. The wave vector bandwidths are defined by array geometry; $\Delta k_a \approx 2\pi/NL_1$ and $\Delta k_3 \approx 2\pi/L_3$. Thus a measurement has an ambiguity of including \pm wave numbers. Note, however, that $\phi(-k_1, k_3, -\omega) \equiv \phi(k_1, k_3, \omega)$. One can argue that if there is a wave propagating as $k_1 y_1 - \omega t$, so that the locus $\omega/k_1 = U_c$ lies in the first quadrant, $\omega > 0$, and $k_1 > 0$, then any pressures in the $k_1 < 0$ $\omega > 0$ quadrant must be secondary unless there is a pressure source downstream that is generating disturbances against the flow direction. The above equation may be approximated for narrow frequency and wave number filter bands,

$$\overline{p^2}(\omega, \Delta\omega) \approx 2 |S_T(k_a)|^2 \Delta\omega \Delta k_a \Delta k_3 \phi_p(\vec{k}_a, \omega) \quad (7.143)$$

where

$$\vec{k}_a \approx k_a, 0$$

if we neglect the contribution from $-k_1$.

A final aspect is that the relationship between L and δ^* must be such as to emphasize the nonconvected pressures. Thus, for a dimensionless frequency $\omega\delta^*/U_\infty \approx 1.0$, one must have $k_a \delta^* < 1$. This requires that $L/\delta^* > \pi$ and for $L_1/L_3 = 2/3$ that $L_1/\delta^* > 2$.

The reader may inquire about the use of a single transducer large enough to minimize the acceptance at wave numbers $k_1 = k_c \gg 2\pi/L_1$ so as to act as a low-pass spatial filter. Such an attempt has been made,¹³⁷ but unfortunately such a transducer has a large acceptance in the region $|k| \leq k_0$. Since these disturbances are often more intense than pressures in the range $k_0 < k_1 \ll k_c$, the measurements were not successful. The use of large transducers for the purpose of discriminating against pressures in the wave numbers near $k_1 = k_c$ in favor of acoustic pressures at lower wave numbers is often attempted. Note, however, that even with large transducers there is a frequency below which the sensor fails to totally discriminate. This frequency for a circular transducer of radius R_T is

$$\omega < \pi \frac{U_c}{R_T}$$

The reader may now recall the condition that was applied to measurements of wall pressure spectra at a point. There we introduced the conservative criterion for a circular transducer that the typical measurement is unaffected by spatial averaging for $\omega < U_c/a$, where a is the microphone radius.

We have discussed only the simplest type of wave vector filter. Maidanik¹⁴² has proposed using time delays among the elements of the array for the purpose of steering. He has also¹⁴² proposed the use of continuous arrays. This device consists of a flush-mounted porous plate backed by a cavity filled with a fluid with density $\rho_1 c_1$. One end of the cavity is terminated with a $(\rho_0 c_0)$ material, and a microphone is placed at the other. The microphone is therefore coupled to the flow medium $\rho_0 c_0$ by the transducer medium $\rho_1 c_1$. The pressures transduced from the outer medium to the inner are propagated to the transducer. If the sound speed in the cavity is less than the sound speed of the flowing fluid, the acceptance wave number in the cavity ω/c_1 will be greater than k_0 in the outer fluid. The transducer will therefore respond to low wave number pressures. In addition to wave vector filters, which consist of an array of discrete elements, some investigators have used plates.^{143,144} As discussed in the preceding chapter, a finite plate, through its resonances, has a set of discrete wave number acceptance regions that can be exploited to produce measurements of low wave number pressure.

The results of attempts at measuring boundary layer pressures with spatial filters are summarized and compared with existing analytical models in Figures 7.41 and 7.46. (See also Section 7.5.2) Blake and Chase¹⁴⁵ used an array of four condenser microphones. The measurements were contaminated by the background noise of the wind tunnel facility, but the results illustrated techniques of wave number calibration and data reduction. The measurements did show that $\phi_p(k_1 \ll \omega/U_c, k_3 = 0, \omega)$ was on the order of 10 dB less than the spectrum level predicted by Equation (7.133).^{*} The experiment was repeated with improved transducers and under improved facility conditions by Jameson,¹⁴⁶ who showed that the low wave number spectrum level was less than that of Blake and Chase by 10 dB. More recently, Farabee and Geib¹⁴⁷ repeated the measurements under the more favorable conditions of a thick boundary layer in a quiet facility, using four-, five-, and six-element arrays of condenser microphones. Their measurements ($8590 < R_\theta < 28500$) were conducted in the range of wave number

$$1.3 < k_1 \delta^* < 1.7$$

and over the frequency range

$$4.5 < \frac{\omega \delta^*}{U_\infty} < 32$$

The acoustic wave number was contained in the range

$$0.65 < k_\theta \delta^* < 1.16$$

In their test program Geib and Farabee¹⁴⁷⁻¹⁴⁹ were also able to vary both δ^* and wall roughness. Figure 7.46 shows $\phi_p(k_1 \delta^*, 0, \omega \delta^*/U_\infty)$ determined from measurements using Equation (7.143) for both types of walls¹⁴⁷; a frequency dependence $(\omega \delta^*/U_\infty)^{-n}$ where $n = 4$ to 6 was observed. Additional data and analysis is presented in Reference 242.

^{*}Note that all the attempted measurements were made with spatial filters that selected a range of transverse (k_3) wave numbers centered on $k_3 = 0$. Therefore all measurements represent $\phi_p(k_1, 0, \omega)$.

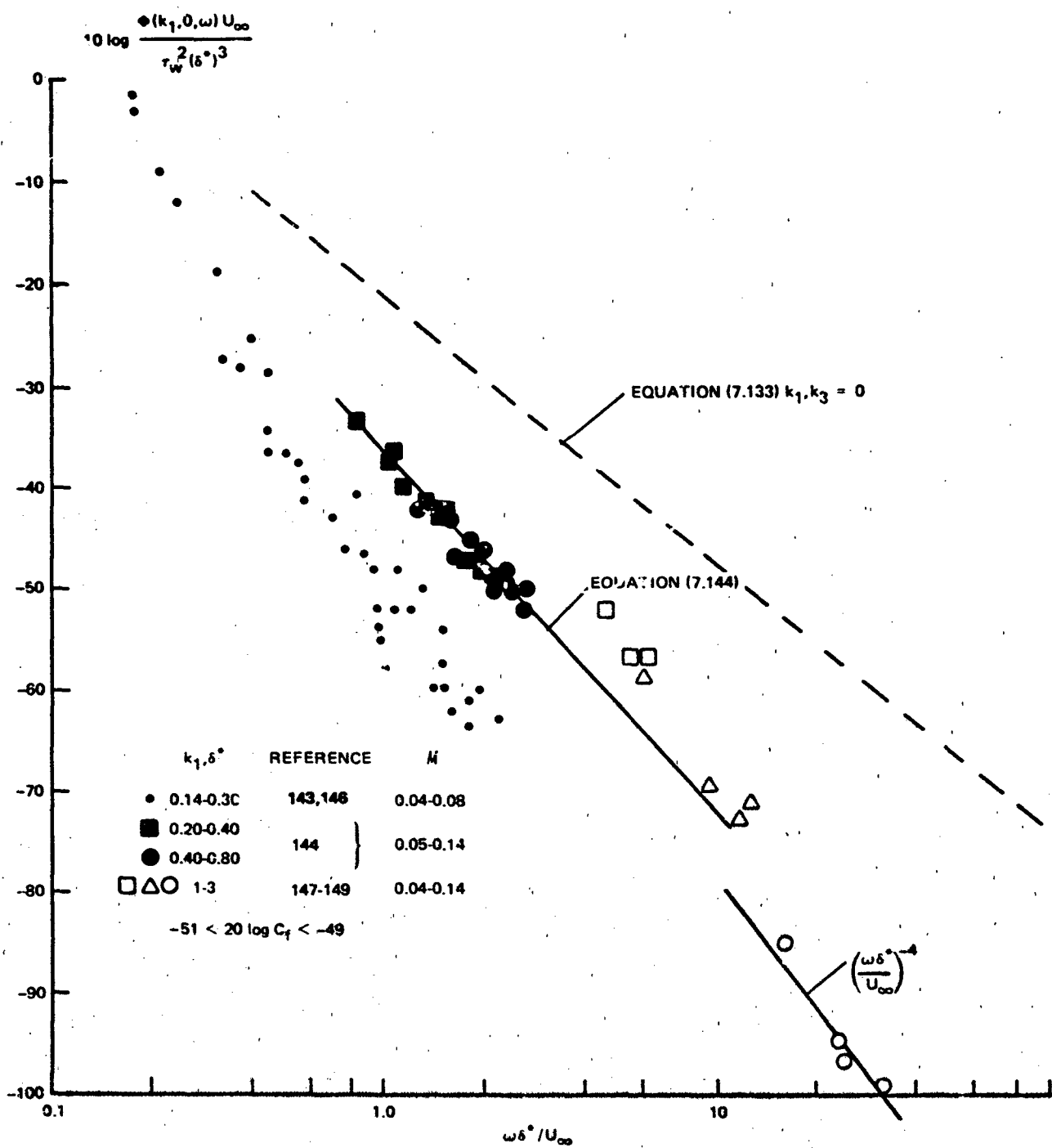


Figure 7.46 - Frequency Dependence of Wall Pressure at Low Wave Number Measured in Various Facilities

The measurements by Jameson¹⁴³ and Martin¹⁴⁴ shown in the figure were accomplished using vibrating plates^{143,144} and membranes¹⁴⁴ as spatial filters.* The boundary-layer pressures excite these structures in their resonant modes of vibration. By selecting the responses of specific modes of wavelengths λ_{p1} , λ_{p3} , the effective force on the panel, which is related to the pressure spectrum, can be calculated. Formulations relating the panel vibration to the wave number spectrum of an excitation were discussed in Chapter 6, and specific cases will be examined in Chapter 8; thus the wave vector filtering aspects are not discussed in detail here. The results of Martin, obtained on a 20 in by 2 in membrane and a 20 in by 5 in steel plate, are in substantial agreement with those of Geib and Farabee. The plates were aligned so that their longest dimension was in the direction of the flow. Because of the large number of modes whose flow responses he was able to sample, Martin was able to determine separately both k_1 dependence and $\omega\delta^*/U_\infty$ dependence within a domain of roughly

$$0.2 < k_1 \delta^* < 0.9$$

and

$$0.8 < \frac{\omega\delta^*}{U_c} < 5$$

Within this domain Martin determined, by a least-squares fit, that

$$\frac{\phi_p(k_1, 0, \omega)}{\tau_w^2 \delta^{*3}} = a_2 \left(\frac{\omega\delta^*}{U_\infty} \right)^{-3.6} (k_1 \delta^*)^{0.31} \quad (7.144)$$

where $a_2 \approx 3 \times 10^{-4}$ for $5100 < R_\theta < 11000$. This equation is shown in Figure 7.41 and 7.46 with points from Martin's results. Various wave numbers were sampled by the modes of his membrane and plate. These modes were selected so that the plate wave number in the spanwise direction was much smaller than the streamwise wave number.

*The idea has also recently been examined theoretically by Kudashev and Yablounik,¹⁵⁰ apparently without knowledge of the work of Jameson and Martin.

The measurements by Jameson¹⁴³ ($\sim 2600 < R_0 < \sim 6730$) were obtained on a flat wall that was the extension of one wall of an open jet wind tunnel. His plate dimensions were 10.8 in by 7.2 in, with $\delta^* \approx 0.14$ in. The boundary layer at the measurement station was probably not equilibrium, but the measured δ^* could be approximated using Equation (7.35). On the whole, the results cover a range of streamwise wave numbers between $0.14 (\delta^*)^{-1}$ and $1.7 (\delta^*)^{-1}$. Although there does not appear to be a dependence on wave number consistently shown by the different investigations, the combined results of all three sets of investigations suggest a frequency dependence of $(\omega \delta^* / U_\infty)^{-m}$ where m is between 3.6 and 6.5 (Jameson's results) and a wave number $(k_1 \delta^*)$ dependence that is substantially less pronounced. The functional dependences of the type expressed by Equations (7.48) would thus seem to be roughly supported by the measurements. None of the measurements extends into the range of very low wave numbers, $k_0 \delta < k_1 \delta \ll 1$.

Referring again to Figure 7.41(b), we see selected results for the pressures in the wave number range intermediate between the acoustic convection and flow convection wave numbers. For $\omega \delta^* / U_\infty = 10$, the results of Geib and Farabee can be extracted directly from Figure 7.47, and the empirical equation of Martin is in reasonable agreement with these, as shown. This can only be done for Jameson's and Martin and Leehey's results for $\omega \delta^* / U_\infty = 3$. Since at $\omega \delta^* / U_\infty = 10$ the eddy convection wave number $k_c = \omega / U_c$ is hardly more than a factor of 20 greater than the wave number of major acceptance of each of the wave vector filters k_a , the possibility exists that the array outputs contained a non negligible contribution due to wave numbers $k_1 = k_c$ received into minor lobes of the array. Since $\phi(k_c, 0, \omega)$ is a factor 10^4 to 10^5 times the value at low wave number $\phi(k_1 \ll k_c, 0, \omega)$, the attenuation effects of the microphone size or panel acceptances must be sufficient to suppress the very high wave number acceptance regions of $|\Lambda(k_1 = k_c)|^2$. Spatial filtering of practical transducers is discussed in Section 7.4.6; however, considering the variety of experimental configurations (i.e., microphone arrays, flexible panels, and membranes) that have been used and the reasonably close agreement among the various results, it would appear that if there were convective contamination in the measurements, it did not significantly alter the order of magnitude of the pressure spectra. The spectrum levels measured with wave number filtering are all exceeded by that predicted by Equation (7.133), which is based on two-point cross spectra.

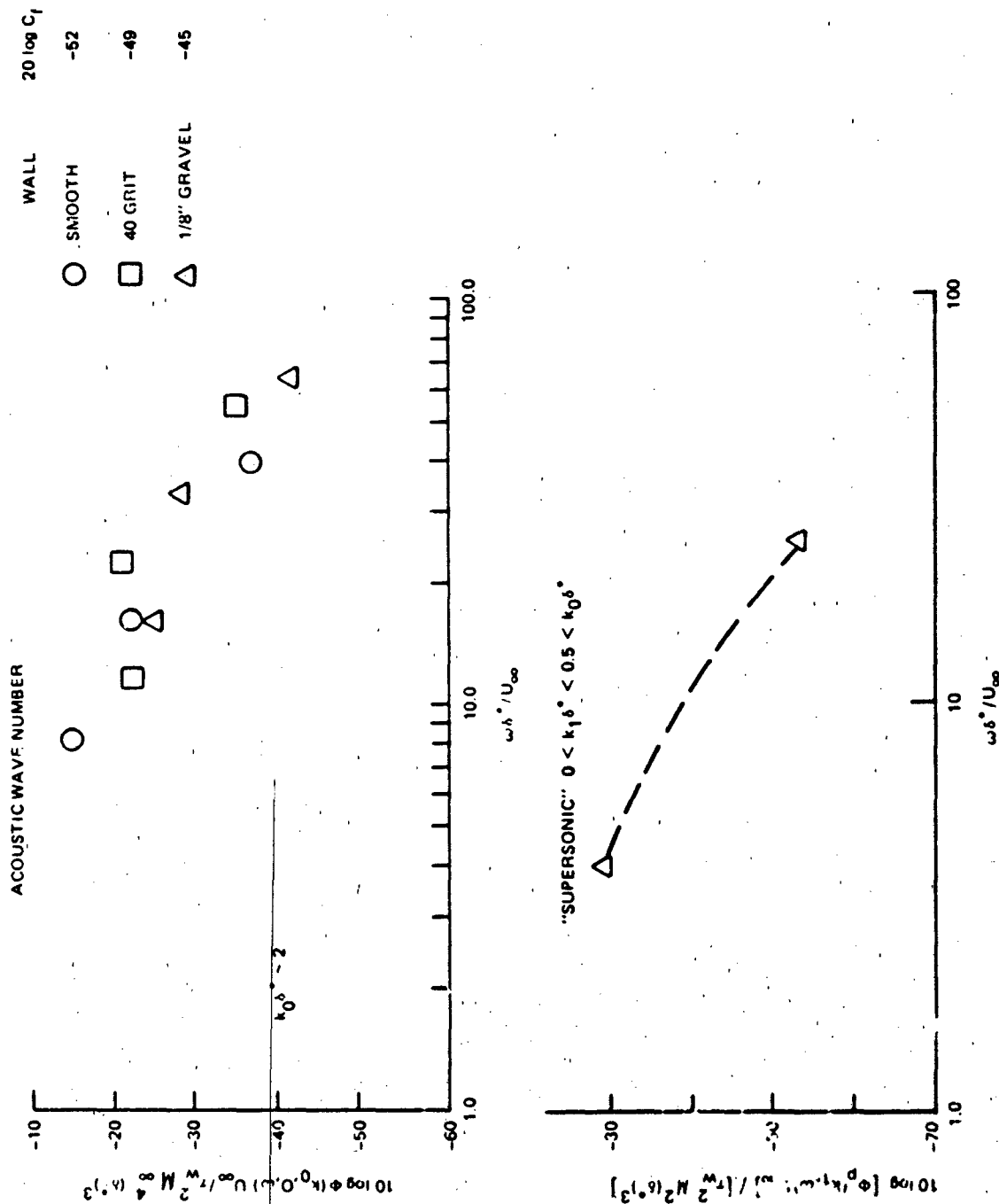


Figure 7.47 - Frequency Spectrum of Wall Pressures in Various Acoustic Wave Number Ranges on Rough Walls for Measurements of Celb and Varabee

In their measurement program Geib and Farabee attempted measurements in the supersonic $k_1 < k_0$ and acoustic $k_1 = k_0$ regions. Figure 7.47 shows the frequency dependence of pressure spectrum levels that were obtained in those wave number ranges over rough walls. The verification of wall-dependent pressure levels at $k_1 = k_0$ was established by the increase in level at this wave number as the wall roughness was increased and the wind speed was maintained constant. Cross-spectral densities between adjacent microphones confirmed that the noise was coming from the roughened region of the wall. In Geib and Farabee's experiment, the wave number filter was positioned at the downstream extremity of a roughened patch on the wind tunnel wall. The possibility exists that sound emanates from the discontinuity between the rough and smooth surfaces; the measurements provide an upper bound in any event. The experimental values of the wave number spectrum are also included in Figure 7.41b for the appropriate dimensionless frequency. The spectrum level at the acoustic wave number, at $k_1 = k_0$, has been extrapolated from the measurements at higher wave number and frequency according to behavior typical of quadrupole radiation (see also Section 7.3.7), i.e.,

$$\left[\frac{\phi_p(k_1, 0, \omega) U_\infty}{\tau_w^2(\delta^*)^3 M_c^4} \right]_{\text{acoustic}} = f \left(\frac{\omega \delta^*}{U_\infty} \right) \delta \left[k_1 \delta^* - \frac{\omega \delta^*}{U_\infty} M \right] \quad (7.145)$$

Finally, the point shown in the supersonic, $k_1 < k_0$, range was obtained using the common-phase mode of the wave vector filter with a bandwidth marked by the -3 dB sensitivity of $0 < k_1 \delta^* < \approx 0.3$. The point shown in Figure 7.41b is therefore an average value over this range of wave numbers; i.e., it represents values of

$$\frac{1}{\Delta k_{1a}} \int_0^{\Delta k_{1a}} \phi_p(k_{1a}, 0, \omega) dk_{1a}, \quad \Delta k_{1a} < k_0$$

To compare the empirically based spectrum of Figure 7.41 to the theoretical spectrum of Figure 7.24 we again note that $\delta/\delta^* \approx 6$ to 10 and that $M_c = 0.07$ in Figure 7.41b. For $k_1 < k_0$, one would expect that the spectrum levels would be dependent on M_c^2 as well as on τ_w^2 and δ^* ; however, the range of experimental conditions has not been large enough to verify this. At $k_0 \delta = (\omega \delta / U_c) M_c$ the experimental levels do not show the local maximum that theory would suggest. In the

intermediate range of $k_0 \delta < k_1 \delta < k_c \delta$, the theory predicts a variety of wave number dependences. In the measurement programs, however, the ranges of wave number were all such that $k_1 \delta > 1$. Therefore the dependence given by Equation (7.102) possibly could not be observed; even $k_0 \delta > 1$ for all the known aerodynamic measurements (compare Figures 7.41a and b). A notable gap in our information concerning the wave number frequency is the lack of measured results to apply to either underwater application, $M_c \approx 0.01$, or to higher speed flow, $M_c \approx 1.0$. In the former case, of particular interest to the hydroacoustics of ships, $k_0 \delta$ will be less than 0.01 in most applications, while structural acceptance will be large near $k_p \delta \approx 2$ (for example). The spectrum of Figure 7.41 is clearly inadequate for this regime, and the only recourse now available is extrapolations using Martin's equation (Equation (7.144)) or the analytical model of Chase,⁸⁶ Equation (7.125).

A novel alternative approach to spatial filtering has been attempted by Emmerling¹²⁶ and Dinkelacker.¹³⁰ They used optical interferometry in which a mirror, consisting of an array of small silver-foil membranes, was placed flush in the wall of a wind tunnel. The membranes were formed by bonding a stretched film over a large circular plate in which several hundred holes (2.5 mm in diameter) were drilled. The spacing between holes was 3 mm. The film over each hole formed an individual membrane. Under the action of boundary-layer pressure fluctuations, the membranes would deflect and these deflections would result in optical interference patterns. Using high-speed photography at 7000 frames per second, they could record a time history of the pressure field over the extended region of the array. By interpreting the optical fringes in each membrane that was photographed, they were able to reconstruct pressure fields, as shown in Figure 7.48. The field of view occupies a region $\Delta y_1 = 1.6\delta$ and $\Delta y_3 = \delta$. The shaded and light regions denote negative and positive pressures, respectively. The flow is from left to right, and one can see the propagation of the correlated pressure disturbance every 2.8 ms ($\tau U_\infty / \delta = 0.77$) for $R_\theta \approx 2000$. One can see that although a generally defined low-pressure region appears to convect, the boundaries and small-scale character of the region is very stochastic. Put in the perspective of the space-time correlations shown in Figure 7.36, this time history illustrates the type of space-time decorrelation that has been observed over times comparable to $\tau U_\infty / \delta = 0.77$ ($\tau U_\infty / \delta \approx 5$).

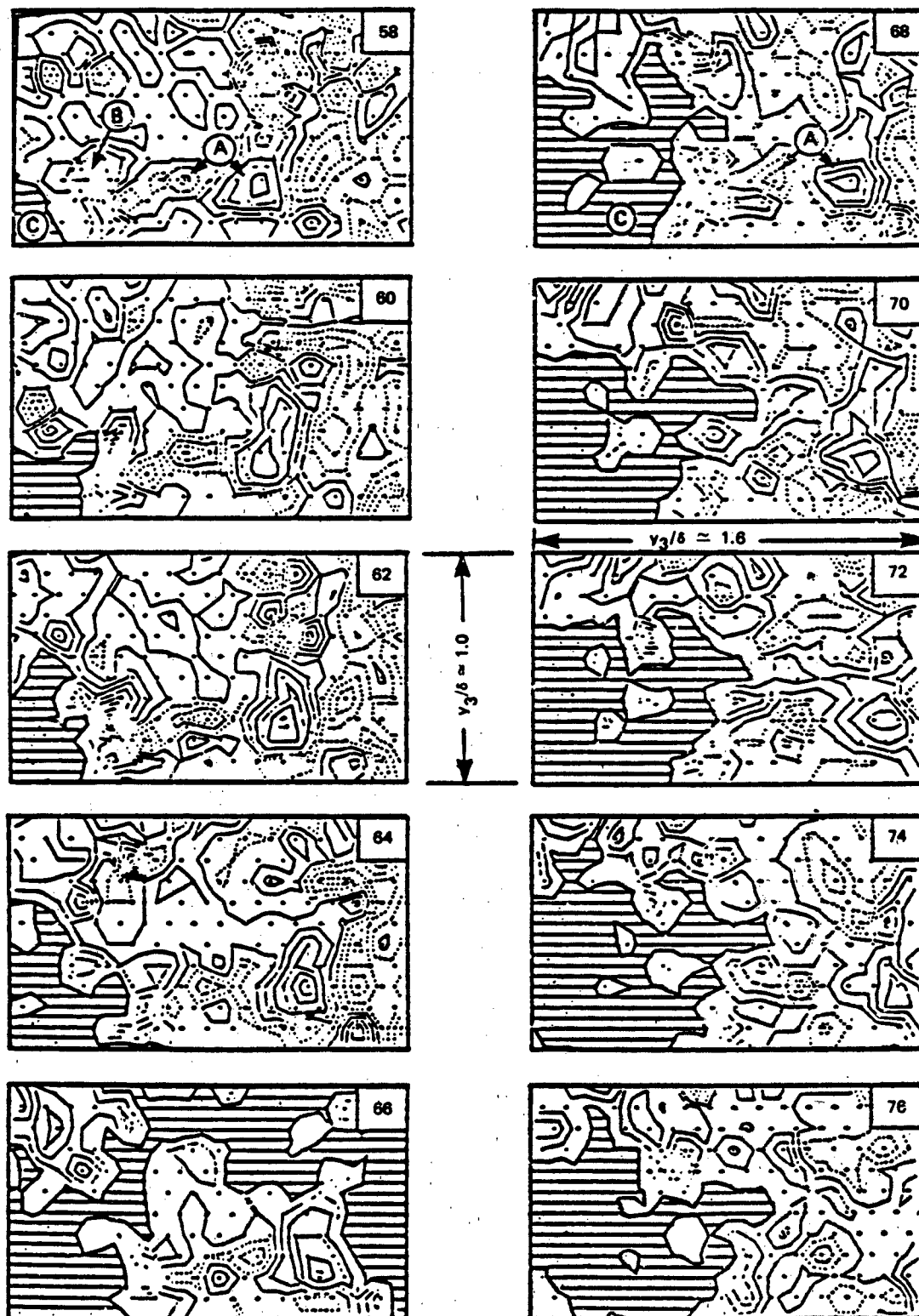


Figure 7.48 - Sequence of Consecutive Pressure Distributions.

Flow from Left to Right, Flow Velocity $U_{\infty} = 8.5$ m/s,

Time Between Consecutive Maps $\Delta t = 0.28$ ms,

Field of Observation 50 mm \times 30 mm

The wave number frequency characteristics of the wall pressure spectrum can be exploited in practical situations in which one is interested in discriminating against near-field flow-induced pseudosound. Using the techniques of array design described here, one can design transducer clusters tailored to respond well to $k_1 = k_o$ while discriminating against the region $k_1 = k_c$. Thus, when transducers are used for oceanographic applications in which they are exposed to local flow-induced pressures, by selectively adjusting size and spacing to the spatial character of the pressure field, the influence of these pressures can be minimized.

7.4.5 Particularities of Rough-Wall Boundary-Layer Pressures

The characteristics of pressure fluctuations have generally been discussed in connection with similar behavior over smooth walls. In general, it can be shown, as in the previous sections, that for $\omega\delta^*/U_\infty < 3$ to 4 (for the rough walls so far examined^{14,20,121,132,151,152}) the convected pressure levels and their spatial correlation can be described in terms of the outer variables τ_w, δ^* and U_∞ (or u_c). In the case of low wave number pressures in a small range of $k_1\delta^*$ near ~ 2 so far observed and for $5 < \omega\delta^*/U_\infty < 20$, the wave number spectrum can also be defined in terms of τ_w^2 and δ^* . As seen in Figure 7.31, however, the convected boundary layer pressures cannot be described in terms of the outer variables at high frequencies.

Instead, inner-wall variables are needed to describe the wall pressure fluctuations. Figure 7.49¹⁴ shows the dimensionless spectrum

$$\frac{\phi_p(\omega) U_\tau}{\tau_w^2 k_g} \text{ vs. } \frac{\omega k_g}{U_\tau}$$

which is the counterpart to Figure 7.32 for smooth walls. The collapse of the various spectra for the frequency $\omega k_g/U_\tau > 3$ suggests the existence of a nearly universal spectrum description; for $k_g U_\tau/\nu = 117$ the spectra are in disagreement. Aupperle and Lambert found an empirical relationship to describe their results, which is

$$\frac{\phi_p(\omega) U_\tau}{\tau_w^2 k_s C_f} = f\left(\frac{\omega k_s}{U_\tau}\right)$$

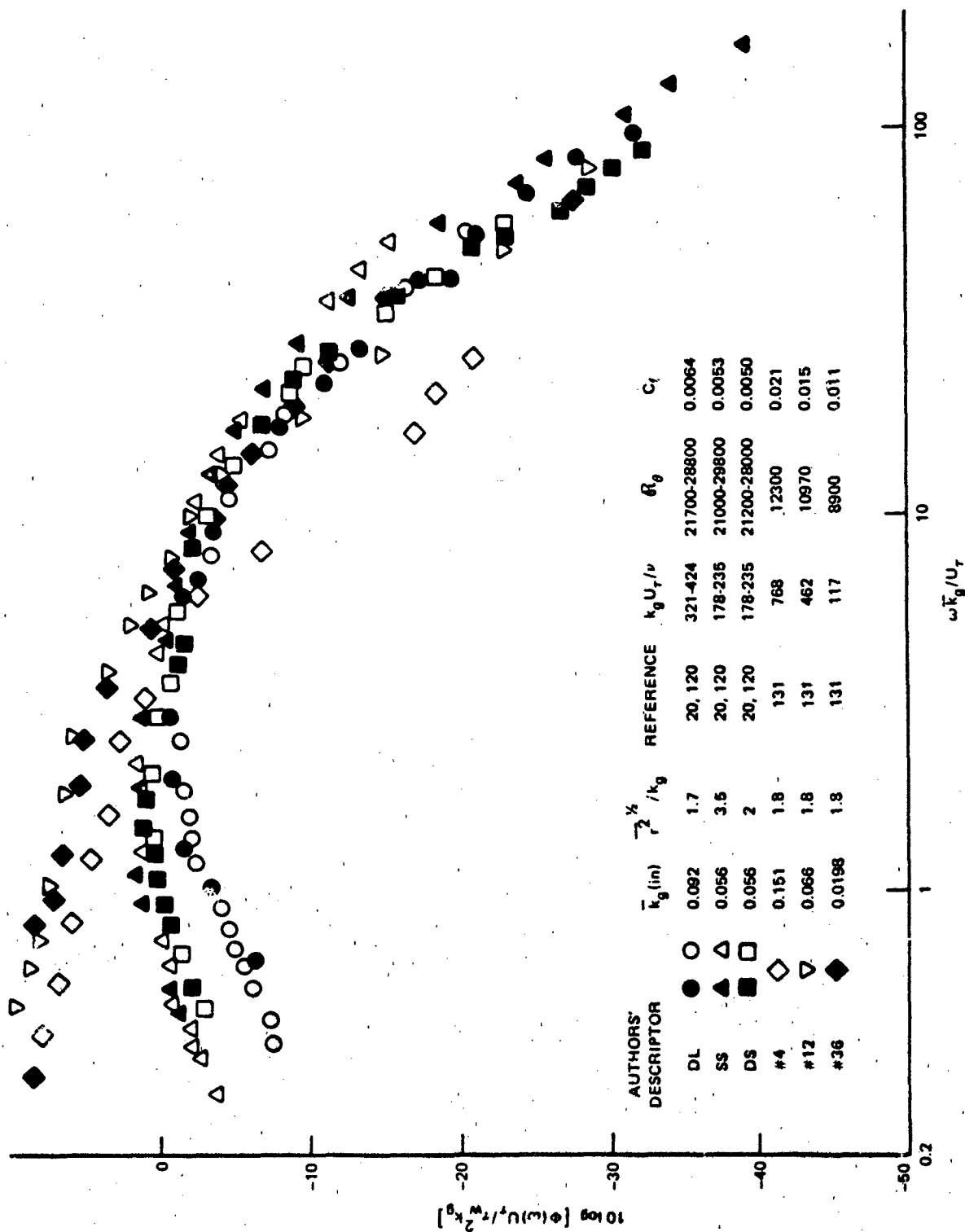


Figure 7.49 - Rough Wall Pressure Spectra Normalized on Wall Variables

This representation brought the spectrum on the wall for which $k_g U_\tau / \nu = 117$ into a somewhat better alignment with the other spectra than the nondimensionalization shown in Figure 7.49. Furthermore, the results DL and SS of references 20 and 121 also roughly (within 5 to 10 dB) conformed to those of Aupperle and Lambert, but generally the representation in Figure 7.49 was better for those spectra. The effectiveness of the inner variable nondimensionalization emphasizes the importance of interstitial flow in determining the high-frequency pressure fluctuations. Note that the convection velocity of high-frequency pressure fluctuations is on the order of $U_c/U_\tau = 8$ to 9. Correspondingly, the region of $\omega k_g/U_\tau$ dependence begins at $\omega k_g/U_c = 0.5$ to 1. This value suggests that the largest of the locally convected eddies is on the order of 6 to 10 times k_g . Burton¹⁵¹ has measured pressure-velocity correlations and has found them to be generally similar to those over smooth walls.²⁷

7.4.6 Effects of Transducer Size and Shape: The Response Function

Although some influences of finite transducer size have been discussed in connection with boundary-layer pressure measurement, some practical and theoretical aspects warrant further discussion. The subject has been given analytical and experimental attention by Corcos,^{132,135} Foxwell,¹⁵³ Gilchrist and Strawderman,¹⁵⁴ Chase,¹⁵⁵ Geib,¹⁵⁶ White,¹⁵⁷ Kirby,¹⁵⁸ Chandiramani,¹³⁵ Willmarth and Roos,¹⁵⁹ Bull and Thomas,¹⁶⁰ and Haddle and Skudrzyk.¹⁶¹

These effects can best be discussed within the framework of low-pass spatial filtering (Equation (7.140)). The autospectral density of the output of a single finite transducer is ($|A(k)|^2 \equiv 1$)

$$\phi_{p_M}(\omega) = \iint_{-\infty}^{\infty} |S_T(\vec{k})|^2 \phi_p(\vec{k}, \omega) d^2\vec{k} \quad (7.146)$$

where the Fourier transform of the sensitivity function is

$$S_T(\vec{k}) = \frac{1}{A_T} \iint_{A_T} e^{-i\vec{k} \cdot \vec{y}} s_T(\vec{y}) d^2\vec{y} \quad (7.147)$$

and $S_T(\vec{y}) = 0$ outside the boundary of the sensor. If $S_T(\vec{y}) \equiv 1$, the transducer responds to local pressures uniformly everywhere on its sensitive region. If we introduce Equation (7.134), we find that the ratio of the measured autospectral density to the actual spectral density at a point is

$$\frac{\phi_{PM}(\omega)}{\phi_p(\omega)} = \iint_{-\infty}^{\infty} |S_T(\vec{k})|^2 \phi_{1,3}(k_1, k_3, \omega) k_1 dk_3 \quad (7.148)$$

An expression for $\phi_{1,3}(k_1, k_3, \omega)$ can be taken from Equation (7.133) as $\phi_p(\vec{k}, \omega) / \phi_p(\omega) = \phi_{1,3}(k_1, k_3, \omega)$. Corcos^{132,162} carried out this integration for circular and square transducers with uniform sensitivity, while Kirby¹⁵⁸ and White¹⁵⁷ extended the results to other shapes. White¹⁵⁷ and Chase¹⁵⁵ considered the averaging effect of nonuniform sensitivity distributions. Gilchrist and Strawderman¹⁵⁴ had earlier attempted to account for nonuniform local sensitivity by defining for a circular transducer an effective radius

$$R_{eff}^2 = \int_0^{R_T} S_T(r) r dr \leq R_T^2 \quad (7.149)$$

and then assuming that the actual transducer responded to pressures as if it were actually a smaller transducer with uniform sensitivity over radius R_{eff} . The wave number function for a circular transducer of radius R_T is

$$|S_T(\vec{k})|^2 = 4 \left(\frac{J_1(kR_T)}{kR_T} \right)^2 \quad (7.150)$$

where

$$k = (k_1^2 + k_3^2)^{1/2}$$

and

$$S_T(\vec{y}) = 1 \quad |\vec{y}| < R_T$$

$$= 0 \quad \text{otherwise}$$

At large wave numbers $kR > 1$

$$|S_T(\vec{k})|^2 \approx \frac{8}{\pi} (kR_T)^{-3} \cos^2 \left(kR_T + \frac{\pi}{4} \right)$$

For a rectangular transducer, $S_T(\vec{k})$ is given in Equation (7.137).

Actual transducers have sensitivity functions that are maximum at the center and fall off near the edges. Measurements of $S_T(\vec{y})$ have been made on hydrophones by Gilchrist and Strawderman and on a condenser microphone by Bruel and Rasmussen¹⁶³ (see also reference 145). Figure 7.50a shows a typical hydrophone function¹⁵⁷; Figure 7.50b shows a measured function $|S_T(k)|^2$ for a typical condenser microphone¹⁴⁷ compared to Equation (7.150) for a transducer of the same radius but uniform sensitivity. We see that the actual acceptance at high wave numbers is at least 10 dB smaller than the acceptance of a transducer of uniform sensitivity.

Chase¹⁵⁵ has determined theoretically what characteristics of $S_T(\vec{y})$ influence the high wave number acceptance of real transducers. For an axisymmetric circular transducer, his result is obtained from Equation (7.146), which becomes

$$S_T(k) = 2 \int_0^1 J_0(kR_T z) S(z) z dz$$

where $z = R/R_T$. By integrating by parts and replacing the Bessel function by

$$J_0(\xi) = 2^{-\frac{1}{2}} \pi^{-1} \int_0^\infty dx x^{-\frac{1}{2}} e^{-\xi x}$$

$$\cdot \left\{ \left(1 + \frac{ix}{2}\right)^{-\frac{1}{2}} \exp \left[i \left(\xi - \frac{\pi}{4} \right) \right] + \left(1 - \frac{ix}{2}\right)^{-\frac{1}{2}} \exp \left[-i \left(\xi - \frac{\pi}{4} \right) \right] \right\}$$

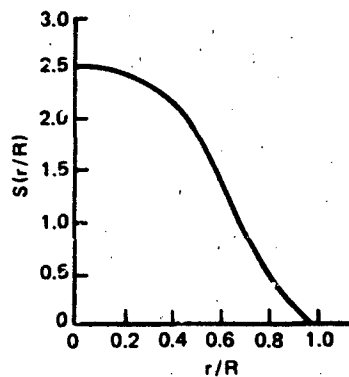
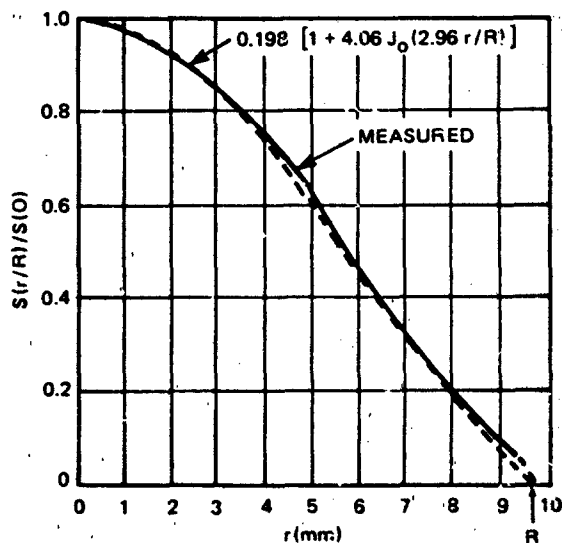
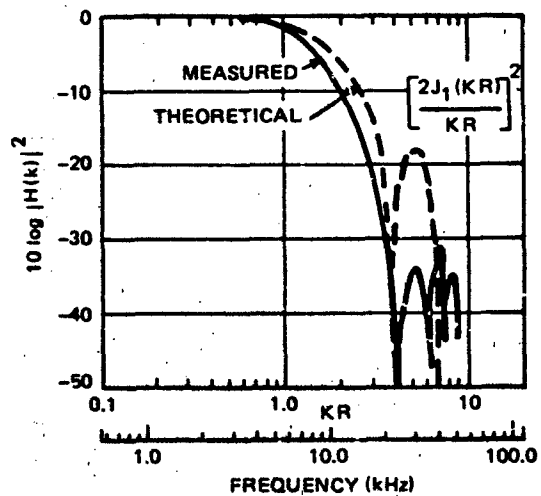


Figure 7.50a - Sensitivity Distribution Measured on the Face of a Piezoelectric Drystal Hydrophone¹⁵⁷



SENSITIVITY DISTRIBUTION



RESPONSE KERNEL

Figure 7.50b - Sensitivity Distribution and Corresponding Response Kernel for a Commonly Used Condenser Microphone. The Theoretical Response Kernel was Computed from the Indicated Functional Approximation to the Measured Sensitivity Distribution^{145,147,163}

Figure 7.50 - Sensitivity Distributions and Response Kernels for Commonly Used Transducers

Chase determined

$$S_T(k) = 2 \sum_{m=0}^M (-1)^m \left\{ \left(\frac{2}{\pi} \right)^{\frac{1}{2}} (kR_T)^{-2m-3/2} \left[S_T^{2m}(1) \cos \left(kR_T + \frac{\pi}{4} \right) \right. \right. \\ \left. \left. (kR_T)^{-1} S_T^{2m+1}(1) \sin \left(kR_T + \frac{\pi}{4} \right) \right] - \left[\frac{(2m+1)!}{2^{2m}(m!)^2} S_T^{2m+1}(0) (kR_T)^{-2m-3} \right] \right\} \quad (7.151)$$

for $kR_T > 1$, where

$$S_T^m(z) = \frac{d^m S_T(z)}{dz^m}$$

and $(m!) = 1 \cdot 2 \cdot 3 \cdot 4 \dots m$, $0! = 1$. For $kR_T \leq 1$, one can approximate $S_T(k)$ with Equation (7.150) using R_{eff} defined as Equation (7.149). It is apparent for most transducers that $S_T^m(0)$ is small or zero.

We consider two examples; in the first, the transducer has a uniform sensitivity

$$S_T^o(1) = 1, S_T^n(0) = 0$$

and

$$S_T^n(z) = \delta(1-z)$$

All terms of Equation (7.151) are important, but the first is most important (for $kR_T > 1$) so that

$$S_T(k) \approx 2 \cdot \left(\frac{2}{\pi} \right)^{\frac{1}{2}} (kR_T)^{-3/2} S_T^o(1) \cos \left(kR_T + \frac{\pi}{4} \right) \quad kR_T > 1$$

and

$$|S_T(k)|^2 \approx \frac{8}{\pi} (kR_T)^{-3} \cos^2 \left(kR_T + \frac{\pi}{4} \right) \quad kR_T > 1$$

If, instead, we have $S(R/R_T)$, as shown in Figure 7.50, then $S_T^0(1) = 0$, $s_T^n(0) = 0$, but $S_T^1(1) = a$. The first term of the expansion is zero, but the second and largest term (for $kR_T > 1$) is

$$S_T(k) \approx 2(-1) \left(\frac{2}{\pi}\right)^{1/2} (kR_T)^{-5/2} a \sin\left(kR_T + \frac{\pi}{4}\right)$$

and

$$|S_T(k)|^2 = \frac{8}{\pi} (kR_T)^{-5} a^2 \sin^2\left(kR_T + \frac{\pi}{4}\right)$$

The dependence at large wave number for this sensitivity has an extra $(kR_T)^{-2}$ because of the nonvanishing slope of the sensitivity function at the periphery of the transducer. If both the sensitivity and its first derivative vanish, we have

$$|S_T(k)|^2 \approx (kR_T)^{-7}$$

at large wave number.

Measurements of the effects of spatial averaging have been provided by Geib,¹⁵⁶ Willmarth and Roos,¹⁵⁹ and Bull and Thomas.¹⁶⁰ The results are most often presented in the form

$$\frac{\phi_{p_M}(\omega)}{\phi_p(\omega)} = \sigma_M \left(\frac{\omega R_T}{U_c} \right) \quad (7.152)$$

Figure 7.51 shows a comparison of measured results that have been extracted from Geib¹⁵⁶ and Willmarth and Roos,¹⁵⁹ and theoretical results of $S_T(R) = 1$ by Corcos¹³² and $S_T(r)$ of Figure 7.50 by White.¹⁵⁷ In both theoretical results a pressure field with the cross-spectral density of wall pressure as Equation (7.133) was assumed. It is clear that there is no universally acceptable function with which to predict exactly the effect of hydrophone size. Indeed, the theoretical results show that the averaging effect is very sensitive to $S_T(R)$ near the periphery. Thus it is not surprising that $\sigma(\omega R_T/U_c)$ for condenser and pinhole microphones are somewhat

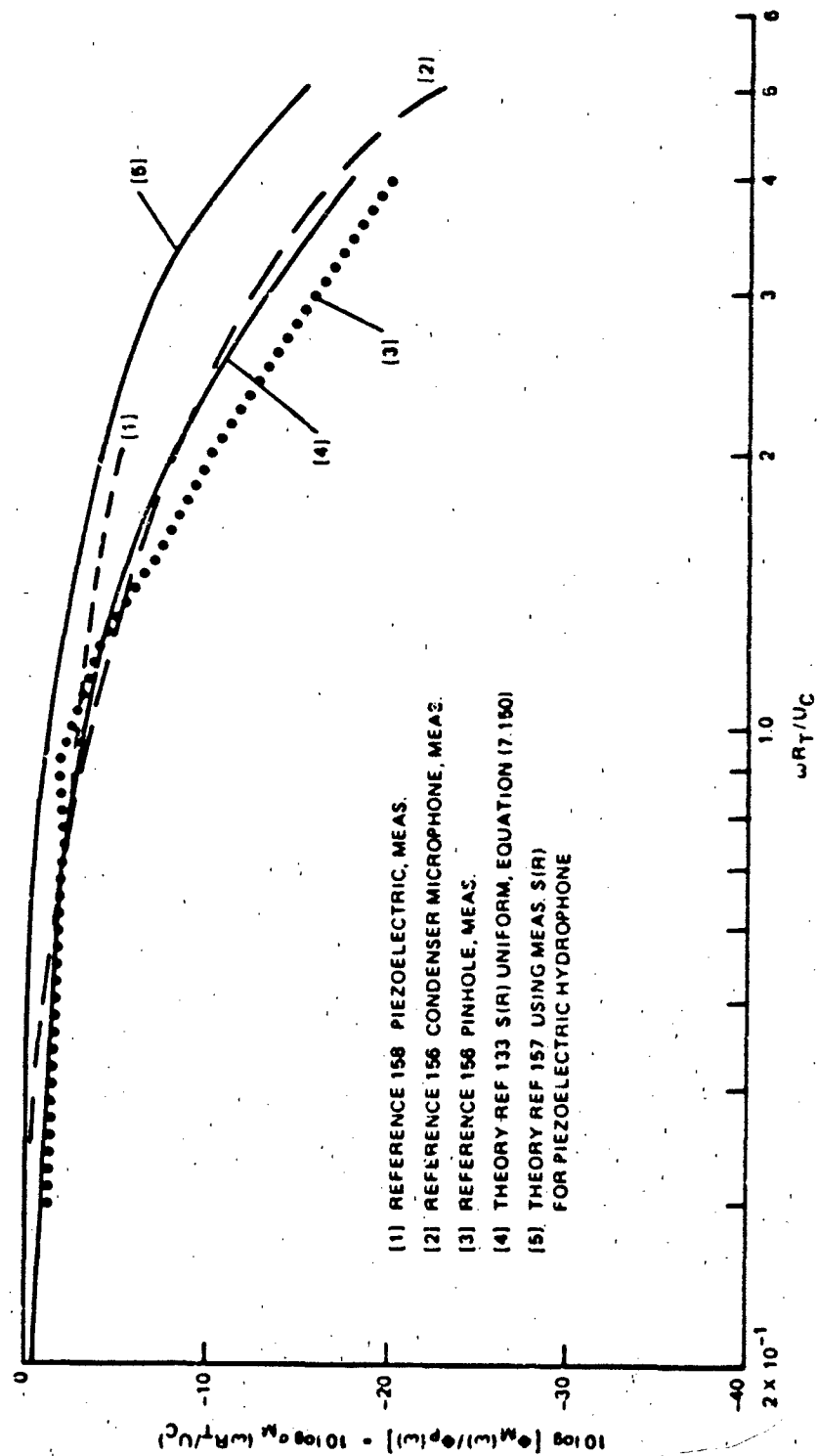


Figure 7.51 - Effect of Spatial Averaging on Wall Pressure Spectrum Observed in Various Facilities

different than for hydrophones. Bull and Thomas¹⁶⁰ showed that slightly different autospectra could be obtained with pinhole and condensor microphones of the same nominal geometric diameter when $\omega R_T / U_c > 1$.

Finally, effects of hydrophone geometry have been explored by Kirby¹⁵⁸ and Haddle and Skudrzyk.¹⁶¹ Generally, when a transducer is longer in one direction than another, autospectra of wall pressures are lowest when the long dimension of the transducer is aligned with the flow direction. This behavior would be expected on the basis of spatial anisotropy of the pressure fluctuations in the plane of the wall, as shown in Figures 7.27 and 7.39. Theoretical results by Corcos show that spatial averaging by square transducers (of length L_T) is less severe than by round transducers for which $L_T = 2R_T$.

7.4.7 Transduction of Boundary-Layer Pressure Through Rubber Blankets

When a transducer exposed to subsonic boundary-layer flow is shielded from that flow with a compliant fluid layer, it may then discriminate very well against high wave number components near $k = k_c$. The discrimination can be estimated very accurately from formulations derived by Maidanik¹⁶⁴ and Maidanik and Reader.¹⁶⁵ The geometry of the transducer (or array of transducers) is shown in Figure 7.52. The moving fluid of density ρ_o and speed of sound c_o is separated from the transducer system in a rigid plane by a second layer of parameters ρ_r and c_r . The thickness of the layer is h . In the most general case, the interface between the $\rho_o c_o$ fluid and the $\rho_r c_r$ fluid would be maintained by an elastic film. This case has been covered by Maidanik.¹⁶⁵ For many applications, particularly underwater, the r layer is an elastomer that is assumed to be fluid-like. In an aerodynamic application, the system could be a porous plate situated at $y_2 = 0$ between the o fluid and the r fluid (see Maidanik¹⁴¹ and Section 7.4).

The simplest approach (and one that applies in many practical situations) is to assume that the properties ρ_r and c_r of the viscoelastic layer are similar enough to those of the external fluid, ρ_o and c_o . Further, assume that the turbulent pressure sources, i.e., the Reynolds stress tensor, in the moving fluid are unaffected by the presence of the elastomer. Thus posed, the solution of this problem may be written straightforwardly by applying Equation (7.77). It is assumed that the viscoelastic displaces the Reynolds stresses a distance $y_2 = -h_r$ from the rigid surface. Therefore Equation (7.77) shows that as long as

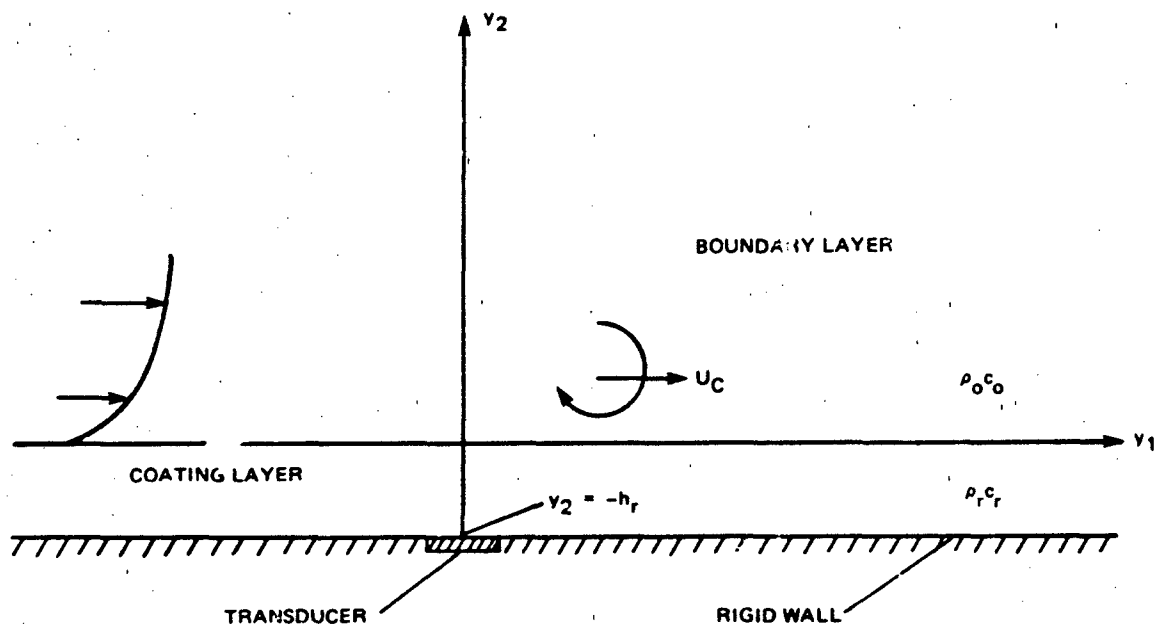


Figure 7.52 - Geometry of a Hydrophone Beneath a Viscoelastic Layer

$$\left[T_{ij}(y_2, \vec{k}, \omega) \right]_{\text{no layer}} = \left[T_{ij}(y_2, \vec{k}, \omega) \right]_{\text{layer}}$$

then

$$\frac{\left[p(\vec{k}, \omega) \right]_{\text{layer}}}{\left[p(k, \omega) \right]_{\text{no layer}}} = \exp \left[i h_r (k_o^2 - k^2)^{1/2} \right] \quad (7.153)$$

Accordingly, the wave number spectrum on the surface behaves as

$$\left[\phi_p(\vec{k}, \omega) \right]_{\text{layer}} = \left[\phi_p(\vec{k}, \omega) \right]_{\text{no layer}} \quad k \leq k_o \quad (7.154)$$

and

$$\left[\phi_p(k, \omega) \right]_{\text{layer}} = \left[\phi_p(\vec{k}, \omega) \right]_{\text{no layer}} e^{-2h_r k} \quad k > k_o$$

In the case of a single small transducer $[S_T(k) = 1]$ reacting to boundary-layer pressure, its autospectrum is controlled by wave numbers $k_1 \approx k_c$; thus it will relate to that of an uncovered transducer by

$$\frac{\phi_m(\omega)}{\phi_p(\omega)} \approx \exp\left(\frac{-2\omega h_r}{U_c}\right) \quad (7.155)$$

This ratio is plotted in Figure 7.53 as a function $\omega h_r/U_c$ and $\omega h_r/U_\infty$, alternately assuming $U_c = 0.6 U_\infty$ and $0.8 U_\infty$.

We now consider again the problem of discrimination. For $k_c h_r > 1$, Equation (7.155) shows that the wall pressures are attenuated as long as $k_c > k_r$ also. Thus the coating permits discrimination of subsonic convected wave number components compared to contributions for which $k h_r < 1$. If the pressure field on the interface of the outer fluid and the coating has an acoustic component, $k \leq k_o = k_r$ ($\rho_o = \rho_r$, $c_o = c_r$), superimposed on the boundary-layer pressures, the coating permits a noninterfered reception of the acoustic field.

The results of this section and the sections that dealt with spatial filtering provide the designer with many options for discriminating against the pseudonoise of boundary layers. When $\phi_p(\vec{k}, \omega)$ contains components of interest (say acoustic information) in the low wave number end of the spectrum, a suitably designed coated transducer system can be successfully used as an acoustic receiver even though it may be physically close to a moving turbulent fluid.

Maidanik^{164,165} has considered a larger number of possibilities than the simple example considered here. These cases include combinations of properties of the outer and coating fluids as well as the effects of a plate at the interface.^{164,166} For a simple coating, if $c_o > c_r$ and $\rho_o = \rho_r$, then resonance situations are generated in the wave number range $\omega/c_o = k_o < k < k_r = \omega/c_r$ because of reflections at the fluid interface. Even for c_o and c_r differing by 30%, effects on transmission can be important. If $c_r > c_o$, resonance conditions can also be generated when the coating is thick enough. For thin enough coatings, say $k_r h_r \ll 1$ ($k_r h_r \approx 0.1$ will satisfy this constraint), pressures in the wave number range $k < k_r$ are transmitted without change.

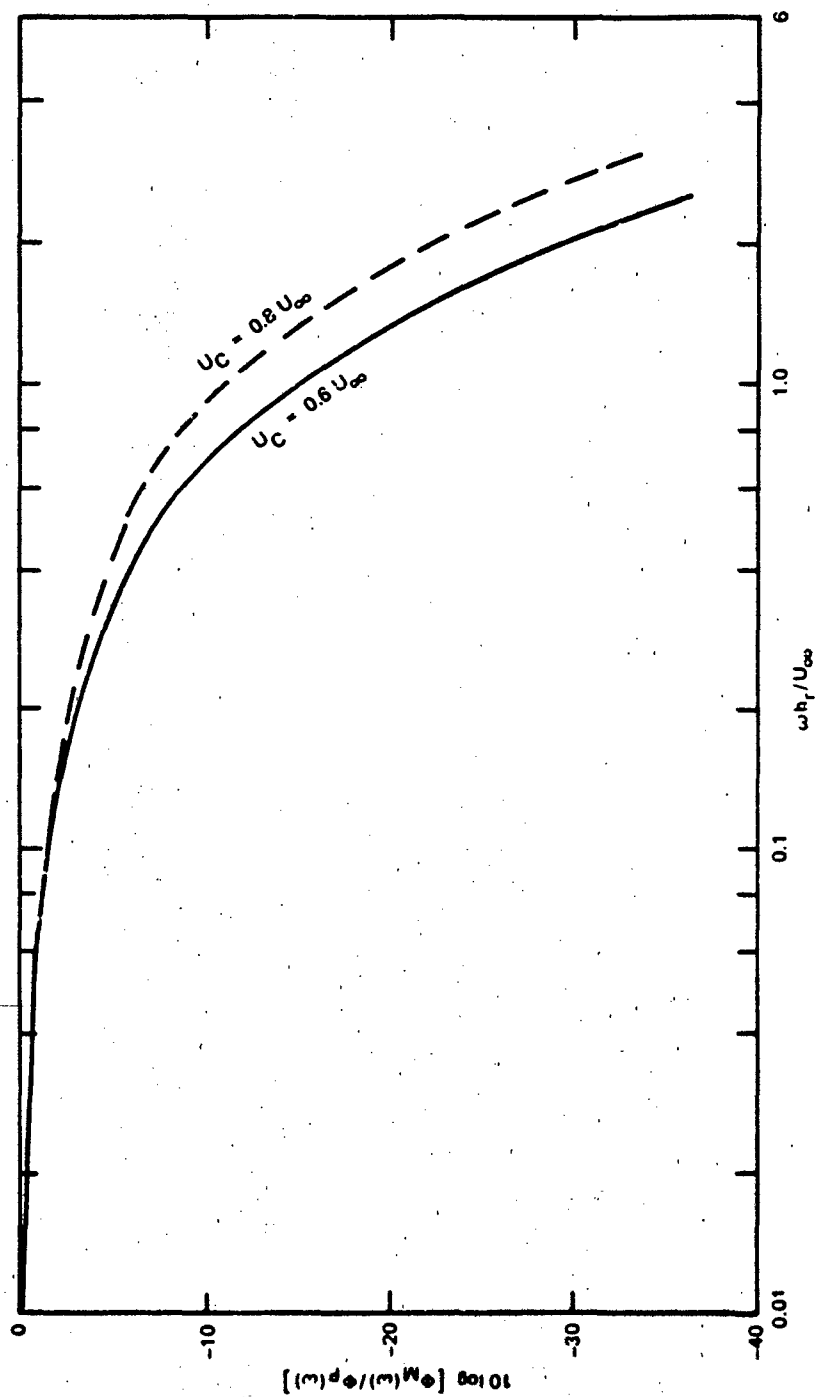


Figure 7.53 - Attenuation of Wall Pressure Autospectrum at a Point on a Rigid Surface Covered with an Elastomeric Layer of Thickness h_r
(See Equation (7.155))

7.4.8 Pressure Fluctuations in Turbulent Pipe Flow

This topic is treated here only as an extension of our discussion of turbulent boundary-layer pressures. Because there has been interest from time to time in measurements in water and because water tunnel facilities are not common, some work has been conducted in pipe flows. Already included in this chapter is work done by Bakewell and Lumley,⁴¹ Laufer (channel flow),⁴⁸ Morrison and Kronauer,⁹³ and Robertson et al.²² In many cases, the physics of wall layers in pipe flow and boundary layers is the same. Perhaps the most extensive characterization of pipe flow turbulence is that of Laufer.¹⁶⁷ Many investigators have used pipe flows for measurements in fluids with polymer additives. The wall shear coefficient can be very simply determined in pipe flows by using Equation (7.6). The static pressure difference ΔP over a length L gives τ_w as

$$\tau_w = \Delta P \frac{d}{2L}$$

where d is the diameter of the pipe. Near the wall, turbulence intensities are similar to those measured in turbulent boundary layers.¹⁶⁷

Wall pressure fluctuations on pipe walls have been measured by von Winkle,¹⁶⁸ Corcos et al.,^{133,169} Bakewell et al.,^{170,171} DeMetz and Jorgensen,¹⁷² and Greshilov et al.¹⁷³ Measurements have been made in a water channel flow by Greshilov and Lyamshev.¹⁷⁴ Figure 7.54 shows the autospectra that have been made dimensionless on the average discharge velocity \bar{U} , and d the diameter of the pipe or the height of the channel. The spectra are of the form

$$\overline{p^2} = \int_0^{\infty} G(f) df$$

This dimensionless form has been adopted by all measurement programs. Cross-spectral densities $\phi_p(\omega, \vec{r})$ are qualitatively similar to those in boundary layers, shown in Figures 7.37 and 7.38, and the convection velocity converges asymptotically to $0.65 U_{CL}$ at high frequencies. The measurements of Greshilov et al. on smooth and rough walls of a water channel disclosed a more rapid loss of streamwise coherence

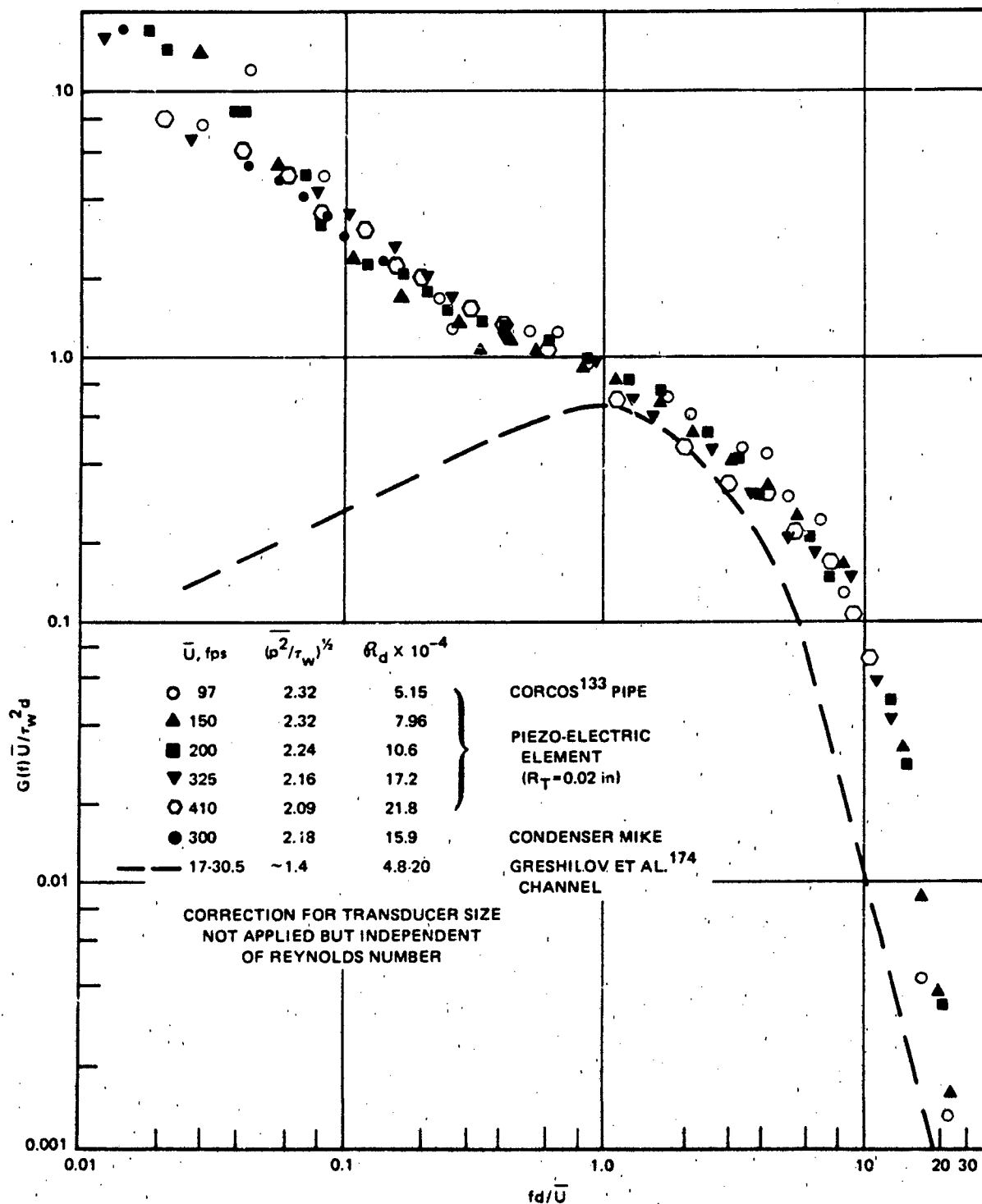


Figure 7.54 - One-Sided Frequency Spectra of Turbulent Pressure at the Wall (Pipe Flow and Channel Flow)

of pressure similar to that illustrated in Figure 7.37a for the boundary layer. Generally, the measurements on smooth walls of channels¹⁷⁴ and pipes^{169,172} behave in a form roughly similar to the functions for boundary-layer pressures.

7.5 TURBULENT FLOW OVER CURVED SURFACES

This section summarizes some characteristics of various types of flow that exist in boundary layers on curved surfaces. They can be classified as "equilibrium" in only a few very special cases; they include both external or internal flows, and none of them may be considered homogeneous in one or more coordinate directions in the plane of the surface. Therefore the balance of published work on these topics cannot be generalized to yield simple prediction schemes. Here we only illustrate the extent to which the noise-producing characteristics of various flow types deviate from those well-documented for equilibrium boundary layers. These characteristics are the magnitude, frequency spectral form, and the temporal and spatial statistics of boundary-layer pressure in local regions of the flow, as well as the overall spatial variation of these properties at various points on surfaces.

We discuss

1. Transition to turbulence
2. Favorable and adverse static pressure gradients
3. Axially symmetric flow on circular cylinders

It is expected that the reader will find more detailed discussions of the general flow characteristics and prediction schemes based on the growing modes of the Orr-Sommerfeld equation in the extensive surveys of Schlichting,¹ Hinze,² Cebeci and Smith,³ Bradshaw,¹⁵ and Lin.⁹⁷

7.5.1 Transition to Turbulence

Mollo-Christensen⁵⁴ gives a very brief and clearly presented survey of the aspects of transition from laminar to turbulent flow. Hinze² gives another survey, highlighting the unsteady aspects of the transition process. In both surveys, the similarities and dissimilarities of the transition mechanics and the fully developed turbulence production are discussed.

The transition process is illustrated in Figure 7.55. The flow is presumed to encounter the surface at $y_1 = 0$. For a short distance, the flow is disturbance free and truly laminar. Near $R_1 = 10^6$ Tollmein-Schlichting¹ waves begin; these disturbances are analytically predictable as eigenfunctions of the Orr-Sommerfeld equation

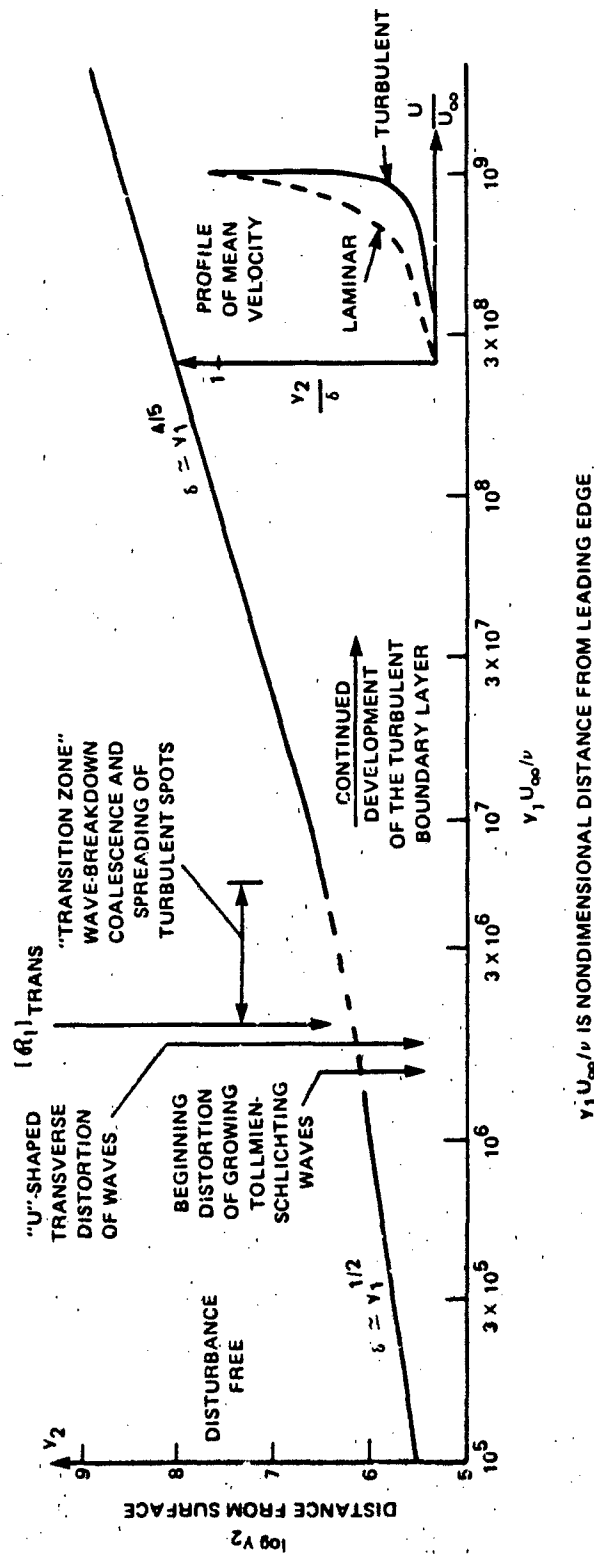


Figure 7.55 - Schematic of a Developing Transitional Boundary Layer. Various Stages of Two- and Three-Dimensional Wave Motion Are Shown

(see Chapter 3, Section 7.3.5, and Lin⁹⁷). They have wave fronts along y_3 and propagate at a wave speed roughly on the order of $U_\infty/2$. The generally used and convenient computation scheme is to compute the complex eigenvalues of the homogeneous equation ((Equation 7.114) with $\tilde{q}=0$). When, for either component of disturbance, u_1 , the computed amplification of the disturbance grows from e^9 to e^{11} times an initial value, i.e.,

$$\ln \left[\frac{u_1(y_1, \omega)}{u_1(y'_1, \omega)} \right] = \int_{y'_1}^{y_1} \alpha_1(y_1) dy_1 = \alpha_1 S = n \quad (7.156)$$

Where $n = 9$ to 11 , $\alpha_1(y_1)$ corresponds to streamwise-varying $U(y_1, y_2)$, and y'_1 is the streamwise location of the initial value, the transition is said to occur. The value of y'_1 generally lies at the leading edge or at the forward stagnation point of the body where the flow is presumed to be disturbance free. It is often found that the value of y_1 for which calculated and measured transition occurs is such that $n = 9$ even though the flow disturbances should hardly be considered to be first order with such a large amplification. Further downstream the disturbance wave fronts become distorted in the transverse direction distortion of the upstream loop of the resulting vortex-like wave front resembling a U (see Hama^{53,175}). The fluid motion within the U-shaped loops becomes turbulent by $R_1 = 2 \times 10^6$, resulting in the occurrence of "spots" of turbulence,^{176,177} which spread streamwise and laterally as they propagate downstream.^{107,178} The occurrence of these spots increases both temporally and spatially until they coalesce into a fully developed turbulence region, $R_1 = 10^7$.

This process is dependent on both the streamwise Reynolds number and the magnitude of the static pressure gradient. An adverse pressure gradient (a positive value of $\partial P/\partial y$) brings on transition to turbulence at a lower value of R_1 , while, conversely, a favorable gradient (negative value of $\partial P/\partial y_1$) will delay the transition to turbulence. The process of transition is also aggravated by surface roughness (e.g., Klebanoff and Tidstrom¹⁷⁹), surface compliance and flexibility,¹⁸⁰⁻¹⁸² and freestream turbulence (e.g., Hall and Gibbings¹⁸³), and it can be influenced by ambient acoustic levels (e.g., Shapiro¹⁸⁴ and Schilz et al.¹⁸⁵⁻¹⁸⁷).

For two-dimensional shapes, airfoils, hydrofoils, and the like, approximate methods are summarized by Schlichting,¹ with results of measured boundary-layer properties given in numerous NACA reports. The case of a flat plate is useful for rough calculations. Transition Reynolds numbers¹⁸⁸ are given in the now well-known Figure 7.56¹⁸⁹ for a range of turbulence intensities in the freestream.

The calculation of the Reynolds number of transition, R_1 , is an involved subject well beyond the scope of this work. However, it is useful, in the context of making approximate noise and vibration estimates, to review the results of some recent work of Niedzwecki¹⁹⁰ and Casarella et al.,¹⁹¹ which deals with the location of transition on bodies of revolution. They have calculated the transition location on a series of elliptical head forms whose shapes are illustrated in the upper half of Figure 7.57 (from Lauchle¹⁹²). The parameter t refers to the ratio of the major-to-minor axis of the forebody. The figure shows the locations of the minimum pressure coefficient and of transition points, determined according to the "Smith-Gabrioni" criterion that $\alpha_1 s = 9$ to 11 (see Equation (7.156)), for five values of Reynolds number. For the shape $t = 0.5$, the transition point moves farthest downstream for the range of $R_D = U_\infty D/\nu$ shown. The transition depends primarily on the value of a parameter β_ℓ , determined by the static pressure gradient and defined as

$$\beta_\ell = \frac{s}{U_m} \frac{dU_m}{ds} \frac{1}{P_3^2(s)}$$

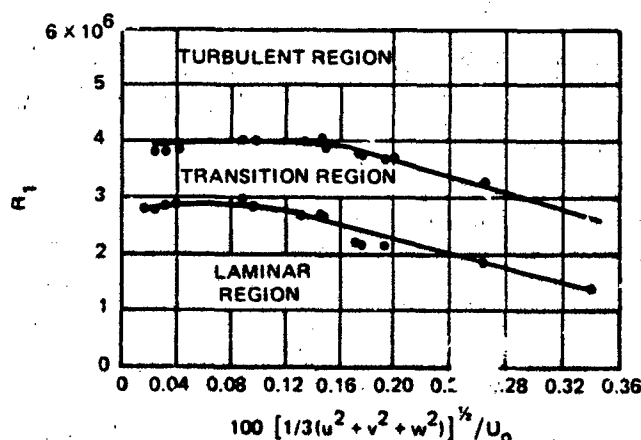


Figure 7.56 - Effect of Turbulence on y_1 Reynolds Number of Transition. Flat Plate, Zero Pressure Gradient.¹⁸⁹

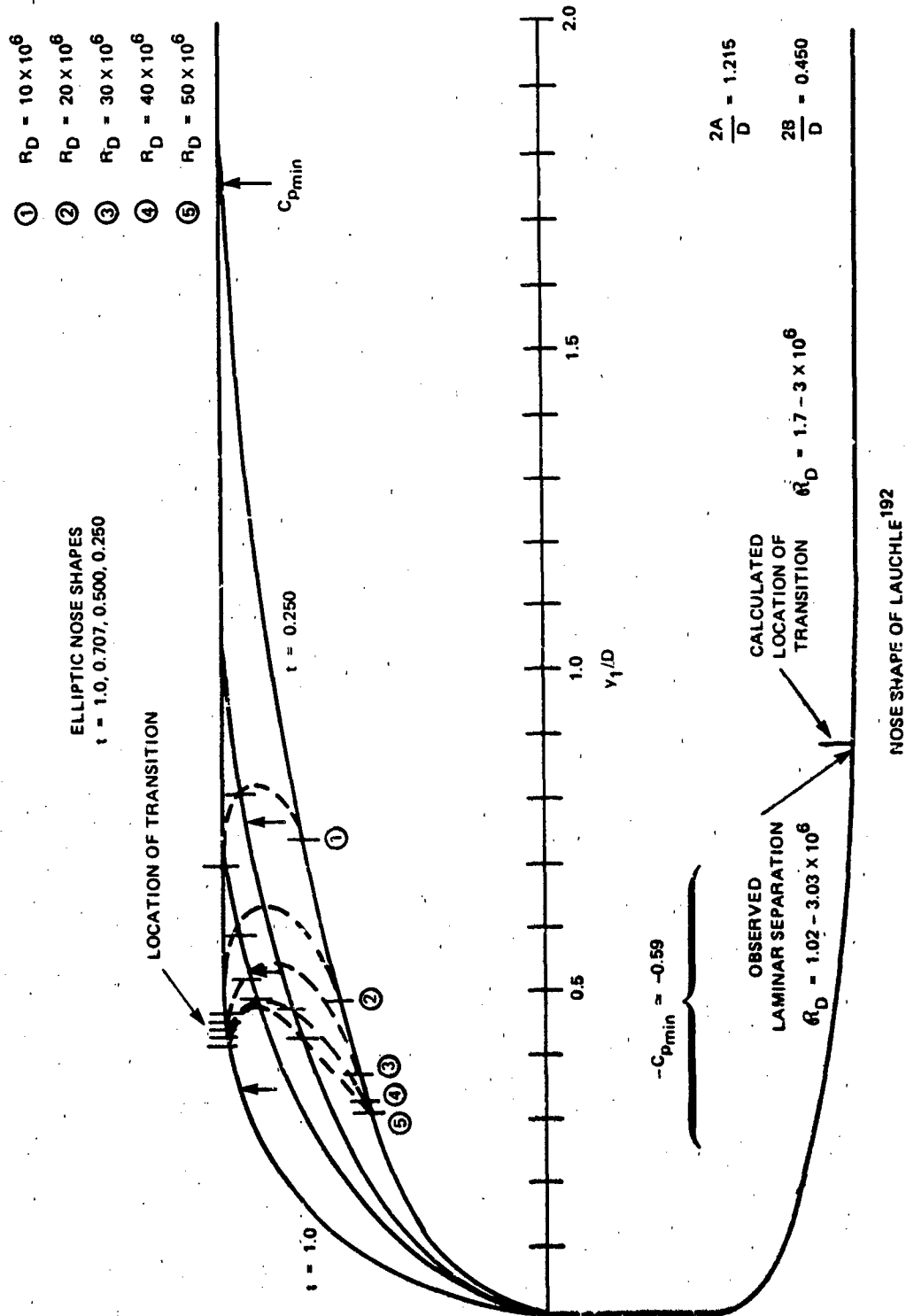


Figure 7.57 - Effects of Nose Shape and Reynolds Number on the Location of Transition¹⁹¹

where

$$P_3^2(s) = \frac{s U_m(s) r^2(s)}{2 \int_0^s U_m(S) r^2(S) dS}$$

s is the streamwise distance along the body, $r(s)$ is the local radius of the body, and $U_m(s)$ is the local potential (freestream) velocity outside the boundary layer. The derivative dU_m/ds determines the static pressure gradient $[(\partial P/\partial s) = -U_m(\partial U_m/\partial s)]$ for a given body shape and dominates the variation of β with s for the shapes shown. The factor $P_3^2(s)$ lies within the limits of 1/2 and 2 for axisymmetric flow. In judging the relative extents of a series of candidate designs, Casarella et al.¹⁹¹ suggested that β should be as large as possible; the condition $\beta = 0$ occurs at the point of minimum pressure. When $C_{p_{min}}$ is also as far from the stagnation point as possible, these two requirements ensure a long region of favorable pressure gradient (accelerating flow). As a practical matter, when $R_D > 30 \times 10^6$ for these bodies, transition can be extended only as far as $C_{p_{min}}$.

The lower half of Figure 7.57 shows another headform and its transition location calculated by Lauchle.¹⁹² In this case the region of $C_{p_{min}}$ is extended (i.e., a large region of $\beta=0$). For the values of R_D shown, laminar separation was experimentally observed near the indicated location. Thus, as a practical matter, transition on this body was limited by the downstream extremity of the minimum pressure region.

Boundary-layer properties can be approximated in the turbulent region using the relationships of Section 7.2 as long as the ratio of the body curvature to boundary-layer thickness is very large and one can estimate the origin of the turbulent boundary layer. The coordinate distance y_1 in those equations is replaced by the streamwise distance s along the surface of the body measured from the transition point. Those equations will also apply approximately to airfoils of small thickness-to-chord ratio. For bodies of revolution, the boundary-layer thickness is much thinner¹⁹¹ (for a given dP/ds) than on the two-dimensional form. For laminar flow over a flat surface, the displacement thickness (Equation (7.28)) is given by

$$\delta^* = 1.72 y_1 \left(\frac{\nu}{U_\infty y_1} \right)^{1/2} \quad (7.157)$$

which can be rewritten simply as

$$\frac{R_{\delta^*}}{(R_1)^{1/2}} = 1.72 \quad (7.158)$$

For a body of revolution, R_{δ^*} can be rewritten as a function of $R_D = U_\infty D/\nu$ and s/D where s is the streamwise distance from the stagnation point. This relationship is written

$$\frac{R_{\delta^*}}{(R_D)^{1/2}} = f \left(\frac{s}{D} \right) \quad (7.159)$$

where f is a function of the geometry alone. If it is assumed that the boundary layer is identical to that which would develop on a flat plate, i.e., Equation (7.157) with s replacing y_1 , then Equation (7.159) takes on a limiting form

$$\left(\frac{R_{\delta^*}}{(R_D)^{1/2}} \right)_{\text{flat}} = 1.72 \left(\frac{s}{D} \right)^{1/2} \quad (7.160)$$

Figure 7.58 compares Equations (7.159) (reference 191) and (7.160) for the elliptical head forms shown in Figure 7.57. The calculations illustrate the effect of body shape in altering the development of laminar flow. Calculations of R_{δ^*} extend roughly up to the transition points shown in Figure 7.57. Other boundary-layer length scales are expected to be in the same proportion to δ^* as they are on planar laminar flow; $\delta = 2.96\delta^*$, $\delta^*/\theta = 2.59$. Since on a flat plate, the local friction coefficient in laminar flow takes on the form¹

$$C_f = \frac{0.664}{(R_1)^{1/2}} \quad (7.161a)$$

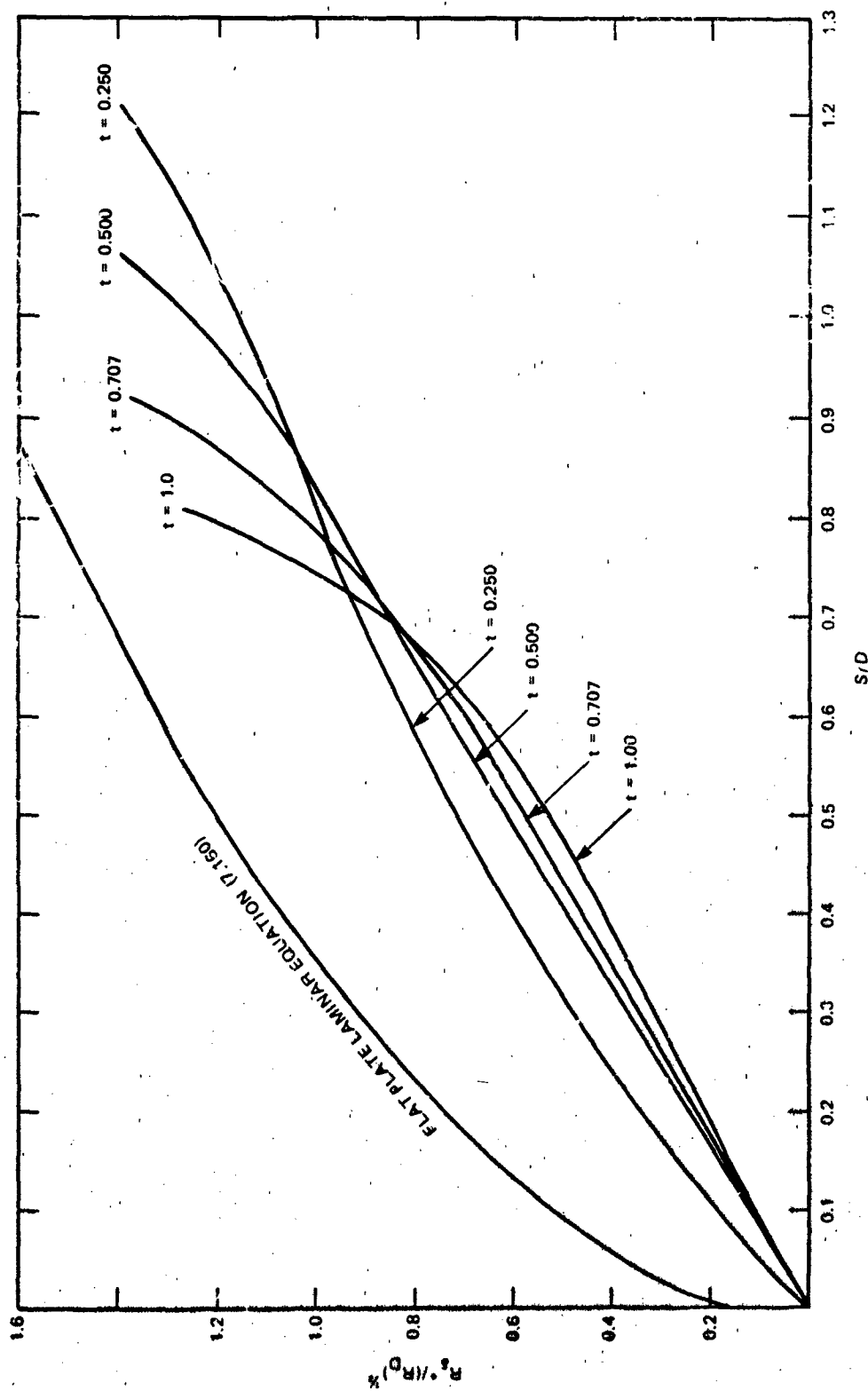


Figure 7.58 - Dimensionless Displacement Thickness for Ellipsoidal Forebodies,
 $t = 1.0, 0.707, 0.50, 0.25$ ¹⁹¹

it is reasonable to utilize Equation (7.158) to approximate C_f in laminar flow on a body of revolution as

$$C_f \approx \frac{1.12}{R_{\delta^*}} \quad (7.161b)$$

The wall-shear coefficient in the turbulent boundary layer exceeds the coefficient in the laminar flow.

The boundary-layer properties in the transition zone have been estimated by Dhawan and Narasimha¹⁹³ using combinations of relationships appropriate to either fully laminar flow or fully turbulent flow. Figure 7.59 shows computed and measured values of R_δ for one case described. The transition Reynolds number R_T is defined as the value of R_1 for which the flow is turbulent approximately 0.01 of the time. This is defined as the location of the onset of transition. When turbulence occurs 0.99 of the time, $\gamma = 0.99$, the boundary-layer thickness is well approximated by Equation (7.10) with R_1 replaced by $R_1 - R_T$. The virtual origin of the turbulent boundary layer is therefore determined by the onset of transition (R_T). The local wall-shear coefficient in the transition zone is hypothesized to be given by Equation (7.161a) in the laminar region and by Equation (7.35) (adjusted with R_1 replaced by $R_1 - R_T$) in the turbulent zone. Thus the local wall-shear coefficient is given by

$$(C_f)_{\text{trans}} = (1-\gamma) (C_f)_{\text{lam}} + \gamma (C_f)_{\text{turb}}$$

where the subscripts lam and turb refer to Equations (7.161) and adjusted Equation (7.36), respectively. The curve marked A in Figure 7.59 was calculated in this manner.

The pressure fluctuations beneath a transitional boundary layer have been measured extensively by DeMetz and Casarella^{194,195} over smooth walls and by Gedney¹⁹⁶ over both smooth and rough flat plates. In these measurements, the transition region was developed in a range of zero to mildly favorable pressure gradients bounded by

$$\frac{y_1}{U_m} \frac{dU_m}{dy_1} = 0 \text{ to } 0.15$$

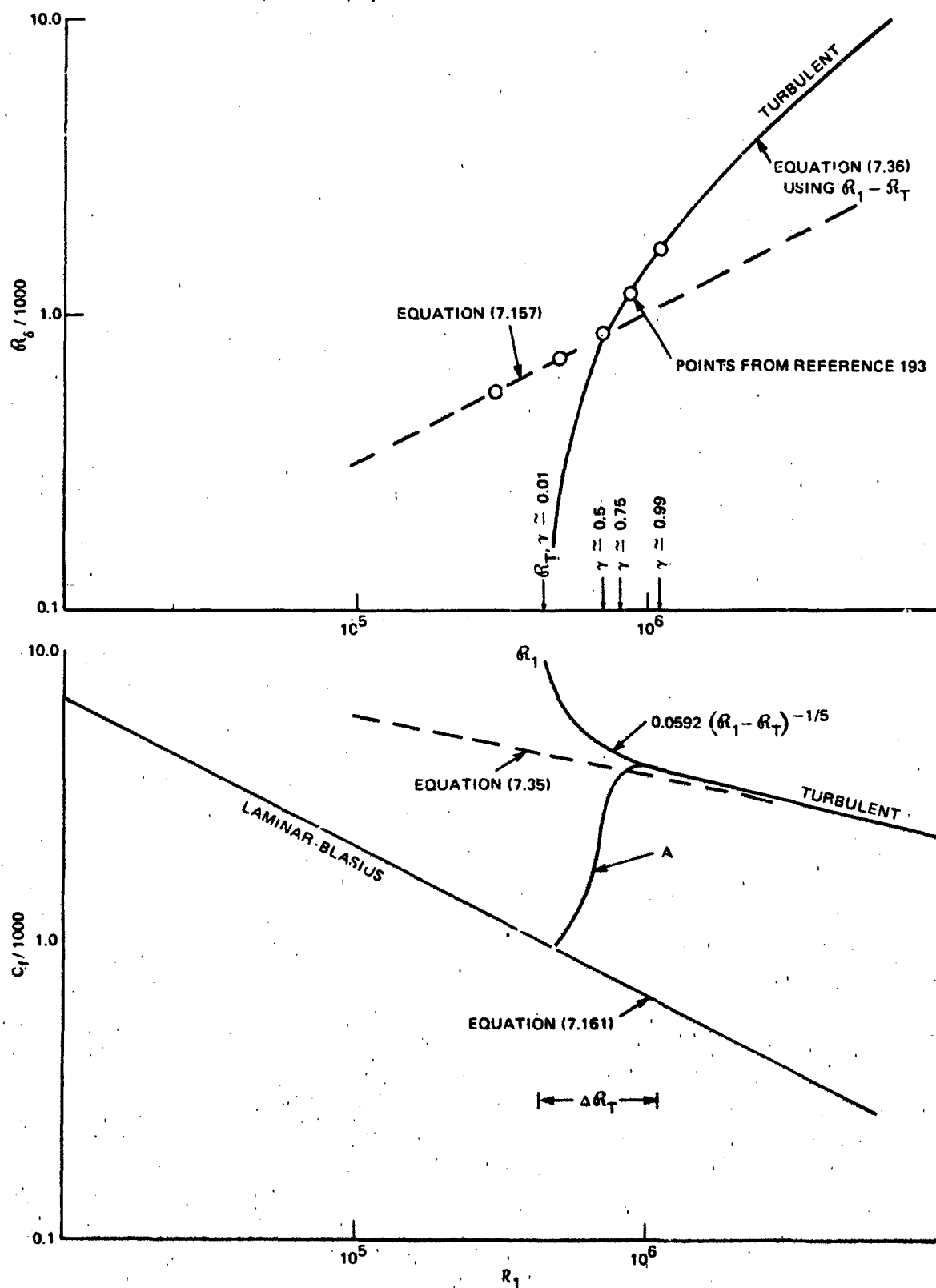


Figure 7.59 - Local Boundary-Layer Thickness and Wall Shear Coefficient as a Function of Reynolds Number in a Smooth-Wall Transition Zone

The range of R_1 over which intermittent transitional flow has been observed was

$$10^6 < R_1 < 9.1 \times 10^6$$

$$(R_0 = 0.9 \times 10^3 \text{ to } 1.9 \times 10^3)$$

In both investigations, the time dependence of the pressure fluctuations observed at a point in the zone of intermittent turbulence (near $R_1 \approx 3 \times 10^6$ in Figure 7.55) resembled a gated random noise function with a random burst duration and period. Letting the narrowband pressure level during the burst be $\overline{p_b^2}$ and the long-time mean-square pressure be $\overline{p^2}$, DeMetz and Casarella found that in a frequency band Δf

$$\overline{p^2}(f, \Delta f) = \frac{1}{\gamma} \overline{p_b^2}(f, \Delta f) \quad (7.162)$$

where γ is an intermittency factor. This factor is simply the ratio of the average burst length T_B to the average time interval between burst T_p

$$\gamma = \frac{T_B}{T_p}$$

Thus Equation (7.162) suggests that the pressure spectral density in the intermittent zone may be written

$$\frac{[\Phi_p(\omega)]_{\text{int}} U_\infty}{\tau_w^2 \delta^*} \approx \gamma \left[\frac{\Phi_p(\omega) U_\infty}{\tau_w^2 \delta^*} \right]_{\text{fully developed}} \quad (7.163)$$

where an appropriate value of C_f is determined by the value attained at the end of the transition zone. This relationship was confirmed by Gedney's measurements, at least for $\gamma > 0.6$. The intermittency variable γ was found by DeMetz and Casarella¹⁹⁵ to be distributed throughout the transition zone in the manner of

$$\gamma = \frac{1}{2} \left[1 \pm \operatorname{erf} \left\{ \left[(R_1 - R_1)_{\gamma=0.5} \right] \sqrt{\left(\frac{\Delta R_T}{6} \right)} \right\} \right] \quad (7.164)$$

where the error function has the asymptotic properties given on page 980, $(R_1)_{\gamma=0.5}$

is the Reynolds number at which the intermittency is 1/2, and ΔR_1 is the Reynolds number interval of the transition zone as defined by measured limits of $\gamma = 0.01$ and $\gamma = 0.99$. Equation (7.164) is shown in Figure 7.60. Dhawan and Narasimha¹⁹³ found similar behavior for velocity fluctuations with

$$\Delta R_1 \approx 5 \Delta R_T \left[(R_1)_{\gamma=0.01} \right]^{0.8}$$

for a wide variety of published data, for which $(R_1)_{\gamma=0.01}$ is the nominal transition Reynolds number. DeMetz and Casarella's measurements of pressure spectra did not reflect the occurrence of periodic Tollmein-Schlichting waves as precursors to the bursts of velocity disturbances that had been reported by Schubauer and Klebanoff.¹⁷⁸

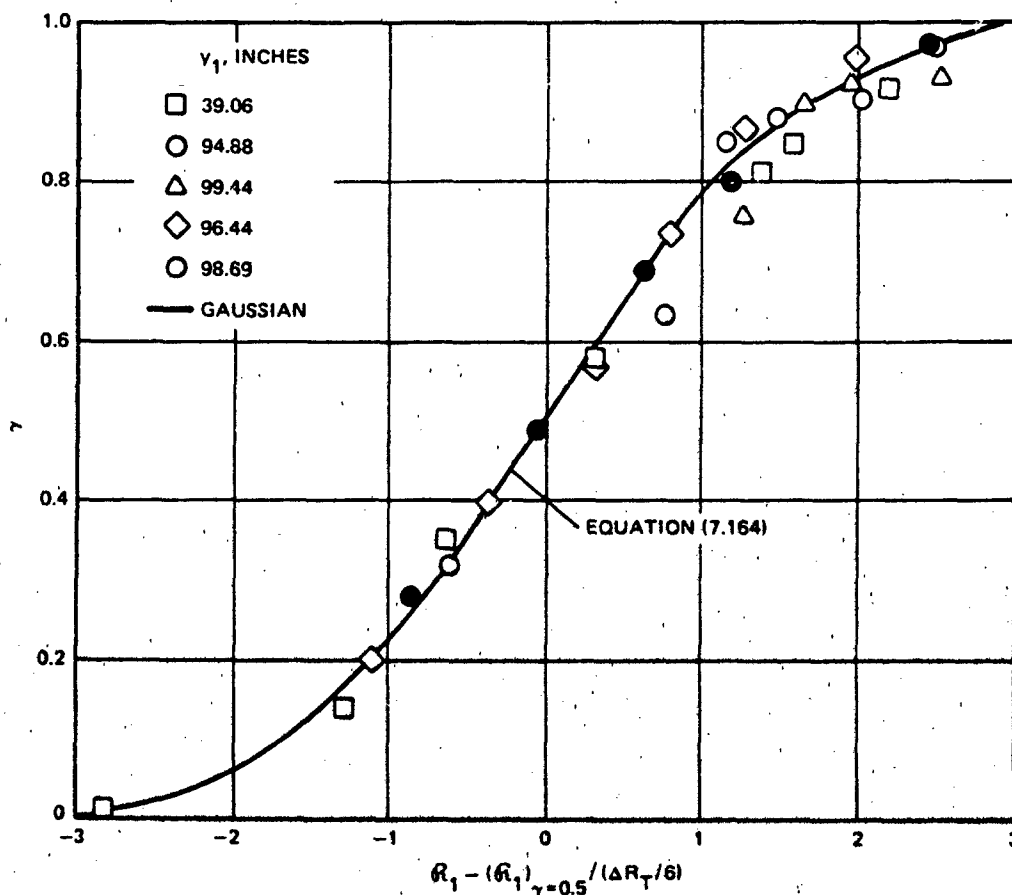


Figure 7.60 - Normalized Intermittency Distributions for Laminar Turbulent Boundary Layer Transition on Smooth Walls¹⁹⁵

This is perhaps due to an inadequacy in available signal-to-noise ratio in pressure measurement. However, the intermittency observed in the wall pressure signal and the space-time spreading character of convected pressure bursts closely resembled the observations of turbulent velocities in "spots" by Schubauer and Klebanoff.¹⁷⁸ Therefore Equation (7.162) shows that the level of the spectral density of the wall pressure, conditionally sampled only within the interval of a burst, is independent of the duration of the burst, a result that is not unlike the observed behavior of the velocity spectra in this intermittent zone.

Subsequent measurements by Huang and Hannan¹⁹⁷ are somewhat contradictory to those of DeMetz and Casarella. These measurements were made on axisymmetric head forms at $R_D \approx 1.3 \times 10^6$ to 2.2×10^6 . The momentum-thickness Reynolds numbers R_θ were roughly on the order of 400 to 900, compared to the value of 1900 in DeMetz's experiment. Huang and Hannan did not measure spectral densities of wall pressure, but they observed that time histories of pressure signals did not display the intermittency shown in the experiment of DeMetz. Furthermore, laminar separation occurred on one of Huang's forms. On this body, the minimum pressure coefficient reached -0.4 within a short distance of the stagnation point. The total root-mean-square pressure fluctuations are shown in Figure 7.61a. In the separation zone they exceeded $0.14 q_\infty$, where q_∞ is the freestream dynamic pressure. In the region of the fully developed turbulent boundary layer, Huang found that $\overline{p^2}^{1/2} \approx 0.015 q$. On a second head form on which laminar separation was not observed, it was found, in the region of transition occurring just downstream of the minimum pressure ($C_{p_{min}} = -0.19$), that $\overline{p^2}^{1/2} \approx 0.038 q$ for $R_\theta \approx 460$. This magnitude is in excess of that measured in the fully developed region downstream, and it is therefore in contradiction with the measurements of DeMetz and Casarella and Cedney. The reason for the discrepancy may lie in the difference in R_θ between the two measurements and therefore in differing values of τ_w . Pressure fluctuation measurements made on a waterborne body of revolution by Nisewanger and Sperling¹⁹⁸ qualitatively agree with DeMetz' in showing no anomalously large pressure fluctuations in the transition zone. Measurements in the fully developed region have been made by Bakewell.¹⁷¹

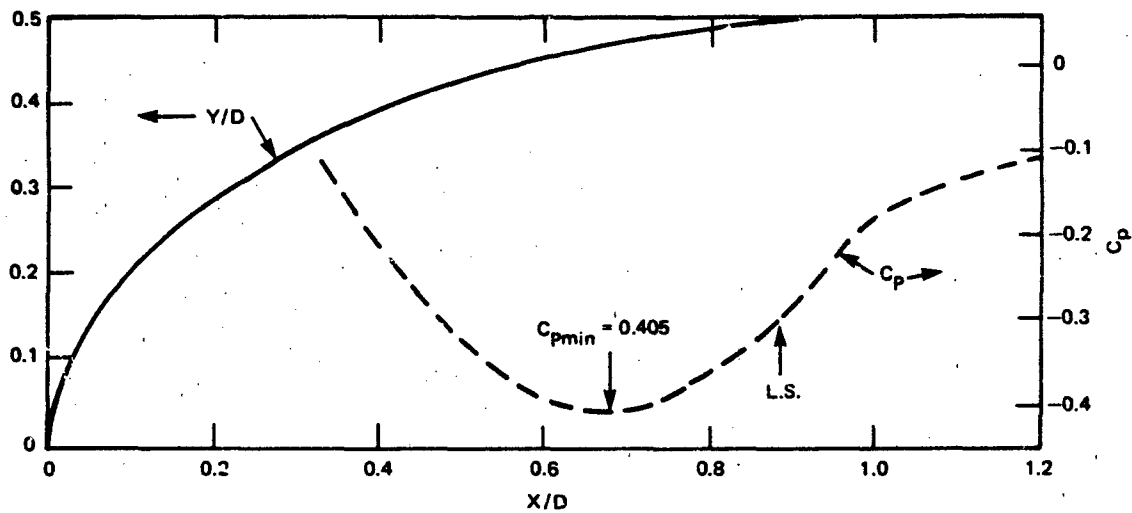


Figure 7.61a - Surface Profile and Pressure Coefficient of Headform S-2

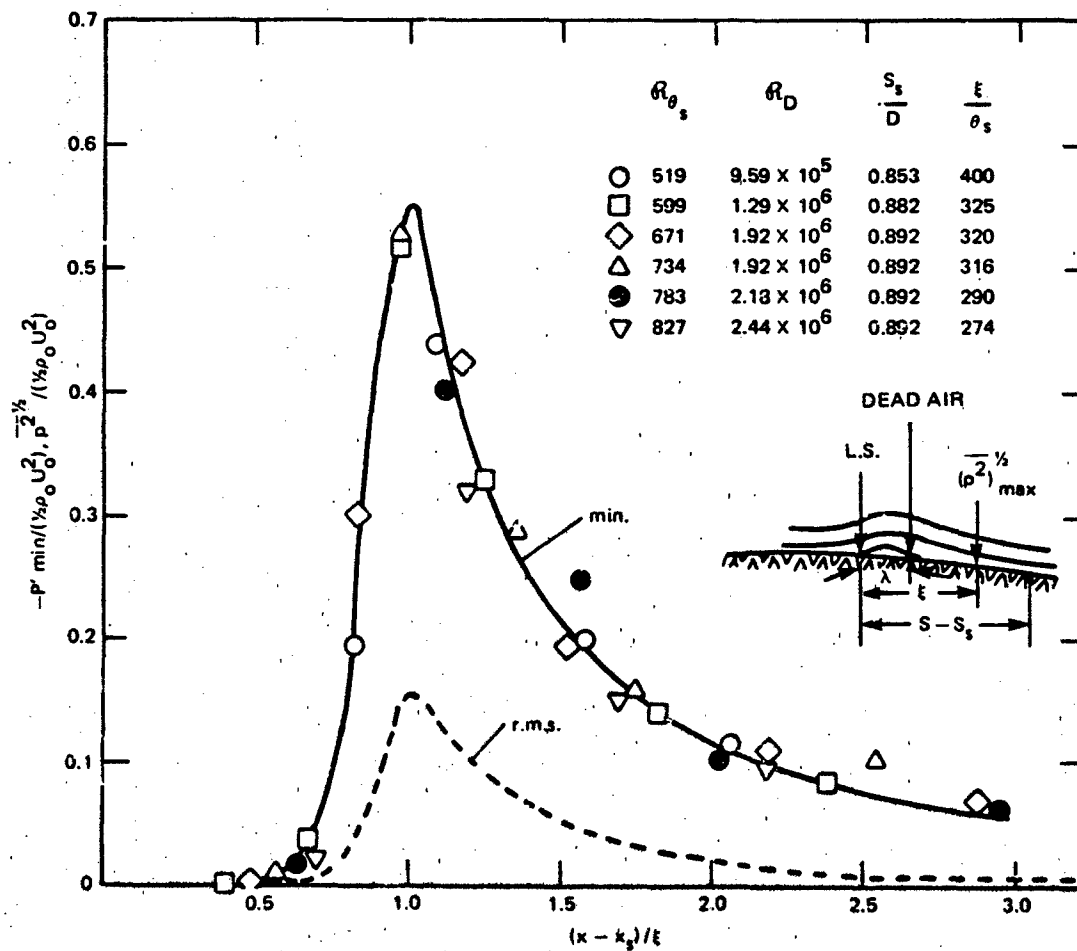


Figure 7.61b - Root-Mean-Square and Negative Peak Wall Pressure Fluctuations Immediately Behind Laminar Separation (Short Bubble) of Headform S-2

Figure 7.61 - Surface Pressures, Fluctuating and Mean, on a Body of Revolution with Laminar Separation. 197

7.5.2 Adverse and Favorable Static Pressure Gradients in Fully Developed Turbulence

The characteristics of turbulent boundary layers in the presence of severe gradients of static pressure are difficult to quantitatively characterize because the behavior is a multivariable problem. Simple analytical prediction schemes, such as those presented in Section 7.2 for flat plates and zero gradient, are difficult to find in the literature. Experimental evidence of boundary layer development, e.g., references 199-202, shows that the local mean properties (δ^* , θ , C_f , etc.) are very much influenced by the upstream character as well as by the local value of the pressure gradient. This effect of the upstream gradient has also been observed in some of the turbulence characteristics.

These flows are also nonequilibrium except in those relatively rare cases in which⁶

$$\Pi_1 = \frac{\delta^*}{\tau_w} \frac{\partial p}{\partial y_1} = \text{constant}$$

which implies that the local freestream velocity behaves in one possible form as

$$U_\infty \propto [y_1 - (y_1)_0]^a$$

and

$$\delta^* \frac{U_\tau}{U_\infty} \propto [y_1 - (y_1)_0]$$

Equation (7.27b) then shows that C_f is a constant throughout such a region. These types of flow were examined by Bradshaw⁴³; measurements of wall-shear coefficients in the presence of adverse pressure gradients on rough walls were made by Perry and Joubert.^{12,13} The wake function of Coles⁹ very well characterizes the mean velocity distribution in these boundary layers except in regions closer to the wall than $(y/\delta^*) \cdot (U_\infty/U_\tau) < 0.1$ where inside a short zone of overlap the law of the wall is satisfied.^{12,203}

Computation schemes for estimating wall shear using semiempirical routines have been suggested by a number of investigators, e.g., Ludwig and Tillmann,²⁰⁴ Ross,²⁰⁵ Diewert and Abbott,²⁰⁶ Bradshaw, et al.,²⁰⁷ Patel and Head,²⁰⁸ Dvorak,²⁰⁹ Mellor and Gibson,²¹⁰ White,²¹¹ and Howarth.²¹² Those of White and Howarth are the simplest. Virtually all the prediction techniques utilize the momentum-integral equation (Equation (7.27b)), which we rewrite in the form

$$\frac{d\theta}{dy_1} = \frac{C_f}{2} + \frac{\theta(2+H)}{2q} \frac{\partial P}{\partial y_1} \quad (7.165)$$

to emphasize the competing roles of the wall shear and pressure gradient in the boundary-layer growth. Depending on the relative magnitudes of the terms on the right-hand side, the boundary-layer growth is controlled by C_f or $\partial P/\partial y_1$. This is reflected in the presentation of wall pressure statistics later in this section. Another parameter often used as a length scale and already introduced in Section 7.2 is

$$\Delta = \delta^* \left(\frac{2}{C_f} \right)^{1/2}$$

Measurements of wall pressure fluctuations in adverse pressure gradients (decelerating flow) have been made by Schloemer¹²¹ on a smooth wind tunnel wall in both positive and negative gradients. Hodgeson¹²³ on a smooth glider wing in flight, Bradshaw^{43,207} in a wind tunnel equilibrium boundary layer with a positive gradient, Burton²¹³ on smooth and rough wind tunnel walls with positive and negative gradients, Blake²¹⁴ at the trailing edge of a flat strut (see also Chapter 9), and by Lauchle,¹⁹² Nisewanger and Sperling,¹⁹⁸ and Bakewell¹⁷¹ on bodies of revolution. It is not possible to present these results in a general form; therefore some representative data are shown for illustrative purposes. Figure 7.62 shows wall pressure spectra for positive gradients in the dimensionless form using dynamic pressure and displacement thickness. In the context of Equation (7.165), the wall shear and pressure gradients are tabulated, showing a domination of the boundary-layer growth by the static pressure increase. The two most strongly influenced flows are those of Burton and Blake, where flow separation was closely approached. Because of the

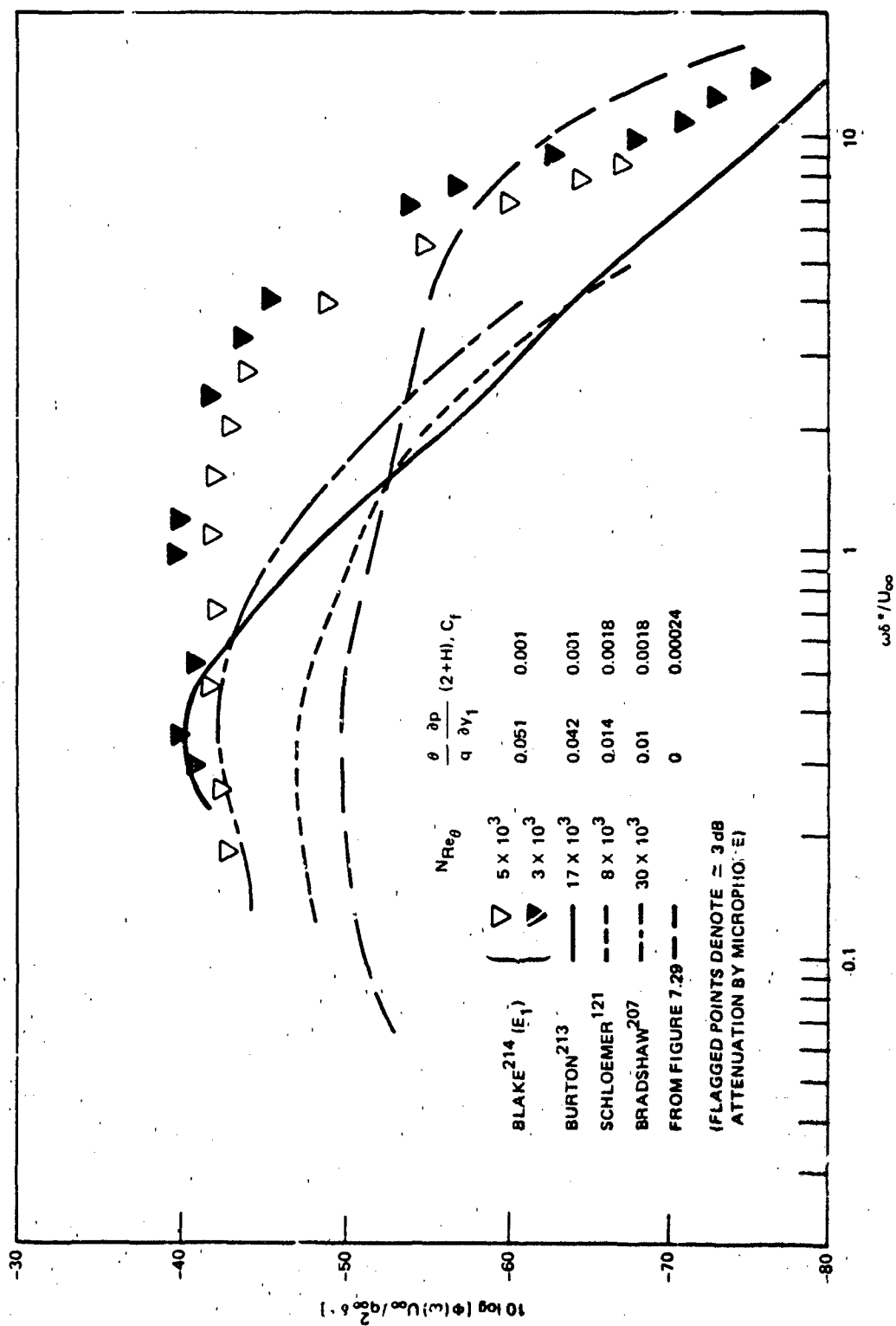


Figure 7.62 - Comparison of Various Measurements of Autospectra of Wall Pressures in Positive (Adverse) Pressure Gradients on Smooth Walls

relative unimportance of wall shear, in these cases it makes more sense to non-dimensionalize on dynamic pressure than on wall shear stress. The effect of the pressure gradient is to increase the spectrum level up to a magnitude of 10^{-4} in the most severe cases examined so far. The spectrum shape apparently depends on the upstream history of the development of the boundary layer, since there is no correlation of the results with Reynolds number, wall shear, or pressure gradient. The dependence on upstream history is most evident in Burton's case. As the flow progressed into a region of positive pressure gradient, at low frequencies, $\omega\delta^*/U_\infty < 2$, the pressures gradually increased from an initial value given by $\nabla p = 0$ to the value shown; at higher frequencies the spectrum levels diminished. A roughly similar effect was observed at and near the trailing edge of a flat strut.²¹⁴ Here again the dimensionless frequency below which levels increased and above which they decreased was between $\omega\delta^*/U_\infty = 1$ and 2.

On sand-roughened walls, Burton's measurements showed that the dimensionless spectral density was relatively weakly dependent on the magnitude of the pressure gradient. The spectrum level shown in Figure 7.62 is within a factor of 3 of those measured on the roughened wall. Furthermore, for the roughness used, as the pressure gradient increased, the spectrum level actually decreased in magnitude by as much as a factor of 2.5.

In the cases of negative (favorable) gradients shown in Figure 7.63, Burton's measurements on smooth and rough walls show a strong dependence on the wall shear stress and displacement thickness. However, in these cases the pressure gradient term never exceeded the magnitude of the wall-shear coefficient. Therefore the influence of the wall was relatively more important than in the cases of the positive gradients. A general characteristic of the pressure spectra for both types of gradients is that the maximum spectrum level is within a band of frequencies $0.1 < \omega\delta^*/U_\infty < 4$.

The spatial characteristics of wall pressure are even less precisely summarized than the frequency dependence at a point. Table 7.3 lists some of the critical parameters that may be used in connection with Equation (7.133). Generally, the cross-spectral densities are spatially nonstationary, i.e., depending very much on the location of measurement. The convection velocities deduced from these measurements therefore vary from 30% to 40%, depending on frequency and transducer separation. Table 7.3 shows representative numerical values for parameters,

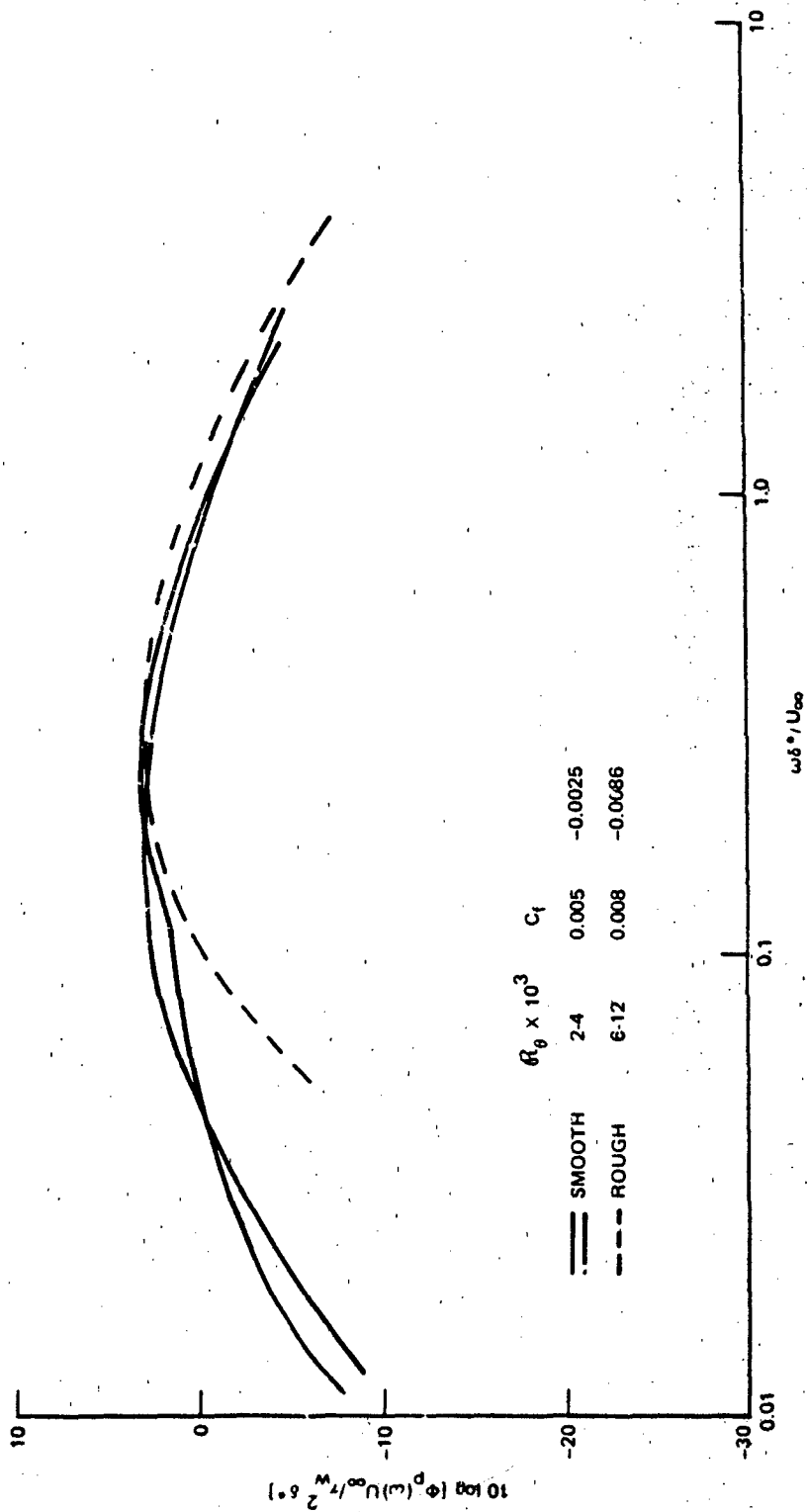


Figure 7.63 - Autospectra of Wall Pressure Fluctuations at Points on Smooth and Rough Walls in Boundary Layers with Adverse Pressure Gradients²¹³

TABLE 7.3
REPRESENTATIVE PARAMETERS* FOR BOUNDARY LAYER PRESSURES IN PRESSURE GRADIENTS

Source	$\frac{\theta(2+1)}{q} \frac{dP}{dy_1}$	C_f	R_θ	H	$\frac{\phi_p(\omega) U_\infty}{q^2 \delta^*}$	Ω	γ_1	γ_3	U_c
Blake, smooth ²⁰	0	0.0024	12,000	1.2	-49	0.3	0.11	0.8	0.6
Blake, rough ²⁰	0	0.0055	24,000	1.5	-43	0.5	0.3	0.8	0.5
Burton, smooth fav. ²¹³	-0.0025	0.005	3,000	1.3	-44	0.3	0.1	0.5	0.6
Burton, rough iav. ²¹³	-0.0086	0.008	9,000	1.5	-39	0.3	0.2	0.5	0.6
Schloemer, smooth fav. ¹²¹	-0.0035	0.0045	1,400	1.35	-48	0.3	0.9	0.5	0.5
Schloemer, smooth ¹²¹	0	0.003	5,000	1.34	-50	0.3	0.1	0.6	0.7
Burton, smooth adv. ²¹³	0.042 0.027	0.001 0.001	26,000	1.8	-41 -48	0.4 0.4	0.77 0.32	0.7	0.45-0.6
Burton, rough adv. ²¹³	0.021	0.0004	20,000 40,000	2.5	-45	0.5	0.35	0.7	0.4
Schloemer, smooth adv. ¹²¹	0.013	0.0018	8,000	1.58	-47	0.3	0.15	0.8	
Blake, smooth adv. ²¹⁴ (trailing edge)	0.051	~0.001	35,200	1.74	-40	1	0.34	0.8	0.55

The spectrum level $\phi_p(\omega)$ is given at its maximum value occurring at the dimensionless frequency $\omega \delta^/U_\infty \equiv \Omega$ tabulated.

extracted from various sources, by fitting Equations (7.129) to experimental data. Generally, as the negative gradients increase in magnitude so does the transverse correlation of pressures, while the streamwise correlation is only slightly affected. This implies that, compared to a zero gradient, there is a larger transverse extent, but a decay distance that corresponds to the same number of disturbance wavelengths. For positive gradients, the streamwise correlation decreases as the gradient increases. In most cases this behavior is associated with a streamwise statistical nonhomogeneity in the flow, which could possibly enhance the low wave number levels of wall pressures. For all types of gradients, the effect of wall roughness is to reduce the streamwise correlation without affecting the transverse length scale.

Assuming that the wall pressures are at least locally homogeneous in the plane of the surface, Equation (7.133) will still yield the wave number spectrum. When the streamwise correlation is reduced by a positive pressure gradient or by increasing wall roughness, γ_1 increases. This reduces $\phi_p(\vec{k}, \omega)$ near $k_1 = \omega/U_c$ and increases $\phi_p(\vec{k}, \omega)$ for $k_1 \ll \omega/U_c$. This increase will persist until $\gamma_1 > 1$. For higher wave numbers, i.e., $k_1 > \omega/U_c$, the increase in the spectrum level will continue to be proportional to the increase in γ_1 . On the other hand, while γ_1 increases, the experimental results suggest that U_c decreases. This gives rise to an effect on the lateral k_3 behavior that can be somewhat offsetting. In Equation (7.133), the limit of $k_3 < \omega/U_c$ suggests that the spectrum level will decrease as U_c^2 . Thus whether in fact a given condition will change the form of $\phi_p(\vec{k}, \omega)$ will depend largely on the relative changes in U_c and γ_1 . Furthermore, for still lower wave numbers, say $k_1 \ll \omega/U_c$ where the representation of Equation (7.133) is probably invalid, i.e., where Figures 7.41 and 7.46 apply for homogeneous boundary layers, there is no existing experimental data.

The only direct measurements of the wave number spectrum in the positive (adverse) pressure gradient have been provided by Moeller et al.²¹⁵ The boundary layer was developed on a smooth wall and forced nearly to separation. Within the range of their parameters ($0.6 < k_1 \delta^* < 2$) pressure fluctuations gradients obeyed

$$\frac{\phi_p(k_1, 0, \omega) U_\infty}{q^2(\delta^*)^3} = 30 \left(\frac{\omega \delta^*}{U_\infty} \right)^{-3.6} (k_1 \delta^*)^{0.31} \pm 4 \text{ dB}$$

which is the same functional form given by Martin¹⁴⁴ (Equation (7.144)).

7.5.3 Pressure Fluctuations Beneath Separated Turbulent Flow

The process of separation of turbulent boundary layers is temporally unsteady and spatially ill defined, as shown by the measurement of Kline and Runstadler,⁵⁰ Sandborn and Kline,²¹⁶ Sandborn and Liu,²¹⁷ and Simpson et al.²¹⁸ The intermittency is a function of distance from the wall into the flow as well as streamwise location, following the same integral of the normal distribution as observed in the transition flows²¹⁸ (Equation (7.164)). In the work of Simpson et al., the separation point was defined when the flow reversal of separation occurred half the time; for distances of 3δ to 4δ upstream and downstream of this point, the intermittent character of the separation was clearly evident. Velocity (rms) maxima of 25% of the freestream velocity were observed in this region. These velocity maxima were observed at distances from the wall near the point for which the curvature of the mean velocity profile vanished, i.e., where

$$\frac{\partial^2 U_1}{\partial y_2^2} = 0$$

Observed values of boundary-layer length scales at separation are given by Sandborn and Kline and Simpson et al. Generally, the shape factor at separation (δ^*/θ) depends on the value of δ^*/δ . Extensive data on turbulent velocities and Reynolds stresses are given by Simpson.²¹⁸ Blake²¹⁴ gives turbulent velocities and spectra for various separation zones at trailing edges. Studies and prediction schemes for turbulent boundary-layer separation are plentiful; e.g., the experimental results of Perry and Fairlie²¹⁹ and the prediction criteria of Stratford,²²⁰ Goldschmied,²²¹ and Cebeci,²²² were all recently compared by Tsahalis and Telionis.²²³

Pressure fluctuations beneath turbulent separated flows have not been well described. Measurements have been conducted in hydraulic jumps,²²⁴ but these cannot be generalized. Measurements downstream of a flow spoiler mounted on a wall have been conducted.²²⁵ Compared to pressure spectrum levels observed on smooth walls with no spoilers, the maximum pressure level behind the spoiler was largest for frequencies less than $\omega h/U_\infty < 1.5$, where h is the height of the spoiler. This point is the location of reattachment of the flow.²²⁶ The total root-mean-square pressure at this point²²⁷ was on the order of

$$\overline{p}^{1/2} \approx 0.06 \left(\frac{1}{2} \rho_o U_\infty^2 \right)$$

where U_∞ is the freestream speed, compared to

$$\overline{p}^{1/2} \approx 0.005 \left(\frac{1}{2} \rho_o U_\infty^2 \right)$$

on smooth planar boundaries.

Other measurements beneath separated flow at trailing edges of airfoils by Mugridge²²⁸ and Blake²¹⁴ are described in Chapter 9.

7.5.4 Thick Axisymmetric Turbulent Boundary Layers: The Circular Cylinder

This topic has only relatively recently received extensive investigation. An initial experimental investigation was that of Richmond,²²⁹ some of whose work has been more recently summarized by Willmarth and Yang²³⁰ and Afzal and Narasimha.²³¹ The subject of laminar turbulent transitional flows has been examined by Yasuhara.²²⁶ Currently there is no universally accepted similarity law for the mean velocity profile, although there have been suggestions by Richmond,²²⁹ Rao,²³² Cebeci,²³³ Reid and Wilson,²³⁴ White,²³⁵ Chase,²³⁶ and Afzal and Narasimha.²³¹ Furthermore, Cebeci²³³ has a semiempirical predication technique for estimating the local wall shear coefficient and the axial growth of the boundary layer. More recent experimental results than Richmond's in addition to those just mentioned^{230,231} include measurements by Rao and Keshavan,²³⁷ and Willmarth et al.²³⁸ Willmarth et al. obtained measurements of the mean velocity profile and wall-shear coefficient on thin cylinders for which $2\delta/d \approx 37$, where a is the radius of the cylinder and δ is the boundary-layer thickness.

The transverse curvature of axisymmetric flow makes it necessary to redefine the boundary layer displacement thickness δ^* as

$$\left(\delta^* + \frac{d}{2} \right)^2 - \left(\frac{d}{2} \right)^2 = 2 \int_{d/2}^{(\delta+d)} \left(1 - \frac{U_1}{U_\infty} \right) r dr^2$$

and the momentum thickness θ as

$$\left(\theta + \frac{d}{2} \right)^2 - \left(\frac{d}{2} \right)^2 = 2 \int_a^{(\delta+a)} \left(1 - \frac{U_1}{U_\infty} \right) \left(\frac{U_1}{U_\infty} \right) r dr$$

The mean velocity profile should depend on the dimensionless lengths yU_τ/ν and $dU_\tau/2\nu$ (where $y=r-d/2$) near the wall of the cylinder and on y/δ and $2\delta/d$ in the wake region of the cylinder. Therefore one would expect analogous dimensionless forms to Equations (7.13) through (7.16) to apply to the axisymmetric boundary layer. Thus we expect

$$\frac{U_1}{U_\tau} = F\left(\frac{rU_\tau}{\nu}, \frac{2y}{d}\right)$$

in the wall region and

$$\frac{U_\infty - U_1}{U_\tau} = G\left(\frac{r}{\delta}, \frac{2\delta}{d}\right)$$

in the wake region. Among the proposed forms of F are various logarithmic functions reviewed by Afzal and Narasimha. These functions are supported by experimental results in various ranges of $dU_\tau/2\nu$ and (or) $d/2\delta$. Functions of the form²³⁷

$$\frac{U_1}{U_\tau} = A \ln \left[\frac{dU_\tau}{2\nu} \ln \left(\frac{r}{a} \right) \right] + B$$

(where $r=d/2$ is the surface of the cylinder) reduce to a logarithmic profile in the limit of

$$1 < \frac{2r}{d} < 2$$

i.e., in this region the mean velocity follows

$$\frac{U_1}{U_\tau} = A \ln \left[\frac{\left(r - \frac{d}{2}\right) U_\tau}{\nu} \right] + B$$

Chase²³⁶ proposed a more complex form ($r \geq d/2$)

$$\frac{U_1}{U_\tau} = \frac{dU_\tau}{2v} \ln \frac{2r}{d}, \quad 0 < \frac{dU_\tau}{2v} \ln \left(\frac{2r}{d} \right) < 7.4 \quad (7.166a)$$

and

$$\frac{U}{U_\tau} = 2.5 \ln \left[\frac{dU_\tau}{2v} \ln \left(\frac{2r}{d} \right) - 4.9 \right] + 5.1 \quad (7.166b)$$

$$7.4 < \frac{dU_\tau}{2v} \ln \left(\frac{2r}{d} \right) < \infty$$

These functions have been derived using arguments analogous to that of Millikan.¹⁰ They are compared to measurements of Willmarth et al. in Figure 7.64 for two extreme values of $2\delta/d$. For comparison, Willmarth et al. also show Equation (7.21) for the smooth plane boundary layer. Equation (7.166b) reduces to Equation (7.21) when $(d-2r)/d < 1$.

Another pair of formulations by Afzal and Narasimha gives, in the wall region,

$$\frac{U}{U_\tau} = 2.5 \ln \left(r - \frac{d}{2} \right) \frac{U_\tau}{v} + C + O \left(\frac{2v}{dU_\tau} \right)$$

and in the wake region

$$\frac{(U_\infty - U)}{U_\tau} = -2.5 \ln \left[\frac{\left(r - \frac{d}{2} \right)}{\delta} \right] + D \left(\frac{2\delta}{d} \right) + O \left(\frac{U_\tau}{U_\infty} \right)$$

with a wall-shear coefficient given by

$$\left(\frac{2}{C_f} \right)^{1/2} = 2.5 \ln \frac{\delta U_\tau}{v} + D + C + O \left(\frac{C_f}{2} \right)^{1/2}$$

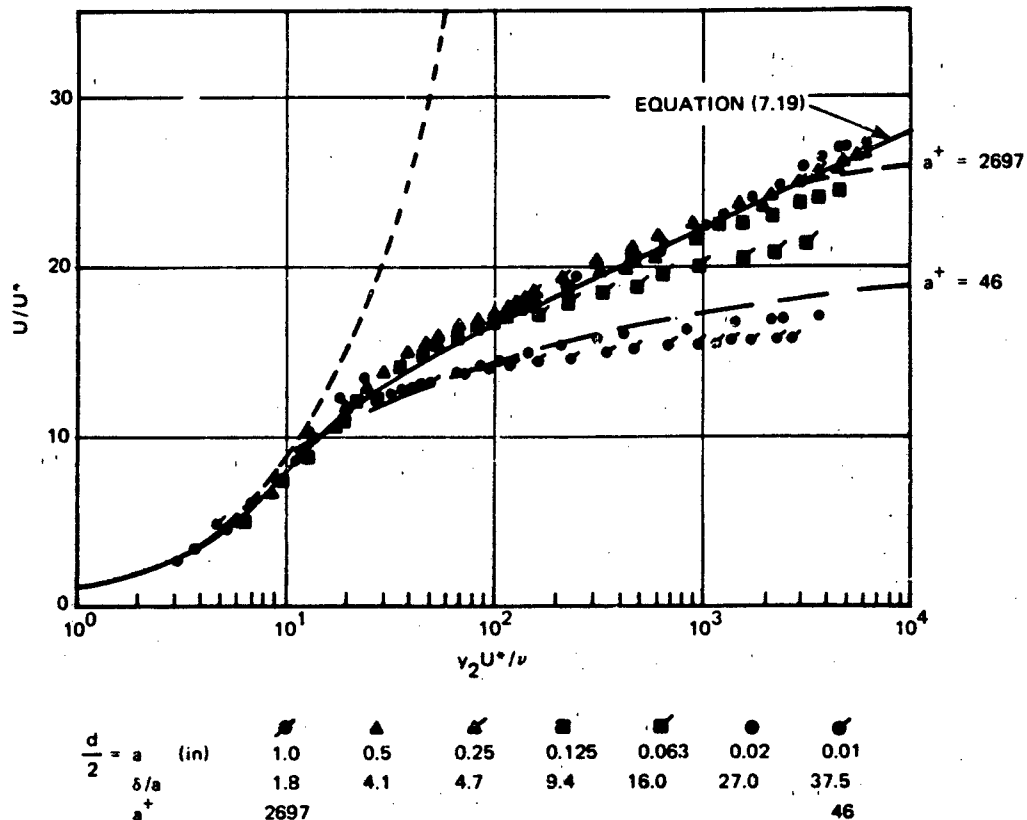


Figure 7.64 - Seven Representative Velocity Profiles in Wall Coordinates Showing the Influence of Increasing Transverse Curvature.

—, Flat Plate, Coles (1955)⁹; $a^+ = 33.4$,
 --- Chase²³⁶ Equation (7.166)

The values D and C depend on $2\delta/d$ and $dU_t/2\nu$, respectively. They have been determined from a compilation of available measurements. For $dU_t/2\nu > 400$, $C \approx 5.5 \pm 0.5$, but for $dU_t/2\nu \approx 20$ to 200 there does not seem to be a clearly defined dependence (see Figure 7.65). For $1 < d/2 < 10$, $D \approx 2d/2\delta$, compared to a value of 2.5 for smooth planar boundary layer.

Wall pressure fluctuations have been measured only by Willmarth et al.^{230,238} The spectral density on a cylinder for which $2\delta/d = 2$ is shown in Figure 7.66 in dimensionless form. In this case the spectrum has been normalized on the mean square $\overline{p^2}$, which can be evaluated once C_f is determined using the above equation. Compared to the spectra measured on a smooth plane surface, the pressures measured

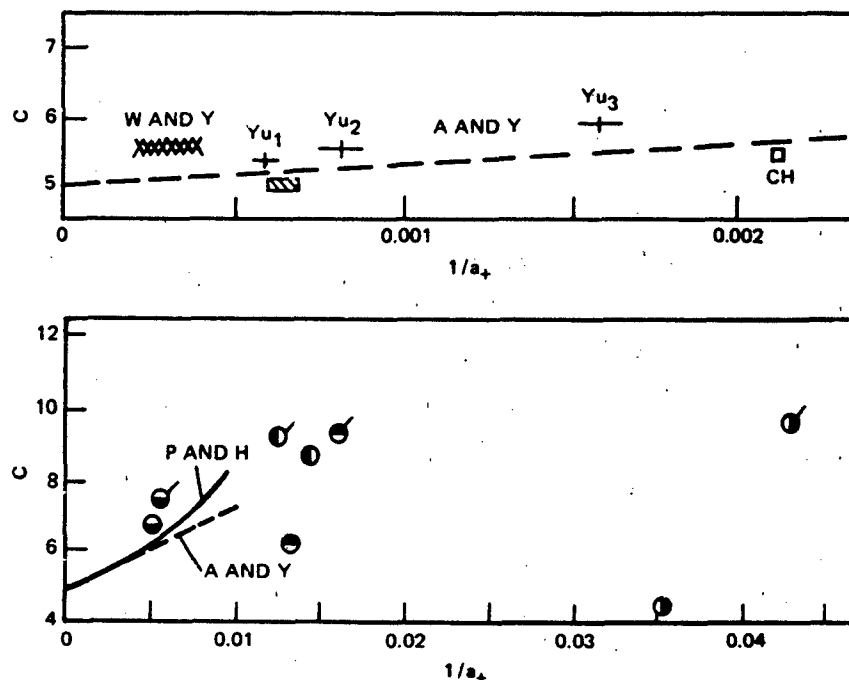


Figure 7.65 - Variation of Additive Term in Law of the Wall with Respect to Inverse of Frictional Reynolds Number. (Top) W and Y, Willmarth and Yang; R, Richmond; C, Chin et al.; A and Y, Afzal & Yajnik. (Bottom) P and H, Patel and Head. Half-Filled Circles are from Rao and Keshavar's Data. Circles with Flags are the Corresponding Point when Skin Friction Obtained by Patel Is Employed. From Reference 231

on the cylinder have slightly larger contributions at higher frequencies and lesser at lower frequencies. Measurements²³⁸ on a cylinder for which $2\delta/d = 4$ gave similar results; the same value of mean-square pressure was observed, but less contribution at frequencies greater than $\omega\delta^*/U_\infty = 10$ occurred.

The cross-spectral densities $\phi(r_1, 0, \omega)$ and $\phi(0, r_3, \omega)$ were similar to those measured on the planar surface (Figures 7.37), but the transverse (r_3) function did not show a single dependence on $\omega r_3/U_c$ for all frequencies and separations. Considerably less correlation was observed for $r_3/\delta^* = 0.72$ than for $r_3/\delta^* = 0.19$. Convection velocities were essentially the same as those measured on the flat surface (Figure 7.38a).

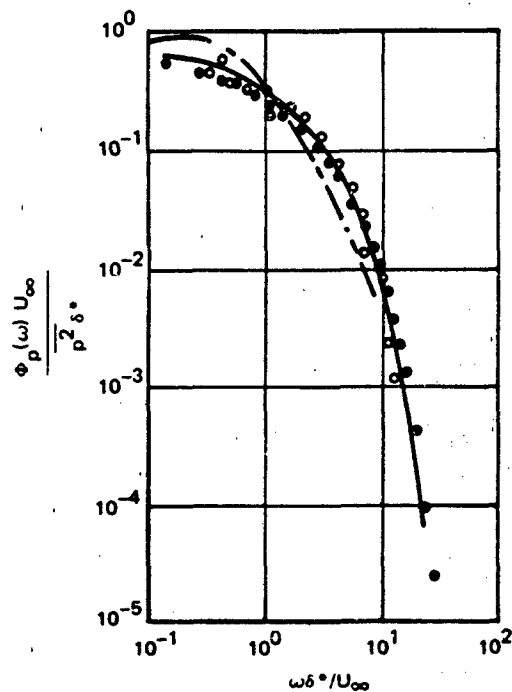


Figure 7.66 - Measured Wall Pressure Spectra. •, $2\delta/d = 2$,
 $R/\delta^* = 0.07$, $R_{\delta^*} = 32,100$; ○ $2\delta/d = 4$; ---, $2\delta/d = 0$,
 $R/\delta^* = 0.10$, $R_{\delta^*} = 25,400$, Bull; —, $2\delta/d = 0$,
 $R/\delta^* = 0.06$, $R_{\delta^*} = 49,400$, Willmarth and Roos.¹⁵⁹
 $p^2_{y_2}/\tau_\omega = 2.39$, Cylinder; 2.6 Plane Corrected
for Transducer Size (R/δ^*).
From Willmarth^{230,238}

7.6 REFERENCES

1. Schlichting, H., "Boundary Layer Theory," McGraw-Hill Book Co., 7th ed. (1979).
2. Hinze, J.O., "Turbulence," 2nd ed., McGraw-Hill Book Co. (1975).
3. Townsend, A.A., "The Structure of Turbulent Shear Flow," Cambridge University Press, 2nd ed. (1976).
4. Cebeci, T. and A.M.O. Smith, "Analyses of Turbulent Boundary Layers," Academic Press (1974).
5. Cebeci, T. and P. Bradshaw, "Momentum Transfer in Boundary Layers," McGraw-Hill Book Co. (1977).
6. Rotta, J.C., "Turbulent Boundary Layers in Incompressible Flow," Prog. Aero. Sci., Vol. 2, pp. 1-220 (1962).
7. Clauser, F.H., "The Turbulent Boundary Layer," in Advances in Applied Mechanics, Vol. IV, No. 1 (1956).
8. Prandtl, L., "Essentials of Fluid Dynamics," Hafner Publishing Co. (1952).
9. Millikan, C.B., "A Critical Discussion of Turbulent Flows in Channels on Circular Tubes," 5th Int. Cong. for Appl. Mech., Cambridge, Mass. (1938).
10. Coles, D., "The Law of the Wake in the Turbulent Boundary Layer," J. Fluid Mech., Vol. 1, pp. 191-226 (1956).
11. Nikuradse, J., "Laws of Flow in Roughness," NACA TM 1292 (1950). Translation of "Strömungsgesetze in rauhen Rohren" VDI-Forschungsheft 361. Beilage zu "Forschung auf dem Gebiete des Ingenieurwesens" Ausgabe 3 Band 4 (Jul/Aug 1933).
12. Perry, A.E. and P.N. Joubert, "Rough-Wall Boundary Layers in Adverse Pressure Gradients," J. Fluid Mech., Vol. 17, pp. 193-211 (1963).
13. Perry, A.E., W.H. Schofield and P.N. Joubert, "Rough-Wall Turbulent Boundary Layers," J. Fluid Mech., Vol. 37, pp. 383-413 (1969).
14. Blake, W.K., "Turbulent Velocity and Pressure Fields in Boundary-Layer Flows Over Rough Surfaces," Symposium on Turbulence in Liquids, Univ. of Missouri, (4-6 Oct 1971).

15. Bradshaw, P. (ed.), "Turbulence", Vol. 12, Topics in Applied Physics, Springer-Verlag (1976).
16. McCarthy, J.H., "Ship Boundary-Layer Research Since About 1974; A Progress Report," 18th ATTC, U.S. Naval Academy, Annapolis, Md. (Aug 1977).
17. von Karman, T., "Über laminare und turbulente Reibung," ZAMM, Vol. 1, p. 233 (1912). English Translation, NACA TM 1092.
18. Hama, F.R., "Boundary-Layer Characteristics for Smooth and Rough Surfaces," Trans. Soc. Nav. Arch. Marine Eng., Vol. 62, pp. 333-358 (1954).
19. Liu, C.K., S.J. Kline and J.P. Johnston, "An Experimental Study of Turbulent Boundary Layer on Rough Walls," Thermosciences Division, Dept. of Mechanical Eng., Stanford University Report MD-15 (1966).
20. Blake, W.K., "Turbulent Boundary Layer Wall Pressure Fluctuations on Smooth and Rough Walls," J. Fluid Mech., Vol. 44, pp. 637-660 (1970).
21. Colebrook, C.F. and C.M. White, "Experiments with Fluid Friction in Roughened Pipes," Proc. Roy. Soc. Lon., Vol. A161, pp. 367-381 (1937).
22. Robertson, J.M., J.D. Martin and T.H. Burkhart, "Turbulent Flow in Rough Pipes," I & E.C. Fundamentals, Vol. V.7, pp. 253-265 (1968).
23. Uram, E.M., "Turbulent Boundary Layers on Rough Surfaces," Sc.D. Thesis Mech. Eng. Dept., Stevens Institute of Technology, Hoboken, N.J. (1966).
24. Arndt, R.E.A. and A.T. Ippen, "Cavitation Near Surfaces of Distributed Roughness," M.I.T. Hydrodynamics Laboratory Report 104 (1967).
25. Klebanoff, P.S., "Characteristics of Turbulence in a Boundary Layer with Zero Pressure Gradient," NACA Report 1247 (1955).
26. Bull, M.K., "Wall-Pressure Fluctuations Associated with Subsonic Turbulent Boundary Layer Flow," J. Fluid Mech., Vol. 28, pp. 719-754 (1967).
27. Willmarth, W.W. and C.E. Wooldridge, "Measurements of the Fluctuating Pressure at the Wall Beneath a Thick Turbulent Boundary Layer," J. Fluid Mech., Vol. 14, pp. 187-210 (1962). Corrigendum: J. Fluid Mech., Vol. 21, pp. 107-109 (1965).
28. Wooldridge, C.E. and W.W. Willmarth, "Measurements of the Correlation Between the Fluctuating Velocities and Fluctuating Wall Pressures in a Thick Turbulent Boundary Layer," Univ. of Michigan Tech Report No. 02920-2-T (1962).

29. Yeh, F. and E.C. Nickerson, "Air Flow over Roughness Discontinuity," Fluid Dynamics and Diffusion Laboratory, College of Engineering, Colorado State University (1970).
30. Corrsin, S. and A.L. Kistler, "Freestream Boundaries of Turbulent Flows," NACA TN 3133 (1954).
31. Antonia, R.A. and R.E. Luxton, "The Response of a Turbulent Boundary to a Step Change in Surface Roughness, Part 1: Smooth to Rough," J. Fluid Mech., Vol. 48, pp. 721-761 (1971).
32. Taylor, G.I., "Statistical Theory of Turbulence, Parts I-IV," Proc. Roy. Soc., Vol. A151, pp. 421-478 (1935).
33. Taylor, G.I., "The Spectrum of Turbulence," Proc. Roy. Soc., Vol. A164, pp. 476-490 (1938).
34. Favre, A.J., J.J. Gaviglio and R. Dumas, "Space Time Double Correlations and Spectra in a Turbulent Boundary Layer," J. Fluid Mech., Vol. 2, pp. 313-342 (1957).
35. Favre, A.J., J.J. Gaviglio and R. Dumas, "Further Space-Time Correlations of Velocity in a Turbulent Boundary Layer," J. Fluid Mech., Vol. 3, pp. 344-356 (1957).
36. Favre, A.J., "Review on Space-Time Correlations in Turbulent Fluids," ASME J. Appl. Mech., Vol. 32, pp. 241-257 (1965).
37. Favre, A., J.J. Gaviglio and R. Dumas, "Structure of Velocity Space-Time Correlations in a Boundary Layer," Phys. Fluids Suppl., pp S138-S145 (1967).
38. Grant, H.L., "The Large Eddies of Turbulent Motion," J. Fluid Mech., Vol. 4, pp. 149-190 (1958).
39. Tritton, D.J., "Some New Correlation Measurements in a Turbulent Boundary Layer," J. Fluid Mech., Vol. 28, pp. 439-462 (1967).
40. Blackwelder, R.F. and L.S.G. Kovasznay, "Time Scales and Correlations in a Turbulent Boundary Layer," Phys. Fluids, Vol. 15, pp. 1545-1554 (1972).
41. Bakewell, H.P. and J.L. Lumley, "Viscous Sublayer and Adjacent Wall Region in Turbulent Pipe Flow," Phys. Fluids, Vol. 10, pp. 1880-1889 (1967).

42. Gupta, A.K., J. Laufer and R.E. Kaplan, "Spatial Structure in the Viscous Sublayer," J. Fluid Mech., Vol. 50, pp. 493-512 (1971).
43. Bradshaw, P., "Inactive Motion and Pressure Fluctuations in Turbulent Boundary Layers," J. Fluid Mech., Vol. 30, pp. 241-258 (1967).
44. Einstein, H.A. and H. Li, "The Viscous Sublayer Along a Smooth Boundary," J. ASCE, Engineering Mech. Div. EM2, Paper 945-1 (1956).
45. Eckelmann, H., "Experimentelle Untersuchungen in einer turbulenten Kanalströmung mit starken viskosen Wandschichten," Max-Planck Institut für Strömungsforschung, Göttingen, Report No. 48 (1970).
46. Phillips, O.M., "The Irrotational Motion Outside a Free Turbulent Boundary," Proc. Camb. Phil. Soc., Vol. 51, pp. 220-229 (1955).
47. Townsend, A.A., "The Structure of the Turbulent Boundary Layer," Proc. Camb. Phil. Soc., Vol. 47, pp. 375-374 (1951).
48. Laufer, J., "Investigation of Turbulent Flow in a Two-Dimensional Channel," NACA Report 1053 (1951).
49. Willmarth, W.W. and T.J. Bogar, "Survey and New Measurements of Turbulent Structure Near the Wall," Phys. Fluids, Vol. 20, Part II, pp. 69-521 (1977).
50. Kline, S.J. and P.W. Runstadler, "Some Preliminary Results of Visual Studies of the Flow Model of the Wall Layers of the Turbulent Boundary Layer," ASME J. Appl. Mech., Vol. 26, pp. 166-170 (1959).
51. Schraub, F.A. and S.J. Kline, "A Study of the Structure of the Turbulent Boundary Layer with and without Longitudinal Pressure Gradients," Report MD-12 Thermosciences Division, Dys. Mech. Eng., Stanford University, Stanford, Ca. (1965).
52. Kline, S.J., W.C. Reynolds, F.A. Schraub and P.W. Runstadler, "The Structure of Turbulent Boundary Layers," J. Fluid Mech., Vol. 30, pp. 741-773 (1967).
53. Hama, F.R., "Progressive Deformation of a Perturbed Line Vortex Filament," Phys. Fluids, Vol. 4, pp. 526-534 (1963).
54. Mollo-Christensen, E., "Physics of Turbulent Flow," AIAA Journal, Vol. 9, pp. 1217-1228 (1971).

55. Tu, B. and W.W. Willmarth, "An Experimental Study of the Structure of Turbulence Near the Wall through Correlation Measurements in a Thick Turbulent Boundary Layer," Rep. 02920-3-T, Univ. Mich., Dept. of Aerospace Eng., Aerodynamics Laboratory (Mar 1966).
56. Willmarth, W.W. and B. Tu, "Structure of Turbulence in the Boundary Layer near the Wall," Phys. Fluids Suppl., pp. S134-S137 (1967).
57. Offen, G.R. and S.J. Kline, "Combined Dye-Streak and Hydrogen Bubble Visual Observations of a Turbulent Boundary Layer," J. Fluid Mech., Vol. 62, pp. 223-239 (1974).
58. Offen, G.R. and S.J. Kline, "A Proposed Model of the Bursting Process in Turbulent Boundary Layers," J. Fluid Mech., Vol. 70, pp. 209-228 (1975).
59. Laufer, J. and M.A. Badri Narayanan, "Mean Period of the Turbulent Production Mechanism in a Boundary Layer," Phys. Fluids, Vol. 14, pp. 182-183 (1971).
60. Rao, K.N., R. Narasimha and M.A.B. Narayanan, "The Bursting Phenomenon in Turbulent Boundary Layer," J. Fluid Mech., Vol. 48, pp. 339-352 (1971).
61. Lu, S.S. and W.W. Willmarth, "Measurements of the Structure of the Reynolds Stress in a Turbulent Boundary Layer," J. Fluid Mech., Vol. 60, pp. 481-511 (1973).
62. Lu, S.S. and W.W. Willmarth, "Measurement of the Mean Period Between Bursts," Phys. Fluids, Vol. 16, pp. 2012-2013 (1973).
63. Kovasznay, L.S.G., V. Kibens and R.F. Blackwelder, "Large Scale Motion in the Intermittent Region of a Turbulent Boundary Layer," J. Fluid Mech., Vol. 41, p. 283-325 (1970).
64. Corino, E.R. and R.S. Brodkey, "A Visual Investigation of the Wall Region in Turbulent Flow," J. Fluid Mech., Vol. 37, pp. 1-30 (1967).
65. Grass, A.J., "Structural Features of Turbulent Flow over Smooth and Rough Walls," J. Fluid Mech., Vol. 50, pp. 233-255 (1971).
66. Fage, A. and H.C.H. Townend, "An Examination of Turbulent Flow with an Ultramicroscope," Roy. Soc. London, Phil. Trans. Ser. A, Vol. 135, pp. 656-677 (1932).
67. Burton, T.E., "The Connection Between Intermittent Turbulent Activity near the Wall of a Turbulent Boundary Layer with Pressure Fluctuations at the Wall," Mass. Inst. Tech. Acoustics and Vibration Lab. Report 70208-10 (Jun 1974).

68. Kim, H.T., S.J. Kline and W.C. Reynolds, "The Production of Turbulence Near a Smooth Wall in a Turbulent Boundary Layer," J. Fluid Mech., Vol. 50, pp. 133-160 (1971).
69. Willmarth, W.W. and S.S. Lu, "Structure of the Reynolds Stress Near the Wall," J. Fluid Mech., Vol. 55, pp. 65-92 (1972).
70. Gupta, A.K. and R.E. Kaplan, "Statistical Characteristics of Reynolds Stress on a Turbulent Boundary Layer," Phys. Fluids, Vol. 15, pp. 981-985 (1972).
71. Wallace, J.M., H. Eckelmann and R.S. Brodkey, "The Wall Region in Turbulent Shear Flow," J. Fluid Mech., Vol. 54, pp. 39-48 (1972).
72. Brodkey, R.S., J.M. Wallace and H. Eckelmann, "Some Properties of Truncated Turbulence Signals in Bounded Shear Flows," J. Fluid Mech., Vol. 63, pp. 209-224 (1974).
73. Kraichnan, R.H., "Pressure Fluctuations in Turbulent Flow over a Flat Plate," J. Acoust. Soc. Am., Vol. 28, No. 3, pp. 378-390 (1956).
74. Lilley, G.M. and T.H. Hodgson, "On Surface Pressure Fluctuations in Turbulent Boundary Layers," The College of Aeronautics Cranfield, CoA Note No. 101. Also AGARD Report 276 (1960).
75. Lilley, G.M., "Wall Pressure Fluctuations Under Turbulent Boundary Layers at Subsonic and Supersonic Speeds," The College of Aeronautics Cranfield, CoA Note 140 (1963).
76. Lilley, G.M., "Pressure Fluctuations in an Incompressible Turbulent Boundary Layer," The College of Aeronautics Cranfield, CoA Note 133 (1960).
77. Ffowcs Williams, J.E., "Surface-Pressure Fluctuations Induced by Boundary-Layer Flow at Finite Mach Number," J. Fluid Mech., Vol. 22, pp. 507-519 (1965).
78. Corcos, G.M., "The Structure of the Turbulent Pressure Field in Boundary Layer Flows," J. Fluid Mech., Vol. 18, pp. 353-377 (1964).
79. Kraichnan, R.H., "Noise Transmission from Boundary Layer Pressure Fluctuations," J. Acoust. Soc. Am., Vol. 29, No. 1, pp. 65-80 (1957).
80. Kraichnan, R.H., "Pressure Field within Homogeneous Anisotropic Turbulence," J. Acoust. Soc. Am., Vol. 28, No. 1, pp. 64-72 (1956).

81. Gardner, S., "On Surface Pressure Fluctuations Produced by Boundary Layer Turbulence," *Acoustica*, Vol. 16, No. 2, pp. 67-74 (1965).
82. White, Frank M., "A Unified Theory of Turbulent Wall Pressure Fluctuations," USN USL Report 629 (1964).
83. Mawardi, O.K., "On the Spectrum of Noise from Turbulence," *J. Acoust. Soc. Am.*, Vol. 27, No. 3, pp. 442-445 (1955).
84. Powell, A., "Aerodynamic Noise and the Plane Boundary," *J. Acoust. Soc. Am.*, Vol. 32, No. 8, p. 982 (1960).
85. Chase, D.M., "Wavevector-Frequency Spectrum of Turbulent Boundary-Layer Pressure," *Proc. Symp. on Turbulence in Liquids*, University of Missouri (4-6 Oct 1971).
86. Chase, D.M., "Modeling the Wave-Vector Frequency Spectrum of Turbulent Boundary Layer Wall Pressure," *J. Sound Vib.*, Vol. 70, pp. 29-67 (1980).
87. Meecham, W.C. and M.T. Tavis, "Theoretical Pressure Correlation Functions in Turbulent Boundary Layers," *Phys. Fluids*, Vol. 23, pp. 1119-1131 (1980).
88. Phillips, O.M., "On the Aerodynamic Surface Sound from a Plane Turbulent Boundary Layer," *Proc. Roy. Soc.*, Vol. A234, pp. 327-335 (1956).
89. Phillips, O.M., "On Aerodynamic Surface Sound," *ARC RM 2099* (Mar 1955).
90. Landahl, M.T., "A Wave-Guide Model of Turbulent Shear Flow," *J. Fluid Mech.*, Vol. 29, pp. 441-459 (1967).
91. Landahl, M., "A Wave-Guide Model for Turbulent Shear Flow," *NASA CR 317* (1965).
92. Bergeron, R.F., "Aerodynamic Sound and the Low-Wavenumber Wall-Pressure Spectrum of Nearly Incompressible Boundary-Layer Turbulence," *J. Acoust. Soc. Am.*, Vol. 54, No. 1, pp. 123-133 (1973).
93. Morrison, W.R.B. and R.E. Kronauer, "Structural Similarity for Fully Developed Turbulence in Smooth Tubes," *J. Fluid Mech.*, Vol. 39, pp. 117-141 (1969).
94. Morrison, W.R.B., K.J. Bullock and R.E. Kronauer, "Experimental Evidence of Waves in the Sublayer," *J. Fluid Mech.*, Vol. 47, pp. 639-656 (1971).

95. Bullock, K.J., R.E. Copper and F.H. Abernathy, "Structural Similarity in Radial Correlations and Spectra of Longitudinal Velocity Fluctuations in Pipe Flow," J. Fluid Mech., Vol. 88, pp. 585-608 (1978).
96. Courant, R. and D. Hilbert, "Methods of Mathematical Physics, Vol. 1," Wiley Interscience Publishers (1966).
97. Lin, C.C., "The Theory of Hydrodynamic Stability," Cambridge University Press (1966).
98. Schubert, G. and G.M. Corcos, "The Dynamics of Turbulence Near a Wall According to a Linear Model," J. Fluid Mech., Vol. 29, pp. 113-135 (1967).
99. Hussain, A.K.M.F. and W.C. Reynolds, "The Mechanics of an Organized Wave in Turbulent Shear Flow," J. Fluid Mech., Vol. 41, pp. 241-258 (1970).
100. Hussain, A.K.M.F. and W.C. Reynolds, "The Mechanics of an Organized Wave in Turbulent Shear Flow, Part 2 - Experimental Results," J. Fluid Mech., Vol. 54, pp. 241-261 (1972).
101. Reynolds, W.C. and A.K.M.F. Hussain, "The Mechanics of an Organized Wave in Turbulent Shear Flow, Part 3 - Theoretical Models and Comparisons with Experiments," J. Fluid Mech., Vol. 54, pp. 262-288 (1972).
102. Davis, R.E., "On the Turbulent Flow over a Wavy Boundary," J. Fluid Mech., Vol. 42, pp. 721-731 (1970).
103. Davis, R.E., "On Prediction of the Turbulent Flow Over a Wavy Boundary," J. Fluid Mech., Vol. 52, pp. 287-306 (1972).
104. Landahl, M.T., "Wave Breakdown and Turbulence," SIAM J. Appl. Math., Vol. 28, pp. 735-756 (1975).
105. Bark, F., "On the Wave Structure of the Wall Region of a Turbulent Boundary Layer," J. Fluid Mech., Vol. 70, pp. 229-250 (1975).
106. Landahl, M.T., "Wave Mechanics of Breakdown," J. Fluid Mech., Vol. 56, pp. 775-802 (1977).
107. Klebanoff, P.S., K.D. Tidstrom and L.M. Sargent, J. Fluid Mech., Vol. 12, pp. 1-35 (1962).
108. Lin, C.C., "On Taylor's Hypothesis and the Acceleration Terms in the Navier-Stokes Equations," Q. Appl. Math., Vol. 10, pp. 295-306 (1953).

109. Lumley, J.L., "Interpretation of Time Spectra Measured in High-Intensity Shear Flows," Phys. Fluids, Vol. 8, pp. 1056-1062 (1965).

110. Fisher, M.J. and P.O.A.L. Davies, "Correlation Measurements in a Non-frozen Pattern of Turbulence," J. Fluid Mech., Vol. 18, pp. 97-116 (1965).

111. Chase, D.M., "Space-time Correlations of Velocity and Pressure and the Role of Convection for Homogeneous Turbulence in the Universal Range," Acoustica, Vol. 22, pp. 303-320 (1969).

112. Bull, M.K., "Properties of the Fluctuating Wall-Pressure Field of a Turbulent Boundary Layer," AASO Rep 234 University of Southampton, England (1963).

113. Bull, M.K., J.F. Wilby and D.R. Blackman, "Wall Pressure Fluctuations in Boundary Layer Flow and Response of Simple Structures to Random Pressure Fields," AASO Report 243, University of Southampton, England (1963).

114. Willmarth, W.W., "Wall Pressure Fluctuations in a Turbulent Boundary Layer," J. Acoust. Soc. Am., Vol. 28, pp. 1048-1053 (1956).

115. Willmarth, W.W., "Pressure Fluctuations Beneath Turbulent Boundary Layers," Ann. Rev. Fluid Mech., Vol. 7, pp. 13-38 (1975).

116. Willmarth, W.W., "Space-Time Correlations of the Fluctuating Wall Pressure in a Turbulent Boundary Layer," J. Aero. Sci., Vol. 25, pp. 335-336 (1958).

117. Mull, H.R. and J.S. Algranti, "Flight Measurement of Wall Pressure Fluctuations and Boundary Layer Turbulence," NASA TN D-280 (October 1960).

118. Tack, D.H., M.V. Smith and R.F. Lambert, "Wall Pressure Correlations in Turbulent Air Flow," J. Acoust. Soc. Am., Vol. 38, pp. 410-418 (1961).

119. Harrison, M., "Pressure Fluctuations on the Wall Adjacent to a Turbulent Boundary Layer," David Taylor Model Basin Report 1260 (1960).

120. Blake, W.K., "Turbulent Boundary Layer Wall Pressure Fluctuations on Smooth and Rough Walls," M.I.T. Acoustics and Vibration Laboratory Report 70208-1 (1969).

121. Schloemer, H.H., "Effects of Pressure Gradients on Turbulent Boundary Wall Pressure Fluctuations," USL Report 747, U.S. Navy Underwater Sound Laboratory (1966). Also J. Acoust. Soc. Am., Vol. 42, pp. 92-113 (1967).

122. Hodgeson, T.H., "On the Dipole Radiation from a Rigid and Plane Surface," Proc. Purdue Noise Control Conf. (1971).
123. Hodgeson, T.H., "Pressure Fluctuations in Shear Flow Turbulence," Ph.D. Thesis, Faculty of Eng. Univ., London (1962).
124. Serafini, J.S., "Wall-Pressure Fluctuations and Pressure-Velocity Correlations in a Turbulent Boundary Layer," AGARD Rep. No. 453 (1963).
125. Blake, W.K. and L.J. Maga, "On the Flow-Excited Vibrations of Cantilever Struts in Water. II. Surface-Pressure Fluctuations and Analytical Predictions," J. Acoust. Soc. Am., Vol. 57, pp. 1448-1464 (1975).
126. Emmerling, R., G.E.A. Meier and A. Dinkelacker, "Investigation of the Instantaneous Structure of the Wall Pressure Under a Turbulent Boundary Layer Flow," AGARD-CP-131 (1973).
127. Emmerling, R., "The Instantaneous Structure of the Wall Pressure Under a Turbulent Boundary Layer Flow," Rept. No. 56/1973, Max Planck Institute fur Stromungsforschung, Gottingen (1973).
128. Bull, M.K., "On the Form of the Wall-Pressure Spectrum in a Turbulent Boundary Layer in Relation to Noise Generation by Boundary Layer-Surface Interactions," Proc. Symp. on Sound Generation in Turbulence (1979).
129. Priestly, J.T., "Correlation Studies of Pressure Fluctuations on the Ground Beneath a Turbulent Boundary Layer," N.B.S., Report 8942 (1966).
130. Dinkelacker, A., M. Hessel, G.E.A. Meier and G. Schewe, "Investigation of Pressure Fluctuations Beneath a Turbulent Boundary Layer by Means of an Optical Method," Phys. Fluids, Vol. 20, pp. 5216-5224 (1977).
131. Aupperle, F. A. and R.F. Lambert, "Effects of Roughness on Measured Wall Pressure Fluctuations Beneath a Turbulent Boundary Layer," J. Acoust. Soc. Am., Vol. 47, pp. 359-370 (1970).
132. Corcos, G.M., "The Resolution of Pressure in Turbulence," J. Acoust. Soc. Am., Vol. 35, pp. 192-199 (1963).
133. Corcos, G.M., J.W. Cuthbert and W.A. vonWinkle, "On the Measurement of Turbulent Pressure Fluctuations with a Transducer of Finite Size," Univ. of California Inst. Eng. Research Report Ser. 82, No. 12 (Nov 1959).

134. Wills, J.A.B., "Measurements of Wave Number/Phase Velocity Spectrum of Wall Pressure Beneath a Turbulent Boundary Layer," J. Fluid Mech., Vol. 45, pp. 65-90 (1971).

135. Chandiramani, K.L., "Interpretation of Wall Pressure Measurements Under a Turbulent Boundary Layer," Bolt Beranek and Newman Report 1310 (1965).

136. Chandiramani, K., "Fundamentals Regarding Spectral Representation of Random Fields-Application to Wall-Pressure Field Beneath a Turbulent Boundary Layer," Bolt Beranek and Newman Report 1728 (1968).

137. Chandiramani, K.L. and W.K. Blake, "Low-Wave Number Content of the Spectrum of the Wall Pressure Under a Turbulent Boundary Layer," Bolt Beranek and Newman Report 1557 (1968).

138. Maidanik, G. and D.W. Jorgensen, "Boundary Wave Vector Filters for the Study of the Pressure Field in a Turbulent Boundary Layer," J. Acoust. Soc. Am., Vol. 42, pp. 494-501 (1967).

139. Jorgensen, D.W. and G. Maidanik, "Response of a System of Point Transducers to Turbulent Boundary-Layer Pressure Field," J. Acoust. Soc. Am., Vol. 43, pp. 1390-1394 (1968).

140. Maidanik, G., "Flush-Mounted Pressure Transducer Systems as Spatial and Spectral Filters," J. Acoust. Soc. Am., Vol. 42, pp. 1017-1024 (1967).

141. Maidanik, G., "System of Small-Size Transducers as Elemental Unit in Sonar System," J. Acoust. Soc. Am., Vol. 44, pp. 488-496 (1968).

142. Maidanik, G., "Wavevector Filters Designed to Explore Pressures Induced by Subsonic Turbulent Boundary Layers," Second USA/FRG Hydroacoustics Symposium (Jan 1971).

143. Jameson, P.W., "Measurement of the Low-Wavenumber Component of Turbulent Boundary Layer Pressure Spectral Density," Proc. 4th Symp. on Turbulence in Liquids (Sep 1975).

144. Martin, N.C., "Wavenumber Filtering by Mechanical Structures," M.I.T. Ph.D. Thesis (Jan 1976).

145. Blake, W.K. and D.M. Chase, "Wavenumber-Frequency Spectra of Turbulent Boundary Layer Pressure Measured by Microphone Arrays," J. Acoust. Soc. Am., Vol. 49, pp. 862-877 (1971).

146. Jameson, P.W., "Measurement of Low Wave Number Component of Turbulent Boundary Layer Wall Pressure Spectrum," BBN Report 1937 (1970).

147. Farabee, T.M. and F.E. Geib, Jr., "Measurement of Boundary Layer Pressure Fields with an Array of Pressure Transducers in a Subsonic Flow," NSRDC Report 76-0031 (1976). Also Proc. 6th Int. Cong. Instrumentation in Aerospace Facilities, Ottawa, Canada (1975).

148. Geib, F.E., Jr. and T.M. Farabee, "Measurement of Boundary Layer Pressure Fluctuations at Low Wavenumber on a Smooth Wall," Paper Presented at 91st Meeting of the Acoustical Society of America, Washington, D.C. (1976).

149. Farabee, T.M. and F.E. Geib, Jr., "Measurement of Boundary Layer Pressure Fluctuations at Low Wavenumber on a Rough Wall," Paper Presented at 91st Meeting of the Acoustical Society of America, Washington, D.C. (1976).

150. Kudashev, E.B. and L.P. Yablonik, "Determination of the Frequency-Wave-Vector Spectrum of Turbulent Pressure Fluctuations," Sov. Phys. Ac., Vol. 23, pp. 351-354 (1978).

151. Burton, T., "On the Generation of Wall Pressure Fluctuations for Turbulent Boundary Layers Over Rough Walls," Acoustics and Vibration Laboratory, M.I.T. Report 70208-4 (1971).

152. O'Keefe, E.J., M.J. Casarella and F.C. DeMetz, "Effect of Local Surface Roughness on Turbulent Boundary Layer Wall Pressure Spectra and Transition Burst Onset," DTNSRDC Report 4702 (1975).

153. Foxwell, J.H., "The Wall Pressure Spectrum Under a Turbulent Boundary Layer," Admiralty Underwater Weapons Establishment Tech Note, 218/66 Portland, England (Aug 1966).

154. Gilchrist, R.B. and W.A. Strawderman, "Experimental Hydrophone-Size Connection Factor for Boundary Layer Pressure Fluctuations," J. Acoust. Soc. Am., Vol. 38, pp. 298-302 (1965).

155. Chase, D.M., "Turbulent Boundary Layer Pressure Fluctuations and Wave Number Filtering by Non-Uniform Spatial Averaging," J. Acoust. Soc. Am., Vol. 46, pp. 1350-1365 (1969).

156. Geib, F.E., Jr., "Measurements on the Effect of Transducer Size on the Resolution of Boundary Layer Pressure Fluctuations," J. Acoust. Soc. Am., Vol. 46, pp. 253-261 (1969).
157. White, P.H., "Effect of Transducer Size, Shape, and Surface Sensitivity on the Measurement of Boundary Layer Pressure," J. Acoust. Soc. Am., Vol. 41, pp. 1358-1363 (1967).
158. Kirby, G.J., "The Effect of Transducer Size, Shape, and Orientation on the Resolution of Boundary Layer Pressure Fluctuations at a Rigid Wall," J. Sound Vib., Vol. 10, pp. 361-368 (1969).
159. Willmarth, W.W. and F.W. Roos, "Resolution and Structure of the Wall Pressure Field Beneath a Turbulent Boundary Layer," J. Fluid Mech., Vol. 22, pp. 81-94 (1965).
160. Bull, M.K. and A.S.W. Thomas, "High Frequency Wall Pressure Fluctuations in Turbulent Boundary Layers," Phys. Fluids, Vol. 19, pp. 597-599 (1976).
161. Haddle, G.D. and E.J. Skudrzyk, "The Physics of Flow Noise," J. Acoust. Soc. Am., Vol. 56, pp. 130-157 (1969).
162. Corcos, G.M., "The Resolution of Turbulent Pressures at the Wall of a Boundary Layer," J. Sound Vib., Vol. 6, pp. 59-70 (1967).
163. Bruel, P.V. and G. Rasmussen, "Free-Field Response of Condenser Microphones," Bruel and Kjaer Tech. Rev. No. 2, pp. 1-15 (1959).
164. Maidanik, G., "Domes Sonar System," J. Acoust. Soc. Am., Vol. 44, pp. 113-124 (1968).
165. Maidanik, G. and W.T. Reader, "Filtering Action of a Blanket Dome," J. Acoust. Soc. Am., Vol. 44, pp. 497-502 (1968).
166. Maidanik, G., "Acoustic Radiation from a Driven Infinite Plate Backed by a Parallel Infinite Baffle," J. Acoust. Soc. Am., Vol. 42, pp. 27-31 (1967).
167. Laufer, J., "The Structure of Turbulence in Fully Developed Pipe Flow," NACA Report 1174 (1954).
168. von Winkle, W.A., "Some Measurements of Longitudinal Space Time Correlations of Wall Pressure Fluctuations in Turbulent Pipe Flow," U.S. Navy Underwater Sound Laboratory USC Report 526 (1961).

169. Corcos, G.M., "The Structure of the Turbulent Pressure Field in Boundary Layer Flows," Univ. Cal. Inst. of Eng. Research, Report Series 183, No. 4 (1963).
170. Bakewell, H.P., G.F. Carey, J.J. Libuha, H.H. Schloemer and W.A. von Winkle, "Wall Pressure Correlations in Turbulent Pipe Flow," U.S. Navy Underwater Sound Laboratory, USC Report 559 (1962).
171. Bakewell, H.P., "Longitudinal Space-Time Correlation Function in Turbulent Airflow," J. Acoust. Soc. Am., Vol. 35, pp. 936-937 (1963).
172. DeMetz, F.C. and D.W. Jorgensen, "Measurement of the Boundary Layer Pressure Fluctuations Associated with Turbulent Air Flow in a Rigid Pipe," NSRDC Report 3707 (1971).
173. Greshilov, E.M., A.V. Evtushenko and L.M. Lyamshev, "Hydrodynamic Noise and the Toms Effect," Sov. Phys. Acoust., Vol. 21, pp. 247-251 (1975).
174. Greshilov, E.M. and L.M. Lyamshev, "Spectrum and Correlation of Wall Pressure Fluctuations in Flow Past a Rough Wall," Sov. Phys. Acoust., Vol. 15, pp. 104-106 (1969).
175. Hama, F., J.D. Long and J.C. Hegarty, "On Transition from Laminar to Turbulent Flow," J. Appl. Phys., Vol. 28, pp. 388-394 (1957).
176. Emmons, H.W., "The Laminar-Turbulent Transition in a Boundary Layer, Part I," J. Atm. Sci., Vol. 18, pp. 490-498 (1951).
177. Emmons, H.W. and A.E. Bryson, "The Laminar Turbulent Transition in a Boundary Layer," Proc. 1st Nat. Congress of Theoretical and Applied Mech., pp. 859-868 (1951).
178. Schubauer, G.B. and P.S. Klebanoff, "Contributions on the Mechanics of Boundary Layer Transition," NACA Report 1289 (1956).
179. Klebanoff, P.S. and K.D. Tidstrom, "Mechanism by which a Two-Dimensional Roughness Element Induces Boundary Layer Transition," Phys. Fluids, Vol. 15, pp. 1173-1188 (1972).
180. Kaplan, R.E., "The Stability of Laminar Incompressible Boundary Layers in the Presence of Compliant Boundaries," M.I.T. ASRL Report TR 116-1 (1964).
181. Garrellick, J.M. and M.C. Junger, "The Effect of Structureborne Noise in Submarine Hull Plating on Boundary Layer Stability," Cambridge Acoustical Assoc. Report ONR-CR 289-017-1F (1977).

182. Landahl, M.T., "On the Stability of a Laminar, Incompressible Boundary Layer Over a Flexible Surface," J. Fluid Mech., Vol. 13, pp. 609-632 (1962).
183. Hall, D.J. and J.C. Gibbings, "Influence of Stream Turbulence and Pressure Gradient upon Boundary Layer Transition," J. Mech. Eng. Sci., Vol. 14, pp. 134-146 (1972).
184. Shapiro, P.J., "The Influence of Sound Upon Laminar Boundary Layer Instability," M.I.T. Acoustics and Vibration Laboratory, Report 83458-83560-1 (Sep 1977).
185. Mechel, F. and W. Schilz, "Studies on the Effect of Sound on Boundary Layers in Air," Acoustica, Vol. 14, pp. 371-381 (1964).
186. Schilz, W., "Studies on the Effect of Flexural Boundary Vibrations on the Development of the Boundary Layer," Acoustica, Vol. 15, pp. 6-10 (1969).
187. Schilz, W., "Experimental Studies of the Effect of Sound on Boundary Layers in the Atmosphere," Acoustica, Vol. 16, pp. 208-223 (1965/66).
188. Schubauer, G.B. and H.K. Skramstad, H.K., "Laminar Boundary Layer Oscillations and Stability of Laminar Flow," J. Aero. Sci., Vol. 14, pp. 69-78 (1947).
189. Schubauer, G.B. and P.S. Klebanoff, "Investigation of Separation of the Turbulent Boundary Layer," NACA Report 1030 (1951).
190. Niedzwecki, J., "Laminar and Turbulent Uncompressible Boundary Layers on Bodies of Revolution in Axial Flow," Ph.D. Thesis, Catholic University of America, Dept. of Mech. Eng. (1977).
191. Casarella, M.J., J.T.C. Shen, and B.E. Bowers, "On the Evaluation of Axisymmetric Firebody Shapes for Delaying Laminar-Turbulent Transition, Part 1, Background and Analyses of the Problem," DTNSRDC Report 77-0074 (Aug 1977).
192. Lauchle, G.L., "Noise Generated by Axisymmetric Turbulent Boundary-Layer Flow," J. Acoust. Soc. Am., Vol. 61, pp. 694-702 (1977).
193. Dhawan, S. and R. Narasimha, "Some Properties of Boundary Layer Flow During the Transition from Laminar to Turbulent Motion," J. Fluid Mech., Vol. 3, pp. 418-436 (1958).

194. DeMetz, F.C. and M.J. Casarella, "An Experimental Study of the Intermittent Properties of the Boundary Layer Pressure Field During Transition on a Flat Plate," NSRDC Report 4140 (Nov 1973).

195. DeMetz, F.C. and M.J. Casarella, "An Experimental Study of the Intermittent Wall Pressure Bursts During Natural Transition of a Laminar Boundary Layer," AGARD-NATO Fluid Dynamics Panel, Brussels, Belgium (Sep 1973).

196. Gedney, C.J., "Wall Pressure Fluctuations During Transition on a Flat Plate," M.I.T. Acoust. and Vibration Lab. Rep. 84618-1 (Apr 1979).

197. Huang, T.T. and D.E. Hannan, "Pressure Fluctuations in the Regions of Flow Transition," DTNSRDC Report 4723 (Dec 1975).

198. Nisewanger, C.R. and F.B. Sperling, "Flow Noise Inside Boundary Layers of Buoyancy-Propelled Test-Vehicles," U.S. Naval Ordnance Test Station, NAVWEPS Report 8519, MATS TP 3511 (1965).

199. Clauser, F.H., "Turbulent Boundary Layers in Adverse Pressure Gradients," J. Aero. Sci., Vol. 21, pp. 91-108 (1954).

200. Scottron, V., "Turbulent Boundary Layer Characteristics Over a Rough Surface in an Adverse Pressure Gradient," NSRDC Report 2659 (1967).

201. Goldberg, P., "Upstream History and Apparent Stress in Turbulent Boundary Layers," M.I.T. Gas Turbine Lab. Report No. 85 (1966).

202. Tillmann, W., "Investigations of Some Particularities of Turbulent Boundary Layers on Plates," British Volkenrode Translation No. 45 (Jun 1946).

203. Perry, A.E. and W.H. Schofield, "Mean Velocity and Shear Stress Distributions in Turbulent Boundary Layers," Phys. Fluids, Vol. 16, pp. 2068-2074 (1972).

204. Ludwig, H. and W. Tillmann, "Investigations of the Wall Shearing Stress in Turbulent Boundary Layers," NACA TM 1285 (May 1950).

205. Ross, D., "A Physical Approach to Turbulent-Boundary-Layer Problems," A.S.M.E. Transactions, Vol. 121, pp. 1219-1254 (1954).

206. Diewert, G.S. and D.E. Abbott, "Analytical Prediction of the Incompressible Turbulent Boundary Layer with Arbitrary Pressure Distribution," J. Hydro-nautics, Vol. 4, pp. 27-34 (1970).

207. Bradshaw, P., D.H. Ferriss and N.P. Attwell, "Calculation of Boundary Layer Development Using the Turbulent Energy Equation," J. Fluid Mech., Vol. 28, pp. 593-616 (1967).
208. Patel, V.C. and M.R. Head, "A Simplified Version of Bradshaw's Method for Calculating Two-Dimensional Turbulent Boundary Layers," Aero. Quart., Vol. 21, pp. 243-263 (1970).
209. Dvorak, F.A., "Calculation of Turbulent Boundary Layers on Rough Surfaces in Pressure Gradient," AIAA J., Vol. 7, pp. 1752-1759 (1969).
210. Mellor, G.L. and D.M. Gibson, "Equilibrium Turbulent Boundary Layers," J. Fluid Mech., Vol. 24, pp. 225-254 (1966).
211. White, F., "A New Integral Method for Analysing the Turbulent Boundary Layer with Arbitrary Pressure Gradient," ASME Trans. J. Basic Eng., Vol. 91, pp. 371-378 (1969).
212. Howarth, L., "The Theoretical Determination of the Lift Coefficient for a Thin Elliptic Cylinder," Proc. Soc., Vol. A149, pp. 558-586 (1935).
213. Burton, T.E., "Wall Pressure Fluctuations at Smooth and Rough Surfaces under Turbulent Boundary Layers with Favorable and Adverse Pressure Gradients," M.I.T. Acoustics and Vibration Lab. Report 70208-9 (1973).
214. Blake, W.K., "A Statistical Description of the Pressure and Velocity Fields at the Trailing Edges of a Flat Strut," NSRDC Report 4242 (Dec 1975).
215. Moeller, M., P. Leehey and N.C. Master, "Low-Wavenumber Levels of Turbulent-Boundary-Layer Wall-Pressure Fluctuations in Zero and Adverse Gradients," M.I.T. Acoustics and Vibration Lab. Report 82464-2 (1978).
216. Sandborn, V.A. and S.J. Kline, "Flow Models in Boundary Layer Stall Inception," ASME Trans. J. Basic Eng., Vol. 83, pp. 317-327 (1961).
217. Sandborn, V.A. and C.Y. Liu, "On Turbulent Boundary Layer Separation," J. Fluid Mech., Vol. 32, pp. 293-304 (1968).
218. Simpson, R.L., J.H. Strickland and P.W. Barr, "Features of a Separating Turbulent Boundary Layer in the Vicinity of Separation," J. Fluid Mech., Vol. 79, pp. 553-594 (1977).

219. Perry, A.E. and B.D. Fairlie, "A Study of Turbulent Boundary Layer Separation and Reattachment," J. Fluid Mech., Vol. 69, pp. 657-672 (1975).

220. Stratford, B.S., "The Prediction of Separation of the Turbulent Boundary Layer," J. Fluid Mech., Vol. 5, pp. 1-16 (1959).

221. Goldschmied, F.R., "An Approach to Turbulent Incompressible Separation Under Adverse Pressure Gradients," J. Aircraft, Vol. 2, pp. 108-115 (1965).

222. Cebeci, T., "The Behavior of a Turbulent Flow Near a Porous Wall with Pressure Gradient," AIAA J., Vol. 8, pp. 2152-2156 (1970).

223. Tsahalis, D.T. and D.P. Telionis, "On the Behavior of Turbulent Boundary Layers Near Separation," AIAA J., Vol. 13, pp. 1261-1262 (1975).

224. Schiebe, F.R. and C.E. Bowers, "Boundary Pressure Fluctuations Due to Macroturbulence in Hydraulic Jumps," Proc. Symp. on Turbulence in Liquids, Rolla, Mo. (1971).

225. Jorgensen, D.W., "Measurements of Fluctuating Pressures on a Wall Adjacent to a Turbulent Boundary Layer," DTMB Report 1744 (1963). Also J. Underwater Acoustics, Vol. 13, pp. 329-336 (1963).

226. Yasuhara, M., "Experiments on Axisymmetric Boundary Layers Along a Long Cylinder in Incompressible Flow," Trans. Japan Soc. Aero. Space Sci., Vol. 2, pp. 72-76 (1959).

227. Greshilov, E.M., A.V. Evtushenlev and L.M. Lyamshev, "Spectral Characteristics of the Wall Pressure Fluctuations Associated with Boundary Layer Separation Behind a Projection on a Smooth Wall," Soviet Physics-Acoustics, Vol. 15, pp. 29-34 (1969).

228. Mugridge, B.D., "Turbulent Boundary Layers and Surface Pressure Fluctuations on Two-Dimensional Aerofoils," J. Sound Vib., Vol. 18, pp. 475-486 (1971).

229. Richmond, R.L., "Experimental Investigation of Thick Axially Symmetric Boundary Layers on Cylinders at Subsonic and Hypersonic Speeds," Thesis Cal. Inst. Tech. (1957). Also Hypersonic Research Project Memo No. 39.

230. Willmarth, W.W. and C.S. Yang, "Wall Pressure Fluctuations Beneath Turbulent Boundary Layers on a Flat Plate and a Cylinder," J. Fluid Mech., Vol. 41, pp. 47-80 (1970).

231. Afzal, N. and R.N. Narasimha, "Axisymmetric Turbulent Boundary Layer Along Circular Cylinder at Constant Pressure," J. Fluid Mech., Vol. 74, pp. 113-128 (1976).
232. Rao, G.N.V., "The Law of the Wall in a Thick Axisymmetric Turbulent Boundary Layer," J. Appl. Mech. Trans. ASME, Vol. 34, pp. 237-238 (1967).
233. Cebeci, T., "Laminar and Turbulent Incompressible Boundary Layers on slender Bodies of Revolution in Axial Flow," J. Basic Eng. Trans. ASME, Vol. 92, pp. 545-554 (1970).
234. Reid, R.O. and B.W. Wilson, "Boundary Flow Along a Circular Cylinder," Hydraul. Div. Proc. ASCE, Vol. 3, pp. 21-40 (1963).
235. White, F.M., "An Analysis of Axisymmetric Turbulent Flow Past a Long Cylinder," J. Basic Eng. Trans. ASME, Vol. 94, pp. 200-206 (1972).
236. Chase, D.M., "Mean Velocity Profile of a Thick Turbulent Boundary Layer Along a Circular Cylinder," AIAA J., Vol. 10, pp. 849-850 (1972).
237. Rao, G.N.V. and N.R. Keshavan, "Axisymmetric Turbulent Boundary Layers in Zero Pressure Gradient Flows," J. Appl. Mech. Trans. ASME, Vol. 39, pp. 25-32 (1972).
238. Willmarth, W.W., R.E. Winkel, L.K. Sharma and T.J. Bogar, "Axially Symmetric Turbulent Boundary Layers on Cylinders: Mean Velocity Profiles and Wall Pressure Fluctuations," J. Fluid Mech., Vol. 76, pp. 35-64 (1976).
239. White, F.M., "Viscous Fluid Flow," McGraw Hill (1974).
240. Ffowcs Williams, J.E., "Boundary-Layer Pressures and the Corcos Model: Development to Incorporate Low Wave Number Constants," J. Fluid Mech., Vol. 125, pp. 9-25 (1982).
241. Ffowcs Williams, J.E. and Pursehouse, M., "A Vortex Sheet Modelling of Boundary-Layer Noise," J. Fluid Mech., Vol. 113, pp. 187-220 (1981).
242. Huang, Y.F. and Geib, F.E., "Estimation of the Wavevector-Frequency Spectrum of Turbulent Boundary Layer Wall Pressure By Multiple Linear Regression," A.S.M.E. Symposium on Turbulence Induced Vibration and Noise of Structures (Nov 1983).
243. Panton, R.L. and Linebarger, J.H., "Wall Pressure Spectra Calculations for Equilibrium Boundary Layers," J. Fluid Mech., Vol. 65, pp. 261-287 (1974).
244. Panton, R.L. et al., "Low-Frequency Pressure Fluctuations in Axisymmetric Turbulent Boundary Layers," J. Fluid Mech., Vol. 97, pp. 299-319 (1980).

CHAPTER 8

BOUNDARY-LAYER-INDUCED VIBRATION AND NOISE

8.1 INTRODUCTION

Noise radiated from boundary layers on surfaces originates from two sources: direct radiation from the flow and surface vibration. If the surface is flat and rigid, the only radiation possible has been shown by Powell¹ (Section 2.4.4) to be quadrupole and radiated only by the volume distribution of Reynolds stresses in the boundary layer. Ffowcs Williams² has further shown that the radiation is quadrupole even if the surface moves but is still infinite and perfectly homogeneous. In both of these cases the surface simply acts as a reflector. If the surface moves at all and is in any way inhomogeneous (say by adding stiffeners), even though the boundary layer flow is strictly homogeneous in the plane of the surface, there is additional radiation due to the induced vibration of the body. Furthermore, if the body is not spatially continuous in the plane of the boundary layer but is terminated as with a trailing edge, Powell³ showed that there is a dipole source established at the edge. This topic will be covered in Chapter 9. This chapter is concerned with the following aspects of the problem:

1. Flow-induced structural vibration of structures of large curvature and methods of prediction and extrapolation,
2. Structural radiation of these flow-excited structures and prediction techniques,
3. Theory and experimental evidence for direct radiation from boundary layers.

In the determination of flow-induced vibration we shall put Chapters 6 and 7 to work. Recall that Chapter 6 covered the important mechanisms for the flow-induced vibration of structures in terms that relate to the space-time matching of the structural acceptance and the hydrodynamic exciting forces. Estimates of the structural response and its resulting acoustical radiation were predicated on a knowledge of the input power to the structure from the flow. This power can be determined once the wave vector spectrum of the exciting pressures is known; Chapter 7 has given both empirical and theoretical descriptions of the wave vector spectrum of turbulent boundary-layer pressure. Similar descriptions can be determined for other flow types once a spatial mapping of the exciting pressures has been determined. The first part of this chapter serves two important purposes. On one hand, it provides a discussion of the important problem of boundary-layer-induced vibration and noise. It also serves the more general purpose of outlining

a methodology for combining the principles of Chapters 6 and 7 in order to analytically model the flow-induced vibration and sound from other flow types.

In the final segment of the chapter, an assessment of direct flow radiation from turbulent boundary layers (requiring no surface vibration) versus noise from flow-induced vibration is given. The relative importance of edges (surface discontinuities) and vibration in overwhelming this noise is illustrated.

8.2 FLOW-EXCITED STRUCTURAL VIBRATION

8.2.1 General Method

If the structure is well enough defined that one can identify individual panel elements and then determine the vibration (and sound) fields from the elements, the methods of normal modes (and in some instances the power balances of statistical energy analysis) as introduced in Chapter 6 can be used with good results. These techniques or modifications thereof have been used in a large number of cases.⁴⁻²⁷ Measurements of boundary-layer-induced vibration and noise appear in references 16-30; however, these generally deal with the flow excitation of single baffled plates or membranes.^{16-25,28,29} Flow excitation of a periodically stiffened membrane,²⁶ space vehicle,²⁷ and commercial aircraft³⁰ have also been reported. Analytical approaches to the problem that have avoided relying on normal mode analyses have been applied to the directly induced convective wave motions in panels,³¹ radiation from large (heavily damped nonreverberant) plates in which various aspects of thick-plate dynamics are introduced,³² and general analyses of radiation from stiffened flexible surfaces without assumptions of interplate independence.³³⁻³⁶ Review papers by Leehey cover the early period of research³⁷ and introduce the method of normal modes.³⁸ The panels are always assumed to be linearly excited by the flow; i.e., no influence of the panel motion on the flow is considered. The effects of wall vibration on the turbulence have been theoretically examined by Ffowcs Williams³⁹ and Davis,^{40,41} who found influences on the Reynolds stresses. The only controlled experiments using panels are those of Mercer,⁴² who found no influence on mean boundary-layer properties and Izzo⁴³ who found enhancement of streamwise velocity fluctuations at the frequency of vibration for $dU_t/v > 3$, where d is the amplitude of wall motion. Other work in the area of interaction effects has been done by those interested in the generation of water waves (see references 102 and 103 of Chapter 7).

Boundary-layer-induced vibration is made complicated (and interesting) by the fact that the wave number spectrum of surface pressures is not independent of wave number, as it is for point forces. As illustrated in Figures 7.24, 7.39, 7.40, and 7.41, the pressures are concentrated within a well-defined region near $k_1 = \omega/U_c$. There may also be a subordinate concentration of pressure components near the acoustic wave number, $|k| \approx k_0$, as shown in Figure 7.39. If the panel has any resonant modes whose wave number of resonance coincides with $k_1 = \omega/U_c$, it will preferentially accept power from the flow in these modes of vibration. As discussed in Section 6.5, certain modes of vibration also preferentially radiate sound, and it is often the case that preferentially excited modes differ from preferentially radiating modes. Therefore caution must generally be observed in applying the methods of Chapter 6 to boundary-layer problems.

The situation to be considered is shown in Figures 8.1-8.5. It is required to evaluate Equation (6.40a), which is rewritten, for the autospectral density of the modal pressure in terms of the wave number frequency spectrum of wall pressure,

$$\phi_{p_{mn}}(\omega) = \frac{1}{A_p^2} \iint_{-\infty}^{\infty} \phi_p(\vec{k}, \omega) |S_{mn}(\vec{k})|^2 dk_1 dk_3 \quad (8.1)$$

where $|S_{mn}(\vec{k})|$ is the shape function (Equation (6.39)). The mean-square modal velocity, averaged in time and over the surface of the panel, is given by Equation (6.41), which is repeated:

$$\overline{v_{mn}^2} = \frac{\pi A_p^2 \phi_{p_{mn}}(\omega_{mn})}{M^2 \eta_T \omega_{mn}} \quad (8.2)$$

where ω_{mn} is the resonance frequency of the m, n mode.

The wave number integral in Equation (8.1) is to be evaluated over all wave numbers k_1 and k_3 . Near the convective ridge, $k_1 \approx \omega/U_c$, as shown by Equation (7.133), $\phi_p(\vec{k}, \omega)$ decreases as $(k_3 \delta^*)^{-2}$ for $k_3 > \gamma_3 \omega/U_c$ (γ_3 given beneath Equation (7.130)). At lower wave numbers nothing is known, but it is assumed that k_1 or k_3 dependencies are similar. As shown in Figures 8.1, and 8.3, the maximum values of

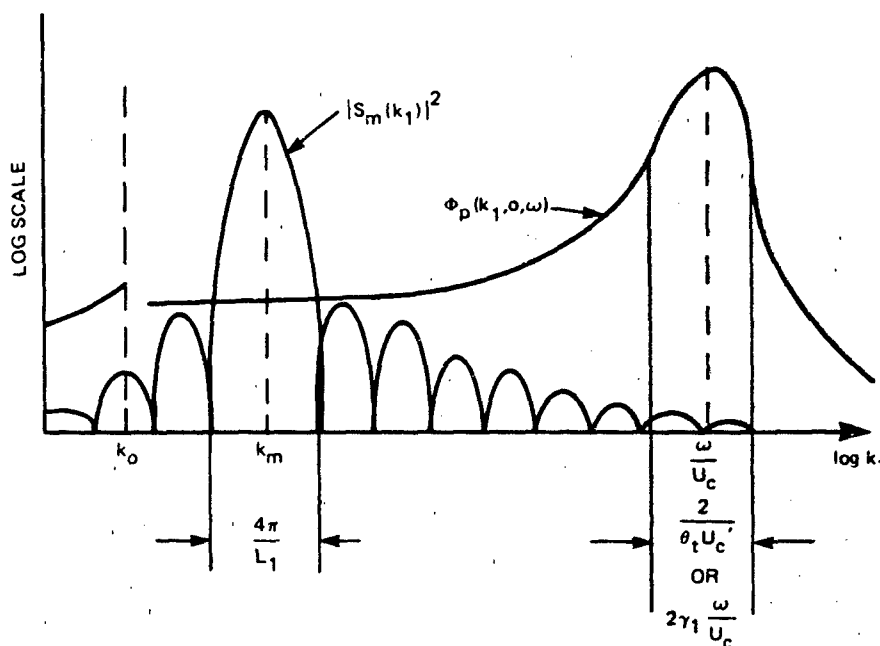


Figure 8.1 - Comparison of Panel Acceptance $|S_{mn}(k)|^2$ with Wall Pressure Spectrum $\phi_p(k_1, 0, \omega)$ for Hydrodynamically Fast Flexural Modes, Case A. The Functions Are Illustrated for $k_3 = \text{constant}$

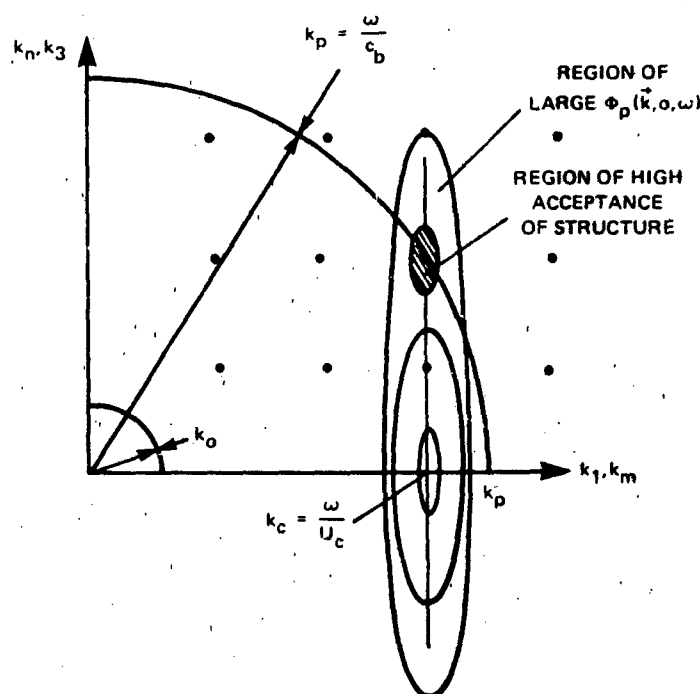


Figure 8.2 - Superposition of the $|S_{mn}(\vec{k})|^2$ Lattice and $\phi_p(\vec{k}, \omega)$ in the k_1, k_3 Plane for Hydrodynamically Slow Flexural Modes, $c_b < U_c$, Case C. Case B, Hydrodynamic Coincidence, Occurs When $k_c = k_n = k_1$

the pressure spectrum and the shape function do not necessarily overlap. In the case shown, the convective wave number is greater than the wave number of free bending waves k_b because $U_c < c_b$. In Figure 8.3 the bending wave number k_b is greater than $k_c = \omega/U_c$ because the free bending wave speed c_b is less than the convection velocity. The points that form the lattice in the figures represent the matrix of all possible values of $k_1 = k_m$ and $k_3 = k_n$ for which $|S_{mn}(\vec{k})|^2$ is maximum, i.e., for all possible resonant modes of the panel. When one of these points coincides with the value of the wave number of free bending waves

$$k_b = \frac{\omega}{c_b} \quad (8.3)$$

a resonance will occur at that frequency. For plates

$$c_b = (\omega \kappa c_L)^{1/2} \quad (8.4)$$

so

$$k_b = \left(\frac{\omega}{\kappa c_L} \right)^{1/2}$$

where $\kappa = h/(12)^{1/2}$ is the radius of gyration of the plate, h is the thickness, and c_L is the longitudinal wave speed of the material (see Chapter 6 for full details). One of these points is shown as the crosshatched region in Figure 8.2 and Figure 8.3. In Figure 8.3 it is shown coinciding with the region of high-pressure spectral density, i.e.,

$$k_m = \frac{\omega}{U_c}$$

Alternatively, in Figure 8.2, the panel acceptance lies in the nonconvective, low wave number tail of the wall pressure spectrum. The wave number bandwidth of $\phi_p(\vec{k}, \omega)$ is $2\gamma_1 \omega/U_c$, as indicated by the spectrum function (Equation (7.133)). Near the acoustic wave number $k_1 = k_o$, the curve of $\phi_p(\vec{k}, \omega)$ is shown discontinuous, reflecting the uncertainty concerning values there. Recall that γ_1 is the decay

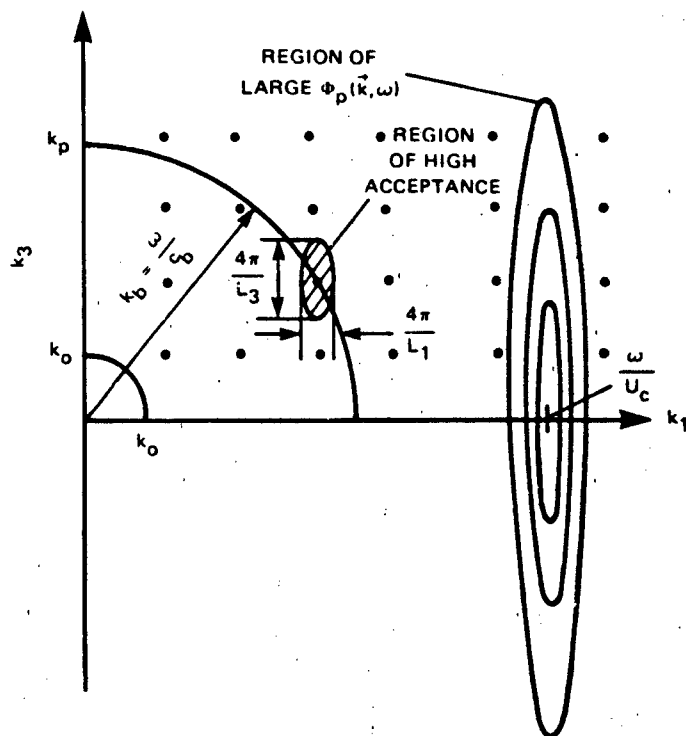


Figure 8.3 - Superposition of $|S_{mn}(\vec{k})|^2$ Lattice and $\Phi_p(\vec{k}, \omega)$ in the k_1, k_3 Plane for Hydrodynamically Fast Bending Modes, $c_b > U_c$, Case A

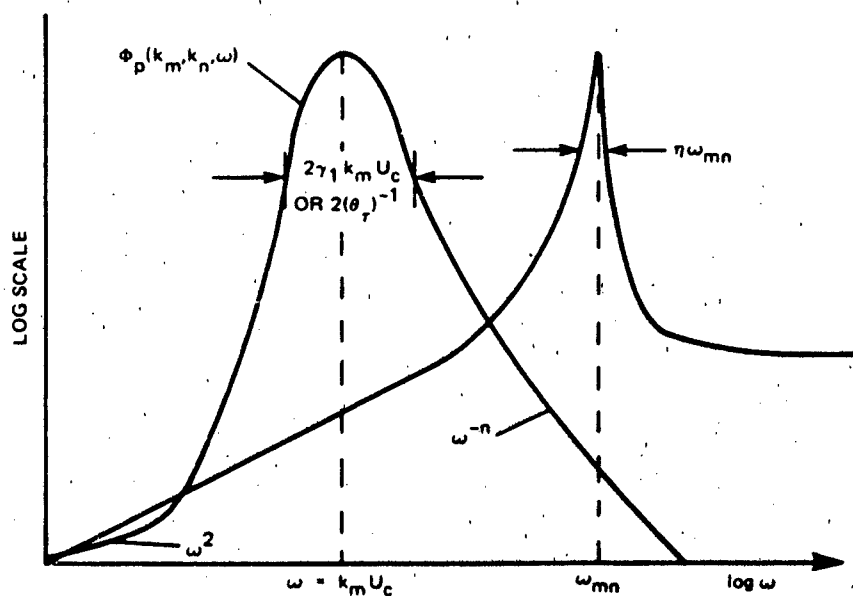


Figure 8.4 - Illustration of $\Phi_p(\vec{k}, \omega)$ for Fixed $k_1 = k_m$ and $k_3 = k_n$ Versus ω and of Frequency Resonance of the Panel Acceleration $\omega^2 \Phi_{mn}(\omega)$ of a Hydrodynamically Fast Mode, $\omega_m/k_m > U_c$

constant of the longitudinal cross-spectral density. An alternative bandwidth may be deduced from the exponential moving axis decay illustrated in Figure 7.35 and leading to a nonvanishing value of $\phi_m(\omega - U_c k_1)$ when $k_1 \ll \omega/U_c$. This bandwidth is $\Delta k_c \approx 2(\theta_\tau U_c)^{-1}$, where θ_τ is the time constant (or eddy life time) of exponential decay, assuming a moving axis correlation function of $\exp(-|\tau|/\theta_\tau)$. The bandwidth of the acceptance of the mode with which Δk_c is to be compared is

$$\Delta k_1 = \frac{4\pi}{L_1}, \Delta k_3 = \frac{4\pi}{L_3}$$

The relative shapes of frequency functions are shown in Figure 8.1. The spectrum function $\phi_p(k_m, k_n, \omega) = \phi(k_p, \omega)$ has a peak at $\omega = k_1 U_c = k_m U_c$. From Equation (7.133) the breadth of the peak is $2\gamma_1 k_m U_c$, or $2/\theta_\tau$. The breadth in the resonance of mode is $\eta_T \omega_{mn}$. The frequency regions of $\phi_p(k_p, \omega)$ include the convective region near $k_m U_c$ as well as the low wave number high-frequency pressures. Experimental data for this spectral region is given in Figure 7.46. At very low frequencies (of little practical value except at very low convection speeds) $\phi_p(k_p, \omega)$ depends on ω^2 .

8.2.2 Effects of Hydrodynamic Coincidence on Single-Mode Response

The various regions of hydrodynamic and acoustic wave number coincidence depend on the relative magnitudes of c_o, c_b , and U_c . Figure 8.5 shows that since c_b increases with frequency, as frequency increases the relationship among phase speeds varies. If the structure is a membrane, characterized by a constant phase speed c_m , the relationship among speeds does not change. For example, since the membrane speed is independent of frequency, the simultaneously acoustically fast and hydrodynamically fast ($c_m > U_c, c_m > c_o$) modes are possible, and these will radiate effectively at all frequencies.

The autospectrum of modal pressure can be simply evaluated from Equation (8.1) for all wave number combinations, even when k_m and ω/U_c coincide, when certain criteria are satisfied. As long as the bending wave speed and the convection velocity do not coincide ($c_b \neq U_c$), the following requirements, originally due to Dyer,⁵ must be met.

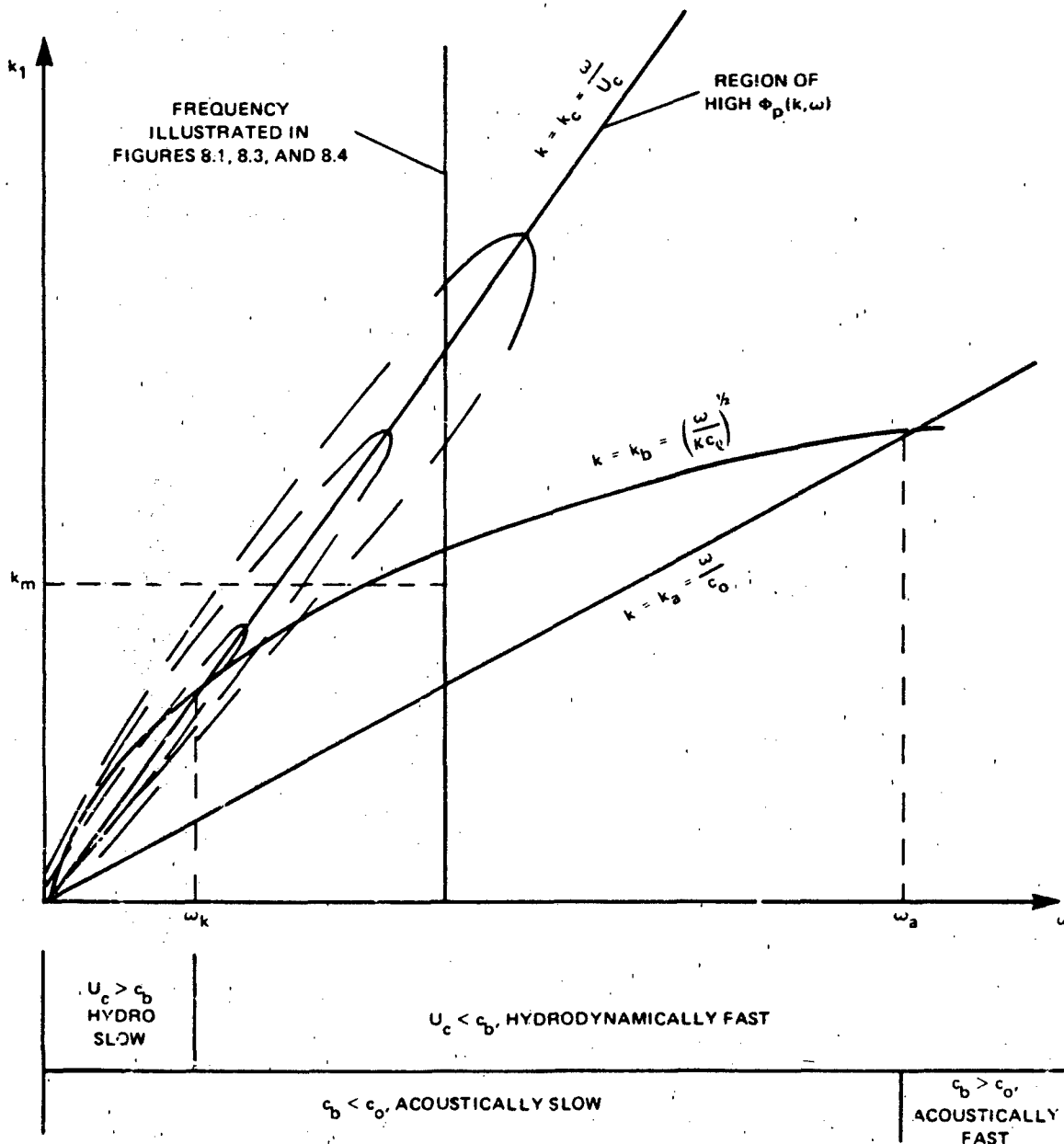


Figure 8.5 - Wave Number Frequency Loci of Important Coincidence Regions of Panel Acceptance $|S_{mn}(k)|^2$ and $\phi_p(\vec{k}, \omega)$. Regions of Acoustic and Hydrodynamic Coincidence Are Shown. The Value k_m Represents the Value of k_1 for the Hydrodynamically Fast Mode Depicted in Figures 8.1, 8.3, and 8.4

1. $\eta \omega_{mn} \ll 2\gamma_1 k_m U_c$. Put in alternative terms, $\eta \omega_{mn} \ll 2/\theta_T$. This means simply that the vibration decay must not be significant within an eddy life time.

2. $4\pi/L_1 \ll 2\gamma_1 \omega/U_c$. Put in alternative terms, $4\pi/L_1 \ll 2/\theta_T U_c$. This means that the distance an eddy travels in its life time $\theta_T U_c$ must be less than the stream-wise length of the panel divided by 2π .

A criterion similar to number 1 above has been derived by Phillips⁶ in connection with wind-generated water waves in which methods similar to those of this chapter were used. Coincidence effects between the wind speed and wave speed were also examined.

Under these circumstances the autospectrum $\phi_{P_{mn}}(\omega)$ will be broad enough that Equation (8.2) is valid and the integral in Equation (8.1) can be separated. There are three regions of wave number.

Case A. $k_m \ll \omega/U_c$. This case is illustrated in Figure 8.1. Assuming that the dominant part of the integral comes from the region of $k_1 \approx k_m$, Equation (8.1) becomes

$$\begin{aligned} \left(\phi_{P_{mn}}(\omega) \right)_{\text{low}} &= \frac{1}{A_p^2} \phi_P \left(k_m, k_n \ll \frac{\omega}{U_c} \right) \iint_{-\infty}^{\infty} |S_{mn}(\vec{k})|^2 d\vec{k} \\ \left(\phi_{P_{mn}}(\omega) \right)_{\text{low}} &= \frac{(2\pi)^2}{A_p^2} \phi_P \left(k_m, k_n \ll \frac{\omega}{U_c}, \omega \right) \end{aligned} \quad (8.5)$$

Since the velocity $\omega/k_m > U_c$, these modes are termed hydrodynamically fast (HF) and the associated mean-square surface velocity for the mn mode is

$$\overline{v_{mn}^2}_{\text{HF}} = \frac{(2\pi)^2 \pi A_p}{M^2 \eta_T \omega_{mn}} \phi_P \left(k_m, k_n \ll \frac{\omega_{mn}}{U_c}, \omega_{mn} \right) \quad (8.6)$$

where $M = m_s A_p$ and m_s is the total (structural plus added) mass per unit area of the panel. This case of low wave number occurs in most underwater applications.

The additional possible contribution that comes from the tail of $|S_m(k_1)|^2$ for $k_1 > k_m$ can be determined by using Equation (6.59) for a simply supported panel or Equation (6.61) for a panel clamped along $y = \pm L_1/2$. For the simply supported case the effective value of $|S_m(k_1)|^2$ is

$$|S_m(k_1)|^2 \approx \frac{1}{2} - \frac{16L_1}{(k_m L_1)^2} \left(\frac{k_m}{k_1}\right)^4 \quad (8.7)$$

where the $(\text{sine})^2$ has been replaced by its average, $1/2$. Thus, letting $k_1 = \omega/U_c$, we have the contribution from the convective ridge:

$$\begin{aligned} \left(\phi_{p_{mn}}(\omega)\right)_{\text{conv}} &\approx \frac{2}{\pi} \frac{\phi_p(\omega_{mn}) \gamma_1 \gamma_3}{\left[\left(\frac{\gamma_3 \omega \delta^*}{U_c}\right)^2 + (k_n \delta^*)^2\right]} \cdot \frac{(\delta^*)^2}{A_p} \\ &\cdot \frac{8}{(k_m L_1)^2} \left(\frac{k_m U_c}{\omega}\right)^4 \end{aligned} \quad (8.8)$$

The pressure spectrum is the sum of the low and convected wave number contributions, however, the relative importance of Equations (8.5) and (8.8) will depend on the parameters of the problem. Generally, it is assumed that $\left(\phi_{p_{mn}}(\omega)\right)_{\text{conv}}$ is negligible. If the edges are clamped, Equation (6.61) shows that an even lower response, by an additional multiplicative factor $(k_m U_c / \omega)^2$, will result from the flow.

Case B. $k_m = \omega/U_c$ or $c_b = U_c \cos \alpha_m$. The peak of the acceptance function coincides with the peak in the wave number spectrum of the pressure. In this case the flow convection velocity is greater than the phase speed of bending waves. Therefore, at some angle to the flow α_m , the trace velocity $U_c \cos \alpha_m$ matches c_b . If there is a mode resonant at the associated wave number, that mode will be preferentially excited.

Equation (8.1) becomes

$$\phi_{p_{mn}}(\omega) = \frac{(2\pi)^2}{A_p} \phi_p\left(k_n, k_m = \frac{\omega}{U_c}, \omega\right) \quad (8.9)$$

so that the modal vibration level of such hydrodynamically coincident (HC) modes is

$$\overline{v_{mn}^2}_{HC} = \frac{(2\pi)^2 \pi A_p}{M^2 \eta_T \omega_{mn}} \phi_p \left(k_n, k_m = \frac{\omega}{U_c}, \omega_{mn} \right) \quad (8.10)$$

Introducing Equation (7.133), we have

$$\overline{v_{mn}^2}_{HC} = \frac{4\pi \phi_p(\omega_{mn}) A_p}{M^2 \eta_T \omega_{mn}} \frac{\delta^{*2} \frac{\gamma_3}{\gamma_1}}{\left[\left(\frac{\gamma_3 \omega_{mn} \delta^*}{U_c} \right)^2 + (k_n \delta^*)^2 \right]} \quad (8.11)$$

Case C. $k_m \gg \omega/U_c$. In this case, since $k_m < k_p$, we write $k_m = k_p \cos \alpha_m$. Therefore the condition can be rewritten

$$\frac{\omega}{c_p} \cos \alpha_m > \frac{\omega}{U_c}$$

or

$$c_b < U_c \cos \alpha_m \quad (8.12)$$

This condition therefore requires that $c_b < U_c$, or it is said that the mode is "hydrodynamically slow" (HS) (see Figure 8.5). For flexural waves on plates there is a specific frequency, called the hydrodynamic coincidence frequency, at which $c_b = U_c$. This frequency is defined as

$$U_c = c_p = (\omega_h \kappa C_\ell)^{1/2}$$

or

$$\omega_h = \frac{U_c^2}{\kappa C_\ell} \quad (8.13)$$

values of coincidence frequency for steel and aluminum panels are given in Figure 8.1. Since all resonant modes satisfy the equation for the resultant wave number,

$$k_p = k_{mn} = (k_m^2 + k_n^2)^{1/2} \quad (8.14)$$

Equation (8.13) is a limiting condition. When $k_m > \omega/U_c$, k_p must also be greater than ω/U_c , so that the frequency is below the hydrodynamic coincidence frequency.

For this case, Equation (8.1) becomes

$$\phi_{p_{mn}}(\omega) = \frac{(2\pi)^2}{A_p} \phi_p(k_n, k_m > \frac{\omega}{U_c}, \omega) \quad (8.15)$$

With Equation (7.133) and Equation (8.2) we have for the modal velocity of hydrodynamically slow (HS) modes

$$\overline{v_{mn}^2} = \frac{4\pi \phi_p(\omega_{mn}) A_p}{M^2 \eta_T \omega_{mn}} \frac{\gamma_1 \gamma_3 \left(\frac{\omega \delta^*}{U_c}\right)^2 \delta^{*2}}{\left[\left(\frac{\gamma_3 \omega \delta^*}{U_c}\right)^2 + (k_n \delta^*)^2\right] \left[\left(\frac{\gamma_1 \omega \delta^*}{U_c}\right)^2 + (k_p \delta^* \cos \alpha_m)^2\right]} \quad (8.16)$$

An additional contribution comes from the maximum of $\phi_p(\vec{k}, \omega)$ coinciding with the wave number extremes of $|S_{mn}(\vec{k})|^2$. This contribution is often neglected. The cases B and C, since they pertain to the conditions of U_c on the order of the bending wave speed, are generally more important in aeroacoustics than in underwater applications. With Equation (6.58) this contribution to $\phi_{p_{mn}}(\omega)$ is written

$$\left[\phi_{p_{mn}}(\omega)\right]_{\text{conv}} \approx \frac{16}{\pi} \frac{1}{(k_m L_1)^2} \cdot \phi_p(\omega) \cdot \frac{\delta^{*2}}{A_p} \frac{\gamma_1 \gamma_3}{\left[\left(\frac{\gamma_3 \omega \delta^*}{U_c}\right)^2 + (k_n \delta^*)^2\right]} \quad (8.17)$$

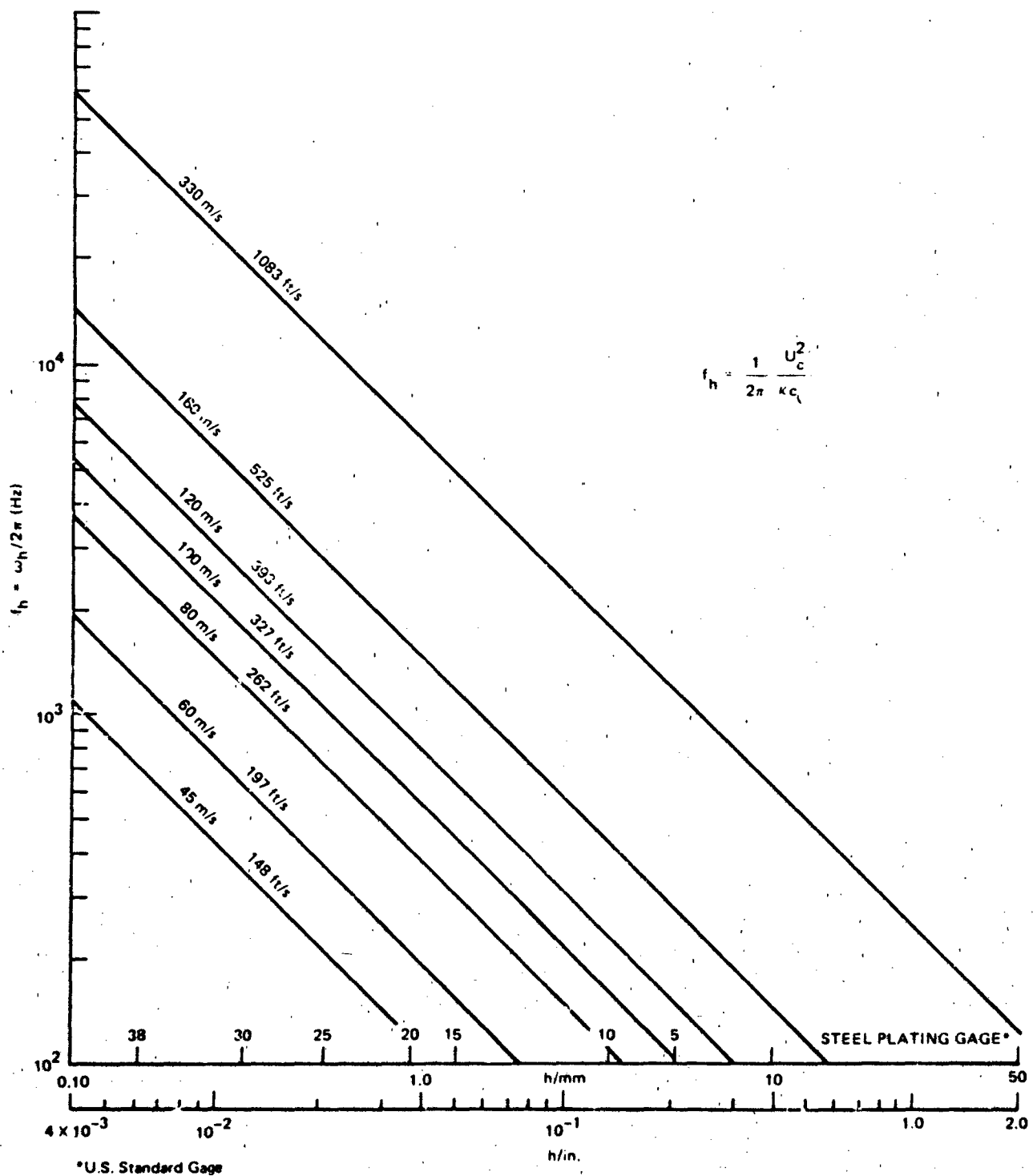


Figure 8.6 - Hydrodynamic Coincidence Frequencies for Flexural Bending Waves in Panels of Steel or Aluminum ($c_\ell \sim 5100$ m/s) of Various Thicknesses and Flow Velocities ($U_c \sim 0.7 U_\infty$). See Equation (8.13)

These relationships indicate different dependence of the modal velocity on ω depending on which case applies. To illustrate the differences in the response of the modes as a function of flow velocity in the various coincidence regions, we let the wall pressure spectral density be approximated by

$$\Phi_p(\omega) \approx a_c C_f^2 \left[\frac{1}{2} \rho U_\infty^2 \right]^2 \left(\frac{\omega \delta^*}{U_\infty} \right)^{-1} \frac{\delta^*}{U_\infty} \quad 0.5 < \frac{\omega \delta^*}{U_\infty} < 10 \quad (8.18)$$

which is indicated by experimental data discussed in Section 7.4.1, and the low wave number spectrum of pressure is given by

$$\Phi \left(k \ll \frac{\omega}{U_c}, 0, \omega \right) \approx a_c C_f^2 \left[\frac{1}{2} \rho U_\infty^2 \right]^2 \left(\frac{\omega \delta^*}{U_\infty} \right)^{-4} \frac{\delta^{*3}}{U_\infty} \quad (8.19)$$

a modification of Equation (7.144)). Thus we find the mean-square modal velocity:

a. $U_c \ll \omega/k_m$ ($U_c \ll c_b$ or $\omega \ll \omega_h$) hydrodynamically fast resonant modes

$$\overline{V_{mn}^2}_{HF} \approx \pi a_c^3 \frac{U_\infty^2}{\eta_T} \left(\frac{U_\infty}{c_o} \right)^2 \left(\frac{U_\infty}{\omega_{mn} \delta^*} \right)^3 \left(\frac{\rho_o c_o}{\rho_p h \omega_{mn}} \right)^2 \frac{\delta^{*2}}{A_p} C_f^2 \quad (8.20a)$$

b. $U_c = \omega/k_m$ ($\omega = \omega_h$), hydrodynamically coincident modes

$$\overline{V_{mn}^2}_{HC} \approx \pi a_c \frac{\gamma_1}{\gamma_3} \frac{U_\infty^2}{\eta_T} \left(\frac{U_\infty}{c_o} \right)^2 \left(\frac{U_\infty}{\omega_{mn} \delta^*} \right)^2 \left(\frac{\rho_o c_o}{\rho_p h \omega_{mn}} \right)^2 \frac{\delta^{*2}}{A_p} C_f^2 \quad (8.20b)$$

c. $U_c \gg \omega/k_m$ ($U_c \gg c_b$, $\omega \ll \omega_h$), hydrodynamically slow modes

$$\overline{V_{mn}^2}_{HS} \approx \pi a_c \frac{\gamma_1}{\gamma_3} \frac{U_\infty^2}{\eta_T} \left(\frac{U_\infty}{c_o} \right)^2 \left(\frac{\rho_o c_o}{\rho_p h \omega_{mn}} \right)^2 \frac{\delta^{*2}}{A_p} C_f^2 \frac{1}{(k_m \delta^*)^2} \quad (8.20c)$$

where it has been assumed that $k_m \delta^*$, $k_n \delta^*$ $\ll 1$. Thus, at flow velocities sufficiently less than the bending wave speed, the mean-square modal panel velocity will increase as U_∞^7 . The dependence will fall off to $U_\infty^{3.6}$ at flow convection velocities greater than c_b . This noninteger power arises from $U_\infty^4 C_f^2$, which becomes $U_\infty^{3.6}$ by virtue of Equation (7.35), which shows $C_f \approx U_\infty^{-1/5}$. The modal velocity is also dependent on the mode order at frequencies significantly above the hydrodynamic coincidence frequency. The thickness of the panel enters by influencing the mass impedance ($\rho_p h \omega$) and by changing the coincidence frequency since ω_h increases with a decrease in the thickness of the panel.

8.2.5 Empirical Confirmation

These results have been given some support by the experimental results of Maestrello.²⁹ Figure 8.7 shows the mean-square amplitudes of various modes of aluminum panels as functions of speed normalized on the acoustic wave speed in air. The speeds for which the bending wave and convection speeds become equal are designated as U_m in the legend. For speeds very much different from U_m (either above or below) the behavior with Mach number indicated by Equations (8.20a) and (8.20c) is qualitatively represented by the measurements. Near hydrodynamic coincidence, the curves of $\langle y^2 \rangle$ versus U_∞/c_o show either a peak or a smooth transition.

An effort by Maestrello²² to predict this panel motion by using essentially the same theory as that presented here was only partially successful. Although the speed dependence was properly predicted, the levels were overpredicted by as much as 10 dB. Differences between measurement and calculation of this order are common.^{14,16} Another comparison between measurement and theory is shown in Figure 8.8. Measurements at the center of a panel of the mean-square displacements of the 11th mode were obtained by Tack and Lambert. Their theory, developed along similar lines as that presented here, but using a contemporary analytical representation of the wall pressure correlation derived by Dyer⁵ and fitted to their measurements,¹⁸ compares favorably to their measurements of vibration. Also shown is Equation (8.20a), which underpredicts the measurements. Since the dimensionless frequency range is low, Figure 7.46 shows that the low wave number limit of Equation (7.133) may apply. This gives, instead of Equation (8.20a),

$$\overline{v_{mn}^2} = \pi \frac{\gamma_1}{\gamma_3} a_c \frac{U_\infty^2}{n_T} \left(\frac{U_\infty}{\omega_m \xi^*} \right)^2 \left(\frac{\rho_o U_o}{\rho_p h \omega_m} \right)^2 \frac{\delta^{*2}}{A_p} C_f^2 \quad \begin{matrix} \omega > \omega_h \\ c_b < U_c \end{matrix} \quad (8.21)$$

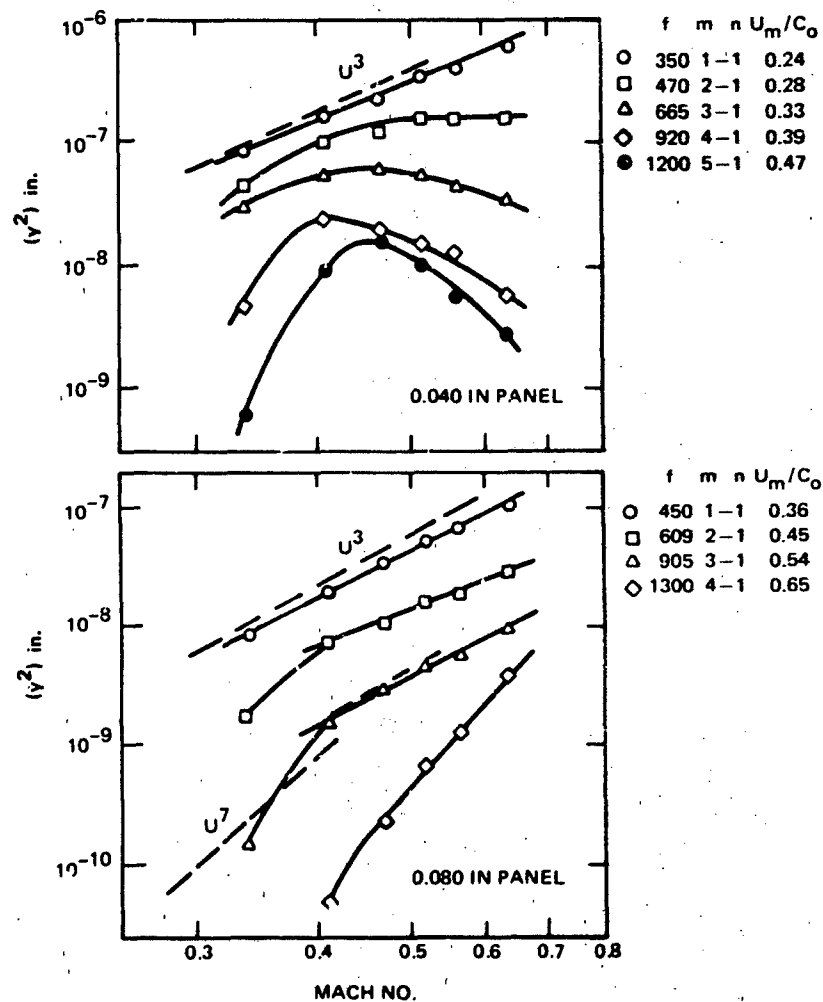


Figure 8.7 - Modal Mean-Square Displacement of Aluminum Panels;
 $L_1 = 12$ in., $L_3 = 7$ in., $\delta^* = 0.15$ to 0.17 in., $U_c = 0.8 U_\infty$.

U_m Denotes Speeds for which c_b and U_c Become Equal
 for Longitudinal Mode Order m .

(Adopted from Ref. 29, Copyright Academic Press)

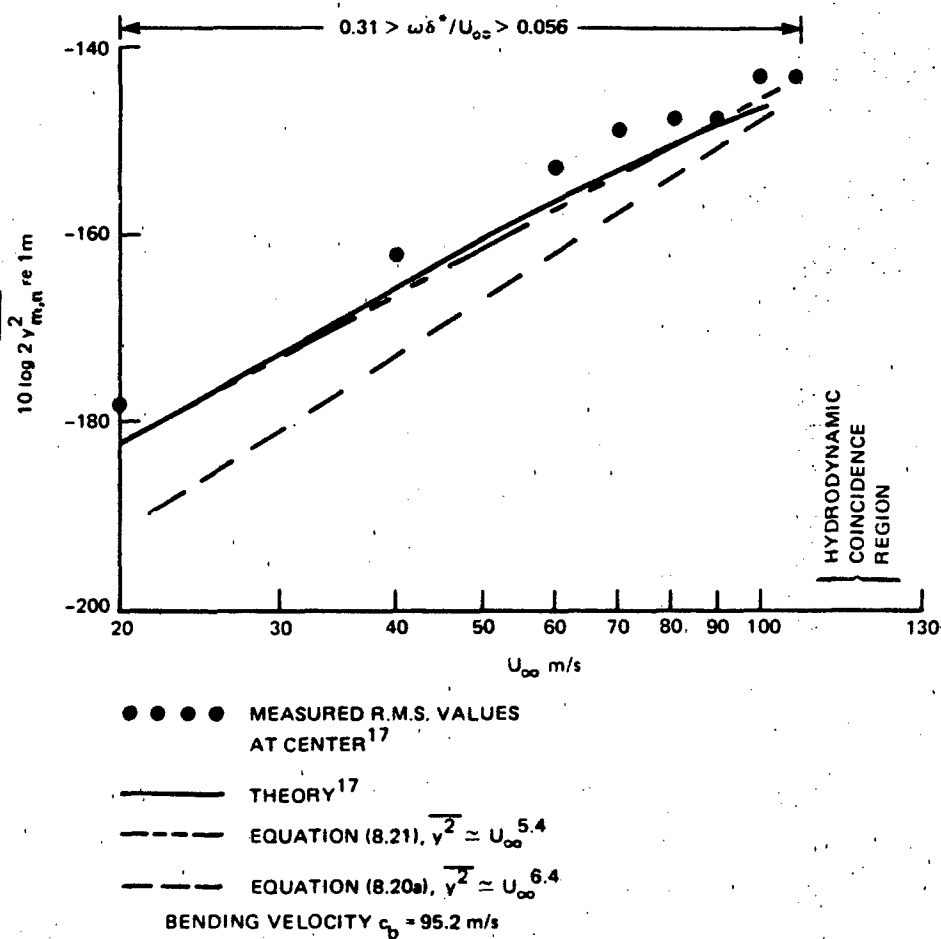


Figure 8.8 - Boundary-Layer-Induced Vibration Amplitude of n^{th} Mode of a Brass Panel (0.475 m \times 0.0254 m \times 0.00153 m).

$f_{11} = 1100$ Hz, $\delta^* \approx 0.0009$ m, $C_f \approx 3 \times 10^{-3}$
at 50 m/s, and $\eta_T \approx 0.01$

This equation, with $a_c = 1$ and $\gamma_1/\gamma_3 = 1/6$, more closely predicts the measured amplitudes. It also approximates, with $C_f \propto U_\infty^{-0.2}$, the observed dependence on speed. Also, since at coincidence $U_c = (0.7 \text{ to } 0.8) U_\infty = c_b$, the coincidence range is approached by the measurements. Generally, for good prediction it is necessary, in any case, to use measured wall pressure statistics obtained in the same facility as the vibration measurements. Herein can lie one source of error because of the difficulties in measurement of wall pressure statistics and the sensitivity of those statistics to the boundary-layer development already described in Section 7.4. A second difficulty lies in uncertainties in estimating the loss factor for a panel. The use of panels for deducing wave number spectra of wall pressures has been demonstrated by Jameson⁴⁴ and Martin⁴⁵ (see Figure 7.46). In those researches it has been shown that careful measurements of total damping must be included in the experimental program.

8.2.4 Average Response of Many Modes

For frequencies well above the hydrodynamic coincidence frequency, $\omega \gg \omega_h$ (see Figures 8.1, 8.3, 8.5, and 8.6), the mode order does not explicitly enter the expressions for modal velocity because the wave number spectrum of the excitation is nearly independent of wave number. This fact greatly simplifies calculation of total mean-square response. Using the methods of Section 6.3.2 we find in such cases, using Equations (6.47), (6.50), and (8.6), that the mean-square velocity in the band $\Delta\omega$ is

$$\overline{V_{HF}^2}(\omega, \Delta\omega) = \frac{\pi^2}{M^2} \frac{A_P^2}{\eta_T \omega} \cdot \frac{\phi_P\left(k_P < \frac{\omega}{U_c}, \omega\right) \Delta\omega}{\kappa c_\ell}, \quad \begin{matrix} \omega \gg \omega_h \\ U_c \ll c_P \end{matrix} \quad (8.22)$$

which may be rewritten in the form analogous to Equation (6.52b)

$$\overline{V_{HF}^2}(\omega, \Delta\omega) = \frac{8\pi^2}{M \eta_T} G_\infty \phi_P\left(k_P < \frac{\omega}{U_c}, \omega\right) \frac{\Delta\omega}{\omega}, \quad \omega \gg \omega_h \quad (8.23)$$

for Case C, where G_∞ is the point admittance of an infinite plate, $G_\infty = (8m_s \kappa c_\ell)^{-1}$. The mass per unit area includes the added mass (see Section 6.7.6).

At frequencies less than ω_h , (i.e., hydrodynamically slow modes) the plate wave number k_p is greater than the convection wave number. By virtue of Equation (7.21), and as illustrated in Figures 8.2 and 8.5, there will be a mode wave number $k_m < k_p$ that will match ω/U_c and be well excited by the convected pressures. Therefore one cannot assume that all modes included in $\Delta\omega$ are equally well excited by the boundary layer pressures.* The situation is further illustrated in Figure 8.9. All modes for which $k_m = \omega/U_c$ are both resonant and well excited in the band Δk coincident with $\Delta\omega$. By Equation (8.14) and the coincidence condition

$$\begin{aligned} c_p &= U_c \cos \alpha_m \\ &= U_c \frac{k_m}{(k_m^2 + k_n^2)^{1/2}} \end{aligned}$$

which is rewritten

$$\left(k_m - \frac{U_c}{2\kappa c_l}\right)^2 + k_n^2 = \left(\frac{U_c}{2\kappa c_l}\right)^2 \quad (8.24)$$

This relationship defines the condition for coincidence with mode m , and it represents the circle with radius $U_c/2\kappa c_l$ shown in Figure 8.9. The coincident modes are shown by both the intersection of circles in Figure 8.9, or by the cross-hatched region in Figure 8.2. Ffowcs Williams and Lyon⁷ first recognized this significance of coincidence. Their expression for the mean-square velocity results from accounting for separate classes of modes: those which are inside the semicircle (Case C), those at the intersection of circles (Case B), and those outside the semicircle (Case A). Thus the total mean-square response is

*Note that this aspect of flow response is simplified in the case of membrane-like motions for which the phase speed of flexural waves c_m is independent of frequency. Reference to Figure 8.5 will show that in these cases if $U_c = c_m$ there will be hydrodynamically coincident modes at all frequencies.

$$\overline{v^2}(\omega, \Delta\omega) = \sum_{mn}^{\text{HF}} \overline{v_{mn}^2} + \sum_{mn}^{\text{HC}} \overline{v_{mn}^2} + \sum_{mn}^{\text{HS}} \overline{v_{mn}^2}, \quad \omega \leq \omega_h$$

$$= \overline{v_{\text{HF}}^2} + \overline{v_{\text{HC}}^2} + \overline{v_{\text{HS}}^2}$$

where each summation is to be approximated with a wave number integral over the respective annular segment of radius k_p and radial increment

$$\Delta k = \frac{\Delta\omega}{2k_p \kappa c_\ell}$$

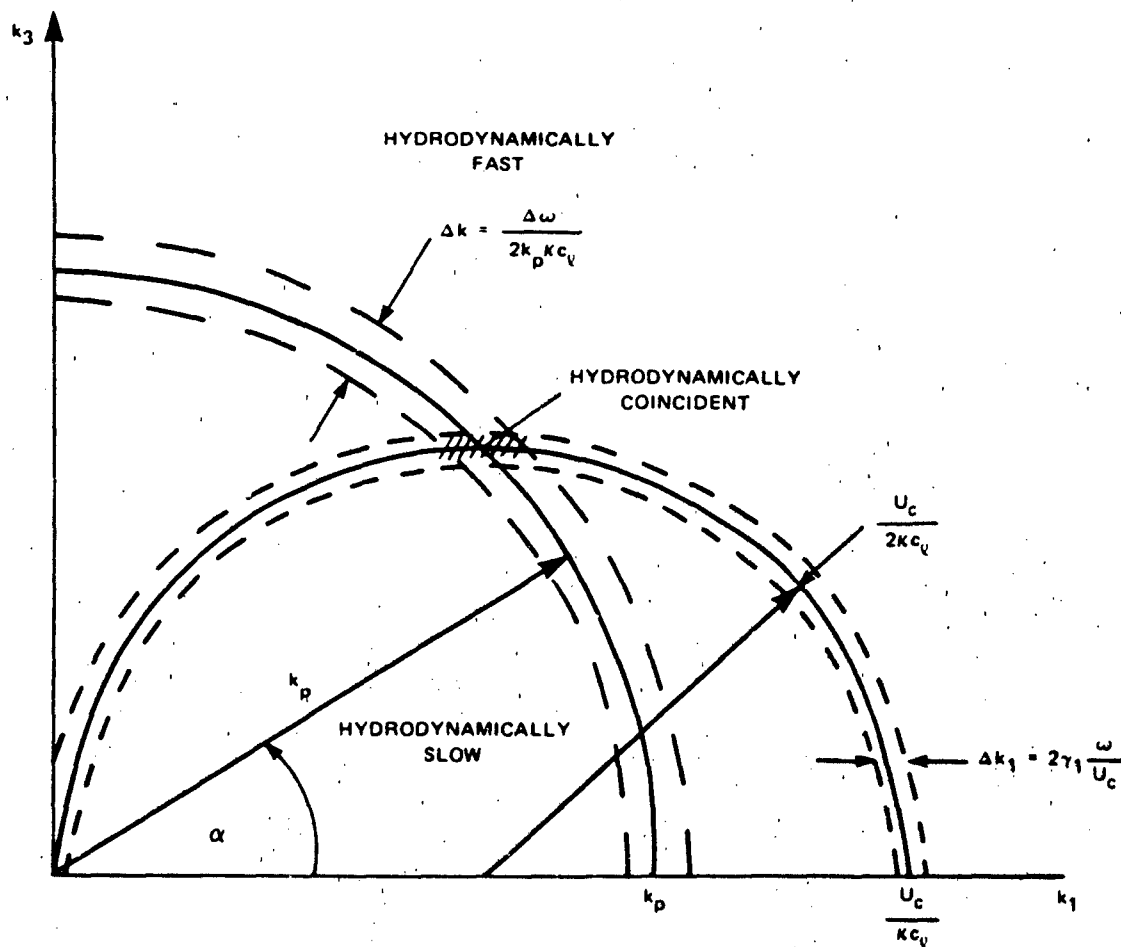


Figure 8.9 - Illustration of Wave Number Bands for Multimodal Response of Flow-Excited Flexural Vibration at Frequencies Below the Hydrodynamic Coincidence Frequency

The intersection of circles that gives the contribution of the coincident modes is given by

$$\alpha = \alpha_m = \cos^{-1} \left(\frac{c_b}{U_c} \right)$$

or

$$\alpha_m = \cos^{-1} \left(\frac{\omega}{\omega_h} \right)^{1/2} \quad (8.25)$$

The mode density in the wave number plane is given by the number of modes per unit wave number area. This is

$$\frac{\Delta N}{\Delta k_1 \Delta k_3} = \frac{1}{\frac{\pi}{L_1} \cdot \frac{\pi}{L_3}} = \frac{A_p}{\pi^2}$$

The summation then includes three terms of the form exemplified by

$$\begin{aligned} \overline{V_{HS}^2} &= \int_0^{\alpha_h} \overline{V_{mn}^2}_{HS} \frac{A_p}{\pi^2} \cdot k \Delta k d\alpha \\ &= \int_0^{\alpha_h} \overline{V_{mn}^2} \left(\frac{A_p}{2\pi^2 \kappa c_l} \right) d\alpha \end{aligned}$$

and similarly for $\overline{V_{HF}^2}$ with $\alpha_h < \alpha < \pi/2$, and for $\overline{V_{HC}^2}$ with $\alpha_m - (\Delta\alpha_m/2) < \alpha < \alpha_m + \Delta\alpha_m/2$. The bandwidth of the coincidence region is, referring to Figure 8.9

$$\Delta k_1 = 2\gamma_1 \frac{\omega}{U_c}$$

$$= \Delta(k_p \cos \alpha_m) = k_p \sin \alpha_m \cdot \Delta\alpha_m$$

that the included angle of the coincidence region is given by

$$\Delta \alpha_m = \frac{2\gamma_1}{\sin \alpha_m} \cdot \frac{c_p}{U_c}$$

s the total mean-square velocity at frequencies below coincidence $\omega < \omega_h$ is a function of the terms

$$\overline{v}_{HS}^2 = \frac{2}{\pi} \frac{\phi_p(\omega) \Delta \omega \delta^{*2}}{\rho_p^2 h^2 \eta_T \omega \kappa c_\ell} \left(\frac{\omega \delta^*}{U_c} \right)^{-2} \frac{\gamma_3 \cdot \gamma_1 \left(\frac{\omega}{\omega_h} \right)^{\frac{1}{2}} \left(1 - \frac{\omega}{\omega_h} \right)^{\frac{1}{2}}}{\gamma_3^2 + \left(1 - \frac{\omega}{\omega_h} \right)}, \quad (8.26a)$$

$$\overline{v}_{HC}^2 = \frac{4}{\pi} \frac{\phi_p(\omega) \Delta \omega \delta^{*2}}{\rho_p^2 h^2 \eta_T \omega \kappa c_\ell} \cdot \left(\frac{\omega}{\omega_h - \omega} \right)^{\frac{1}{2}} \cdot \frac{\gamma_3 \left(\frac{\omega \delta^*}{U_c} \right)^{-2}}{\gamma_3^2 + \left(1 - \frac{\omega}{\omega_h} \right)} \quad (8.26b)$$

$$\overline{v}_{HF}^2 = \frac{2}{\pi} \frac{\phi_p(\omega) \Delta \omega \delta^{*2}}{\rho_p^2 h^2 \eta_T \omega \kappa c_\ell} \left(\frac{\gamma_1 \gamma_3 \left(\frac{\omega \delta^*}{U_c} \right)^{-2}}{\gamma_3^2 + \left(1 - \frac{\omega}{\omega_h} \right)} \right) \cdot \frac{\sin^{-1} \left(\frac{\omega}{\omega_h} \right)^{\frac{1}{2}}}{\gamma_1 + 1} \quad (8.26c)$$

$\omega < \omega_h$. In the limit of $\omega \ll \omega_h$, Equation (8.26b) is the largest, meaning that total response is dominated by whichever modes are hydrodynamically coincident that band. At very low frequencies,

$$\overline{v}^2 (\omega \ll \omega_h, \Delta \omega) = \overline{v}_{HC}^2 (\omega \ll \omega_h, \Delta \omega)$$

$$\overline{v}^2 (\omega \ll \omega_h, \Delta \omega) = \frac{4}{\pi} \frac{\phi_p(\omega) \Delta \omega}{\rho_p^2 h^2 \omega^2 \eta_T} \frac{\gamma_3}{\left(\gamma_3^2 + 1 \right)} \left(\frac{\omega_h}{\omega} \right)^{\frac{1}{2}} \quad (8.27)$$

which is to be compared to Equation (8.22) for the alternative limit at high frequencies. Equation (8.27) shows that the mean-square velocity reduces to

$$\overline{V^2} (\omega < \omega_h, \Delta\omega) \propto \left(\frac{\omega^{-2} \tau_w^2}{\rho_p^2 h^2 \eta_T} \right) \left(\frac{\phi_p \left(\frac{\omega \delta^*}{U_\infty} \right) \frac{\Delta\omega \delta^*}{U_\infty}}{\tau_w^2} \right) \left(\frac{\omega_h}{\omega} \right)^{1/2} \quad (8.28a)$$

or in the range of Equation (8.18), this gives

$$\overline{V^2} (\omega < \omega_h, \Delta\omega) \propto \frac{U_\infty^2}{\eta_T} \left(\frac{\rho_o}{\rho_p} \right)^2 \left(\frac{\delta^*}{h} \right)^{2.5} \left(\frac{U_\infty}{\omega \delta^*} \right)^{2.5} \left(\frac{U_\infty}{c_L} \right)^{0.5} \left(\frac{\Delta\omega}{\omega} \right) C_f^2 \quad (8.28b)$$

which shows that the vibration level can be reduced by mass loading (increasing ρ_p or h) or by damping. Equation (8.22), with Equation (8.19), on the other hand, reduces to the alternate proportionality forms

$$\overline{V^2} (\omega > \omega_h) = \overline{V_{HF}^2} (\omega > \omega_h)$$

$$\overline{V^2} (\omega > \omega_h, \Delta\omega) \propto \frac{\tau_w^2 \omega^{-2}}{\rho_p^2 h^2 \eta_T} \frac{\Delta\omega}{\omega} \left(\frac{\omega_h \delta^*}{U_\infty} \right)^{3-n} \left(\frac{\omega}{\omega_h} \right)^{2-n} \quad \begin{matrix} \omega \gg \omega_h \\ U_c \ll C_p \end{matrix} \quad (8.29a)$$

$$\propto \frac{U_\infty^2}{\eta_T} \left(\frac{\rho_o}{\rho_p} \right)^2 \left(\frac{\delta^*}{h} \right)^3 \left(\frac{U_\infty}{\omega \delta^*} \right)^n \frac{U_\infty}{c_L} \left(\frac{\Delta\omega}{\omega} \right) C_f^2, \quad n = 4 \quad (8.29b)$$

showing that, as with the modal amplitude, the dependence on speed at low speeds is more pronounced than at high speeds. Perhaps closer to the coincidence frequency the wave number spectrum (Equation (7.133)) applies, giving

$$\overline{V_{HF}^2} (\omega > \omega_h, \Delta\omega) \approx \left(\frac{\rho_o}{\rho_p} \right)^2 \frac{U_\infty^6}{\eta_T h^3} C_f^2, \quad (U_c < C_p)$$

is relationship shows a slightly weaker dependence on speed than Equation (8.29b), which is valid at lower frequencies. Now, accounting for the fact that C_f should vary roughly as $U_\infty^{-0.2}$, the dependence on speed at a fixed frequency indicated by these formulae is ($U_c \approx 0.8 U_\infty$)

$$\overline{v}^2 \sim U_\infty^{6.6}$$

$$U_c \ll c_b \text{ or } \omega \gg \omega_h$$

$$\sim U_\infty^{5.6}$$

$$U_c < c_b \text{ or } \omega > \omega_h$$

$$\sim U_\infty^{4.6}$$

$$U_c \gg c_b \text{ or } \omega \ll \omega_h$$

Dimensionless frequency dependence is dominated by Equations (8.22) and (8.27), giving the approximate spectral form shown in Figure 8.10. The break point between $\omega^{-1/2}$ and ω^{-1} is determined by the value of $\omega \delta^*/U_\infty$ for which $\phi_p(\omega)$ changes from $\phi_p(\omega) = \text{constant}$ to $\phi_p(\omega) = \omega^{-1}$. The value of n from Figure 7.46 is $n = 4$. Experimental support for the spectral form is given by measurements of Moore³⁰ and Chang and Leehey,²⁶ whose measurements display much the same character as shown in Figure 8.10.

Evidence for a direct vibration field in panels due to local response to the advecting boundary-layer flow has been experimentally observed by Maestrello²² and Leehey and Davies³² and theoretically examined by Leehey and Davies.³² Cross correlations of flow-induced panel vibration of large panels disclosed a wave component traveling at the speed U_c and superimposed on the reverberant field (which is covered by the above analysis). The condition has been observed both above and below hydrodynamic coincidence. The analysis of Leehey and Davies³² shows that the character of the traveling wave at the speed U_c , disclosed by a cross-spectral density of panel vibration of points separated by r_1 , has an amplitude proportional

$$\phi_{vv}(r_1, 0) \sim \phi_p e^{-\gamma_1 \omega r_1 / U_c}$$

i.e., the decay rate of the vibration matches that of the boundary layer. This component of vibration is present for all frequencies below the fundamental resonance frequency of the panel as well as at higher frequencies. The direct component

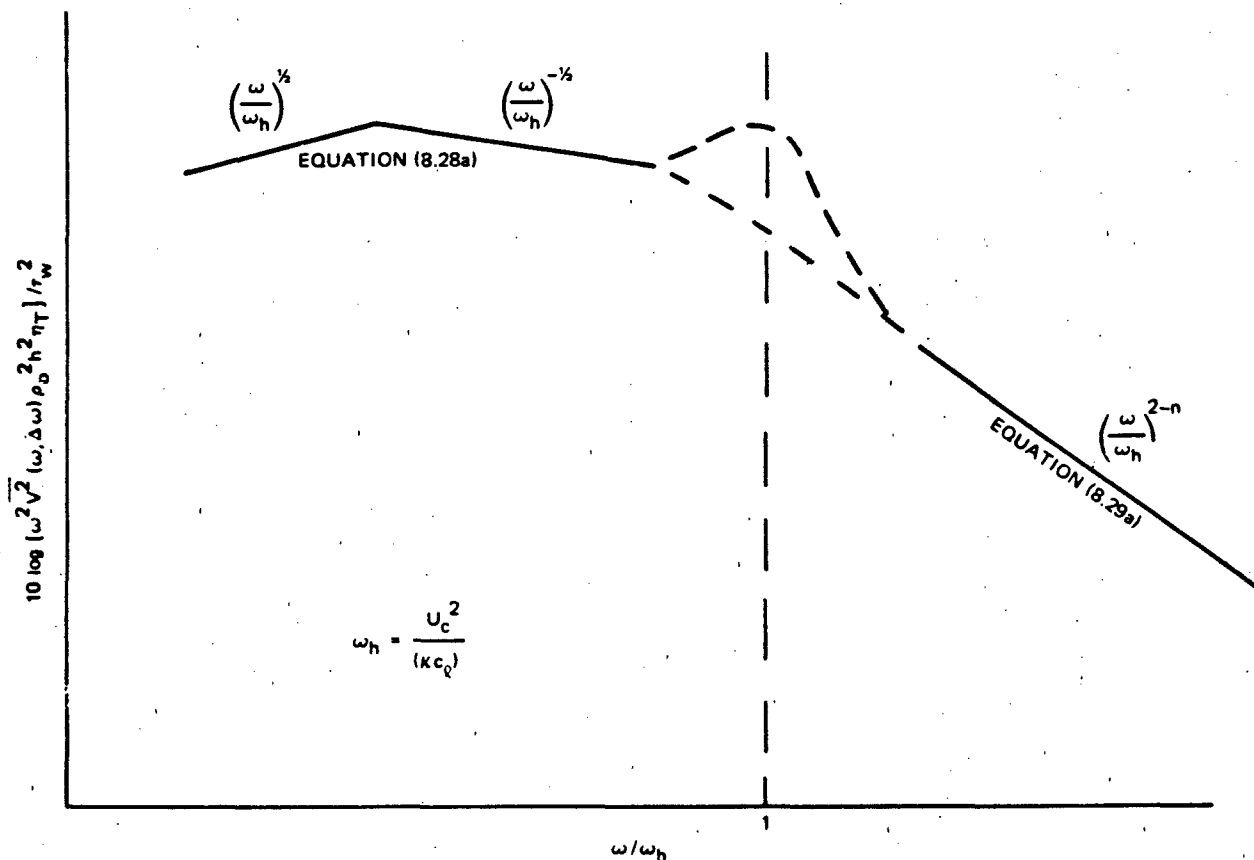


Figure 8.10 - Illustration of the General Theoretical Features of the Frequency Spectrum of Flexural Acceleration ($\omega^2 \phi_{VV}(\omega)$) as Measured in a Proportional Frequency Band, $\Delta\omega \propto \omega$

comes from all lateral modes with resonance frequencies above the frequency in question, while the reverberant response comes from modes with resonance frequencies less than that frequency. The direct response can occur whether or not Dyer's criteria Section 8.2.2 are satisfied by the panel, although the reverberant motion controls the energy in the panel when Dyer's criteria are satisfied.

8.3 SOUND FROM FLOW-INDUCED VIBRATION

The methods of Sections 6.5.3 and 6.5.5 can be applied using the modal and total response velocities to determine modal sound pressures and far-field sound power levels. However, due regard must be paid to the relative importance of hydrodynamically and acoustically coincident modes. It is possible to have simultaneously

hydrodynamically coincident ($U_c > c_b$), and acoustically fast ($k_o > k_p$) modes. For $p < 1$ it is also possible to have hydrodynamically coincident edge and corner modes, the likelihood being more noise from the edge modes (see Figure 8.11). In such cases the radiated sound power in a bandwidth should be carefully evaluated. Therefore, using Equation (6.82) the radiated sound power in a frequency band $\Delta\omega$ is

$$P_{\text{rad}}(\omega, \Delta\omega) \approx \int_{\omega+\Delta\omega/2}^{\omega+\Delta\omega/2} \sum_{\substack{mn \\ \text{modes} \\ \text{in } \Delta\omega}} \pi_{mn}(\omega) d\omega$$

which reduces to

$$P_{\text{rad}}(\omega, \Delta\omega) = \rho_o c_o A_p \sum_{\substack{mn \\ \text{modes} \\ \text{in } \Delta\omega}} \sigma_{mn} \overline{v_{mn}^2}(\omega_{mn}) \quad (8.30)$$

where σ_{mn} is the radiation efficiency of the m,n mode, rather than Equation (6.89b). It follows that Equation (6.89b) results from applications of statistical energy analysis. An independent average mean-square panel velocity and an average mean-square radiation efficiency are used in that approach.

Davies²⁵ has used both calculation methods (Equation (8.30) and (6.89b)) to predict the radiated sound power from thin aerodynamically excited, baffled panels. His calculations are compared to his measurements in Figure 8.12. The measurements were made in a reverberant enclosure around a test section of a subsonic wind tunnel. The panel was mounted in the rigid tunnel wall. The theoretical sound power spectral densities from Equations (8.2) and (8.30) give $\pi_{\text{rad}}(\omega) \Delta\omega = P_{\text{rad}}(\omega, \Delta\omega)$,

$$\pi_{\text{rad}}(\omega) = \frac{\rho_o c_o A_p \pi}{m_s^2 \eta_T \omega} n(\omega) \left(\overline{\sigma_{mn}(\omega)} \overline{\phi_{p_{mn}}(\omega)} \right) \quad (8.31a)$$

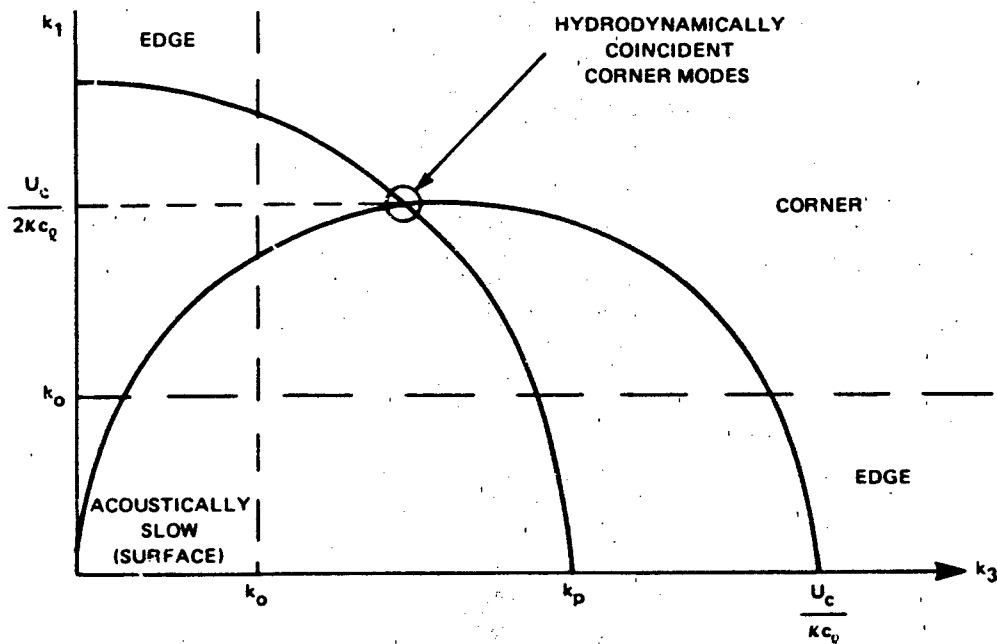


Figure 8.11a - Frequencies Below Hydrodynamic Coincidence in a Typical Aeroacoustic Application for Hydrodynamically Slow Acoustically Slow Edge and Corner Modes. Hydrodynamically Coincident Edge Modes Occur When $U_c/2kc_l \leq k_o \leq U_c/kc_l$

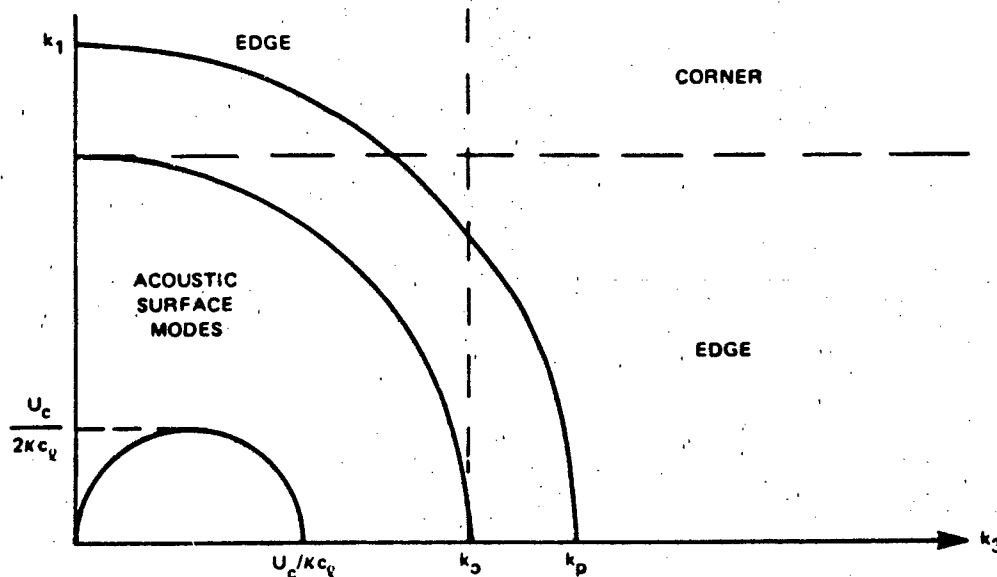


Figure 8.11b - Frequencies Above Hydrodynamic Coincidence in a Typical Hydroacoustic Application of Hydrodynamically Fast-Acoustically Slow Modes

Figure 8.11 - Classifications of Hydrodynamic and Acoustic Mode Types in Various Applications

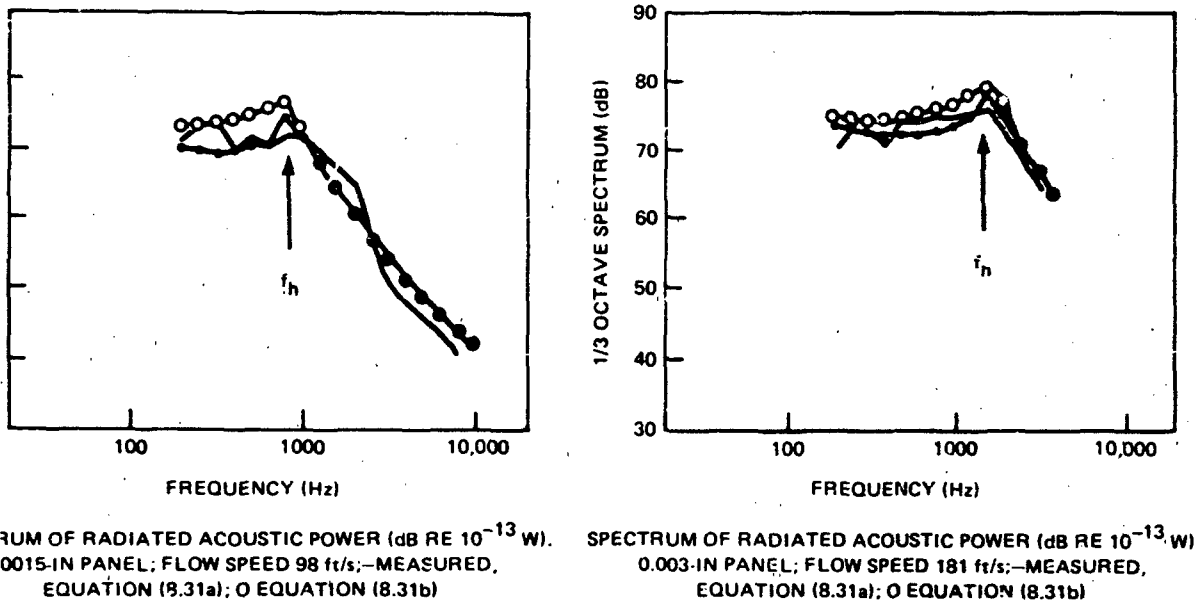


Figure 8.12 - Acoustic Radiation from Thin Panels Beneath an Aerodynamic Boundary Layer²⁵

the alternative estimate (Equation (6.89b)) is

$$\pi_{\text{rad}}(\omega) \approx \frac{\rho_o c_o A_p \pi}{m_s^2 \eta_T \omega} n(\omega) \frac{\sigma}{\phi_{p_{mn}}}(\omega) \quad (8.31b)$$

σ are given in Section 6.5.5 and the vinculae over quantities denote

$$\bar{a} = \frac{1}{n_s(\omega) \Delta\omega} \sum_{\substack{mn \\ \text{modes} \\ \text{in } \Delta\omega}} a_{mn}$$

Figure 8.12 shows measured radiated sound power in one-third octave frequency bands for two panels of area dimensions $L_1 = 0.33$ m and $L_2 = 0.28$ m. These are compared with theoretical estimates that were made using the modal averages in Equations (8.31a) and (8.31b). At frequencies below coincidence, $f < f_h$, the theoretical estimate is independent of the method of modal summation (Equation (8.31a) vice (8.31b)) because some modes are hydrodynamically coincident. However, at higher frequencies

the estimates are not sensitive to summation technique because there is no preferential modal excitation by the boundary-layer pressure at wave numbers $k_1 < \omega/U_c$. Finally, note that the estimates shown in Figure 8.12 utilized measurements, in the same facility, of boundary-layer pressure statistics and measured panel loss factors η_T .

An extensive series of calculations of sound power have also been made by both Maestrello²² and Aupperle and Lambert.¹⁴ Their calculations were performed using the normal mode approach of Chapter 6 and Equation (7.133) for the pressure spectrum. The calculations of Aupperle and Lambert are compared in Figure 8.13 with experimental results of Ludwig¹⁶ obtained in a reverberant chamber. A digital computer was used to calculate the modal summations as given by Equation (8.31a). The difference between theoretical values for the assumed clamped and unclamped panels is due to the effect of the clamping boundary condition on the modal shape function (see Section 6.4). The acoustic coincidence frequency for Ludwig's panels

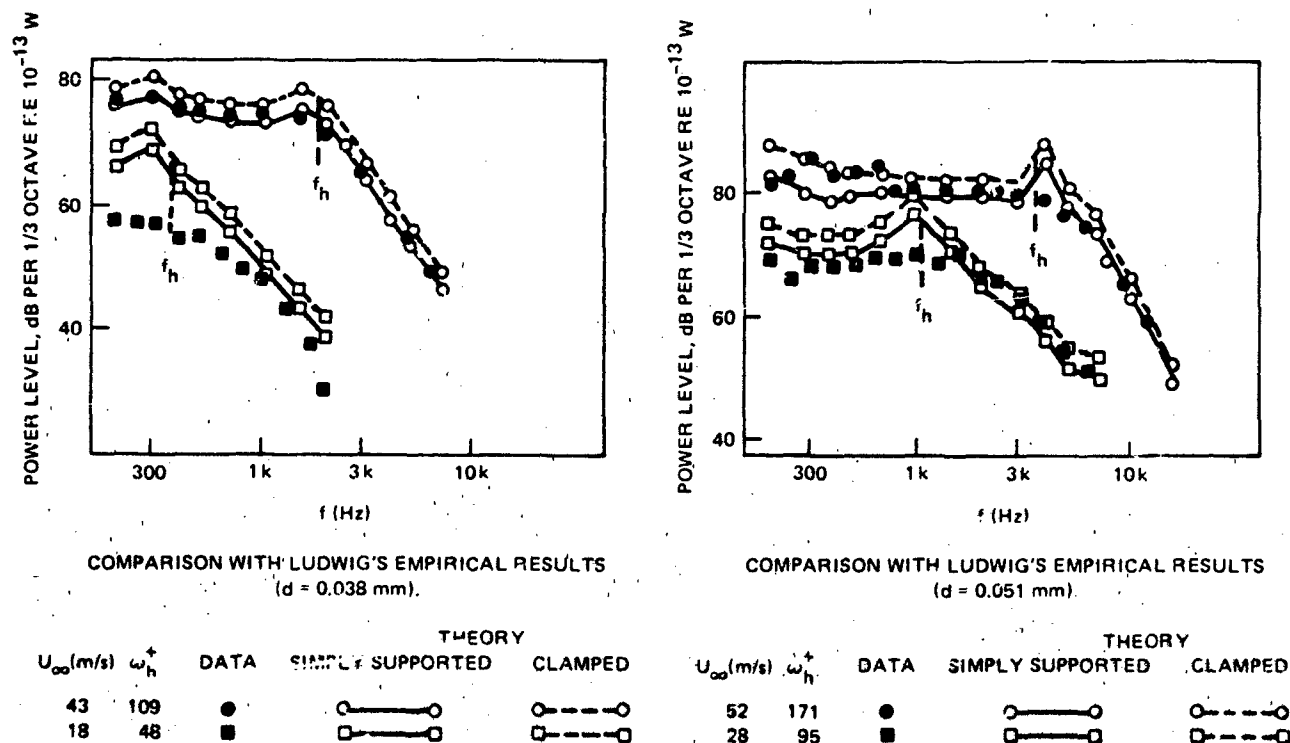


Figure 8.13 - Acoustic Radiation from Thin Panels (with $L_1 = 0.279$ m)
Beneath an Aerodynamic Boundary Layer¹⁴
(Copyright Academic Press)

was calculated at 220,000 Hz; thus the radiation was controlled by edge and corner modes. Theoretical estimates for Ludwig's case had also been successfully performed earlier by White¹² using an analysis similar to that of Aupperle and Lambert. The earliest theoretical work directed at corroborating Ludwig's results was that of Ffowcs-Williams and Lyon,⁷ who were able to predict roughly the observed dependence of sound on speed and panel thickness.

Calculations of flow-induced vibration of a cylindrical pipe were performed by Rattayya and Junger.⁸ The radius of the cylinder was assumed to be much greater than δ . The normal mode analysis was used; the mean-square flexural velocity was determined using the mode density for cylindrical shells.

An extensive summary of computational techniques for predicting flow-induced vibration and noise has been prepared by Leibowitz.¹⁰

The only reported measurements of flow-induced noise and vibration of panels beneath pressure gradients are those of Chang and Leehey.²⁶ In that case

$$\frac{\theta(2+H)}{q} \frac{\partial P}{\partial y_1} \approx 0.0084$$

which, compared to the data in Table 7.2, is a situation with a weak adverse pressure gradient. Estimates of noise and vibration were compared to measurements of those quantities using the methods of Chapter 8 and Equation (7.133). The comparisons were as good as those made in cases involving zero pressure gradients. At frequencies less than the hydrodynamic coincidence frequency, the panel vibration levels were overestimated by the theory by about 7 dB.

8.4 GENERAL RULES FOR HYDROACOUSTIC SIMILARITY AND NOISE CONTROL

In a practical situation, we are interested primarily in vibration as sensed by an accelerometer and either sound pressure level, sensed at some given distance from the noise source, or sound power. The preceding results can be used to provide general rules for flow, acoustic, and structural similitude. These rules may be used to plan scaled model simulations, performance estimations for design modifications, and noise control measures. The two expressions for root-mean-square accelerations ($a^2 = \omega^2 V^2$) may be written from Equations (8.28a) and (8.29a) as

$$\overline{a^2} \propto \frac{\rho_o^2 U_\infty^4}{\rho_p^2 h^2 \eta_T} \left(\frac{U_\infty}{c_\ell} \right)^{\frac{1}{2}} \left(\frac{U_\infty}{\omega \delta^*} \right)^{\frac{1}{2}} \left(\frac{\delta^*}{h} \right)^{\frac{1}{2}} \left(\frac{\Delta \omega}{\omega} \right) C_f^2 \quad \omega \ll \omega_h \quad (8.32a)$$

$$\overline{a^2} \propto \frac{\rho_o^2}{\rho_p^2} \frac{U_\infty^4}{h^2 \eta_T} \left(\frac{U_\infty}{c_\ell} \right) \left(\frac{U_\infty}{\omega \delta^*} \right)^{n-2} \left(\frac{\delta^*}{h} \right) \left(\frac{\Delta \omega}{\omega} \right) C_f^2 \quad \omega \gg \omega_h \quad (8.32b)$$

with values of $\omega_h = 2\pi f_h$ given in Figure 8.6. Both of these show that the acceleration measured in proportional bands conforms to the general behavior

$$\overline{a^2} \propto U_\infty^4 L^{-2} \eta_T^{-1} \left(\frac{\rho_o}{\rho_p} \right)^2 \cdot f \left(\frac{U_\infty}{c_\ell} \right) \cdot g \left(\frac{\omega L}{c_\ell} \right) \cdot h \left(\frac{U_\infty L}{\nu} \right) \quad (8.33)$$

where $f(x)$, $g(y)$, and $h(z)$ are functions of structural Mach number, reduced frequency, and flow Reynolds number for which length L is a conveniently selected linear dimension (plate thickness, model length, etc.).

Vibration control may be achieved by a number of measures indicated by Equations (8.32). Figure 8.14 illustrates for $\omega > \omega_h$ the most important of these for hydroacoustic applications using the notation

$$\Delta L_A = 10 \log \frac{\overline{a^2}}{a_o^2}$$

where variables with subscript o represent the original value of the parameter. Dependence on speed is shown to be the most prominent variable (δ^* assumed constant), while dependence on panel properties is somewhat weaker. Dependence on U_∞ is predicated on an assumed $n = 4$ for $\phi_p(k_1 \ll \omega/U_c, \omega)$. Sound control is discussed later.

Equation (8.33) shows clearly that scaled model similitude can only be achieved when certain parameter ratios are maintained. Reynolds number similarity is required so that the wall-shear coefficient and displacement thickness are in same size ratio as the model and prototype geometries (see Section 7.2). Similarity in the Mach number U_∞/c_ℓ establishes that the effects of hydrodynamic coincidence are

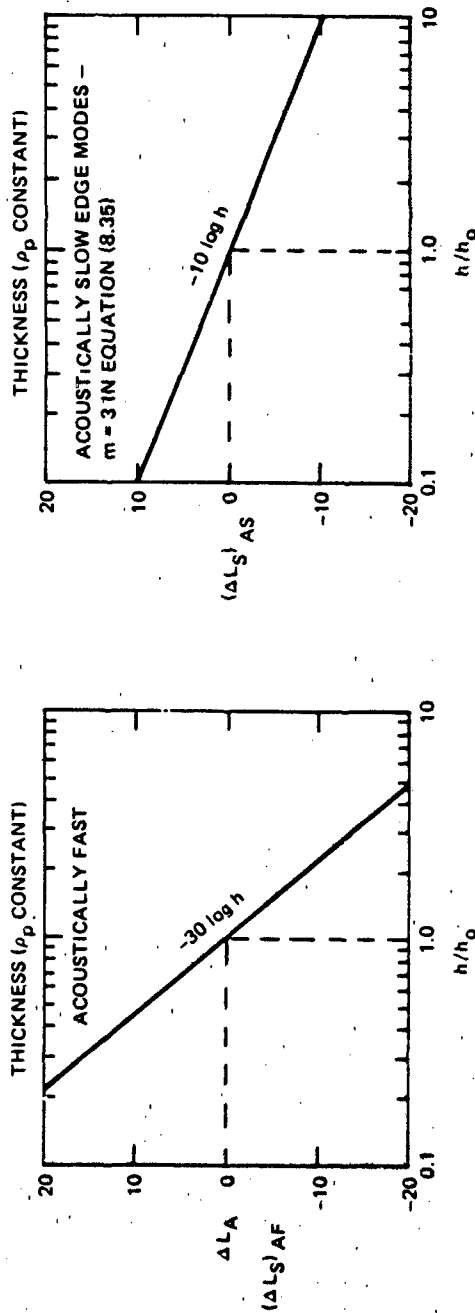
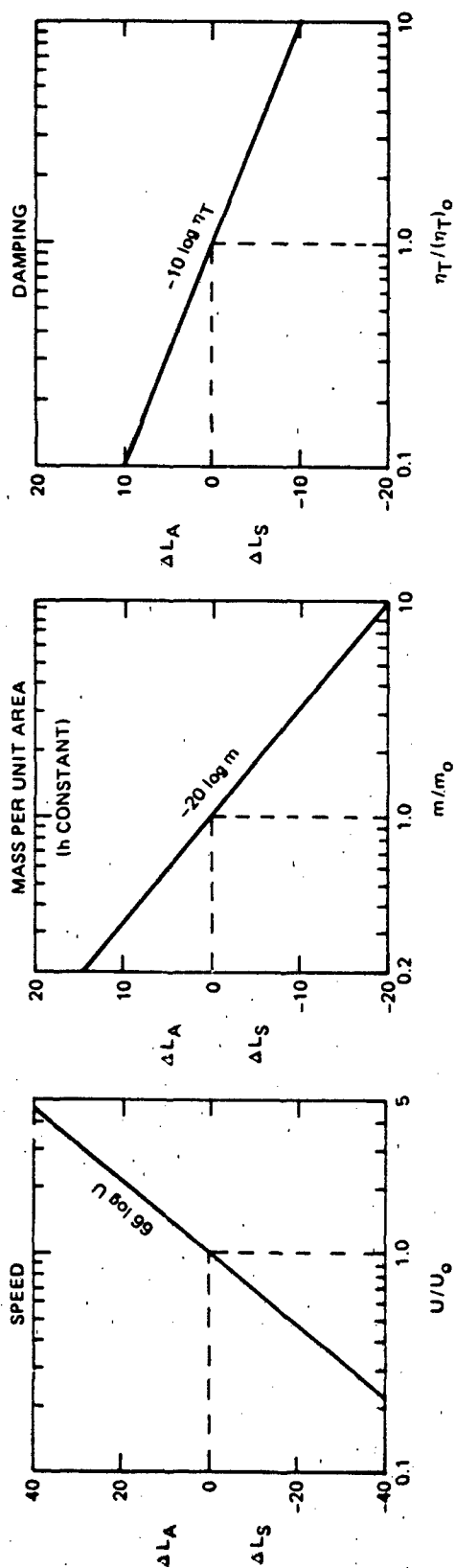


Figure 8.14 - Theoretical Parametric Dependences of Flow-Induced Panel Vibration, L_A , and Sound Radiation L_s when $\omega > \omega_h$. For Acoustically Fast (AF) Bending Modes ($\lambda_b > \lambda_0$), ΔL_s Follows ΔL_A ; for Acoustically Slow (AS) Modes ($\lambda_b < \lambda_0$) ΔL_s Depends Differently on h (e.g., as Edge Modes) but Depends on η_T, m , and U_∞ as for ΔL_A

appropriately simulated, while scaled frequencies ($\omega L/c_l$, $\omega h/c_l$, etc.) establish modal similarity. Except for the effect of Reynolds number similarity, by constructing model and prototype structures of the same materials and operating them at the same velocity, hydroacoustic similitude is maintained. When comparisons are made at scaled frequencies

$$(\omega L)_m = (\omega L)_p$$

problems with explicit flow modeling are largely circumvented, with the possible exception of Reynolds number dependence of the flow. Such dependence may, for example, be important if boundary-layer separation occurs on the model. The Reynolds numbers of model flow will generally be lower in proportion to the geometric scale ratio. Also, damping must be properly simulated in the model, since it linearly controls the resonant acceleration response. According to the above method, when $U_{\infty m} = U_{\infty p}$, $c_{l m} = c_{l p}$, etc., then

$$10 \log \overline{a_p^2} = 10 \log \overline{a_m^2} + 20 \log \frac{L_m}{L_p}$$

$$(\omega L)_m = (\omega L)_p$$

for model (m)-to-prototype (p) scaling.

Sound pressure and sound power levels may be similarly expressed by invoking general representations as used above. Sound power is related to the mean-square velocity (Equations (8.28a) and (8.29a)) through an expression of the form of Equation (8.30),

$$P_{\text{rad}}(\omega, \Delta\omega) = \rho_o c_o A_p \cdot \left[\sigma \left(\frac{\omega L}{c_o} \right) \right] \cdot \overline{v^2}(\omega, \Delta\omega)$$

where $\sigma(\omega L/c_o)$ now represents the fact that the radiation efficiency will be generally dependent on the wavelength of sound relative to a geometric length scale of the body. Furthermore, the sound pressure level, $\overline{p_a^2}$, will depend on $\rho_o c_o$.

the sound power, and the square of a linear dimension, say L^2 , which represents the range distance squared for direct-path radiation for sound in an unbounded medium or the room constant for reverberant radiation in an enclosure. Thus

$$P(\omega, \Delta\omega) \propto \frac{\overline{p_a^2}(\omega, \Delta\omega) L^2}{\rho_o c_o}$$

For sound fields developed in semireverberant enclosures or when the reverberant level has not been assessed, it is best to consider sound pressures at corresponding (scaled) distances.

Accordingly, we may now write the mean-square sound pressure level below the hydrodynamic coincidence

$$P(\omega, \Delta\omega) \propto \left(\frac{\rho_o}{\rho_p}\right)^2 \frac{U_\infty^2 C_f^2}{\eta_T} \left(\frac{\delta^*}{h}\right)^{2.5} \left(\frac{U_\infty}{c_\ell}\right)^{0.5} \left(\frac{\omega \delta^*}{U_\infty}\right)^{-2.5} \left(\frac{\Delta\omega}{\omega}\right) \overline{\sigma}\left(\frac{\omega L}{c_o}, \frac{c_o}{c_\ell}\right) (\rho_o c_o)^2$$

$$\omega \ll \omega_h \quad (8.34a)$$

and above the hydrodynamic coincidence frequency

$$P(\omega, \Delta\omega) \propto \left(\frac{\rho_o}{\rho_p}\right)^2 \frac{U_\infty^2 C_f^2}{\eta_T} \left(\frac{U_\infty}{c_\ell}\right) \left(\frac{\delta^*}{h}\right)^3 \left(\frac{\omega \delta^*}{U_\infty}\right)^{-n} \left(\frac{\Delta\omega}{\omega}\right) \overline{\sigma}\left(\frac{\omega L}{c_o}, \frac{c_o}{c_\ell}\right) (\rho_o c_o)^2$$

$$\omega \gg \omega_h \quad (8.34b)$$

where the value $n = 4$ can be deduced from measurements shown in Figure 7.46. These are relationships corresponding to the acceleration response. In deriving these expressions the proportionality

$$A_p \propto L^2$$

is used. Similar relationships could be derived for the acoustic power by multiplying the pressure squared by $L^2(\rho_o c_o)^{-1}$.

Acoustic similitude also requires that the size of the body and the wavelength of vibration are in proportion to the acoustic wavelength. Thus, by maintaining both the same structural material and the same acoustic medium, the similitude described above can be maintained. Under these conditions we have a very simple relationship between the sound pressure levels of the model and prototype:

$$10 \log (\overline{p_a^2}(\omega, \Delta\omega))_p = 10 \log (\overline{p_a^2}(\omega, \Delta\omega))_m$$

$$(\omega L)_m = (\omega L)_p$$

Possible limitations of Reynolds number dissimilitude in scaling the sound pressures exist as in scaling vibration levels.

The possible importance of fluid loading in connection with vibration similitude has been overlooked. The degree of fluid loading is expressed by the factor $c_o/(\rho_p h \omega)$, which will be a constant when the above requirements of similitude are met. This is especially important when η_{rad} exceeds η'_{mech} , as described in Chapter 6.

Dissimilarity in Reynolds number can be reduced only by increasing the size of the model, under the constraints provided above. If the Reynolds number is large enough, so that the flow is fully turbulent, dissimilarity will not be a serious effect in modeling, because δ^* and C_f are slowly varying functions of Reynolds number.

A more serious deficiency in model testing will often be caused by unavoidable differences in mechanical loss factor. These differences can be caused by details of prototype construction that are not recreated in the model. These details can then influence intercomponent coupling loss factors in complex structures, as well as the boundary conditions of resonant structural members.

The above relationships may be constructively used to estimate possible noise control measures. Consider a composite structure of N_p panels of dimensions L_1, L_2 and thickness h subjected to boundary-layer flow. If we are interested in a hydroacoustic application with $\omega > \omega_h$ and with edge mode radiation, then, from Chapter 6, equations (6.90d) and (6.90e),

$$\bar{\sigma} \propto \frac{(L_1+L_3)}{A_p k_p} \left(\frac{k_o}{k_p} \right)^m \quad m = 2 \text{ to } 3$$

re (ignoring water loading) $k_p = (\omega/\kappa c_\ell)^{1/2}$, and we can write

$$(\omega, \Delta\omega) \propto N_p \left(\frac{\rho_o}{\rho_p} \right)^2 \frac{U_\infty^2 c_f^2}{(\eta_r + \eta_m)} \left(\frac{U_\infty}{c_\ell} \right) \left(\frac{\delta^*}{h} \right)^3 \left(\frac{\omega \delta^*}{U_\infty} \right)^{-n} (\rho_o c_o)^2 \frac{(L_1+L_3)}{A_p k_p} \left(\frac{k_o}{k_p} \right)^m \quad (8.35)$$

the radiated noise in a proportional frequency band ($\Delta\omega/\omega = \text{constant}$).*

The most effective noise control measure is to increase ρ_p , by mass loading, without also increasing Young's modulus. This measure increases the impedance of structure, ρ_p^2 , while also increasing k_p by decreasing c_ℓ . This last measure will reduce $\bar{\sigma}$. Unfortunately, it is not often practical or desirable to increase mass of the radiator. One possible noise control measure that is not acceptable in this case is to add ribbing for the purpose of stiffening. This measure will increase both N_p (the number of separate radiating panels) and therefore the total perimeter $N_p(L_1+L_3)$ of the radiating surface. Accordingly, a removal of stiffeners will reduce the noise. The addition of mechanical damping, η_m , will be effective when $\eta_m \geq \eta_r$. If, as is possible in water, $\eta_r > \eta_m$, then since

$$\eta_r = \frac{\rho_o c_o}{\rho_p h \omega} \cdot \bar{\sigma}$$

addition of stiffeners will have no effect on the sound field because the ratio

$$\frac{\bar{\sigma}}{\eta_m + \eta_r} = \frac{\bar{\sigma}}{\eta_r} = \frac{\rho_p h \omega}{\rho_o c_o} \quad (8.36)$$

will be unaffected by the addition of the stiffeners. A reduction in the relative velocity between the surface and the fluid can reduce the noise by U_∞^7 ($n=4$).

For acoustically fast surface modes, i.e., ω vibration modes for which $\lambda_b > \lambda_o$, and level reductions follow reductions in vibration level. Letting ΔL_s denote decibel reductions,

*Neglecting any interpanel interactions, see ref 27, which could cause selected number transmissions from panel to panel.

$$\Delta L_s = 10 \log \frac{\overline{p_{rad}^2}}{\left(\overline{p_{rad}^2}\right)_o}$$

where $\left(\overline{p_{rad}^2}\right)_o$ denotes the original value,

$$\Delta L_s = \Delta L_A$$

when $\sigma_{rad} = 1$, in Equation (8.34b). Therefore the charts in Figure 8.14 apply to sound reductions of such modes. Acoustically slow bending modes, however, generally radiate as edge modes for which Equation (8.35) applies. This alters the dependence of ΔL_s on thickness h , but otherwise ΔL_s follows ΔL_A .

Other reductions in noise may be brought about by less obvious methods. Reductions in the wall-shear coefficient should effect a proportionate reduction in $\overline{p_a^2}$. Modifications to the flow in order to adjust the spectrum level of wall pressures are perhaps possible, but there exists no systematic method for doing this.

8.5 HISTORICAL NOTES ON MODELING $\Phi_p(\vec{k}, \omega)$

It is of interest to point out some highlights of the evolutionary development of this topic. Prior to the analysis of White¹² in 1966 there had been theoretical work by Maidanik and Lyon⁴⁶ in 1961 as well as the previously mentioned work in 1963 by Ffowcs Williams and Lyon⁷ and Tack and Lambert¹⁷ in 1962. These followed Myer's⁵ analysis, later further formalized by Maidanik,⁴⁷ of the response of plates to random pressure fields. The approach was substantially the same as that used in Chapter 6, except that it was performed in the time and space rather than the frequency and wave number domain. That analysis departed from the one used in this book in the postulations regarding the statistical nature of the pressure field.

Myer assumed a delta function correlation function of the form

$$R_{pp}(\vec{r}, \tau) = A_c \delta(r_1 - U_c \tau) \delta(r_3) \exp\left(-\frac{|\tau|}{\theta_\tau}\right) \quad (8.37)$$

where A_c is a correlation area of the pressure fluctuations.

function models the pressure fluctuations with a life-time θ_τ in a frame of reference moving at U_c . The use of delta-function approximation for convected low excitation functions had been adopted earlier for structural predictions by Lyon.^{18,19} Their use simplifies analysis, but the validity of the results obtained must be restricted to situations in which the acoustic wavelength, structural wavelength, and the size of the structure are all much greater than the spatial integral scales Λ_i of the wall pressure.

The criteria in Section 8.2.1 were essentially the results of Equation (8.37) giving a wave number spectrum, determined by transforming Equation (8.37), using Equation (3.51),

$$\phi_p(\vec{k}, \omega) = \frac{\overline{p^2 A_c}}{4\pi^3} \frac{\theta_\tau}{1 + \theta_\tau^2 (k_1 U_c - \omega)^2} \quad (8.38)$$

This function has all the necessary features to qualitatively match the wave number dependence shown in Figure 7.41; there is a local maximum at $k_1 = \omega/U_c$ and a wave-number-independent function for $k_1 \ll \omega/U_c$, although it has an erroneous frequency dependence. Tack and Lambert, Ffowcs Williams and Lyon, and Rattayya and Junger used this delta-function model for boundary-layer pressure in subsequent work. The constant θ_τ was determined from the moving axis correlation (see, for example, Figure 7.36). Integral correlation lengths of the pressure field were determined from the spatial correlations in narrowbands.¹⁷ The ratio of magnitudes of the spectrum at $k_1 = \omega/U_c$ and that at $k_1 \ll \omega/U_c$ is

$$\frac{\phi_p\left(\omega, k_1 \ll \frac{\omega}{U_c}\right)}{\phi_p\left(\omega, k_1 = \frac{\omega}{U_c}\right)} = \frac{1}{1 + \theta_\tau^2 \omega^2}$$

If $\theta_\tau \approx 5\delta^*/U_\infty$, the ratio at $\omega\delta^*/U_\infty \approx 10$ is

$$10 \log \frac{\phi_p\left(\omega, k_1 \ll \frac{\omega}{U_c}\right)}{\phi_p\left(\omega, k_1 = \frac{\omega}{U_c}\right)} \approx -27$$

Comparison to Figure 7.41 will show that this delta-function model overestimates the pressures at low wave numbers compared to those at wave numbers near $k_1 = k_c$. Furthermore, this simple model gives an ω^{-2} frequency dependence at small values of k_1 , indicating that the discrepancy between Equation (8.38) and the measured values in Figure 7.46 will increase with increasing frequency.

It was recognized by Ffowcs Williams and Lyon⁷ and Lyon¹¹ that an "effective" correlation area rather than the flow correlation area was required to estimate panel vibration for cases in which $c_b > U_c$. The effective area was dependent on the ratio of the bending wavelength to δ^* . In the context of Equation (8.1) this "effective" correlation area was actually the low wave number spectrum evaluated near $k_1 = k_p$; i.e.,

$$\overline{p^2 A_t}(k_p) = 2\pi \cdot \int_0^{2\pi} \int_{-\infty}^{\infty} \phi_p(k_1 = k_p \cos \theta, k_3 < k_p \sin \phi, \omega) d\phi d\omega$$

They evaluated this function using space-time statistics of the convected pressures by using the rough approximations that near $k_1 = \omega/U_c$

$$\phi_p(k_1, k_3, \omega) \approx \phi_1(k_1) \phi_3(k_3) \delta(k_1 U_c - \omega)$$

The function $\phi_1(k_1)$ is taken as the frequency spectrum $\phi_p(\omega/U_c)$; Hodgeson's^{48,49} glider wing results were used to approximate this function. The lateral function was just the Fourier transform of the lateral correlation function assumed to be of the form $\exp(-2|r_3|/\delta^*)$. The correlation area A_t replaced A_c in Equation (8.38) or their analysis.

6 DIRECT RADIATION FROM TURBULENT BOUNDARY LAYERS

The pressure anywhere in the fluid due to a volume of turbulent fluid adjacent to a flat, rigid homogeneous surface is given formally by Equation (7.69). This relationship is the result of Powell's imaging argument discussed in Chapter 2. That the radiation is quadrupole is a conclusion reached by neglecting the surface integral of surface stresses. Phillips^{50,51} reached a similar conclusion, namely,

dipole radiation from incompressible homogeneous turbulent flow on a flat, surface is identically zero. Mawardi⁵² estimated noise from the quadrupole in much the same manner as that for subsonic free shear flows in Section 8.6.1.

Qualitative Analysis of Direct Radiation

8.6.1 Landahl's Argument for Dipole Radiation. Landahl's⁵³ argument concerns the relative magnitudes of the surface and volume integrals in the far field. At distances far from the surface, Equation (7.58) is written

$$p(\vec{x}, t) = -\frac{1}{2\pi c_0^2} \frac{x_i x_j}{r^3} \iiint_V \left[\frac{\partial^2 T_{ij}}{\partial t^2} \right] dV(\vec{y}) +$$

$$\frac{1}{2\pi c_0} \frac{x_i}{r^2} \iint_S \left[\frac{\partial T_{i2}}{\partial t} \right] dS(\vec{y})$$

T_{ij} has been reintroduced, and the theorems derived in Chapter 2 have been

Landahl postulated that in the boundary layer bursting process (see Section 8.6.1), a localized reaction pressure of order $\rho u'^2$ is impressed on the wall, where u' is the velocity fluctuation amplitude during a burst. The horizontal length scale (say, an integral scale) of this pressure is designated as ℓ_H . The time derivatives are on the order of u'/ℓ , where ℓ is the vertical length scale of the bursting zone. Following a short analysis, he found that the first term in Equation (7.58) gives an instantaneous far-field pressure of order $(U_\infty/c_0)^2$ smaller than the second term which he considers a dipole term. The idea has been questioned by⁵⁴ in a more recent analysis which accounts for the phasing of the apparent source terms." The wall shear stresses considered by Landahl would act as a generator of sound energy, thus limiting the magnitude of $\phi_p(k_1 \leq k_0, \omega)$. See also Section 8.6.2.

2.6.1.2 Effects of Slight Surface Curvature. Another possible noise source arises from curvature of the boundary, as discussed by Meecham.⁵⁵ Powell's imaging argument relies on spatial homogeneity of flow on a perfectly flat surface. Meecham argues that finite curvature of a perfectly rigid surface will prevent the surface integrals of the type

$$p_o = \frac{\partial}{\partial x_1} \iint_S \frac{l_1 p \left(y, t - \frac{r}{c_o} \right)}{r} dS(y) \quad (8.40)$$

in Equation (2.62) from canceling as they did in Section 2.4.4. By analogy to the incompressible flow about a large cylinder of radius R , Meecham postulated that the difference between the physical flow and the image flow for an acoustic field should be of the type

$$(\text{physical flow}) - (\text{image flow})$$

$$\left(\frac{\delta}{R} \right) (\text{image flow})$$

where δ is the thickness of the boundary layer. The ratio δ/R is zero in the case of a flat surface. Thus, if the pressure on the interior of the surface in the image flow is of order $\alpha \rho_o U^2$, with the turbulence length scale l , where α is a coefficient, then the difference between the physical and image flows is finite and of the analytical form

$$p_{\text{physical}} - p_{\text{image}} = \frac{1}{r} \cdot \frac{U_\infty}{c_o} \cdot \alpha \rho U_\infty^2 \cdot l \left(\frac{\delta}{R} \right)$$

Therefore, to the quadrupole contribution is added a dipole-like contributor for which the far-field intensity per unit area is

$$I_D = \alpha^2 r^{-2} \rho M^3 U_\infty^3 \left(\frac{\delta}{R} \right)^2 \quad (8.41)$$

is not identically zero except when $R \rightarrow \infty$. The analysis shows that the radiation will also increase with a reduction in the radius of curvature of the surface. The quadrupole component, although indirectly altered by curvature through its effect in the boundary layer, is not directly effected by the curvature. Other calculations of a rotating cylinder and flow over a bump in a wall are worked out in Cham.⁵³

In the limit of very small radius of curvature, say a trailing edge, there is at least a surface discontinuity which, as Powell has shown,³ raises the dipole radiation to greatly exceed the quadrupole. This is discussed in Section 8.6.2 and in greater length in Chapter 9.

3 Efforts at Measuring Direct Radiation. Measurements of flow-induced noise for various types of flows have been attempted. In no case is there a fully satisfactory theory with which to quantify and generalize the results. The measurements of Skudrzyk and Haddle⁵⁶ deal with noise radiated by a roughened rotating disk. That radiation was due to the flow on the disk, as was deduced from the change in noise with roughness.

Radiated noise from smooth and rough rotating disks was reported by Chanaud.⁵⁷ A roughness was applied to the plane of the disk, with a resultant increase in sound radiation compared to the smooth disk. The roughness was a 2-in strip applied to a portion of a 12-in-diameter disk. The increase was observed predominantly in the region $0 < \phi < 60$ deg, where $\phi = 0$ is the plane of the disk. The maximum sound intensity was observed at an angle of 15 deg to 30 deg to the plane of the disk over a frequency range from 3150 Hz to 20,000 Hz. The sound from the rough disk was associated with a standing vortex pattern causing an oscillatory flow around the edge of the disk. The directivity for the smooth disk was nearly $\sin^2 \phi$ -like. The total sound power from the roughened disk was observed to increase as U^6 . This speed dependence is similar to that of the Aeolian tone (see p. 5) and given by Meecham's dimensional analysis above.

Although the radiation was increased by roughness over an entire frequency band ranging from 100 Hz to 20 kHz, the greatest increase was observed for frequencies above 3000 Hz. This frequency can be nondimensionalized on k_g and U_g , as in eq. 7.49. Using the parameters of Chanaud's measurements and the flow characteristics of disks reported by Cham and Head,⁵⁸ it is found that this lower limit

of frequency corresponds to $\omega k_g / U_\tau \approx 4.5$. In Figure 7.49, this frequency is seen to be the lower limit on which the wall pressure spectrum is controlled by roughness variables. This similarity suggests a noise mechanism controlled by flow around the elements. The directivity observed in Chanaud's measurements in this frequency range also suggests a source in the shear stress dipoles. As shown in Equation (2.73) (as well as in Equation (8.39)), the shear stress dipole, being directive in the plane of the surface, has its maximum directivity there. Thus the concentration of sound at angles within 30 deg of the plane of the disk is suggestive of this mechanism.

Another measurement by Barker⁵⁹ utilized a rotating spiral-shaped plate enclosed in a drum. In this program a polymer additive was added to the water in the drum, causing a reduction in the wall pressure spectrum levels of up to 10 dB for frequencies greater than $\omega \delta^*/U \approx 6$, where U is the spiral speed. Sound pressure levels in the tank were observed to decrease over frequencies greater than 1000 Hz for concentrations of 100 and 200 ppmw.

Radiated noise from torpedo-like bodies of revolution has been reported by Lauchle⁶⁰ and by Haddle and Skudrzyk.⁶¹ The latter measurements were made in the far field of a buoyantly propelled vehicle. Speculation that the noise was not due to surface vibration resulted from similar noise levels being observed with both aluminum shell and solid wooden bodies. Lauchle's measurements were conducted on the flat nose of the body of revolution. He used his measurements to postulate an effective noise source located at the zone of laminar to turbulent boundary-layer transition.

Noise from curved surfaces such as those in all the experiments above may be expected simply on the basis of surface nonuniformity, as implied by Meecham's analysis. In addition, the lack of statistical homogeneity of flow near the nose of a body of revolution violates all the analytical requirements that were needed in Chapter 2 to specify simple quadrupole radiation as the sole noise source; i.e., a lack of statistical homogeneity in the surface pressures is certain to enhance the low wave number wall pressures, but whether this increase at wave numbers near k_0 is sufficient enough remains to be established.

8.6.2 Recent Analyses of Direct Radiation

8.6.2.1 Background. In recent years there has been interest in quantifying the direct sound levels to be expected from turbulent boundary layers formed on rigid surfaces. Recall that in Section 2.4.4 this sound was shown to be caused by combinations of a quadrupole system of sources and surface shear stresses, the latter arising from the viscous interaction of the flow with the wall. Furthermore, it was pointed out that noise from the volume distribution of Reynolds stresses would be relatively inefficiently radiated on hard walls compared to flow over soft walls.³ Ffowes Williams⁶² speculated that there is a theoretical possibility of direct radiation from Reynolds stresses in transition zones compared to that in homogeneous boundary layers because of the exponentially growing Tollmein-Schlichting waves in the former zones. This possibility can be readily traced to an enhancement of the low wave number contribution at

$$k_1 \leq k_o \ll \frac{\omega}{c_r}$$

where c_r is the hydrodynamic propagation velocity in the stress tensor that appears in the integral, Equation (7.74). This integral shows that direct radiation or unattenuated propagating pressure disturbances can only occur when $(k_o^2 - k^2)^{1/2}$ is real, i.e., when $k < k_o$. Disturbances that grow exponentially as they propagate are relatively rich in low wave number content compared to disturbances in homogeneous turbulence fields, and those disturbances which are frozen in convection do not possess low wave number components.

Further treatment of transition noise as if from exponentially growing disturbances has been given by Dolgova⁶³ under the hypothetical assumption of the existence of exponentially growing one-dimensional surface pressure waves throughout the entire transition zone. Such pressures in transitional boundary layers have not been observed,^{64,65} at least not within developing boundary layers in small pressure gradients. Furthermore, normal pressures exerted on the surface will only radiate as octupoles (rigid) or quadrupoles (soft), as shown below. These factors suggest that sound radiation from such wall pressures must be negligible.

Acoustic radiation from developed boundary layers was evaluated by Vecchio and Wiley⁶⁶ using a theory that results from the retention of the surface integral over S_o in Equation (2.78), but with zero motion on the boundary and with zero shear stress, $\tau'_{ni} = 0$. The quadrupole contribution was ignored in favor of this surface integral of the normal stresses, $p\delta_{ni}$. The integrals over the outside surface, S_1 , were taken as zero. The use of equations in this form is in direct violation of Powell's reflection theorem for turbulence-generated noise over rigid planar surfaces. In his original paper, Powell warned against such manipulations; the normal stresses, he said, are merely a consequence of the reflections of the volume distribution and should not be considered separately from the quadrupole contribution.

8.6.2.2 Analytical Fundamentals. One way in which the hydrodynamic pressures may be seen to give the radiated sound field is by rewriting the stress tensor, following Lighthill,⁶⁷ as

$$\frac{\partial \rho u_i u_j}{\partial t} = p_{ij} \frac{\partial u_j}{\partial y_k} + p_{jk} \frac{\partial u_i}{\partial y_k} - \frac{\partial}{\partial y_k} (\rho u_i u_j u_k + p_{ik} u_j + p_{jk} u_i) \quad (8.42)$$

The third term is a third-order octupole term that may be ignored in favor of the first two terms. In a shear flow, the first-order term in the right-hand side is

$$\frac{\partial \rho u_1 u_2}{\partial t} = p \frac{\partial U_1}{\partial y_2} \quad (8.43)$$

where p is the fluctuating pressure and $\partial U_1 / \partial y_2$ is the mean velocity gradient. Now, since we are interested in rigid surfaces, $u_n = 0$; Equation (2.81) may be rewritten to give the far-field fluctuating pressure

$$p_a(\vec{x}, t) = \frac{\partial^2}{\partial x_1 \partial x_2} \iiint_{V_o} \frac{\left[T_{12}(\vec{y}, t - \frac{r}{c_o}) + T_{12}(\vec{y}', t - \frac{r'}{c_o}) \right]}{r} dV(\vec{y})$$

where $\vec{y} = y_1, y_2, y_3$ and $\vec{y}' = y_1, -y_2, y_3$. The T_{12} is antisymmetric about $y_2 = 0$, because $u_n = 0$ forces $T_{12}(y_2=0) = 0$. Now, if the thickness of the boundary layer is small compared to both the distance to the field point r and the acoustic wavelength, we can approximate

$$\begin{aligned} [T_{12}] &\approx [T_{12}]_{(y_2=0)} + \left[\frac{\partial T_{12}}{\partial y_2} \right] y_2 \\ &\approx \left[\frac{\partial T_{12}}{\partial y_2} \right] y_2 \end{aligned}$$

so that the far-field pressure becomes

$$p_a(\vec{x}, t) \approx \frac{\partial^2}{\partial x_1 \partial x_2} \iiint_{V_0} \frac{2}{r} \left(\frac{\partial T_{12}(\vec{y}, t - \frac{r}{c_0})}{\partial y_2} \right) y_2 dV(\vec{y})$$

which, by Equation (2.58) (since $y_2 T_{12}(\vec{y}, t) \rightarrow 0$ as $y_2 \rightarrow \infty$), and with Equation (9.43) is

$$\begin{aligned} p_a(\vec{x}, t) &\approx \frac{\cos \theta \sin^2 \theta}{2\pi r c_0} \iiint_{V_0} y_2 \frac{\partial^3 T_{12}}{\partial t^3} \left(\vec{y}, t - \frac{r}{c_0} \right) dV(\vec{y}) \\ &\approx \frac{\cos \theta \sin^2 \theta}{2\pi r c_0} \iiint_{V_0} \frac{dU_1}{dy_2} y_2 \frac{\partial^2 p}{\partial t^2} \left(\vec{y}, t - \frac{r}{c_0} \right) dV(\vec{y}) \end{aligned} \quad (8.44)$$

where the flow (1) direction is parallel to the x axis in Figure 2.1 and ϕ is taken as $\pi/2$. Since the vertical distribution of the boundary-layer pressure is stochastic, the integral cannot be evaluated except perhaps in terms of statistical properties, as outlined in Section 7.3. In any case, in order for acoustic radiation to occur, the boundary-layer pressure field must have non zero contributions in the

in wave number range, $|k| < k_0$, in the sense of Equation (7.74), and the acoustic radiation will still be of the inefficient octupole type (quadrupole over soft surfaces).

6.2.3 Deductions Based on Models of Surface Pressure at $k_1 \leq k_0$. The problem of radiated sound from wall turbulence has also been examined using Equation (7.77) from the standpoint of the wall pressure in the wave number range $|k| \leq k_0$. The frequency spectrum of the mean-square pressure at a point is given by an integral over all $\vec{k} = k_1, k_3$ of the product $|\tilde{p}(k, \omega)|^2$. This involves the singularity $(k_0^2 - k^2)$ as k approaches k_0 that cannot be integrated. Taken at face value, this indicates the existence of a peak of indeterminate level in the wave number spectrum $\phi_p(k_1 = k_0)$, illustrated in Figure 7. The origin of this singularity lies in the assumption of a spatially homogeneous source layer of infinite extent and therefore over infinite volume. Berger⁶⁸ argued that the singularity can be removed through the realization that the physical boundary layer extends over a finite region rather than indefinitely, as assumed by the simple theory. The formal development replaces the complete Fourier transform (over $-\infty < y_1, y_3 < \infty$) appearing in Equation (7.77) with partial transforms extending over $-L_1, -L_3 < y_1, y_3 < L_1, L_3$. The resulting alternative permits integration through $k - k_0$ leading to a value at $|k| = k_0$ relative to that at $|k| = 0$ which is

$$\phi_{pp}(|k| = k_0, \omega) \approx \left(\frac{\omega L}{c_0} \right) \phi_{pp}(|k| = 0, \omega). \quad (8.45)$$

over a range of wave numbers $|k| \delta < c_0/\omega L$ centered on k_0 . The singularity is removed, but it is possible that $\omega L/c_0 \gg 1$, permitting a relatively large spectrum level at incidence. In a more recent paper, Ffowcs Williams⁷³ elucidates more clearly the analytical nature of this apparent singularity.

Other attempts at dealing with the singularity postulate the removal of energy from the acoustic medium either by dissipation^{54,69} or wall compliance.^{3,25,70} The effect of wall compliance interjects a surface integral of finite value that is added to Equation (7.69) (see Equation (2.80)). The surface reacts to pressures generated by T_{ij} so that u_n does not vanish, as previously assumed. The equation for the transformed wall pressure that replaces Equation (7.77) is³

$$\tilde{p}(\vec{k}, \omega) = \int_{-\infty}^{\infty} \frac{Q_{ij}(y_2, \vec{k}, \omega) e^{iy_2(k_o^2 - k^2)^{1/2}}}{\rho_o \omega} dy_2 \cdot \frac{Z_a Z_p}{Z_a + Z_p} \quad (8.46)$$

ere

$$Z_a = \frac{\rho_o \omega}{(k_o^2 - k^2)^{1/2}}$$

the acoustic impedance,

$$Z_p = \frac{m_s \omega^2 (1 - i\eta_T) + k^4 D}{i\omega}$$

the wall impedance, and

$$Q_{ij}(y_2, \vec{k}, \omega) = i \tilde{T}_{ij}(y_2, \vec{k}, \omega) \left[(k_o^2 - k^2)^{1/2} \delta_{i2} + k_i \right] \cdot \left[(k_o^2 - k^2)^{1/2} \delta_{j2} + k_j \right]$$

r a rigid wall, $Z_p \rightarrow \infty$ and Equation (8.46) reverts to Equation (7.74). Equation .46) is derived in the following way: Equations (2.79) and (2.80) are transformed th the use of Equation (7.73); Equation (2.79) gives the surface pressure in terms the normal velocity and the image system of Reynolds stresses. In turn, the rface pressure and the normal velocity are related by Equation (6.21), giving nally the normal velocity in terms of the image system of Reynolds stresses, the oustic impedance, and the plate impedance. Together with the transformed Equa- on (2.79) and the symmetry $Q_{ij}(y_2) = Q_{ij}(-y_2)$, Equation (8.46) results.

Addressing the case of $|k| \rightarrow k_0$ and a mass-controlled boundary impedance, i.e., $m_s \omega \gg Dk_0^4$, we find

$$\phi_{pp}(|k|=k_0, \omega) = \left[1 + \left(\frac{m_s \omega}{\rho_o c_o} \right)^2 \right] \phi_{pp}(|k| \rightarrow 0, \omega) \quad (8.47)$$

alternatively, if the waves in the plate become acoustically coincident, i.e., $k_p = k_0$ or $m_s \omega^2 = Dk_0^4$, we have

$$\phi_{pp}(|k|=k_0=k_p, \omega) = n_T^2 \left[1 + \left(\frac{m_s \omega}{\rho_o c_o} \right)^2 \right] \phi_{pp}(|k|=0, \omega) \quad (8.48)$$

In the above, $\phi_{pp}(|k|=0, \omega)$ is not the value that would be obtained on a hypothetically rigid surface, but rather on the impedance boundary itself, i.e.,

$$\phi_{pp}(|k|=0, \omega) = \left[\phi_{pp}(|k|=0, \omega) \right]_{\text{rigid}} \left(\frac{m_s^2 \omega^2}{\rho_o^2 c_o^2 + m_s^2 \omega^2} \right) \quad (8.49)$$

where $\left[\phi_{pp}(|k|=0, \omega) \right]_{\text{rigid}}$ is given by Equation (7.86b). Therefore, when the surface mass impedance becomes less than of order $\rho_o c_o$, the zero wave number intercept is reduced by the impedance ratio squared. In the limit of $m_s \rightarrow 0$, of course, the boundary is pressure release, i.e., zero pressure fluctuations, and $\phi(\vec{k}, \omega)$ is identically zero for all k . In hydroacoustic applications, the fluid loading factor $\rho_o c_o / m_s \omega$ is often of order unity, so that no singularity can occur at $|k| = k_0$ although there may be some enhancement by a factor of 2 there. This is because for any value of $m_s \omega$ between infinity (rigid) and $\rho_o c_o$ (acoustically transparent) the spectral density of the pressure will vary by at most a factor of 2. If the induced waves in the surface boundary are acoustically coincident, yet the total mechanical damping is small ($n \ll 1$), Equation (8.48) indicates a reduction in the spectrum level.

The spectrum level of wall pressure at $|k| = k_0$ on a mass-controlled impedance boundary may then be written in terms of the $k = 0$ intercept of the spectrum on a rigid boundary in order to emphasize the relative magnitude of the acoustic component:

$$\phi_{pp}(k=k_o, \omega) = \frac{\rho_o^2 \omega^2}{2 c_o^2} \left[\phi_{pp}(|k|=0, \omega) \right]_{\text{rigid}} \quad (8.50)$$

Dissipation in the acoustic impedance, Z_a , arises in the turbulent boundary through fine-grain (high-wave number) Reynolds stresses acting on the large- (low wave number) pressure waves. The attenuation of the sound increases the wall shear and is most pronounced for grazing sound, i.e., when $\vec{k} = k_o$.⁹ has shown that such effects give rise to a change in Z_a in Equation (8.46) at

$$Z_a = \frac{\rho_o \omega}{\left(k_o^2 - k^2 \right)^{1/2} + \left(\frac{k^2 \kappa U_\tau}{2\omega} \right) \alpha_o}$$

(Section 7.2) U_τ is the friction velocity, κ is the von Karman constant (0.4) α_o is a complex factor that depends on the quantity

$$\frac{41\nu\omega}{\kappa^2 U_\tau^2}$$

presence of α_o in the impedance removes the singularity at $k = k_o$. In the range $1 < \omega\delta^*/U_\infty < 10$ and for R_{δ^*} between 10^4 and 10^7 , Howe found that the real part that accounts for attenuation lies between 0.2 and 3.4. The wave number sum of pressures on a rigid surface ($Z_p \rightarrow \infty$) is then⁶⁹

$$\phi_p(|k|=k_o, \omega) = \frac{4}{\kappa^2 \left(\frac{U_\tau}{c_o} \right)^2 R_e(\alpha_o)} \left[\phi_p(|k|=0, \omega) \right]_{\text{rigid}} \quad (8.51)$$

typical values of $U_\tau/U_\infty \approx 0.03$ and $U_\infty/c_o \approx 0.01$ in hydroacoustic applications, Equation (8.51) shows that the introduction of dissipation does not remove the real peak at $|k| \rightarrow k_o$, i.e., the wall impedance dominates the pressure transformation (8.46).

2.4 Some Formulas for Quantitative Estimations of Sound Radiation. The relationship between the surface pressure on a rigid wall beneath the turbulent boundary layer and the radiated sound pressure above it is indirect. The reflection principle (Section 2.4.4) shows that in evaluating the far-field sound one must account only for the secondary waves, as given by the surface pressures, but also the primary waves emanated from the Reynolds stresses as sources. When the surface that supports the boundary layer is planar and rigid, the surface acts simply as a reflector and no special radiated sound component can be identified with the surface pressures alone. Equation (2.81) gives the sound field in this case. It is possible, however, to rewrite Equation (2.81) (or Equation (2.60) with 2π replacing π to account for the pressure doubling caused by specular reflection) in terms of transformed variables, and this was done in Section 3.6.1.

Smol'yakov^{71,72} approached a rough estimation of direct quadrupole radiation essentially in this manner, using a form of dimensional analysis identical to that in Section 2.3.3 and leading to Equation (2.64). The sound intensity averaged over solid angle in the far field was thus represented as

$$\bar{I}(r, \omega) \propto \frac{1}{\rho_0 c_0^5 r^2} \iiint \frac{(\overline{u_1 u_2})^2}{\Lambda} \overline{u_1^2}^2 dv$$

$$\bar{I}(r, \omega) \frac{(4\pi r^2)}{A_p} = \frac{a}{\rho_0 c_0^5} \int_c^\infty \frac{(\overline{u_1 u_2})^2}{\Lambda} \overline{u_1^2} dy_2 \quad (8.52)$$

where $\bar{I}(r, \omega)/A_p$ represents the radiated acoustic intensity per unit area of panel, a is a constant to be determined, and $\Lambda \approx \overline{u_1 u_2} (dU_1/dy_2)^{-1}$ and $\overline{u_1 u_2} \approx \overline{u_1^2}(y_2)$.

The integral in Equation (8.52) was evaluated using empirical relationships for $\overline{u_1^2}(y_2)$ and $U(y_2)$. The integral was repeated for parameters that are appropriate for low-speed jets; using measured values of jet noise intensity and values of the integral so determined, a was evaluated. Applying that value of a to the boundary

, Smol'yakov determined that the pressure spectral density ($\bar{\Phi}_{\text{Prad}}(r, \omega)$) and $-\infty < \omega < \infty$ of sound behaved roughly as

$$\bar{\Phi}_{\text{Prad}}(r, \omega) \frac{4\omega r^2}{A_p} = \frac{\tau_w^{2\delta*}}{U_\infty} M^4 (4 \times 10^{-2}) R_x^{-2/5} \left(\frac{\omega \delta^*}{U_\infty} \right)^{-1} \quad (8.53)$$

$\omega \delta^* / U_\infty < \Omega_2$ where

$$\Omega_1 = 0.35 R_x^{-1/10} \quad \Omega_2 = 1.7 \times 10^3 R_x^{2/5}$$

the spectrum dropping off precipitously outside these limits. The estimate is and subject to the following criticisms: The matching of acoustic and turbulence scales may be dissimilar in boundary layers and jets, the hydroacoustic coupling may depend on the length scale $u_1 u_2 (du_1/dy_2)^{-1}$, and the imaging effect of the surface has not been accounted for. Nevertheless, as we shall see, the levels indicated by equation (8.53) are, practically speaking, negligible for most hydroacoustic calculations.

A variant to the analysis used in Section 3.6.1 may be used to relate the radiated sound pressure to low wave number wall pressures in the range $k_1, k_3 < k_0$. The radiated sound pressure spectrum and the wall pressure spectrum at supertrace wave numbers can be related in an approximate sense to a low wave number sum of the source stress tensor.

To accomplish this, Equation (3.62) can be rewritten in the form

$$\bar{\Phi}_{\text{Prad}}(\vec{x}, \omega) = \frac{1}{4\pi^2} \frac{\omega^4}{c_0^4 r^2} \left[\frac{x_1 x_j x_k x_l}{r^4} \right] (2\pi)^3 A_p \delta \Phi_{ijkl}(|k| \leq k_0, \omega) \quad (8.54)$$

the radiation corresponding to Equation (2.81) and the geometry of a turbulence boundary layer lying in the 1,3 plane. The quantity $A_p \delta$ replaces V_J as the volume of the turbulent region and $\Phi_{ijkl}(|k| \leq k_0, \omega)$ represents a net contribution of all trace wave numbers denoted as k_r in Equation (3.62). Now the (x_i/r) are direction cosines of the field point, all less than or equal to unity. Since we are interested in an upper bound to the boundary-layer radiation, these terms are

ped. The spectrum function $\phi_{ijkl}(\vec{k}, \omega)$ in Equation (8.54) differs from that used surface pressure fluctuations in Section 7.3.1, Equation (7.86a), in that a δ -dimensional wave number spectrum has been used in Equation (8.54).

If it is assumed that the boundary-layer thickness is very small so that $\delta \ll 1$, the correct order of magnitude relationship between $\phi_{ijkl}(\vec{k}_{1,3}, \omega)$ and $\phi_{ijkl}(\vec{k}, \omega)$ is*

$$\phi_{ijkl} = \rho_0^2 \frac{\overline{u_i u_j} \overline{u_k u_l}}{(2\pi)^4} \iiint_0^\delta R_{ijkl}(\vec{r}, \tau) e^{-i(\vec{k} \cdot \vec{r} - \omega \tau)} d^3 r d\tau$$

$$\phi_{ijkl} = \frac{1}{(2\pi)^3} \iiint R_{ijkl}(\vec{r}_{13}, y'_2 - y_2, \tau) e^{-i(\vec{k}_{13} \cdot \vec{r}_{13} - \omega \tau)} d^2 r_{13} d\tau$$

ng

$$\begin{aligned} \phi_{ijkl}(\vec{k}, \omega) &= \frac{\rho_0^2 U_\tau^4}{2\pi} \int_c^\delta \phi_{ijkl}(\vec{k}_{13}, y'_2 - y_2, \omega) e^{-ik_2(y'_2 - y_2)} d(y'_2 - y_2) \\ &= \frac{\rho_0^2 U_\tau^4 \delta}{2\pi} \phi_{ijkl}(\vec{k}_{13}, \omega) \end{aligned} \quad (8.55)$$

e it has been approximated that $\overline{u_i u_j} = U_\tau^2$. Substituting Equation (8.55) into Equation (8.54), we obtain a relationship that parallels Equation (7.86a):

*Note that these relationships are only approximate since the strengths of the olds stresses have been approximated by an average over boundary-layer thick- and correlations between two vertical points have been approximated as depend- crudely on the difference $r_2 = y'_2 - y_2$, also note that wave numbers in the plane he surface are denoted by \vec{k}_{13} .

$$\phi_{\text{P rad}}(r, \omega) \frac{U_{\infty}}{\delta} \approx \frac{\omega^4}{C_0^4} \frac{A_P}{r^2} \rho_0^2 U_{\tau}^4 \delta^3 \left[\frac{\phi_{1jkl}(|k_{13}| \leq k_0, \omega)}{\delta^2} \frac{U_{\infty}}{\delta} \right] \quad (8.56)$$

ctrum function in brackets is dimensionless. Rewriting Equation (7.86a),

$$\phi_{\text{pp}}(\vec{k}_{13}, \omega) \frac{U_{\infty}}{\delta} \approx \rho_0^2 U_{\tau}^4 M_{\infty}^2 \left(\frac{\omega \delta}{U_{\infty}} \right)^2 \delta^2 \left[\frac{\phi_{1jkl}(|k_{13}| \leq k_0, \omega)}{\delta^2} \frac{U_{\infty}}{\delta} \right] \quad (8.57)$$

see that the surface pressure spectrum becomes a measure of the net strength quadrupole source spectrum. Therefore it can be used to estimate the source in Equation (8.56).

seen in Section 7.4.4, experimental evidence for a magnitude of $\phi_{\text{pp}}(\vec{k}_{13}, \omega)$ $|k_{13}| = k_0$ is scant (Figure 7.47), but nonetheless the available measurements represent upper bounds. The representation used in Figure 7.47 has been as a universal spectrum. Accordingly, the spectrum of radiated quadrupole can be written in dimensionless form

$$\frac{\phi_{\text{P rad}}(r, \omega)}{\rho_0 U_{\tau}^4} \frac{U_{\infty}}{\delta^*} \approx \frac{A_P}{r^2} \left[\frac{\omega \delta^*}{U_{\infty}} \right]^2 M^4 \left[\frac{\phi_{\text{pp}}(|k_{13}| \leq k_0, \omega) \frac{U_{\infty}}{\delta}}{\rho_0^2 U_{\tau}^4 M^2 \delta^{*3}} \right] \quad (8.58)$$

he spectrum in brackets is the (assumed universal) function of $\omega \delta^*/U_{\infty}$ given in Figure 7.47. Note that this spectrum function represents the effective quadrupole source strength and that at a given value of $\omega \delta^*/U_{\infty}$ the intensity increases as accordance with basic principles. Equation (8.58), with Figure 7.47, therefore serves as an alternative to Equation (8.53) for estimating direct quadrupole on.

compare the quadrupole radiation with the dipole radiation that would be d from a ribbed structural panel for which Equation (8.15) and (8.31) apply,

$$\frac{\overline{\phi_{p_{rad}}(r, \omega)}}{\rho_o^2 U_\tau^4} = \frac{\pi}{4} \left(\frac{A_p}{r^2} \right) \frac{\eta_r}{\eta_T} \frac{\rho_o c_o}{\rho_p c_l} \frac{(\delta^*)^2}{\kappa h} \left[\frac{\phi_{pp}(|k_{1,3}|=k_p, \omega) \frac{U_\infty}{\delta^*}}{\rho_o^2 U_1^4 \delta^{*2}} \right] \quad (8.59)$$

, as before, $\phi_{pp}(k_{1,3}=k_o, \omega)$ is the wave number frequency spectrum of boundary-pressure evaluated at wave numbers k_p . The spectrum function $\overline{\phi_p}(r, \omega)$ represents a sound pressure averaged over a solid angle in the far field as it has been deduced from arguments involving the total sound power. It therefore represents a bound to the maximum sound pressure that could be observed at high light speeds in the far field.

The quadrupole radiation is apparently dominated by dipole sound whenever any of scattering mechanism (ribs, edges, etc.) is present. Three basic problems examined below to illustrate this dominance of scattering mechanisms at both low and high Mach numbers. Figure 8.15 shows sketches of three conceptual radiators; a thin homogeneous boundary layer on a rigid plate is shown in (a), a planar laminar boundary layer on a ribbed (flexible) structure is shown in (b), and a turbulent boundary layer exiting a rigid half plane is shown in (c). In this third case, which is discussed at length in Chapter 9, the sound is radiated because eddies are convected past a pointed trailing edge. The noise has been called "trailing edge noise." Now, the far-field sound pressure levels for cases (a) and (b) are given in Equations (8.58) and (8.59), respectively. The sound pressure level for trailing edge noise that will be derived in Chapter 9 is (see Equation 8.60).

$$\frac{\overline{\phi_{p_{rad}}(r, \omega)} \frac{U_\infty}{\delta^*}}{\rho_o^2 U_\tau^4} = \frac{1}{4\pi^2} \frac{A_p}{r^2 \gamma_3} \left(\frac{\delta^*}{x_1} \right) M \left[\frac{\phi_{pp}(\omega) \frac{U_\infty}{\delta^*}}{\rho_o^2 U_\tau^4} \right] \quad (8.60)$$

0.8 (given in Section 7.4.1 with the point pressure spectrum $\phi_{pp}(\omega)$). The term (δ^*/x_1) is the ratio of the displacement thickness of the boundary layer to streamwise length of the plate, x_1 . We assume that the boundary layer begins at the leading edge of the plate which is many acoustic wavelengths away and not

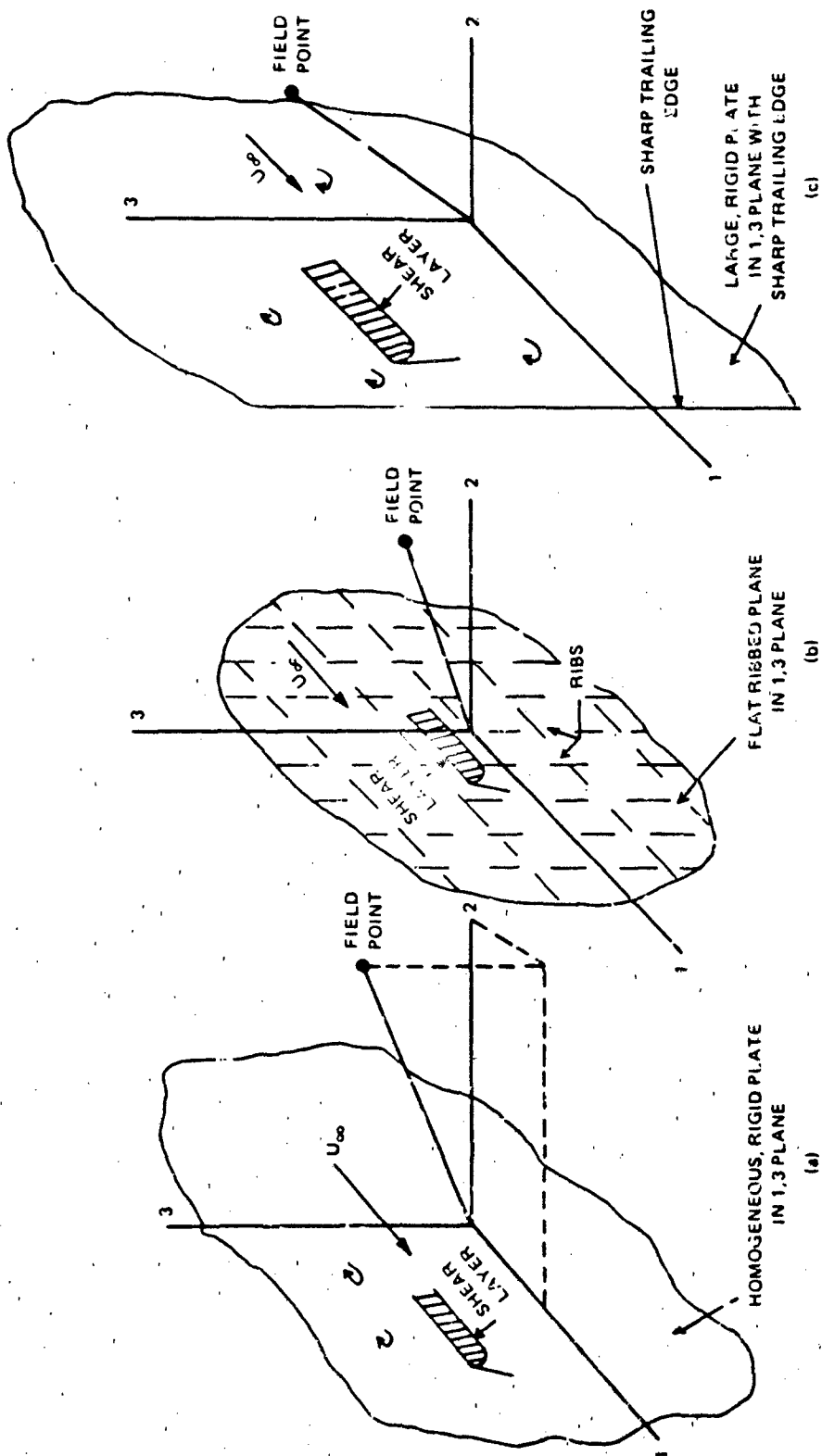


Figure 8.15 - Illustrations of Three Radiation Problems Involving Turbulent Boundary Layers on Planar, or Nearly Planar, Surfaces

exposed to any inflow disturbances that may create additional "leading edge" noise. Therefore δ^*/X_1 is given by Equations (7.34) ($n=9$) and (7.35):

$$\frac{\delta^*}{x_1} = 0.037 R_1^{-1/5}$$

Equation (8.60) gives an average per solid angle in the far field since the directivity factors have been integrated out; in the standard coordinate system with $\phi = \pi/2$ and $\theta = 0$ corresponding to the flow direction,

$$\begin{aligned} \overline{\phi_{\text{P rad}}}(r, \omega) &= \frac{1}{4\pi} \cdot 4 \int_0^\pi d\phi \int_0^\pi d\theta \phi(r, \theta, \phi, \omega) \sin \theta \\ &= \frac{\pi}{8} \left[\phi_{\text{P rad}}(r, \omega) \right]_{\text{maximum in space}} \end{aligned}$$

Figure 8.16 shows the three sound pressure spectra for a low-speed flow referred to a unit panel area, A_p . Equation (8.58) and (8.53) of Smol'yakov are shown for the quadrupole radiation. Recalling that both the edge and vibration-induced levels are averages over a spherical surface in the acoustic far field and that the quadrupole levels represent peak levels occurring at arbitrary points in the far field, we see that the total sound power cannot possibly dominate the other sound components except at the highest frequencies. The discussion also suggests that the acoustic radiation will be dipole whenever finite surfaces are placed in low-velocity flow, not only because these surfaces may generate their own additional turbulence, but also because they provide a mechanism for altering the fundamental noise-producing physics that converts the turbulent energy to acoustic energy. Figure 8.16 further serves to indicate why measurements of direct radiation are likely to be dominated by the particular experimental arrangement, and measurements should probably be viewed as dipole generated rather than quadrupole generated until clearly shown to be otherwise.

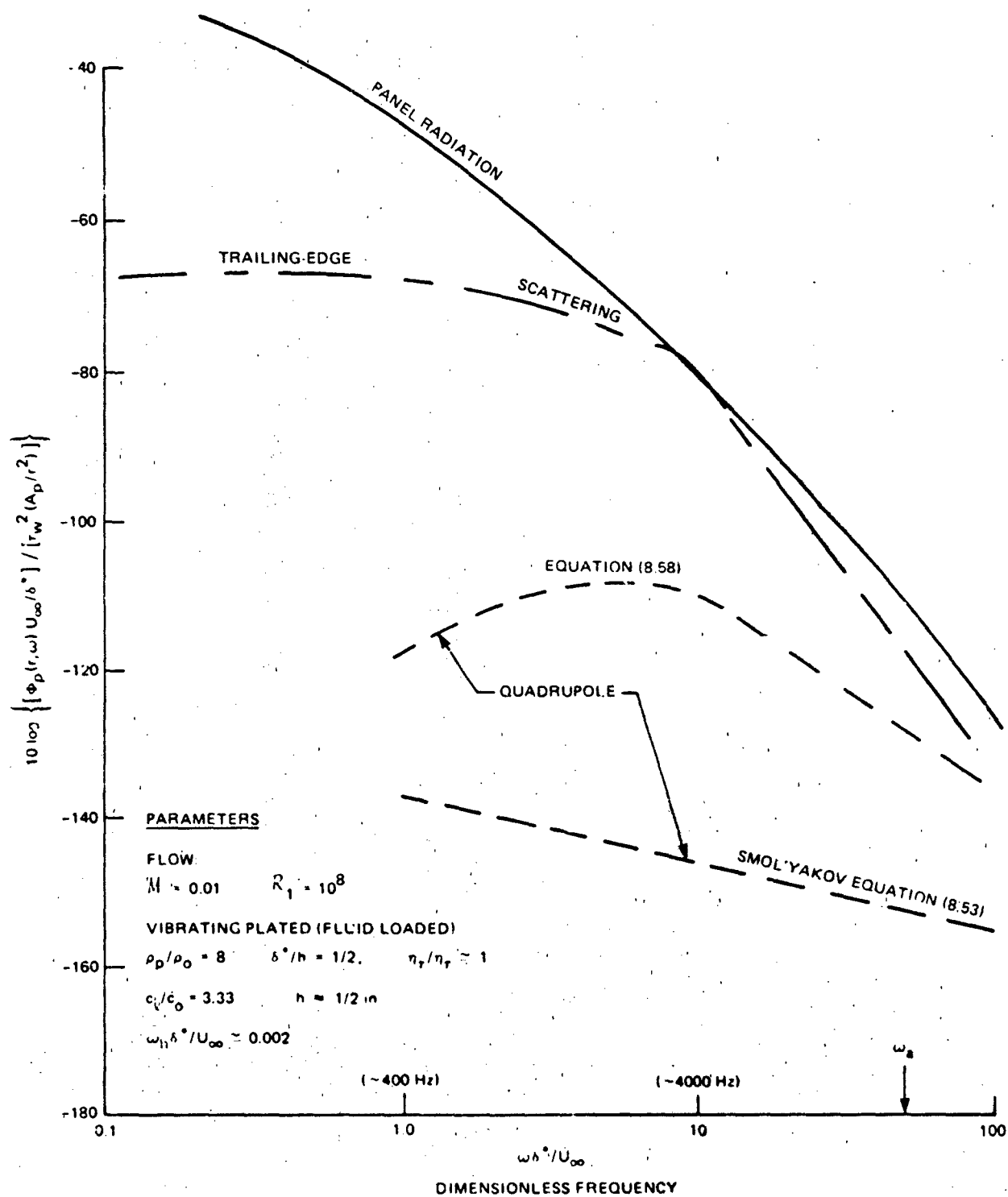


Figure 8.16 - Estimates of Far-Field Acoustic Levels to Be Expected from the Various Boundary-Layer Flows Shown in Figure 8.15. Numbers in Parentheses Denote Approximate Frequencies

A source of inhomogeneity that has not been included in the discussion, but which could, at least conceptually, cause higher levels of direct radiation is afforded by separating and transitional flows. However, these have not been systematically examined from this point of view. If shear stress fluctuations are ignored, the radiation will still be quadrupole, but the level will be enhanced due to some spatial nonuniformity that increases the low wave number pressure.

The example given in Figure 8.16 is intended only as illustrative; it is not indicative of the actual levels to be expected in other more practical arrangements. Differences in circumstances could cause variations of more than ± 10 dB in any of the particular noise levels. However, the relative levels would remain substantially as shown, and, except at moderately high wave number, $k_1 \delta / 10 = k_1 \delta^* > 10$ where the analysis is not valid, the direct radiation is not expected to yield an appreciable contribution.

In higher-speed flows, the quadrupole component can gain in importance, as shown in Figure 8.17. Here, for flows past rigid planes and half-planes, the quadrupole and dipole noise sources can both be important, especially at high frequencies. This importance has been demonstrated in a number of aeroacoustic experiments with wall jets. The next chapter includes examples of measured trailing edge noise from wall jets which may exceed the quadrupole noise of free jets only at low frequencies (e.g., Figure 9.45). Figure 8.17 suggests that this can be the case when $\omega \delta^* / U_\infty$ is less than unity or so. When the flow is bounded by a thin, flexible panel, vibration-induced radiation may be important at low to moderate frequencies, depending of course on the magnitude of the radiation damping relative to the total damping. Figure 8.17 should be regarded only in a qualitative sense, since the actual noise will be dependent on the conditions of the experiment.

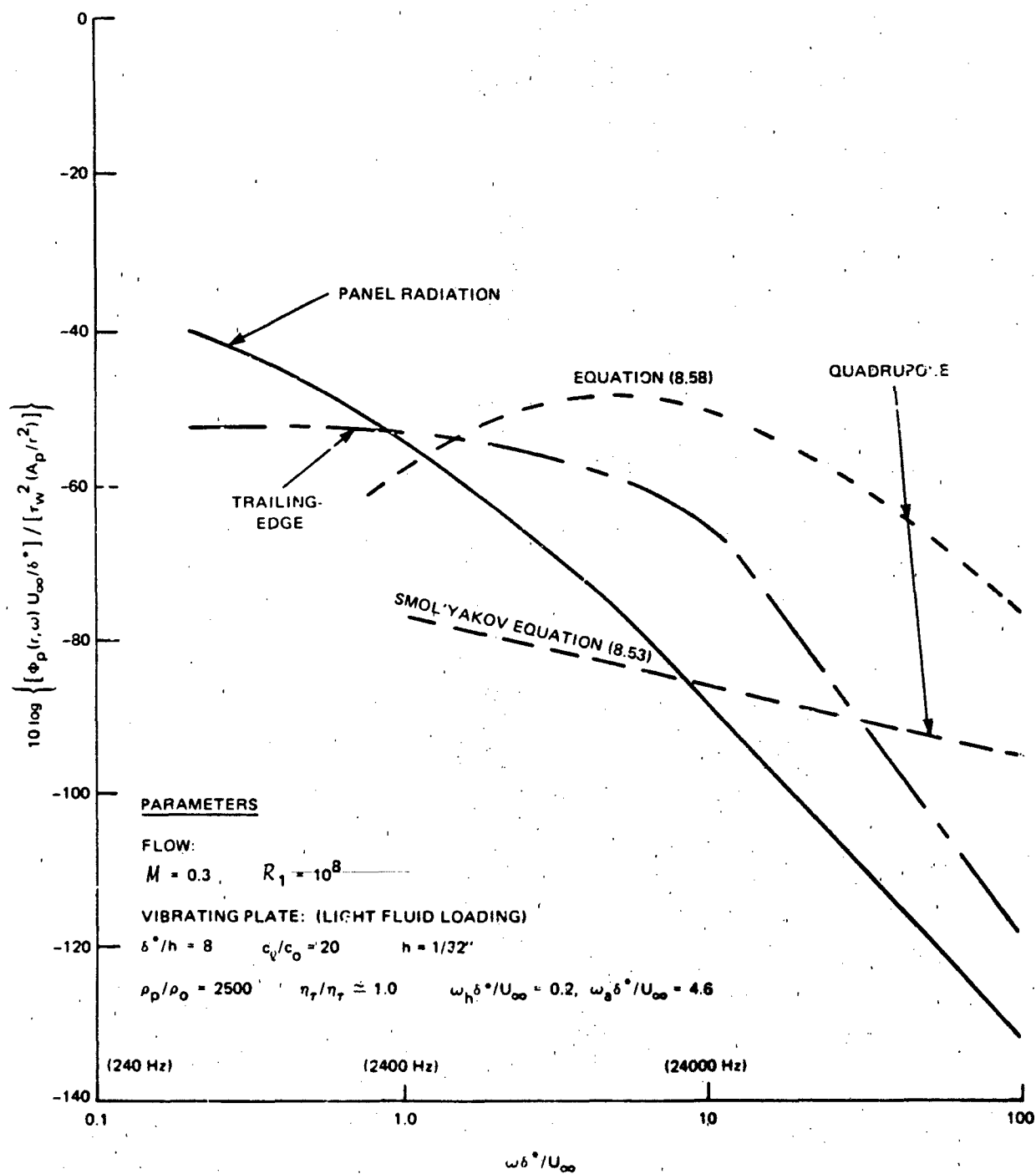


Figure 8.17 - Estimates of Far-Field Acoustic Radiation to Be Expected from the Various Boundary-Layer Flows Shown in Figure 8.15. Numbers in Parentheses Denote Approximate Frequencies

8.7 REFERENCES

1. Powell, A., "Aerodynamic Noise and the Plane Boundary," J. Acoust. Soc. Am., Vol. 32, pp. 982-990 (1960).
2. Ffowcs Williams, J.E., "Sound Radiation from Turbulent Boundary Layers Formed on Compliant Surfaces," J. Fluid Mech., Vol. 22, pp. 347-358 (1965).
3. Powell, A., "On the Aerodynamic Noise of a Rigid Flat Plate Moving at Zero Incidence," J. Acoust. Soc. Am., Vol. 31, pp. 1649-1653 (1959).
4. Kraichnan, R.H., "Noise Transmission from Boundary Layer Pressure Fluctuations," J. Acoust. Soc. Am., Vol. 29, pp. 65-80 (1956).
5. Dyer, I., "Response of Plates to a Decaying and Convecting Random Pressure Field," J. Acoust. Soc. Am., Vol. 31, pp. 922-928 (1959).
6. Phillips, O.M., "On the Generation of Waves by Turbulent Wind," J. Fluid Mech., Vol. 2, pp. 417-445 (1957).
7. Ffowcs Williams, J.E. and R.H. Lyon, "The Sound from Turbulent Flows Near Flexible Boundaries," Bolt Beranek and Newman, Inc., Report 1054 (Aug 1963).
8. Rattayya, J.V. and M.C. Junger, "Flow Excitation of Cylindrical Shells and Associated Coincidence Effects," J. Acoust. Soc. Am., Vol. 36, pp. 878-884 (1964).
9. Cremer, L. et al., "Structure-Borne Sound," Springer-Verlag (1973).
10. Leibowitz, R.C., "Vibroacoustic Response of Turbulence Excited Thin Rectangular Finite Plates in Heavy and Light Fluid Media," J. Sound Vib., Vol. 40, pp. 441-495 (1975).
11. Lyon, R.H., "Boundary Layer Noise Response Simulation with a Sound Field," Acoustical Fatigue in Aerospace Structures, Ch. 10, Syracuse University Press (1965).
12. White, P.H., "Transduction of Boundary Layer Noise by a Rectangular Panel," J. Acoust. Soc. Am., Vol. 40, pp. 1354-1362 (1966).
13. Davies, H.G., "Excitation of Fluid-Loaded Rectangular Plates and Membranes by Turbulent Boundary Layer Flow," ASME Winter Annual Meeting, Paper 70-WA/DE-15 (1970).

14. Aupperle, F.A. and R.F. Lambert, "Acoustic Radiation from Plates Excited by Flow Noise," J. Sound Vib., Vol. 26, pp. 223-245 (1973).
15. Chandiramani, K.L., "Vibration Response of Fluid Loaded Structures to Low-Speed Flow Noise," J. Acoust. Soc. Am., Vol. 61, pp. 1460-1470 (1977).
16. Ludwig, G.R., "An Experimental Investigation of the Sound Generated by Thin Steel Panels Excited by Turbulent Flow (Boundary Layer Noise)," UTIA Report 87, University of Toronto (Nov 1962).
17. Tack, D.H. and R.F. Lambert, "Response of Bars and Plates to Boundary-Layer Turbulence," J. Aero. Sci., Vol. 29, pp. 311-322 (1962).
18. Lyon, R.H., "Propagation of Correlation Functions in Continuous Media," J. Acoust. Soc. Am., Vol. 28, pp. 76-79 (1956).
19. Lyon, R.H., "Response of Strings to Moving Noise Fields," J. Acoust. Soc. Am., Vol. 33, pp. 1606-1609 (1961).
20. el Baroudi, M.Y. et al., "An Experimental Investigation of Turbulence-Excited Panel Vibration and Noise (Boundary Layer Noise)," AGARD Report 465 (1963).
21. el Baroudi, M.Y., "Turbulence-Induced Panel Vibration," UTIAS Report No. 98, University of Toronto (Feb 1964).
22. Maestrello, L., "Measurement of Noise Radiated by Boundary Layer Excited Panels," J. Sound Vib., Vol. 2, pp. 100-115 (1965).
23. Maestrello, L., "Use of Turbulent Model to Calculate the Vibration and Radiation Responses of a Panel with Practical Suggestions for Reducing Sound Level," J. Sound Vib., Vol. 3, pp. 407-448 (1967).
24. Maestrello, L., "Radiation from and Panel Response to a Supersonic Turbulent Boundary Layer," Boeing Flight Sciences Laboratory Report D1-82-0719 (Sep 1968).
25. Davies, H.G., "Sound from Turbulent-Boundary Layer Excited Panels," J. Acoust. Soc. Am., Vol. 49, pp. 878-889 (1971).
26. Chang, Y.M. and P. Leehey, "Vibration of and Acoustic Radiation from a Panel Excited by Adverse Pressure Gradient Flow," MIT Acoustic and Vibration Lab. Report 70208-12 (1976).

27. Chang, Y.M., "Acoustical Radiation from Periodically Stiffened Membrane Excited by Turbulent Boundary Layer," MIT Acoustics and Vibration Lab. Report 70208-11 (1975).
28. Chandiramani, K.L. et al., "Structural Response to In-Flight Acoustic and Aerodynamic Environments," Bolt Beranek and Newman, Inc., Report 1417 (1966).
29. Maestrello, L., "Measurement and Analyses of the Response Field of Turbulent Boundary Layer Excited Panels," J. Sound Vib., Vol. 2, pp. 270-292 (1965).
30. Moore, J.A., "Response of Flexible Panels to Turbulent Boundary Layer Excitation," MIT Acoustics and Vibration Lab. Report 70208-3 (1969).
31. Bhat, W.V. and J.F. Wilby, "Interior Noise Radiated by an Aeroplane Fuselage Subjected to Turbulent Boundary Layer Excitation and Evaluation of Noise Reduction Treatments," J. Sound Vib., Vol. 18, pp. 449-464 (1971).
32. Leehey, P. and H.G. Davies, "The Direct and Reverberant Response of Strings and Membranes to Convecting Random Pressure Fields," J. Sound Vib., Vol. 38, pp. 163-184 (1975).
33. Feit, D., "Flow-Noise Radiation Characteristics of Elastic Plates Excited by Boundary Layer Turbulence," Cambridge Acoustical Associates Report U-279-199 (1968).
34. Ffowcs Williams, J.E., "The Influence of Simple Supports on the Radiation from Turbulent Flow Near a Plane Compliant Surface," J. Fluid Mech., Vol. 26, pp. 641-649 (1966).
35. Crighton, D.G. and J.E. Ffowcs Williams, "Real Space-Time Green's Functions Applied to Plate Vibration Induced by Turbulent Flow," J. Fluid Mech., Vol. 38, pp. 305-313 (1969).
36. Crighton, D.G., "Radiation from Turbulence Near a Composite Flexible Boundary," Proc. Roy. Soc. London, Vol. A.314, pp. 153-173 (1970).
37. Leehey, P., "A Review of Flow Noise Research Related to the Sonar Self-Noise Problem," Arthur D. Little Report 4110366 (1966).
38. Leehey, P., "Trends in Boundary Layer Noise Research," Aerodynamic Noise, Proc. AFOSR-UTIAS Symposium, Toronto (May 1968).

39. Ffowcs Williams, J.E., "Reynolds Stress Near a Flexible Surface Responding to Unsteady Air Flow," Bolt Beranek and Newman, Inc., Report 1138 (1964).
40. Davis, R.E., "On the Turbulent Flow Over a Wavy Boundary," J. Fluid Mech., Vol. 42, pp. 721-731 (1970).
41. Davis, R.E., "On Prediction of the Turbulent Flow over a Wavy Boundary," J. Fluid Mech., Vol. 52, pp. 287-306 (1976).
42. Mercer, A.G., "Turbulent Boundary Layer Flow Over a Flat Plate Vibrating with Transverse Standing Waves," St. Anthony Falls Hydraulic Laboratory, University of Minnesota, Report 41, Ser. B. (1962).
43. Izzo, A.J., "An Experimental Investigation of the Turbulent Characteristics of a Boundary Layer Flow over a Vibrating Plate," General Dynamics Electric Boat Division Report U417-69-049 (1969).
44. Jameson, P.W., "Measurement of the Low-Wave Number Component of Turbulent Boundary Layer Pressure Spectral Density," Proc. 4th Symp. on Turbulence in Liquids (Sep 1975).
45. Martin, N.C., "Wavenumber Filtering by Mechanical Structures," MIT Ph.D. Thesis (Jan 1976).
46. Maidanik, G. and R.H. Lyon, "Response of Strings to Moving Noise Fields," J. Acoust. Soc. Am., Vol. 33, pp. 1606-1609 (1961).
47. Maidanik, G., "Use of Delta Function for the Correlations of Pressure Fields," J. Acoust. Soc. Am., Vol. 33, pp. 1598-1606 (1961).
48. Hodgeson, T.H., "On the Dipole Radiation from a Rigid and Plane Surface," Proc. Purdue Noise Control Conf. (1971).
49. Hodgeson, T.H., "Pressure Fluctuations in Shear-Flow Turbulence," Ph.D. Thesis, Faculty of Eng. Univ., London (1962).
50. Phillips, O.M., "On Aerodynamic Surface Sound From a Plane Turbulent Boundary Layer," Proc. Roy. Soc., Vol. A234, pp. 327-335 (1956).
51. Phillips, O.M., "On Aerodynamic Surface Sound," ARC RM 2099 (Mar 1955).
52. Mawardi, O.K., "On the Spectrum of Noise from Turbulence," J. Acoust. Soc. Am., Vol. 27, pp. 442-445 (1955).

53. Landahl, M.T., "Wave Mechanics of Boundary Layer Turbulence and Noise," J. Acoust. Soc. Am., Vol. 57, pp. 824-831 (1975).
54. Howe, M.S., "The Role of Surface Shear Stress Fluctuations in the Generation of Boundary Layer Noise," J. Sound Vib., Vol. 65, pp. 159-164 (1979).
55. Meecham, W.C., "Surface and Volume Sound from Boundary Layers," J. Acoust. Soc. Am., Vol. 37, pp. 516-522 (1965).
56. Skudrzyk, E.J. and G.P. Haddle, "Noise Production in a Turbulent Boundary Layer by Smooth and Rough Surfaces," J. Acoust. Soc. Am., Vol. 32, pp. 19-34 (1960).
57. Chanaud, R.C., "Experimental Study of Aerodynamic Sound from a Rotating Disk," J. Acoust. Soc. Am., Vol. 45, pp. 392-397 (1969).
58. Cham, T. and M.R. Head, "Turbulent Boundary Layer Flow on a Rotating Disk," J. Fluid Mech., Vol. 37, pp. 129-147 (1969).
59. Barker, S.J., "Radiated Noise from Turbulent Boundary Layers in Dilute Polymer Solutions," Phys. Fluids, Vol. 16, pp. 1387-1393 (1973).
60. Lauchle, G.C., "Noise Generated by Axisymmetric Turbulent Boundary-Layer Flow," J. Acoust. Soc. Am., Vol. 61, pp. 694-703 (1977).
61. Haddle, G.D. and E.J. Skudrzyk, "The Physics of Flow Noise," J. Acoust. Soc. Am., Vol. 46, pp. 130-157 (1969).
62. Ffowcs Williams, J.E., "Flow-Noise," Chapter 6, Underwater Acoustics, Vol. II, V.M. Albers, ed., Plenum Press (1967).
63. Dolgova, I.I., "Sound Field Radiated by a Tollmein-Schlichting Wave," Sov. Phys. Acoust., Vol. 23, pp. 259-260 (1977).
64. DeMetz, F.C. and M.J. Casarella, "An Experimental Study of the Intermittent Properties of the Boundary Layer Pressure Field During Transition on a Flat Plate," NSRDC Report 4140 (Nov 1973).
65. DeMetz, F.C. and M.J. Casarella, "An Experimental Study of the Intermittent Wall Pressure During Natural Transition of a Laminar Boundary Layer," AGARD-NATO Fluid Dynamics Panel, Brussels, Belgium (Sep 1973).
66. Vecchio, E.A. and C.A. Wiley, "Noise Radiated from a Turbulent Boundary Layer," J. Acoust. Soc. Am., Vol. 53, pp. 596-601 (1973).

67. Lighthill, M.J., "On Sound Generated Aerodynamically. II. Turbulence as a Source of Sound," Proc. Roy. Soc., Vol. A222, pp. 1-32 (1957).
68. Bergeron, R.F., "Aerodynamic Sound and the Low-Wave Number Wall-Pressure Spectrum of Nearly Incompressible Boundary Layer Turbulence," J. Acoust. Soc. Am., Vol. 54, pp. 123-133 (1973).
69. Howe, M.S., "The Interaction of Sound with a Low Mach Number Wall Turbulence Shear Flow," J. Sound Vib., Vol. 65, pp. 159-164 (1979).
70. Ffowcs Williams, J.E., "Surface-Pressure Fluctuations Induced by Boundary-Layer Flow at Finite Mach Number," J. Fluid Mech., Vol. 22, pp. 507-519 (1965).
71. Smol'yakov, A.V., "Quadrupole Emission Spectrum of a Plane Turbulent Boundary Layer," Sov. Phys. Acoust., Vol. 19, pp. 165-168 (1973).
72. Smol'yakov, A.V., "Intensity of Sound Radiation from a Turbulent Boundary Layer on a Plate," Sov. Phys. Acoust., Vol. 19, pp. 271-273 (1973).
73. Ffowcs Williams, J.E., "Boundary Layer Pressures and the Corcos Model: A Development to Incorporate Low-Wavenumber Constraints," J. Fluid. Mech., Vol. 125, pp. 9-25 (1982).

CHAPTER 9

THE HYDROACOUSTICS OF NONCAVITATING LIFTING SURFACES

9.1 INTRODUCTION

In many engineering applications, the noise and vibration produced by lifting surfaces dominates all other structural acoustic sources. In contrast to the flow noise of shells and flat surfaces previously discussed, lifting surfaces are not hydrodynamically and acoustically homogeneous. Thus the fluid dynamics of the surface can be complicated by the coexistence of a multiplicity of flow regimes at different sections of the surface. In rotating machinery (fans, propellers, turbines, and the like), the relative velocity between the appropriate solid surface and the fluid is often maximum at the blade tips, making lifting surface noise dominant in systems that include rotating components. In a very real sense this chapter provides the fundamentals for treating the noise of fans and rotors by mechanisms discussed in Chapter 10. Lifting surfaces in general provide important edge effects that influence both the fluid dynamics of the surface and the acoustic radiation efficiency. The surface may not be acoustically compact in that the product of the chord and acoustic wave number may be much larger than unity. In these cases simple formulas for estimating and scaling noise using the simple point-dipole radiation formula (Chapters 2 and 5) are not valid. As a structure, the surface may be a cantilever possessing a particularly low input impedance at the tip and along the leading and trailing edges. Finally, the unstable nature of the shear flow leaving the trailing edge may give rise to a correlated discrete vortex structure that will also be a source of noise and lifting surface vibration.

The general hydroacoustic mechanisms common to all types of lifting surfaces are discussed in this chapter.* Section 9.2 discusses the various sources and their important time and length scales. The implications of these scales in determining the general acoustic aspects of the problem are described, and the resulting speed and directivity dependences are given. Section 9.4 is a review of important aerodynamic characteristics of steady and unsteady boundary-layer and wake flow. In particular, statistical properties of various flow regimes are presented in dimensionless form for later use in quantifying input force representations in the acoustic problems. Sections 9.3 and 9.6 discuss leading- and trailing-edge noise

*Particular characteristics of rotating machinery are discussed in Chapter 10.

from rigid surfaces from various points of view that lead to alternative normalization and scaling relationships. Flow-induced vibration and its effect on the Helmholtz instabilities of trailing-edge flow are discussed in Section 9.7, which also includes the subject of hydrofoil singing.

9.2 FUNDAMENTALS OF LIFTING-SURFACE NOISE

9.2.1 Classifications of Flow Disturbances

The flow environment of the typical lifting surface is illustrated in Figure 9.1. The worst case is depicted; a turbulent flow is incident on the surface and a turbulent boundary layer is convected past the trailing edge. The occurrence of new disturbances in the trailing-edge wake due to shear flow instabilities raises the possibility of additional noise. In real situations any combination of all or some of the sources depicted can occur. The view is from the intersection of a plane $(y_1, y_2, 0)$ with the surface, which is supposed to lie nearly in the $(y_1, 0, y_3)$ plane. The flow field is roughly parallel to the y_1, y_3 plane, except for the effect of finite angle of attack, thickness, and camber. The incident turbulence is regarded as linear superposition of wave harmonics of amplitude u_0 and length scales Λ , where Λ also represents the correlation radius of the ingested eddy, which is presumed to convect at speed U_c and is on the order of $0.9 U_\infty$. The interaction of this turbulence with the lifting surface causes unsteady loading and thus sound. At frequencies high enough that leading and trailing edges are more than an acoustic wavelength apart, this interaction may be localized at the edge, in which case it may be called "leading-edge" noise. To a first approximation, the statistics of the incident turbulence are generally regarded as stationary in time and space, and Taylor's hypothesis of frozen convection (Chapter 3) is assumed for the eddies as the hydrofoil cuts through the turbulent field.

A boundary layer develops on the hydrofoil at the leading edge, and, depending on the angle of attack, the velocity (Reynolds number) of the inflow, and the curvature of the leading edge (affecting the local pressure distribution), the flow may separate there. If this occurs, intense pressure fluctuations with root-mean-square values on the order of 0.1 times the dynamic pressure are likely to occur beneath and just downstream of the separation zone (see Section 7.5.1). Whether or not separation occurs, turbulent boundary-layer flow will totally envelop both sides of the lifting surface when the Reynolds number based on chord is somewhat greater

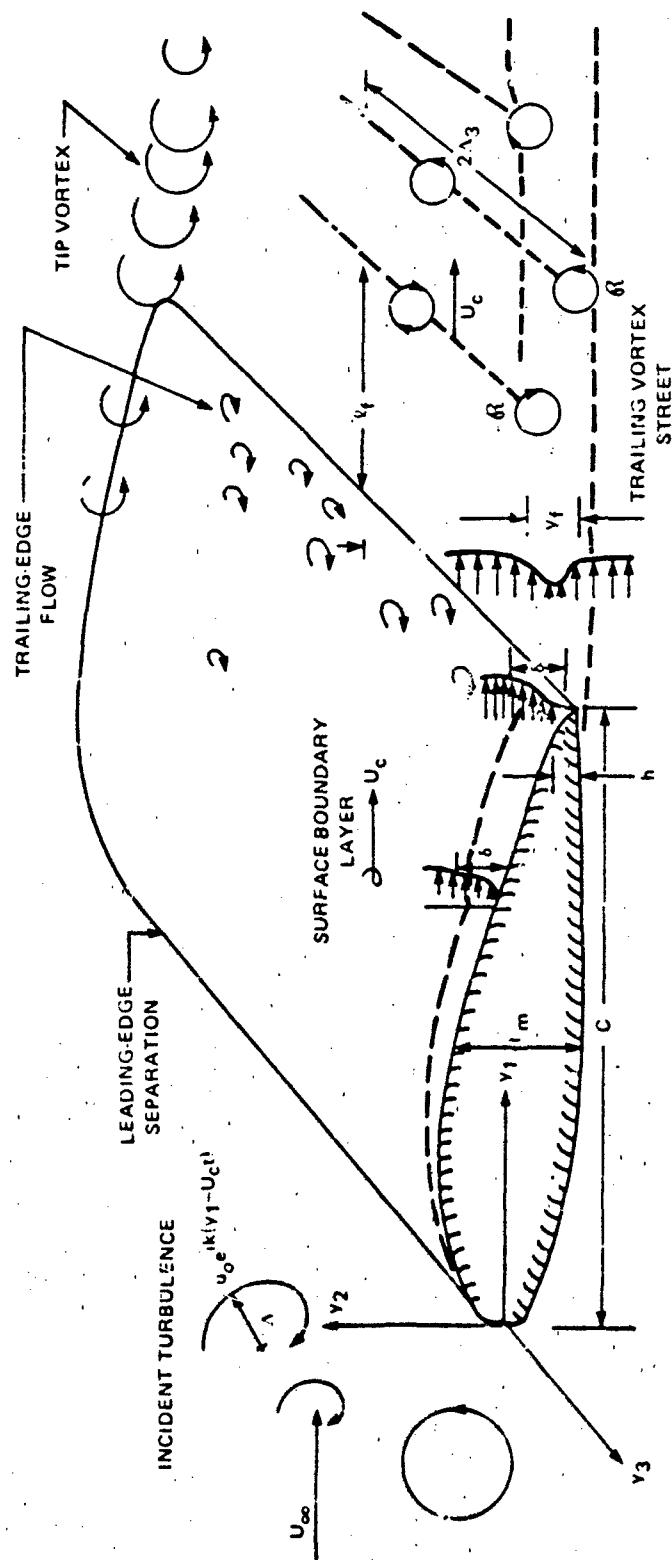


Figure 9.1 - Illustration of Hydrodynamic Sources of Lifting Surface Noise.
Section $(y_1, y_2, 0)$ Is Typical of Sections Existing Along the Span

than a limiting value on the order of 10^6 . Transition is dependent on angle of attack, roughness, upstream turbulence, and chordwise thickness distribution. Because of the convergence of the upper and lower sides of the hydrofoil, the flow decelerates and the associated adverse pressure gradient causes a general thickening of the boundary layer near the trailing edge compared with what it would be on a flat surface at the same Reynolds number. This property depends on the variation of the section thickness, particularly near the trailing edge; the flow may separate and shed vorticity into the wake. Even when turbulent separation or vortex shedding does not occur at the trailing edge, the passage of the turbulence in the boundary layer by the edge generates sound, called "trailing-edge" sound, in the same physical way that leading-edge noise is generated. Trailing-edge noise of this type is most intense with very sharp trailing edges.

At a Reynolds number high enough that turbulent boundary layers occur on the surfaces, the occurrence of tones depends strongly on the geometry of the trailing edge. For certain geometries with or without this separation, the wake of the hydrofoil is a two-sided shear flow with disturbances that are similar to those in the wakes of circular cylinders. The intrinsic instability of these flows often results in the formation of additional vorticity in the wake. This occurs particularly if the location of separation at the edge is well defined (for example, when the edge is blunt). Then the formation of the vortex-street wake is a primary source of tonal vibration and noise. On the other hand, for less blunt, i.e., sharper, trailing edges, the flow separation at the edge may not be as well defined as, for example, on sharp edges at high Reynolds number, in which case the wake vorticity will very likely be disordered. Laminar-flow airfoils (or, say, for Reynolds numbers less than 10^6) with sharp trailing edges often generate ordered vortex streets with high tonal quality. These characteristics are discussed in detail in Sections 9.4 and 9.5.2.

If the ends of the hydrofoil are not embedded in end plates, a tip vortex is also probable. The unsteadiness and strength of the vortex depend on the lift developed by the hydrofoil and its boundary layer.

9.2.2 Characteristic Length and Time Scales for Acoustic and Aerodynamic Classifications

We proceed now to a general discussion of the important time and length scales of the various flow types. These characteristics determine not only aerodynamic

classifications of sources, but also acoustic classifications as well as the theoretical approaches to the treatment of each source with regard to noise estimations. Table 9.1 provides a list of primary sources and a summary of the most general characteristics of each important flow source discussed in this chapter. Thus two general classes of aeroacoustic sources are possible: noise due to turbulence-edge interactions and noise due to vortex-street wakes. The former classification includes both trailing-edge and leading-edge noise; the latter is a trailing-edge phenomenon and is influenced strongly by Reynolds number effects. The aspects of the flow on the hydrofoil controlled by viscosity, e.g., the boundary layer, wake flow, and leading-edge laminar flow, depend on Reynolds number. In some cases, flow-induced forces result in hydrofoil vibration, and this vibration often supports and augments fluid forces because of a phase lock between the fluid and structure motions. The vibration may also increase the noise by creating additional radiation from the surface motion as well as by increasing the magnitudes of the flow-induced forces just mentioned. Whereas the dependence of total sound power on speed is generally quite regular, for example, U_∞^5 to U_∞^6 for rigid surfaces, the dependence is more complicated and is not characterized by simple formulas when surface vibration occurs. A qualitative illustration portraying the relative spectral forms of the types of noise in relation to one another (as if measured with proportional frequency bands) is shown in Figure 9.2. The frequencies are those which would be expected in the far field of a rigid lifting surface advancing into turbulent fluid, for which a specific numerical example is given at the end of the chapter. Separate measurements of leading- and trailing-edge noise was the subject of an experimental program of Olsen.¹

The vortex-street wake flow behind hydrofoils (see Section 9.4.2, is dependent on Reynolds number in much the same fashion as it is behind cylinders. Figure 9.3 shows a collection of flow visualizations in the wakes of lifting surfaces with blunt trailing edges. Figures 9.3a and 9.3b (reference 2) show the effect of angle of attack on the orderly vortex structure downstream of an airfoil for which $U_\infty C/\nu = R_c = 2.3 \times 10^5$ where C is the chord. The surface is thus the "laminar-flow" type, but the general features of the wake share much in common with ordered wakes at larger Reynolds numbers. The photographs illustrate the existence of a dominant structure that can be disorganized by the introduction of both the asymmetry and turbulence that is brought on by increasing the angle of attack. At a 3 deg angle of attack, the disordered boundary-layer flow just upstream of the trailing edge

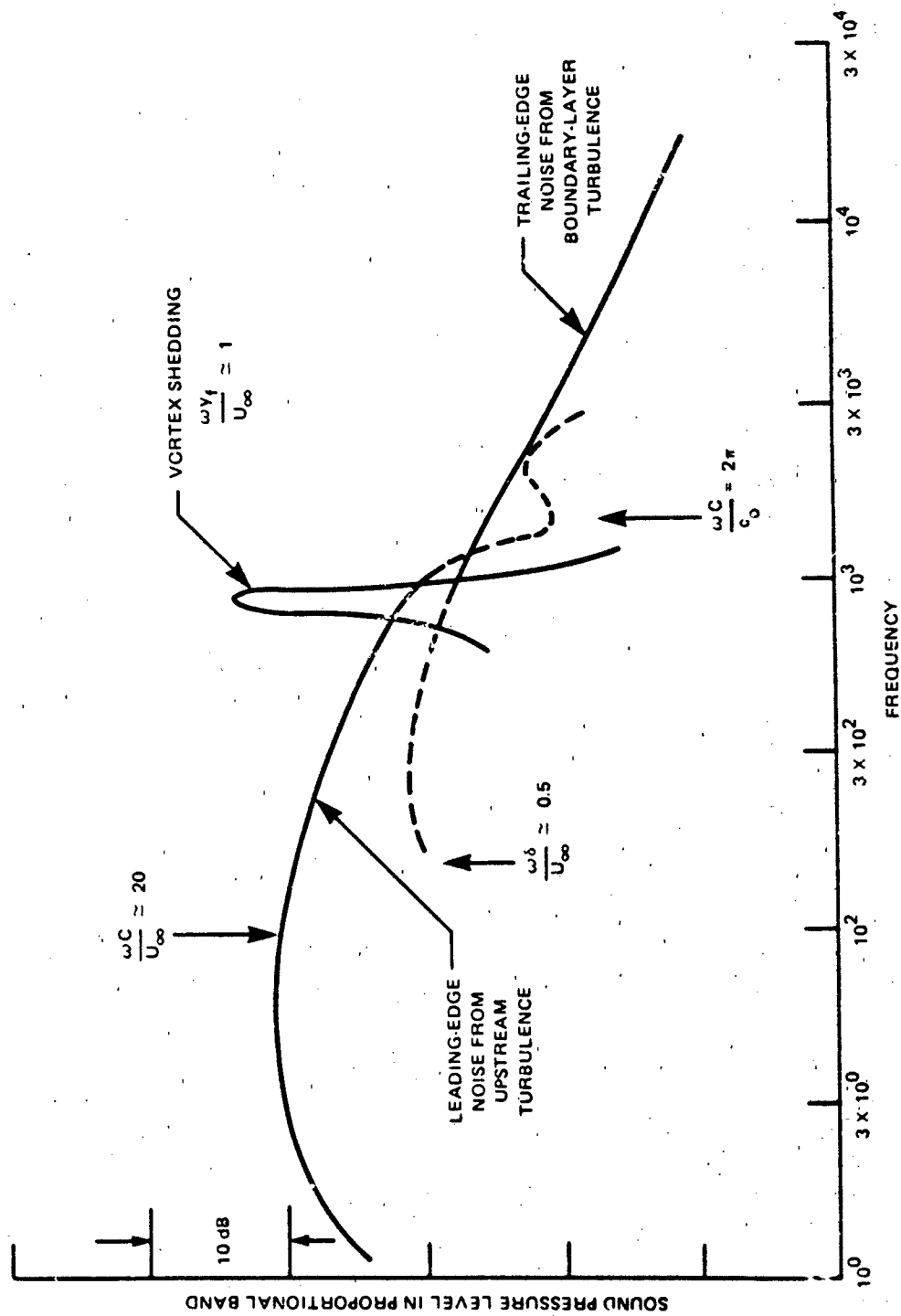


Figure 9.2 - Illustration of Flow-Induced Noises for a Hydrofoil of 3-ft Chord, 0.4-in Trailing Edge Advancing into Turbulent Fluid at 100 ft/s

TABLE 9.1 - PROMINENT HYDROACOUSTICAL SOURCES FOR TRANSLATING HYDROFOILS

Flow Disturbance	Hydrodynamic Characteristic	Acoustical Limitations
Rigid Hydrofoils		
Upstream Turbulence	<p>$\omega C/2U_\infty < 20$ - Flow induces oscillating angle of attack. Leading and trailing edges flow coupled, and the disturbance results in perturbation of the overall lift coefficient. Sections 9.2.3.4, 9.3.1, 9.3.2, 9.3.3, 9.3.4.</p>	<p>$\omega C/c_0 < 2\pi$ - Leading and trailing edges within an acoustic wavelength; simple theory of compact dipole radiation applies. $I \propto U_\infty^6$.</p>
		<p>$\omega C/c_0 > 2\pi$ - Surface behaves as a diffractor. Simple dipole theory not adequate for prediction of power or directivity. $I \propto U_\infty^5$.</p>
	<p>$\omega C/2U_\infty > 20$ - Induces pressure fluctuations local to leading edge; length scales of incident eddies become comparable to leading-edge thickness; practical consequence is an influence on boundary layer growth near the leading edge. Near the trailing edge, noise is dominated more by boundary-layer turbulence. Sections 9.2.3.4, 9.3.2.</p>	<p>$\omega C/c_0 > 2\pi$ - Radiation possible due to compact edge force when the edge radius is less than reciprocal wave number of incident turbulence. $I \propto U_\infty^5$.</p>
Boundary-Layer Turbulence	<p>Broadband in frequency ($\omega \delta/U_\infty < 100$). Turbulence convected past trailing edge becomes effective as edge noise. Practical limit on frequency may be $\omega C/2U_\infty > 10$. Sections 9.6.3.1, 9.6.3.2.</p>	<p>As edge noise source, $\omega \delta/U_\infty > 0.5$, $\omega C/2U_\infty > 10$, $\omega C/c_0 > 2\pi$ otherwise not distinct from other source due to incident turbulence. Here $I \sim U_\infty^5$ and is broadband in frequency and much dependent on edge contour of hydrofoil. Sharp edge is the best radiator.</p>

Trailing-Edge Vortex Shedding

Very dependent on Reynolds number and edge geometry.

a. $R_c < 0$ (10^6) Laminar flow possibly extant on most of the surface. Mechanism of tonal production open to debate but due to hydroacoustic instabilities in wake. Sections 9.4.2, 9.6.2.2.

b. $R_c > 0$ (10^6) Turbulent flow extant on the foil. Near wake of trailing edge most important in establishing tonal character. Trailing-edge geometry influences strength and frequency of formation of wake vorticity. $\omega_f/U_\infty \approx 1$, where y_f relates to shear-layer thickness and roughly of order of trailing-edge thickness. Sections 9.4.2, 9.4.3, 9.5.1, 9.5.2, 9.6.2.

Flexible Hydrofoils

Upstream Turbulence

$\omega C/2U_\infty < 1$ - Induced oscillating lift is maximum, so phase between ingested disturbance and resultant vibration could lead to hydroelastic coupling causing larger or greater forced response. Section 9.7.1.

Radiated sound from forces affected only by change in force magnitude. Additional sound (interfering or reinforcing that from forces) could come from surface motion; no universal speed dependence of noise.

Trailing-Edge Vortex Shedding

Hydroelastic coupling between trailing edge and Helmholtz instability of shear layer resulting in force augmentation. Because $\omega C/2U_\infty > 1$, primary hydroelastic effect of mean flow on vibration is nonlinear damping with small speed-dependent inertial loading. Phenomenon is called singing and often results in fixed frequency over a restricted speed range due to coincidence of resonance with vortex formation. Sections 9.7.1, 9.7.2.

Additional noise from vibration as well as from force augmentation; no universal speed dependence of noise.

Boundary-Layer Turbulence

Little hydroelastic coupling; however, both surface and trailing-edge flow may cause multimodal vibration. Section 9.7.1 and Chapter 8.

Enhanced radiation due to vibration.

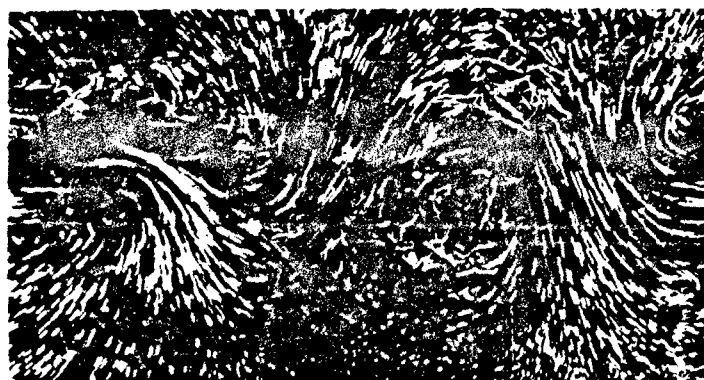
Forces are localized at the trailing edge. For $\omega C/c_0 < 2\pi$ the compact theory applies and $I \propto U_\infty^6$. For $\omega C/c_0 > 2\pi$, edge noise mechanism predominates and $I \propto U_\infty^5$. These exponents apply for $F^2 \propto U_\infty^4$ only.



(a) $\alpha = 0 \text{ deg}$ $R_h = 1.96 \times 10^4$



(b) $\alpha = 3 \text{ deg}$ $R_h = 1.96 \times 10^4$



(c) $\alpha = 0 \text{ deg}$ $R_h = 3.4 \times 10^3$

Figure 9.3 - Photographs of Trailing-Edge Flow Fields.

(a) and (b), Airfoil² $R_c = 2.3 \times 10^5$, $h/C = 0.028$.

(c) Flat Strut, $h/C = 0.24$

(Photographs (a) and (b) taken from Ref. 2, (c) taken from Ref. 3)

(tripped by laminar boundary-layer separation) becomes entrained in the vortex cores, but the geometry of the vortex field does not appear to be greatly influenced by the upstream turbulence. In both cases the frequency of vortex formation ω_s increases nearly linearly with speed in such a way that $\omega_s \approx U_\infty/h$ (increasing slightly with Reynolds number and angle of attack). Figure 9.3c shows another type of visualization as effected by the motions of phosphorescent particles on the surface of a water channel.³ Here the Reynolds number based on the thickness of the trailing edge is somewhat smaller than in the other cases illustrated. These vortices (see Figure 9.1) generally extend only over a spanwise segment $2\Lambda_3$. The noise emanated because of the formation of such orderly vortex streets is generally nearly tonal, as illustrated in Figure 9.2.

In the case of leading-edge-turbulence interactions, the unsteadiness in the inflow induces an angle of attack oscillation on the hydrofoil. The frequency of this oscillation is on the order of $\omega \approx U_\infty/\Lambda$. The response of the flow on the hydrofoil will depend on how well the flow adjusts to this oscillation in angle of attack. Clearly, if Λ is made larger than or on the order of the chord C , then the entire chord will be enveloped by the gust. This condition may be stated as $C/\Lambda \approx 2\pi fC/U_\infty$, or

$$\frac{\omega C}{U_\infty} \ll 1$$

When this condition is met by the incident turbulence, the lifting surface responds as a unit; i.e., the fluid dynamics of both the leading and the trailing edge are not physically separate and the gust will induce both a moment and a lift on the surface. As C/Λ increases, i.e., as the length scale of the incident turbulence decreases in relation to the chord, the response to the disturbances will become more localized near the leading edge. When C/Λ is much greater than unity,

$$\frac{\omega C}{U_\infty} \gg 1$$

the response will begin to diminish with increasing frequency. The study of the unsteady dynamics of hydrofoils in response to incident gusting can be found in texts by Bisplinghoff et al.⁴ and Newman.⁵

Sounds emitted by the interaction of a sharp leading edge with small-scale upstream turbulence or by the interaction of a sharp trailing edge with boundary-layer turbulence or with wall-jet turbulence have many general features in common. In both cases, appreciable sound will be emitted only when the scale Λ of the turbulence is greater than the radius of curvature of the edge. Furthermore, when both $\omega C/2U_\infty > 1$ and $\omega C/c_0 > 1$, as is often the case when such noise has practical importance, the surface may be considered as a half-plane because leading and trailing edges are aerodynamically and acoustically uncoupled.

9.2.3 Low and High Frequency Limits of Theory

9.2.3.1 Statement of the Problem. In Chapter 5 it was seen that the acoustic radiation intensity emanating from a cylinder shedding a vortex-street wake in a moving fluid was very simply expressed in terms of the mean square of the fluctuating force exerted on the cylinder by the fluid. This result, also illustrated in Chapter 2, has general application to any body placed in the flow as long as the dimension of the disturbing body in the flow direction is smaller than an acoustic wavelength. The effect of the cylinder is twofold; it creates a new fluid dynamic disturbance, but as an acoustic effect it behaves as a low-wave-number scatterer, the effect of which may be expressed analytically by replacing the physical cylinder by a distribution of concentrated forces in the fluid that are the result of "hydrodynamic" scattering. In the case of small cylinders, the fluctuating force is simply the unsteady force exerted on the fluid and concentrated in a region very much smaller than an acoustic wavelength. In the case of lifting surfaces, this result has immediate and straightforward application only at low frequencies for which $\omega C/c_0 \ll 1$. At frequencies that are often of practical interest, the acoustic wavelength is shorter than the chord of the lifting surface, i.e., $\omega C/c_0 > 1$, so that the surface is a much more complicated scatterer, and some other analytical formulation must be used. The purpose of this section is to set down the fundamentals that lead to acoustic distinctions such as compact and noncompact chords. This is done in a very idealized way by postulating a local dipole distribution concentrated along a trailing edge. The geometrical effects of extended surfaces were first recognized by Powell⁶; later Ffowcs Williams and Hall⁷ formalized the mathematical treatment of the flow noise of half-planes. The general approach of Ffowcs Williams and Hall is followed here.

We consider the acoustics of lifting surfaces to be governed by the ratio of the chord C to the wavelength λ_a . If $C/\lambda_a < 1$

$$\frac{\omega C}{c_o} < 2\pi$$

and the surface is considered acoustically compact. The problem then reduces to one like that of Section 5.6.3, where we provide an expression for the force in Equations (2.77). This force fluctuation may be due to either ingestion of turbulence in the inflow or to trailing-edge vortex shedding.

In the alternative limit of high frequency

$$\frac{\omega C}{c_o} > 2\pi$$

the leading and trailing edges are at least a wavelength apart, in which case acoustical interference of leading- and trailing-edge noises may occur at specific field points and alter both the directivity and the dependence on Mach number of the sound. Now, when both $\omega C/U_\infty > 1$ and $\omega C/c_o > 2\pi$, the flow-induced noise from the leading and trailing edges approaches independence both hydrodynamically and acoustically. In this class of problems it is useful to consider the leading-edge noise separately from the trailing-edge noise. The latter is likely to be caused by both convection of the boundary-layer eddy field past the edge and the generation of new wake vorticity. If the complication of flow-induced vibration does not exist, the noise from the more nearly homogeneous boundary layer on segments of the surface that are an acoustic wavelength or more from either edge will be minimal. This is because the surface acts as a reflector to quadrupole radiation from the eddy field in the sense of Powell (see Section 2.4.4).

9.2.3.2 General Theory for a Localized Dipole Field. Here we consider scattering effects on the sound from a given source distribution at frequencies $\omega C/U_\infty > 1$ alternately located near surfaces for which $\omega C/c_o \ll 2\pi$ or for which $\omega C/c_o \gg 2\pi$. The acoustic source is assumed to be manifested primarily as a localized dipole caused by the fluid motion. The dipole source may be due to forces exerted on either the edge of a large lifting surface or on an acoustically compact flow

spoiler aligned with the trailing edge of the surface. The dimension of the forcing region is presumed to be smaller than an acoustic wavelength, for example, on the order of a turbulent length scale or the trailing-edge thickness h , as in the case of vortex shedding. We seek to know what difference it makes to the radiated sound field that the source is situated near the large blade surface rather than near cylinders or other acoustically compact bodies. Where vortex shedding in the wake is concerned, for example, hydrodynamic forces are concentrated at the trailing edge⁸ regardless of the value of $\omega C/c_0$. The surface model is a semi-infinite half-plane coincident with the $y_1 < 0, y_2 = 0$ plane, as illustrated in Figure 9.4. This time, rather than aligning the axis of the coordinate system with the axis of the force, it is more convenient to align the axis with the edge of the plate.

A given dipole strength of frequency ω is assumed to be described by

$$F_2(\omega, \vec{y}; t) = F(\vec{y}, \omega) e^{-i\omega t} \quad (9.1)$$

where $F_2(\vec{y}, \omega)$ is the generalized time Fourier transform of the source strength $f(\vec{y}, t)$, for example, the $\rho(\vec{\omega} \times \vec{u})$ of equation 2.87 with a Fourier transform, Equation (2.104). The source concentration is located a distance $y_1 = \ell_0$ downstream of the edge, and it may be distributed over a length $\Delta y_3 = \ell_3$ parallel to the edge. Equation (2.74) with only the dipole source term retained can be put into Helmholtz form (Equation (2.106)); specifically,

$$\nabla^2 P_a(\vec{y}, \omega) + k_0^2 P_a(\vec{y}, \omega) = \frac{\partial F_2(\vec{y}, \omega)}{\partial y_2} \quad (9.2)$$

where $P_a(\vec{y}, \omega)$ is the generalized Fourier transform of the acoustic pressure. The scattering half-plane surface is rigid; thus the normal derivative of the acoustic pressure vanishes, i.e.,

$$\frac{\partial P_a(\vec{y}, \omega)}{\partial y_2} = 0 \quad \theta = \pm \pi \quad (9.3)$$

The Green function for the problem also satisfies Equation (2.113), namely,

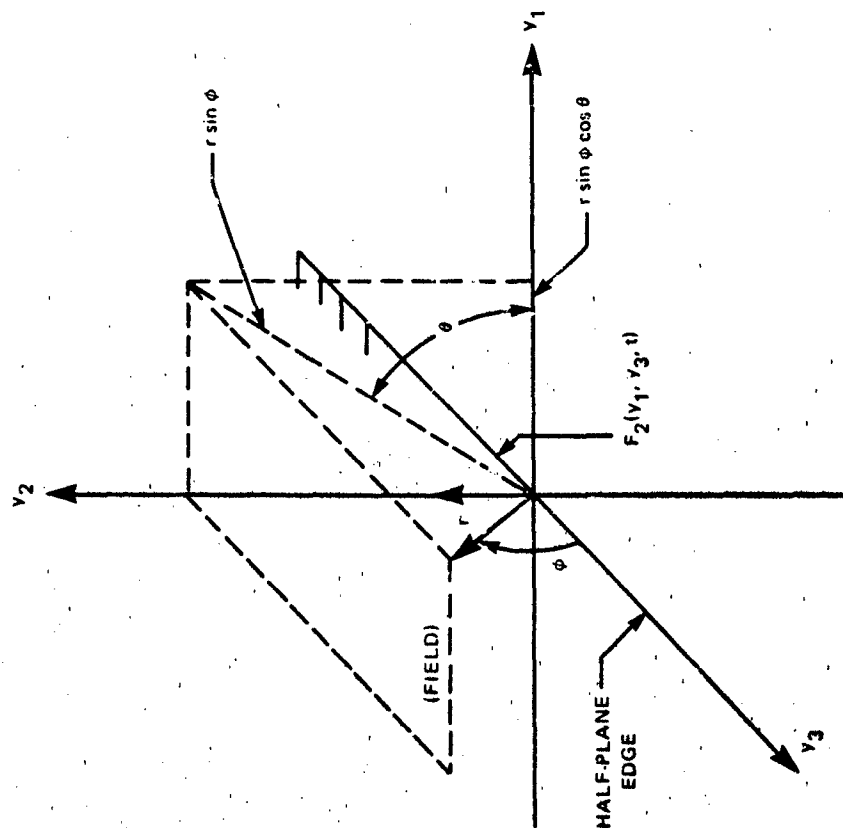


Figure 9.4a - Point Dipole Source Near a Half-Plane;
Case for Which $\omega C/c_0 \gg 1$

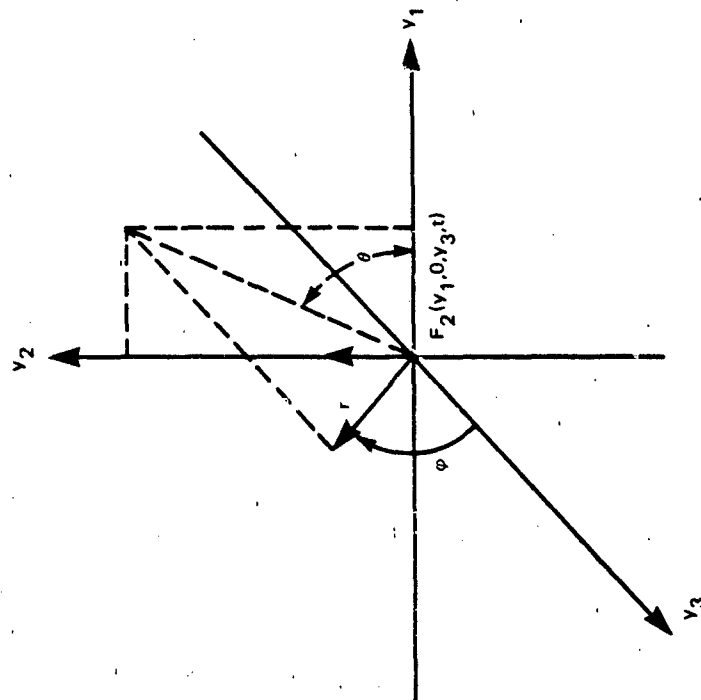


Figure 9.4b - Point Dipole Source in Free
Space; Case for Which $\omega C/c_0 \ll 1$

Figure 9.4 - Surface Geometries for Compact Dipole Sources in Free Space
and Near a Half-Plane

$$\nabla_{\vec{x}}^2 G(\vec{y}, \vec{x}) + k_o^2 G(\vec{y}, \vec{x}) = \delta(\vec{x} - \vec{y}) \quad (9.4)$$

with the boundary condition

$$\frac{\partial G}{\partial n} = \frac{\partial G}{\partial x_2} = 0 \quad \theta = \pm \pi \quad (9.5)$$

This function is given by Ffowcs Williams and Hall⁷ as a specific case of the more general formulations for wedges derived by MacDonald.⁹ Crighton and Leppington¹⁰ have derived the Green function as a special scattering problem by using the Wiener-Hopf technique. Howe¹¹ has used the three-dimensional function in a form valid for sources near the edge and a far-field observation point to derive a two-dimensional function. An extensive survey is given by Bowman et al.¹²

The Green function for the special case of a source near the edge of the plane $\vec{y} = (r_o, \theta_o, \phi_o)$ and a distant field point $\vec{x} = (r, \theta, \phi)$ is

$$G(\vec{x}, \vec{y}, \omega) = \frac{e^{ik_o r}}{4\pi r} \left[1 + \frac{2e^{-i\pi/4}}{\pi^{1/2}} (2k_o r_o \sin \phi_o)^{1/2} \sin \frac{1}{2} \theta_o (\sin \phi)^{1/2} \sin \frac{1}{2} \theta \right]$$

$$k_o r_o \ll 1, k_o r \gg 1 \quad (9.6)$$

The acoustic pressure is given by an analog for Equation (2.115). Following the methods of Chapter 2,

$$P_a(\vec{x}, \omega) = \iiint_V \frac{\partial F_2(\vec{y}, \omega)}{\partial y_2} G(\vec{x}, \vec{y}, \omega) dV(\vec{y}) \quad (9.7a)$$

or

$$P_a(\vec{x}, \omega) = - \iiint_V F_2(\vec{y}, \omega) \frac{\partial G(\vec{x}, \vec{y}, \omega)}{\partial y_2} dV(\vec{y}) \quad (9.7b)$$

This equivalence is insured by the fact that

$$\begin{aligned}
 & \iiint \frac{\partial}{\partial y_2} [F_2(\vec{y}, \omega) G(\vec{x}, \vec{y}, \omega)] dy_1 dy_2 dy_3 \\
 &= \int_{y_1 > 0} \int_{-\infty}^{\infty} F_2(y_1, y_2=0^+, y_3) G(\vec{x}_1, y_1, y_2=0^+, y_3, \omega) dy_1 dy_3 \\
 & - \int_{y_1 > 0} \int_{-\infty}^{\infty} F_2(y_1, y_2=0^-, y_3) G(\vec{x}_1, y_1, y_2=0^-, y_3, \omega) dy_1 dy_3 \\
 &= 0
 \end{aligned}$$

because $F_2(y_1, y_2=0^+, y_3) = F_2(y_1, y_2=0^-, y_3)$ and $\partial G / \partial y_2 = 0$ on the half-plane. The normal derivative of G on the plane is

$$\frac{\partial G}{\partial y_2} = \frac{1}{r_o \sin \phi_o} \frac{\partial G}{\partial \theta_o} \approx \frac{e^{ik_o r}}{4\pi r} \cdot \frac{e^{-i\pi/4}}{2(\pi)^{1/2}} \left(\frac{2k_o}{r_o \sin \phi_o} \right)^{1/2} \sin^{1/2} \phi \cos \frac{\theta_o}{2} \sin \frac{\theta}{2} \quad (9.8)$$

and the localized dipole strength per unit volume can be written

$$F_2(\vec{y}, \omega) = F_2(\omega) 2\Lambda_3 \delta(y_3) \delta(y_2) \delta(y_1 - \ell_o) \quad (9.9)$$

where $F_2(\omega)$ may be equated to the frequency spectrum of a force per unit span, the correlation length along the span is $2\Lambda_3$, and $2k_o \Lambda_3 \ll 1$. This may be done for a dipole source distribution near a surface because the integral of $\rho(\vec{\omega} \times \vec{u})$ over the source volume in such cases represents the net force imparted to the fluid. This force has an equal and opposite reaction directly on the rigid plate and it will be presumed to have an effective location ℓ_o with respect to the edge. Substitution of Equations (9.8) and (9.9) into Equation (9.7b) yields the far-field pressure

$$P_a(\vec{x}, \omega) = \frac{-k_o [F_2(\omega) 2\lambda_3] \sin^{1/2} \phi \sin \frac{\theta}{2} e^{ik_o r}}{4\pi(2\pi)^{1/2} r(k_o \ell_o)^{1/2}} \quad (9.10)$$

where $F_2(\omega) 2\lambda_3$ represents the magnitude of the force, or the net dipole strength. The frequency spectrum of the far-field radiated pressure is proportional to the square of the magnitude of $P_a(\vec{x}, \omega)$ (see, e.g., Equation (2.124) or (3.39)). Furthermore, we assume that the length of the edge is L_3 and that there are $L_3/2\lambda_3$ uncorrelated dipoles per unit spanwise length, each with a frequency spectrum $\phi_f(\omega)$. The autospectral density of far-field acoustic pressure is then the summation over all the uncorrelated contributions from the point dipoles,

$$\phi_{p_{rad}}(\vec{x}, \omega) = \frac{k_o^2 |\sin \phi| \sin^2 \left(\frac{\theta}{2}\right)}{32\pi^3 r^2 (k_o \ell_o)} \cdot \left[\frac{L_3}{\ell_c} \phi_f(\omega) \ell_c^2 \right] \quad (9.11)$$

= (Sound pressure from each local dipole)
 • (Number of dipoles) • (Spectrum level
 of a typical dipole element)

The factor $\phi_f(\omega) \ell_c L_3$ is the spectral density of the net mean-square dipole strength exerted on the fluid and $\ell_c = 2\lambda_3$.

In an identical manner we can find the radiated sound pressure from the same distribution of point dipoles, but now in free space where scattering boundaries are absent. This dipole distribution is still synonymous with a force distribution. Invoking Equation (2.110) and the free-space Green function Equation (2.108) (or just using Equation (2.77) directly), the spectrum of the radiated sound pressure is

$$\left[\phi_{pp_a}(\vec{x}, \omega) \right]_{compact} = \frac{k_o^2 \sin^2 \theta}{16\pi^2 r^2} \left[\frac{L_3}{\ell_c} \phi_f(\omega) \ell_c^2 \right] \quad (9.12)$$

where, again, $\phi_f(\omega) \ell_c L_3$ is the net oscillating lift force spectrum induced on the fluid, and $\ell_c = 2\lambda_3$. This pressure would be radiated if the same force were present near a very small nonreflecting boundary, as illustrated in Figure 9.4b. Equation (9.12) should therefore be compared to Equation (5.49), with due regard to differences in notation. The validity of Equation (9.12) for airfoils has been confirmed by directivity measurements by Hersh and Meecham,¹³ Siddon,¹⁴ and Clark and Ribner,¹⁵ as well as in appropriate references cited in Chapter 5.

9.2.3.3 Implications of Noncompactness to Dependence on Speed. The striking differences between the half-plane and free-space radiation, as expressed in the two equations above, are in the directivity and the dependence on the acoustic wave number. As in Chapter 5, we can assume that the spanwise correlation length is independent of speed, but that the spectrum of the oscillating force is given in terms of a dimensionless spectral density, i.e.,

$$\phi_f(\omega) = \left(\frac{1}{2} \rho_o U_\infty^2 \right)^2 \ell_o^2 \phi_p \left(\frac{\omega \ell_o}{U_\infty} \right) \frac{\ell_o}{U_\infty} \quad (9.13)$$

For simplicity, the function $\phi_p(\omega \ell_o / U_\infty)$ is also assumed to be a dimensionless "hay-stack" spectrum with its maximum value centered on $\omega \ell_o / U_\infty = \pm 1$. The length scale ℓ_o is a characteristic of the fluid disturbance that produces the force (for example, a cylinder diameter or a trailing-edge thickness). Substitution of Equation (9.13) into Equations (9.11) and (9.12) gives alternative representations for the mean-square radiated sound pressure:

$$\begin{aligned} \overline{p_a^2}(\vec{x}) &= \int_{-\infty}^{\infty} \phi_{p_{\text{rad}}}(\vec{x}, \omega) d\omega \\ &\approx 2 \phi_{p_{\text{rad}}} \left(\vec{x}, \frac{\omega \ell_o}{U_\infty} \right) \Delta \left(\frac{\omega \ell_o}{U_\infty} \right) \end{aligned}$$

where $\Delta(\omega \ell_o / U_\infty)$ is the bandwidth of the excitation spectrum. Thus the mean-square pressure in each case is given by

$$\left[\overline{p_a^2(\vec{x})} \right]_{\text{compact}} = \frac{a_2}{64\pi^2} \frac{\ell_c L}{r^2} \rho_o^2 U_\infty^4 \left(\frac{U_\infty}{c_o} \right)^2 \sin^2 \theta \quad (9.14a)$$

and

$$\left[\overline{p_a^2(\vec{x})} \right]_{\text{edge}} = \frac{a_1}{128\pi^3} \frac{\ell_c L}{r^2} \rho_o^2 U_\infty^4 \frac{U_\infty}{c_o} |\sin \phi| \sin^2 \frac{\theta}{2} \quad (9.14b)$$

These formulas disclose that the difference in wave number dependence of the sound pressure in the two cases gives rise to different speed dependence. The coefficients a_n arise from weighted integrals of the pressure spectrum

$$a_n = \int_0^\infty \phi_{\text{rad}} \left(\frac{\omega \ell_o}{U_\infty} \right) \left(\frac{\omega \ell_o}{U_\infty} \right)^n d \left(\frac{\omega \ell_o}{U_\infty} \right)$$

where $n = 2$ in free space and $n = 1$ for the half-plane. Furthermore, the directivities of the two cases provide for no sound in the fluid plane normal to the axis of the force, but on the surface of the plane the sound is maximum. The intensity on the surface is, in fact, double the value that it attains in a direction normal to the surface. Furthermore, the speed dependence is U_∞^5 for the force situated near the half-plane and U_∞^6 for a similar forcing mechanism acting on an acoustically compact boundary. These differences are illustrated in Figure 9.5.

In more physically realizable situations, the distance to the field point r will also exceed the chord; in this case the dependence on speed will still be U_∞^5 , but the directivity pattern will roughly resemble $\sin^2 \theta$ directivity. This is because the $y_2 = 0$, $y_1 < 0$ plane will be a fluid plane as $|y_1| > C$, and it must also be a plane of asymmetry on which $p_a = 0$. Figure 9.5 shows the hypothetical case of a given surface of chord C with an acoustic wave number increasing because of the speed dependence of the forcing function. The break point of U_∞^6 to U_∞^5 occurs when

$$\frac{k_o C}{2\pi} \geq \frac{C}{2\pi \ell_o} \quad M > 1$$

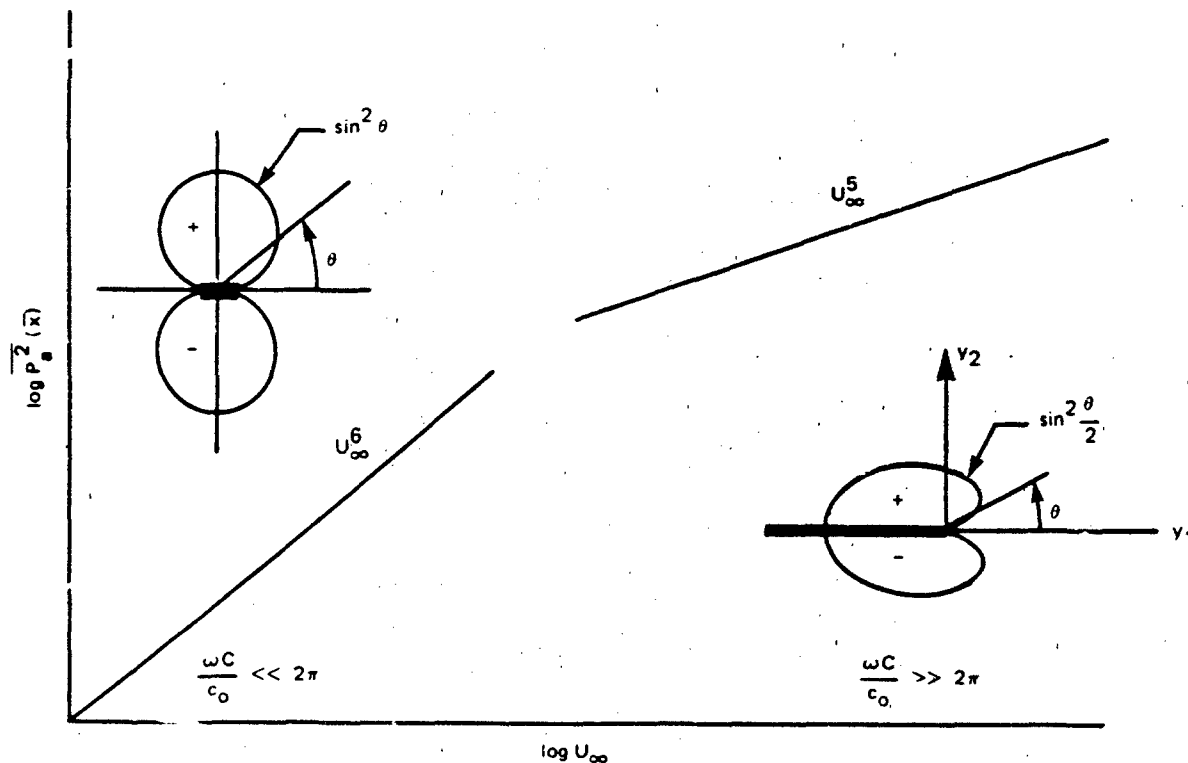


Figure 9.5 - Illustration of the Speed Dependence of Noise from a Localized Force on a Rigid Surface as the Acoustic Wavelength Decreases with an Increase in Speed-Dependent Frequency, i.e., as $k_0 C = C/\lambda_0 M$. Also Shown Are Free-Space and Half-Plane Directivity Functions for the Theoretical Problem

To illustrate this numerically, for the case of vortex shedding shown in Figure 9.3 the ratio of fluid length scale to the chord is

$$\frac{\ell_0}{C} = \frac{h}{C} = 0.028$$

so that the condition is

$$M > 0.18$$

In aeroacoustic applications this Mach number is often exceeded, but in water Mach numbers rarely exceed 0.05. Thus vortex shedding noise from a rigid lifting surface of this geometry will show a U_∞^6 speed dependence in water and U_∞^5 to U_∞^6 dependence in air, depending on the specific value of M .

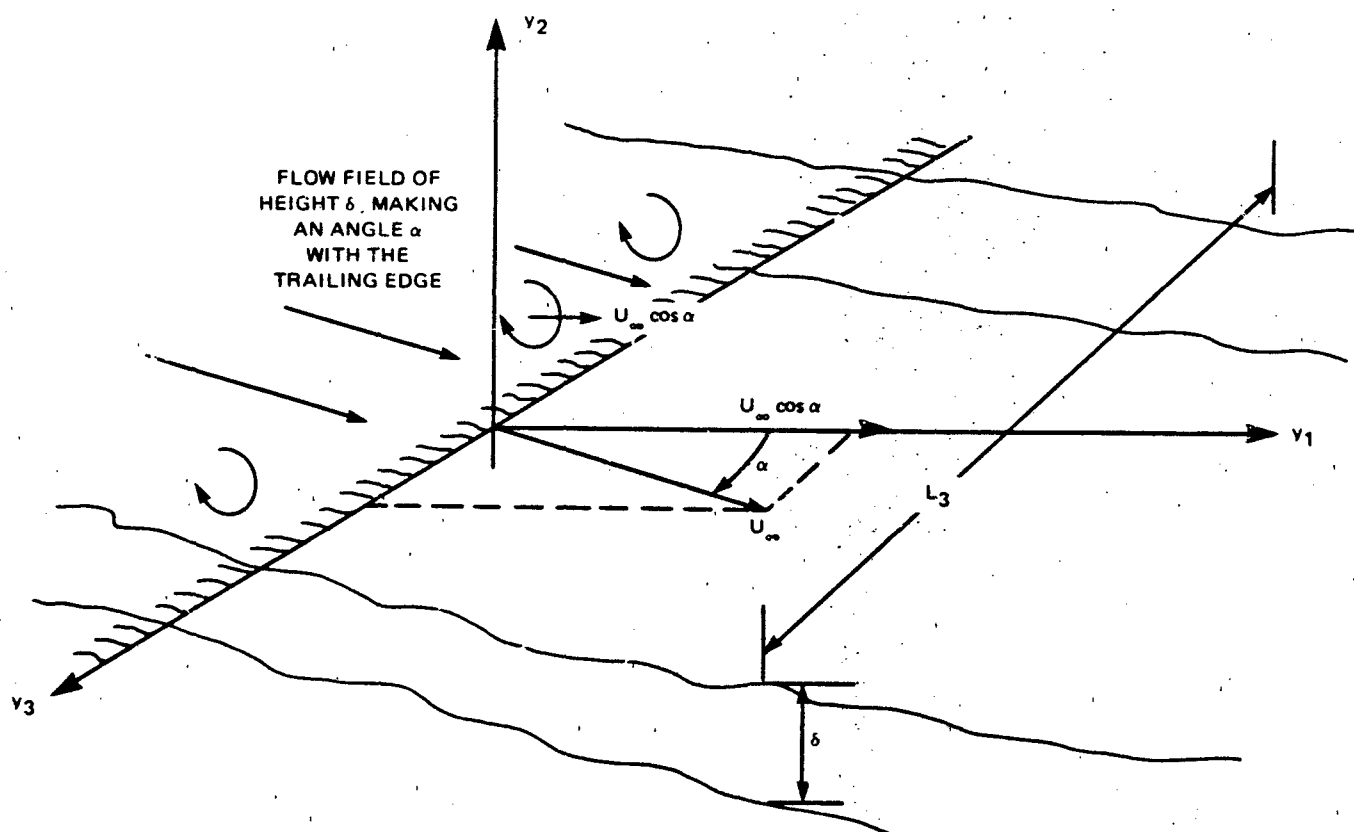


Figure 9.6 - The Geometry of a Wall Jet That Is Incident on the Trailing Edge of a Semi-Infinite Half-Plane

9.2.3.4 Radiation from Turbulence Convected Past a Half-Plane Edge. We now examine a related problem of important practical significance, i.e., the generation of high-frequency noise due to the interaction of upstream turbulence with a leading edge. The problem is straightforwardly solved as an extension of the above development. Ffowcs-Williams and Hall quantified the dipole noise, which is caused by the passage of turbulent eddies convected close to a sharp edge; this noise is radiated as U_∞^5 when the surface is largely flat. The situation, shown in Figure 9.6, is also one for which $\omega C/c_0 \gg 2\pi$. The flow is assumed to be of thickness δ and width L_3 , encountering the edge on an angle α with the normal to the trailing edge. The edge coincides with the y_3 axis and the turbulence character is not presumed to be influenced by the edge, i.e., no new hydrodynamic disturbances are supposed to be generated at the edge.* We use Equation (2.115) for the radiated pressure at frequency ω

*Other theoretical arguments that have been put forth in this regard are discussed in Section 9.6.3.1.

due to a fluctuating Reynolds stress as approximated by $\rho_0 u_i u_j$ in Equation (2.52). The analog to Equation (9.12) is

$$P_a(\vec{x}, \omega) = \iiint_V T_{ij}(\omega) \frac{\partial^2 G(\vec{x}, \vec{y}, \omega)}{\partial y_i \partial y_j} dV(\vec{y}) \quad (9.15)$$

where the integration extends over the entire volume of flow.

We can simplify the analysis by noting that because of the existence of a mean shear flow, the Reynolds stress can be considered to be dominated by functions of the form

$$T_{ij}(\omega) \approx \rho_0 U_i(\vec{y}) u_j(\vec{y}, \omega)$$

where U_i is the mean velocity in either the y_1 or y_3 direction and u_j is the j th stochastic component of that velocity. Note also the requirement that only terms in the mean stress tensor for which

$$\frac{\partial U_1}{\partial y_j} \neq 0$$

will be included. Furthermore, we now specify the situation that

$$\frac{\partial U_1}{\partial y_j} = \frac{dU}{dy_2}$$

is the only nonvanishing mean-shear term in the stress tensor. Therefore T_{ij} will include only the two terms:

$$T_{12} \approx \rho_0 U_\infty \cos \alpha u_2(\vec{y}, \omega) = \rho_0 U_1 u_2(\vec{y}, \omega)$$

$$T_{32} \approx \rho_0 U_\infty \sin \alpha u_2(\vec{y}, \omega) = \rho_0 U_3 u_2(\vec{y}, \omega)$$

plus the second-order products of turbulent quantities. The field is therefore decomposed into one parallel and another normal to the trailing edge. The problem is now most conveniently solved by invoking spherical coordinates. Thus

$$\begin{aligned}
 dV(\vec{y}) &= r_o^2 \sin \phi_o \, dr_o \, d\theta_o \, d\phi_o \\
 \frac{\partial^2 G(\vec{x}, \vec{y})}{\partial y_i \partial y_j} &= \frac{1}{r_o \sin \phi_o} \frac{\partial^2 G(\vec{x}, r_o, \theta_o)}{\partial \theta_o \partial r_o} \\
 &= + \frac{e^{ik_o r} e^{i\pi/4}}{4\pi r} \frac{(2k_o \sin \phi)^{1/2} \sin \frac{\theta}{2} \cos \frac{\theta_o}{2}}{\pi^{1/2} 2r_o^{3/2} \sin \phi_o} \quad (9.16)
 \end{aligned}$$

The trace components of mean velocity in the r and θ directions are

$$U_r = U_1 \cos \theta_o \sin \phi_o + U_3 \cos \phi_o$$

$$U_\theta = -U_1 \sin \theta_o$$

Treating first the contribution due to flow parallel to the edge, i.e., involving $U_3 \cos \phi_o$, it is found that this part of the volume integral contains functions dependent on r_o, ϕ_o, θ_o of the type

$$I_3 = \int_0^\phi dr_o \int_0^\pi d\phi_o \int_{-\pi}^\pi d\theta_o \cdot u_\theta(r_o, \phi_o, \theta_o) \cos \phi_o \cdot \frac{\cos \frac{\theta_o}{2}}{r_o^{3/2} \sin \phi_o} \cdot r_o^2 \sin \phi_o$$

If we make the assumption that $u_\theta(\phi_o) = u_\theta(-\phi_o)$, i.e., that there is no asymmetry about the $y_3 = 0$ axis, then the integration $0 < \phi_o < \pi/2$ cancels that due to $\pi/2 < \phi_o < \pi$, resulting in

$$I_3 \equiv 0$$

For flow normal to the edge there are two terms. The first is $U_r u_\theta$ and contains the function

$$I_{\frac{1}{\theta}} = \int_0^\delta \int_0^\pi \int_{-\pi}^\pi u_\theta(r_o, \theta_o, \phi_o) \cos \theta_o \sin \phi_o \cdot \frac{\cos \frac{\theta_o}{2}}{r_o^{3/2} \sin \phi_o} r_o^2 \sin \phi_o dr_o d\phi_o d\theta_o$$

The second, involving $U_\theta u_r$, contains the function

$$I_{\frac{1}{r}} = - \int_0^\delta \int_0^\pi \int_{-\pi}^\pi u_r(r_o, \theta_o, \phi_o) \sin \theta_o \cdot \frac{\cos \frac{\theta_o}{2}}{r_o^{3/2} \sin \phi_o} r_o^2 \sin \phi_o dr_o d\phi_o d\theta_o$$

Neither of these integrals can be shown to vanish identically by using symmetry arguments; therefore both must be formally retained. Thus $P_a(\vec{x}, \omega)$ is given by

$$P_a(\vec{x}, \omega) \approx \frac{\rho_o e^{ik_o r}}{8\pi r} \frac{e^{i\pi/4}}{\pi^{1/2}} (2k_o \sin \phi)^{1/2} \sin \frac{\theta}{2} \cdot \int_0^\delta \int_0^\pi \int_{-\pi}^\pi U_1(-u_r \sin \theta_o + u_\theta \cos \theta_o \sin \phi_o) \cos \frac{\theta_o}{2} r_o^{1/2} dr_o d\phi_o d\theta_o \quad (9.17)$$

The integrand of Equation (9.17) shows the important result that eddies that lie close to the surface and are well upstream of the edge, $\theta \approx \pm\pi$, do not contribute to the sound. It is only when the $\cos \theta_o/2$ term takes on finite values that an eddy is capable of radiating noise. If the thickness of the turbulent flow field is δ , then only those eddies which are located within a radius of 2δ or so of the edge contribute strongly to the radiation. After passing the edge, eddies will continue to be sources, depending on the orientation of the velocity disturbances relative to the edge of the flow field. To determine the dependence of sound on parameters, the integral in Equation (9.17) will be assumed to extend over a correlation volume determined by the correlation radius of an eddy. The magnitude of $P_a(\vec{x}, \omega)$ will therefore be measured in terms of an eddy scale Λ_o . Furthermore, all components of the

turbulence will be given a common scale of intensity, $u_2(\vec{y}, \omega)$. In this case the Fourier amplitude of the sound pressure becomes

$$P_a(\vec{x}, \omega) \approx \frac{\rho_o e^{i(k_o r + \pi/4)}}{8\pi^{3/2} r} U_1 u(\omega) \Lambda_o (2k_o \Lambda_o \sin \phi)^{1/2} \sin \frac{\theta}{2} \quad (9.18)$$

As before, the autospectral density of the radiated sound pressure can be approximated with the square of the Fourier amplitude to obtain

$$\Phi_{p_{rad}}(\vec{x}, \omega) \approx \left[\frac{\rho_o^2 \Lambda_o^2 U_\infty^2 \cos^2 \alpha \overline{u_2^2}}{r^2 32\pi^3} \Phi_{22}(\omega) k_o \Lambda_o \sin \phi \sin^2 \frac{\theta}{2} \right] \frac{V}{\frac{4\pi}{3} \Lambda_o^3} \quad (9.19)$$

where V/Λ_o^3 expresses the number of uncorrelated eddies and $\Phi_{22}(\omega)$ is the frequency spectrum of the eddies. This equation can be converted to a form useful for scaling by assuming that the volume within which the eddies can effectively radiate sound is roughly (for flow on one side)

$$V \approx \delta^2 L_3$$

where δ is the length scale of the flow and L_3 is the spanwise segment of the edge that is enveloped by the moving fluid. Then, ignoring numerical factors, we have, for $\Lambda_o \approx \delta$, the autospectrum of the radiated sound pressure behaving as

$$\Phi_{p_{rad}}(\vec{x}, \omega) \approx A \rho_o^2 U_\infty^4 \frac{U_\infty}{c_o} \frac{\delta L_3}{r^2} \cos^3 \alpha |\sin \phi| \sin^2 \frac{\theta}{2} \cdot \overline{u_2^2} \frac{\Phi_{22}(\omega)}{U_\infty^2} \left[\frac{\omega \delta}{U_\infty \cos \alpha} \right] \quad (9.20)$$

where A is constant. The turbulence intensity is assumed to be proportional to U_∞ , while the frequency is determined by the rate of encounter of the eddies with the edge. This rate should be proportional to $\delta/(U_\infty \cos \alpha)$ or equivalently $\ell_o/(U_\infty \cos \alpha)$. If we now invoke Taylors' hypothesis of frozen convection past the edge (Chapter 3), then we write

$$\phi_{22}(\omega) = \phi_{22}(k_1) (U_\infty \cos \alpha)^{-1}$$

where $\phi_{22}(k_1)$ is the wave number spectrum of the normal component of the incident turbulence. The sound pressure spectrum expressed as a function of the dimensionless frequency $\omega\delta/(U_\infty \cos \alpha)$ is given by

$$\phi_{p_{rad}} \left(\vec{r}, \frac{\omega\delta}{U_\infty \cos \alpha} \right) \approx A_0^2 U_\infty^2 \left(\frac{U_\infty}{c_0} \right) \frac{\delta L_3}{r^2} (\cos^2 \alpha) |\sin \phi| \sin^2 \frac{\theta}{2} \frac{1}{u_2^2} \left[\frac{\phi_{22}(k_1 \delta)}{\frac{1}{u_2^2}} (k_1 \delta) \right] \quad (9.21)$$

This relationship is the major conclusion of this section, and it is used throughout this chapter. It applies to flows incident on the edge from either $y_1 > 0$ or $y_1 < 0$, and it should be compared with Equations (9.11) and (9.14). The U_∞^5 dependence on speed arises in the case discussed here because the interaction of the edge with the turbulence results in a localized edge dipole source with a magnitude proportional to $\rho_0 U_\infty^2$. Furthermore, Equation (9.21) brings out the effect of yawing the edge at an angle α to the mean flow. The spectrum level will decrease as $\cos^2 \alpha$ until the source terms whose magnitudes are quadratic in the turbulent field quantities begin to dominate the radiation. The result shows that this type of dipole sound will be most intense for flow across the edge rather than for flow along the edge. The level is proportional to a transverse cross-sectional area of the flow region measured in multiples of $L_3 \delta$ or $L_3 \lambda$. The acoustically active segment of the surface has also been shown to be measured in multiples of the height of the wall jet or boundary layer, or of the eddy scale.

Extensive experimentation, some of which is described in Section 9.3, has been carried out by NASA and its contractors and used to develop a variety of semi-empirical prediction techniques for noises produced by trailing edges scrubbed with turbulent flow. These techniques, summarized by Fink,¹⁶ essentially use Equation (9.21) as a basis, with the length scale δ replaced by some geometric dimension. For example, for jets exhausting over trailing edges, δ is replaced by the diameter of the jet.

9.3 NOISE FROM INFLOW UPSTEADINESS

9.3.1 Elements of Unsteady Airfoil Theory

9.3.1.1 Outline of the General Theory. This topic is of such broad naval and aeronautical interest that it has been treated elsewhere; the reader is referred specifically to books by Bisplinghoff et al.⁴ and Newman⁵ for developments of the general theory. A general treatment of the lift fluctuations on a body of arbitrary geometry in unsteady flow has been given by Sevik.¹⁷ In this section only the preliminaries that pertain to unsteady lifting surfaces are outlined in order to fix ideas and to illustrate the limitations and idealizations of the theory.

The problem really deals with determining the distribution of unsteady pressure on a lifting surface that results from a time-varying change in angle of attack to the inflow. This angle of attack can be altered because of a heaving or pitching motion of the surface in a steady flow (commonly called "Theodorsen's problem").^{18,19*} In either case the initial disturbance is a relative vertical velocity between the lifting surface and the incoming fluid. In the mathematical problem posed in Figure 9.7 the airfoil is of infinitesimal thickness, representing a plane discontinuity in the y_1, y_3 plane in the three-dimensional problem, or a line discontinuity in the two-dimensional problem. The flow is assumed to be inviscid, so that the vortex sheet in the $C/2 < y_1 < \infty$ plane is in direct response to the requirement that fluid pass the trailing edge tangent to the surface. This boundary condition is known as the Kutta condition. All the vorticity disturbances in the wake considered later in this chapter are the result of viscous flow instabilities assumed to be superimposed on the potential flow. The Kutta condition as stated here applies to the potential flow. Now, as a point of complication, one must assume that the unsteady viscous and potential flows are not wholly independent. Therefore the terms "unsteady Kutta conditions," and "partial Kutta conditions" often appear in the literature. These simply mean that some kind of condition of boundedness has been placed at the trailing edge. Figure 9.3a helps to illustrate the notion of "inner" and "outer" flow regions; the smoke patterns close to the surface are drawn into the viscous vortex wake, while the streamline, which is a distance of only one trailing-edge thickness away, passes by the airfoil surface without distortion. Therefore, to the degree

*There is also a response to chordwise motion, or gusts,²⁰⁻²² but this is small when accompanied by a vertical, or transverse, velocity fluctuation.

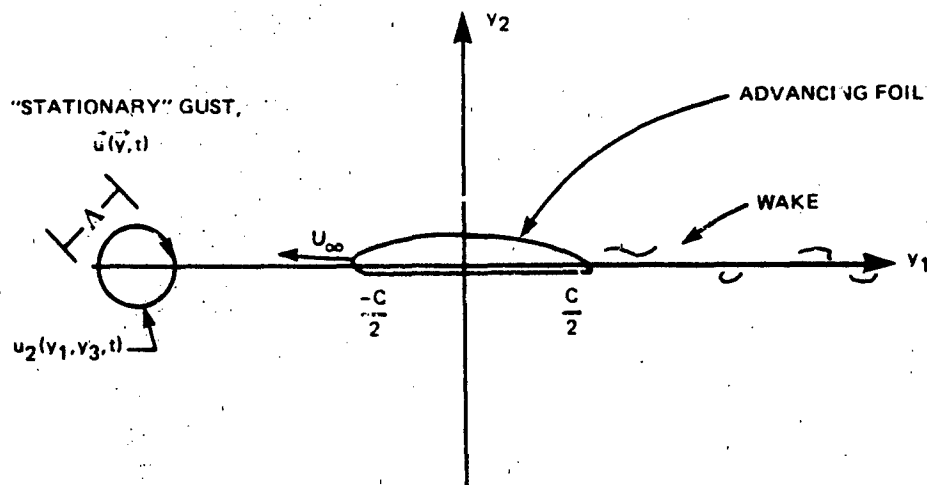


Figure 9.7a - Physical Problem of Unsteady Inflow

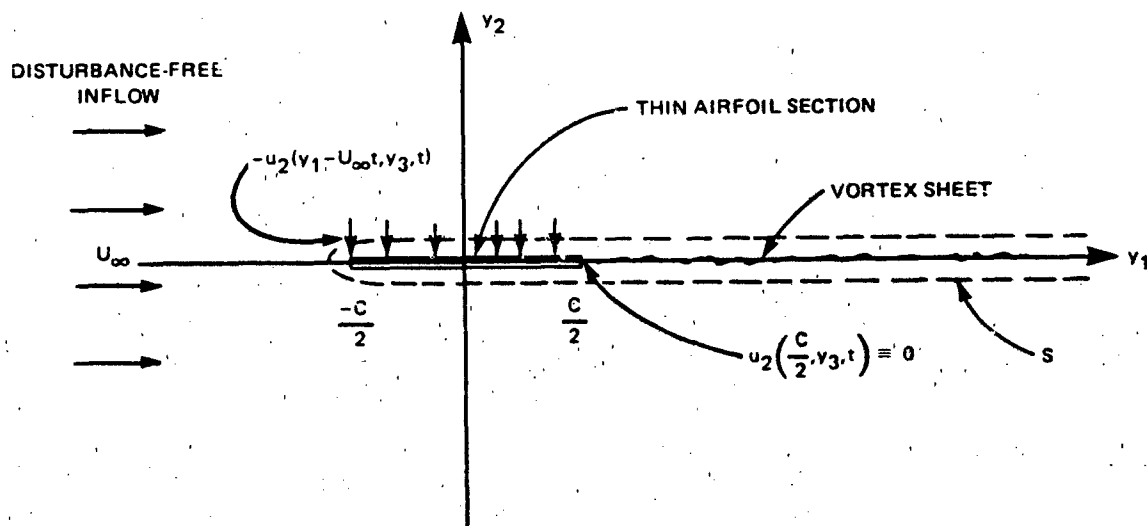


Figure 9.7b - Mathematical Idealization of a Cut in the y_1, y_3 Plane

Figure 9.7 - The Physical and Idealized Perspectives of an Airfoil Responding to an Unsteady, Yet Statistically Stationary, Inflow

that the outer potential flow is unaffected by the inner viscous wake, it is possible to keep these flow regimes dynamically separate.

The mathematical problem of the unsteady flow is set up in the following way. The plane $-C/2 < y_1 < \infty$ is a discontinuity we include within a surface S . On this plane we must allow vorticity to be present, for without circulation around the lifting surface there can be no lift. Flow outside S is inviscid and irrotational. Therefore Equation (2.86) is useful because it exposes the direct influence of the vorticity. Incompressible flow will be assumed and all the vorticity (incident, bound, and trailing) is restricted to lie in a sheet of infinitesimal thickness, i.e.,

$$\begin{aligned}\vec{\omega}(\vec{y}, t) &= \vec{\omega}(y_1, y_3) \delta(y_2) & -\frac{C}{2} < y_1 < \infty \\ &= 0 & y_1 < -\frac{C}{2}\end{aligned}\quad (9.22)$$

Since the vorticity is

$$\vec{\omega} = \nabla \times \vec{u}$$

we can define a stream function

$$\vec{u} = \nabla \psi \quad \vec{u} = \nabla \times \vec{\psi}$$

so that

$$\nabla^2 \psi_3 = -\vec{\omega}_3(y_1, y_3, t) \delta(y_2) \quad (9.23)$$

In writing Equation (9.23) it has been assumed that

$$\vec{U} = (U_\infty, 0, 0)$$

so that only one component of $\vec{\omega}$ is important and

$$\nabla \psi = 0$$

This condition is obviously met in the two-dimensional problem since $\partial\psi_3/\partial y_3 = 0$.

A solution to Equation (9.23) follows directly from the methods of Chapter 2, e.g., Equation (2.56) with the retardation condition dropped (for this hydrodynamic problem in which $U_\infty/c_0 \rightarrow 0$), so that

$$\psi_3(\vec{y}, t) = \frac{+1}{4\pi} \iiint \frac{\omega_3(Y_1, Y_3, t) \delta(Y_2)}{|\vec{y} - \vec{Y}|} dV(\vec{Y}) \quad (9.24)$$

Since

$$u_2 = \frac{\partial\psi_1}{\partial y_3} - \frac{\partial\psi_3}{\partial y_1}$$

Equation (9.24) gives the velocity on the cut in the vertical direction as*

$$u_2(y_1, 0, y_3, t) = \frac{1}{4\pi} \iint_{Y_1 > -C/2} \frac{\omega_3(Y_1, Y_3, t) (y_1 - Y_1)}{[(y_1 - Y_1)^2 + (y_3 - Y_3)^2]^{3/2}} dY_1 dY_3 \quad (9.25)$$

If two-dimensionality is now assumed, by taking $\omega_3(y_1, y_3) = \omega_3(y_1)$ we find, upon integration over $-\infty < Y_3 < \infty$,

$$u_2(y_1, t) = \frac{1}{2\pi} \int_{-C/2}^{\infty} \frac{\omega_3(Y_1, t) dY_1}{y_1 - Y_1} \quad (9.26)$$

Similarly, for the two-dimensional problem the streamwise velocity is found in stages that utilize Equation (9.23):

*Note that for airfoils of finite span there will be a tip vortex, $\psi_1 \neq 0$, adding another component to the down wash (Chu and Widnall²³).

$$u_1(y_1, y_2, 0, t) = \frac{1}{4\pi} \iiint \frac{\omega_3(\vec{Y}, t) (y_2 - Y_2)}{[(y_1 - Y_1)^2 + (y_2 - Y_2)^2 + Y_3^2]^{3/2}} dV(Y)$$

$$= \frac{1}{2\pi} \iint \frac{\omega_3(Y_1, t) \delta(Y_2) (y_2 - Y_2) dY_2 dY_1}{[(y_1 - Y_1)^2 + (y_2 - Y_2)^2]}$$

from which

$$u_1(y_1, 0^+, 0, t) = \frac{1}{2} \omega_3(y_1) \quad y_2 \rightarrow 0^+ \quad -\frac{C}{2} < y_1 < \frac{C}{2}$$

$$u_1(y_1, 0^-, 0, t) = -\frac{1}{2} \omega_3(y_1) \quad y_2 \rightarrow 0^- \quad -\frac{C}{2} < y_1 < \frac{C}{2} \quad (9.27)$$

Equation (9.27) is determined by deforming the Y_1 integration into contours in the upper and lower complex $(Y_1 + iY_2)$ plane and evaluating the residues at $Y_1 = y_1 \pm i|y_2|$.

Equations (9.26) and (9.27) give the velocities on the surface surrounding the bound vortex sheet in the $-C/2 < y_1 < \infty$ plane, and they form the starting point for most analytical treatments of thin airfoil theory. To find the lift we must find the pressure jump across the surface of the airfoil. It is expedient to rewrite Equation (2.86) as

$$\nabla_{1,3} \left[p(\vec{y}, t) + \frac{1}{2} \rho_o u^2 + \rho_o \frac{\partial \phi(\vec{y}, t)}{\partial t} \right] = 0$$

Upon formal integration, this gives the conditions on either the upper or the lower surface (i.e., above or below the slit $-C/2 < y_1 < \infty$). For example, on the upper surface,

$$p_u + \frac{1}{2} \rho_o u_u^2 + \rho_o \frac{\partial \phi_u}{\partial t} = P_\infty + \frac{1}{2} \rho_o U_\infty^2 \quad (9.28)$$

where P_∞ and U_∞ are freestream conditions. The vorticity outside the slit is zero; therefore the velocity on the surfaces $y_2 = 0^+$ and $y_2 = 0^-$ of the slit has been

written in the form of a potential jump

$$\vec{u} = \pm \nabla \phi_s$$

introduced in the above equations.

The problem now is to find a relationship between the imposed downwash on the airfoil $u_2(y_1, 0, t)$ and the wake vorticity $\omega(y_1, 0, t)$ that results. To do this the boundary condition imposed at the trailing edge, i.e., at $y_1 = C/2$ is $u_2(C/2, 0, t) = 0$. This condition means that the gradient of pressure across the wake at the trailing edge and downstream is zero, i.e.,

$$-\frac{1}{\rho_0} \frac{\partial p(y_1 = \frac{C}{2})}{\partial y_2} = j_\infty \frac{\partial u_2}{\partial y_1} + \frac{\partial u_2}{\partial t} = 0,$$

so that by Equation (9.28) (letting $u^2 = 2U_\infty u + U_\infty^2$)

$$U_\infty \frac{\partial u_1(\frac{C}{2}, 0, t)}{\partial y_1} + \frac{\partial u_1(\frac{C}{2}, 0, t)}{\partial t} = 0$$

This is a condition that also ensures that the flow is tangential to the trailing edge. Therefore, using Equation (9.27), we can write the kinematic condition for the generation of vorticity in the wake as

$$\omega_3(y_1, t) = \omega_3(y_1 - U_\infty t) \quad -\frac{C}{2} < y_1 < \infty \quad (9.29)$$

The boundary condition of known $u_2(y_1, t)$ on the remainder of the airfoil segment gives another requirement on $\omega_3(y_1, t)$: by Equation (9.26) and

$$u_2(y_1, t) + \frac{1}{2\pi} \int_{-C/2}^{C/2} \frac{\omega_3(Y_1, t)}{(y_1 - Y_1)} dY_1 = -\frac{1}{2\pi} \int_{C/2}^{\infty} \frac{\omega_3(Y_1 - U_\infty t)}{(y_1 - Y_1)} dY_1 \quad (9.30)$$

for $-C/2 < y_1 < C/2$. The velocity $u_2(y_1, t)$ is the prescribed vertical velocity (downwash) on the airfoil. The pressure distribution on the airfoil is found from Equation (9.28)

$$\Delta p = -\rho_o U_\infty (u_u - u_l) - \rho_o \frac{\partial(\phi_u - \phi_l)}{\partial t}$$

where the potential jump is

$$\phi_u - \phi_l = \int_{-\infty}^{y_1} (u_u - u_l) dy_1$$

Therefore, using Equation (9.27),

$$\Delta p = -\rho_o U_\infty \omega_3(y_1, t) - \rho_o \frac{\partial}{\partial t} \int_{-C/2}^{y_1} \omega_3(y_1, t) dy_1 \quad (9.31)$$

The unsteady lift per unit span is

$$\frac{dL}{dy_3} = \int_{-C/2}^{C/2} \Delta p(y_1, t) dy_1 \quad (9.32)$$

Equations (9.29), (9.30) and (9.31) (or the three-dimensional equivalent involving Equation (9.25)) are the general equations of unsteady airfoil theory. The procedures for their solution involve the inversion of Equation (9.30), which is a singular integral equation. The solution now requires the specific formulation of the incident velocity $u_2(y_1, 0, t)$. These solutions are given in all the references cited in this section. A novel approach to the acoustic problem which determines $\omega_3(y_1, t)$ from an incident vortex has been given recently by Howe.²⁴

9.3.1.2 Aerodynamic Influence Functions. The inversion of Equation (9.30) to find ω_3 is dependent on knowledge of the nature of the downwash $u_2(y_1, y_3, t)$ on the strip.

$-C/2 < y_1 < C/2$, $(1/2) L_3 < y_3 < (1/2) L_3$ where L_3 is the span of the lifting surface. Suppose now the circumstance shown in Figure 9.7a, in which a gust flows into the leading edge of a rigid airfoil. We write the turbulence $u_2(y_1, y_3, t)$ in terms of its generalized Fourier transform, i.e.,

$$u_2(k_1, k_3, \omega) = \frac{1}{(2\pi)^3} \iiint_{-\infty}^{\infty} u(y_1, y_3, t) e^{-i(\vec{k} \cdot \vec{y}_{13} - \omega t)} d\vec{y}_{13} dt \quad (9.33)$$

The space-time variation of the downwash of each wave number relative to the fixed surface of the airfoil is

$$-u_2(y_1, y_3, t) = -u_2(k_1, k_3, \omega) e^{+ik_1(y_1 - U_\infty t) + ik_3 y_3} \quad (9.34)$$

where U_∞ refers to the velocity of the surface relative to the convection velocity of the gust.

The solution of Equation (9.30) with Equation (9.34) for a one-dimensional turbulent field,^{4,5} such that $k_3 L_3 \ll 1$ and $L_3/C \gg 1$, yields the standard two-dimensional Sears function,²⁵ which relates the lift per unit span to the incident downwash amplitude as

$$\frac{dL(k_1)}{dy_3} = \pi \rho_o C U_\infty u_2(k_1, \omega) S_e \left(\frac{k_1 C}{2} \right) e^{-i\omega t} \quad (9.35)$$

where $k_1 C/2 = \omega C/2U_\infty$. The Sears function gives the amplitude and phase (relative to the disturbance at the midchord):

$$S_e \left(\frac{k_1 C}{2} \right) = \frac{\frac{2i}{\pi} \left(\frac{2}{k_1 C} \right)}{H_1^{(2)} \left(\frac{k_3 C}{2} \right) + i H_0^{(2)} \left(\frac{k_1 C}{2} \right)} \quad (9.36)$$

where $H_1^{(2)}$ and $H_0^{(2)}$ are cylindrical Hankel functions (see Abramowitz and Stegun.²⁶) The Argand diagram of this function is shown as the solid-line spiral in Figure 9.8.

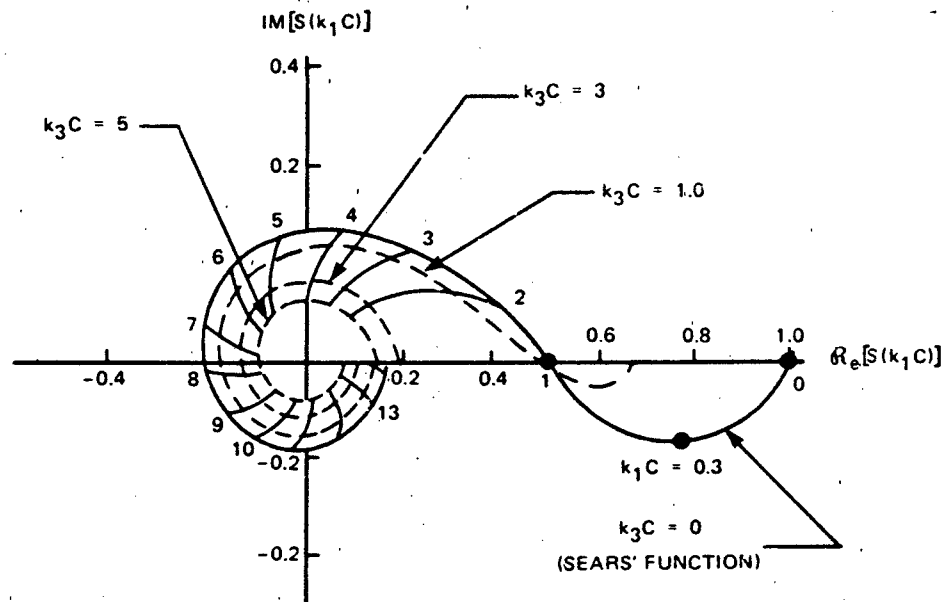


Figure 9.8 - Unsteady Aerodynamic Loading Functions for One- and Two-Dimensional Gusts, $k_1 C = C/U$ ³⁵

For wave numbers $k_1 C = \omega C/U_\infty > 2$, function is roughly circular, but with a slowly decreasing radius as $k_1 C$ increases. Of particular interest in the following discussion is the square of the amplitude, which has been approximated by Liepmann²⁷ as

$$\left| S_e\left(\frac{k_1 C}{2}\right) \right|^2 = \frac{1}{1 + \pi k_1 C} \quad (9.37)$$

which bears a close resemblance to the exact function throughout $k_1 C > 0$. The lift coefficient corresponding to this wave number component of the turbulence is defined as

$$C_L(k_1) = \frac{1}{\frac{1}{2} \rho_0 U_\infty^2 c} \frac{dL(k_1)}{dy_3} e^{-i\omega t} \quad (9.38a)$$

$$C_L(k_1) = 2\pi \frac{u_2(k_1, \omega)}{U_\infty} S_e\left(\frac{k_1 C}{2}\right) \quad (9.38b)$$

For cases in which neither the airfoil span nor the spanwise wavelength of the incident turbulence are effectively infinite with respect to the chord, a variety of attempts have been made to invert Equation (9.30). One early attempt that resulted in numerically computed response functions was that of Reissner.^{28,29} Recently, Mugridge^{30,31} determined an approximate closed-form expression for the lift coefficient in terms of a correction factor to the traditional Sears function. In the notation of Equation (9.38), that result is

$$|C_L(k_1, k_3)| = 2\pi \left| \frac{u_2(k_1, k_3, \omega)}{U_\infty} \right| \left| S_e\left(\frac{k_1 C}{2}\right) \right| |F(k_1, k_3)| \quad (9.39a)$$

where the correction function is

$$|F(k_1, k_3)|^2 = \frac{\frac{2}{\pi^2} + \left(\frac{k_1 C}{2}\right)^2}{\left(\frac{k_3 C}{2}\right)^2 + \left(\frac{k_1 C}{2}\right)^2 + \frac{2}{\pi^2}} \quad (9.39b)$$

An approximation by Filotas³²⁻³⁴ for the two-dimensional lift function such that

$$|C_L(k_1, k_3)| = 2\pi \left| \frac{u_2(k_1, k_3, \omega)}{U_\infty} \right| \left| S_{2D}\left(\frac{k_1 C}{2}, \frac{k_3 C}{2}\right) \right| \quad (9.40)$$

is

$$S_{2D}\left(\frac{k_1 C}{2}, \frac{k_3 C}{2}\right) = \frac{\exp \left\{ \frac{-ik_1 C}{2} \left[\sin \beta - \frac{\pi \beta \left(1 + \frac{1}{2} \cos \beta\right)}{1 + \pi k C \left(1 + \frac{1}{2} \cos \beta\right)} \right] \right\}}{\left[1 + \pi \frac{k C}{2} \left(1 + \sin^2 \beta + \frac{\pi k C}{2} \cos \beta\right) \right]^{1/2}} \quad (9.41)$$

where $k^2 = k_1^2 + k_3^2$ and $\sin \beta = k_1/k$. This formula was derived for an airfoil of infinite span. Graham³⁵ numerically computed the exact loading functions for an airfoil of infinite span and varying $k_3 C$. These results are shown as the dotted line spirals in Figure 9.8 for selected values of $k_3 C$. In the limit of $k_3 \rightarrow 0$,

Graham's function matches the Sears function. The amplitude-squared of Graham's function is plotted in Figure 9.9. For use in approximations, a closed-form expression is necessary, and this has been fitted to Graham's exact calculations:

$$|S_{2D}(k_1 C, k_3 C)|^2 = |S_e(k_1 C)|^2 \frac{1 + 3.2(k_1 C)^{1/2}}{1 + 2.4(k_3 C)^2 + 3.2(k_1 C)^{1/2}} \quad (9.42)$$

It is useful to represent the exact form as an approximate correction to the Sears function.

The aerodynamic influence function for a two-dimensional gust incident on an airfoil of finite span has been derived by Chu and Widnall.²³ Their results can be used to numerically examine the loading at the tip in particular.

Influence functions have also been determined for compressible flow. Although hydrodynamic Mach numbers are generally negligible, except in regions of two-phase flow, compressibility effects become important when the product of Mach number and

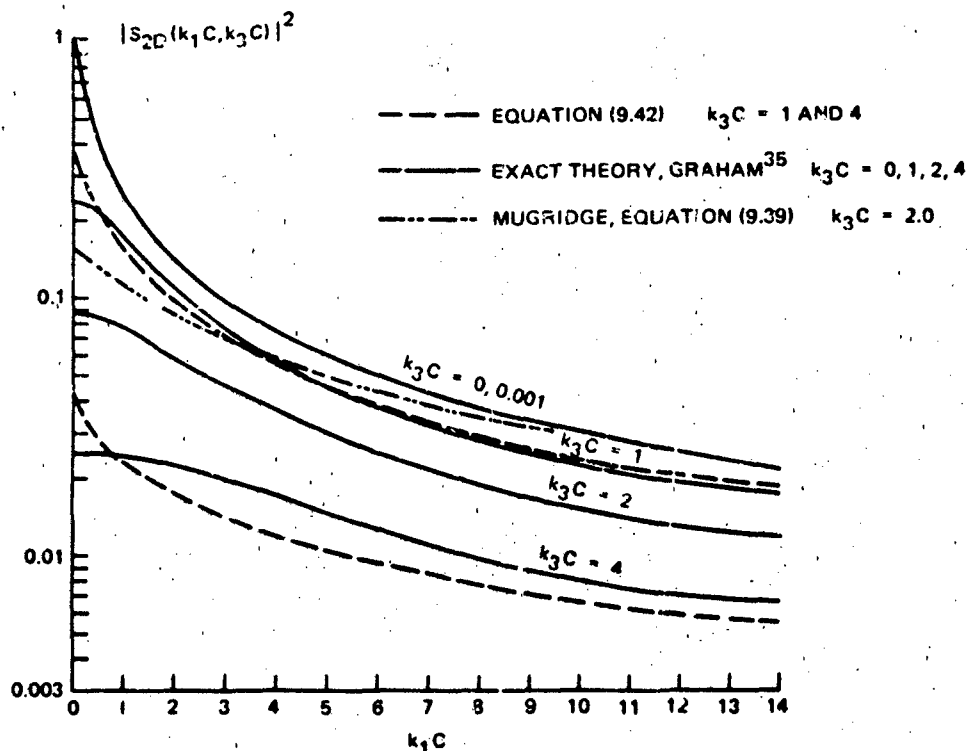


Figure 9.9 - Aerodynamic Response Functions to One- and Two-Dimensional Gusts

reduced frequency, Mk_1C , approaches unity. Essentially, this means that retardation effects must be included in Equation (9.24) and succeeding integrals. Since $k_1 = \omega/U_\infty$, this product is $\omega C/c_0$; it can be large at high frequencies and nonnegligible even for low Mach number. The above expressions are strictly valid in the limit of $Mk_1C < 1$. More general expressions have been given by Graham,³⁶ Osborne,³⁷ Chu and Widnall,^{23,38} Amiet,^{39,40} Adamczyk,⁴¹ Kemp and Homicz,⁴² and Miles.^{43,44} For purposes of rough acoustic approximations, the result of Adamczyk,⁴¹ later corroborated by Amiet,⁴⁰ may be reduced to an approximate closed form

$$S_{2D}(k_1C, k_3C=0) \approx \frac{e^{-i\pi/2}}{\left(\frac{\omega C}{2U_\infty} \cdot \frac{\omega C}{2c_0}\right)^{1/2}} \quad (9.43)$$

for $(\omega C/c_0)(1-U_\infty/c_0) > 1.5$, say. This lower limit on $\omega C/c_0$ is established by the error function,²⁶ which is within 5% of its asymptotic value (unity) used in Equation (9.43) when its argument exceeds 1.5.

The pressure difference between the upper and lower surfaces has been given by a number of investigators in the form (with the origin at midchord)

$$\Delta P(y_1, y_3, k_1, k_3, \omega) = 2\rho_0 U_\infty u_2(k_1, k_3, \omega) \left(\frac{\frac{C}{2} - y_1}{\frac{C}{2} + y_1}\right)^{1/2} S_{2D}(k_1C, k_3C) \cdot e^{i(k_3y_3 - \omega t)} \quad (9.44)$$

$$Mk_1C < 1$$

See, for example, Filotas,³² Chu and Widnall,^{23,38} Osborne,³⁷ Amiet,^{39,45} Adamczyk,⁴¹ Kemp and Homicz,⁴² and Fugita and Kovasznay.⁴⁶ This form reflects the classical chordwise behavior of the steady and unsteady lift distribution, namely, a maximum at the leading edge $y_1 = -C/2$ and zero at the trailing edge $y_1 = C/2$. Integration of Equation (9.44) yields the lift, while multiplication of ΔP by y_1 followed by integration yields the moment. These manipulations show that the center of (both steady and unsteady) lift occurs at $y_1 = -C/4$, i.e., one-fourth of the chord downstream of the leading edge.

An asymptotic formula for the pressure jump which is valid for high frequencies, $\omega C/U_\infty > 1$ and $\omega C/c_o > 1$, can be derived from expressions given by Amiet.⁴⁰ This expression is

$$\Delta P(y_1, y_3, k_1, k_3, \omega) = -\rho_o U_\infty u_2(k_1, k_3, \omega) \frac{e^{i(k_3 y_3 - \omega t)}}{[\pi y_1 (k_3 - i k_1)]^{1/2}} \cdot e^{-i M k_o y_1 - (k_3^2 - k_o^2)^{1/2} y_1} (-1)^{1/2} = -i \quad (9.45)$$

for $M \rightarrow 0$ but $M k_1 C/2 = \omega C/2c_o > 1.5$. This formula shows evanescent waves emanating from the leading edge for $k_3 > k_o$, but acoustic waves for $k_3 < k_o$.

9.3.2 Oscillatory Lift Spectra from Ingested Turbulence

For use in estimating acoustic radiation and flow-induced vibration, we require the appropriate force coefficient. The above expressions for $C_L(k_1, k_3)$ and ΔP can be used to determine the spectra of oscillatory lift and surface pressure. The total time-dependent lift due to all the wave number components k_1, k_3 is found from integration of Equation (9.44):

$$\mathcal{L}(t) = \pi \rho_o U_\infty C \int_{-L_3/2}^{L_3/2} \iiint_{-\infty}^{\infty} u_2(k_1, k_3, \omega) S_{2D}\left(\frac{k_1 C}{2}, \frac{k_3 C}{2}\right) \cdot e^{+i(k_3 y_3 - \omega t)} dk_1 dk_3 d\omega dy_3 \quad (9.46)$$

$$= \pi \rho U_\infty C L_3 \iiint u_2(k_1, k_3, \omega) S_{2D}\left(\frac{k_1 C}{2}, \frac{k_3 C}{2}\right) \left(\frac{\sin \frac{1}{2} k_3 L_3}{\frac{1}{2} k_3 L_3}\right) e^{-i\omega t} dk_1 dk_3 d\omega$$

The result is essentially in the form of Equation (9.40) except that it includes the averaging of the span-varying phase of the upstream turbulence. In fact, as L_3

increases, the only important contribution to the integral comes from values of k_3 which are much less than $1/L_3$. Also, Equation (9.46) is perfectly general; $S_{2D}(k_1 C, k_3 C)$ can theoretically represent any lifting surface response function. The generality in Equation (9.46) includes a provision that Taylor's hypothesis need not strictly apply because we have maintained the possibility of separate k_1 and ω dependence in $u_2(k_1, k_3, \omega)$. The frequency spectrum of the lift function is related to the temporal correlation function by

$$\int_{-\infty}^{\infty} \phi_l(\omega) e^{-i\omega\tau} d\omega = \int_{-\infty}^{\infty} \mathcal{L}(t) \mathcal{L}(t+\tau) dt$$

Therefore, using Equation (2.133), we find that in the case of spatially and temporally stationary gusts the frequency spectrum of the lift fluctuation is

$$\phi_l(\omega) = \pi^2 \rho_0^2 U_\infty^2 C^2 L_3^2$$

$$\overline{u_2^2} \int_{-\infty}^{\infty} \int \phi_{22}(k_1, k_3, \omega) \left| S_{2D}\left(\frac{k_1 C}{2}, \frac{k_3 C}{2}\right) \right|^2 \left(\frac{\sin \frac{1}{2} k_3 L_3}{\frac{1}{2} k_3 L_3} \right)^2 dk_1 dk_3 \quad (9.47)$$

where $\overline{u_2^2}$ is the mean-square component of velocity normal to the span. This is the formal statement of the oscillatory lift in terms of the wave number frequency spectrum of the incident turbulence, $\phi_{22}(k_1, k_3, \omega)$, which behaves generally as discussed in Sections 3.6.3 and 7.2.

This relationship is in a form completely compatible with the relationships of Chapter 6 for flow-induced vibration and of Equation (9.12) for direct dipole radiation from a surface with an acoustically compact chord.

A relationship of this type was first derived by Liepmann,²⁷ but his considerations were limited only to gusts for which $k_3 = 0$ and $L_3 \rightarrow \infty$. In that special case, the result can be written directly from our Equation (9.38) because no consideration of spanwise phase variation is needed. Liepmann's results were in a form that utilized structural impedance representations in much the same manner as that described in this text. The approach was later applied to aircraft surfaces

by Diederich.⁴⁷ The more general case of an airfoil of finite span was then later derived by Liepmann⁴⁸ by assuming that the locally induced pressure distribution was identical to that which would occur if both the airfoil and the gust had infinite span. Therefore the airfoil locally responded in strips of width k_3^{-1} along the span. The total response is just the resultant of the loading on each strip, with account taken of the phase from strip to strip. The result can be obtained from Equation (9.45) simply by letting $S_{2D}(k_1 C/2, k_3 C/2) = S_e(k_1 C/2)$. Liepmann considered two limiting cases of Equation (9.47), $L_3/\Lambda_3 \gg 1$ and $L_3/\Lambda_3 \ll 1$, where Λ_3 is the integral length scale of turbulence in the direction of the span.

A more general formalism of the problem for applications to three-dimensionally varying turbulence is due to Ribner.⁴⁹ The response is written as an integral over all three wave number components,

$$\phi_l(\omega) \sim \iiint \phi_{u_2}(\vec{k}, \omega) S(\vec{k}) d\vec{k}$$

For the surface of infinitesimal thickness the response function can be written as

$$S(\vec{k}) = S_{2D}(k_1, k_3)$$

and we retrieve Equation (9.47), in which the response kernel is permitted to be a function only of the directional wave numbers in the plane of the surface. Another generalization introduced by Miles⁵⁰ allows the gust to have a convection velocity unequal to the translation velocity of the fluid. This allows the gust encounter velocity and the mean flow velocity to differ, influencing the phase between the downwash and the lift but not the magnitude of the lift. It appears from calculations based on the theory that the effect will be small for gust convection velocities on the order of $0.9 U_\infty$ to U_∞ . Response functions for a more general case of nonstationary turbulence have been numerically calculated by Verdon and Steiner.⁵¹

The derivation of relationships that give the dependence of the lift on the length scale of the turbulence is most simply done by resorting to a separable model for the turbulence, such as that used in Sections 3.6.3.2 and 7.2.5. Furthermore, recall that the integral length scale of a correlation function is related

to the wave number spectrum by Equation (3.82b) and similarly for the time scale. If it is assumed that the span is substantially larger than the integral correlation scale in that direction, then the lift spectrum is of the form

$$\phi_L(\omega) = \pi^2 \rho_\infty^2 U_\infty^2 (CL_3)^2 \frac{\Lambda_3}{u_2^2 \pi} \cdot \int_{-\infty}^{\infty} \left(\frac{\sin \frac{k_3 L_3}{2}}{\frac{k_3 L_3}{2}} \right)^2 dk_3$$

$$\cdot \int_{-\infty}^{\infty} \phi_{22}(k_1) \phi_m(k_1 U_\infty - \omega) \left| S_{2D}\left(k_1, 0\right) \right|^2 dk_1 \quad (9.48)$$

for $\Lambda_3/L_3 < 1$. The correlation of turbulence in directions perpendicular to the surface was assumed to be unity, i.e., the correlation function is taken to be $R_{22}(r_2, y_2) = 1$, which is consistent with the thin-airfoil hypothesis. Furthermore, the wave number spectra are assumed to be of the form

$$\phi_{jl}(k_1) = \frac{1}{\pi} \frac{\Lambda_1}{1 + (\Lambda_1 k_1)^2} \quad (9.49)$$

which is the transform (e.g., Equation (3.77)) of a correlation function $\exp -r_1/\Lambda_1$. The sine integral is exactly $2\pi/L_3$, and, under the assumption of frozen convection, $\phi_m(k_1 U_\infty - \omega)$ is replaceable by $\delta(k_1 U_\infty - \omega)$. Incorporating these two values, Equation (9.69) becomes

$$\frac{\phi_L(\omega)}{\left(\frac{1}{2} \rho_\infty U_\infty^2 \right)^2 (CL_3)^2} =$$

$$C_L^2(\omega) = 4\pi^2 \frac{u_2^2}{U_\infty^2} \left[\frac{1}{U_\infty} \phi_{22}\left(\frac{\omega}{U_\infty}\right) \right] \frac{2\Lambda_3}{L_3} \left| S_e\left(\frac{\omega C}{2U_\infty}\right) \right|^2 \quad (9.50a)$$

or, more generally,

$$\overline{C_L^2(\omega)} = 4\pi^2 \frac{U_\infty^2}{U_\infty^2} \phi_{22}(\omega) \left[\left| A \frac{\omega C}{2U_\infty} \right|^2 \right] \quad (9.50b)$$

The function in brackets, $A(\omega C/(2U_\infty))$, has been called the aerodynamic admittance function (Figure 9.10), and its general expression can be deduced by comparing Equations (9.48) and (9.50), as shown below. The spectrum function $\phi_2(\omega) = U_\infty^{-1} \phi_2(\omega/U_\infty)$ is the point wave number spectrum of the downwash convected in a frame of reference moving with the lifting surface. The lateral integral length scale is a function of the wave number $k_1 = \omega/U_\infty$; in this regard it is appropriate to look at Λ_3 in terms of the limit

$$\lim_{k_3 \rightarrow 0} \int_{-\infty}^{\infty} \phi_{22}(k_1, k_3, \omega) dk_1 = \frac{\Lambda_3(\omega)}{\pi} \phi_{22}\left(k_1 = \frac{\omega}{U_\infty}\right)$$

when the behavior of Λ_3 with frequency is known.

Experimental verification of Equations (9.48) and (9.50) for fixed single airfoils has been provided by the measurements of Jackson et al.,⁵² who obtained the frequency spectra of lift fluctuations induced by incident grid turbulence. The airfoil was a NACA 0015 section with aspect ratio (L_3/C) of 2.68; the measurements were conducted in configurations with and without end plates at a chordwise Reynolds number of 1.6×10^4 . Figure 9.10 shows the measured values of the admittance

$$\left| A\left(\frac{\omega C}{2U_\infty}\right) \right|^2 = [\phi_2(\omega)]^{-1} \iint \phi_{22}(k_1, k_3, \omega) \left| S_{2D}\left(\frac{k_1 C}{2}, \frac{k_3 C}{2}\right) \right|^2 \cdot \left(\frac{\sin \frac{1}{2} k_3 L_3}{k_3 L_3/2} \right)^2 dk_1 dk_3 \quad (9.51)$$

The spectrum of the turbulence

$$\phi_2(\omega) = \iint_{-\infty}^{\infty} \phi_{22}(k_1, k_3, \omega) dk_1 dk_3$$

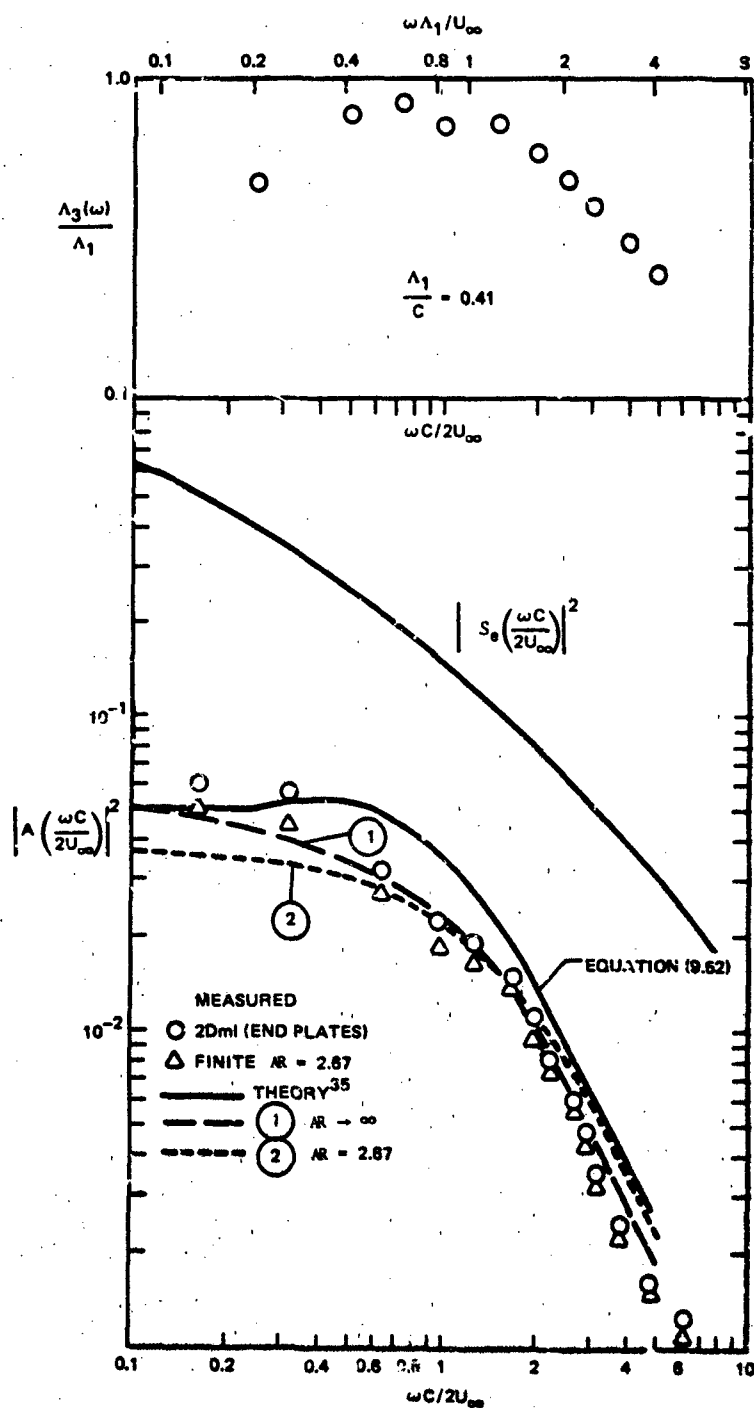


Figure 9.10 - Unsteady Aerodynamic Admittance Functions, Comparison of Experiment and Theory for the Integral Scales Shown

was determined by measurement with a hot wire anemometer. The Sears function, which applies to a one-dimensional gust (Equation (9.38)) greatly exceeds the measured admittance. In the case of the experiment, the span was larger than Λ_3 , and apparently the installation of end plates did not influence C_L^2 . In their program, Jackson et al.⁵² also measured the spanwise correlation functions of the turbulence at a variety of frequencies. From their correlations, values of $\Lambda_3(\omega)$ were computed; these are included at the top of Figure 9.10. Using the values of $\Lambda_3(\omega)$, the approximation of the admittance function in Equations (9.50) is

$$\left| A \left(\frac{\omega C}{2U_\infty} \right) \right|^2 = \frac{2\Lambda_3(\omega)}{L_3} \left| S_e \left(\frac{\omega C}{2U_\infty} \right) \right|^2 \quad (9.52)$$

which is basically a strip theory that utilizes the Sears function. The lines labeled 1 and 2 in the figure were calculated numerically by Jackson et al.⁵² using Graham's³⁵ influence function and fitted analytical functions to the measured streamwise and spanwise turbulence characteristics to obtain $\phi_{22}(k_1, k_3, \omega)$. They assumed frozen convection of the turbulence. In subsequent work it was found⁵³ that $A(\omega C/2U_\infty)$ is slightly sensitive to modest angles of attack at low frequencies.

An alternate to Equation (9.50) is Filotas' result,³⁴ which has the approximate form

$$\left| A \left(\frac{\omega C}{2U_\infty} \right) \right|^2 = \frac{\ln \left[1.2 + \pi^2 \left(\frac{\omega C}{U_\infty} \right)^2 \right]}{\ln \left[1.2 + 3\pi^2 \left(\frac{\omega C}{2U_\infty} \right)^2 \right]}, \quad \frac{\omega C}{2U_\infty} \gg \frac{C}{2\Lambda_3} \quad (9.53)$$

$$= \frac{\ln \left[1.2 + \pi^2 \left(\frac{C}{2\Lambda_3} \right)^2 \right]}{\ln \left[1.2 + 3\pi^2 \left(\frac{C}{2\Lambda_3} \right)^2 \right]}, \quad \frac{\omega C}{2U_\infty} \ll \frac{C}{2\Lambda_3}$$

which also agrees with Graham's measurements in Figure 9.10 when $2\Lambda_3/C \approx 0.7$. This function gives a frequency-independent admittance function at low frequencies which increases monotonically as the lateral integral scale increases. At the higher frequencies $\omega/U_\infty > 1/\Lambda_3$ and the admittance function is scale independent.

9.3.3 Surface Pressures Resulting From Unsteady Loads

Measurements of surface pressure fluctuations on a NACA 0012 airfoil in a turbulent stream were made by Paterson and Amiet.^{54,55} The Reynold's number based on chord varied over the approximate range 5×10^5 to 26×10^5 , with $0.1 < M < 0.5$. Figure 9.11 shows a selection of the measured results that have been made dimensionless on the parameters shown. In their measurement program, as in that of Jackson et al.,⁵² supporting turbulence wave number spectra and spanwise correlations were obtained. Their theoretically determined pressures were obtained from the full relationship from which Equation (9.45) was derived, but their formulation was valid at high frequencies and Mach numbers, i.e., without the restriction $Mk_1C < 1$. A simplified relationship for the surface pressures for completely incompressible flow

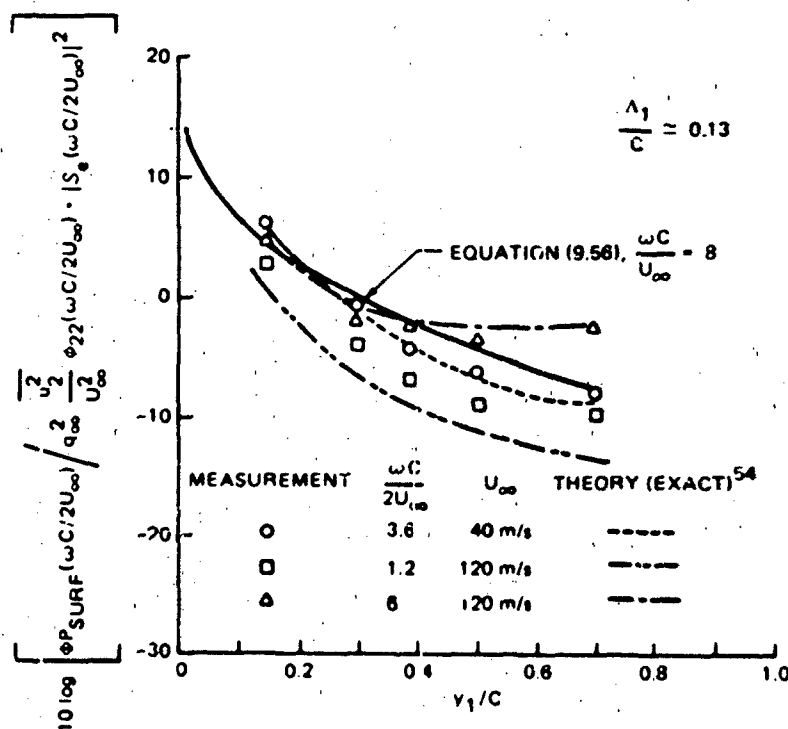


Figure 9.11 - Spectral Densities of Surface Pressures Induced by Ingested Turbulence on an Aerofoil

can be derived from Equation (9.44) using the above approach. The pressure difference between the upper and lower surface is actually

$$\Delta P(y_1, y_3, k_1, k_3, \omega) = 2p_s(y_1, y_3, k_1, k_3, \omega)$$

where $p_s(\vec{y}, \vec{k}, \omega)$ is the surface pressure on one side of the airfoil. The autospectral density of the surface pressure is then obtainable from Equation (9.44) as

$$\phi_{p_s}(y_1, \omega) = \rho_0^2 U_\infty^2 \overline{u_2^2} \left[\frac{\frac{C}{2} - y_1}{\frac{C}{2} + y_1} \right] \cdot \iint_{-\infty}^{\infty} \phi_{22}(k_1, k_3, \omega) \left| S_{2D}\left(\frac{k_1 C}{2}, \frac{k_3 C}{2}\right) \right|^2 dk_1 dk_3 \quad (9.54)$$

Equation (9.54) differs from that of Amiet and Equation (9.45) in the absence of a phase function that accounts for the chordwise propagation and the interference of pressures across the surface at high frequencies $M k_1 C > 1$. The use of Equation (9.49) for the spanwise wave number spectrum and the frozen convection approximation (Equations (3.83) and (3.95)) gives

$$\frac{\phi_{p_s}(y_1, \omega)}{q_\infty^2} = 4 \frac{\overline{u_2^2} \phi_{22}(\omega)}{U_\infty^2} \left(\frac{\frac{C}{2} - y_1}{\frac{C}{2} + y_1} \right) \int_{-\infty}^{\infty} \left| S_{2D}\left(\frac{\omega C}{2U_\infty}, \frac{k_3 C}{2}\right) \right|^2 \dots \frac{\Lambda_3(\omega)}{\pi [1 + (\Lambda_3(\omega) k_3)^2]} \cdot dk_3 \quad (9.55)$$

To determine a closed-form approximation for this integral we cannot simply introduce the Sears function because of the necessity of integrating over all spanwise wave numbers. To this end we introduce the approximation to Graham's two-dimensional influence function (Equation (9.42)), which requires integration of

$$I_3 = \int_{-\infty}^{\infty} \frac{1 + 3.2 \left(\frac{\omega C}{U_\infty} \right)^{1/2}}{1 + 3.2 \left(\frac{\omega C}{U_\infty} \right)^{1/2} + 2.4 (k_3 C)^2} \cdot \frac{\Lambda_3(\omega)}{\pi [1 + (\Lambda_3(\omega) k_3)^2]} dk_3$$

The lateral wave number response function begins to diminish as $k_3 C > (\omega C/U_\infty)^{1/4} > 1$, while the turbulence spectrum decays when $k_3 > \Lambda_3^{-1}$. Thus these two functions may be decoupled in alternate limits depending on Λ_3 , C , and $\omega C/U_\infty$, which we shall write

$$I_3 \approx 1 \text{ for } \frac{\Lambda_3}{C} > 1 \text{ or } > \left[\frac{1 + 3.2 \left(\frac{\omega C}{U} \right)}{2.4} \right]^{1/2}$$

$$I_3 \approx \frac{\Lambda_3}{C} \left[\frac{1 + 3.2 \left(\frac{\omega C}{U} \right)}{2.4} \right]^{1/2} \text{ for } \frac{\Lambda_3}{C} \ll \left[\frac{1 + 3.2 \left(\frac{\omega C}{U} \right)}{2.4} \right]^{1/2}$$

Carrying out the integration,⁵⁶ the entire function is

$$I_3 = \frac{\left[\frac{2.4}{1 + 3.2 \left(\frac{\omega C}{U} \right)^{1/2}} \right]^{1/2} \frac{C}{\Lambda_3(\omega)} - 1}{\frac{2.4}{1 + 3.2 \left(\frac{\omega C}{U} \right)^{1/2}} \left(\frac{C}{\Lambda_3(\omega)} \right)^2 - 1}$$

Introducing the simplification of I_3 into Equation (9.55), a nondimensional form for the autospectrum of the surface pressure at y_1 is found as

$$\frac{\phi_{p_s} \left(y_1, \frac{\omega C}{U_\infty} \right)}{q_\infty^2 \left(\frac{u_2^2}{U_\infty^2} \right) \cdot \phi_{22} \left(\frac{\omega C}{U_\infty} \right) \cdot \left| s_e \left(\frac{\omega C}{2U_\infty} \right) \right|^2} = 4 \left(\frac{\frac{C}{2} - y_1}{\frac{C}{2} + y_1} \right) \text{ for } \frac{\Lambda_3}{C} > 1, \text{ or } > \left[\frac{1 + 3.2 \left(\frac{\omega C}{U} \right)}{2.4} \right]^{1/2}$$

or

$$= 4 \left(\frac{\frac{C}{2} - y_1}{\frac{C}{2} + y_1} \right) \frac{\Lambda_3}{C} \left[\frac{1 + 3.2 \left(\frac{\omega C}{U_\infty} \right)}{2.4} \right]^{1/2} \quad \text{for } \frac{\Lambda_3}{C} < \left[\frac{1 + 3.2 \left(\frac{\omega C}{U_\infty} \right)}{2.4} \right]^{1/2} \quad (9.56)$$

where $-C/2 < y_1 < C/2$.

This approximation agrees reasonably well with the measured results of Paterson and Amiet⁵⁴; however, the more exact numerical evaluation of Amiet predicts the observed relative trends more accurately. The surface pressures, both measured and predicted, show a maximum at the leading edge; the prediction in fact shows a singularity there. This is a consequence of applying a Kutta condition at the trailing edge, i.e., $\partial R / \partial y_2 = 0$, and leaving the boundary condition at the leading edge unspecified. In reality, the singularity is removed by either laminar flow separation or finite curvature effects.

9.3.4 Observations of Noise from Inflow Inhomogeneities

Equation (9.12) can be adopted directly when $k_0 C < 2\pi$. In dimensionless form, this is

$$\frac{\phi_{\text{rad}}(r, \theta, \omega)}{q_\infty^2 M^2} = \frac{\sin^2 \theta}{4\pi^2} \cdot \left(\frac{L_3}{r} \right)^2 \left(\frac{\omega C}{2U_\infty} \right)^2 \overline{C_L^2(\omega)}, \quad \frac{\omega C}{c_0} < 2\pi \quad (9.57)$$

where $\overline{C_L^2(\omega)}$ is the spectrum of the net oscillatory lift (Equation (9.50b)). At higher frequencies such that the chord can no longer be considered small, the expressions of Paterson and Amiet⁵⁴ can be approximated to give

$$\frac{\phi_{\text{rad}}(r, \theta, \omega)}{q_\infty^2 M^2} \approx \frac{2 \sin^2 \frac{\theta}{2}}{\pi^2} \cdot \left(\frac{L_3}{r} \right)^2 \frac{2\Lambda_3}{L_3} \frac{u_2^2}{U_\infty^2} \phi_{22}(\omega) \quad \text{for } \frac{\omega C}{c_0} > 2\pi \quad (9.58)$$

and for $2\Lambda_3/L_3 \ll 1$, which is identical in parametric form to Equation (9.21). In both equations, the vector $(r, \theta) = (r, 0)$ points into the direction of the flow, while

the vector $(r, \theta) = (r, \pi)$ points downstream. These two relationships can be compared with measurements. It is convenient to express the acoustical effects of finite chord as a ratio of Equations (9.57) and (9.58). To this end, Equation (9.50a) can be used for the lift spectrum to obtain

$$\frac{\phi_{p_{rad}}(r, \theta, \omega)_{edge}}{\phi_{p_{rad}}(r, \theta, \omega)_{compact}} \approx \frac{8}{\pi \frac{\omega C}{c_0}} \quad (9.59)$$

if the differences in directivity are ignored by taking field points directly normal to the surface $\theta = \phi = 90^\circ$.

Measurements of sound due to the interaction of airfoils with upstream turbulence* have been made by Clark and Ribner,¹⁵ Dean,⁵⁷ Fink,⁵⁸ Amiet,⁵⁹ and Paterson and Amiet^{54,55} for airfoils responding to upstream turbulence, and by Fujita and Kovasznay⁴⁶ for an airfoil responding to a periodic time-varying wake defect. Clark and Ribner present no spectral densities of radiated noise, but confirm the general validity of Equation (9.12) and (9.57) through correlations of the oscillating lift and radiated sound pressure. Measurements by Paterson and Amiet are shown in Figure 9.12 in nondimensional form. These measurements were obtained at the same time as data for surface pressures shown above in Figure 9.11. The flagged points denote frequencies for which $\omega C/c_0 > 2\pi$ and Equation (9.57) are not expected to hold. The dotted line in the figure is the square of the reduced frequency times the spectrum of oscillatory lift; the latter was calculated using Equation (9.50a). The solid lines are the more precise theoretical values calculated by Paterson and Amiet,^{54,55} which are valid for all values of $M\omega C/2U_\infty = \omega C/c_0$. At frequencies small enough that acoustic effects are insignificant, the dimensionless sound pressures are very accurately predicted by the simple dipole relationship (Equation (9.57)). The dimensionless sound pressures of Dean⁵⁷ and Fink^{58,60} are shown in Figures 9.13 and 9.14, respectively. The ordinates reflect the different normalizations that were used by the investigators, and all measured values can be seen to be equally well predicted by the theory.

*Measurements of noise from rotors and fans are discussed in Chapter 10.

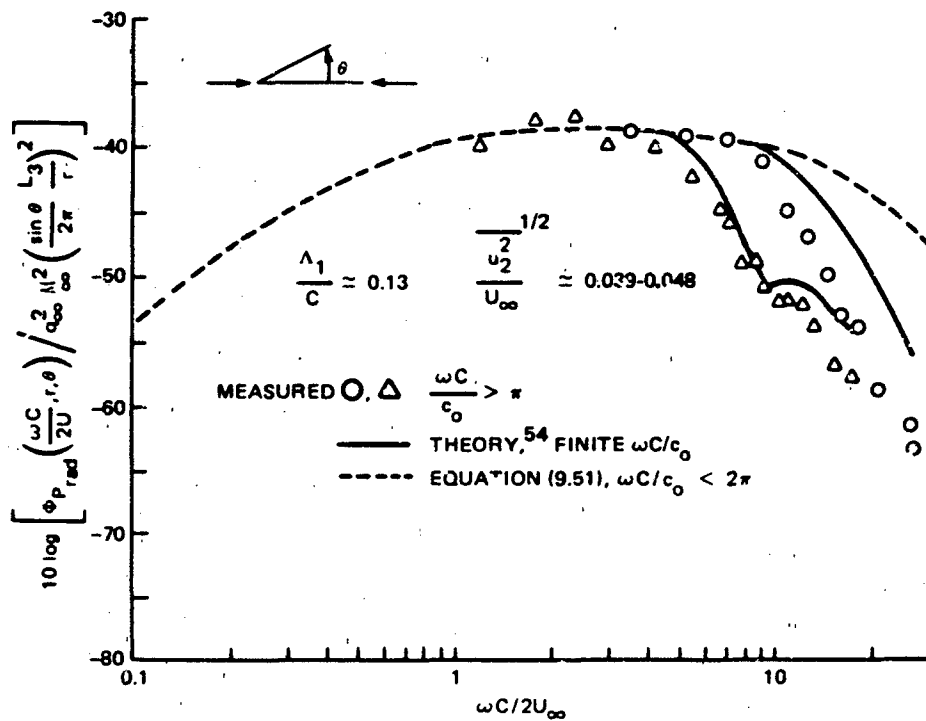


Figure 9.12 - Spectral Density of Radiated-Noise Resulting from Turbulence Ingestion to an Airfoil; Comparison of Measurement and Theory

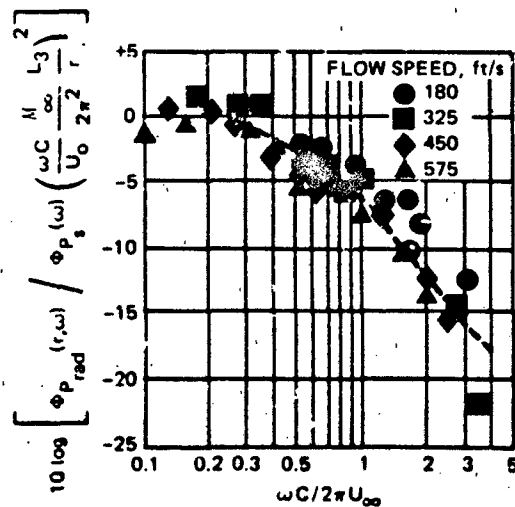


Figure 9.13 - Radiated Sound Pressure Levels from an Airfoil in Turbulent Flow. Noise Levels Have been Nondimensionalized on the Surface Pressure, Spectrum Measured at the Quarter-Chord Point⁵⁷

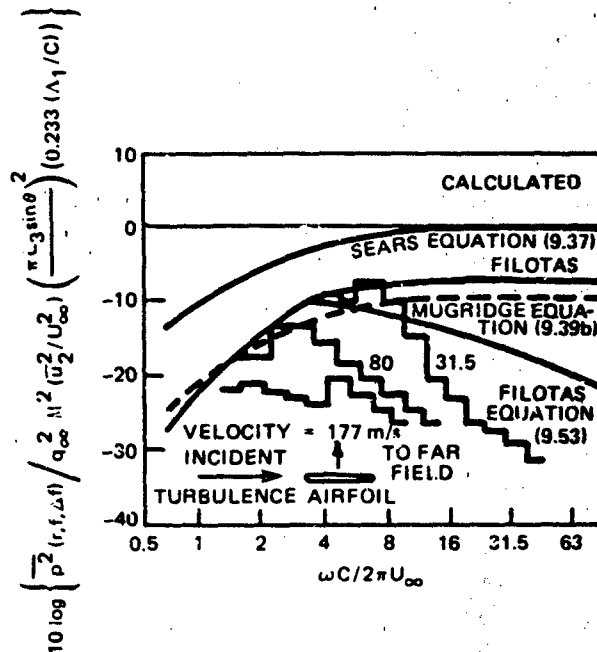


Figure 9.14 - Radiated Sound Pressure Levels from a Rigid Airfoil Responding to Inflow Turbulence Created by a Grid Upstream.

Measurements and Theory Are Taken from Fink^{58,60},
 Filter Band $\Delta f = 0.233f$, $\Lambda = 32$ cm, $\Lambda_3 = 1.9$ cm,
 $C = 46$ cm, and $L_3 = 53$ cm

Dean's form of nondimensionalization is found by combining Equations (9.56), (9.57), and (9.50) to obtain a function that is independent of $|A|^2$; i.e.,

$$\frac{\phi_{\text{prad}}(r, \theta, \omega)}{\phi_{\text{ps}}\left(y_1 = -\frac{C}{4}, \frac{\omega C}{U_\infty}\right)} = \frac{(2\pi)^2}{24} \frac{\Lambda_3}{L_3} \cdot \left\{ x \frac{x}{\Lambda_3} \left[\frac{1 + 3.4(\omega C / U_\infty)^{1/2}}{2.4} \right]^{1/2} \right\}$$

$$\left(\frac{\omega C}{U_\infty} \frac{M}{2\pi} \frac{L_3}{r} \right)^2$$

depending on the limits as stated for Equation (9.56). Note that when $\Lambda_3/L_3 > 1$, Λ_3/L_3 is replaced by unity. At very low frequencies this factor approaches $(2\pi)^2/24 \approx 1.6$ in agreement with the notion that when $\Lambda_3 > C$ on L_3 , the deft response of the airfoil is correlated and it radiates over a correlation area equal to (CL_3) . Figure 9.13 indicates that at high frequencies Λ_3/L_3 is smaller than unity and the sound radiation process is more limited by the local leading edge; i.e., the correlation area becomes less than (CL_3) .

The form of Fink's nondimensionalization may be found by combining Equations (9.49), (9.50), and (9.57) to obtain

$$\frac{\overline{p^2(f, \Delta f)}}{q_\infty^2 M_\infty^2 \frac{u_\infty^2}{U_\infty^2} \left(\frac{L_3}{r}\right) \left(0.233 \frac{\Lambda_1}{C}\right) (\pi \sin \phi)^2} = \left(\frac{fC}{U_\infty}\right)^3 \left|A\left(\frac{\omega C}{U_\infty}\right)\right|^2 \frac{4}{1 + \left(\frac{\omega \Lambda_1}{U_\infty}\right)^2}$$

The notations to Dean, Filotas, and Mugridge refer to the various approximations to the admittance function. Note that when $\omega C/c_0 > 2\pi$, Equation (9.57) does not hold; for $U_\infty = 31.5$ and 80 m/s of Fink's measurements this occurs when $\omega C/2\pi U_\infty = 10.5$ and 4.1 , respectively. As described below, this may account for the remaining discrepancy between Equation (9.53) and the measurements.

Semiempirical prediction techniques for other forms of leading-edge noise in more complex arrangements have been reviewed by Fink.¹⁶

The discrepancies between the observed levels of noise and those computed from the theory of the simple dipole can be looked at as the ratio of the finite to point radiated noise levels. Figure 9.15 shows the ratio derived in three ways. The theoretical values of Paterson and Amiet^{54,55} (Figure 9.15) show an interference pattern in the frequency region $2\pi < \omega C/c_0 < 4\pi$ that agrees with the measured values. This behavior has been shown as a ratio of the sound predicted by the exact theory to that predicted for the point dipole. The simple asymptote for high frequency (Equation (9.59)) is numerically larger than the heuristic correction function proposed by Hayden,⁶¹ which is

$$\frac{[\phi_{\text{Prad}}(r, \omega)]_{\text{finite}}}{[\phi_{\text{Prad}}(r, \omega)]_{\text{point}}} \approx \frac{1}{1 + \left(\frac{\omega C}{2c_0}\right)^2} \quad (9.60)$$

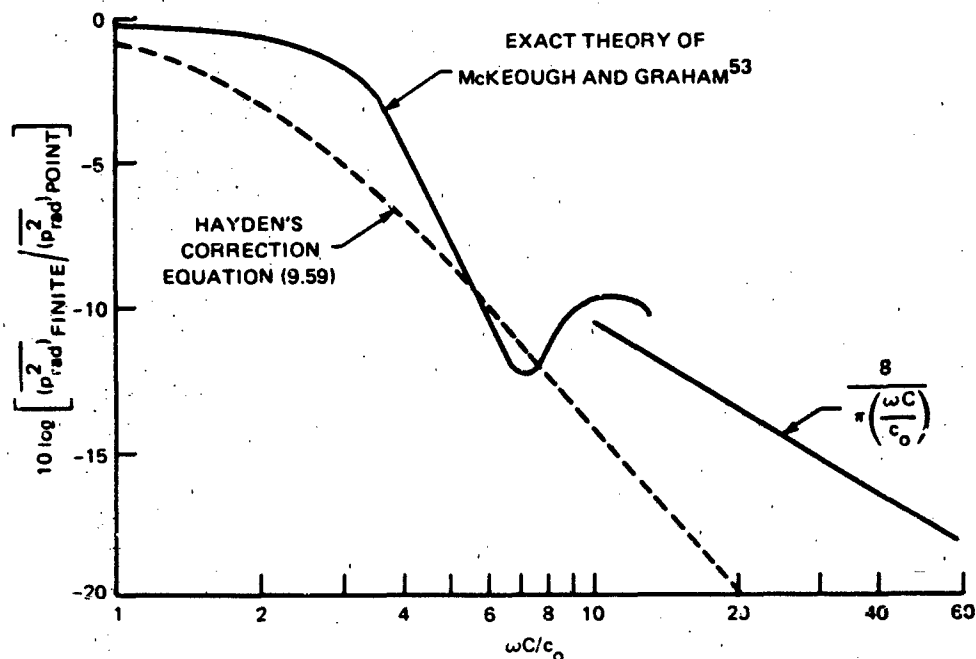


Figure 9.15 - Reduction of Sound from Unsteady Flow Over Lifting Surfaces.
Reduction Caused by Finite Chord Relative to Acoustic Wavelength

Although Hayden's function appears to roughly describe the trend shown by the exact theory at low frequencies in Figure 9.15, it does not appear to agree at high frequencies with either the frequency dependence or the speed dependence that one would expect for the half-plane versus point-dipole radiation.

The time-dependent lift, surface pressure, and radiated sound from an airfoil cutting through stationary wakes has been treated theoretically by Fujita and Kovasznay,⁴⁶ Mayer,⁶² and Lefcort.⁶³ Measurements to corroborate the theory have been made by Fujita and Kovasznay with simultaneous surface and far-field pressure measurements. The configuration examined by Fujita and Kovasznay has direct application to the radiated sound from a single stator blade responding to the wake of a passing upstream rotor blade. The mean velocity defect in the wake causes a time-dependent perturbation on the angle of attack of the fixed airfoil. This variation in downwash caused by the wake of an upstream body moving relative to the airfoil can be designated as $u_2(y_0 - y_1)$, so that the maximum value of u_2 occurs at $y_1 = y_0$. The time-dependent downwash is $u_2(y_0 - U_\infty t)$, referring time to the

instant that the leading edge coincides with y_0 . The oscillation in angle of attack is $u_2(y_0 - U_\infty t)/U_\infty$. The appropriate form of Equation (9.44) for the surface pressure in this case is

$$\Delta p(y_1, \omega, t) = 2\rho_0 U_\infty u_2(\omega) \left(\frac{\frac{C}{2} - y_1}{\frac{C}{2} + y_1} \right)^{1/2} S_e \left(\frac{\omega C}{2U_\infty} \right) e^{-i\omega t} \quad (9.61)$$

This form arises from

$$\begin{aligned} \int_{-\infty}^{\infty} u_2(k_1, k_3, \omega) dk_1 &= \int_{-\infty}^{\infty} u_2(k_1, 0) \delta(\omega - U_\infty k_1) dk_1 \\ &= u_2\left(k_1 = \frac{\omega}{U_\infty}\right) \\ &= U_\infty u_2(\omega) \end{aligned}$$

where

$$u_2(k_1) = \frac{1}{2\pi} \int_{-\infty}^{\infty} u_2(y_1) e^{-ik_1 y_1} dy_1$$

is the spatial Fourier transform of the downwash with a span-independent downwash being assumed. The time-dependent pressure differential across the airfoil at chordwise location y_1 is

$$\begin{aligned} \Delta P(y_1, t) &= \int_{-\infty}^{\infty} \Delta P(y_1, \omega, t) d\omega \\ &= 2\rho_0 U_\infty \left(\frac{\frac{C}{2} - y_1}{\frac{C}{2} + y_1} \right)^{1/2} \int_{-\infty}^{\infty} u_2(\omega) S_e \left(\frac{\omega C}{2U_\infty} \right) e^{-i\omega t} d\omega \quad (9.62) \end{aligned}$$

Equation (9.62) can be integrated over the span to determine the instantaneous time-dependent lift and subsequently the sound.

In the experiment of Fujita and Kovasznay,⁴⁶ a fixed airfoil was positioned along the radius of a rotating rod and both were placed in the open-jet wind tunnel, which exhausted into an anechoic chamber. The alignment was such that the wake of the rod impinged along the leading edge of the airfoil twice per revolution of the rod. This arrangement represents, idealistically, viscous rotor/stator interactions due to the presence of inlet or outlet guide vanes. Figure 9.16 shows time records of the instantaneous surface pressure distribution, lift coefficient, time derivative of the lift coefficient, and radiated sound. At the angle of attack of 10 deg the effect of the wake was to initiate leading-edge separation, which subsequently reattached as the airfoil progressed into the wake. This caused the rate of change of the lift coefficient $dC_L/d(tU_\infty/C)$ to nearly double for that case. The pressure distribution shows the square-root functional increase in pressure at the leading edge except when separation occurred. The measurements of the radiated noise from the transient response of an airfoil passing through the wake defect of a cylinder, agreed with predictions based on Equation (9.57) and measured lift coefficients. In their case the radiated sound pressure was determined in the time domain. They evaluated

$$\frac{p(r,t)}{qM \left(\frac{1}{2\pi} \frac{L_2}{r} \right)} = \left\{ \frac{dC_L \left(\frac{tU_\infty}{C} \right)}{d \left(\frac{tU_\infty}{C} \right)} + \frac{C_L \left(\frac{tU_\infty}{C} \right)}{\frac{2r}{C}} \right\} \cos \theta$$

which includes the full effects of acoustic time retardation.

9.4 VISCOUS EFFECTS: BOUNDARY-LAYER AND VORTEX-WAKE DEVELOPMENT

These flow types include all flow on the lifting surfaces whose characteristics are determined by the shear flow adjacent to the surface and in the trailing-edge wake.

The discussion is restricted to flow over rigid lifting surfaces. Consideration of surface flexure and hydroelastic coupling to the fluid motions, which are related to singing, are reserved for Section 9.7. The areas considered are

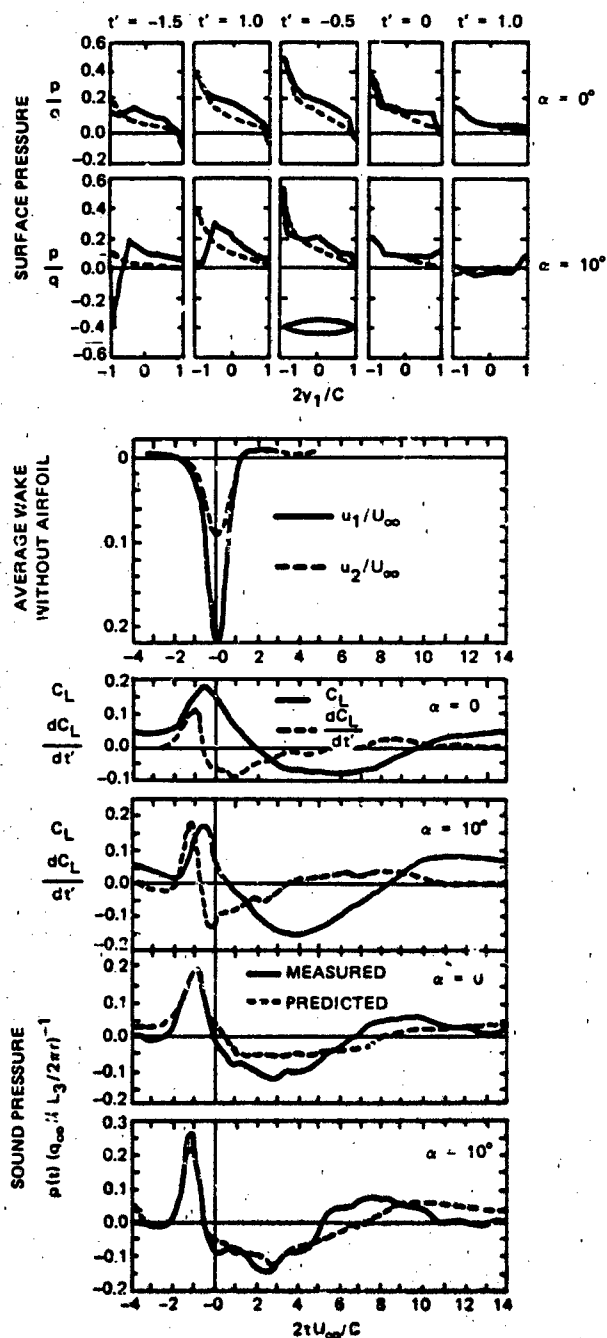


Figure 9.16 - Surface Pressure, Lift Coefficient, and Sound Pressure Caused by the Illustrated Shear Flow Passing by a Sharp-Edged Airfoil ($R_c = 2.5 \times 10^5$). Airfoil Is a Symmetrical Circular-Arc Section with $h_m/C = 0.14$. Adopted from Fujita and Kovasznay⁴⁶

1. Boundary-layer growth on lifting surfaces
2. The onset of vortex shedding
3. Influences of edge geometry on flow structure
4. Alternative definitions of Strouhal number
5. Flow-induced trailing-edge pressures and forces

4.1 Boundary-Layer Growth on Lifting Surfaces

This aspect of lifting-surface hydrodynamics has an indirect influence on radiated noise. For airfoils with undisturbed inflow, the static pressure gradient influences the laminar boundary-layer growth and laminar turbulent transition. References given in Sections 4.3.2.7 and 7.5 apply here. In addition, Schlichting⁶⁴ summarizes methods of calculation and some experimental observations, including characteristics of the Joukowski airfoil and many of the NACA lifting sections. Abbott and von Doenhoff⁶⁵ provide a compilation of most general lifting characteristics of NACA sections. When the flow remains laminar beyond the point of minimum pressure, laminar separation can occur as the static pressure gradient becomes adverse. In these cases, if the separation is intermittent because of unsteady inflow conditions, the temporal variation of section lift coefficients can also be aggravated. This situation has been observed by Fujita and Kovasznay,⁴⁶ who also report an associated increase in radiated noise. Certain section shapes are designed to retard laminar turbulent transition by appropriate location of the point of maximum thickness. Generally, the transition and separation characteristics of lifting sections are also dependent on the angle of attack. Often at moderate angles of attack the separated flow very near the leading edge will reattach itself to the foil as it becomes turbulent, initiating the turbulent boundary layer. Characteristics of the NACA 0012 section are given by Gault,⁶⁶ Peterson,⁶⁷ von Doenhoff⁶⁸ and of the Joukowski section by Schlichting.⁶⁴ The transition behavior on these sections makes scaling of model measurements somewhat difficult because of large changes with Reynolds number.⁶⁹ However, for values of Reynolds number based on chord that are greater than 10^6 , the flow will most likely be turbulent, at least downstream of the point of maximum thickness unless the boundary layer is tripped at the leading edge. Another situation in which the simple boundary-layer equations will fail to adequately predict the flow is the case of high-lift sections, which are thick sections designed (e.g., Leibick⁷⁰) for maximum lift at high Reynolds

number. These are designed for maximum loading without turbulent boundary-layer separation.

The characteristics of boundary-layer development on lifting surfaces with oscillating angle of attack have been mostly examined for the purpose of assessing the effects for large fluctuations in angle of attack on laminar separation. Emphasis in that work has generally been directed toward problems of dynamic stalling and flutter. Computations of Tollmein-Schlichting wave stability have been made by Chu⁷¹ on a Joukowski airfoil shape for angle of attack oscillations from 0 deg, 0.95 deg, and 3 deg. At $R_c = 1.5 \times 10^6$, little change in the point of neutral stability was computed for an oscillation of 0.95 deg, but the point moved forward from the 45% chord point to the 15% chord point for a 3-deg oscillation. The effect was calculated for a reduced frequency ($\omega c/2U_\infty$) of 0.25. However, no substantial change in the boundary displacement thickness or wall-shear stress (less than 10%) was computed downstream of the midsection of the surface.

The boundary-layer thickness and wall-shear coefficients along the contours of lifting surfaces can be computed using any number of the techniques summarized by Schlichting.⁶⁴ The method of Truckenbrodt seems to be well used; the earlier equations by Gruschwitz have been verified by the measurements on an airplane wing in flight by Stuber.⁷² All prediction techniques require the static pressure distribution for the lifting section as a starting point. The momentum thickness (Equation (7.33a)), is then integrated using estimates of the shape factor and wall-shear coefficient. The initial condition for the calculation requires the knowledge of the momentum thickness at the end of the transition zone. Schlichting⁶⁴ gives a worked example. Note that although Equations (7.34) and (7.36) give a rough measure of θ/C near the trailing edge, the estimates do not generally agree with measured values of the detailed variation along the surface, especially at angles of attack. However, these equations give rough order-of-magnitude values on lightly loaded sections which may be relied on when other computation tools are unavailable. An example with the commonly used NACA 0012 section is given in Figure 9.17. The actual momentum thickness near the trailing edge exceeds the values predicted with Equations (7.34) and (7.36) because of the influence of the airfoil curvature in establishing an adverse pressure gradient. At the trailing edge, θ and δ^* should therefore depend on Reynolds number, thickness, and angle of attack. At a 0-deg angle of attack it will be assumed in Section 9.6 that for the naturally developing

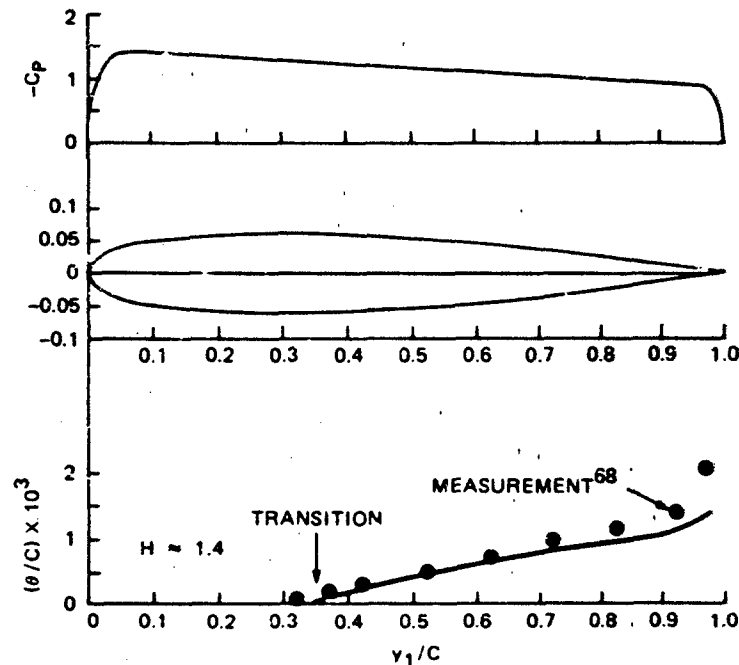


Figure 9.17 - Characteristics of Boundary Layer Growth
on NACA-0012 Section at $R_c = 7.6 \times 10^6$

turbulent boundary layer, i.e., no turbulence stimulators (trips) at the leading edge, $\delta^*/h_m = \text{constant}$, where h_m is the maximum thickness.

Later measurements on an NACA 63-009 section in a wind tunnel are shown in Figure 9.18. This thin, uncambered section shows two practical aspects of the viscous flow. At a 0-deg angle of attack the static pressure gradient is small, and, assuming that transition occurs near the leading edge, Equations (7.34) and (7.36) adequately predict the momentum thickness. At a 4-deg angle of attack there is a strongly adverse pressure gradient near the leading edge, and laminar separation occurs over a region of $\delta C \approx 0.006C$, as indicated by the arrow; at the point of reattachment the flow was turbulent. (This airfoil stalled at an 8.5-deg angle of attack.) Downstream of reattachment, the remainder of the section had an adverse pressure gradient. The simple boundary-layer equation fails to predict this case, which is initiated (tripped) by the separated flow and controlled by a pressure gradient.

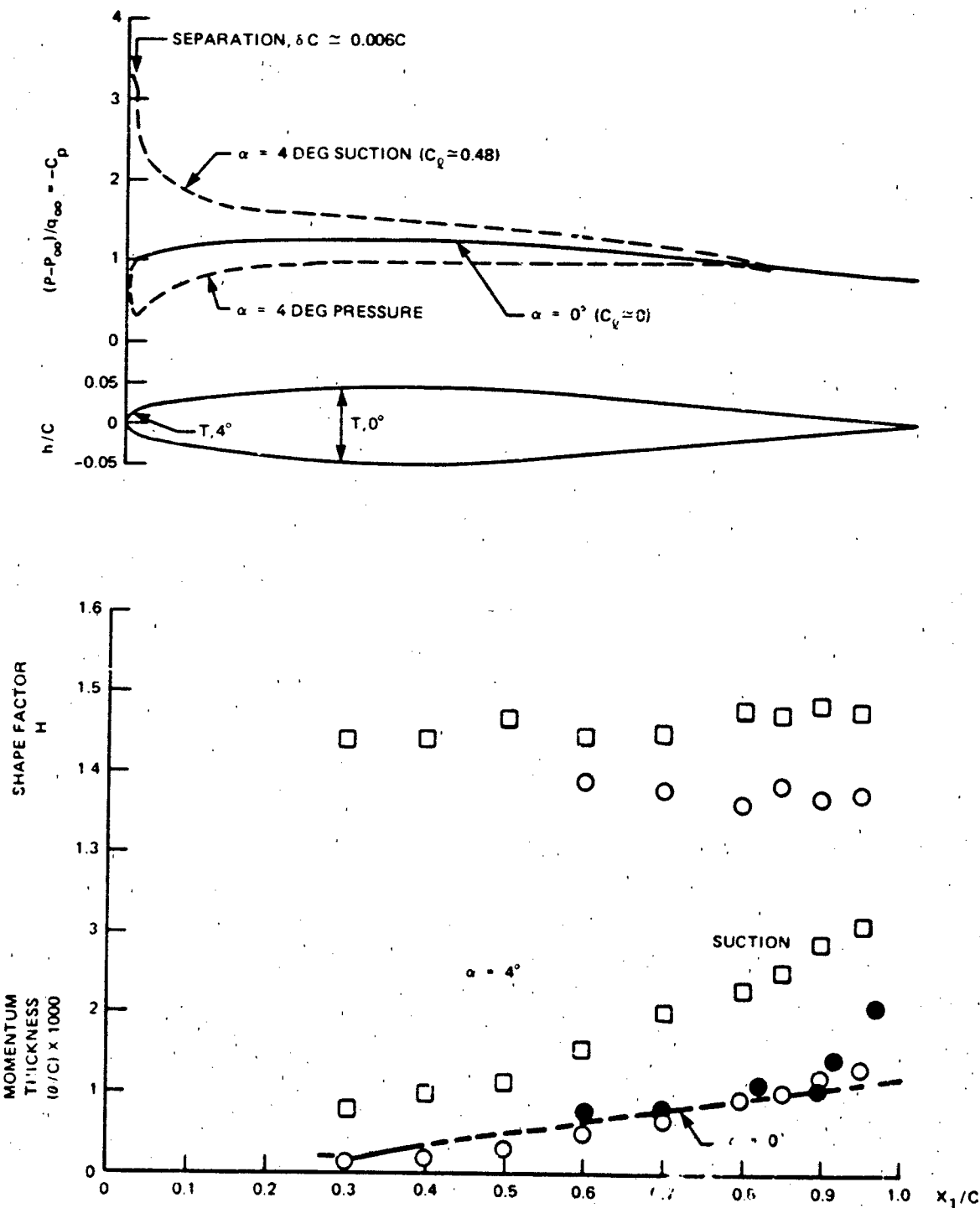


Figure 9.18 - Characteristics of Boundary-Layer Growth on a Thin Airfoil Section, NACA 63-009, $R_c = 5.8 \times 10^6$, $M = 0.167^{66}$, Closed Points, $\alpha = 0^\circ$, Open Points, $\alpha = 4^\circ$

In estimating the momentum thickness at the trailing edges of lifting surfaces, as long as the pressure gradient is not severe and laminar separation does not trip the boundary layer, it appears that the simple formulae in Equations (7.34) and (7.36) will give an approximate value for acoustic estimations. This value will probably be conservative, and it will probably lead to slight overestimates of the characteristic frequencies that are based on the dimensionless scaling $\omega\delta/U$, $\delta \approx 10\theta$. The effects of surface roughness can be included in the procedures outlined by Schlichting⁶⁴ (see also Section 7.2).

9.4.2 Conditions for Vortex Formation at Trailing Edges of Rigid Surfaces

9.4.2.1 Sharp Trailing Edges. The natural generation of acoustic or vibration tones by rigid lifting surfaces is ultimately controlled by the production of periodic vortex-street wakes at the trailing edges. As a practical issue, the prediction of the tone frequencies and the reliable prevention of the tones is of first-order importance in both hydro and aero-acoustics. Continuous-spectrum sound which will occur (and be occasionally co-existent with tones) may be of secondary importance. The latter is important, for example, for high-performance aircraft wings which employ lift-augmentation devices.

We are interested in a reasonably precise description of the unsteady fluid mechanics of trailing edges. First, we require a reliable method of predicting the conditions for the occurrence or nonoccurrence of tones and their frequencies. Second, an understanding of the fluid mechanical causes for the generation of vortex-street wakes is helpful in either explaining or discovering noise and vibration control methods. Third, analytical modeling of both the near-field surface pressures and far-field sound pressures of various types of flows, (both continuous-spectrum and tone produced) requires some physical notion of the statistical structure of the near wakes of the edges.

In the present context, the most elementary wake-producing surface is the thin flat plate. When laminar viscous flow exists on both sides of a thin flat plate, periodic vortex formation occurs, very much like those shown in Figure 9.3(a) and (b), and Figure 5.1. In fact, the mean velocity profiles and the dynamics of wake instabilities of laminar wakes of both cylinders and flat plates are qualitatively identical, as discussed in Section 5.2. The theoretical determinations of wave speeds and wavelengths of unstable modes of laminar wakes of flat plates following

the same format as outlined in Section 3.2 has been done by Sato and Kuriki⁷³ and Mattingly and Criminale.⁷⁴ The mean velocity profile chosen for the calculation of Figures 5.6 and 5.7 was taken from the work of Sato and Kuriki. For Reynolds numbers exceeding $U_\infty b/\nu > 8$ (where b is a wake width defined by Equation (5.3)), such wakes are theoretically unstable. At Reynolds numbers up to 700, the wave mechanical properties compare favorably with each other and with Figure 5.7.

At high Reynolds numbers, such that the boundary layers on each side of the flat plate are fully turbulent upstream of the trailing edge, the wake generates no periodic disturbance. In fact, measurements of Chevray and Kovaszny⁷⁵ show that the shear layers shed at the trailing edge simply merged to form a stable wake. The trailing edge of the "flat plate" had a slight taper of a 0.13-deg included angle, a base height h (trailing-edge thickness) of only 0.025 cm, and a relatively thick boundary layer such that $2\theta/h = 46$, where θ is the momentum thickness of the boundary layer at the trailing-edge. For comparison, the wake Reynolds number was on the order of $U_\infty b/\nu = 10^4$, with b determined in the same manner as for the laminar wakes discussed above. It is apparent, therefore, that for flat plates or thin airfoils with sharp trailing edges (with sharpness defined in small fractions of 2θ), a limiting Reynolds number based on chord exists above which periodic wake disturbances should not be expected. This Reynolds number, $U_\infty C/\nu$, where C is the chord, has been found by Patterson et al.⁷⁶ to be dependent on the angle of attack of the airfoil and to be in the range 8×10^5 to 2.4×10^6 for an NACA 0012 airfoil. The relationship to boundary-layer development is clear, since Figure 7.55 indicates that the turbulent breakdown of Tollmein-Schlichting waves occurs at R_g , in excess of roughly 1.5×10^6 , so that substantial laminar flow should be expected on the surfaces of thin airfoils only up to $R_c = 1.5 \times 10^6$. This limit might be slightly higher on thick airfoils with large regions of favorable pressure gradient forward of the mid chord.

Note that hypotheses of coupling existing between wake instabilities and Tollmein-Schlichting waves in the laminar boundary layers of lifting surfaces have been put forth by some investigators via Tam,⁷⁷ Longhouse,⁷⁸ Archibald,⁷⁹ and Fink⁸⁰ to explain certain observed "jumps" in a uniform increase of frequency of vortex formation (or acoustic tones) with forward velocity. Furthermore the acoustic tones generated by airfoils at $R < 2 \times 10^6$ have been eliminated by the abovementioned investigators by roughening or serrating the leading edges of their airfoils.

9.4.2.2 Blunt Trailing Edges and Wake Geometry. Airfoils with squared-off blunt trailing edges may be expected to generate periodic vortex sheets and acoustic tones whether the boundary layers on the airfoil are laminar or turbulent. The discussion which follows generally applies to both laminar and turbulent upstream flows, but the specific examples will be those for which turbulent upstream flow exists. Measurements of the flow structure in near-wakes of blunt edges have been made by Eagleson et al.,⁸¹ Blake,⁸²⁻⁸⁴ and Bearman⁸⁵; extensive flow visualizations, such as that resulting in Figure 9.3(c), have been made by Meyers,² Greenway and Wood,³ Mattingly and Criminale,⁷⁴ Seshagiri,⁸⁶ and Wood.⁸⁷ Measurements by Brooks and Hodgeson⁸⁸ of sound levels emitted by an NACA 0012 airfoil at $R_c \approx 3 \times 10^6$ (with boundary layer tripping that resulted in a relatively large momentum thickness at the trailing edge, $\theta/C \approx 4.3 \times 10^{-3}$ where $C = 61$ cm) showed that weakly periodic vortex shedding occurred when $2\theta/h \approx 2.1$ and 2.8 , but not when $2\theta/h = 5$ or infinity (sharp edge). A working criterion for "bluntness" may therefore be $2\theta/h$ in excess of 5 to prevent vortex shedding with turbulent flow airfoils, since collective observations^{75,88} show that tones are not generated at values of 5, 46, and ∞ .

The mechanics of vortex formation behind the squared-off blunt edges (Figure 9.19(a)) is strongly nonlinear and not amenable to the same methods of linear stability theory introduced in Chapters 3 and 5. For small values of $2\theta/h$, the shear layers in the near wake may be analytically regarded as a pair of vortex sheets. As the sheets move downstream, their response to any small perturbation will result in the formation of vortices. The numerical computations of the motions of a pair of such vortex sheets by Abernathy and Kronauer⁸⁹ and Boldman et al.⁹⁰ shown in Figure 9.20 show this tendency very well. The computed successive stages of deformation of a pair of vortex sheets at various times following some initial disturbance to the originally parallel sheets, show matured deformations which are clustered into local concentrations of vorticity. The least stable of all possible arrangements is the one for which the ratio of the streamwise to cross-stream distances between cluster centers corresponds closely to that between vortices in the actual wake shown in Figure 9.3(c). The computed spacings are also similar to those which have been found to be most stable by von Karman and Rubach.^{91,92} Figure 9.20 also shows a parallel between the wavelength of small amplitude wave-like oscillation, and the streamwise spacing of large-scale concentrations of vorticity which is very much like that observed for other hydrodynamically unstable motions discussed in Chapter 3.

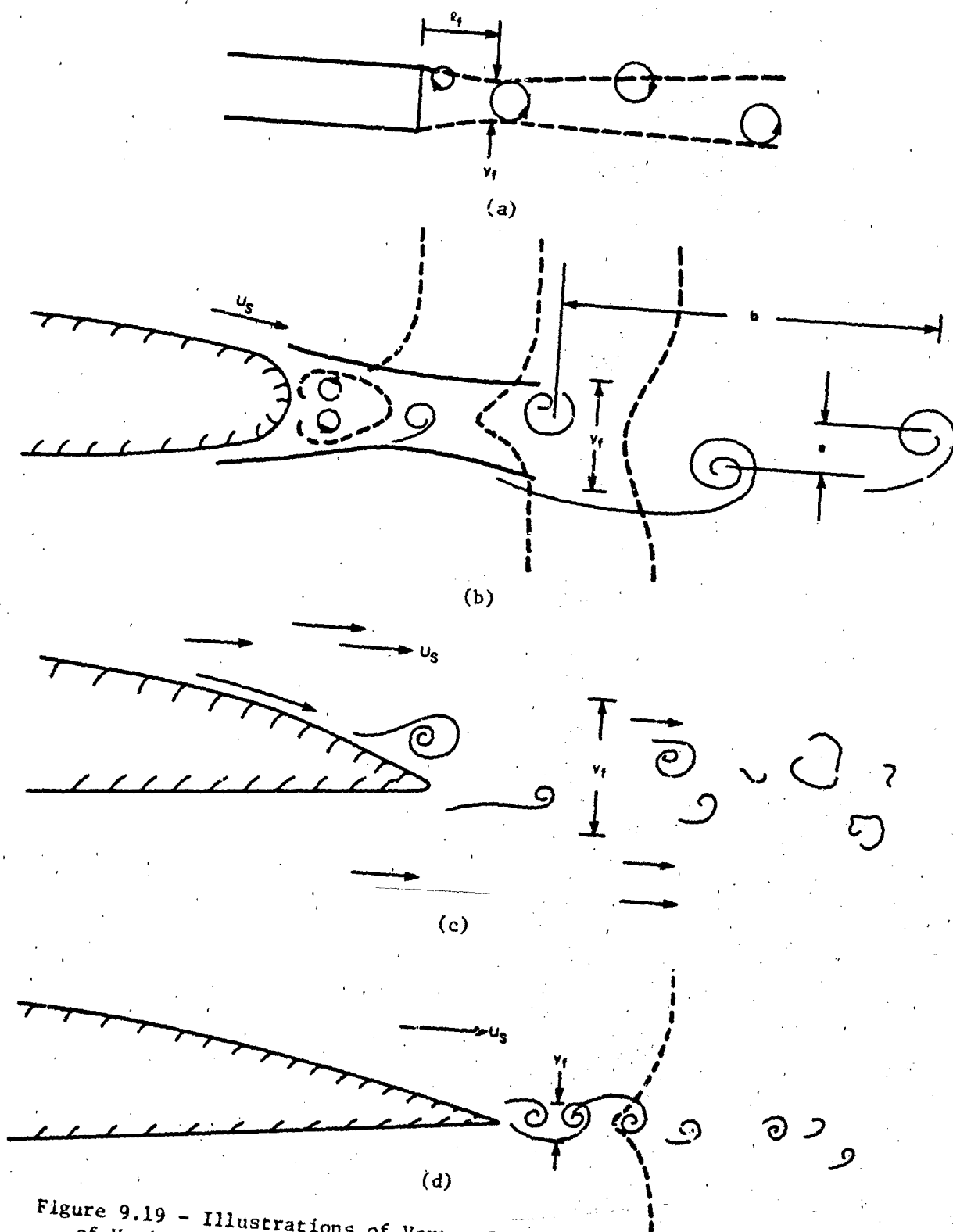


Figure 9.19 - Illustrations of Vortex Street Development Downstream of Various Trailing Edges. Blunt (a), (b); Beveled (c), (d)

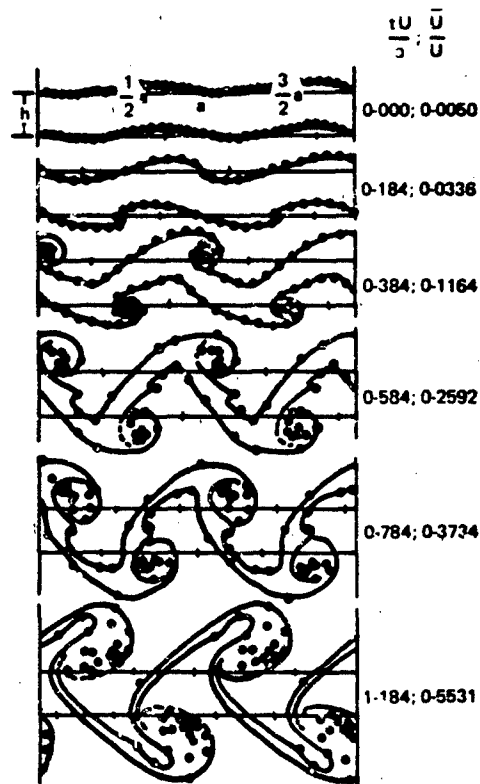


Figure 9.20 - Vortex Street Formation with $h/a = 0.281$, $A = -0.0250a$,
 $y = (\coth \pi h/a)^{1/2}$, and $\Delta t = 0.004a/u^{89}$

Measurements of velocity fluctuations in the near-wake of a squared-off blunt trailing edge by Bearman⁸⁵ and Blake^{82,83} suggest that the shed vortices reach full strength of formation at a distance ℓ_f on the order of $0.8 h$. Figure 9.21 shows the vortex geometry in the wakes of blunt trailing edges with various base modifications that have been shown effective in altering the occurrence of vortex shedding. Apart from their importance in suppressing vortex shedding, experiments with splitter plates in particular disclose important qualities of the shear-layer dynamics that affect vortex formation. As also illustrated in Figure 9.19 all vortex-street wakes have the property that the intensity of velocity fluctuations in the upper and lower shear layers of the wake grow in intensity along loci, as shown in selected parts of the figures. These loci contract just downstream of the trailing edge as the velocity fluctuations increase in intensity. At the point of minimum shear-layer width the velocity fluctuations also attain an absolute maximum. This distance from the edge is called the vortex formation length,⁸⁵ ℓ_f , and the wake width, y_f . These have special importance in determining the frequency of vortex formation.^{82,83} Both ℓ_f and y_f

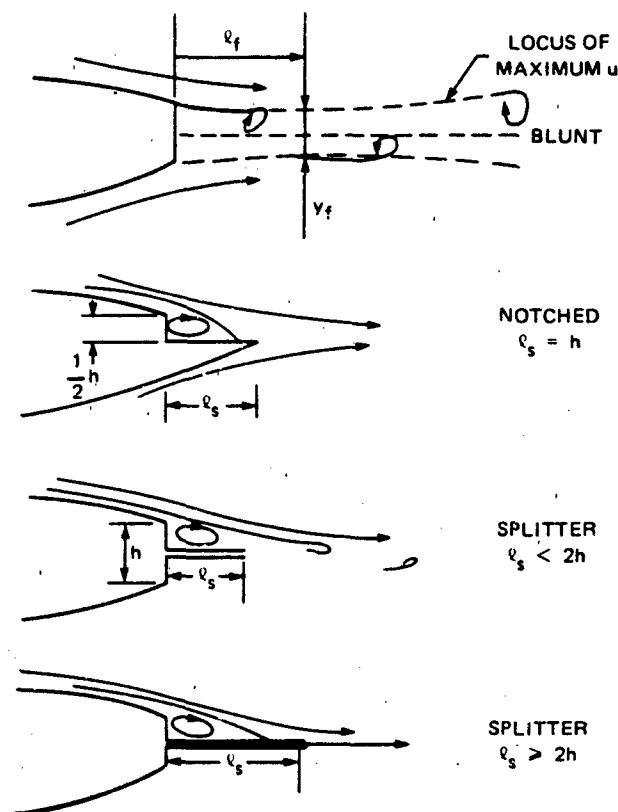


Figure 9.21 - Splitter Plates and Illustrations of Streamlines

are approximately equal to the thickness of the trailing edge for squared-off edges. Various splitter plate modifications shown in Figure 9.21(c) and (d) have been shown used to reduce the intensity of the vortex street wake.⁸⁵ When the length of the splitter plate is greater than the base height, the vortex formation dynamics are affected. Shorter splitter plate lengths only serve to extend the formation length without significantly affecting the wake intensities. The splitter plates longer than $2h$ not only extend the formation length, but the individual shear layers begin to break down before vortex formation, so that the vortex shedding becomes suppressed. No vortex shedding occurs for lengths greater than $3h$. Therefore, the length of the splitter plate, or the length of the notch shown in Figure 9.21 (b), must extend beyond the full extent of the natural length of formation, at least $1.5h$, in order to be effective in both delaying and weakening vortex formation. Such splitter plate lengths inhibit "communication" between the shear layers, while the sufficiently long notches delay the formation of one shear layer with respect to the other for at least one-half wavelength of oscillation of the shear layer.

recall (Section 5.4) that splitter lengths equal to $2.65d$ annihilated the occurrence of periodic vortex shedding from cylinders of diameter d .

9.4.3 Suppression of Vortex Shedding With Changes in Edge Geometry









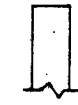

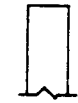









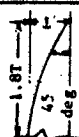









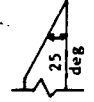
In the case of sharp edges on laminar-flow airfoils, vortex formation can be suppressed by the use of leading-edge trips to promote fully developed turbulent boundary layers, as described in Section 9.4.2.1. Even hydroelastic effects in sharp-edged, turbulent-flow hydrofoils are minimal, as discussed in Section 9.7.2. For turbulent-flow airfoils at greater Reynolds numbers, suppression of vortex shedding is less straightforward. The remainder of this subsection is devoted to lifting surfaces with turbulent flow upstream of the trailing edges.

It has long been appreciated that the audible tones emanated by marine propellers can be changed and even eliminated by somehow sharpening the trailing edges of the propeller blades and turbine blades. Much of the early experience was concerned with the elimination of vortex shedding tones by modification of trailing edges as summarized in Table 9.2 from Cumming.⁹³ The procedure generally followed was to measure the frequency and relative amplitudes of the flow-induced vibration of hydrofoils. Donaldson,⁹⁴ Heskestad and Olberts,⁹⁵ Ippen et al.,⁹⁶ and Toebs and Tagleson⁹⁷ were able to quantify the influences of trailing-edge modification on vibration amplitude in this manner.

The ranking of edge shapes by each investigation shows remarkable consistency in view of the fact that there are factors involving coupling of the vortex shedding with the structural resonances that can influence relative levels. For example, the relationship between the frequency of vortex shedding and speed can change when either the geometry or the damping is altered. This change could have an effect on the hydroelastic coupling that is important to the generation of the tones. The shapes used by Heskestad and Olberts are of particular interest because they are unsymmetrical. Figure 9.19(c) and (d) shows illustrations of vortex structures as deduced from flow measurements behind beveled trailing edges. Generally, unsymmetrically beveled trailing edges effect the most reduced hydroelastic response. A relative amplitude of zero should be viewed somewhat qualitatively since they may cause varying levels of trailing-edge noise (described in Section 9.6) even though they do not emit strong tonals.

To understand the causes for the different regimes of shedding that occur on various trailing-edge shapes and in particular the general effectiveness of bevelled

TABLE 9.2
TRAILING-EDGE SHAPES, THEIR RELATIVE SENSITIVITIES TO SINGING, AND THEIR PARAMETERS FOR SCALING

Donaldson 94		Heskestad and Olberts 95		Ippen 96		Blake et al. 8			
Geometry	Relative Amplitude	Geometry	Relative Amplitude	Geometry	Relative Amplitude	Geometry	Relative Amplitude	γ_f / t	U_s / U_∞
	360%		380%		320%				
	260				280				
	230		190						
	100		100		100		100	0.9	1.25
	48		43				100	1.0	1.05
	22		31		80				
	20		38		70				
	0		3		60		1.4-1.5	0.5	1.05
	0		0						
	0		0				0.4-0.6	0.8	1.2
			0						

edges in suppressing vortex shedding, near-wake development has been examined. Figure 9.22 summarizes the velocity profiles in the near wake of a bevelled trailing edge of the type used by Heskestad and Olberts to radically suppress vortex shedding. The wake is typical of those shed from such beveled edges^{82,84} as shown in Figure 9.19(c). A transient flow reversal has been observed which occurs in the separated flow at the edge and beneath which the static pressure is constant. It is also clear from the wake survey shown in the figure that the fluid disturbances increase in intensity as the flow progresses downstream in the developing wake. The turbulent flow of the normal boundary layer type exists up to position D and the flow separates at position 13.

An organized wake develops and causes pressures at the edge due to both the local separated flow at the edge and to a developing ordered vortex structure in the near wake. We shall see in section 9.5.3 that these surface pressures induced by the local flow are generally characterized by a broad frequency range; while those generated by the organized wake structure are characterized by a more narrow bandwidth centered on the so-called "vortex-shedding" frequency, ω_s .

To observe the connection between the fluctuating surface pressures and wake development, a series of space-time correlations between surface pressure fluctuations and streamwise velocity fluctuations (both filtered in 1/10-octave frequency bands centered on the vortex shedding frequency) were determined by measurement. As shown in the lower part of Figure 9.22, the rms pressures attain a maximum value at a point just upstream of where the stagnation point has been estimated to occur. The pressures then fall off roughly as $(x-x_s)^{-1/2}$ where $(x-x_s)$ is the distance from the stagnation point x_s . The reason for this behavior is examined in Sections 9.5.1 and 9.5.2. The center of Figure 9.22 shows correlations defined as

$$\tilde{R}_{p_G u_1}(r_1) = \frac{\overline{p_G(t) u_1(r_1, t)}}{\overline{p}^{1/2} U_\infty}$$

The pressure fluctuations were measured at the position of maximum intensity, position G in Figure 9.22, and the velocity fluctuations were measured at locations in the wake at which focal maxima in velocity occurred, i.e., along the loci y_u and y_L . These loci are considered to be the upper and lower shear layers, respectively. These pressure-velocity correlations allow mapping of the wake disturbances and

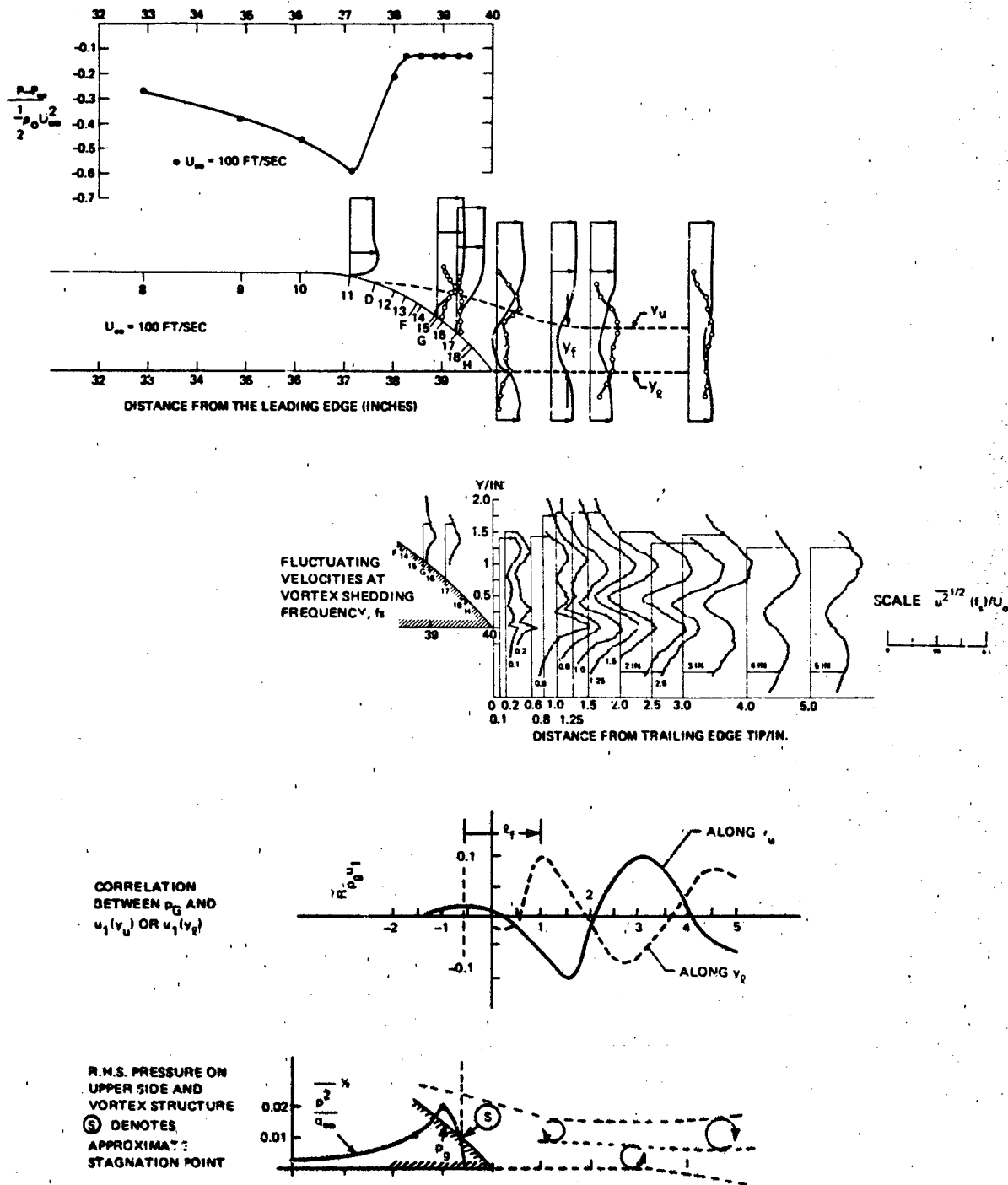


Figure 9.22 - Flow Structure and Pressure Distributions on a Beveled Trailing Edge (#6, Table 9.3, p. 974)

air connection with the flow-induced surface pressures. The correlations suggest that the unsymmetrical bevel provided a spatial delay between primary motions of the rear layer by at least one-half wavelength. This is indicated by the one-half wave clearance of \bar{K}_{pu} in the separated zone. Once both layers are clear of the edge, they still interact to generate a clearly defined structure. This behavior, as discussed later, is strongly dependent on Reynolds number. A vortex structure indicated by both the correlations and by the traces of y_u and y_l is shown in the lower part of the figure. The vortex cores are located so that they are tangent to both the approximate wake centerline to either y_u or y_l . This type of "modeling" of the vortex street has been verified as valid simulation by computations and observations Schaefer and Eskinazi.⁹⁸

Another case for which the wake development occurs, but is less ordered, with a local separated flow being more prominent in determining surface pressures on a trailing edge, is shown in Figure 9.23. Upstream of the separation point, the pressure-velocity correlation is essentially the same as that observed in attached boundary layers (see Chapter 7). Downstream of separation, the correlation function drops slightly with distance downstream, reaches a maximum at the apex of the edges, and then diminishes. This shows an aperiodic vortex structure which generates the surface pressure at position G. This position is within an eddy scale of the apex, and the relatively large correlation of the pressure with the velocity above is caused by the flow-edge interaction. The wake width y_f at this point is partially descriptive of the spectrum of surface pressures near the apex of the edge. This point is pursued in Section 9.5.3. Recent work⁸¹ explores the close structural similarities between periodic and random wake structures. These types of correlation measurement have also been made on various types of airfoils and trailing edges Bearman,⁸⁵ Hansen,⁸⁹ Mugridge,^{30,100} and Blake⁸²⁻⁸⁴ to elucidate features of wake growth and to explain the behaviors of notched trailing edges and splitter plates.

1.4 Alternative Definitions of Strouhal Numbers

Definitions of Strouhal numbers for vortex shedding from lifting surfaces are varied. This is largely due to the wide range of geometries and flow regimes which may exist for lifting surfaces at a given value of Reynolds number. Flow quality, stream of the edge, boundary-layer thickness, edge geometry, and edge thickness are all important in determining the frequency of vortex shedding. Since the

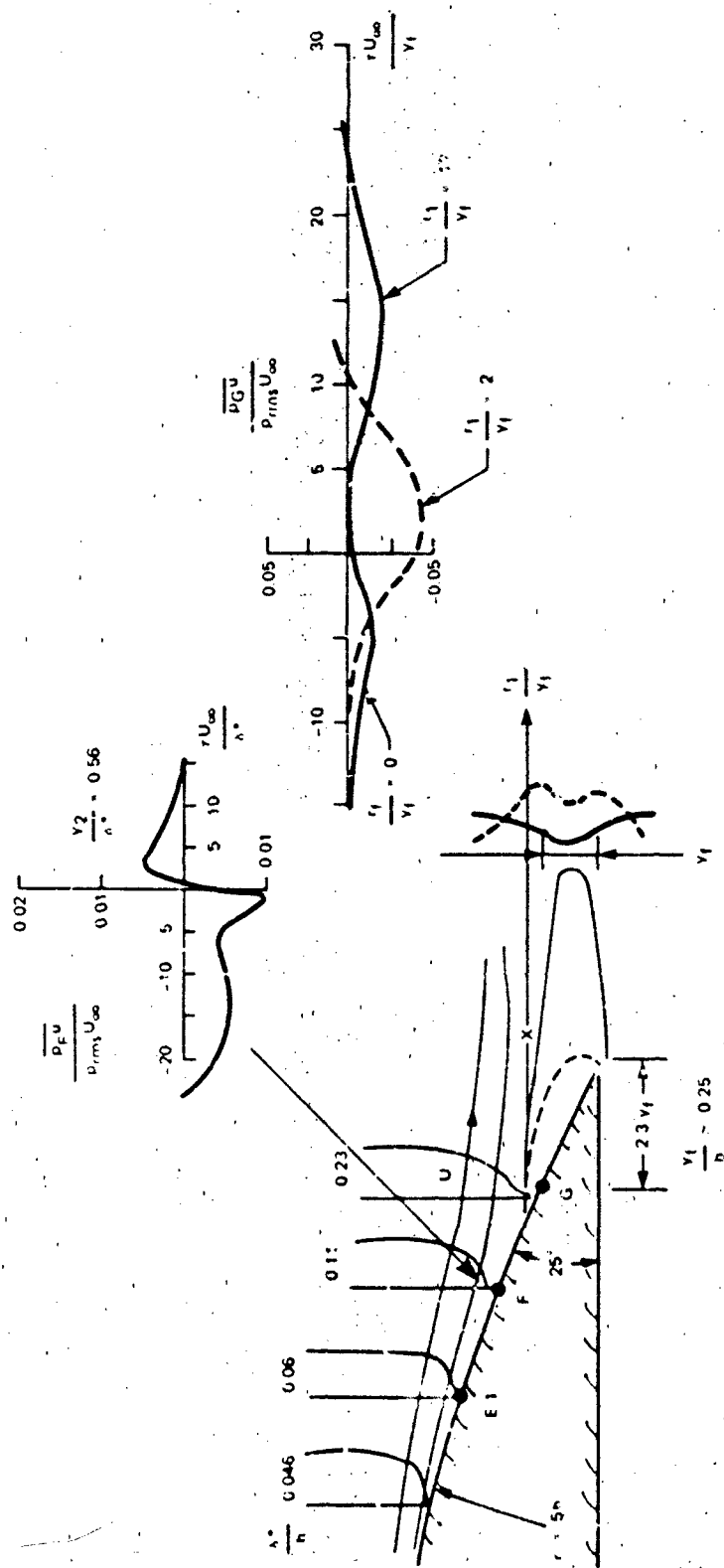


Figure 9.23 - The Development of the Large-Scale Wake Structure Downstream of a Thin Nonsymmetric Wake, as Indicated by the Behavior of Pressure Velocity Correlations

Strouhal number brings in only one additional parameter (viz., length) in addition to the shedding frequency f_s and the velocity U_∞ , various definitions of Strouhal number have appeared in the literature as knowledge of trailing edge flows has developed over the years. Each definition depends on which fluid mechanical property of the edge flow is important in the given case. The most important definitions are reviewed under the two general qualifications of laminar or turbulent upstream boundary layers.

9.4.4.1 Laminar-Flow Airfoils. For laminar flow off blunt trailing edges, a relationship reported by Bauer¹⁰¹ is

$$\frac{f_s(h+2\delta^*)}{U_s} \approx 0.2 \text{ to } 0.24 \text{ for } 3 \times 10^4 < R_c < 3 \times 10^5 \quad (9.63)$$

where U_s is defined below in equation (9.66). In this formula δ^* was calculated using a Blasius formula for the boundary layer. For very blunt edges for which $2\delta^*/h \ll 1$, this formula is identical with that of wakes of cylinders. Considering the complete similarity between the two classes of wake, corresponding values of Strouhal number are expected. Another relationship, defined by Paterson et al.⁷⁶ over a Reynolds number range for which laminar-turbulent transitional flow is involved at sharp edges ($3 \times 10^5 < R_c < 15 \times 10^5$) is

$$\frac{2f_s \delta}{U_\infty} \approx 0.11 \text{ for } 3 \times 10^5 < R_c < 15 \times 10^5 \quad (9.64)$$

where δ is the boundary layer thickness based on the assumption of laminar flow at the trailing edge. Other measurements of Hersh and Hayden¹⁰² suggest that this Strouhal number ranges from 0.13 to 0.16 over the range $R_c = 8 \times 10^4$ to 4×10^5 . Thus Strouhal numbers for sharp-edged laminar flow airfoils appear to be between 0.11 and 0.16 over the collective range $8 \times 10^4 < R_c < 1.5 \times 10^6$. Base thickness probably does not enter as a parameter unless h is order $2\delta^*$ or larger, in which case Equation (9.63) applies.

In the case of thin-edged airfoils, the vortex formation frequency is not linear with speed. This is because $\delta \sim 1/(U)^{1/2}$ (see Section 7.5); thus Equation (9.64) gives

$$f_s \propto U_\infty^{3/2}$$

9.4.4.2 Turbulent-Flow Airfoils. Regarding singing tones from hydrofoils with blunt edges at high Reynolds number, Gongwer¹⁰³ observed that the singing tone of a hydrofoil increased in frequency as the base thickness of the trailing edge h was reduced, and that the increase was not inversely proportional to the geometric thickness but rather to an effective thickness somewhat larger than h . For hydrofoils which were either swept (yawed) or not he found that

$$\frac{f_s (h+2\delta^*)}{U_\infty \cos \alpha} = 0.18 \text{ for } 1.5 \times 10^6 < R_c < 7.8 \times 10^6 \quad (9.65)$$

where α is the sweep angle of the trailing edge relative to the flow vector and δ^* is the boundary-layer displacement thickness at the trailing edge of thickness h . The formula was derived for hydrofoils with circular trailing edges and the range of Reynolds numbers sufficient for turbulent blade flow. Subsequently it has also been found to apply to blunt squared-off edges; and momentum thickness rather than δ^* is now often used in its definition. This value is slightly smaller than the Strouhal number for circular cylinders (Chapter 5) or for the identically defined Equation (9.63), but it is a constant for the range of R_c examined. Gongwer's results are also noteworthy because, using Equation (9.65), he confirmed that trailing-edge vortex formation near the tips of propeller blades was the source of marine propeller singing. Equation (9.65) is probably the most simple formulation for estimating vortex-shedding frequencies, although other definitions of Strouhal numbers that apply to more general trailing-edge shapes are discussed below. For blunt, squared-off trailing edges the Strouhal number defined in Equation (9.65) has the value indicated by recent work^{3,82,83,85} of 0.23 to 0.24 for values of R_c collectively between 1.4×10^4 and 2×10^6 . In all the experiments cited, the upstream boundary layer was thin in comparison to the base height. In these cases, the increase of vortex shedding frequency with velocity is linear.

More recent work^{82,83} has disclosed that Equation (9.65) will not account for vortex shedding behind edges such as those shown in Figure 9.22. A common feature between both the blunt and beveled edges as shown in Figure 9.22 is the occurrence of shear-layer trajectories y_ℓ and y_u and of an absolute maximum in shear-layer velocity fluctuation at some location downstream of the apex of the edge and in the near wake. This maximum occurs at the minimum value of $\Delta y = y_u - y_\ell$, which shall be called y_f . This cross-wake scale is analogous to the cylinder diameter in Chapter 5. Furthermore, following the notion introduced by Roshko (Chapter 5) that the velocity governing vortex shedding is

$$U_s = U_\infty \left[1 - (C_p)_s \right]^{1/2} \quad (9.66)$$

where $(C_p)_s$ is either the static base pressure coefficient or the pressure coefficient in the trailing-edge separation zone, the definition








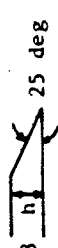
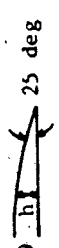

$$\frac{\omega_s y_f}{U_s} = \frac{2\pi f_s y_f}{U_s} \approx 1 \quad (9.67)$$

appears to be valid for a large range of trailing-edge geometries. This dimensionless representation is supported by considerations of wake stability. Calculations⁸³ were made of the eigenfunctions of the Orr-Sommerfeld equation for a variety of mean velocity profiles described by Equation (5.2). For a range of minimum velocities $-0.1 < U_m < 0.3$, the calculated perturbation velocities $\hat{u}(\vec{y}, t)$ traveling at wave speed C_r are least stable at frequencies given by

$$0.85 < \frac{\omega_s y_f}{U_s} < 1.0 \quad (9.68)$$

Table 9.3 shows a listing of $\omega y_f / U_s$ for a variety of trailing edges on simple airfoil shapes. Generally, the total momentum thickness of the incident boundary layer $2\theta_b$ was only a small fraction of the trailing-edge thickness. However, edge 7 has a

TABLE 9.3
STROUHAL NUMBERS²⁹ BASED ON y_f

Edge Shape *	$R_h \times 10^{-4}$	$\omega_s y_f / U_s$	$2\theta_b / h$	y_f / h	U_s / U_∞	k_f / h	$2\Delta_3 / y_f$	Reference
1 	2.4 ^{**} , [†]	0.97	0.05	0.7	1.25	1.0	--	85
2 	2.4 ^{**} , [†]	0.92	0.05	0.5	--	2.2	--	85
3 	1.7-2.8 ^{**}	0.83	--	0.56	1.06	4.7	--	99
4 	2-3 ^{**}	0.94	--	0.51	--	2.2	--	99
5 	2.6-21	1.0	0.06	0.8	1.25	0.75	7.0	82
6 	10-21	1.0	0.05	0.5	1.05	1.0	7.0	82
7 	2.8	0.85	0.26	1.0	1.05	0.9	--	8
8 	2.6-5.2 [†]	1.0	0.05	0.8	1.1	2.5	Equation 9.83	8
9 	3.6-5.2	--	--	0.4	--	--	Equation 9.83	82
10 	1.1	[§] =1	2.2	1.5	[§] =1	--	3.0	88

* Incident boundary layers were all turbulent.

** Values of y_f are approximated from published results in references 42 and 51.

[†] Boundary-layer thicknesses was 0.5h for edges 1 and 2, estimate $\theta_b \approx \delta/10$.

[‡] A periodic wake was observed at these Reynolds numbers only when this edge was given a forced oscillation with r.m.s. displacement of 0.019h.

[§] Assumed.

averaging tail section and a total momentum thickness $h/4$. Other pertinent information is included in the table for guidance concerning the ranges of validity of the Strouhal number definition.

The relationship between the vortex-shedding frequency and the mean drag coefficients induced by vortex streets on cylinders was discussed in Chapter 5. The discussion is expanded here, but, rather than basing the analysis on the vortex-street drag, we substitute the base pressure or the pressure coefficient beneath a separated flow at the trailing edge. Both Bearman^{85,104} and Hansen⁹⁹ observed that the base pressure coefficient, and therefore the vortex wake drag coefficient, increases with an increase in the formation length of vortices. The importance of this result in terms of wake dynamics can be seen by referring to Equation (5.37), which shows that the mean drag coefficient is a function of both the strength of the vortices and their separation ratio, a/b (h/l in Chapter 5); the spacing of the realized vortices is shown in Figures 9.19 and 9.22. The minimum mean drag induced by the vortex street as derived at the end of Section 5.3.1 is uniquely determined by the translation velocity of the vortices, the geometry of the wake; in these terms it is independent of the characteristic of the body. Recall that following Schwanauer, Bearman¹⁰⁵ differentiated equation (5.37) with respect to the spacing ratio to determine a/b as a function of a known vortex speed relative to the mean flow velocity, U_v , that satisfies this requirement of minimum drag. Since, by Equation (5.21), U_v is also a function of Γ , b , and a/b , Bearman expressed the result in the unique functional relationship

$$\frac{a}{b} = F_1\left(\frac{U_v}{U_\infty}\right)$$

and b are determined by measurement behind blunt bodies. Since we can write

$$f_s = \frac{U_c}{b} = \frac{\omega_s}{2\pi}$$

where U_c is the convection velocity of the vortex and

$$\frac{U_c}{U_\infty} = \frac{U_\infty - U_v}{U_\infty}$$

and since

$$U_c \propto U_s = U_\infty (1 - (C_p)_o)^{1/2}$$

then the functional dependence is rewritten as

$$S_B = \frac{f_s a}{U_s} = F\left(\frac{U_s}{U_\infty}\right) \quad (9.69)$$

which is an analog in the far wake of Equation (9.67). This function is shown in Figure 9.24 in the form of a compilation of experimental data from a wide variety of sources. The reduced base pressure coefficients observed with splitter plates result in values of U_s/U_∞ closer to unity and therefore lower Strouhal numbers owing to an altered wake structure.

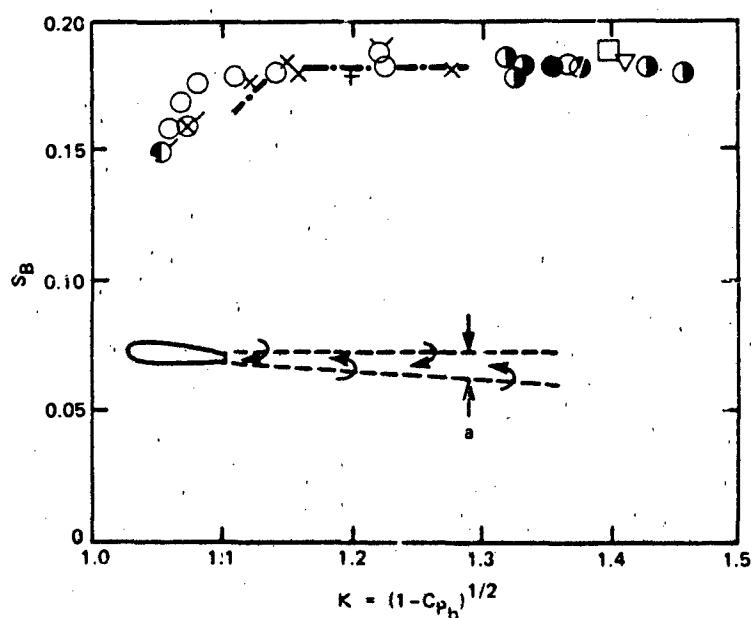


Figure 9.24 - Bearman's Universal Strouhal Number Versus K for Assorted Bluff Body Shapes Including Flat Plates with Bluff Trailing Edges, Cylinders, Wedges, and Airfoils with Blunt and Beveled Trailing Edges. Adapted from a

Figure Prepared by Bearman¹⁰⁴

Another definition of Strouhal number, given by Hansen⁹⁹ utilizes the momentum thickness of the wake determined at the formation zone, θ_w . Hansen found the vortex-shedding frequencies from his blunt and modified trailing edges to satisfy the relationship

$$\frac{\omega_s \theta_w}{2\pi U_s} \cdot \frac{U_s \theta_w}{\nu} = 0.0728 \left(\frac{U_s \theta_w}{\nu} - 1038 \right)$$

$$S_{\theta_w} R_{\theta_w} = 0.0728 (R_{\theta_w} - 1038) \quad (9.70)$$

or

$$3 \times 10^3 < R_{\theta_w} < 1.2 \times 10^4$$

This relationship was adopted from one used by Roshko.¹⁰⁶ It was subsequently found⁸³ to overestimate (by nearly a factor of 2) the vortex-shedding frequency of blunt edge 5 in Table 9.3, but it accurately predicted the frequencies of edge 6. The overall range of validity of Equation (9.70) may then apparently be extended to

$$3 \times 10^3 < R_{\theta_w} < 5 \times 10^4$$

The base pressure coefficients on all the airfoils for which Equation (9.70) seems to hold are all less than -0.3; thus this value perhaps sets an upper limit on C_{p_b} for which this definition appears to be valid. Also note that when $C_{p_b} \geq -0.3$, $\theta_w/U_\infty < 1.15$, which correlates with the occurrence of nonconstant and decreasing values of Bearman's definition in Figure 9.24. The wake momentum thickness is related to the drag coefficient C_D of the airfoil section. Since the drag on the airfoil is roughly equal to the time rate of change of fluid momentum of the wake in the flow direction; see Equation (5.23)), it is found that

$$\frac{2\theta_w}{h_m} = C_D \quad (9.71)$$

for airfoils on which the flow is separated only in the vicinity of the trailing edge; h_m is the maximum thickness of the airfoil.

Equations (9.65), (9.68), (9.69), and (9.70) provide alternative definitions of the predominant Strouhal number for vortex shedding. To date, the analogous definitions of Equations (9.68) and (9.69) appear to be of universal validity, applying to a wide range of geometrical forms. It is clear that Gongwer's definition, although it is most simple in terms of the easily obtained quantities on which it is based, will not adequately scale the shedding frequencies from the nonblunt edges in Table 9.3. On the other hand, the estimations of vortex spacing, the shear layer thicknesses y_f and a , and wake momentum thickness are not known a priori for many applications. Thus, unless one has a situation approximately covered by the cases in Table 9.3, Equation (9.69) must be used judiciously for estimating frequencies in noise estimates.

9.5 SELF-INDUCED SURFACE PRESSURE FLUCTUATIONS

It is important to give separate consideration to the characteristics of surface pressures on wings and hydrofoils because of the variety of flow regimes that are typical of such bodies and because of the intimate relationship between the surface pressures and radiated sound and vibration. This section is concerned with self-generated pressure fluctuations due to viscous boundary layer and wake flow of the body and as such they are considered self-induced. These pressures are, to a first approximation unaffected by inflow disturbances except when those disturbances affect the boundary-layer transition. The flow regimes that exist on a lifting surface in a given situation have been shown in the previous section to be controlled by a mix of Reynolds number and geometric effects. In order to isolate these effects, the distinctions between tonal and turbulent pressure fluctuations discussed in Section 9.4 are expanded below. As brought out in connection with the beveled trailing edge with upstream turbulent boundary layers,

periodic disturbances are due to the generation of the periodic vortex street, the turbulent flow near the blade surface will generate local pressure fluctuations.

5.1 Tonal Surface Pressures From Vortex Shedding: Theory

The problem considered here is the establishment of surface pressures (causing unsteady lift) due to the formation of the vortex. Of interest are the magnitudes and variation of the pressure fluctuations over the surface of the lifting surface in terms of the strength and geometrical characteristics of the vortex street. Obviously, there are many parallels between such wake-induced disturbances generated by both cylinders and airfoils. In mathematical modeling of the phenomenon, a point of departure is that the lifting surface chord and length are much larger than a streamwise vortex spacing so that, for the sharp-edged surface especially, the trailing-edge region is effectively represented by a rigid semi-infinite half-plane of infinitesimal thickness. The important subject of vortex shedding forces on vibrating airfoils is reserved for Section 9.8. In the course of comparing the analytical results with measured pressures, it shall be shown that the correct analytical result can only be given when no Kutta condition is applied at the trailing edge; it cannot be given when a full Kutta condition is applied, as it was above in modeling the response of the airfoil to inlet turbulence. Furthermore, the spanwise scale of the vorticity will be regarded large in comparison to the vortex spacing so that modeling may consider a locally two-dimensional periodic vortex street in the wake of the edge. These results are especially realistic if consideration is restricted to surface pressures in the near field of the edge. The topic has been similarly treated by Davis¹⁰⁷ (radiated sound), Blake^{83,108} (surface pressures), and Howe¹⁰⁹ (surface pressures and radiated sound).

The pertinent geometry, shown in Figure 9.25b, is an idealization of the actual wake structures suggested by Figure 9.22 in Section 9.3, and idealized in Figure 9.25 as a wavelike vorticity distribution moving in the $y_1 > 0$ direction. The wake circulation distribution $\Gamma = \kappa(\xi_1, \xi_2, t)$ is given by

$$\kappa(\xi_1, \xi_2, t) = \gamma_0 \delta(\xi_2) e^{+ik_w(\xi_1 - U_c t)} d\xi_1 \text{ for } \xi_1 \geq l_f \quad (9.73)$$

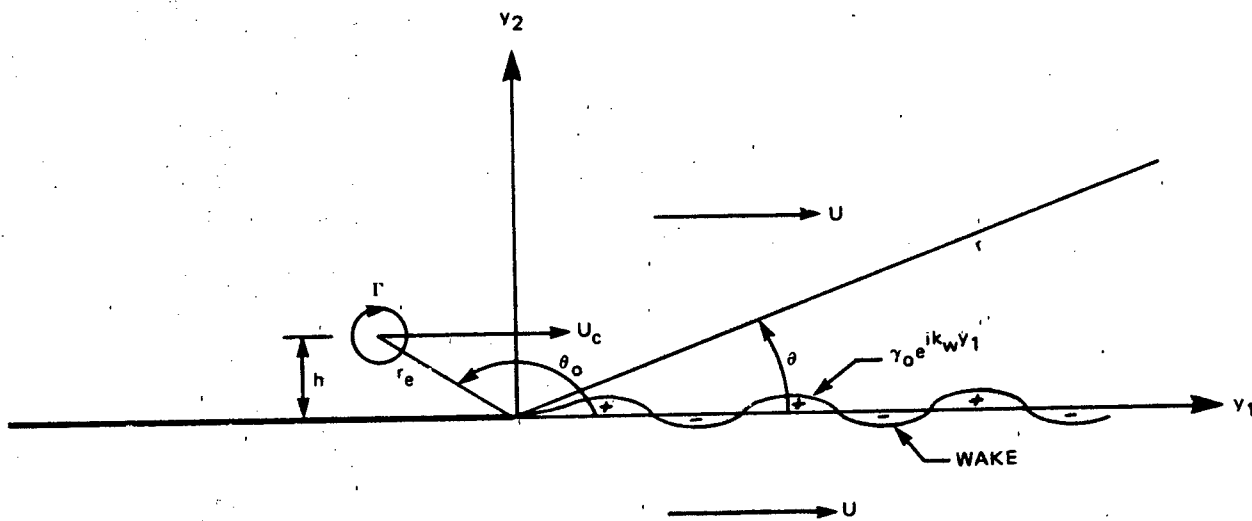


Figure 9.25a - Convected Eddies and Trailing Edge-Scattering

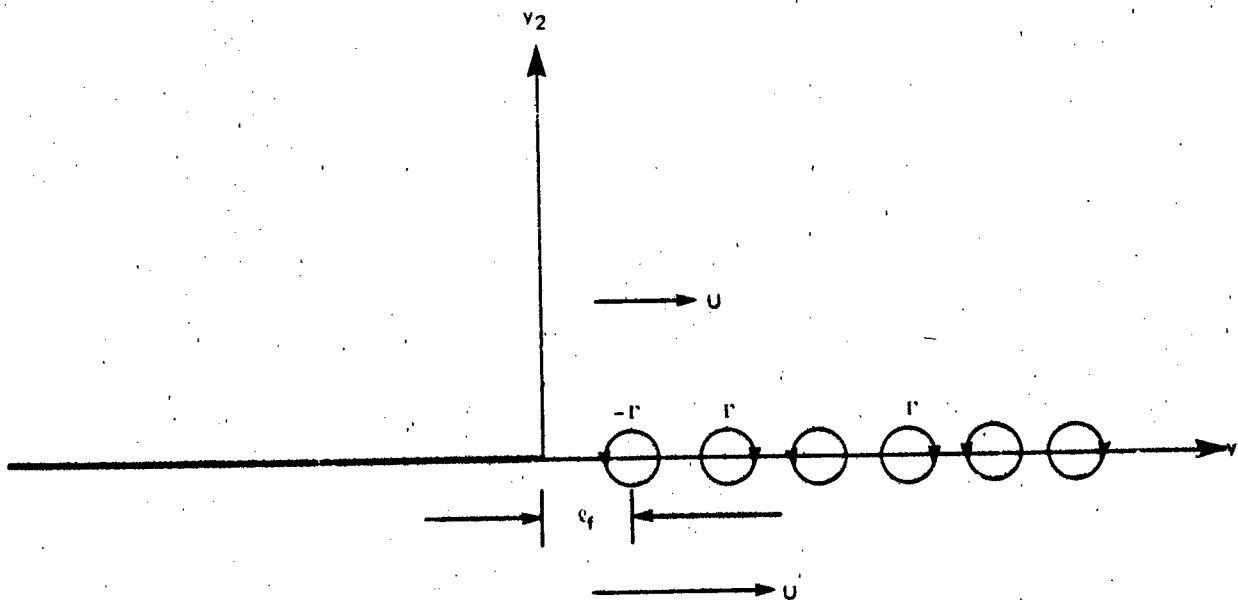


Figure 9.25b - Shedding of Discrete Vortices

Figure 9.25 - Idealizations of Two Trailing-Edge Flow Problems

re ξ_1, ξ_2 are dummy variables introduced to identify coordinates in the wake.

factor γ_o is the circulation distribution in the wake, and it is related to the circulation of vortices, Γ_o , that may be experimentally determined. The vortex circulation is just the integral of $\Gamma(\xi_1, \xi_2, t)$ over a half wavelength π/k_w :

$$\Gamma_o = \int_{y_1 - \pi/2k_w}^{y_1 + \pi/2k_w} \gamma_o e^{ik_w(\xi_1)} d\xi_1$$

$$\Gamma_o = \frac{2\gamma_o}{k_w} = 2 \frac{\gamma_o U_c}{\omega} \quad (9.74)$$

modeling the wake vorticity to have wavelike structure along $\xi_1 > \xi_f$ rather than > 0 , flexibility is maintained to allow for effects of delayed vortex growth as the case of trailing edges with splitter plates.

The surface pressure generated by the vortex street can be shown to be singular at the trailing edge as long as a complete Kutta condition is not applied. The vortex street generates a potential field $\phi_h(y_1, y_2, t)$, which causes a pressure given by the unsteady Bernoulli equation, Equation (2.88):

$$\frac{-p(y_1, 0^+, t)}{\rho_o} = \frac{\partial \phi_h(y_1, 0^+, t)}{\partial t} + U_c \frac{\partial \phi_h(y_1, 0^+, t)}{\partial y_1} \quad (9.75)$$

re $\phi_h(y_1, 0^+, t)$ is evaluated on the upper surface of the half-plane, $y_2 = 0^+$ (see Figure 9.25). Pressures on opposite sides are out of phase, i.e., $p(x_1, 0^+, t) = -p(x_1, 0^-, t)$. The potential needed is the real part of the complex value

$$\phi_h(y_1, y_2) = \text{Re}_j \phi_h(Z_1, Z_o)$$

re Re_j is the real part of $\phi_h(Z_1, Z_o)$ with respect to the complex notation j .

The hydrodynamic potential around the plate due to a point vortex is found most expediently by analytically mapping the field of a vortex near a surface into that near a half-plane, as illustrated in Figure 9.26. The theory and techniques for doing this are discussed extensively by Milne-Thompson.¹¹⁰ The potential due to the vortex in the ξ plane is

$$\phi(\xi, \xi_0) = j \frac{\Gamma}{2\pi} \ln \frac{\xi - \xi_0}{\xi - \xi_0^*} \quad (9.76)$$

here $\xi = \xi_1 + j\xi_2$ is a complex variable and ξ_0^* is the complex conjugate of ξ_0 . The ξ plane is mapped into the Z plane according to the function

$$\xi = jZ^{1/2}$$

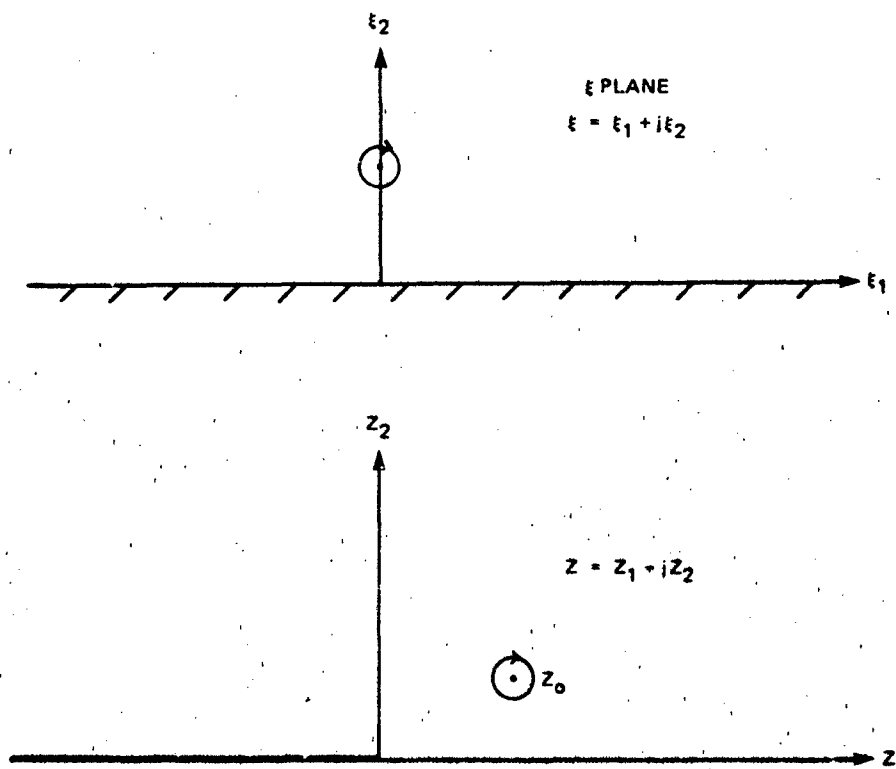


Figure 9.26 - Mapping Function for Vortices Near the Sharp Edge of a Half-Plane

that the complex potential in the Z , or physical, plane is

$$\phi(Z, Z_0) = j \frac{\Gamma}{2\pi} \ln \frac{jZ^{1/2} - jZ_0^{1/2}}{jZ^{1/2} + jZ_0^{*1/2}} \quad (9.77)$$

we have defined $Z = Z_1 + jZ_2$, using j rather than i to emphasize the use of complex variable theory here as an expedient and to keep it formally distinct from the local time dependence.

The complex velocity due to this vortex is

$$u_1 - ju_2 = \frac{d\phi}{dZ} = j \frac{\Gamma}{2\pi} \frac{(Z Z_0)^{1/2}}{Z^2 - Z Z_0}$$

Z_0 is the location of the vortex. Note that as $Z \rightarrow 0$, i.e., at the edge, the velocity has a square-root singularity,

$$u_1 - ju_2 \rightarrow - \frac{j\Gamma}{2\pi} \frac{1}{(ZZ_0)^{1/2}} \quad (9.78)$$

which would be canceled by adding vorticity to the wake if we were to apply a Kutta condition at the edge.

To apply this potential to the problem shown in Figure 9.38a, we introduce Equation (9.77), to give

$$\phi_h(y_1, 0^+, t) = \frac{j\gamma_0}{2\pi} \int_{\xi_f}^{\infty} \ln \frac{(y_1)^{1/2} - j(\xi_1)^{1/2}}{(y_1)^{1/2} + j(\xi_1)^{1/2}} e^{ik_w(\xi_1 - U_c t)} d\xi_1 \quad (9.79)$$

Equation (9.73) is used to model a continuous distribution of vorticity that starts at $\xi_1 = \xi_f$ and continues in periodic fashion indefinitely downstream.

By integrating by parts we find the potential induced by the entire periodic wake to be

$$\phi_h(y_1, 0^+, t) = \frac{\gamma_0}{2\pi} \int_{l_f}^{\infty} \frac{e^{-ik_w \xi_1}}{-ik_w} \left(\frac{y_1}{\xi_1} \right)^{1/2} \frac{d\xi_1}{y_1 + \xi_1} \quad (9.80)$$

$$- \frac{j\gamma_0}{2\pi} \left\{ \frac{e^{-ik_w l_f}}{-ik_w} \ln \left[\frac{(y_1)^{1/2} - j(l_f)^{1/2}}{(y_1)^{1/2} + j(l_f)^{1/2}} \right] \right\}$$

where l_f is the formation distance of vortices downstream of the edge. The integral simplifies into alternate forms depending on the relative magnitudes of y_1 and l_f . In the case of $y_1 \gg l_f$ the approximation

$$\ln \frac{(y_1)^{1/2} - j(l_f)^{1/2}}{(y_1)^{1/2} + j(l_f)^{1/2}} \approx -2j \left(\frac{l_f}{y_1} \right)^{1/2} \quad \frac{y_1}{l_f} \gg 1$$

holds. The integrals reduce to a pair⁵⁶ (for $y_1 > l_f$)

$$\frac{(y_1)^{1/2}}{-ik_w} \int_{l_f}^{\infty} \frac{e^{ik_w \xi_1}}{(\xi_1)^{1/2}} \frac{d\xi_1}{y_1 + \xi_1}$$

$$\frac{(y_1)^{1/2} e^{ik_w y_1}}{-ik_w} \left[\int_z^{\infty} \frac{e^{-ik_w z}}{z(z-y)^{1/2}} dz + \frac{e^{ik_w y_1}}{y_1} \int_0^{l_f} \frac{e^{-ik_w z}}{z^{1/2}} dz \right]$$

$$= \frac{\pi}{-ik_w} \left\{ e^{ik_w y_1} \left[1 - \text{Erf}(ik_w y_1)^{1/2} \right] - (ik_w y_1)^{-1/2} \cdot \text{Erf}(ik_w l_f)^{1/2} \right\}$$

The function $\text{Erf}(ik_w l_f)^{1/2}$ is the error function for which the asymptotic formulae are²²:

$$\text{Erf}(ik_w l_f)^{1/2} \approx 1 - \frac{e^{-i(k_w l_f + \pi/4)}}{(\pi k_w l_f)^{1/2}} \quad k_w l_f > 1 \quad (9.81a)$$

$$\approx (k_w l_f)^{1/2} e^{-i(k_w l_f + \pi/2)} \quad k_w l_f < 1 \quad (9.81b)$$

when $k_w l_f$ and $k_w y_1$ are on the order of unity, neither equation applies. Therefore a set of alternate first-order closed-form expressions for the mean-square amplitude of the surface pressure are found for various cases that depend on where $k_w y_1$ and $k_w l_f$ stand with respect to unity:

$$\frac{\overline{p^2}}{\rho_o^2 U_s^2 \left(\frac{\Gamma_o}{2\pi y_f} \right)^2} \approx \frac{\pi^2}{16} \frac{U_c}{U_s} \frac{y_f}{y_1} \quad \text{for } 1 > k_w y_1 \gg k_w l_f \quad (9.82a)$$

in which the only important length scales are y_1 and y_f ;

$$\frac{\overline{p^2}}{\rho_o^2 U_s^2 \left(\frac{\Gamma_o}{2\pi y_f} \right)^2} \approx \frac{\pi}{4} \frac{U_c}{U_s} \frac{y_f}{y_1} \left[1 - 4 \left(\frac{k_w l_f}{\pi} \right)^{1/2} \cos \left(k_w l_f - \frac{\pi}{4} \right) + \frac{4k_w l_f}{\pi} \right]$$

for $k_w y_1 \gg k_w l_f > 1$ (9.82b)

and finally

$$\frac{\overline{p^2}}{\rho_o^2 U_s^2 \left(\frac{r_o}{2\pi y_f} \right)^2} \approx \frac{\pi}{4} \frac{U_c}{U_s} \frac{y_f}{y_1} \left[1 - 4 \left(\frac{k_w l_f}{\pi} \right)^{1/2} \cos \left(k_w l_f - \frac{\pi}{4} \right) \left(1 - \frac{(\pi)^{1/2}}{2} \right) \right]$$

$$\text{for } k_w y_1 > 1 \gg k_w l_f \quad (9.82c)$$

to complete the set of limits that apply whenever $y_1 \gg l_f$. Equation (9.82a) applies closer to the edge than a wake wavelength and requires a very short formation zone. Equation (9.82c) applies at distances far from the edge but requiring a short formation zone. Equation (9.82b), on the other hand, applies at distances far from the edge when the formation zone is large.

In the alternative limit of $l_f \gg y_1$ the \ln term in Equation (9.79) reduces to $2j (y_1/l_f)^{1/2}$ for the entire region of integration. The resulting integral is $1 - \text{Erf}(ik_w l_f)^{1/2}$. Accordingly, when $k_w l_f \gg 1$, the expression for the pressure becomes

$$\frac{\overline{p^2}}{\rho_o^2 U_s^2 \left(\frac{r_o}{2\pi y_f} \right)^2} = \frac{1}{4} \frac{U_c}{U_s} \frac{y_f}{l_f} \frac{y_f}{y_1} \text{ for } k_w l_f \gg 1 > k_w y_1$$

$$\text{or } k_w l_f \gg k_w y_1 > 1 \quad (9.82d)$$

However, when $k_w l_f \ll 1$, the alternate limit for the error function leads to

$$\frac{\overline{p^2}}{\rho_o^2 U_s^2 \left(\frac{r_o}{2\pi y_f} \right)^2} \approx \frac{\pi}{4} \frac{l_f}{y_f} \frac{y_f}{y_1} \text{ for } 1 \gg k_w l_f \gg k_w y_1 \quad (9.82e)$$

In all the above expressions $k_w l_f$ has been rewritten as $(U_s/U_c) (l_f/y_f)$. Equations (9.82d) and (9.82e) give similar values of p^2 and therefore a smooth transition of parametric behavior in the overlap region of $k_w l_f = k_w y_1$. However, for $k_w l_f \gg 1$ this smooth transition does not occur for the asymptotic forms. Therefore, for the special case of $y_f = l_f$ and $k_w l_f \gg 1$, an adequate expression is

$$\frac{\overline{p^2}}{\rho_o^2 U_s^2 \left(\frac{r_o}{2\pi y_f} \right)^2} = \frac{\pi}{36} \frac{U_c}{U_s} \frac{y_f}{y_1} \quad \text{for } k_w y_1 \approx k_w l_f \gg 1 \quad (9.82f)$$

In all the expressions for pressure it can be seen that both the formation length and the wake thickness enter as pertinent length scales depending on the domain of dependence. When $k_w l_f$ is much less than unity, Equations (9.82a,b,c) show that the pressure becomes largely independent of l_f . Equations (9.82a,b,c) show that when $k_w l_f$ decreases toward zero the pressure increases at all values of $k_w y_1$.

We conclude from the above analysis that pressures due to periodic vortex shedding are maximum near the trailing edge, with amplitudes falling off as $1/(X)^{1/2}$ and that the formation length l_f may be important in determining the proximity of the vortex street to the edge and therefore the maximum pressure induced. The pressures become theoretically singular as the trailing edge is approached; however this behavior should be expected only until y_1 is on the order of a viscous length $(\nu/\omega)^{1/2}$, i.e., as long as

$$\begin{aligned} \frac{y_1}{y_f} &> 0 \left(\frac{\nu}{y_f U_\infty} \frac{U_\infty y_f}{\omega} \right)^{1/2} \\ &> 0 \left(R_{y_f}^{-1/2} \right) \end{aligned}$$

Comparison with experimentally determined pressures are given in the next section.

9.5.2 Measured Pressures From Vortex Shedding

We have already seen in Section 9.4, Figure 9.22, that measured fluctuating pressures near a trailing edge with vortex shedding are maximum just upstream of the stagnation point. A clearer perspective may be gained from Figure 9.27, which shows these pressures to be generated on a blunted airfoil,^{83,111} edge number 7 in Table 9.3 of Section 9.4. Note the logarithmic scale for the mean-square pressures which have been normalized on the freestream dynamic pressure. Other parameters that apply to the wake, the importance of which are discussed in Section 9.4, are also shown. Figure 9.28 shows a $y_1/y_f - \omega y_f/U_s$ mapping of the pressures which are strongly tonal but also have significant continuous-spectrum character. The continuous-spectrum pressures upstream of the edge are independent of the bluntness, and they are generated by the local boundary-layer flow, as discussed in Chapter 7.

To compare these tonal pressures to Equations (9.82), the parameter Γ_o must be determined from the measurements of wake properties. Schaefer and Eskinazi analytically modeled the vortex streets behind cylinders with an array of Rankine vortices (see, e.g., Section 4.3.2.1) of radius r_o . A comparison of measured and computed velocity fluctuations confirmed that the wake may be approximated by vortex cores, as shown in Figure 9.22 and 9.27. Accordingly, a mean-square value of Γ_o may be defined as

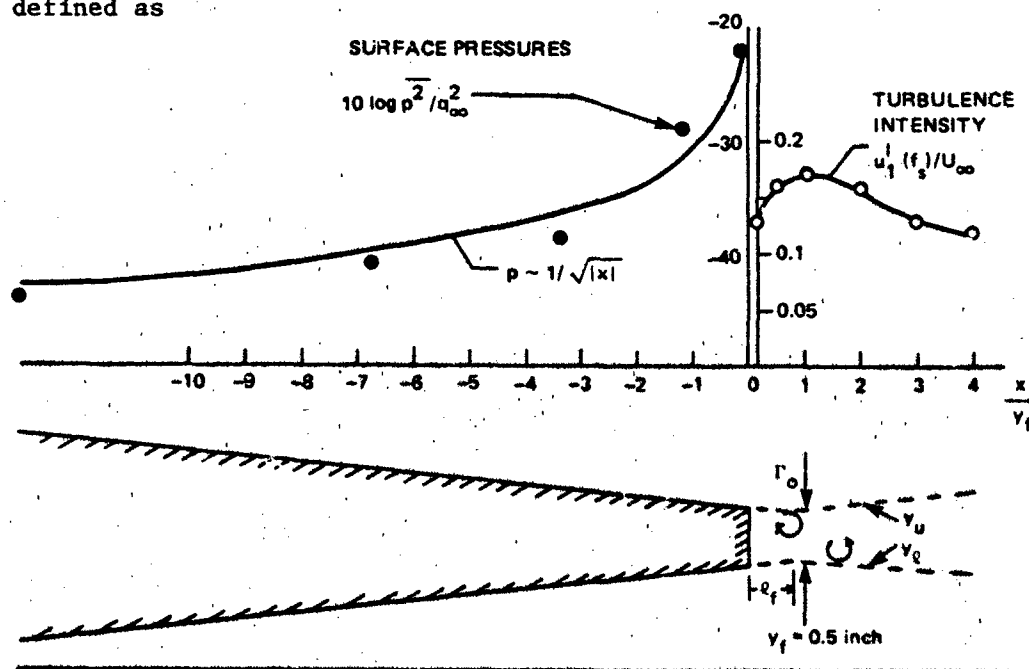


Figure 9.27 - Profiles of Surface Pressure and Velocity Fluctuations at the Blunt Trailing Edge of a Tapered Airfoil (#7, Table 9.3, p. 969) Measurements Were Made at $U_\infty = 100$ ft/sec

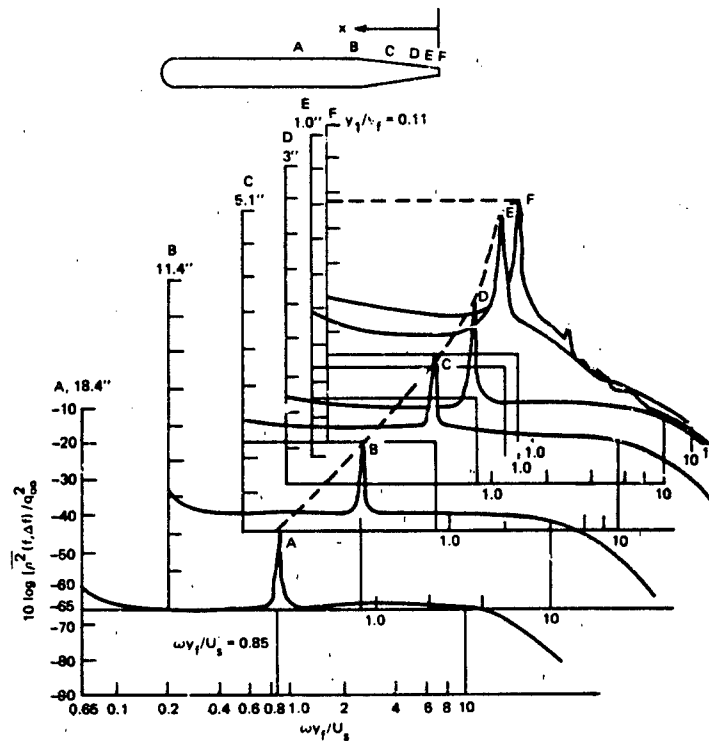


Figure 9.28 - Contour of Spectral Densities of Surface Pressures Generated on a Trailing Edge with Vortex Shedding

$$\begin{aligned} \Gamma_o^2 &= \overline{(2\pi r_o u_m)^2} \\ &= 4\pi^2 r_o^2 \overline{u_m^2} \end{aligned}$$

where $\overline{u_m^2}$ is measured along the loci y_l and y_u . Since at the formation point

$$4r_o = y_f$$

we have

$$\Gamma_o^2 = \left(\frac{\pi}{2}\right)^2 \overline{u_m^2} y_f^2 \quad (9.83)$$

Measurements of surface pressure obtained on some of the edges that appear in Table 9.3, normalized as suggested by Equation (9.82), are shown in Figure 9.29. Comparisons are also made with each of the theoretical values of the surface pressure. The factor Λ_3 is the spanwise correlation length, which will be discussed in

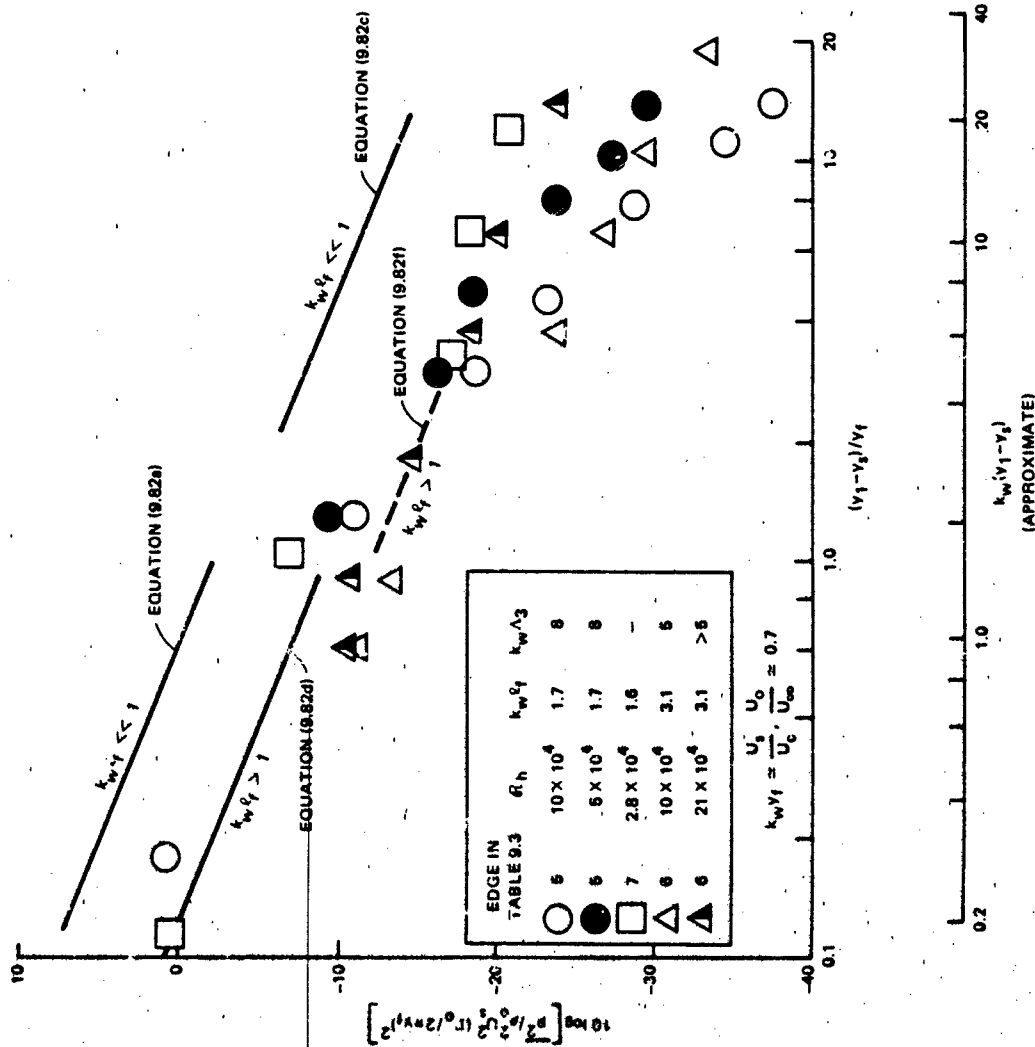


Figure 9.29 - Vortex-Induced Surface Pressures on Trailing Edges of Airfoils. Normalization Is Based on Wake Variables: Circulation, Shear Layer Thickness, and U_s . See Table 9.3

Section 9.5.4, but it has the same significance as it does for vortex streets of cylinders. In Figure 9.29, the abscissa is the distance from either the base of a blunt edge ($y_s=0$) or from the stagnation point ($y_s \neq 0$). It is seen that the available experimental data applies to $k_w \ell_f > 1$; Equations (9.82b,d,f) are expected to agree with measurements best. For the parameters of the available measurements, it is difficult to apply Equation (9.82b) because when the conditions of validity for y_1 are reached it also becomes comparable to the transverse correlation length $2\lambda_3$. It is therefore difficult in practical instances to apply Equations (9.82) and retain the conditions of two-dimensional vortex shedding as well. However, Equations (9.82) suggest a sensitivity of the pressure at large distances to formation length. Application of these results to the tonal pressures on laminar-flow airfoils is indicated by the measurements of Archibald.⁷⁹ For $k_w \ell_f \gg k_w y_1 > 1$, the surface pressures will fall off as $(\ell_f)^{-1/2}$. Therefore increasing ℓ_f to be larger than y_f will carry both a reduction in potential flow pressure as well as a possible reduction in both spanwise correlation length and in vortex intensity Γ_o (recall Bearman's⁸⁵ results with splitter plates). If an unsteady Kutta condition had been applied, the measured pressures would not have been predicted. Instead, in the limit of $y_1 \rightarrow 0$ the pressure would decrease to zero and the prediction of peak pressures at the edge would not have been possible.

When $y_1 \gg y_f$, the measured values of the pressure begin to decrease nearly as $(y_1/y_f)^{-3/2}$, but, as discussed earlier, this may be due to the fact that locations far from the edge will not respond to the wake vorticity two dimensionally.

Variations in the magnitude of surface pressure due to Reynolds number and geometrical changes are controlled by changes in the strength Γ_o . Vortex strengths may be determined either by measurement according to Equation (9.83) or from measured surface pressures according to Equation (9.82d) (since this equation conforms best to measured parameters). Figure 9.30 shows a compilation of existing measurements^{83,88} as a function of $R_{y_f} = U_\infty y_f / \nu$. The points are keyed to Table 9.3. For both the squared-off and rounded edges, Γ_o is dependent on R_h at low values. The numbers shown in the figure denote the bandwidths of the pressure spectra when it was determined that they were no longer tonal. These bandwidths are shown as quality factors, $Q = f_s / \Delta f_s$, where Δf_s is the bandwidth of the pressure spectrum at -3 dB points from the maximum. As R_{y_f} increases, the intensity and the quality of the tone increase in a manner similar to the values of cylinders (see Figure 5.15). One would expect that if the parallel continues when R_{y_f} reaches between 10^5 and 10^6 , the

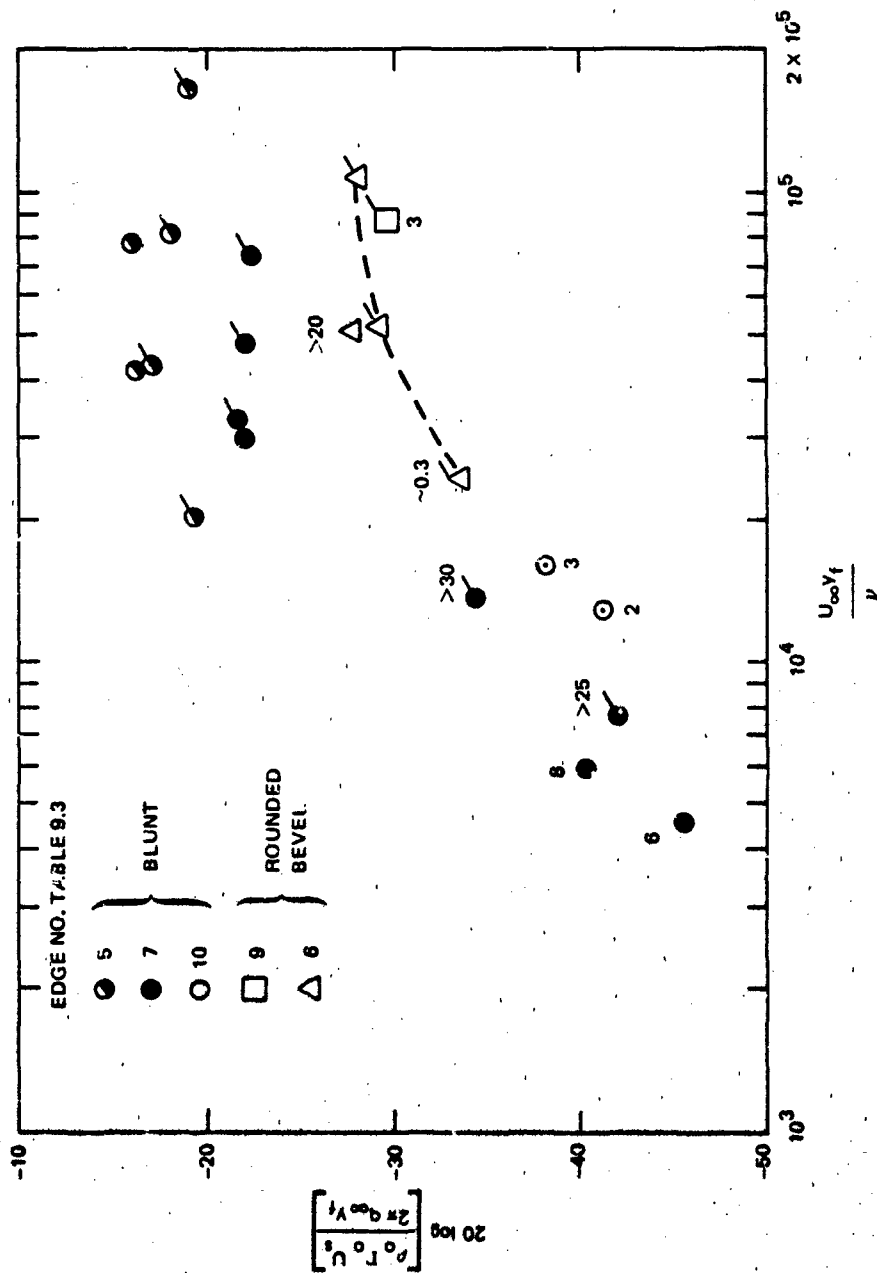


Figure 9.30 - Mean-Square Vortex Strengths for Various Trailing Edges with Vortex Shedding. Unflagged Points Obtained with Wake Intensity Measurements and Eq. 9.82. Flagged Points Obtained with Surface Pressure Measurements and Eq. 9.82d. Numbers Denote Quality Factors $f_s/\Delta f_s = Q$ for $Q < 30$

strengths of the vortices shed by blunt trailing edges should again decrease as they do for circular cylinders. Vortex shedding has not been observed at such large values of R_{y_f} , however.

9.5.3 Pressures From Turbulent Separation

As noted in the last section, both periodic and continuous spectrum pressures may co-exist at trailing edges. Figures 9.31 and 9.32, show autospectra of surface pressures that were measured on edges 5, 6, 8, and 9 of Table 9.3. On the bevelled edges 6, 8, and 9, the pressures were measured on the bevelled side near the apex. In order that the measurements could be compared on a common basis, the continuous (broadband) portion of the spectrum has been nondimensionalized on the variables y_f and U_s , defined in Figures 9.22 and 9.23 and Equation (9.66), as well as the dynamic pressure of the freestream q_∞ . The tonal contribution of the pressure is indicated by the arrow representing a delta function. The total mean-square pressure is therefore given by a mixture of both the random and tonal contributions:

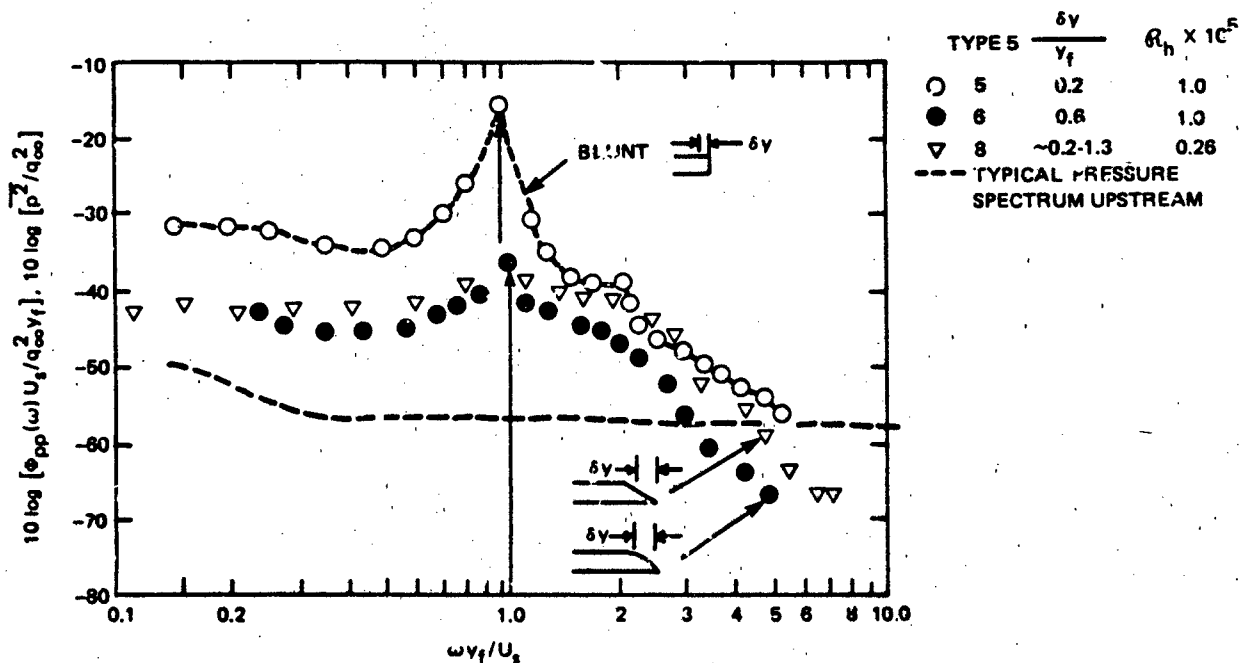


Figure 9.31 - Pressure Spectral Densities on Trailing Edges Nondimensionalized on U_s and y_f (see Table 9.3, p. 969)⁸

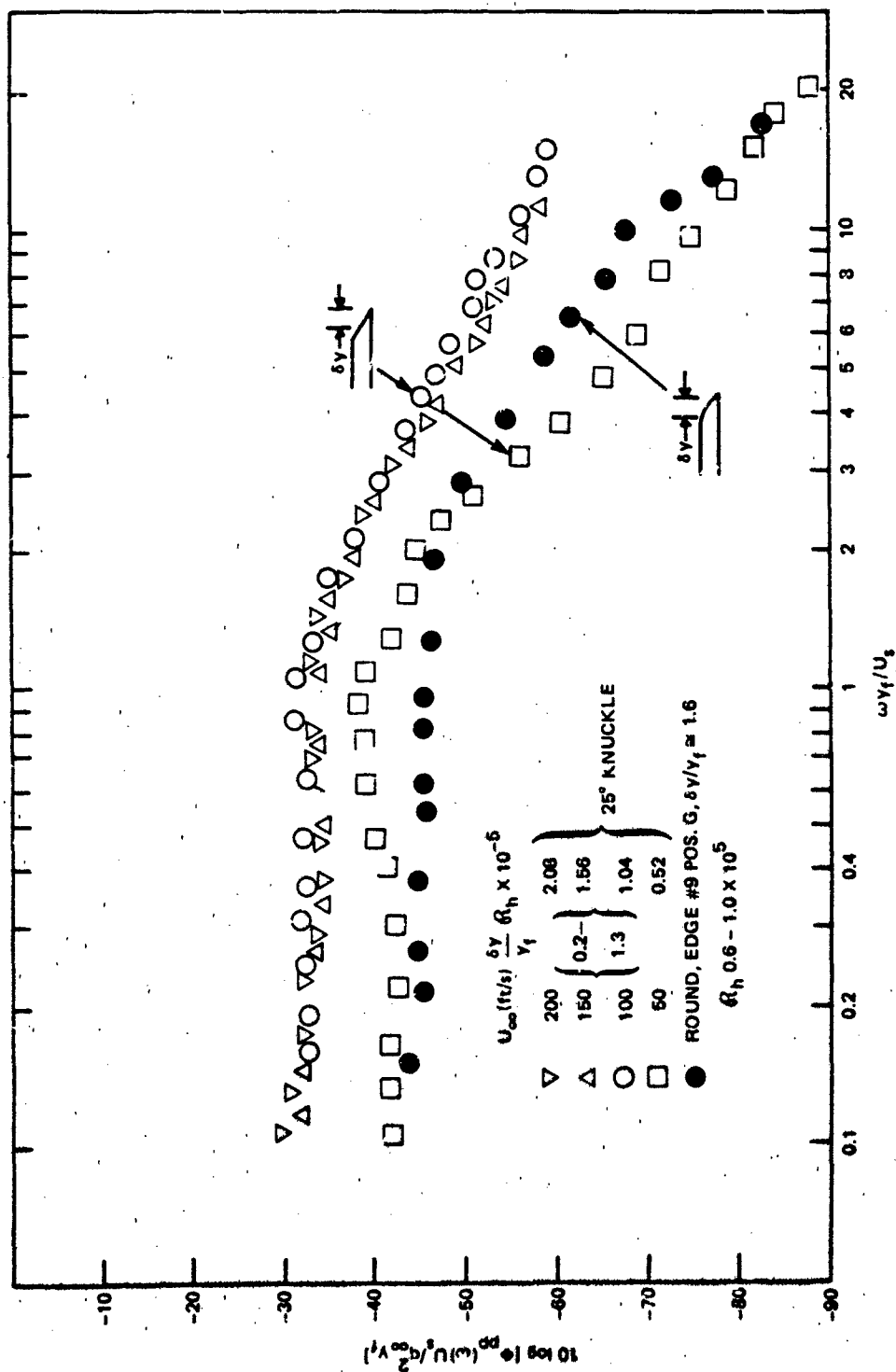


Figure 9.32 - Surface Pressure Spectra Beneath Flow Separation. Open Points: Pressure Spectra at Position F on Beveled Trailing Edge of Figure 9.34; $y_f = 0.7h$ (Assumed Constant for All Speeds, $U_s/U_\infty = (1-C_{ps})^{1/2}$, $C_{ps} = -0.3$). Closed Points: Pressure Spectra at Position G on Rounded Edge of Figure 9.23, $y_f \approx 0.37h$ (Assumed for Speed $U_\infty = 60$ fps to 100 fps, $C_{ps} \approx -0.1$).

$$\frac{\overline{p^2}}{q_\infty^2} = \int_{-\infty}^{\infty} \frac{\phi_{pp} \left(\frac{\omega y_f}{U_s} \right) d \left(\frac{\omega y_f}{U_s} \right)}{q_\infty^2} + \frac{\overline{p_T^2}}{q_\infty^2} \frac{1}{2} \int_{-\infty}^{\infty} \left[\delta \left(\frac{\omega y_f}{U_s} - 1 \right) + \delta \left(\frac{\omega y_f}{U_s} + 1 \right) \right] d \left(\frac{\omega y_f}{U_s} \right)$$

The tonal pressure $\overline{p_T^2}$ is equal to zero for edges 8 and 9, while it attains varying magnitudes on the other edges. The position of measurement of the pressure is given relative to the location of the stagnation point at the edge; this point occurs at the base of the airfoil with edges 1, 3, 5, 7 and at points such as "S" in Figure 9.22 for edges 6, 8, and 9. Included also is an approximate value for the autospectrum of surface pressures induced by the normal turbulent boundary layer upstream of the edge. All spectra show a similar dependence on the dimensionless frequency $\omega y_f / U_s$; either the tone or the maximum in the autospectrum of the continuum occurs near $\omega y_f / U_s = 1$.

As the apex of the beveled trailing edge is approached, the boundary layer experiences an adverse pressure gradient downstream of which the flow may separate, as seen in Figures 9.33 and 9.34. During this process the pressures at frequencies less than $\omega y_f / U_s$ tend to increase, and those above $\omega y_f / U_s$ tend to decrease sharply as the apex of the edge is approached. Figure 9.33 (taken from reference 82) demonstrates this behavior for edge 9 of Table 9.3, which is also shown in Figure 9.23. Upstream of location C, the surface pressures behave statistically just as they do for any fully developed turbulent boundary layer (see Chapter 7). If the edge is not curved as shown, so that separation does not occur at the trailing edge, then the boundary-layer properties remain substantially unaltered up to the apex, as confirmed by the measurements of Brooks and Hodgeson.⁸⁸ Downstream of position C in Figure 9.33 the flow separates, creating the spectrum at G as shown.

Elucidation of the pressure fields beneath zone of separation on the trailing edge is afforded by the flow downstream of a sharpened bevel (edge 8 in Table 9.3), which generates the properties shown in Figure 9.34. Turbulent flow separation at the knuckle causes an abrupt increase in fluctuating pressure as shown by the behavior of spectrum levels at constant values of $\omega y_f / U_s$, the pressures retain a high value throughout the separation zone for $\omega y_f / U_s \leq 10$. At higher frequencies, the increase is localized at the knuckle. Magnitudes of the cross-spectral densities of pressures at different chordwise locations show that the pressure-producing vortex structure remains well correlated as it convects uniformly down the bevel

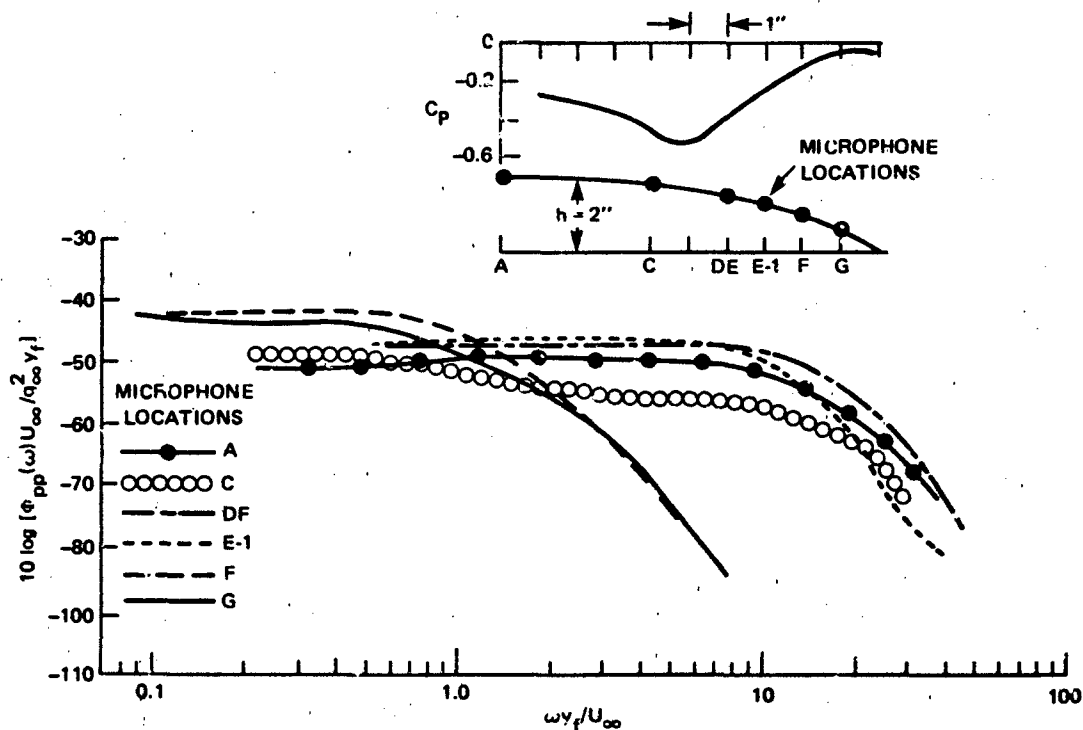


Figure 9.33 - Spectral Densities of Surface Pressures at a Round-Bevel Trailing Edge. The Double Arrow in the Inset Indicates the Zone of Separation. Parameters: Edge 9, Table 9.3, $R_h = 10^5$

and past the apex. The vortical nature of the flow was established⁸³ by flow visualization and correlations of velocity fluctuations. The zone of separation is not one of constant recirculation. Instead, a separation vortex is formed that convects downstream with a reattached flow following it. As the vortex passes roughly halfway down the bevel, separation reoccurs at the knuckle and the process repeats.⁸³ The high-level low-frequency pressures are generated only by the separated vortex, not by the reattached flow. This distinction arises from the observation that the velocity fluctuations near the surface have nearly zero convection velocity, but both the pressure and velocity fluctuations of the large-scale vortical flow convect at $U_c = 0.46 U_\infty$ at $0.7 < \omega y_f / U_\infty < 1.0$. The phase angle of the cross spectrum of pressures was found to vary uniformly with streamwise separation, free stream velocity, and frequency, so that the standard interpretation (see Equation (3.103) or (7.129a)) could be put on the phase. Thus $\omega / U_c = k_c$, where U_c is the convection velocity which lies between $0.35 U_\infty$ and $0.5 U_\infty$, and Figure 9.34 shows values of $k_c y_1$ at selected dimensionless frequencies. As discussed in section 9.6.3 this parameter determines the theoretical behavior of surface pressures induced by aerodynamic

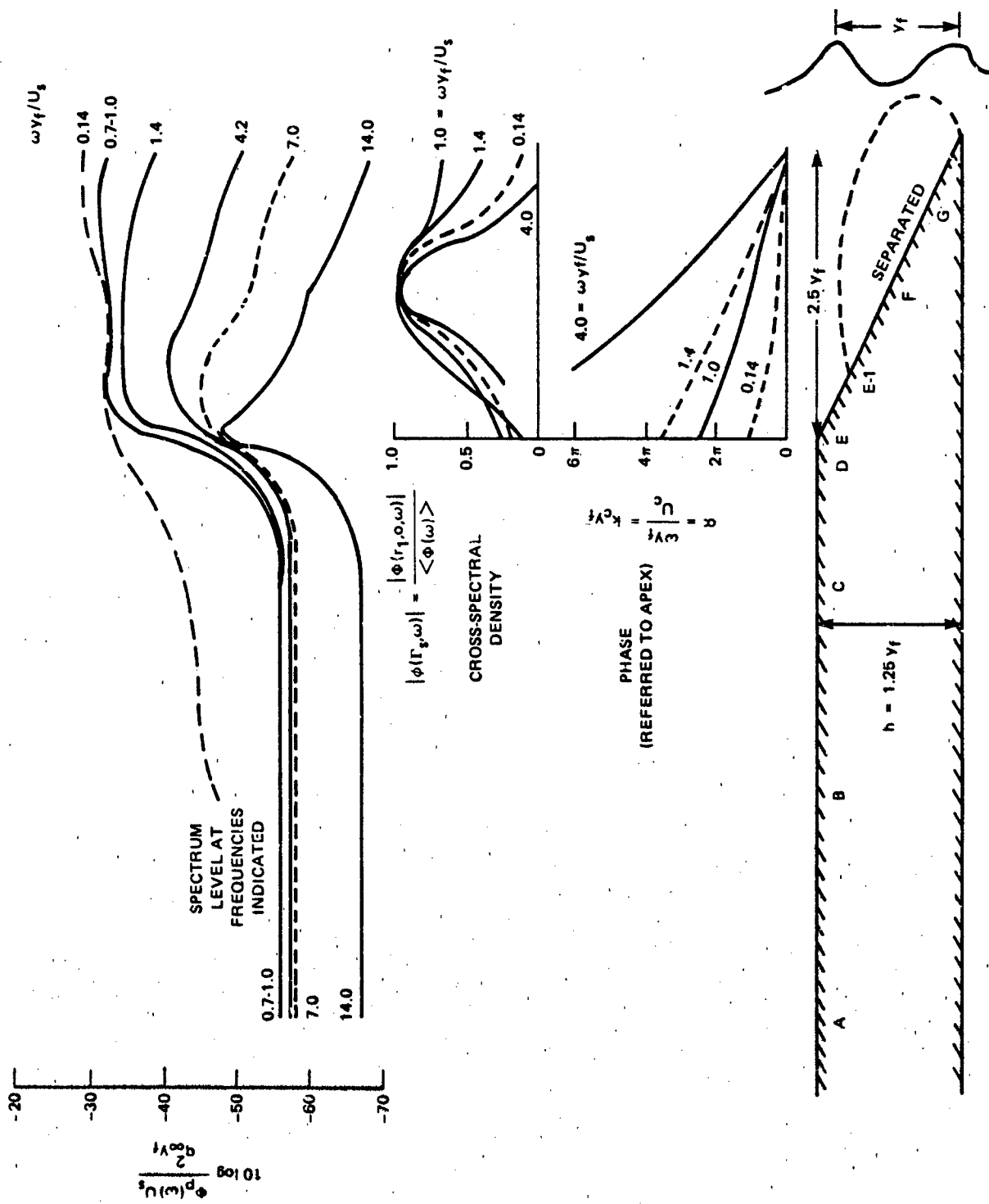


Figure 9.34 - Distribution and Covariance of Pressures on the Beveled Trailing Edge 8, Table 9.3, p. 9-77 at $R_h = 10.4 \times 10^4$

edge scattering. Finally, as Figure 9.32 shows, the random pressures on edges with separation seem to have a characteristic frequency $\omega_f/U_s \approx 1$, and the levels apparently remain reasonably uniform throughout the zone of separation.

9.5.4 Spanwise Correlation Lengths

In section 9.6 it will be shown that the sound radiated by trailing-edge flows is directly proportional to the spanwise integral correlation length. If turbulent separation does not occur, then the spanwise cross-spectral density of pressures near the edge is essentially the same as that shown in Figure 7.37b, which gives

$$\Lambda_3 \approx 1.4 U_c / \omega \quad (9.84)$$

where Λ_3 has been defined by Equation (3.90a).

When separation occurs, the spanwise correlation is more complicated. Measurements at the midpoint of the knuckle bevel (previously shown in Figure 9.34) have two characteristics. As shown in the upper part of Figure 9.35, the normalized cross-spectral density has an envelope that appears to be a function of $\omega r_3/U_c$. Upon close examination of the points, however, one sees that this applies only when $\omega y_f/U_s > 1$. At lower frequencies the cross spectrum is not expressible as a function of $\omega r_3/U_c$; rather, it depends on r_3/y_f . Thus there are two spanwise integral scales for pressures beneath the separation zone,

$$\Lambda_3 \approx y_f \quad \omega y_f/U_s \leq 1 \quad (9.85a)$$

and since for this edge $U_c/U_s \approx 0.46$

$$\Lambda_3 \approx 2.2 U_c / \omega$$

or

$$\Lambda_3 \approx y_f \left(\frac{\omega y_f}{U_s} \right)^{-1} \quad \omega y_f/U_s > 1 \quad (9.85b)$$

When vortex shedding occurs, then spanwise correlation and its physical meaning are completely analogous to the circular cylinder. The lower part of Figure 9.35

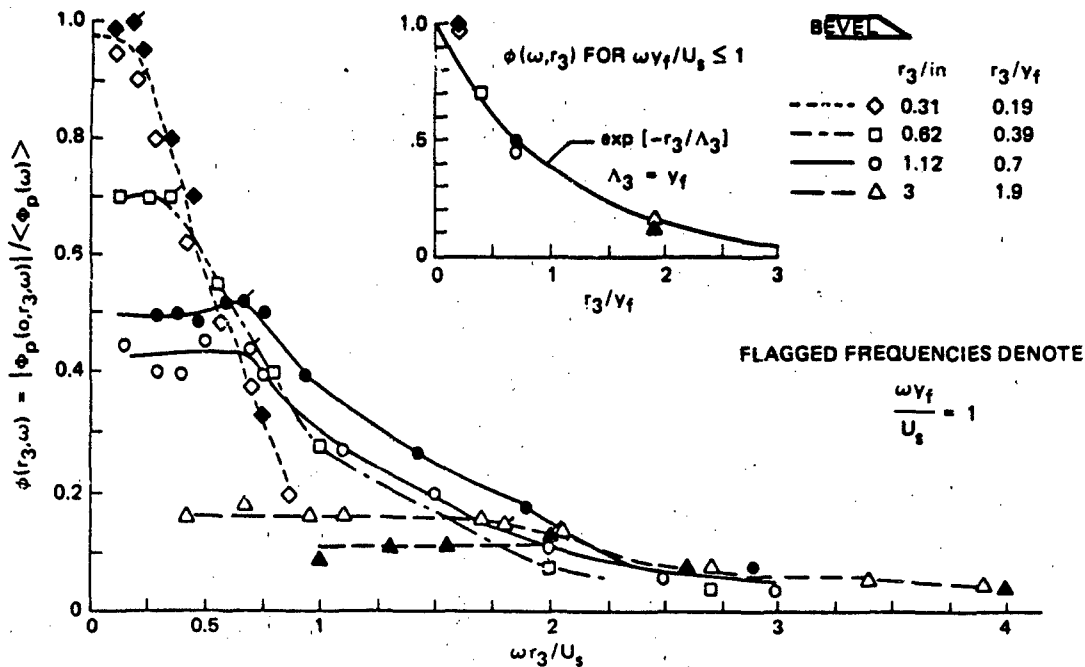


Figure 9.35a - Spanwise Cross Spectral Density on a Trailing Edge with Flow Separation and Continuous-Spectral Pressures

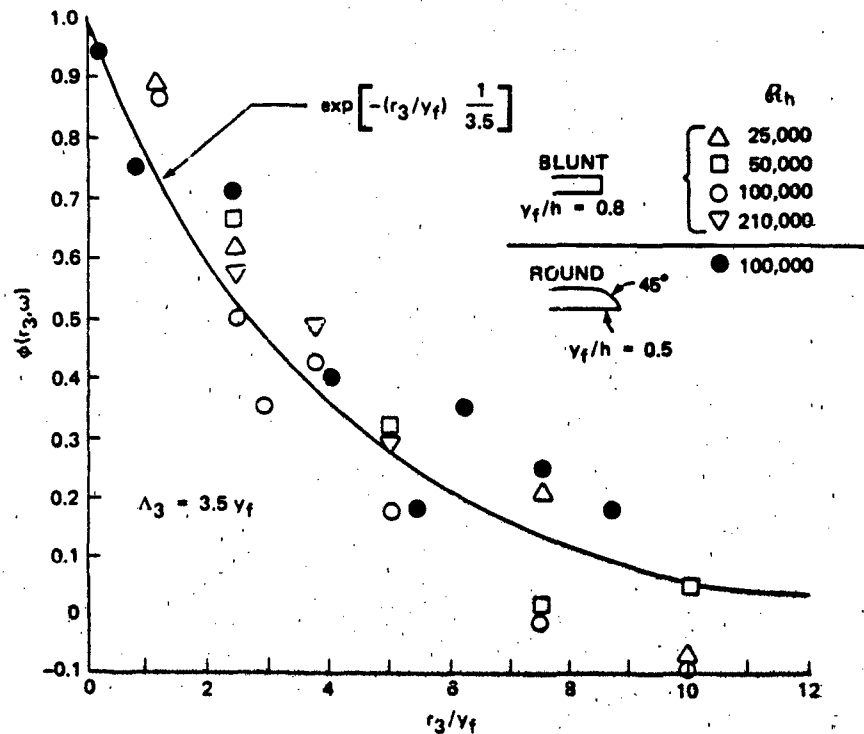


Figure 9.35b - Spanwise Cross Spectral Density of Tonal Pressures on Blunt Trailing Edges with Vortex Shedding

Figure 9.35 - Example of Spanwise Cross Spectra on Trailing Edges 5, 6, and 8 of Table 9.3 with Different Modes of Flow

shows the spanwise correlation of tonal pressures near the trailing edge. For both trailing-edge geometries, the same exponential fit seems to apply. It gives

$$\Lambda_3 \approx 3.8 y_f \quad (9.86)$$

The correlation values presented in Figure 9.35 are the maximum values of the space-time correlation, and they are not known to be influenced by airfoil vibration. Owing to slight yawing of the vortices relative to the trailing edge of the strut, the maximum of space-time correlation was often observed at small values of time delay. For the blunt edge this behavior was minimal, but in the case of the rounded edge a time delay was generally observed.

Measurements of spanwise correlations of velocities in vortex-street wakes of squared-off blunt edges have also been reported by Graham¹¹² for $2.8 \times 10^4 < R_h < 8.3 \times 10^4$. The correlation functions are similar to those shown in Figure 9.36. However, Graham observed generally negative values of the correlation function between $5 < r_3/h < 11$ reaching values of -0.05.

9.5.5 The Flow-Induced Forces at Trailing Edges

In the case of either the tonal or the random pressures, the force on the surface can be formally found by integrating the pressure,

$$f(t) = \int_{\text{surface}} p(\vec{y}, t) d\vec{y} \quad (9.87)$$

Figures 9.27 and 9.29 show that the trailing-edge force due to the vortex shedding is localized. The autospectrum of the force can be written

$$\phi_f(\omega) = \int_{-\infty}^{\infty} \int_{\text{surface}} d\vec{y}_1 \int_{\text{surface}} d\vec{y}_2 \overline{p(\vec{y}_1, t) p(\vec{y}_2, t+\tau)} e^{i\omega\tau} d\tau \quad (9.88)$$

The time and space variation will be separated along the lines used in Sections 3.6.3.3, 5.3.3, 7.2.5, and 7.4.2; an autospectrum function will be factored out from the spatial behavior. The pressures induced by the formation of periodic vortex streets will be deterministic in y_1 , in phase opposition on upper and lower surfaces,

and will have a spanwise stochastic function of position, with integral scale Λ_3 . It is apparent from the measured data that y_1 and y_3 functions of position are analytically separable. Figure 9.29 suggests in fact

$$p(\vec{y}, t) = p_o g\left(\frac{y_1}{y_f}\right) e^{i\phi(\vec{y}_3, t)} e^{-i\omega_s t} \quad (9.89)$$

where $p_o = \rho_o U_s \Gamma / (2\pi y_f)$ and $g(y_1/y_f) = [(y_1/y_f) / 0.12]^{1/2}$ for y_1/y_f less than, say, m , where m is approximately 6. Accordingly, it can be shown that

$$\phi_f(\omega) = \frac{1}{2} \langle F^2(t) \rangle [\delta(\omega + \omega_s) + \delta(\omega - \omega_s)]$$

where

$$\langle F^2(t) \rangle = 4 \left(\frac{\rho_o \Gamma_o U_s}{2\pi y_f} \right)^2 \left[2y_f (0.12m)^{1/2} \right]^2 (2\Lambda_3 L_3) \quad (9.90a)$$

if my_f is less than the chord C or

$$\langle F^2(t) \rangle = 4 \left(\frac{\rho_o \Gamma_o U_s}{2\pi y_f} \right)^2 \left[2y_f \left(0.12 \frac{C}{y_f} \right)^{1/2} \right]^2 (2\Lambda_3 L_3) \quad (9.90b)$$

if the chord is much less than my_f . The assumption has been made that the integral over $g(y_1/y_f)$ is limited only to the $(y_1^{1/2})^{-1}$ region, and that the span is long enough that $L_3 \gg 2\Lambda_3$.

9.6 SOUND FROM TRAILING-EDGE FLOW

9.6.1 Summary

Sound is radiated from trailing-edge flows by two related mechanisms. Tones are generated when periodic vortex shedding occurs. The vortex street in the wake provides distributed aeroacoustic dipole source of strength $\nabla \cdot (\vec{\omega} \times \vec{U})$. If the

frequency is large enough that $\omega C/c_0 > 2\pi$, then the acoustic pressures far from the edge may be determined in a straightforward manner as an extension to the analysis Section 9.2.3.2. The acoustic-field Green function introduced in that section applies to this case, since Equation (9.8) gives the pressure in the fluid resulting from a unit depole source near the trailing edge. The pressure and fluid velocity become singular as the source-distance from the r_0 decreases, in the same way as expressed explicitly for the velocity in the hydrodynamic field of the edge by Equation (9.78) in Section 9.5.1. Thus the two problems are consistent, and this consistency is used below. At lower frequencies such that $\omega C/c_0 < 20$, a low-frequency Green function for the acoustic field (see, e.g., Howe²⁴) must be introduced as an alternative to the half-plane function.

The second mechanism of sound generation at trailing edges arises when vorticity is convected past a trailing edge. The sound is generated as the vorticity in the flow encounters a sharp discontinuity in local impedance ($\rho_0 C_0$ in the fluid compared with infinity on the surface of a rigid knife edge). As far as the mathematical fundamentals of Section 9.2.3.4 are concerned, at first sight they apply equally well to both leading- and trailing-edge sound generator. Physical differences are apparent, however, as indicated by the behavior of surface pressures near the edges. Near the leading edge, the pressure attains a maximum (analytically it becomes unbounded, while at the trailing edge, the unsteady pressures induced by turbulent flow do not increase at the apex of the edge, as discussed in the preceding section. This means that, while leading-edge noise is analytically reasonably well described by the relationships of Section 9.2.3.4, continuous-spectrum trailing-edge noise will differ in level from leading-edge noise, but, as we shall see, it will still be functionally similar. The mathematical dissimilarities are due to the observed fact that the random trailing-edge surface pressures remain finite at the edge. The analytical treatment that may provide such bounded pressures must require that additional vorticity be shed into the wake in response to the hydrodynamic effect of the upstream turbulence, which would otherwise be to create a pressure singularity at the edge as in the leading-edge case. Thus, while leading- and trailing-edge noises at high frequencies are both the result of the scattering due to the impedance discontinuity at the edge, trailing-edge noise is reduced somewhat by a requirement that the surface pressure at the apex should not increase there.

In this section, analytical relationships are derived with which the prediction of sound can be made. Empirically determined vortex strengths or excitation forces, depending on analytical model used, are given to assist in practical situations.

9.6.2 Acoustic Tones From Vortex Shedding

9.6.2.1 Theoretical Relationships. At low Mach number, the wave equation in the Powell (Equation (2.89); see Section 2.5) and Howe¹¹ form is

$$\nabla^2 P_a(\vec{y}, \omega) + k_o^2 P_a(\vec{y}, \omega) = \frac{\partial}{\partial y_2} (\rho_o \omega_3 U_c) \quad (9.91)$$

which resembles Equation (9.2). The vorticity distribution has been specialized to be oriented along the y_3 direction, whence the $\omega_3 U_c$ term is all that remains of $\vec{\omega} \times \vec{U}$. The vorticity is given by the same model as Equation (9.73); however, a statistical variation along the span of the edge is permitted. The correlation length $2\Lambda_3$ of this variation is presumed to be much greater than a streamwise vortex spacing; that is, $2\Lambda_3 k_w \gg 1$. Combination of Equation (9.73), (9.8), and (9.7b), noting that

$$\omega_3(\xi_1, \xi_2, \xi_3, t) = \gamma_o(k_w, \xi_3, \omega) \delta(\xi_2) e^{+ik_w(\xi_1 - U_c t)} d\xi_1 \quad (9.92)$$

yields

$$\xi_1 > 0$$

$$P_a(\vec{x}, \omega) = \frac{e^{ik_o r}}{4\pi r} \cdot \frac{e^{-i\pi/4}}{(2\pi)^{1/2}} (k_o)^{1/2} \sin^{1/2} \phi \sin \frac{\theta}{2}$$

$$\int_{-L/2}^{L/2} \left[\rho_o \gamma_o(k_w, \xi_3, \omega) U_c \right] \int_0^\infty \frac{1}{(\xi_1)^{1/2}} e^{ik_w \xi_1} d\xi_1 d\xi_3 \quad (9.93)$$

The geometry of the wake is shown in Figure 9.25(a). For simplification, it has been assumed that $k_w \ell_f \approx 0$, although it is argued below that there is really no loss in generality by doing so. The integral in Equation (9.93) is evaluated straightforwardly to give

$$P_a(\vec{x}, \omega) = \frac{e^{ik_o r}}{4\pi r} \frac{1}{(2)^{1/2}} \left(\frac{k_o}{k_w}\right)^{1/2} \sin^{1/2} \phi \sin \frac{\theta}{2} \rho_o U_c \int_{-L/2}^{L/2} \gamma_o(k_w, \xi_3, \omega) d\xi_3 \quad (9.94)$$

and $P(\vec{x}, \omega)$ is a random variable because of the stochastic nature of the integral of $\gamma_o(k_w, \xi_3, \omega)$ over the span. By the same steps that led to Equations (5.48) and (5.49), the spectral density of the far-field sound pressure is

$$\phi_{P_{rad}}(\vec{x}, \omega) = \frac{1}{32\pi^2} \left(\frac{k_o}{k_w}\right) |\sin \phi| \sin^2 \frac{\theta}{2} \rho_o^2 \overline{\gamma_o^2} U_c^2 \left(\frac{\ell_c L}{r^2}\right) \quad (9.95)$$

$$\cdot \phi_Y(\omega - \omega_s)$$

where $\phi_Y(\omega - \omega_s)$ is a normalized spectrum function of the wake disturbances such that

$$\int_{-\infty}^{\infty} \phi_Y(\omega - \omega_s) d\omega = 1$$

and

$$\frac{\omega_s y_f}{U_3} \approx 1 \quad (9.96)$$

By Equation (9.74)

$$\overline{\gamma_o^2} = r_o^2 \frac{k_w^2}{4} \quad (9.97)$$

is the mean-square vorticity at a point in the near wake. In Equation (9.95) the factor γ_c appearing in Equation (5.49) has been taken as negligible in comparison to $2\Lambda_3$.

To maintain consistency with Section 9.5.1, Equation (9.82a) can be used to relate the surface pressure near the edge to the quantity $\gamma_0^2 \phi_Y(\omega - \omega_s)$ to obtain

$$\frac{\phi_{P_{rad}}(\vec{x}, \omega)}{\phi_{P_s}(y_1 - y_s, \omega)} = \frac{1}{2\pi^2} \frac{U_s}{c_o} \frac{2\Lambda_3}{y_f} \frac{(y_1 - y_s)L}{r^2} |\sin \phi| \sin^2 \frac{\theta}{2} \quad (9.98)$$

Equation (9.98) has been derived by using functions that depend on the assumption $k_w \ell_f \approx 0$. However, it does not depend on this assumption. The influence of $k_w \ell_f > 0$ is to reduce the magnitude of the surface pressure by a degree proportional to y_f/ℓ_f ; however, the nature of the singularity, which ultimately controls the ratio of far-field to near-field pressures, is identical. Accordingly, even though $\phi_{P_{rad}}(\vec{x}, \omega)$ and $\phi_{P_s}(y_1 - y_s, \omega)$ may be reduced by y_f/ℓ_f , their ratio will be invariant. The position of surface pressure measurement must be in the $(y_1 - y_s)^{-1}$ range for the spectrum level.

Figure 9.36 shows a comparison of the measured sound pressure from a NACA 0012 airfoil with a blunt edge and values predicted using Equation (9.98). The spanwise integral scale Λ_3 was taken from measurements such as shown in Figure 9.35, and the other conditions for the airfoil are as listed in Table 9.3 and shown in Figure 9.30. Both the bandwidth and the integral scale of these pressures show greater randomization than occurs on blunter edges, e.g., edge 5 in Table 9.3, p. 974.

At low frequencies such that $\omega C/c_o < 2\pi$, the above analysis must be adjusted to use a low-frequency Green function. Such functions have been derived by Howe for the circular cylinder¹¹³ and the finite thin airfoil.²⁴ The result obtained is similar to Equation (9.94) but with a different numerical coefficient and with k_o/k_w rather than $(k_o/k_w)^{1/2}$. The associated force on the cylinder is related to $\rho_o \Gamma_o$ by a relationship similar to Equation (5.32). The mean-square sound pressure radiated from the lifting surface as given by Equation (5.53) then applies and is rewritten here for the convenience of the reader

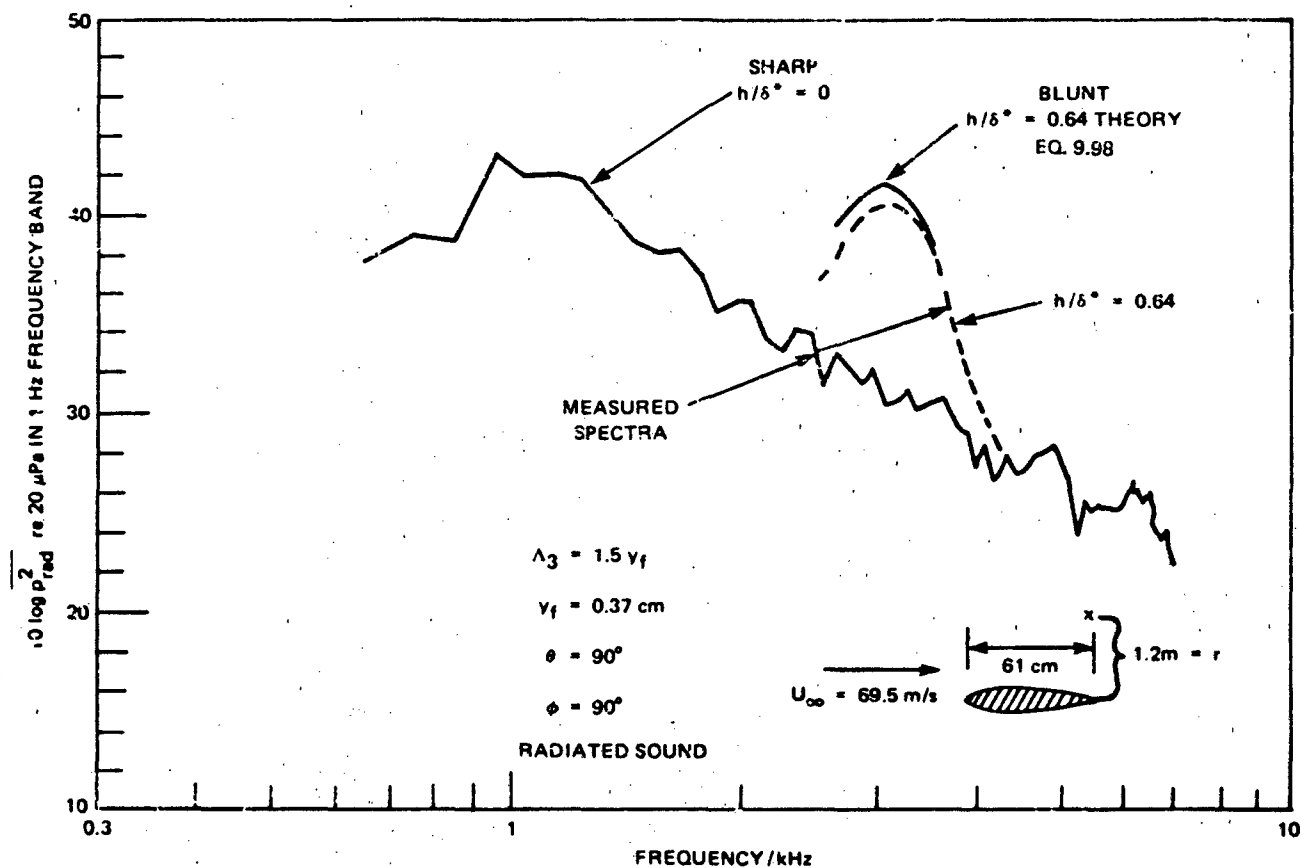


Figure 9.36 - Vortex Shedding Sound from a NACA 0012 Airfoil with a Blunt Trailing Edge Compared with Theory and with Sound Radiated When the Edge Is Sharp

$$\overline{p_a^2}(\vec{x}) = q_\infty^2 M_\infty^2 \left(\frac{\sin \theta}{4\pi} \right)^2 \frac{y_f L}{r^2} \left[\left(\frac{\omega C}{U} \right)^2 \frac{2\Lambda_3}{y_f} \overline{C_L^2} \right] \quad (9.99)$$

where $\theta = 0$ coincides with the wake and where $\overline{C_L^2}$ is now the mean-square lift coefficient based on the chord of the airfoil to be consistent with Equation (9.50a), and y_f represents the length scale such that Equation (9.62) is obeyed. We note that the term in square brackets is independent of the chord by virtue of the fact that the mean-square force as given by Equation (9.90a) is proportional to y_f^2 , not to C^2 .

The far-field pressure in a two-dimensional field was determined by Davis using a matching process. He evaluated the radial fluid velocity resulting from Equation (9.77) at distances far from the edge. He matched the radial velocity to that of the acoustic field radiated from a source near a half-plane. A variation of this approach was used by Clark¹¹⁴ and Clark et al.,¹¹⁵ who expressed the time derivative of the force on the lifting surface in terms of the rate of momentum shed into the wake (see, e.g., Equation (5.23)). The unsteady momentum normal to the plane of the surface and generated in the near wake is responsible for the lift fluctuation causing the noise. To evaluate this momentum it is necessary to determine empirically the correlation volumes for normal (u_2) velocity fluctuations. Agreement between the measured sound pressures and those estimated from the wake momentum flux is to approximately ± 5 dB. Kotake¹¹⁶ developed the formalism for the general treatment of the radiated noise from a surface of arbitrary chord, shedding a wake with an arbitrary circulation distribution. The formalism developed the alternating lift fluctuations along the general lines of the approach of Section 9.3.1.

9.6.2.2 Tones From Laminar-Flow Airfoils. The earliest measurements of sounds from airfoils with vortex shedding are those of Yudin¹¹⁷ on rotating rods already described in Chapter 5. Those measurements were made on blunt-edged surfaces at low Reynolds number. More recent measurements using fixed airfoils in uniform inflow are described below. Since these measurements were made at moderately low Reynolds number, they entail the existence of laminar flow over a substantial segment of the chord. Treatment of tonal sounds therefore will be divided into a review of measurements with laminar flow airfoils and an account of theoretical

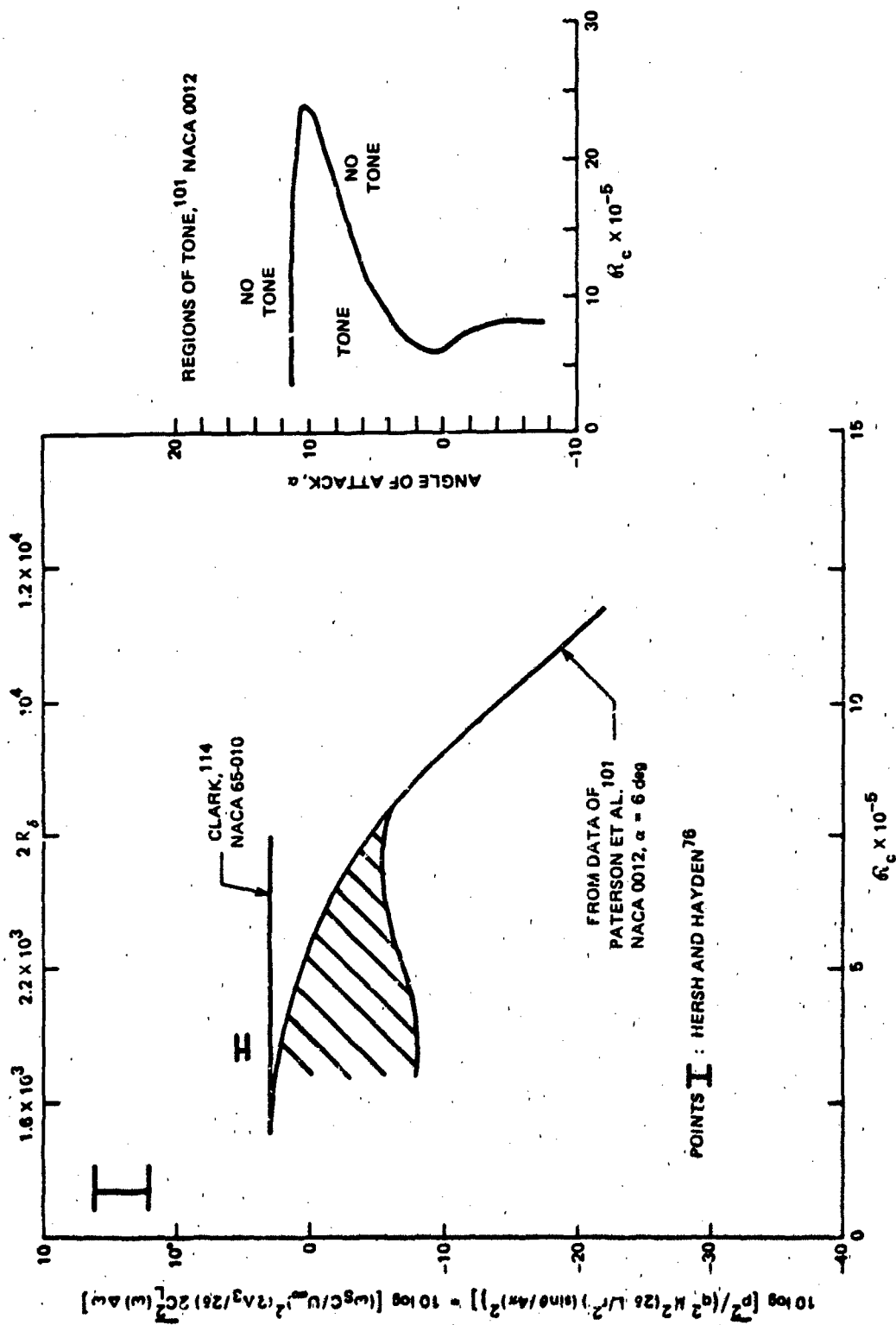


Figure 9.37 - Vortex-Induced Lift Coefficients for Sharp-Edged Airfoils at Small Angles of Attack as Deduced from Measured Dipole Sound. Note That Boundary-Layer Transition

Normally Occurs on Flat Plates when $R_{y_1} > 4 \times 10^6$ (See Chapter 7)

relationships for predicting sounds from blunt-edged surfaces at high Reynolds number. The radiated noise measurements by Clark,¹¹⁴ Paterson et al.,⁷⁶ and Sunyach et al.¹¹⁸ were all conducted for $R_c < 1.5 \times 10^6$. The chord was acoustically compact in those measurements so that radiated noise can be regarded as having been induced in the same manner as for cylinders, and Equation (9.85) applies. Note that C_L^2 may be a spectrum function as in Section 9.3, i.e., the integrated lift coefficient is

$$\overline{C_L^2} = \int_{-\infty}^{\infty} \overline{C_L^2}(\omega) d\omega$$

Since we are dealing with sharp-edged laminar-flow airfoils, the Strouhal number defined by Equation (9.64) applies, so that we replace

$$2\delta = y_f$$

in Equation (9.85).

The noise levels of Clark¹¹⁴ and Paterson et al.,⁷⁶ nondimensionalized in the manner of Equation (9.85), are shown in Figure 9.37. The experiments were conducted on airfoils that had perfectly sharp trailing edges; Clark's airfoils were both uncambered and cambered NACA 65-010 sections; that used by Paterson et al.⁷⁶ was an uncambered sharp-edged NACA 0012. The sound pressure levels given in Figure 9.37 were of high tonal quality.

The dimensionless noise levels are roughly constant at low values of R_c , suggesting that the oscillatory lift is a function of Reynolds number only through its dependence on δ . At a 6-deg angle of attack and at values of $R_c > 7 \times 10^4$, the values reported by Paterson et al. fall off abruptly, possibly because of an influence of turbulent boundary-layer flow on the wake dynamics. Somewhat similar behavior was shown in the experiment of Sunyach et al.¹¹⁸ In that case, a narrow-band radiation was observed at $R_c \approx 10^5$ which disappeared for $R_c \approx 2 \times 10^5$. A connection between the turbulence character of the surface boundary layer and the tone generation has been further substantiated by Paterson et al.⁷⁶ and Hersh and Hayden,¹⁰² who found that tripping the laminar boundary layer to turbulence could eliminate the tone. The existence of the tone also depends on the angle of attack, as seen in the inset of Figure 9.37.

A close examination of the frequency-speed relationship of the tones observed by Paterson et al.⁷⁶ discloses a discontinuous behavior with speed. It was also observed at some speeds that two tones could occur simultaneously. Tam⁷⁷ has postulated that this discontinuous behavior is the result of acoustic coupling between the wake disturbances and Tollmein-Schlichting waves in the transitional boundary layer on the surface. The jump discontinuities are due to phase requirements between the exponentially growing disturbances in the wake and the disturbances in the boundary layer of the airfoil. The waves in the boundary layer then feed the initial waves in the wake.

9.6.2.3 Turbulent Flow Airfoils With Blunt Trailing Edges. In Section 9.6.2.1 we derived a relationship between both the vortex induced surface pressure and the radiated sound for acoustically large rigid airfoils. A useful relationship that may be used in conjunction with Figure 9.30 for rough prediction is found from Equation (9.95):

$$p_a^2(\vec{x}) = \frac{1}{32} q_\infty^2 M_\infty^2 \left(\frac{U_c}{U_\infty} \right) |\sin \phi| \sin^2 \frac{\theta}{2} \frac{2\Lambda_3 L}{r^2} \times$$

$$\left\{ \frac{\rho_o^2 \Gamma_o^2 U_s^2}{(2\pi)^2 q^2 y_f^2} \right\} \quad \text{for } \frac{\omega c}{\omega} > 2\pi \quad (9.100)$$

where $2\Lambda_3$ may be taken from Table 9.3.

For compact turbulent-flow surfaces, Equation (9.90a) (for $C > m y_f$) may be used to find a lift coefficient consistent with the definition Equation (9.50a) in the form

$$\overline{C_L^2} \left(\frac{c}{y_f} \right)^2 = 2\pi \left[\frac{\rho_o^2 U_s^2 \Gamma_o^2}{(2\pi q y_f)^2} \right] \frac{2\Lambda_3}{L_3} \quad (9.101)$$

where the entire bracketed term on the right may be obtained in Figure 9.30(b).

Thus

$$\overline{p_a^2}(\vec{x}) = \frac{(2m)}{16\pi^2} q_\infty^2 M_\infty^2 \sin^2 \theta |\sin \phi| \frac{2\Lambda_3 L}{r^2} \times$$

$$\left(\frac{\rho_o^2 \Gamma_o^2 U_s^2}{(2\pi q y_f)^2} \right) \quad \text{for } \frac{\omega C}{C_o} < 2\pi, \text{ and } C > \sim 6y_f \quad (9.102)$$

In addition to the experimental work of Brooks and Hodgeson⁸⁸ previously described in Section 9.6.2.1, measurements by Olsen and Karchmer¹¹⁹ of dipole sound from co-axial nozzles and from nozzles with splitter plates support the validity of Equations (9.100) through (9.102). Supporting measurements were also made of the wake flow. The vortex-shedding edges were blunt as edge 5 of Table 9.3. Measurements indicated that their wake flow had the following parameters: $R_h \approx 2-6 \times 10^4$, $l_f \approx 2h$, and $y_f \approx 0.9h$. Calculations made with values of $\rho_o \Gamma_o U_s / (2\pi q y_f)$ from Figure 9.21b, $2\Lambda_3 \approx 6y_f$, $U_s \approx 1.3 U_\infty$ gave values of sound pressure that agreed with those measured to within 10 dB; the calculated values were generally high. In their program, Olsen and Karchmer¹¹⁹ varied the flow velocities on the upper and lower surfaces of the plate independently. When the velocities differed by more than a factor of 2 ($U_{\text{upper}}/U_{\text{lower}} \geq 2$), the tonals ceased. As $U_{\text{upper}}/U_{\text{lower}}$ increased from unity, the sound pressure level decreased systematically; a 10-dB reduction occurred when $U_{\text{upper}}/U_{\text{lower}} \approx 2.5$.

9.6.3 Sound From Aeroacoustic Scattering

In this section we consider broadband sound generated at frequencies greater than, say, $\omega C/U_\infty = 2\pi$. In this frequency range, leading and trailing edges may be considered to be aerodynamically decoupled; the leading-edge noise is given by Equation (9.56). This source of trailing-edge noise occurs from jets blowing over simple or slotted trailing edges,^{60-63, 120-130} and turbulent boundary layer flow past sharp-edged airfoils. At finite angles of attack, the tip flow of lifting

surfaces may generate noise.^{131,132} This noise, however, has received very little analytical or experimental attention compared to the attention given to trailing-edge noise. The theory postulates that the noise mechanism is due to the convection of the turbulent eddies in the boundary layer past a sharp edge so that the edge behaves as a scatterer. The general dimensional characteristics of noise from this type of source were considered in Section 9.2.3.3 and the generation process may be considered independent of whether or not the flow is on one or both sides of the edge, except insofar as interaction may occur between the flow and the trailing edge. In this section we characterize the noise in terms of the spectrum of surface pressures and examine dimensionless representations of the sound.

9.6.3.1 A Concise Theory of Edge Noise By Aeroacoustic Scattering. In this section we examine numerous theoretical results that may be used to predict sound pressures due to turbulent flow off trailing edges. Certain simplified analytical problems are discussed to examine separately the importance of various features of the general theoretical treatment. The results derived in this section pertain to the trailing-edge noise from scattering of aerodynamic sources (pertaining to wall jets, flap noise, and boundary layer turbulence convected over trailing edges).

Theoretical treatments of trailing-edge noise by aeroacoustic scattering, beyond the dimensional and heuristic discussions in Section 9.2.3.3, have dealt with three general aspects. The first¹³³⁻¹³⁵ treats the radiated noise field as a boundary-value problem determined by a known pressure field that exists on the rigid boundary. The characteristics of the boundary pressure field are assumed to be proportional to and determined by the hydrodynamic pressures of the turbulent boundary layer on the edge. These results in particular apply only to the extent that there is no hydrodynamic interaction between the edge and the incident eddies and therefore no formation of additional vorticity sources within the wake of the trailing edge. The effect of the sharp trailing edge is to scatter energy from relatively short hydrodynamic (evanescent) waves into the long acoustic waves. The second alternative formulation¹³⁶⁻¹³⁹ deals with the hydroacoustic interactions among the rigid plate, the fluid, and the shear layer in the wake of the edge. The plate-shear layer interaction is assumed to be governed by incompressible equations of fluid motion and gives rise to flow instabilities, while the acoustic scattering effect of the half-plane gives rise to a far-field acoustic radiation. The third class of

problems^{10,11,21,140,141} treats the flow field incident on the edge and in the wake as a distributed source according to Lighthill's analogy. Various combinations of vortex motions^{11,21,141} and surface impedances^{10,140} have been considered in that group of studies. Additional work that does not clearly fall into the three classifications is that of Amiet,¹⁴² which is a direct application of relationships derived in references 40 and 59, and of Tam¹⁴³ and Tam and Reddy,¹²⁶ which is based on a Kraichnan-like model of the surface pressures in terms of the velocity statistics in the wake in connection with an acoustic boundary-value problem in which the surface pressures are the boundary conditions. An extensive and critical review of all these analytical treatments has been given recently by Howe.¹⁴⁴ Also included in that treatment is a unified theoretical analysis from which many of the results from various investigations have been extracted as special cases of a more general theory.

One of the important questions surrounding the theoretical analyses has dealt with the prediction of sound levels from mathematical models of near-field wake velocity statistics¹²⁶ or from wall pressure statistics.¹³³⁻¹³⁵ This work is of use in explaining some of the differences in the observed trailing-edge noise levels in terms of the time and length scales and the intensities of the surface pressures.

Another important question deals with the interaction of the turbulence field with the edge and therefore with the boundary condition to be applied there in analytical treatments of the problem. This boundary condition is used to keep the velocity transverse to the edge finite. A vehicle for doing this is to postulate the shedding of additional vorticity in the wake whose rotation is such as to cancel the transverse velocity induced by the incident primary vortex. In theoretical models the use of Kutta conditions influences only the magnitude of radiated sound, not its dependence on Mach number. The imposition of such conditions should be dependent on the edge geometry and the thickness of the edge in relation to the scale of the incident vorticity. These conditions have been examined for specific situations, all of which deal with half-plane knife edges, by Grighton¹³⁶ and Davis¹⁰⁷ (for a semi-infinite vortex sheet downstream of the plate), Jones¹⁸⁰ (for a stationary vortex with harmonic time dependence), and Howe^{11,21,141,144} (for a turbulence translating past a trailing edge). The unsteady aerodynamic implications of various types of Kutta conditions have also been analyzed using stability theory by Orsag and Crow.¹⁴⁵

A reasonably complete analysis of the problem of trailing-edge noise from sharp edges has been given by Howe.¹⁴⁴ The approach solves Equation (2.89), retaining only the $\vec{\omega} \times \vec{U}$ term for subsonic flow. The turbulent sources are postulated to be in a region above and adjacent to the sharp-edged plate, and in the wake downstream of the edge. The solution of the problem includes both the far-field and surface pressures generated from the edge-flow interaction, Figures 9.4 and 9.6, show the appropriate geometry. Two alternative solutions are produced. The first essentially corresponds to the analysis used in Section 9.6.2.1 in that it does not include a Kutta condition. F_2 in Equation (9.2) is replaced by a distribution of sources $\rho_0 \vec{\omega} \times \vec{U}_c$, just as in Equation (9.91), where $\vec{\omega}$ is a measure of the distribution of random vorticity fluctuations in the turbulent flow and \vec{U}_c is the convection velocity of that vorticity. The length scale in Equation (9.11) ℓ_0 would stand for the variable distance of the incident vorticity from the edge. In Equation (9.11) this would be typified by the shear layer thickness δ . We have seen that such solutions correspond to the case for which surface pressures at the extremity of the trailing edge become infinite in the mathematical sense. It could be argued that this singularity might be removed in a physical sense by the action of viscosity within a distance $y_1 \approx \ell_v$ where ℓ_v is a viscous length scale $(\omega/\nu)^{1/2}$. Howe^{140,144} gives an alternative argument, which employs a Kutta condition as described above (and for which the essentials will follow below). The acoustic source strength $\rho_0 \vec{\omega} \times \vec{U}_c$ is accordingly modified by an amount $-\rho_0 \vec{\omega}_w \times \vec{U}_w$ to account for new vorticity $\vec{\omega}_w$ in the wake convected away at speed U_w . The results of this analysis might be expected to hold for turbulent flow past sharp-edged lifting surfaces for which the included wedge angle is small. Furthermore, as we shall see, the result presented here does not apply to the noise resulting from the formation of periodic wake vorticity due to shear-layer instability.

Postulating that the source region above the downstream of the edge constitutes a region of nonvanishing $\nabla \cdot (\vec{\omega} \times \vec{U})$, Howe obtains an expression for the surface pressures

$$p_s(y_{1,3}, t) = \frac{-\rho_o}{2} \iint_{-\infty}^{\infty} \int_{-\infty}^{\infty} dk_1 dk_3 d\omega \int_0^{\infty} dZ \left\{ 1 + \operatorname{sgn}(y_2) \operatorname{Erf} \left[iy_1(k_1 + \sqrt{k_o^2 - k_3^2} + M_c k_o) \right]^{1/2} \right\} \\ \left\{ \left(1 - \frac{U_w}{U_c} \right) \vec{u} \cdot (\vec{\omega} \times \vec{U}_c) \right\} \frac{i(k_o^2 - k^2)^{1/2} Z}{(k_o^2 - k^2)^{1/2}} e^{i(\vec{k} \cdot \vec{y} - \omega t)} \quad (9.103)$$

where U_c is the local convection velocity of the eddies at a distance Z from the surface, $\operatorname{sgn} y_2 = +1$ for pressures on the same side of the surface as the flow, and $\operatorname{sgn} y_2 = -1$ for pressures on the opposite side and where

$$\vec{L} = \left[k_1, - (k_o^2 - k^2)^{1/2}, k_3 \right]$$

$$\vec{k} = (k_1, k_3)$$

where $(-1)^{1/2} = i$ and $\vec{\omega}$ is the generalized Fourier transform of the source vorticity

$$\vec{\omega}(\vec{k}_{13}, Z, \omega) = \frac{1}{(2\pi)^3} \iiint_{-\infty}^{\infty} e^{-i(\vec{k}_{13} \cdot \vec{y}_{13} - \omega t)} \vec{\omega}(\vec{y}, t) d^2\vec{y}_{13} dt \quad (9.104)$$

The new vorticity generated in the wake in response to the interaction of the incident vorticity with the edge is shed into the wake with such a strength and convection velocity, U_w , to identically cancel the singularity created by the incident vorticity. Evidence for this has been shown in the flow visualization of Yu and Tam.¹²⁹ This accounts for the error function and for the presence of U_w , the convection velocity of eddies in the wake. In writing Equation (9.103), the general result has been specialized to a flow vector perpendicular to the edge, an eddy convection Mach number much less than unity, and the pressure evaluated on the surface of the half plane. The error function in Equation (9.103) has the asymptotic values given earlier in Equation (9.91). The applicability of Equation (9.103)

to pressures near sharp trailing edges has been validated by measurements on opposite sides of sharp-edged airfoils.^{88,146}

The corresponding relationship for the far-field sound pressure consistent with the above is

$$p_r(r, \theta, \phi, t) = \frac{-\rho_o \sin\left(\frac{\theta}{2}\right) (\sin \phi)^{1/2}}{r(2)^{1/2}} \int_{-\infty}^{\infty} d\omega \int_{-\infty}^{\infty} \frac{dk_1}{k_1} \int_0^Z \quad (9.105)$$

$$\left(1 - \frac{U_w}{U_c}\right) \left(\frac{U_c}{c_o}\right)^{1/2} \left[\vec{\mu} \cdot (\vec{\omega} \times \vec{U}_c) \right] e^{-k_1 Z} e^{i(k_o r - \omega t)}$$

where U_c is still a function of Z , and

$$\vec{\mu} = (k_1, -i|k_1|, k_o \cos \phi)$$

The factor $(U_c - U_w)$ arises from the application of the Kutta condition. If the wake vorticity is convected at the same velocity as the incident vorticity, then $U_c = U_w$, and Equation (9.105) shows that there will be no sound at all. Typically, $U_c > U_w$, so one expects sound to be generated. If the Kutta condition had not been applied, then $1 - U_w/U_c$ would be replaced by unity.

Regarding Equation (9.103), the reader will see certain close similarities to Equation (7.77) for the surface pressures beneath subsonic turbulent boundary layers. The transform

$$\vec{\mu} \times (\vec{\omega} \times \vec{U})$$

replaces the transform used earlier

$$\gamma_{1j}(k_{13}, \gamma_2 \omega) \left[\left(k_o^2 - k^2 \right)^{1/2} \delta_{12} + k_1 \right] \left[\left(k_o^2 - k^2 \right)^{1/2} \delta_{j2} + k_j \right]$$

The latter transform came about from having integrated by parts over y_2 . The formality of this equivalency can be deduced from repeating the derivation of Equation (7.77) but with the source term given by Equation (2.89). The notable distinction between surface pressures near the trailing edge and surface pressures upstream of the edge is given by the bracketed term with the error function. As Equations (9.81) show, $\text{Erf} \left\{ 1 \left[y_1 (k_1 + k_3) \right]^{1/2} \right\}$ approaches unity when $y_1 (k_1 + k_3)$ becomes much larger than unity. Accordingly, as long as the wave number spectrum of $\vec{\omega} \times \vec{U}$ is peaked near $k_1 = k_c = \omega / \bar{U}_c$ (as illustrated, for example, in Figure 7.25 or 7.39), the solution given by Equation (9.103) reduces to the form of Equation (7.77) when $y_1 \gg k_c^{-1}$; i.e., the error function gives the familiar pressure doubling at distances far from the edge. If the flow is one sided, existing only in the region $\delta > y_2 > 0$, e.g., as in the case of wall jets, then $p(\vec{y}_{13}, 0^+, t)$ will be finite and essentially the same as that which would exist without an edge. On the opposite side, $p(\vec{y}_{13}, 0^-, t)$, the upstream pressure will vanish as $(k_c y_1)^{-1/2}$.

Alternatively, Equations (9.81) show that when $y_1 = 0$, i.e., at the apex of the edge, $\text{Erf} \left\{ 1 \left[y_1 (k_1 + k_3) \right]^{1/2} \right\}$ is identically zero as required by having utilized the Kutta condition at the edge. The pressure on opposite sides of the surface edge will be 180 deg out of phase due to the presence of the $\text{sgn}(y_2)$ term.

Other assumptions made in the derivation of Equations (9.103) and (9.105) are

1. The eddy field is frozen during the time that it translates past the edge; i.e., in terms of the moving axis correlation time constant, θ_r , (see Figures 3.21 and 7.10) we require that

$$\theta_r U_c \gg \delta$$

where δ is the thickness of the boundary layer.

2. The eddy convection velocity $U_c(y_2)$ is equal to the local mean velocity in the boundary layer.
3. There is no correlation between eddies that translate at different values of $U_c(y_2)$.
4. The wake vorticity created in response to the eddy-edge interaction via the imposition of the Kutta condition is concentrated in a thin sheet, $\delta(y_2)$, and is convected in frozen fashion at velocity U_w . The velocities

$U_c(y_2)$ and U_w are parallel to the wall. The plate is infinitesimally thin, and the mean slip velocity of flow (the velocity just outside the viscous sublayer) is also taken to be U_w .

5. The source term $\vec{\omega} \times \vec{U}$ is such that $\vec{\omega} \times \vec{U} = \vec{\omega} \times \vec{U}$. This requires that

$$\nabla (\vec{\omega} \times \vec{U}) \gg \nabla \left(\frac{d\bar{U}_1}{dy_2} \hat{k} \times \vec{u} \right)$$

where \hat{k} is the unit vector parallel to the edge and \vec{u} is the fluctuating velocity vector. If the above inequality does not hold, it will affect the result through the form of the shed vorticity arising from imposition of the Kutta condition.

9.6.3.2 Radiated Sound Pressure in Terms of Surface Pressure From the foregoing results can be found a useful relationship between the frequency spectra of radiated sound and of surface pressure on planes terminated by rigid knife edges. This relationship will make it unnecessary to devise prediction schemes in terms of vorticity measurements.

The frequency spectral density of the radiated sound pressure at a point in the far field can be written from the above in terms of the surface pressures. The spectrum of the radiated sound

$$\phi_{\text{p rad}}(\vec{r}, \omega) = \frac{1}{4\pi^2} \sin^2 \frac{\theta}{2} |\sin \phi| M_c \frac{L_3^2 \Lambda_3}{r^2} P(\omega) \quad (9.106)$$

where $P(\omega)$ represents the integrated influence of the entire vortical source region, and M_c represents the average convection Mach number of turbulence past the edge. The function $P(\omega)$ is

$$P(\omega) = \int_0^\infty dz \int_0^\infty dz' \rho_0^2 \left(1 - \frac{U_w}{U_c} \right) \frac{U_c}{U_c} U_c^2 \omega_3(z) \omega_3(z') \int_{-\infty}^\infty e^{-k(z+z')} \dots \frac{2\pi}{2\Lambda_3} \phi_{\omega_3 \omega_3} (k_1, k_3 = k_0 \cos \phi, \omega; z, z') dk_1 \quad (9.107)$$

in which we have specialized the source function to $\omega_3 \times \bar{U}_c$; i.e., vorticity parallel to the edge is considered to be the most important radiator at low Mach numbers since $k_c \omega_3 U_c \gg k_o \omega_2 U_c$. The spectrum function $\omega_3(Z)\omega_3(Z')\phi_{\omega_3\omega_3}(k_1, \omega; Z, Z')$ represents the cross-spectrum of vorticity in planes Z and Z' above the plate; $\omega_3(Z)$ represents the magnitude of the vorticity at Z above the plate. Further elaboration is unnecessary because these functions will be cast in terms of the pressures on the surface beneath the shear layer. To relate $P(\omega)$ to physically determinate parameters it will be clear that this relationship is best made in terms of the spectral characteristics in the cross-stream (y_3) direction. Therefore define

$$\phi_{pp}(y_1, k_3, \omega) = \frac{1}{(2\pi)^2} \int_{-\infty}^{\infty} \int_{-\infty}^{\infty} e^{-i(k_3 r_3 - \omega \tau)} p_s(y_1, y_3, t) p_s(y_1, y_3 + r_3, t + \tau) dr_3 d\tau$$

where it is assumed that the spanwise extent of the flow, L_3 , greatly exceeds the integral length scale Λ_3 and that the vorticity is homogeneous within the span L_3 . Accordingly, we find from Equation (9.103) that

$$\phi_{pp}(y_1, k_3, \omega) = \frac{1}{4} \int_0^{\infty} dZ \int_0^{\infty} dZ' \rho_o^2 \left(1 - \frac{U_w}{U_c}\right)^2 U_c^2 \omega_3(Z)\omega_3(Z') \int_{-\infty}^{\infty} e^{-k(Z+Z')} \left(1 + \text{sgn}(y_2) \text{Erf} \left\{1 \left[y_1(k_1 + k_3)\right]^{1/2}\right\}\right)^2 \phi_{\omega_3\omega_3}(k_1, k_3, \omega, Z, Z') dk_1 \quad (9.108)$$

If $\phi_{pp}(y_1, k_3, \omega)$ had not been determined from pressure correlations with zero streamwise separation, i.e., along $r_1 = 0$, there would be two error function terms to further complicate the expression. The spectrum function for the vorticity, $\phi_{\omega_3\omega_3}(k_1, k_3, \omega; Z, Z')$, is peaked at $k_1 = k_c = \omega/U_c$ and $k_1 = 0$; the breadth of the peak in k_1 is on the order of $2/\theta_\tau U_c$, where θ_τ is the moving-axis eddy decay time

constant. Therefore the integrals over k_1 will be dominated by $\vec{k}_{13} = (\omega/U_c, 0)$, and we may approximate the assorted functions of kZ, kZ' , and $(k_1+k_3) y_1$ by their corresponding values at $\omega Z/U_c, \omega Z'/U_c$, etc. Now, if $\omega y_1/U_c \gg 1$ and $y_1(\theta_\tau U_c)^{-1} \gg 1$, the error function term may be decoupled from the spectrum function $\phi_{\omega_3 \omega_3}(\vec{k}, \omega; Z, Z')$ because $\text{Erf} \left[i(k_c y_1/U_c)^{1/2} \right] = 1$ for $\omega y_1/U_c \gg 1$. Therefore, at distances far from the edge, the integral over wave number reduces to $1/\phi_{\omega_3 \omega_3}(k_1, k_3, \omega; Z, Z')$ and the error function term becomes 4.0. Alternatively, if $y_1 = 0$, then $\text{Erf} \left[i(k_c y_1)^{1/2} \right] = 0$, and the integral over k_1 reduces the same way, but the error function term is 1.0.

The expression for the transverse wave number spectrum of surface pressure accordingly reduces to a simpler form:

$$\begin{aligned} \phi_{pp}(y_1, k_3, \omega) &\approx \alpha(y_1) \int_0^\infty dZ \int_0^\infty dZ' \rho_o^2 \left(1 - \frac{U_w}{U_c}\right)^2 U_c^2 \omega_3(Z) \omega_3(Z') e^{-k_c(Z+Z')} \\ &\quad \cdots \int_{-\infty}^\infty \phi_{\omega_3 \omega_3}(k_1, k_3, \omega; Z, Z') dk_1 \end{aligned} \quad (9.109)$$

where

$$\begin{aligned} \alpha(y_1) &= 1 \quad \frac{\omega y_1}{U_c} \text{ and } \frac{y_1}{\theta_\tau U_c} \gg 1 \\ &= \frac{1}{4} \quad y_1 \rightarrow 0 \text{ or } \frac{\omega y_1}{U_c} \ll 1 \end{aligned}$$

Comparing this to the expression for $P(\omega)$, we find that as long as $U_c \approx \bar{U}_c$ (i.e., as long as the eddy convection velocity is basically uniform over all levels Z of the boundary layer) and as long as the spectrum distribution over k_3 is the same for all Z (i.e., basically as long as Λ_3 is constant over Z (see Figure 7.21)), then

$$P(\omega) \approx \frac{2\pi \phi_{pp}(y_1, k_3 = k_o \cos \phi, \omega)}{(2\Lambda_3) \alpha(y_1)}$$

where y_1 must satisfy either of the above conditions. In most practical instances $k_3 \Lambda_3 \rightarrow 0$; therefore the wave number may be effectively evaluated at $k_3 = 0$. An alternate expression for low Mach numbers is therefore

$$P(\omega) = \frac{\phi_{pp}(y_1, \omega)}{\alpha(y_1)} \text{ for } k_3 \Lambda_3 \ll 1 \quad (9.110)$$

where $\phi_{pp}(y_1, \omega)$ is the pressure spectral density at a point y_1 . This expression is particularly convenient for the estimation of the dependence of radiated sound on changes in the statistics of wall pressures.

These relationships apply equally to cases in which the turbulence is either homogeneous or inhomogeneous in the plane of the plate. However, if the flow is inhomogeneous, i.e., as in the case of separated trailing-edge flow, it must be established that

1. the region ℓ_1 of the chord over which the turbulence extends is greater than the streamwise eddy scale; i.e., $\omega \ell_1 / U_c > 1$.
2. the eddy decay length exceeds δ ; i.e., $\delta / U_c \theta_T < 1$.
3. the spanwise correlation length is large enough so that $\omega \Lambda_3 / U_c \gg 1$.
4. $\phi_{pp}(y_1, k_3, \omega)$ is evaluated beneath the separated flow.

For cases in which the flow is two sided, then, to the extent that periodic vortex shedding does not occur, the net radiated sound intensity is just the power sum of contributions from each side of the surface. Finally, when the flow field is controlled by a separation zone near the trailing edge, $\phi_{pp}(y_1, k_3, \omega)$, then the pressures must be chordwise homogeneous over a region δC such that $\omega(\delta C) / U_c \gg 1$. The trailing-edge flows described in Section 9.5.3, in particular in Figure 9.27, fall into this class.

Alternative examples of the use of these equations are given below in which the spanwise statistics are controlled either by a separated flow or a fully developed homogeneous turbulent boundary layer.

- a. Separated flow upstream of the edge.

This case corresponds to the one illustrated in Figure 9.27 in which the boundary layer separates before passing into the wake. Using the above equations, the radiated sound pressure spectrum can be given in the dimensionless form introduced in Section 9.2

$$\frac{\phi_{p_{rad}}(\omega)}{q_{\infty}^2 M_c \left(\frac{L_3 y_f}{r^2} \right) \sin^2 \frac{\theta}{2} |\sin \phi|} = \frac{1}{\pi^2} \frac{\Lambda_3}{y_f} \frac{\phi_p(\omega)}{q_{\infty}^2} \quad (9.111)$$

where $\phi_p(\omega)$ is measured close enough to the edge that $\omega y_1 / U_c < 1$. For use in the order-of-magnitude estimates $\Lambda_3 = y_f$ (Section 9.5.3), $U_s = U_{\infty}$, and pressure spectra are given in Figure 9.31 or 9.32.

b. Spatially homogeneous convected pressures with slight chordwise decay.

This case applies to turbulent flow past sharp edges, blown flaps, and to the parallel wall jet. Using Equation (7.135) we have

$$\begin{aligned} \int_{-\infty}^{\infty} \phi_{pp}(k_1, k_0 \cos \phi, \omega) dk_1 &= \\ \frac{\phi_{pp}(\omega)}{\pi^2} \cdot \frac{\delta^*}{\gamma_3} \int_{-\infty}^{\infty} \frac{\gamma_1 \delta^* dk_1}{\left(\frac{\gamma_1 \omega \delta^*}{U_c} \right)^2 + \left(k_1 \delta^* - \frac{\omega \delta^*}{U_c} \right)^2} &= \\ = \frac{1}{\pi} \phi_{pp}(\omega) \frac{\delta^*}{\gamma_3} \left(\frac{\omega \delta^*}{U_c} \right)^{-1} \end{aligned}$$

which amounts to Equation (9.110) with $\Lambda_3 = U_c / \gamma_3 \omega$. The radiated sound pressure spectrum from the boundary layer on each side of a lifting surface can then be written in a form of the nondimensionalization introduced in Section 9.2 and that will be used subsequently. The sound spectrum from the boundary layer on either side is, then

$$\frac{\phi_{p_{rad}}(\omega)}{q_{\infty}^2 M_c \left(\frac{L_3 \delta^*}{r^2} \right) \sin^2 \frac{\theta}{2} |\sin \phi|} = \frac{1}{4 \gamma_3 \pi^2} \frac{\delta^*}{\omega} \frac{\phi_{pp}(\omega) \left(\frac{\omega \delta^*}{U_c} \right)^{-1}}{q_{\infty}^2} \quad (9.112)$$

where $\phi_{pp}(\omega)$ is measured where $\omega y_1/U_c > 1$. The distinction between Equations (9.111) and (9.112) is essentially that $\Lambda_3 = U_c/\gamma_3\omega$ and that $\alpha(y_1) = 1$ in Equation (9.112). To estimate the far-field sound pressure levels in one-third-octave bands, estimate $\Delta\omega = (1/4)\omega$, $\delta^*/\delta = 1/6$, $\gamma_3 = 0.8$, $U_c = 0.7 U_\infty$, and $\phi_{pp}(\omega\delta^*/U_c)q^{-2}$ given by Figure 7.29. This sound pressure probably represents the minimum sound radiated by a turbulent flow of a homogeneous boundary layer. As shown in Figure 7.62, the surface pressures (even those far enough upstream that $\omega y_1/U_c \gg 1$) can be influenced by local pressure gradients and upstream history, and all these influences appear to increase both the level and the lateral correlation scales of the boundary-layer pressures even when separation does not take place.

Equations (9.111) and (9.112) are of a general form giving a mean-square pressure in a dimensionless form as

$$\frac{\overline{p^2}(\omega, \Delta\omega)}{q_\infty^2 M_\infty \frac{L_3 \delta}{r^2} \sin^2 \frac{\theta}{2} |\sin \phi|} = f\left(\frac{\omega\delta}{U_\infty}\right) \quad (9.113)$$

where $M_\infty = U_\infty/c_0$. This is the same functional form as Equation (9.21).

9.6.3.3 A Note on Evanescent Wave Theories. The hydrodynamic pressures on the surface, due to the boundary layer turbulence convected past the edge, have been represented mathematically as an incident wave field^{134,135} diffracted by the edge. These diffracted waves in fact constitute the sound radiated by the scattering interaction of the edge with the turbulent field. The approach was used by Chandiramani¹³⁴ and Chase¹³⁵ to expose the relationship between the radiated sound and the near-field surface pressures. The theory provides a closed-form relationship between the surface pressures induced by the turbulence upstream of the edge and the radiated sound. The analysis assumes that the incident pressure field is imposed on the surface from a plane immediately above, but not touching, the rigid half-plane. The flow plane extends both upstream and downstream of the edge and the incident wave pressures are presumed to have the same characteristics both upstream and downstream of the edge. The relationship of the incident wave field to the physical pressures that actually exist on the flow-bearing surface has been clarified by Howe.¹⁴⁴ Downstream of the edge and in the wake, $y_2 = 0$, $y_1 < 0$, the

diffracted pressure is zero so the incident wave pressure equals the physical pressure. Far upstream of the edge and on the surface, $y_2 = 0$, $y_1 < 0$, the surface pressure is just twice the incident pressure, due to pressure doubling. In the vicinity of the edge the surface pressure is a complex combination of the incident pressure and the near-field diffracted pressure caused by the interaction of the incident field with the edge.

As discussed by Howe, the analyses of Chandiramani and of Chase correspond with his result¹⁴⁴ for which a closure (Kutta) condition was applied at the trailing edge. Accordingly, as given by Equation (9.110) the surface pressure at points within an eddy scale of the trailing edge was found to be equal to the hydrodynamic pressure in the wake; both pressures are equal to the pressure of the incident wave. In the evanescent wave theory, the pressures are presumed to be homogeneous along the plate.

The result of Chase's analysis can best be written as

$$\phi_{p_{rad}}(\vec{r}, \omega) = \frac{1}{\pi} \frac{L_3}{r^2} \sin^2 \frac{\theta}{2} |\sin \phi| \int_{-\infty}^{\infty} \frac{(k_1 + k_0 \sin \theta) k_0}{(k_1 - k_0 \sin \phi \sin \theta)^2} \phi_1(k_1, k_0 \cos \phi, \omega) dk_1$$

or, in terms of the above,

$$\frac{1}{4} M_c P(\omega) = \frac{2\pi}{2\Lambda_3} \int_{-\infty}^{\infty} \frac{(k_1 + k_0 \sin \theta) k_0}{(k_1 - k_0 \sin \phi \sin \theta)^2} \phi_1(k_1, k_0 \cos \phi, \omega) dk_1$$

The spectrum function $\phi_1(k_1, k_3, \omega)$ applies to the incident wave, which corresponds to the surface pressure spectrum beneath the turbulent flow

$$\begin{aligned} \phi_{pp}(y_1, k_3, \omega) &= \int_{-\infty}^{\infty} \phi_1(k_1, k_3, \omega) dk_1 \frac{\omega y_1}{U_c} \ll 1 \\ &= 4 \int_{-\infty}^{\infty} \phi_1(k_1, k_3, \omega) dk_1 \frac{\omega y_1}{U_c} \gg 1 \end{aligned}$$

The factor 4 accounts for the pressure doubling of the incident wave pressure at the surface far upstream of the edge. For low acoustic wave numbers, $k_0 \ll k_c$

$$\begin{aligned} \frac{1}{4} M_c P(\omega) &\approx \frac{2\pi}{2\Lambda_3} \int_{-\infty}^{\infty} \frac{k_0}{k_1} \phi_1(k_1, k_0 \cos \phi, \omega) dk_1 \\ &\approx \frac{2\pi}{2\Lambda_3} M_c \int_{-\infty}^{\infty} \phi_1(k_1, k_0 \cos \phi, \omega) dk_1 \end{aligned}$$

which is identical to the relationships derived in Equations (9.109) and (9.111).

9.6.3.4 Measured Continuous-Spectrum Trailing-Edge Noise From Rigid Airfoils.

Turbulent trailing-edge noise radiated from sharp-edged airfoils has been measured by Schlinker¹⁴⁷ and by Brooks and Hodgson⁸⁸ on NACA airfoils. In the latter case, the properties of the boundary layer and the surface pressures were measured near the trailing edge; the boundary layer was tripped at the leading edge. In Schlinker's experiment the boundary layer was allowed to transition to turbulence naturally, so that the quantities shown in Figure 9.17 were assumed to apply to the NACA 0012 airfoil. For the NACA 0018 foil ($h_m/C=0.18$) the δ^*/h_m was assumed to have the same value as the NACA 0012 foil. For purposes of comparing Equation (9.112) with Figure 9.38, we note that it can be rewritten for the special case of fully developed and reattached flow on both sides of the airfoil. To account for two sides radiating incoherently, Equation (9.112) is multiplied by two:

$$\begin{aligned} \frac{\phi_{\text{rad}}\left(\frac{\omega\delta^*}{U_\infty}\right)}{q^2 M_\infty \frac{L\delta^*}{r^2} \sin^2 \frac{\theta}{2} |\sin \phi|} &= 2 \frac{C_f^2 \left(\frac{U_c}{U_\infty}\right)^2}{4\pi^2 \gamma_3} \left(\frac{\omega\delta^*}{U_\infty}\right)^{-1} \frac{\phi_{\text{pp}}\left(\frac{\omega\delta^*}{U_\infty}\right)}{\tau_w^2} \\ &\approx (0.042) C_f^2 \left(\frac{\omega\delta^*}{U_\infty}\right)^{-1} \left[\phi_{\text{pp}}\left(\frac{\omega\delta^*}{U_\infty}\right) / \tau_w^2 \right] \end{aligned} \quad (9.114)$$

SCHLINKER¹⁴⁷ (DIRECTIONAL MICROPHONE)

▲▲▲	0018	0.14	0.8×10^6
■ ■ ■	0018	0.28	1.6×10^6
● ● ●	0012	0.14	0.8×10^6
—	0012	0.28	1.6×10^6

BROOKS & HODGESON (POINT MICROPHONE)

— $1.3 \times 10^6 < R_c < 2.8 \times 10^6$
 $0.12 < M < 0.21$

--- EQUATION 9.114, $C_f = 0.002$

$\gamma_3 = 0.8, \Phi_p(\omega \delta^*/U_\infty)/r_w^2$
 OF FIGURE 7.

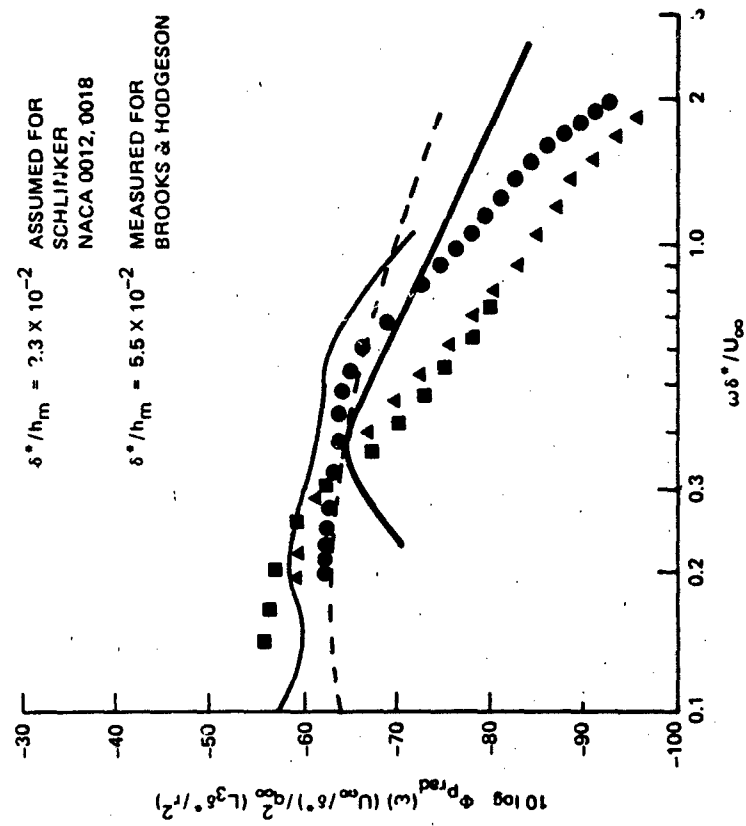


Figure 9.38 - Spectra of Trailing Edge Noise from NACA Airfoils in Uniform Flow, δ^* Is the Boundary Layer Displacement Thickness

where $\gamma_3 \approx 0.8$ and $U_c/U_\infty = 0.7$ for fully developed turbulent boundary layers. The dimensionless wall pressure spectrum is given in Figure 7.31. The wall-shear coefficient has been separated out because of the near universality of the wall pressure spectrum nondimensionalized on τ_w and δ^* . Equation (9.114) applies therefore for both smooth- and rough-surfaced airfoils. For evaluation, C_f and δ^* must be determined.

Figure 9.38 shows spectra of radiated sound for two sets of NACA foils compared with Equation (9.114). The dimensionless form is used to make easy cross-referencing with boundary-layer properties discussed in Chapter 7. Note that the surface pressures measured by Brooks and Hodgeson agreed with those of Figure 7.31 when normalized on τ_w .

In the measurement programs the airfoil-generated noise was difficult to distinguish from other facility background noises. Therefore Schlinker used a directional microphone to discriminate against other sources. Brooks and Hodgeson used a series of free-field microphones over an arc in the θ plane and normal to the surface $\phi = 0$. The directivity $\sin^2 \theta/2$ was verified to the extent that the facility permitted, $45 < \theta < 135$ where $\theta = 0$ coincides with the flow direction. The radiated sound of Brooks and Hodgeson compared well to the estimate of Equation (9.114), but the measurements of Schlinker do not at low frequencies. The reason for this is unknown and beyond explanation without information regarding the boundary layers on the airfoils.

Radiated sound from sharp-edged airfoils is therefore only indirectly determined by the chord. Surface finish, Reynolds number and maximum thickness control the sound radiation through influences on C_f and δ^* . For blunted airfoils that do not shed vortex street wakes, but have a small region of flow separation near the trailing edge, it is likely that enhanced sound will occur at low frequencies and reduced sound at high frequencies, as may be deduced by an examination of the surface pressures in Figure 9.33. Surface pressures near the trailing edge with separated flow have reduced high-frequency content.

9.6.3.5 Measurements of Broadband Noise from Turbulent Wall Jets and Blown Flaps.

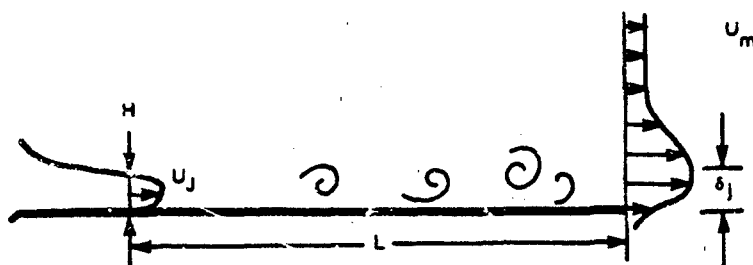
Noise from these one-sided flow geometries has the same physical origin as noise from turbulent boundary-layer flow past sharp trailing edges. Blown flaps and wall jets, however, generate more intense sound pressures. Noise in the form considered

here is also expected to occur on two-sided flows when a velocity differential of more than 2 to 1 exists.¹¹⁹

Available experimental results fall into two classes. First, measurements have been made on compound or slotted blown flaps. The configurations examined^{124,125,127,128} include flap arrangements that turn either into or away from the jet. The results of measurements on these flaps have been examined in detail by Fink,¹⁶ who gives prediction schemes. The second group of measurements, which forms the bulk of available data, was obtained on the simple configurations illustrated in Figure 9.39.

The measurements of Hayden¹²⁰ (aspects of which have been openly published in references 61 and 122) and Grosche¹²¹ were obtained using a wall jet with the axis of the jet parallel to the wall. Their supporting measurements included the mean velocity and thickness of the wall layer at the edge of the plate. The more recent correlation measurements between surface pressure and far-field pressure made by Yu and Tam¹²⁹ were obtained on a similar arrangement. In Hayden's program, the configurations that were tested included the ratio L/D and therefore U_m and δ . Scharton et al.¹²³ and Olsen et al.¹²⁴ examined a series of configurations that represented pressure side blowing of airfoil flaps. The jet was incident on a converging surface, probably producing a favorable wall pressure gradient; measurements included statistics of pressure fluctuations in the vicinity of the edge. Turbulent field quantities in the converging flow were determined only in a case similar to that of Olsen et al.¹²⁷ by Olsen and Boldman.¹²⁵ The program of Tam and Reddy¹²⁶ concerned the reverse situation involving upper (suction) surface blowing. In their case, the wall jet turned through 60 deg and possibly represents an adverse wall pressure gradient. They measured radiated noise and statistics of the turbulent field at the edge, but not surface pressure fluctuations. The measurements of Fink⁵⁶ were conducted on an airfoil section the leading edge of which mated with the ducting of a wind tunnel open jet. The flow was made turbulent upstream of the airfoil using a turbulence grid. Both the intensity and macroscale of the incident turbulence were varied. The noise in these experimental arrangements constitutes edge noise rather than noise from the turbulence contiguous to the wall.

Various measurements are compared within the format of Equation (9.21). The radiated sound pressure measured in a bandwidth $\delta\omega$,



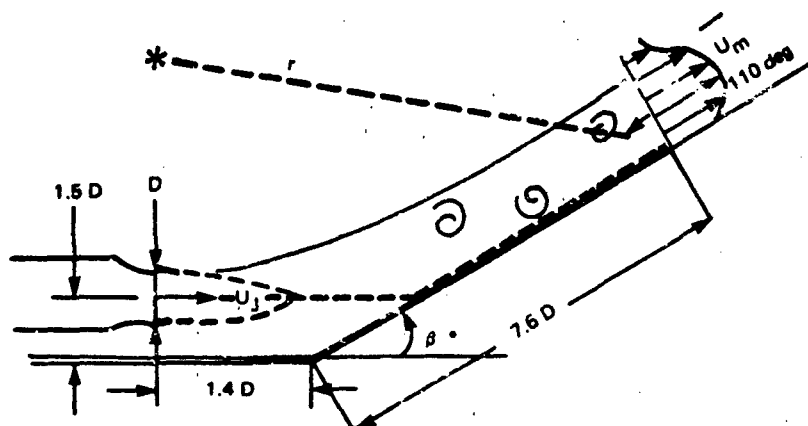
PARALLEL WALL JET

JOSHI ¹³⁰ $0.5 < M < 0.9$

GROSCHKE ¹²¹ $0.5 < M < 1$

HAYDEN ¹²⁰ $0.055 < M < 0.32$

RECTANGULAR JET



CONVERGING WALL JETS

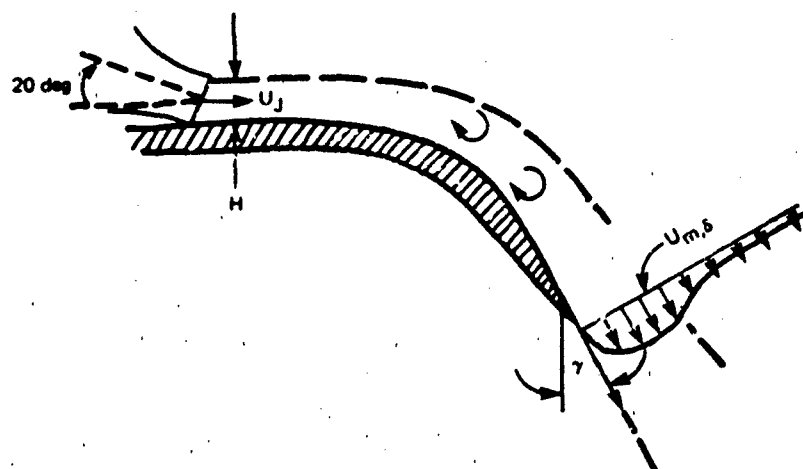
OLSEN ET AL. ¹²⁴ } $M \approx 0.3$

OLSEN AND BOLDMAN ¹²⁵ } $\beta \approx 60$

SCHARTON ET AL. ¹²³ $M = 0.45, \beta = 30$

ROUND JET

ARRANGEMENT OF SCHARTON ET AL. ¹²³

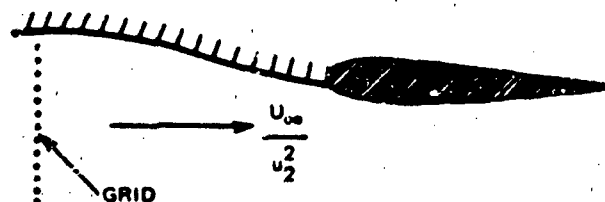


DIVERGING WALL JET

OLSEN ET AL. ¹²⁷ $\gamma = 30 \text{ deg}$

TAM AND REDDY ¹²⁸ $\gamma = 60 \text{ deg}$

RECTANGULAR JET $M = 0.31$



PARALLEL WALL JET

FINK ⁵⁸ $0.09 < M < 0.53$

Figure 9.39 - Experimental Configurations for Measurements of Trailing-Edge Noise from One-Sided Flow

$$\begin{aligned}\overline{p^2}(r, \omega, \Delta\omega) &= 2 \int_{\Delta\omega} \phi_{p_{rad}}(r, \omega) d\omega \\ &= \overline{p^2}(r, f, \Delta f)\end{aligned}$$

can be written in the nondimensional form involving the broadband transverse correlation length of the component of the turbulence normal to the trailing edge:

$$\frac{\overline{p^2}(r, f, \Delta f)}{q_m^2 M_m^2 \frac{L_3 \Lambda_3}{r^2} \frac{\overline{u_2^2}}{U_\infty^2} \sin^2 \frac{\theta}{2} |\sin \phi|} = f\left(\frac{\omega \Lambda_3}{U_\infty}\right) \quad (9.115)$$

for a yaw angle of $\alpha = 0$ deg. The general function $f(\omega \Lambda_3 / U_\infty)$ includes the frequency dependence of the turbulent field as well as the transverse correlation scale. Therefore it should be somewhat dependent on the circumstances surrounding the type of flow studied. Figure 9.40 shows that it is. The noise levels of Fink,⁵⁷ Tam and Reddy,¹²⁶ and Olsen et al.¹²⁴ appear to fall into separate groups of dimensionless spectra, each of which is about 8 dB wide. The free stream reference velocity U_∞ or the maximum velocity in the wall jet U_m at the edge are used synonymously in this figure.

The alternative form of nondimensionalization given by Equation (9.113) utilizes the thickness of the wall jet at the trailing edge, δ_j , in the form

$$\frac{\overline{p^2}(r, f, \Delta f)}{q_m^2 M_m^2 \frac{\delta_j L_3}{r^2} \left(\sin^2 \frac{\theta}{2}\right) |\sin \phi|} = \left(\frac{\omega \delta_j}{U_\infty}\right) \quad (9.116)$$

which is useful especially when the turbulence intensity is unknown. The flow thickness δ_j was measured by Hayden,⁶¹ Grosche,¹²¹ Tam and Reddy,¹²⁶ and Olsen et al.¹²⁷ Spectra are shown in Figure 9.41 in the form of Equation (9.116). Again, the measured values from the co-axial wall jet of Hayden and of Grosche, as well as those of Olsen et al.,¹²⁷ form a series separate from the values of Tam and Reddy obtained on a diverging wall jet. The noise levels of Scharton et al.¹²³ are also included,

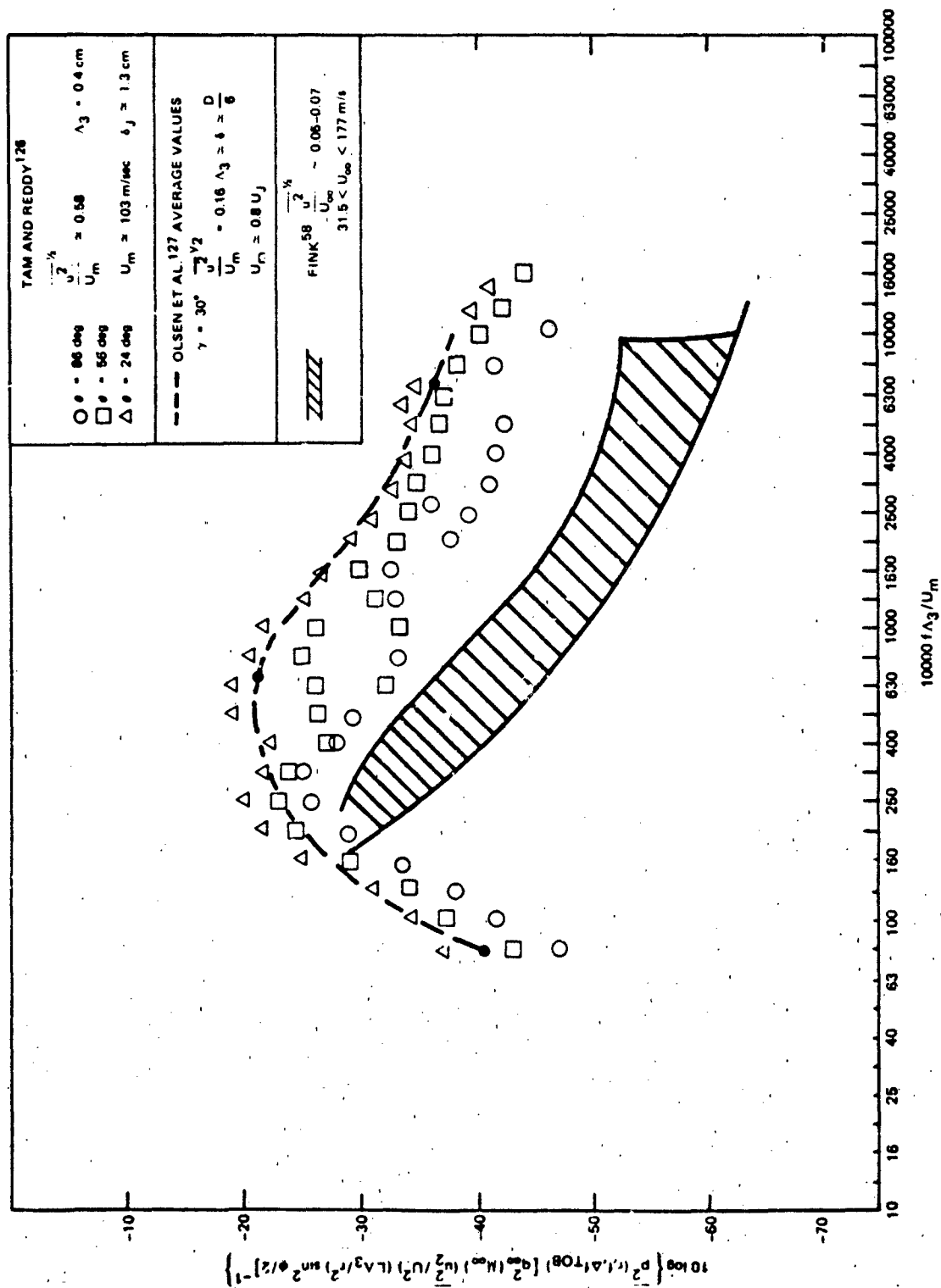


Figure 9.40 - Nondimensional Sound Spectra from Trailing Edges and Blown Flaps Measured in One-Third-Octave Bands, in the Experiments Illustrated in Figure 9.39

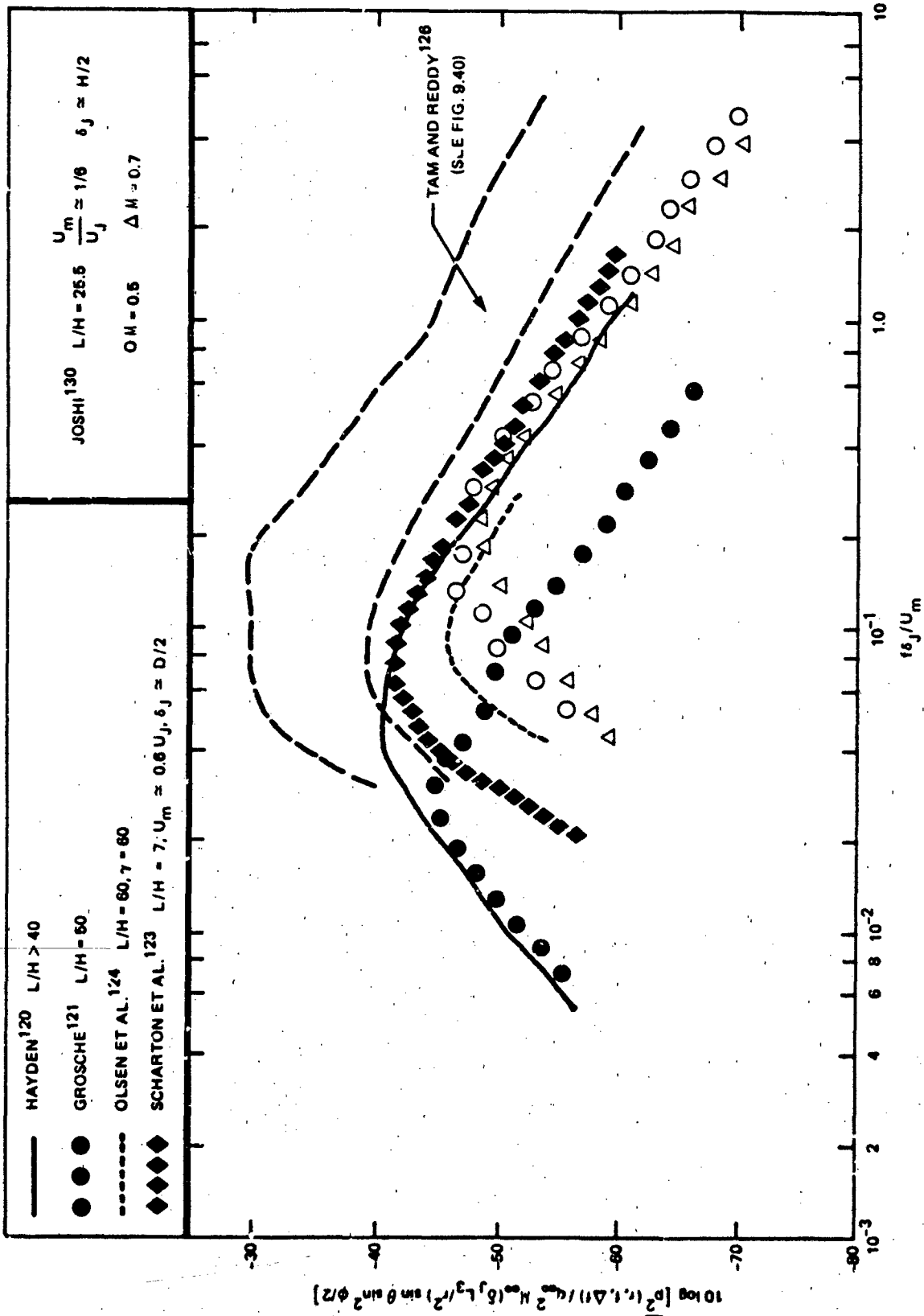


Figure 9.41 - Nondimensional Sound Spectra, in One-Third-Octave Bands of Edge Noise with One Sided Flow. All Cases are for Wall Jets and Blown Flaps as Illustrated in Figure 9.39, U_j is the Exit Velocity of the Jet, U_m is the Maximum Shear Layer Velocity at the Edge

the scales being estimated* as $U_m \approx 0.6 U_o$, $L_j \approx 2D$, and $\delta_j \approx D/2$, where D is the diameter of the circular jet. The collection of data suggests that the dimensionless noise levels from the three types of wall jet appear to increase as the diverging angle of the surface increases. Augmented noise levels were also measured by Olsen et al.¹²⁷ for the converging jet for which $\gamma = 30$ deg are also consistent. The higher levels could be attributable to the large-intensity turbulence levels created at the edge by the jet-wall interaction. There is also a general increase in sound level as L/H increases, shown by Hayden, which has been corroborated by Joshi,¹³⁰ who shows that the overall sound power level increases with L/H from the free jet value to a maximum at $L/H \approx 10$. For larger values of L/H the sound power decreases very slowly, which is probably due to the reduced velocity of eddy convection past the edge at large L/H . The occurrence of maximum sound levels observed for $L/H \approx 10$ is attributable to the relatively intense turbulence field associated with the end of the potential core. Joshi's sound pressures also show maxima near $f\delta_j/U_m \approx 0.15$, where it has been estimated that $\delta_j \approx H$ and $U_m \approx (1/6) U_o$ for $H/L = 25$.

Equation (9.111) may be used to predict the noise from wall jets using measured surface pressure spectra. Figure 9.42 shows such a comparison for the configuration of Scharf et al.¹²³ It is notable that the interaction of the jet with the wall increased the noise of the jet by more than 10 dB.

9.6.3.6 Modifications of the Aerodynamic Scattering Theory for Surfaces of Finite Thickness and Impedance. The preceding theoretical results, as well as most others, are posed for surfaces that are rigid knife edges. In many practical situations, however, edges are neither rigid nor sharp. Therefore modifications to the standard theories are given below for finite-impedance surfaces and wedges as far as the scattering of hydrodynamic waves into acoustic waves is concerned. The variations of the problem of hydroacoustic scattering from edges (either leading or trailing) that are not rigid half-planes and that have been considered by Crighton

*Joshi¹³⁰ reports that for $L/H < 15$ the wall jet mixing characteristics closely resemble those of free jets for these parallel jets. Thus, assuming that the length of the potential core of the jet is $4D$, and using the relationship due to Forstall and Shapiro quoted by Hinze,¹⁴⁸ the velocity U_m is roughly estimated as $U_m/U_o \approx 4H/L$ or $4D/L$.

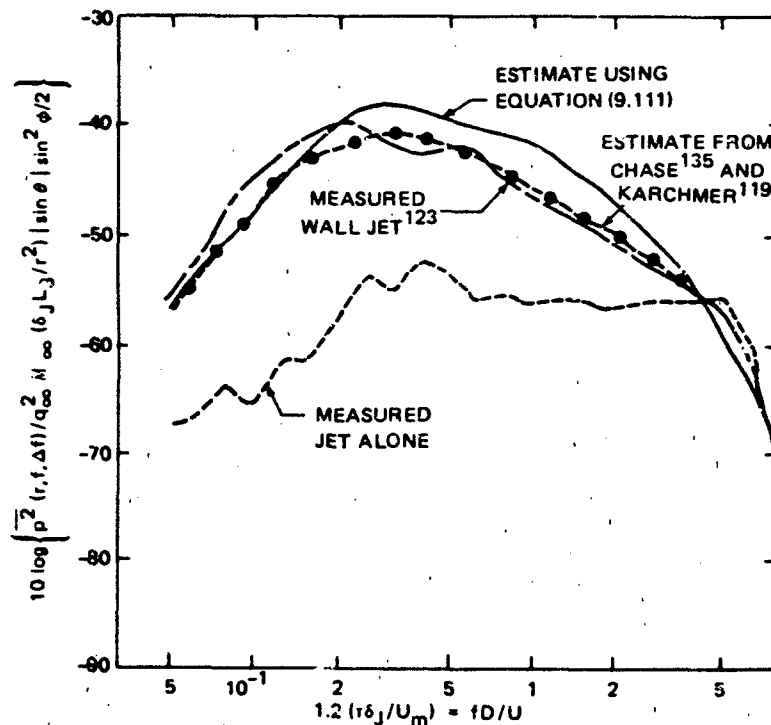


Figure 9.42 - Measured and Predicted Noise from Wall Jet
of Scharton et al.¹²³ Adapted from Chase¹³⁵
(see Figures 9.39 and 9.41).

and Leppington Modify the results of those earlier sections by introducing multiplicative coefficients. Radiated sound pressure spectrum $\phi_{rp}(\omega)$ from the flow of turbulence across a rigid half-plane was already given by Equations (9.11), (9.20), and (9.111) in the form (apart from directivity factors)

$$\phi_{rp}(\omega) = q_{\infty}^2 M_{\infty}^2 \left(\frac{L_j \delta}{r^2} \right) \left(\frac{\omega \delta}{U_{\infty}} \right) \frac{V_c}{\delta^3} \frac{\overline{u^2}}{U_{\infty}^2} \phi_u(\omega) \quad (9.117)$$

where $\overline{u^2}$ represents the magnitude of the mean-square turbulence velocity near the edge, δ is the boundary layer thickness at the edge, $\phi_p(\omega)$ is the frequency spectrum $\overline{u^2}$, and V_c is the correlation volume of the velocities.

Crighton and Leppington's¹⁰ result for the effect of flexural compliance of the surface yields the expression for the limp plane that differs from the rigid plane by

$$\begin{aligned}\phi_{cp}(\omega) &= \phi_{rp} \cdot (48)^{-1} \\ &= q_{\infty}^2 \frac{M_{\infty}}{\beta} \cdot \left(\frac{L_3 \delta}{r^2} \right) \left(\frac{\omega \delta}{U_{\infty}} \right) \frac{v_c}{\delta^2} \frac{\overline{u^2}}{U_{\infty}^2} \phi_u(\omega)\end{aligned}\quad (9.118)$$

The factor β is the fluid loading factor introduced in Chapter 6. Equation (9.118) applies only for $\beta \gg 1$; that is, as the plate becomes more fluid-like, this form of radiation diminishes as $1/\beta$. When the surface impedance is large enough that $\beta \leq 1$, Equation (9.117) holds. The presence of the fluid loading factor in Equation (9.118) implies the existence of additional Mach number dependence of the noise; i.e., the total overall sound pressure for the compliant edge, p_{cp} , will depend as

$$\begin{aligned}\overline{p_{cp}^2} &= \int_{-\infty}^{\infty} \phi_{cp}(\omega) d\omega \\ &= q_{\infty}^2 M_{\infty}^2 \left(\frac{\rho_p}{\rho_o} \right) \frac{h}{\delta} \left(\frac{L_3 \delta}{r^2} \right) \left(\frac{v_c}{\delta^3} \right) \frac{\overline{u^2}}{U_{\infty}^2}\end{aligned}\quad (9.119)$$

The corresponding relationship for the compact force, i.e., dipole, extracted from Equation (9.12), is

$$\overline{p_{dipole}^2} = q_{\infty}^2 M_{\infty}^2 \cdot \left(\frac{L_3 \delta}{r^2} \frac{v_c}{\delta^3} \frac{\overline{u^2}}{U_{\infty}^2} \right)\quad (9.120)$$

showing the same parametric dependencies as Equation (9.119); both expressions give a U_{∞}^6 behavior. This means that the limp panel provides only a modest impedance

discontinuity in the flow. In contrast, the total intensity for the rigid edge has been obtained from Equation (9.117)

$$\overline{p_{rp}^2} \approx U_{\infty}^5 \quad (9.121)$$

When the surface is a wedge rather than a thin half-plane, and the exterior angle of the wedge is $\alpha\pi$, where

$$1 < \alpha \leq 2$$

(with $p/q=2$ for the half-plane problem, 1 for the full-plane, and $3/2$ for a right-angle corner) the adjustment to Equation (9.117) is

$$\phi_{\text{wedge}}(\omega) \approx \phi_{r,p} \cdot \left(\frac{\omega \delta}{U_{\infty}} M_{\infty} \right)^{\frac{2}{\alpha} - 1} \quad (9.122)$$

Regarding the overall sound pressure, the speed dependence of sound from turbulence convected over a wedge would be

$$\overline{p_{\text{wedge}}^2} \approx U_{\infty}^{(4+2/\alpha)} \quad (9.123)$$

with the dependence on the other variables (in Equation (9.117)) retained.

The above theories apply to surfaces of infinitesimal thickness or wedges that come to a point. The results also apply¹⁴⁰ to surfaces of finite thickness whose trailing edges are rounded when the acoustic wavelength exceeds both the thickness of the surface and the radius of curvature of the edge. When the eddy length scale is small compared to the radius of the edge and the acoustic wavelength is long, then the Mach number dependence of the total intensity will still be as shown in Equation (9.121). However, the magnitude of the sound will be less than if the edge were sharp.

With regard to the application of a Kutta condition, no theoretical work of this type has been done on edges that are not sharp. For blunted edges, the results

f Section 9.6.3.1 should apply as long as the base thickness of the edge, h , is small compared with the boundary-layer thickness, shear-layer thickness, and $\delta/U_c \ll 1$. In such cases all the simplifying assumptions leading to Equations 9.103) and (9.105) should hold. For blunt edges for which $\delta \ll h$, $\omega h/U_c > 1$, the applicability of these equations is questioned on the basis of measurements⁸³; however, Equations (9.106) and (9.110) should be approximately valid, at least when the surface pressure wave number spectrum is measured far enough upstream to avoid the near field of the edge.

9.7 FLOW-INDUCED VIBRATION AND SINGING

In this section we consider the flow-induced vibration of lifting surfaces that is caused by each of the excitation mechanisms. As a general rule, in order to apply the methods of Chapter 6, the modal force spectrum must be estimated for the type of flow in question. The necessary additional information is an estimate of structural impedance, and this requires estimates of the mode shape and loss factor. As a first approximation the frequency ranges that are dominated by the respective flow sources will still bear the relationship shown in Figure 9.2. It must be emphasized that the vibration-induced sound will change the relative weights of the different flow sources because the radiation efficiency of the structure may depend on frequency in a fashion differing from the ω^2 dependence of the compact flow dipole. A complication that often arises in the hydroacoustic application is a fluid structure feedback. At low frequencies this feedback may occur in the form of flutter if the fluid disturbances at the leading or trailing edges induce angle-of-attack fluctuations that alter the potential flow and therefore the lift on a flexible hydrofoil. Such fluctuations in angle of attack are important at reduced frequencies that are less than unity so that the aerodynamic influence functions which are large, possess mass, positive damping, and stiffness-like qualities which couple with the structural impedance of the surface thus altering the resonant behavior of the surface. The flutter phenomenon is treated by texts such as Asplinghoff et al.⁴ At higher frequencies, $\omega C/U_m > 2$, the incompressible fluid reaction to unsteady inflow will be a combination of added mass and hydrodynamic damping and apart from viscous effects the interactions are stable and passive. When vortex shedding occurs at blunt trailing edges, however, self excited motions are again possible. When the vortex shedding frequency, or the eigenfrequency of the unstable shear layer in the wake, equals a resonance frequency of the structure,

the hydroelastic coupling can enhance the strength and spanwise correlation of the shed vorticity thus increasing the magnitude of the flow-induced forces.

This section discusses the physical causes and mathematical modeling of both linear and non-linear (self-excited) flow-induced vibration which is controlled by either turbulent boundary layer flow on the blades or by hydroelastic feedback occurring with vortex shedding. The problem of radiated noise from the vibration can be determined for either linear or nonlinear flow excitation using the methods of Section 6.5, once the modal amplitudes are known.

9.7.1 Linear Flow Excitation of Lifting Surfaces

9.7.1.1 Modal Response and Excitation Force Spectra. The vibratory responses as resonant modes of a lifting surface to broad band excitation can be approximated by Equation (6.41). This is rewritten to give the mean-square flexural vibration velocity

$$\overline{v_n^2} = \frac{\pi \phi_{f_n}(\omega_n)}{M^2 \eta_T \omega_n} \quad (9.124)$$

where the mean-square velocity is defined in terms of its spectral density

$$\overline{v_n^2} = 2 \phi_{vv}(\omega_n) \left[(\eta_T \omega_n) \frac{\pi}{2} \right] \quad (9.125)$$

and where $\phi_{f_n}(\omega_n)$ is the autospectrum of the broadband modal force exerted on the surface evaluated at ω_n . This modal force is a convolution of the pressure distribution with the mode shape function, Equation (6.40). The loss factor η_T is the total loss factor (see Section 6.6), which includes the flow-induced hydrodynamic damping; the mass M includes the added mass. For frequency bands $\Delta\omega$ broad enough that enough modes are included to allow a modal average to be taken, Equation (9.124) (or (6.41)) is replaced by Equation (6.51),

$$\overline{v^2}(\omega_o, \Delta\omega) = \frac{\pi \phi_{f_n}(\omega)}{M^2 \eta_T} \cdot \frac{1}{4\pi \kappa C_{lp} \omega_o} \Delta\omega \quad (9.126)$$

when the force excitation has a bandwidth that is less than $\eta_T \omega_n$ then equation 6.34 with $\omega = \omega_n$ applies for the mean square velocity response at resonance.

For fluid excitation caused by boundary-layer flow, the modal force is given directly by Equation (6.40), with specific examples worked out in Section 8.1.2. Since the boundary layers on the airfoil surfaces are uncorrelated, the net mean-square velocity will just be the power sum of the individual responses, i.e.,

$$\overline{v^2}(\omega_o, \Delta\omega) = \left(\overline{v^2}(\omega_c, \Delta\omega) \right)_{\text{upper}} + \left(\overline{v^2}(\omega_o, \Delta\omega) \right)_{\text{lower}}$$

Other than this, the prediction of response is the same. An example has been worked out^{149,150} and is compared with measured responses to boundary-layer turbulence in Figure 9.43, where $m_s = M/A_p$ is the wetted mass per unit area of the hydrofoil.

When fluid excitation is caused by inflow unsteadiness and vortex shedding, account must be taken of the deterministic chordwise variation of unsteady pressures (Figures 9.11 and 9.29) compared to the variation in mode shape $\psi_{mn}(y_1, y_3)$, as developed below. The unsteady chordwise pressure distribution is given by Equations (9.44) and (9.54) (at low frequencies) when excitation comes by incident turbulence, or by Equations (9.87) and (9.89) when excitation comes from vortex shedding. In either case we have a stochastic spanwise variation and a deterministic chordwise variation. The pressure is a superposition of continuous frequency harmonics on the upper and lower surfaces of the lifting surface. These are written

$$\Delta p(y_1, y_3, y_T) = p_u(y_1, y_3, t) - p_l(y_1, y_3, t)$$

$$\Delta p(y_1, y_3, t) = \int_{-\infty}^{\infty} \Delta P(y_1, y_3, \omega) e^{-i\omega t} d\omega \quad (9.127)$$

Following Equation (6.27), the Fourier transform of the modal force imposed by the flow is

$$f_n(\omega) = \int_{A_p} \Delta P(y_1, y_3, \omega) \psi_{mn}(y_1, y_3) dy_1 dy_3 \quad (9.128)$$

*By dividing $f_n(\omega)$ by the planform area one would obtain a modal pressure differential consistent with Equation 6.25.

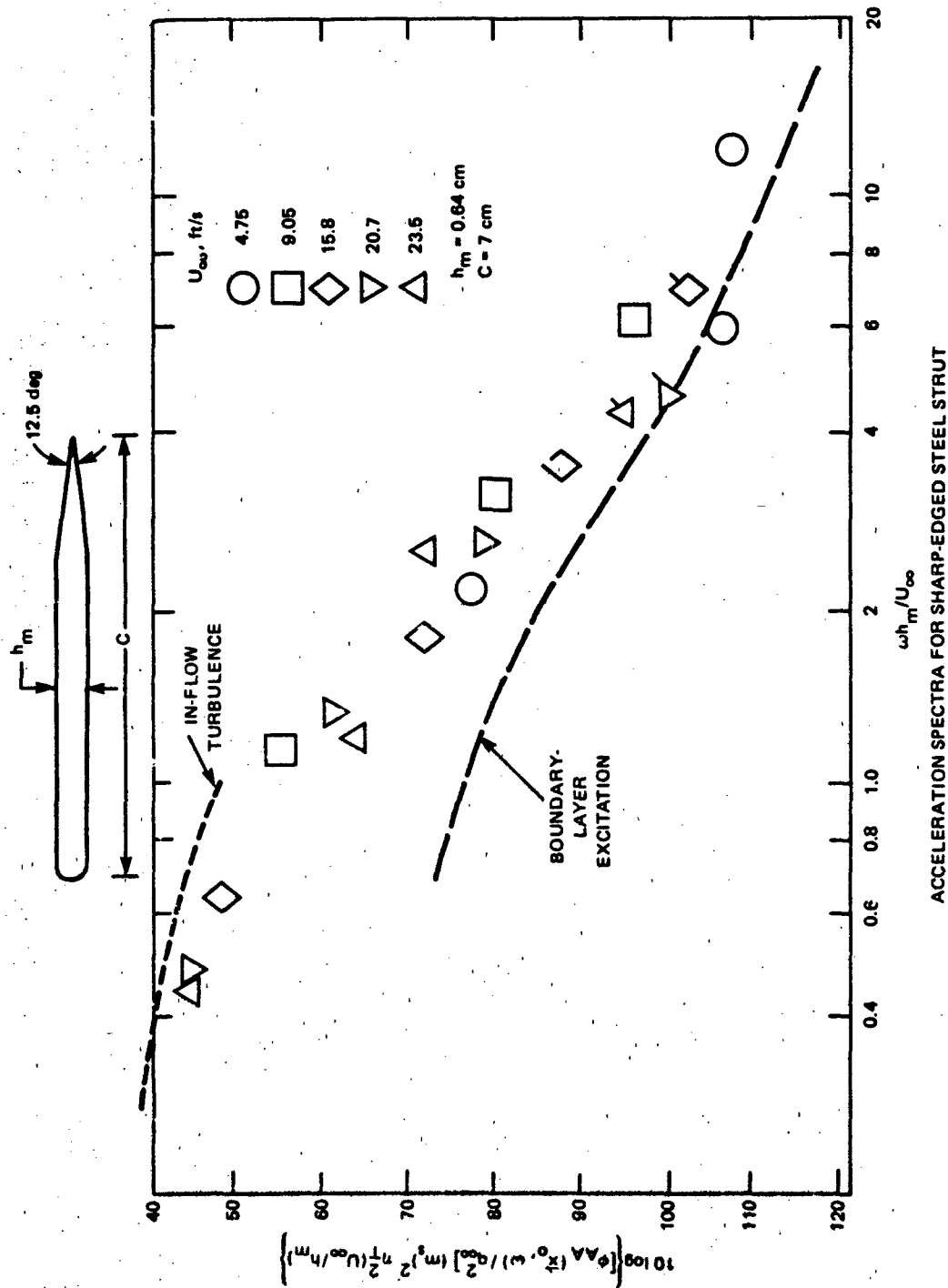


Figure 9.43 - Dimensionless Modal Acceleration of Flow-Excited Cantilever Hydrofoil with a Sharp Trailing Edge in an Open-Jet Water Tunnel. ¹⁴⁹

$10^5 < R_c < 4.9 \times 10^5$, $1.7 \times 10^4 < R_{2\delta} < 7.5 \times 10^4$. 2δ is

Twice the Thickness of the Boundary Layer Leaving the

Trailing Edge; $2\delta/h_m \approx 1.35$

The flow-induced pressures may be separated into a deterministic chordwise variation, $g(y_1)$, and a stochastic spanwise variation, $\Delta p(y_3, \omega)$; i.e.,

$$\Delta P(y_1, y_3, \omega) = \Delta p(y_3, \omega) g(y_1) \quad (9.129)$$

Lifting surfaces are cantilever structures, but Leissa¹⁵¹ has shown that to a rough approximation mode shape functions of cantilever plates can be represented by a separable form as

$$\psi_{mn}(y_1, y_3) \approx \psi_m(y_1) \psi_n(y_3) \quad (9.130)$$

Therefore, in evaluating Equation (9.128), relatively pronounced response can be expected of those modes for which $g(y_1)$ and $\psi_m(y_1)$ are complementary. Figure 9.44 illustrates that for such unsymmetrical (relative to the midchord) loading functions, as provided by inflow turbulence or by vortex shedding, "torsional" modes (as $\psi_1(y_1)$) are most responsive. However, since $g(y_1)$ is peaked near the unrestrained edges and since $\psi_m(y_1)$ is nonzero on the edges, for all orders m of the chordwise vibration pattern it appears that modes of all types will be responsive to flow excitation of these types.

The response of a cantilever beam to inflow turbulence shown in Figure 9.43 has been estimated in the manner indicated above, using Mugridge's³¹ expression of the lift coefficient and Equation (6.34) with $\omega_n = \omega$ for the resonant modal acceleration response spectral density at the resonance frequency is

$$\frac{\phi_{AA} \left(\frac{\omega h}{U_\infty} \right)^2 M^2 \eta_T^2}{q_\infty^2 A_p^2} = \frac{\phi_{fm} \left(\frac{\omega h}{U_\infty} \right)}{q_\infty^2 A_p^2}$$

For modes with uniform response along the chord, i.e., $\psi_{0,n}(\bar{y})$ which are classical beam modes, the modal force simplifies to the resultant force and thus relationship reduces to

$$\frac{\phi_{AA} \frac{\omega h}{U_\infty} M^2 \eta_T^2}{q_\infty^2 A_p^2} = \frac{1}{C_L^2(\omega)}$$

In this case the resultant lift force is applied to the $c/4$ point as indicated in Figure 9.44.

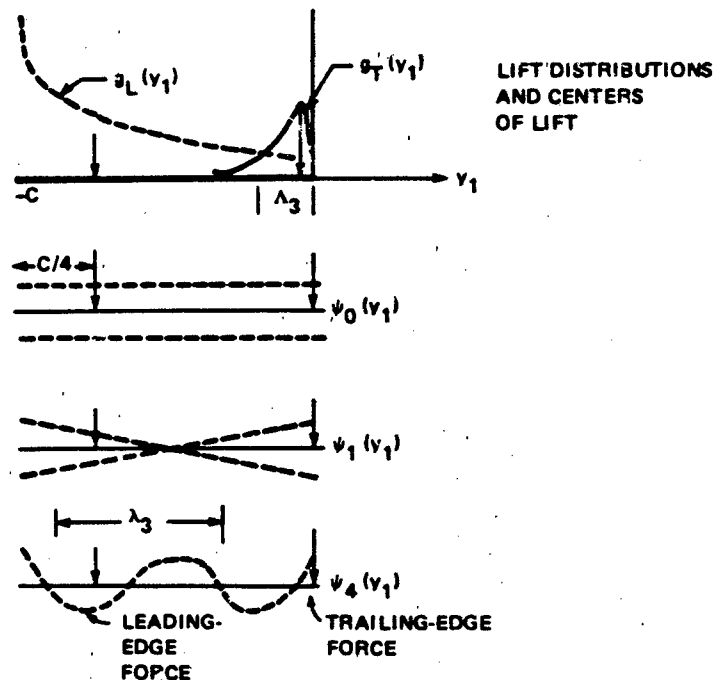


Figure 9.44 - Illustrations of Lift Distributions $g_L(y_1)$ and $g_T(y_1)$ for Leading and Trailing-Edge Pressures and Chordwise Mode Shapes for Structurally Free Leading and Trailing Edges

9.7.1.2 Hydrodynamic Damping. The reaction of the moving fluid to the motion of the hydrofoil can be expressed for each mode as a pressure that is dependent on the amplitude distribution of the hydrofoil. The temporal Fourier transform of this pressure is written¹⁴⁹ as a summation of contributions from all modes.

$$p_h(\vec{y}, \omega) = \sum_{m,n} C_{mn} \left(\frac{\omega C}{2U_\infty} \right) \cdot 2\pi\rho_\infty U_\infty V_{mn}(\omega) \int_A l_{mn}(\vec{y}-\vec{y}_o) \psi_{mn}(\vec{y}_o) d\vec{y}_o \quad (9.131)$$

where $V_{mn}(\omega)$ is the modal amplitude and $l_{mn}(\vec{y})$ is a function that describes the chordwise dependence of the pressure in response to the particular form of $\psi_{mn}(\vec{y})$. If $\psi_m(y_1) = 1$, then $l_{mn}(\vec{y})$ has the same form as $g_L(y_1)$ above and in Equation (9.44). $C(\omega C/2U_\infty)$ is related to the Theodorsen function of unsteady airfoil theory.

Equation (9.131) results from a straightforward application of the unsteady airfoil theory outlined in Section 9.3.1, but the downwash distribution is given by functions

resembling $\psi_{mn}(\vec{y})$. Thus Equation (9.131) has the same form as Equation (9.44). Of importance here are the two chordwise mode shapes shown by $\psi_0(y_1)$ and $\psi_1(y_1)$ in Figure 9.44. For $\psi_0(y_1) = 1$, the force per unit span is

$$\begin{aligned} \frac{dL(\omega)}{dy_3} &= \int_{-C}^0 \Delta p_h(\vec{y}, \omega) dy \\ &= \pi C \rho_0 U_\infty V_n(\omega) \psi_n(y_3) C_T \left(\frac{\omega C}{2U_\infty} \right) \end{aligned}$$

where $C_T(\omega C/2U_\infty)$ is the Theodorsen function^{4,5,18} if $C \ll \lambda_3$ and $C_T(\Omega) = 1/2$ for $\Omega > 1$.

The hydrodynamic exciting pressure $-p_b(\vec{y}, \omega)$ is included on the right-hand side of the structural response function (Equation (6.25) or (6.98)). Therefore, since $\psi_{mn}(\vec{y}) = \psi_n(y_3)$, we can modify Equation (6.99) to include the hydrodynamic reaction superimposed on the hydrostatic added mass and radiation damping. Doing this, we obtain a modified impedance relationship for the general mode order m, n

$$\begin{aligned} &\left[-(m_s + m_{mn}) \omega^2 + i\omega(m_s + m_{mn}) \omega_{mn}(\eta_s + \eta_r) + \omega_{mn}^2 (m_s + m_{mn}) \right] V_{mn}(\omega) \\ &= -i\omega \Delta P_{b_{mn}}(\omega) - i\omega \pi C \rho_0 U_\infty C_{mn} \left(\frac{\omega C}{2U_\infty} \right) V_{mn}(\omega) \end{aligned}$$

where ω_{mn} is the water-loaded resonance frequency. For beam ($m=0$) modes and for $\omega C/2U_\infty > 1$, $C_T(\omega C/2U_\infty)$ is real and positive; therefore the fluid reaction behaves as an additional damping. A hydrodynamic loss factor can therefore be defined as

$$\eta_H = \frac{\pi C \rho_0 U_\infty}{2(m_s + m_{on}) \omega_{on} C} \quad \text{for } \frac{\omega C}{2U_\infty} > 1$$

which increases linearly with the advance speed of the hydrofoil. A more convenient expression of the hydrodynamic damping is a loss factor defined in terms of the added mass,

$$\eta_H' = \frac{\pi \rho_o U_\infty}{2 m_{on} \omega_{on}}$$

Since (Equation (6.91a)) the added mass at low frequencies is given by

$$m_{on} \approx \pi \frac{\rho_o}{4}$$

this hydrodynamic loss factor is given by the simple functions

$$\eta_H' = 2 \left(\frac{\omega C}{U_\infty} \right)^{-1} \quad (9.132)$$

and

$$\eta_H = \eta_H' \left(\frac{m_{on}}{m_s + m_{on}} \right) \quad (9.133)$$

Equation (9.132) applies when the chord is smaller than a spanwise wavelength. For higher-order modes for which the extent of the chord may exceed λ_3 , functions analogous to those discussed in Section 9.3 must replace the two-dimensional Theodorsen function. Functions that are adequate for this purpose have been derived for small aspect ratio wings by Lawrence and Gerber,¹⁵² with experimental verification by Laidlaw and Halfman.¹⁵³ The resulting expression for hydrodynamic damping is

$$\eta_H' = \left(\frac{\omega C}{U_\infty} \right)^{-1}$$

For mode orders with one node line along the chord, i.e. the (1,n) modes, an expression has also been derived.¹⁴⁹ It replaces the $C_r(\Omega)$ function with one appropriate to a chordwise pitching motion for which the fluid applies a moment and it gives a hydrodynamic loss factor double that given by equation (9.132). It is to be noted that this hydrodynamic response is capable of coupling modes since lift induces moments and moments induce lift thus permitting coupling of $n=0$ and $n=1$ motions.

Figure 9.45 shows measured values of η_H' for a number of modes (m,n), where k_m is the chordwise wave number and k_n is the spanwise wave number. Equation (9.132)

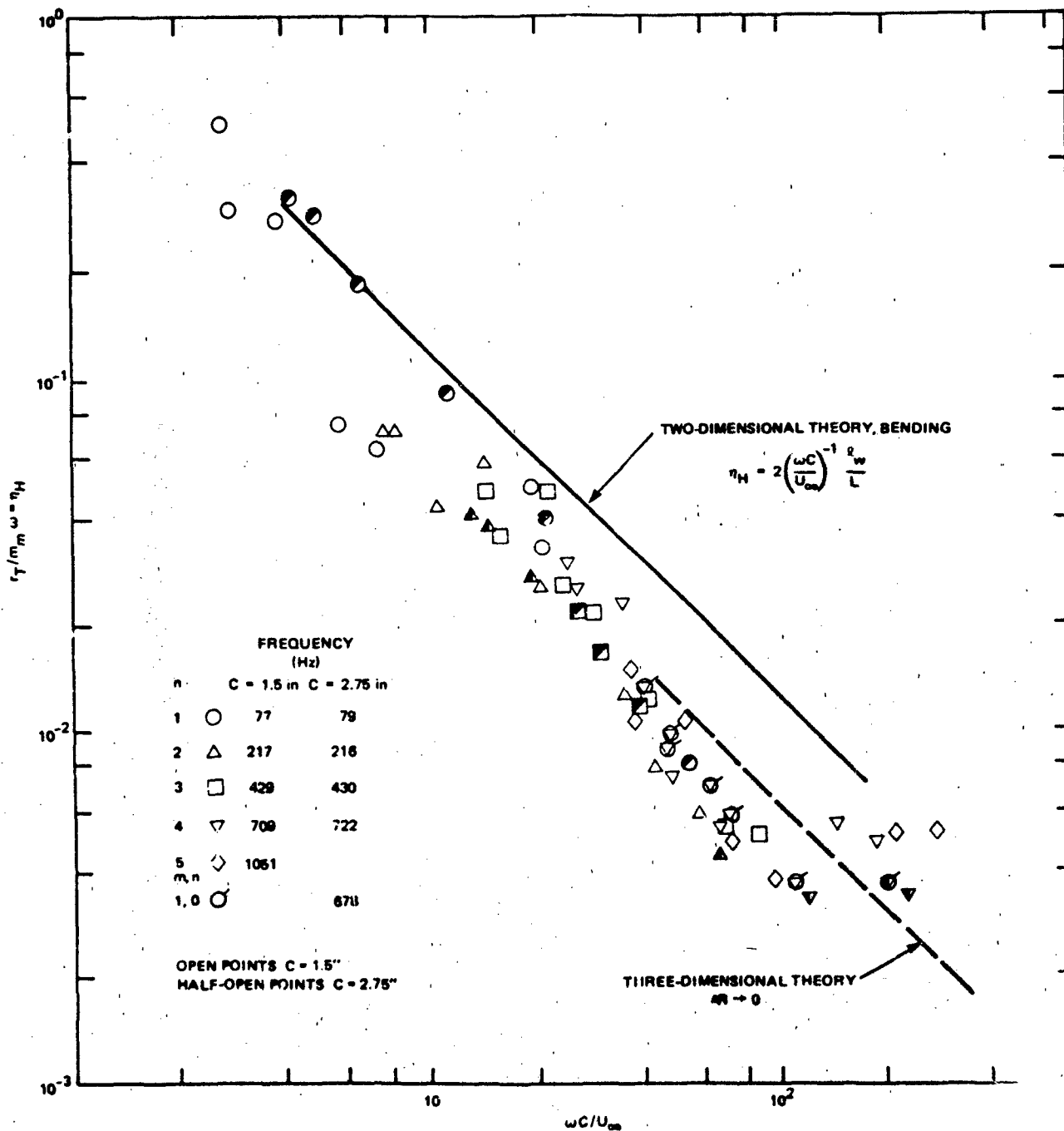


Figure 9.45 - Hydrodynamic Loss Factors as a Function of Reduced Frequency¹⁴⁹

has been drawn in as the "two-dimensional" theory for mode orders (0,n). Using an alternative expression derived by Lawrence and Gerber¹⁵² for vanishing aspect ratio for the case of $\Lambda_3/C \rightarrow 0$, values are found that are one-half of those based on the theory of large aspect ratio (two dimensions). The experimental values of η_H' in Figure 9.45 that are apparently independent of frequency are actually controlled by other hysteretic losses in the test fixture.

9.7.1.3 Viscous Damping. These losses are considered to be important when the flow about the vibrating surface is stagnant and the vibration sets up steady-state eddy currents.^{154,155} For cantilever beams with mode types (0,1) this type damping has been found to be given by¹⁵⁴

$$\eta_V = \frac{4.9}{m_s} \rho_o \left(\frac{2v}{\omega} \right)^{1/2} \left(\frac{m_s}{m_s + m_m} \right) \quad (9.134)$$

9.7.2 Vibration Induced by Vortex Shedding from Cylinders and Airfoils

9.7.2.1 General Characteristics. Detailed measurements of the hydroelastic behavior of fixed hydrofoils excited by vortex shedding forces have been made by Ippen et al.,⁹⁶ Eagleson et al.,¹⁵⁶ Blake,¹¹¹ and Blake et al.⁸ The problem is manifested as a large-amplitude vibration level occurring when the resonance frequency coincides with the frequency of vortex shedding. Figure 9.46 is an illustration of the behavior as observed on a cantilever hydrofoil in a water tunnel.^{8,111} Acceleration was monitored at $y_1 = -0.66C$, $y_3 = 0.285L_3$ (the origin is taken at the intersection of the trailing edge and the root of the hydrofoil) for the trailing edge 7 in Table 9.3 and for the same hydrofoil with a sharp trailing edge. The sharp-edged response that is not tonal is shown in Figure 9.46. For this mode, the vortex-induced vibration level is approximately 50 dB greater at the coincidence speed than it was when the trailing edge was sharp. Figure 9.47 shows the acceleration levels in narrow-spectrum frequency bands for two hydrofoils with specific modes identified. The case is selected for $f_s \neq f_{mn}$ so that the forced nonresonant vibration due to vortex shedding from the hydrofoil with the blunt edge causes an identifiable but low-level peak. The slightly different resonance frequencies of some modes for the two hydrofoils is suspected to be due to their different chords resulting from having shortened a sharp edged foil to create the blunt edge. Similar response characteristics have been observed elsewhere (e.g., references^{77-81,83,93-97,103,156} and the discussion in Section 9.4).

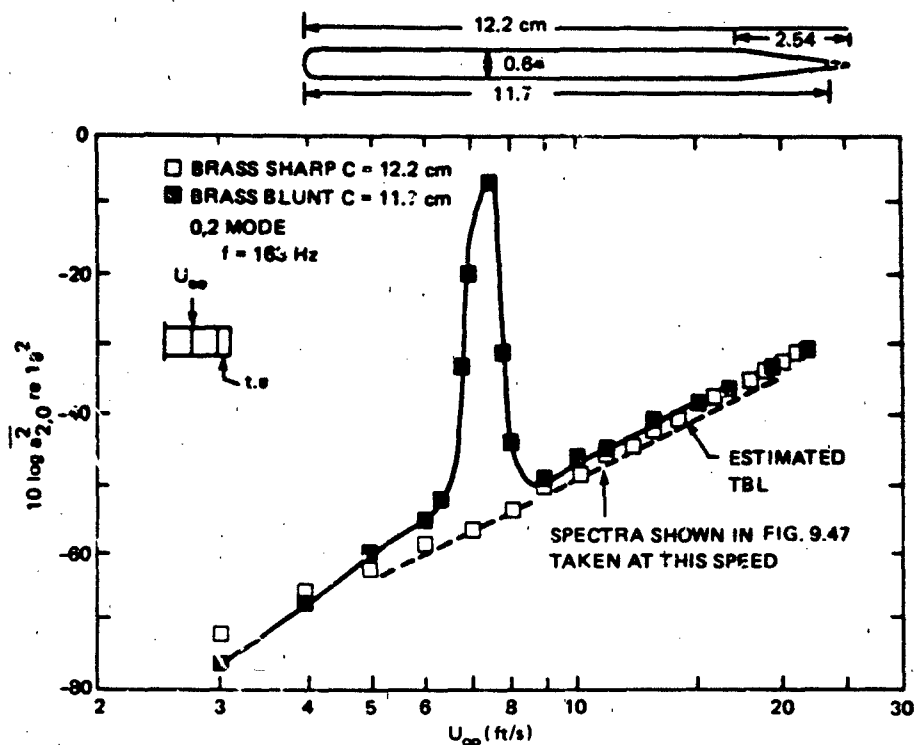


Figure 9.46 - Hydroelastic Response⁸ of 0,2 Mode of a Simple Cantilever Hydrofoil Fitted with a Sharp and a Blunt Trailing Edge, $L_3 = 50.8$ cm. At Coincidence ($\omega_s = \omega_{0,2}$) $R_c = 2.8 \times 10^4$, $R_h = 4 \times 10^3$

Self-sustained vibrations occur as shown in Figure 9.46, when the linear dependence of frequency on speed is interrupted because the vortex shedding "locks-on" to the vibration of the trailing edge. This occurs when the natural vibration frequency and natural shear-layer frequency coincide. In extreme cases the apparent vortex shedding frequency may become fixed and equal to the natural vibration frequency for short speed ranges, as illustrated in Figure 9.48. The phenomenon is another case of the shear layer-body interaction that leads to self-sustained oscillations, as described in Sections 3.3 and 3.4. As the vortex shedding frequency passes through each mode in succession, the step-wise dependence on speed is observed about an average function

$$\frac{\omega_s y_f}{U_s} \approx 1$$

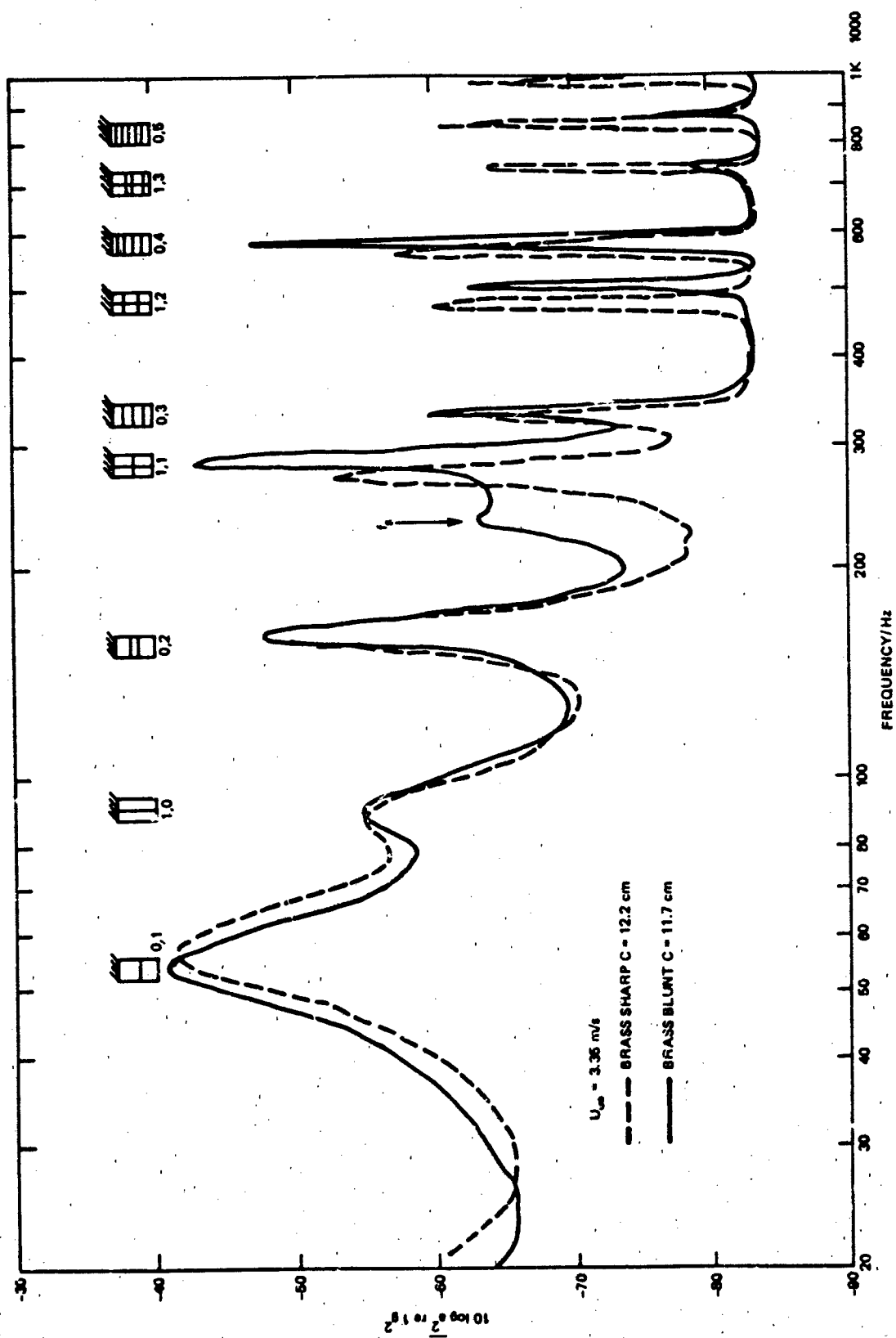


Figure 9.47 - Acceleration Spectrum, Measured in 5-Hz Bands,⁸ for the Hydrofoils
of Figure 9.46. $R_c = 4.1 \times 10^4$, $R_h = 5.9 \times 10^3$

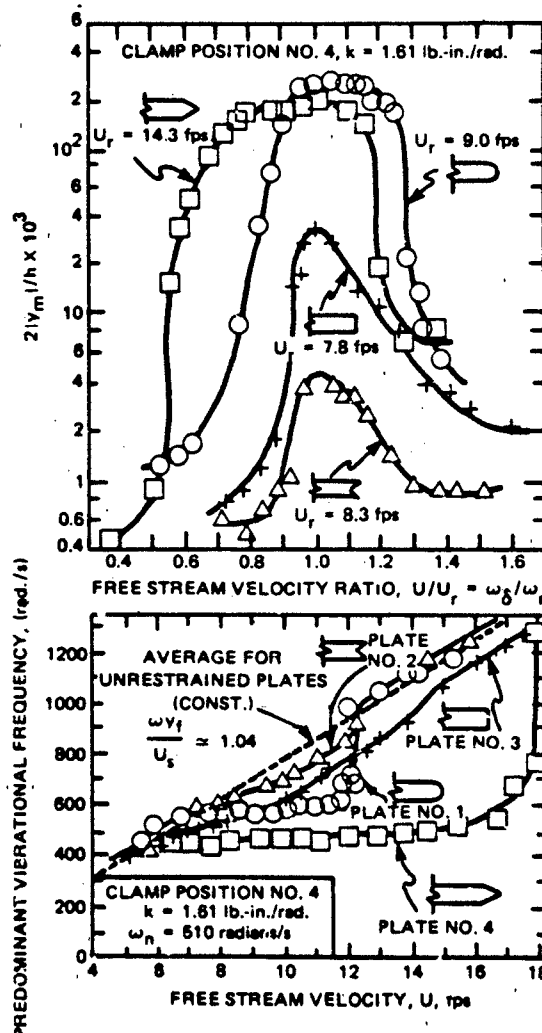


Figure 9.48 - Comparative Dynamic Response⁹⁶ of Spring-Loaded Test Plates Pivoted to Oscillate About the Leading Edge.

$$R_c \approx 1.5 \times 10^5, R_h = 1.9 \times 10^4$$

This behavior is evident in the measurements in Figure 9.48. At these "coincidence" speeds, the observed damping of the mode is reduced to values less than the damping observed when vortex shedding does not occur, as illustrated in Figure 9.49. The observed loss factor near the coincidence velocity $U_\infty = U_{co}$ is substantially less than that observed when the edge was sharp, but at the same velocity the hydrodynamic damping is essentially cancelled by the negative damping associated with the vortex shedding. This behavior, although pronounced when trailing edges are blunt and vortex

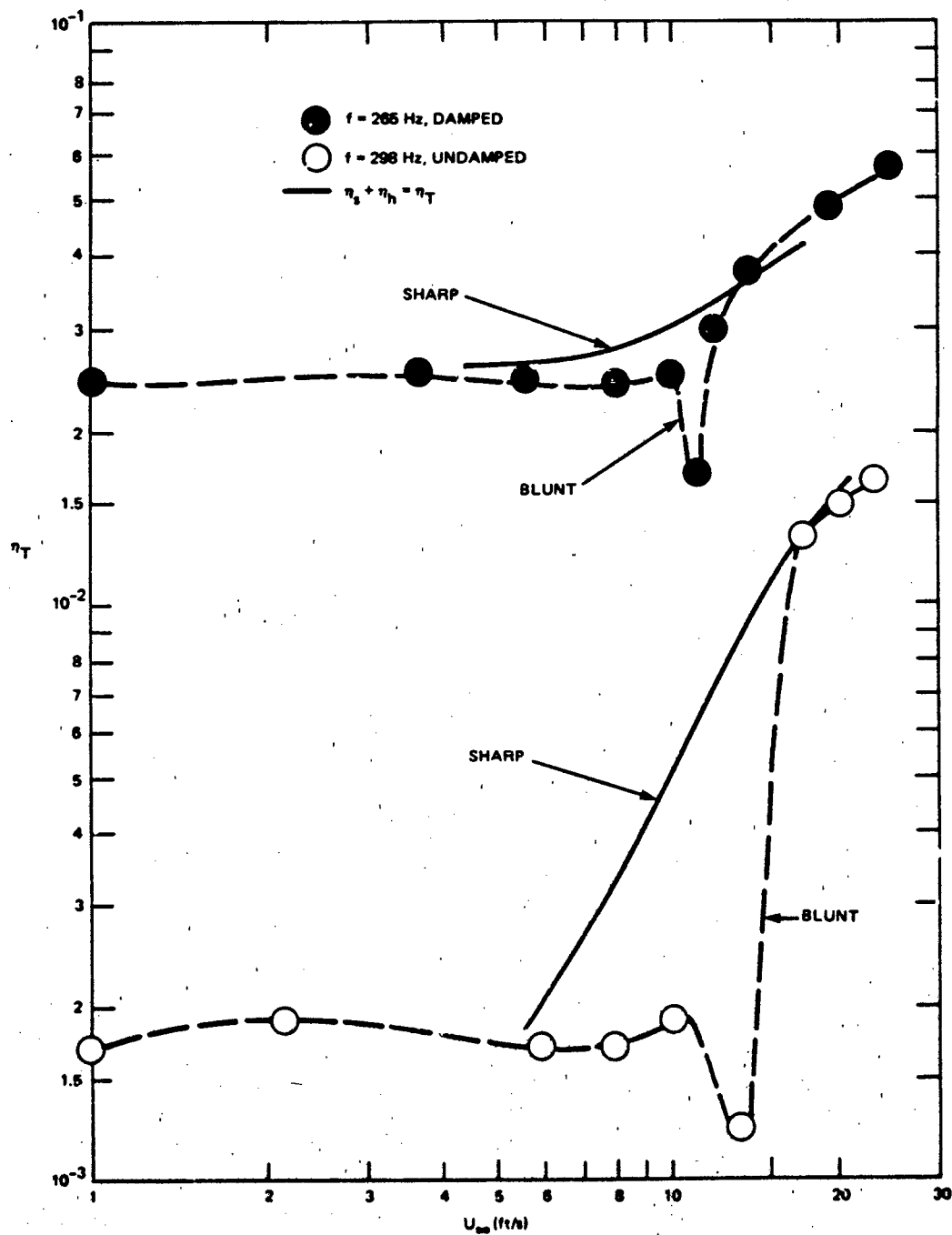


Figure 9.49 - Loss Factors of Hydrofoils with Sharp and Blunt Trailing Edges as a Function of Speed. Reduced Damping at $10 < U_\infty < 20$ Is Due to the Effects of Self-Excitation. Increasing Damping with Speed of Sharp-Edged Hydrofoils is Due to Hydrodynamic Damping⁸

shedding is strongly tonal, is less pronounced when the edge is sharpened by beveling. The general trend of reducing hydroelastic response by modifying the trailing edges of hydrofoils was discussed in Section 9.4 (see also Table 9.2).

Self-sustained vibrations have also been observed in cascades when the coincidence of the vortex-shedding frequency coincides with the frequency of an acoustic cross mode of the duct.¹⁵⁷⁻¹⁶⁰ They also occur with combinations of acoustic modes of ducts and shedding structures.^{161,162} Acoustic reinforcement is provided when the vortex-induced force $f(\vec{y})$, or $\vec{\omega} \times \vec{U}$, coincides with a node in the acoustic cross-mode of the duct. In the case examined by Parker,¹⁵⁶ for example, a lifting surface spanned a duct and reinforcement occurred when the placement of the surface in the y_3 plane coincided with maximum values of $\partial S_{mn}(\vec{y})/\partial y_2$ and when the vortex shedding frequency roughly satisfied

$$\omega_s = C_o k_n$$

here k_n is $\pi n/L_2$ with $n = 0, 1, 2, \dots$ and L_2 is the duct width. $S_{mn}(\vec{y}_o)$ is the acoustic pressure mode shape (see Section 9.8.1), and the acoustic source is given by $f_2(\vec{y}, \omega) = (\partial/\partial y_2) (\omega_3 \times U_c)$ in Equation (9.2). The above resonance condition becomes less able to predict coincidence frequencies as the chord of the airfoil becomes large. The self-excitation comes about because the acoustic particle velocity of the duct medium drives the trailing-edge shear layer.

9.7.2.2 Control by Hysteretic Damping. Since the vortex-induced vibration involves the coupling system with the structural modes of the airfoil with the unstable mode of the wake, it is expected that the introduction of damping into the fluid structure will be effective as a vibration-control technique. To quantify this effectiveness, Equation (6.99) can be adapted to the present case by writing

$$(-i\omega) Z_{mn}(\omega) Y_{mn}(\omega) = \frac{1}{L_3} \int_{-L_3/2}^{L_3/2} f_m'(\omega, y_3) \psi_n(y_3) dy_3 \quad (9.135)$$

where

$$f'_n(y_3, \omega) = \frac{1}{c} \int_{-c/2}^{c/2} \Delta P(y_1, y_3, \omega) \psi_m(y_1) dy_1$$

$$\approx \frac{1}{c} \frac{df(y_3, \omega)}{dy_3} \psi_m(y'_1) \quad (9.136)$$

as long as the chordwise scale of $\Delta P(y_1, y_3, \omega)$ is much smaller than a wavelength of $\psi_m(y_1)$ near the edge $y_1 = y'_1$. The impedance is written

$$(i\omega) Z_{mn}(\omega) = (\omega_{mn}^2 - \omega^2) (m_s + m_{mn}) - i(m_s + m_{mn}) \eta_T \omega_{mn} \omega \quad (9.137)$$

where η_T includes both mechanical, hydrodynamic, and radiation damping, i.e.

$$\eta_T = \eta_s + \eta_r + \eta_H$$

A modal lift coefficient is formed in a fashion which parallels sections 9.5.5. It can be written in the form of a random variable

$$C_L(\omega)_{mn} e^{i\phi} = \int_0^{L_3} \frac{f'_m(y_3, \omega) \psi_n(y_3) dy_3}{q_\infty L_3 c} \quad (9.138)$$

where the prime denotes differentiation by y_3 . Now the autospectrum of the fluctuating lift coefficient can be written as an ensemble of $C_L(\omega) e^{i\phi}$; i.e.,

$$\langle C_L^2(\omega)_{mn} \rangle = \frac{\phi_{fm}(\omega)}{q_\infty^2 c^2 L_3^2} = \frac{\int_0^{L_3} dr_3 \int_{-L_3/2}^{L_3/2} \langle f'_m(y_3) f'_m(y_3+r_3) \rangle \psi_n(y_3) \psi_n(y_3+r)}{q_\infty^2 c^2 L_3^2}$$

This equation reduces as long as $f'_m(y_3)$ is statistically stationary along y_3 and as long as its correlation length is small compared to a half-wave length of $\psi_n(y_3)$. Then we have, using basically the same procedures that led to Equation (5.49) with $\gamma_c = 0$, or to equation (9.101),

$$\langle C_L^2(\omega)_{mn} \rangle = \frac{(\langle (f')^2 \rangle L_3 2\Lambda_3) \psi_m^2(y'_m)}{q_\infty^2 C_L^2 L_3^2} \quad (9.139)$$

if the spanwise correlation length $2\Lambda_3$ is much less than a wavelength of $\psi_n(y_3)$.

Using Equation (9.135) through (9.138), the modal amplitude at any excitation frequency ω can be written in the dimensionless form

$$\left[1 - \left(\frac{\omega}{\omega_{mn}} \right)^2 - i\eta_T \frac{\omega}{\omega_{mn}} \right] \frac{Y_{mn}(\omega)}{y_f} = \left[\frac{\rho_o y_f}{2(m_{mn} + m_s)} \right] \left(\frac{\omega_s}{\omega_{mn}} \right)^2 \left(\frac{\omega y_f}{U_\infty} \right)^{-2} C_L(\omega) e^{i\phi} \quad (9.140)$$

where the phase ϕ is a random variable in the case of uncoupled vortex shedding and it is a function of $y_{mn}(\omega)$ in the case of self-sustained oscillation. At the coincidence condition $\omega = \omega_{mn}$ and when $\omega_{mn} = \omega_s$, the resonant response can be written

$$\frac{Y_{mn}(\omega_{mn})}{y_f} = i \left(\frac{\frac{1}{2} \rho_o y_f}{(m_{mn} + m_s) \eta_T} \right) \left(\frac{\omega y_f}{U_\infty} \right)^{-2} C_L(\omega_{mn}) e^{i\phi} \quad (9.141)$$

which illustrates the importance of a damping parameter that can be written as

$$\mathcal{D}_a = \frac{(m_{mn} + m_s) \omega \eta_T}{\frac{1}{2} \rho_o y_f^2} \quad (9.142)$$

in controlling the flow-induced vibration. The mean-square modal amplitude is

$$\frac{\langle Y_{mn}^2(\omega_{mn}) \rangle}{y_f^2} = p_a^{-2} \left(\frac{\omega y_f}{U_\infty} \right)^{-4} \langle C_L^2(\omega_{mn}) \rangle \quad (9.143)$$

A comparison of Equation (9.139) with Equations (9.90) shows that $\langle C_L^2(\omega_{mn}) \rangle$ can be approximated in terms of the variables in Table 9.3 since

$$\langle C_L^2(\omega_{mn}) \rangle = \frac{\phi_f^2(\omega_{mn}) \psi_m^2(y_{10})}{q^2 (CL_3)^2} \quad (9.144)$$

Equation (9.143) applies whether "self-excited" or linear vibration occurs. When linear vibration occurs, i.e., when airfoil vibration and the vortex shedding remain uncoupled, then the autospectrum of the lift coefficient may be written in terms of the parameters listed in Table 9.3. Thus, using Equation (9.144) the linearly excited motion can be seen to depend on damping in the classical sense, i.e., $Y_{mn}(\omega_{mn}) \approx \eta_T^{-1}$.

The effect of vibration at the trailing edge is to modify the magnitude of $C_L(\omega)$ and lock its phase ϕ into fixed relationship with $Y_{mn}(\omega)$. Accordingly, to restrict $Y_{mn}(\omega)$ by damping serves the twofold purpose of reducing $Y_{mn}(\omega)$ and maintaining $C_L(\omega)$ to the value existing on the rigid surface. The quantification and analytical modeling of this coupling is the subject of the next two sections. Here we examine the effects of increased damping in controlling either the linear or the self-sustained oscillations of elastic hydrofoils and cylinders.

Measured vibration levels on a series of hydrofoils with blunt edges, like number 7 in Table 9.3, are shown in Figure 9.50. The mean-square displacement represents both a time and area average of the motion. The dimensionless amplitudes of both berding (0,n) modes and plate modes (m,n) which involve pitching motion along the chord (flagged points) show identical behavior. For damping parameters that are smaller than 100, the amplitude-squared decreases as η_T^{-4} compared to η_T^{-2} behavior for the linearly excited vibration. The dashed line is a computation

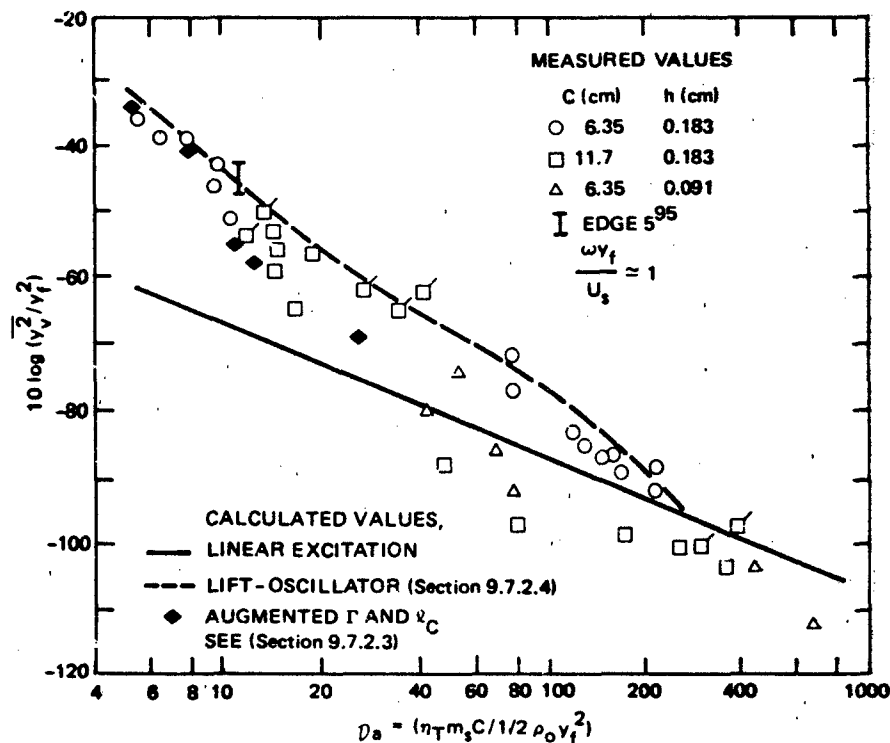


Figure 9.50 - Mean-Square Amplitude of Flexural Vibration of Hydrofoils Excited by Vortex Shedding. Variables Include Mechanical Loss Factor, Plate Density, Chord, Trailing-Edge Thickness, and Vibration Mode Order⁸

using the oscillator model of Hartlen and Currie (Section 9.7.2.4) with the same parameters used in connection with Figure 9.56 (see Section 9.7.2.4). The solid line in the figure describes the linear resonant response to the vortex shedding given by Equation (9.143) with constant lift coefficient. The parameters of Table 9.3 were used to establish its magnitude.

The point included from Ippen et al.⁹⁶ was obtained on an aluminum panel shaped with trailing edge number 5 (Table 9.3). The plate was mounted in a water tunnel so that it underwent a rigid-body pitching motion about its leading edge. Stiffness was provided with leaf springs. In this case the added mass was approximately twice the structure mass. The reported amplitude that was measured at the trailing edge (y_T) has been adjusted according to the formula

$$\overline{y^2} = \frac{y_T^2}{3}$$

to determine the mean-square displacement for the mode shape $\psi_1(y_1)$ in Figure 9.44.

Similar data exist for sustained oscillations of elastically mounted cylinders. In that case the damping parameter is

$$D_{cyl} = \frac{4 M_c (2\pi S_d)^2 \eta_s}{\rho_o d^2}$$

Figure 9.51 shows a compilation by Skop and Griffin¹⁶³ of measurements from various sources where M_c is the mass per unit length of the cylinder, and its accession to inertia.

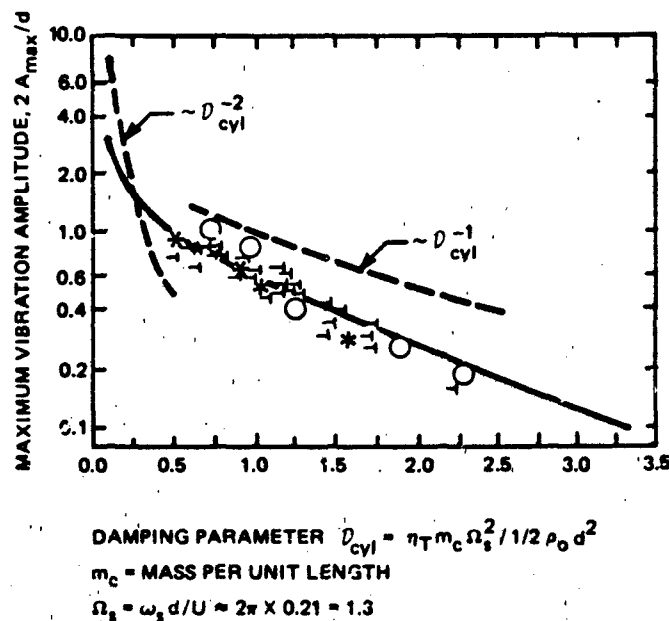


Figure 9.51 - The Maximum Amplitude of Vortex-Excited Oscillation, $2 A_{max}$, for an Elastically Mounted, Rigid Circular Cylinder, as a Function of the Response Parameter D_{cyl} . Data Points from a Number of Investigations Performed in Air and in Water. Adopted from Reference 163 (Copyright Academic Press)

9.7.2.3 Effects of Trailing-Edge Vibration on the Vortex Shedding and Induced Forces. We discussed in Chapter 5 the effects of transverse cylinder motion on the structure of the vortex street. The related effects on the vortex-induced forces were also briefly described in Figure 5.21. We now examine the effects of surface motion in more detail. In the case of vibrating circular cylinders, the results of Jones¹⁶⁴ ($R_D=10^7$) and Bishop and Hassan^{165,166} ($6 \times 10^3 < R_D < 11 \times 10^3$) showed measured effects on both $C_L(\omega)$ and ϕ as the cylinder vibration frequency ω_v was brought into coincidence with the shedding frequency. At the coincidence of $\omega_v = \omega_s$, Jones showed that the phase between the lift and the amplitude was between $-\pi < \phi < 0$, suggesting negative fluid damping. This type of behavior has also been interpreted in terms of Equations (9.140) and (9.142) by Griffin.¹⁶⁷ The augmented lift coefficients are shown in Figure 5.21. Measurements by Toebs¹⁶⁸ in the wake of an oscillating cylinder disclosed that nearly complete correlation of the vortices along the length of the cylinder (within $0.7L$) took place for motion amplitudes of $0.125d$. This amplitude is somewhat larger than the motion occasionally observed in flow-excited cylinders. Recall, for example, the measurements by Leehey and Hanson¹⁶⁹ cited in Chapter 5 which showed enhancement of the lift coefficient with no measurable effect on spanwise correlation for amplitudes of motion equal to $0.03d$. In the context of Equations (9.82), this is interpreted as an increase in the circulation of the vortices which causes a larger lift per unit length of the cylinder. Other measurements Vickery and Watkins¹⁷⁰ and Hartlen et al.¹⁷¹ are in general agreement with the measurements of Jones presented in Figure 5.21 for values of amplitude that are less than $0.6d$. For amplitudes of order d and larger, Vickery and Watkins¹⁷⁰ report that the coefficients decrease again with increasing amplitude.

The effects of transverse vibration on vortex-induced oscillating lift on cylinders have been diagnosed in terms of the component features of increased correlation and wake strength (force per unit length) by Leehey and Hanson¹⁶⁹ and Blevins and Burton.^{172,173} These separate effects are shown in Equation (9.139), which is equally applicable to cylinders ($y_f=d$) or to hydrofoils. From Toebs' measurements, Blevins and Burton deduced that for cylinders

$$\frac{2\Lambda_3}{d} = \frac{(2\Lambda_3)_0}{d} + \frac{100 A}{A_m - A} \quad A < A_m$$

$$= \infty \quad A > A_m$$

where A_m is a threshold amplitude and $A_m = 0.5d$, and $(2\Lambda_3)_0$ is the correlation length when there is no transverse motion. From Toebs' data, $2\Lambda_3 \approx 5d$, but see Figure 5.19 for other values. The effects on the lift fluctuation, which includes the increase in Λ_3 , have been discussed. Measurements¹⁷⁴ at low R_d , $O[500]$, disclose complete correlation of the vortex street with the vibration for $A_m > 0.2D$.

Experimental studies of the effects of trailing-edge oscillation on flow have been made by Wood,⁸¹ Greenway and Wood,³ Blake et al.,^{5,175} Graham and Maull,¹⁷⁶ and Wood and Kirmani.¹⁷⁷ The measurements by Greenway and Wood and by Wood and Kirmani are primarily flow visualizations (see Figure 9.3c) conducted on the surface of a water channel. The hydrofoil pierced the surface from a towing carriage. As it was towed, the flow structure around the hydrofoil was made visible by light-reflecting particles suspended buoyantly on the surface. From measured particle trajectories the circulation distribution could be calculated. Their measurements³ disclosed little change in the geometry of the wake of blunt edges for heaving amplitudes less than $0.10h$. For beveled trailing edges, of the general type resembling number 8 in Table 9.3, but with varying included angle, Greenway and Wood³ ($R_h = 3.4 \times 10^3$) found that although motion generally organized the wake of edges with included angles of 20 to 30 deg, the strength of the vortices was only slightly affected. The strength of vortices shed from the upper (obtuse) corner was less than that of vortices shed from the lower (acute) corner. For included apex angles of greater than 45 deg, a marked increase in strength with motion (of amplitude $0.123h$) was found.

Measurements of surface pressures and their correlation properties on an airfoil shape were conducted with a blunt and a beveled oscillating trailing-edge flap^{8,175} that had a chordwise extent of $3h$, where h is the base height (see Table 9.3, numbers 1, 5, and 8). Measurements of the surface pressure were made to determine any change in the spanwise correlation and the chordwise variation, $g(y_1)$ of Equation (9.89). Regarding the blunt trailing edge, it was found that the chordwise variation was unaffected by the vibration, but it was also found that the spanwise correlation was increased, as shown in Figure 9.52. A nearly identical behavior was shown by Graham and Maull¹⁷⁶ using a similar experimental arrangement at $R_h = 3.5 \times 10^4$. The surface pressures also increase with displacement, with a matching

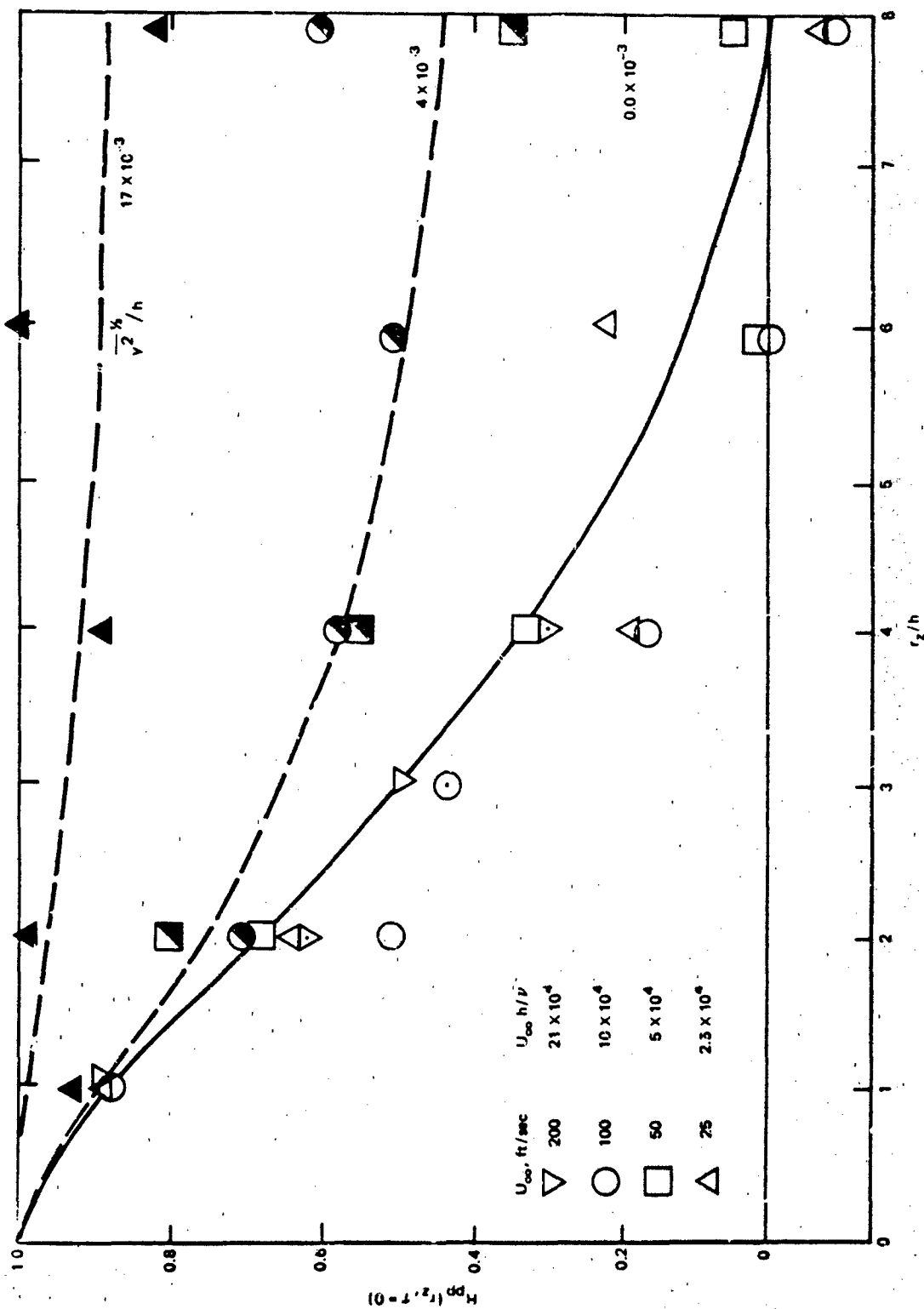


Figure 9.52 - Spanwise Correlations of Vortex-Induced Pressures on Blunt Trailing Edges of Base Height h Undergoing Forced Transverse Oscillation⁸

behavior shown by the vortex strength κ . The increase with motion of the mean-square value and the correlation length of the pressure at $(y_1 - y_s)/y_f \approx 0.1$ is shown in Figure 9.53; the vortex shedding frequency and the oscillation were coincident. The pressure measured with no motion is p_o . There also was a clear phase relationship between the displacement and the surface pressures (Figure 9.54). As the ratio ω_v/ω_s was increased, there were two clearly detectable pressure contributions observed at the frequencies ω_v and ω_s . When $\omega_v/\omega_s > 0.98$, the two pressures could not be distinguished and the phase with respect to the amplitude turned negative. This "entrainment" continued until $\omega_v/\omega_s > 1.05$ and it was the same for the two amplitudes examined. The increase in the magnitude of alternating lift $\bar{C}_L^2(\omega)$ relative to its value with no motion is determined by the changes in $p_o \propto \rho_o \Gamma U_s / (y_f 2\pi) q$, Λ_3 and m , which is assumed to be limited by $m = 2 \Lambda_3 / y_f$. Using Equation (9.90a) this increase is shown as a function of ω_v/ω_s at $y_v^{1/2} = (9 \times 10^{-3})h$ at

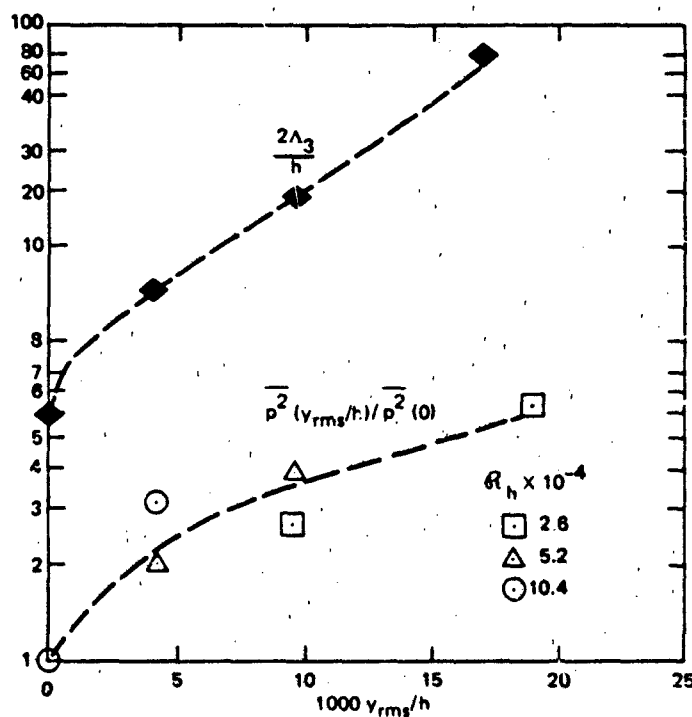


Figure 9.53 - Enhancement of Vortex-Induced Pressures and Spanwise Correlation Lengths as Transverse Displacement is Increased
Relative to $h \approx y_f$ for Blunt Trailing Edge⁸

the bottom of Figure 9.54. The values of augmented pressure p_o and correlation length $l_c = 2\lambda_3$ for this displacement account for a lift increase amounting to 25 dB at $\omega_v/\omega_s \approx 1.02$. The fact that the maximum lift occurs at $\omega_v \neq \omega_s$ has been often observed in the flow excitation of hydrofoils and cylinders, as shown, for example, in Figure 9.53.

As presented in Figure 9.54, the effect of the motion is shown as an increase in lift due to an augmentation of the pressure over p_o and $l_c = 2\lambda_3$ throughout a range of y_v^2/y_f^2 ($y_f=h$) that corresponds to the observed values shown in Figure 9.50. Therefore, for selected observed values of y_v^2/y_f^2 in the nonlinear range, the linear response calculated by Equation (9.143) has been augmented by the parameters shown in Figure 9.53 to give the vibration levels indicated by ♦'s in Figure 9.50. For example, for $D_a = 8$, the observed displacement is $y_v^2/y_f^2 \approx 10^{-2}$. The augmentation in p_o and l_c for this amplitude amounts to 25 dB which, when added to the calculated linear response, accounts for the observed vibration levels.

9.7.2.4 Semiempirical Modeling as a Nonlinear Oscillator. Attempts at theoretically predicting this hydroelastic behavior have been varied. Some of the earlier attempts were based on the direct adaptation of unsteady lifting surface theory to quantify the relationship between the wake circulation Γ and the oscillatory lift and translation of the surface. This was the approach used by Shioiri,¹⁷⁸ Tsakonas and Jacobs,¹⁷⁹ and Arnold et al.¹⁸⁰ It now appears to have two shortcomings. First, a one-to-one relationship was assumed between the average vorticity shed by the mean shear layer of the boundary layer on the hydrofoil surfaces and the rate at which vorticity was entrained in the periodic vortex street. Even in the case of circular cylinders (Section 5.2) in the process of vortex formation the strengths of vortices are known to be modified by freestream turbulence and Reynolds number. Furthermore, the assumption overlooks the fundamentals of vortex sheet stability that are now widely regarded as important in the wake generation process. The second shortcoming has to do with the fact that the theories were essentially two dimensional. Their application in fact would require spanwise correlation lengths of vortices that are many times larger than the chord of the hydrofoil. This is generally not the case. Therefore these theories generally over predicted the magnitudes of hydroelastic

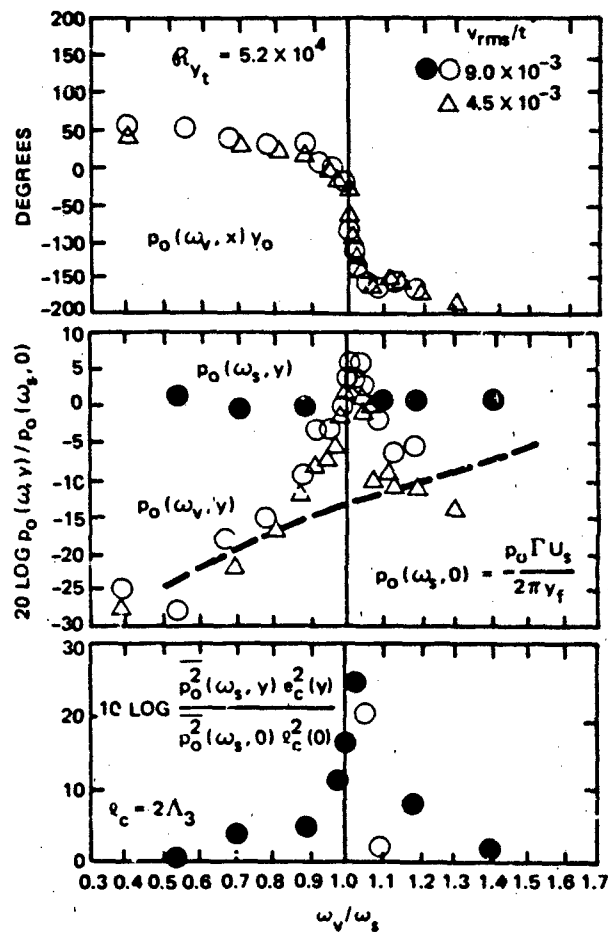


Figure 9.54 - Influence of Vibration Frequency and Transverse Displacement on Phase, Pressure, and Resultant Lift⁸
for Edge 5 (Table 9.3) in Air

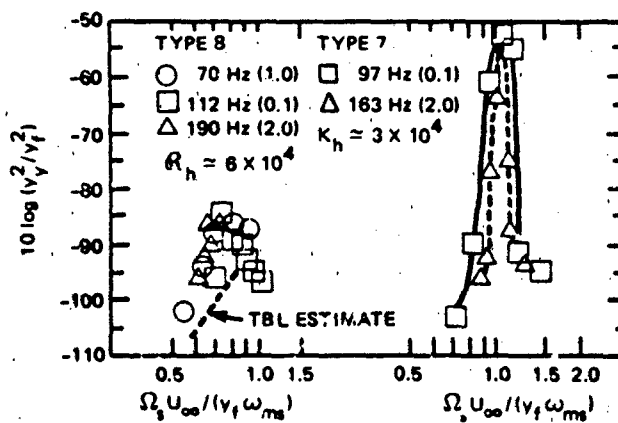


Figure 9.55 - Transverse Modal Displacement as a Function of U_∞ , c , and γ_f for Various Modes of Edges Type 7 and 8⁸
(See Table 9.3)

sponse while properly accounting for the qualitative aspects of observed self-excitation behavior.

Semiempirical analyses, similarly based but relying on more heuristic reasoning, were presented by Ippen et al.⁹⁶ and Eagleson et al.¹⁵⁶ Generally, the lift and moments induced on the hydrofoil by the vortex street were determined using the Theodore function, which is valid for two-dimensional flow. The excitation and moment due to the vortex street was assumed to be proportional to the area of the hydrofoil, the square of the advance velocity (U_∞), and the thickness of the trailing edge. Again, although the general hydroelastic behavior could be described, the amplitudes of motion could not be predicted. However, the role of increased hysteretic structural damping in limiting hydroelastic response could be clearly defined. It was found¹⁵⁶ that the optimum damping for preventing hydroelastic self-excitation was to have η_T from 0.06 to 0.08.

A more recent approach outlined below differs from the earlier ones by not explicitly relying on the theory of unsteady flow about thin lifting surfaces but relying heavily on heuristic reasoning and empirical data. When self-excitation and coincidence occur, the vibration of the hydrofoil is tonal. The occurrence of self-excitation depends on the existence of a relationship between the lift coefficient, $C_L(\omega) e^{i\phi}$, and the amplitude $Y_m(\omega)/y_f$. The effective total loss factor during self-sustained oscillations can be written

$$(\eta_T)_{\text{eff}} = \eta_T \left[1 + D_a^{-1} C_L(\omega) \sin \phi \right] \quad (9.145)$$

where η_T is the total loss factor that would exist without self-excitation, so the effective value can be less than η_T when ϕ lies in the range $-\pi < \phi < 0$. The lift fluctuation in this region acts as a negative damping, which has a minimum value limited by some property of the wake flow.

The nonlinear limiting-cycle character of the oscillating lift resembles the behavior of both the van der Pol and the Rayleigh oscillators. The important characteristic of these oscillators is the nonlinear dependence of fluid damping on the amplitude of the fluid disturbance. The disturbance function used by Hartlen and Currie¹⁸⁰ is the lift oscillation, which in the time domain is defined

$$C_L(t) = \text{Im} \left[\int_{-\infty}^{\infty} C_L(\omega) e^{-i\omega t + i\phi(\omega)} d\omega \right] \quad (9.146a)$$

or

$$C_L(t) = C_L(\omega) \sin(\omega t - \phi) \quad (9.146b)$$

The lift was assumed to satisfy the nonlinear van der Pol equation

$$\begin{aligned} \ddot{C}_L(t) - \alpha \omega_s \dot{C}_L(t) + \frac{\gamma}{\omega_s} [C_L(t)]^3 + \omega_s^2 C_L(t) \\ = b \frac{\dot{y}_{mn}(0,t)}{y_f} \end{aligned} \quad (9.147)$$

where $\dot{y}_{mn}(0,t)$ is the flexural velocity of the trailing edge governed by Equation (6.21) in general, Equation (9.135) in particular, b is a coupling coefficient, and α and γ are positive-valued empirical parameters. When $\dot{C}_L(t)$ is small, the fluid oscillation is a simple harmonic, but negatively damped (compare Equation (6.27)) and therefore able to grow with time. This growth occurs until $\dot{C}_L(t)$ is large enough to make the damping term positive. In the case of a rigid hydrofoil or cylinders $b = 0$, ($y_{mn}(0,t)=0$) and the lift coefficient is given its value on rigid surfaces, which is written

$$C_L(t) = C_{L_0} e^{-i\omega_s t} \quad (9.148)$$

where

$$C_{L_0} = \left(\frac{4\alpha}{3\gamma} \right)^{1/2} \quad (9.149)$$

is the lift coefficient for pressures induced by vortices shed from a rigid trailing edge.

Skop and Griffin^{163,182,183} and Griffin et al.¹⁸⁴ modified the equation for lift somewhat by adding another stiffness term to the equation. This term permitted behavior as a nonlinear spring.

The equation of motion for the mn mode of the lifting surface, or cylinder, vibration in the time domain is, from Equations (9.135) and (9.138),

$$m \ddot{y}_{mn}(t) + \eta_T m \dot{y}_{mn}(t) + k_{mn}^4 y_{mn}(t) = q_\infty C_L(t) \quad (9.150)$$

where $m = m_s + m_{mn}$ is the total wetted mass per unit area, and

$$y_{mn}(t) = Y_{mn}(\omega) \sin \omega t$$

is the lateral displacement of the points of flow separation. Equations (9.147) and (9.150) can be solved approximately and simultaneously without the use of a digital computer when Equation (9.146b) is substituted into Equation (9.147) and the coefficients of sines and cosines are grouped, with high-order terms higher order than \sin^2 or \cos^2 ignored. This operation was followed by Hartlen and Currie, who found for the amplitude, frequency, and phase:

$$C_L(\omega) \cos \phi = \frac{(\omega_{mn}^2 - \omega^2) Y_{mn}(\omega)}{a \omega_s^2 y_f}$$

$$C_L(\omega) \sin \phi = - \frac{\eta_T \omega \omega_{mn} Y_{mn}(\omega)}{a \omega_s^2 y_f}$$

and

$$\left\{ \left[1 - \left(\frac{\omega}{\omega_{mn}} \right)^2 \right] \left[\left(\frac{\omega_s}{\omega_{mn}} \right)^2 - \left(\frac{\omega}{\omega_{mn}} \right)^2 + \alpha \eta_T \frac{\omega_s \omega^2}{\omega_{mn}^2} \right] \right\} - \frac{3}{4} \frac{Y}{a^2} \frac{\omega_{mn}^2 \omega^3}{\omega_s^3} \left(\frac{Y_{mn}(\omega)}{y_f} \right) \left\{ \eta_T \left(\frac{\omega}{\omega_{mn}} \right)^3 + \eta_T \frac{\omega}{\omega_{mn}} \left[1 - \left(\frac{\omega}{\omega_{mn}} \right)^2 \right] \right\} = 0$$

where

$$a = \frac{\rho_o y_f}{2m} \left(\frac{U_\infty}{\omega_s y_f} \right)^2$$

For circular cylinders, y_f is replaced by diameter. A second method is to program Equations (9.11) and (9.147) on an analog computer and determine $y_{mn}(\omega)$, $C_L(\omega)$, and ϕ from observed oscillations in response to small initial conditions. This technique, although it preserves the complete nonlinearity of the functions, is difficult to program. The difficulty arises in the necessity of scaling the amplitudes of the functions and the frequency so that all terms in the equations remain within the dynamic range of the computer. The digital computer was used by Skop and Griffin¹⁶³ and Griffin et al.¹⁸⁴ to solve the linearized equations of Hartlen and Currie in their modified form, which included the fluid stiffness term dependent on $C_L(t)$.

An example of a calculation¹¹¹ for a singing steel hydrofoil similar in geometry to that whose measured response characteristics are shown in Figures 9.46 through 9.48, is shown in Figure 9.56. The coefficient C_{L0} was approximated from the

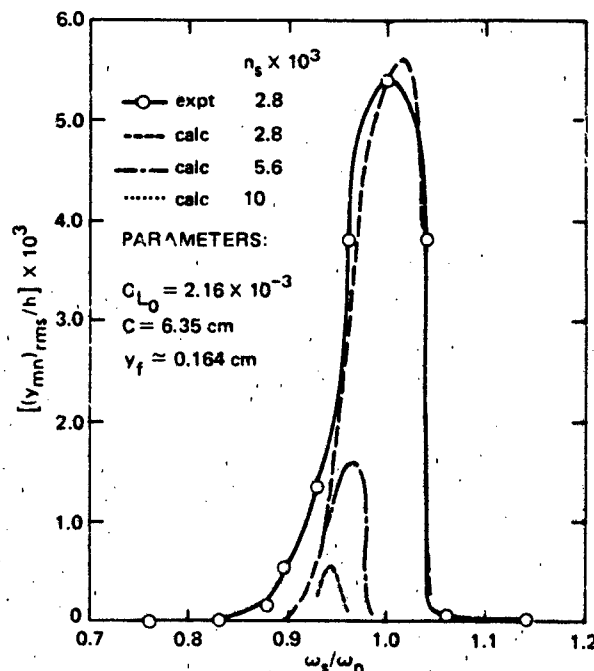


Figure 9.56 - Example of Self-Excited Hydrofoil Vibration
Estimated with the Lift-Oscillator Model¹¹¹

aerodynamic measurements in Figure 9.30 ($\rho U_s / 2\pi q y_f \approx 10^{-2}$ for $R_h = 5 \times 10^3$) and the parameters of the experiment to give $C_{L_0} = 2.2 \times 10^{-5}$. For other applications $C_{L_0}(\omega)$ can be estimated from Equations (9.90) and (9.139) using the parameters in Table 9.3 (p. 969) and Figure 9.30 or for cylinders using the parameters in Chapter 5, Figures 5.15 and 5.18 or Table 5.2. The coefficients $\gamma = 59$ and $b = 1.58$ were determined by trial and error fitting to the measured function $Y_{mn}(\omega)$ v.s. ω_s / ω_{mn} . The subsequent curves were calculated to determine the effect of additional damping. To perform such calculations one needs as initial information the initial damping in the structure which generally lies between 3×10^{-3} and 10^{-2} . The method has been used extensively¹⁸²⁻¹⁸⁴ to estimate the effectiveness of damping cylinders to prevent self-excited vibration (Figure 9.51).

An approach used by Iwan and Blevins¹⁸⁵ and Iwan¹⁸⁶ uses a mathematical model for the unsteady momentum generated in the wake as a power series of time derivatives of the unsteady fluid displacement transverse to the plane of the flow Z . This variable rather than the lift coefficient is used to describe the nonlinear fluid dynamics. The force of the fluid on the cylinder is written (in terms of the variables used in this section) as

$$f(\dot{Z}, \dot{y}) = a \rho_o y_f U_s (\dot{Z} - \dot{y})$$

where $\dot{Z} - \dot{y}$ is the relative velocity between the fluid and the trailing edge (separation points). This force is equal to the rate of momentum transferred to a fluid control volume surrounding the cylinder, determined to be

$$\frac{dM_3}{dt} = \rho_o y_f^2 \omega_s^2 Z - a_1 \rho_o U_s y_f \dot{Z} + a_2 \rho_o \frac{y_f}{U_s} (\dot{Z})^3$$

plus the rate of momentum increase in the control volume

$$\dot{M} = a_o \rho_o y_f^2 \ddot{Z}$$

These definitions are as heuristic as those in the formulation of Hartlen and Currie; they lead inevitably to a nonlinear equation for fluid motion similar to Equation (9.147). However, in this case the problem is set formally along the general lines of the unsteady momentum transfer theory of Section 5.5.

9.8 ILLUSTRATION: ESTIMATION OF RADIATED NOISE FROM A HYDROFOIL

The use of the dimensionless relationships in this chapter for estimating noise from lifting surfaces is illustrated with a specific example. The case considered is somewhat artificial in that the additional radiation from flow-induced vibration is ignored. The hydrofoil illustrated in Figure 9-51 is considered to be translating at a steady velocity into fluid with nearly isotropic turbulence. We require the one-third-octave band levels directly above the hydrofoil. The translation velocity of the fluid with respect to a fixed frame of reference is assumed to be much less than the advance velocity of the hydrofoil. The reader is cautioned that, although a specific quantitative example is given here, it is not in general true that all features of radiated sound may be computed with great precision. Subtleties in viscous flow generation can, as shown in many sections, modify the flow, making prediction difficult. Computations like those shown in this section are valuable in identifying pertinent frequency ranges over which one or another source mechanism should be expected to be important. Their value also lies in setting rough relative orders of magnitude for the various major flow noise sources that may coexist.

The particulars of the hydrofoil shown in Figure 9-57 are:

maximum thickness $h_m \approx 0.1c$, as the NACA 63-009

chord = $C = 0.6$ m

Advance velocity, $U_\infty = 30$ m/s

span = $L_3 = 1.8$ m

Mach number, $M = 0.02$

Acoustic reference range = $R = 1$ m

Trailing edge blunt, thickness, $h = 0.51$ cm

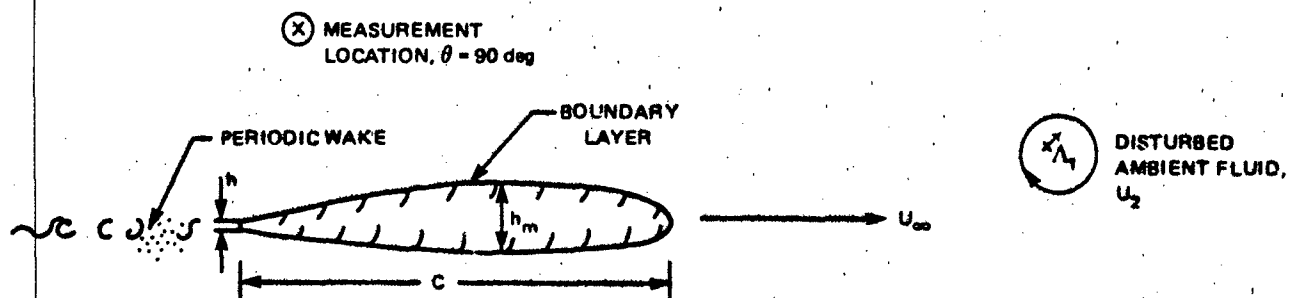


Figure 9.57 - Lifting Surface Advancing into a Disturbed Ambient Fluid

The particulars of the ambient turbulence are

intensity, $\overline{u_2^{1/2}}/U_\infty = 0.02$

macroscales, $\Lambda_1 = 0.25$ m

$\Lambda_3 = 0.25$ m

wave number spectrum:

$$\phi_2(k_1) = \phi_2\left(\frac{\omega}{U_\infty}\right) = \frac{\frac{\Lambda_1}{\pi}}{1 + \left(\frac{\omega\Lambda_1}{U_\infty}\right)^2} \quad \frac{\omega\Lambda_1}{U_\infty} < 10 \quad (9.151a)$$

$$= \frac{\Lambda_1}{\pi} \left(\frac{\omega\Lambda_1}{U_\infty}\right)^{-3} \quad \frac{\omega\Lambda_1}{U_\infty} > 10 \quad (9.151b)$$

The spectrum in Equation (9.151a) fits measured values quite well (reference 148, Chapter 1); the high wave number fall-off in Equation (9.151b) simply accounts for the fact that Equation (9.151a) overestimates measured values when $\omega\Lambda_1/U_\infty > 10$.

All estimations will require the calculation of the dynamic pressure

$$\begin{aligned} q_\infty &= 1/2 \rho_o U_\infty^2 \\ &= 1/2 (10^3 \text{ kg/m}^3) (900 \text{ m}^2/\text{s}^2) \\ &= 4.8 \times 10^{11} \text{ micropascals } (\mu\text{Pa}) \end{aligned}$$

$20 \log q = 234$ reference 1 μPa .

The radiated noise will be calculated for a one-third-octave frequency band; therefore

$$\begin{aligned} \overline{p^2}(R, f, \Delta f) &\approx 2 \phi_{p_{\text{rad}}}(R, \omega) \Delta \omega \\ &\approx \frac{1}{2} \phi_{p_{\text{rad}}}(R, \omega) \omega \end{aligned}$$

The Reynolds numbers appropriate to the hydrofoil are

$$R_c = 18 \times 10^7$$

so that the boundary layer flow is fully turbulent, and

$$R_h = 1.5 \times 10^5$$

Thus the parameters of Table 9.3 and Figure 9.30 will apply to the hydrofoil.

9.8.1 Noise from Inflow Turbulence

The equations appropriate to this calculation are

a. For $\omega C/c < 2\pi$ or $f > 2500$ Hz.

Equation (9.) for the sound pressure level and Equations (9.49) and (9. a) for the unsteady lift spectrum give ($\theta=90$ deg)

$$\overline{p^2}(R, f, \Delta f) = \frac{q_\infty^2 M_\infty^2}{8\pi} \left(\frac{L_3}{r}\right)^2 \cdot \frac{\frac{2\Lambda_3}{L_3}}{1 + \frac{2\pi^2 f C}{U_\infty}} \cdot \left(\frac{2\pi f C}{U_\infty}\right)^2 \frac{\overline{u_2^2}}{U_\infty^2} \frac{\frac{2\pi f \Lambda_1}{U_\infty}}{1 + \left(\frac{2\pi \Lambda_1 f}{U_\infty}\right)^2}$$

b. For $\omega C/c_0 > 2\pi$ or $f > 2500$ Hz.

Equation (9.58) may be used:

$$\overline{p^2}(R, f, \Delta f) =$$

$$\frac{q_\infty^2 M_\infty^2}{8\pi^2} \left(\frac{L_3}{r}\right)^2 \frac{2\Lambda_3}{L_3} \frac{\overline{u_2^2}}{U_\infty} \frac{\left(\frac{2\pi C}{U_\infty}\right)}{\left(\frac{2\pi f C}{U_\infty}\right)^3}$$

However, the limit of $\omega C/2U_\infty$ over which the admittance function has been verified is 10. For an 0.1 thickness to chord ratio of $h_m/C = 0.1$ this limit corresponds to $\omega h_m/U_\infty = 2$. The leading edge noise accordingly cannot be extrapolated into this

range because the aerodynamic functions will be invalidated by the effects of finite thickness. The low-frequency sound levels are thus shown in Figure 9.58 for frequencies less than roughly 200 Hz for $\omega C/c_0 < 1$.

9.8.2 Trailing-Edge Noise

Noise from turbulent flow off the trailing edge is approximated using Figure 9.38 and scaling the levels due to Brooks and Hodgeson to the present parameters in order to compute an upper bound. This noise is expected to be approximated by these data only when $\omega C/c_0 > \pi$. The boundary layer thickness δ is crudely estimated as

$$\delta = 10\theta$$

A lifting surface at zero angle of attack at this Reynolds number is expected to have a boundary-layer growth roughly as that shown in Figure 9.18, which gives

$$\frac{\theta}{C} = 2 \times 10^{-3}$$

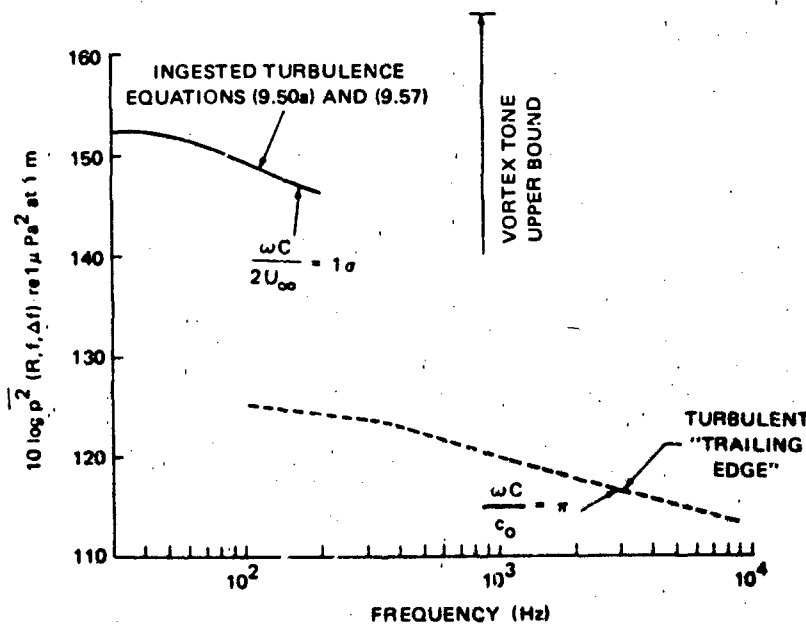


Figure 9.58 - Illustration of Types of Noises and Their Levels Radiated by a Rigid Hydrofoil Moving into Disturbed Water

at the trailing edge. Therefore, since $\delta \approx 1.2$ cm,

$$10 \log \left(\frac{\delta L_3}{R^2} \right) \approx -15$$

Introducing these parameters and using Figure 9.38, the trailing-edge noise is found as the line in Figure 9.58. It was necessary to extrapolate the available data into the required frequency range for frequencies greater than 1 kHz.

9.8.3 Acoustic Tones from Vortex Shedding

First the frequency is calculated from Table 9.3. For the blunt edge on which $\theta/h \ll 1$ and $y_f \approx h$ and $U_s \approx 1.25 U_\infty$, the vortex shedding frequency is given by

$$f = \frac{U_s}{2\pi y_f} = 750 \text{ Hz}$$

An alternative calculation can be made from Gongwer's definition, with which we find

$$f = \left(\frac{U_\infty}{h+2\theta} \right) (0.2) = 800 \text{ Hz}$$

The frequency of the tone is expected to lie between these two estimates. Since $\omega C/c_o > 1$, the radiated noise level of the tone is given by Equation (9.100) (neglecting directivity factors)

$$\overline{p^2} = \frac{1}{32} q_\infty^2 M_\infty^2 \frac{L_3 y_f}{r^2} \left[\left(\frac{\rho_o \Gamma_o U_s}{2\pi q y_f} \right)^2 \frac{U_c}{U_\infty} \left(\frac{2\Lambda_3}{y_f} \right) \right]$$

The ratio of twice the momentum thickness, 2θ , to h is

$$\frac{2\theta}{h} = \frac{2(0.12 \text{ cm})}{0.51} = 0.47$$

which is slightly larger than that of the parent edge, number 7 of Table 9.3 of p. 969.

Therefore the applicable parameters in Table 9.3 p. 969 and Figure 9.30 p. 937 are those for edge numbers 7 and 10 so the term in brackets is

$$\left(\frac{\rho_o \Gamma U_s}{2\pi q y_f} \right)^2 \frac{U_c}{U_\infty} \left(\frac{2\Lambda_3}{y_f} \right) = (0.08)^2 (0.7) (3.7)$$

$$= 0.02$$

the value of Λ_3 for edge 10 is used to adjust for probable reduction spanwise correlation due to the substantial value of $2b/h$. An upper bound to the estimated radiated sound pressure level of the tone is

$$10 \log \overline{p^2} = 234 - 16 - 15 - 20 - 19$$

$$= 164 \text{ re } 1 \mu\text{Pa}$$

This value is indicated by the head of the arrow in Figure 9.58.

9.8.4 Enhancement from Surface Vibration

Vibration of the surface will enhance the radiation by augmenting the trailing-edge forces due to vortex shedding, as seen in Section 9.7.2, as well as contributing to the sound pressure by surface motion. The former will occur at one frequency, while the latter will occur over a continuous range of frequencies.

The added radiation in a broad frequency band due to surface motion will be calculated relative to the direct dipole radiation that was calculated in the last subsection. The calculation is shown for both air and water media in order to illustrate the essential differences in treating problems of flow-induced radiation from surfaces with light and heavy fluid loading. Radiation from the surface is zero in the plane of the surface; it is unbaffled so this requirement is levied by symmetry arguments. The radiated power from multiple modes in the bandwidth $\Delta\omega$ is related to the input power by Equation (6.103); the input power is given by Equation (6.52a). There will be a frequency limit for validity of this relationship which is

$$n(\omega)\Delta\omega \approx n(\omega) \left(\frac{\omega}{4} \right) > 1 \quad (9.152)$$

for one-third-octave bands. To establish this limit for the hydrofoil (with an effective average thickness of $\bar{h} \approx 3/4 h_m$), a limiting frequency is first defined as that for which at least one-half flexural wavelength will fit along the span, i.e.,

$$(\lambda_p)_{\max} = 2L_3$$

and from Equations (6.45) and (6.46a)

$$f_o = \frac{\pi C_L \kappa}{2L_3^2} \approx 37 \text{ Hz}$$

for $C_L = 6100 \text{ m/s}$, $h_m = 0.06 \text{ m}$, and $L_3 = 1.8 \text{ m}$. This is not the fundamental vibration frequency; that frequency depends on both the water loading (added mass) and the boundary conditions, which need not be specified for setting this rough lower bound. Thus resonances may be expected for frequencies above 40 Hz or so and the inequality in Equation (9.152) gives (with Equation (6.47) and neglecting the water loading, which will lower the estimate)

$$n(\omega) \cdot \frac{\omega}{4} \approx \frac{CL_3 f}{2\kappa C_L} > 1$$

or

$$f > \sim 600 \text{ Hz}$$

Above this frequency both $k_p C$ and $k_p L_3 > 1$, so that the mode density of the hydrofoil will be approximated by Equation (6.47). For lower frequencies, the estimates of sound power will be too large in some one-third-octave bands because those bands will not include at least one structural mode.

Therefore the radiated power from structural vibration P_{ST} is given by Equations 5.52a) and (6.103) as

$$P_{ST}(\omega, \Delta\omega) = \frac{\bar{\eta}_{rad}}{\bar{\eta}_{rad} + \bar{\eta}_s} \cdot \frac{\pi \bar{F}_h^2(\omega)}{m_s 4\pi\kappa C_\ell} \quad (9.153)$$

and by analogy to Equation (6.101)

$$\bar{\eta}_r = \beta \bar{\sigma}_r$$

here

$$\beta = \frac{\rho_o C_o}{\rho_p \bar{h}\omega}$$

and

$$\bar{F}_h^2(\omega) = A_o^2 \bar{p}_h^2(\omega)$$

is the mean-square modal force in bandwidth $\Delta\omega$. By Equation (9.144), we have the mean-square modal force

$$\bar{F}_n^2(\omega) = \bar{F}_n^2(\omega) |\psi_{mn}(\vec{y}_e)|^2$$

and, since $|\psi_{mn}(\vec{y}_e)|^2$ may be assumed to be of order unity at the edges,

$$\bar{F}_n^2(\omega) \approx \bar{F}_h^2(\omega)$$

The representative value of the mode shape evaluated at the excitation locations \vec{y}_e is taken to be unity by virtue of the normalization of the function (Equation (6.26)).

The radiated sound power from the direct dipole P_{D1} for which $\omega C/c_0 < 2\pi$, is, from Equation (2.11c) and (9.12),

$$\begin{aligned}
 P_{D1}(\omega) &= \int_0^{2\pi} \int_0^\pi \frac{\overline{p^2}(\omega)}{\rho_0 c_0} r^2 d\theta \cos \theta d\phi \\
 &= \frac{\omega^2 \overline{F_h^2}(\omega)}{(\rho_0 c_0) 8\pi c_0^2} \int_0^\pi \sin^2 \theta \cos \theta d\theta \\
 &= \frac{\omega^2 \overline{F_h^2}(\omega)}{12\pi c_0^2 (\rho_0 c_0)} \quad (9.154)
 \end{aligned}$$

This formula will overestimate the radiated sound by the factor given by Equation (9.59) when $\omega C/c_0 > 2\pi$.

9.8.5 Relative Sound Levels from Surface Motion and Pressures

The required quantity is the ratio of the structural radiation to the direct dipole radiation, which has the general form

$$\frac{P_{ST}}{P_{D1}} \approx 3\pi \frac{\overline{\eta}_{rad}}{\overline{\eta}_{rad} + \overline{\eta}_s} \left(\frac{c_0}{c_p} \right)^2 \quad (9.155)$$

which can be rewritten in terms of the infinite plate impedance

$$\frac{P_{ST}}{P_{D1}} \approx \frac{6}{\pi} \frac{\overline{\eta}_{rad}}{\overline{\eta}_{rad} + \overline{\eta}_s} \cdot \frac{\rho_0 c_0 \lambda_0^2}{R_\infty} \quad (9.156)$$

are, as in Equation (6.52b),

$$R_{\infty} = 8\pi \kappa c_l$$

a property of the bending waves in plates of average thickness \bar{h} .

The equation shows that the balance between the sound power from flow-excited vibration and the flow forces will depend on the damping in the structure, the ratio of the speed of sound in the fluid to the bending wave speed, and the fluid loading factor. Another way of stating this is as a ratio of the radiation damping to the total damping times the ratio of the acoustic impedance to the average plate impedance to a point force. The factor $\rho_o c_o \lambda_o^2$ is the acoustic impedance of the fluid over an area whose dimension is the acoustic wavelength. Equations (9.155) and (9.156) are general for any fluid-structure interaction as long as it may be considered an acoustically compact surface.

These relationships are now used to illustrate the importance of structure-fluid impedance matching for our hydrofoil.

Attention is restricted to the relative importance of radiation and structural damping (the reader can calculate the hydrodynamic damping). Equation (6.87a) gives a simple formula σ_r for unbaffled plates with edge-mode radiation, which can be written*

$$\sigma_r \approx \frac{1}{4} \frac{1}{(k_p L_3)^2} \left(\frac{k_o}{k_p} \right)^2 \quad k_o L_3 > 2\pi \quad \frac{k_o}{k_p} \ll 1$$

which overestimates the radiation efficiency when $k_o L_3 < 2\pi$. Assuming a typical value for $\eta_s \approx 0.01$, the radiation damping will not be important for frequencies such that

$$8\sigma_r < 0.01$$

*Note the change in index notation; L_3 applies to the longer dimension - in this case, the span - and since $k_n > k_m$ is the spanwise wave number, we replace $k_n L_3$ by $k_m L_3$.

For this hydrofoil shape the ratio of the bending wave speed to the acoustic speed in water is

$$\frac{c_p}{c_o} = \frac{k_o}{k_p} = \left(\frac{\omega \kappa c_l}{c_o} \right)^{1/2}$$

$$\approx 0.015 (f)^{1/2}$$

$$< 1 \text{ for } f < 4400 \text{ Hz}$$

and

$$k_p L_3 \approx \left(\frac{\omega}{\kappa C_l} \right)^{1/2} L_3$$

$$= 0.5 (f)^{1/2}$$

so that

$$\sigma_r \approx 10^{-4} (f)^{1/2} \quad f \ll 4400 \text{ Hz}$$

$$\approx 1 \quad f > 4400 \text{ Hz}$$

and

$$\beta = \frac{690}{f}$$

The radiation loss factor is therefore of order

$$\eta_r = 6.9 \times 10^{-2} (f)^{-1/2} \quad f < 4400$$

$$\approx 6.9 \times 10^2 (f)^{-1} \quad f > 4400$$

air, these parameters would be adjusted for the different speed of sound and specific acoustic impedance. The function $\eta_r/(\eta_s + \eta_r)$ is shown graphically in Figure 9.59 for both air and water media. The ratio of structural radiation to total radiation given by

$$\frac{P_{ST}}{P_{DI}} = \frac{\eta_r}{\eta_r + \eta_s} \cdot f^{-2} \cdot \begin{cases} 3 \times 10^7 & \text{water} \\ 3.5 \times 10^2 & \text{air} \end{cases}$$

shown in Figure 9.60.

The sources of radiation in air and water are therefore controlled by different parameters; structural response does not generally play an important role in aero-acoustic excitation problems. Although obtained here for a specific geometry, the result is fairly general. In order for the sound from surface motion to dominate radiated power, the surface density of the structure must be small (to reduce β) damping of the structure must be very light. When the structure is heavily loaded by fluid, the radiated power (in broad-enough frequency bands that include

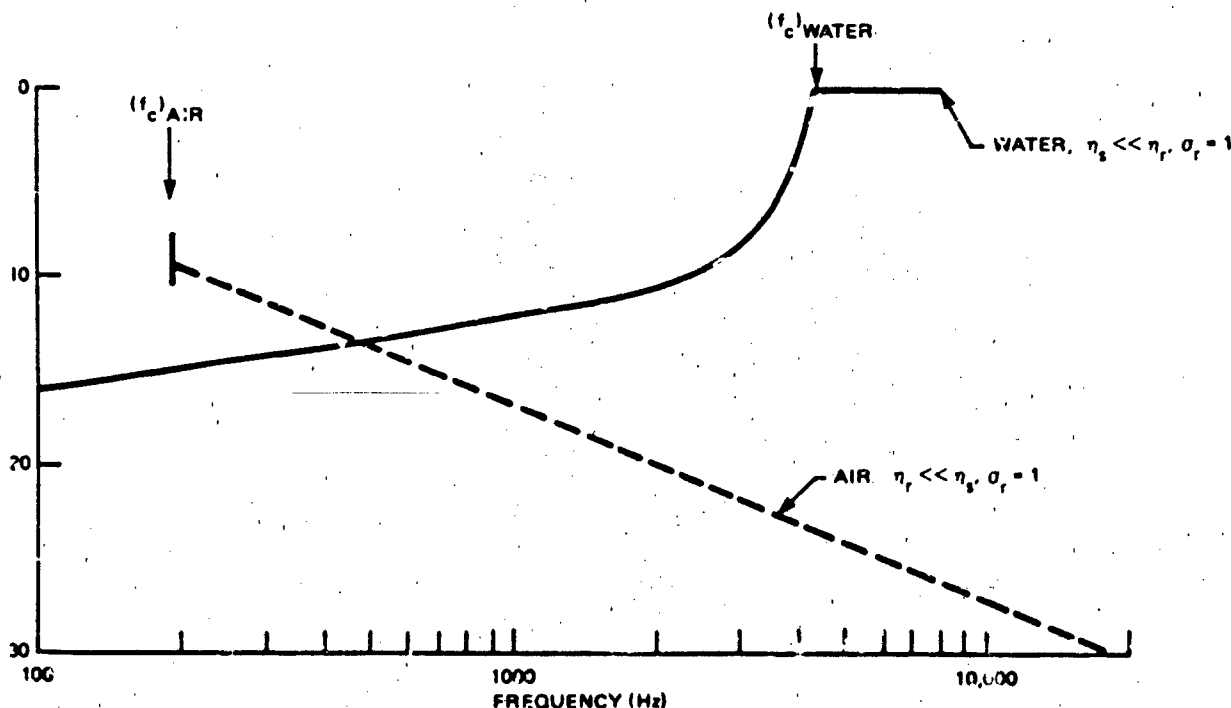


Figure 9.59 - Approximate Ratio of Radiation to Total Loss Factor for A 10% Thickness Hydrofoil, Chord 0.6 m, Span 1.8 m. Radiation Is Assumed To Be Dominated by "Edge" Modes Along the Chord with Spanwise Bending Wavelength Less Than c_0/f . Estimated Acoustic Coincidence Frequency Is f_c

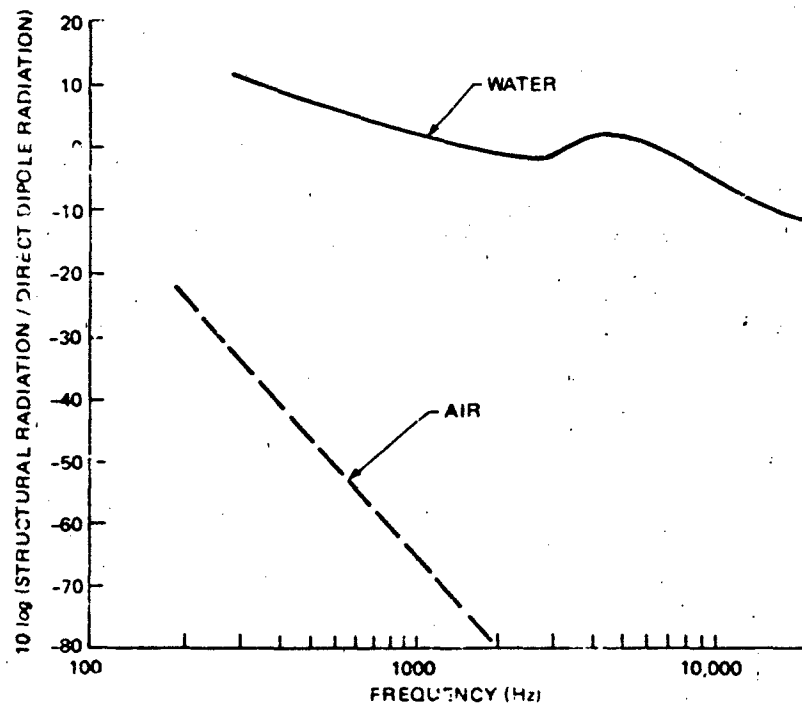


Figure 9.60 - Ratio of Sound Power Radiated by Structural Vibration to that Radiated by Direct Dipole Sound on a Rigid Surface for a 10% Thickness Hydrofoil, Chord 0.6 m, Span 1.8 m

many modes) can be contributed to equally by direct radiation and structural radiation, as in the case of this water-loaded hydrofoil. Only at reasonably large frequencies for which β begins to decrease can one expect the radiated sound power to be dominated by the direct dipole sound. At low frequency, when β is large, the radiated sound can be completely dominated by the excited structural modes.

The example has been worked without regard for such details as modifications of the bending wave speed (c_b) by water loading, boundary conditions on the hydrofoil structure, directivity effects on the sound from structural vibration, and the importance of hydrodynamic damping. These factors would all be taken into account in a second iteration. However, the general results of calculations for air and water media will remain unchanged in the outcome of such an iteration. Other iterations should also reexamine the frequencies less than 600 Hz for which a statistical approach to the structural acoustics is not strictly valid. In those iterations calculations should be performed on a modal basis, account being taken of boundary condition and mode order.

The enhancement of sound by hydroelastic coupling between the vortex street and the hydrofoil is addressed by first computing the damping parameter. At the frequency of 800 Hz, $\eta_s \gg \eta_r$, so that we have

$$\frac{\eta_s m_s C}{\frac{1}{2} \rho_o y_f^2} = \frac{2 \times 10^{-2} (7.7) (0.6)}{(0.8)^2 (0.0051)}$$

$$\approx 30$$

According to Figure 9.44, for this value of the damping parameter, the flow-excited vibration could be enhanced 8 to 15 dB by hydroelastic coupling. This coupling could occur if a resonant mode of the hydrofoil becomes coincident with the vortex-shedding frequency.

Estimations of noise using the formulae in this chapter will rarely give precise absolute values. The value of these estimation procedures is rather their usefulness in scaling noise levels from one hardware design to another. The estimations are of value too in providing rough orders of magnitude of the relative importance of various acoustic sources.

9.9 REFERENCES

1. Olsen, W.A., "Noise Generated by Impingement of Turbulent Flow on Airfoils of Varied Chord, Cylinders, and Other Flow Obstructions," NASA TM X-73464 (1976).
2. Meyers, W.G., "The Effects of Three Trailing Edge Modifications on the Vortex Shedding Frequency and the Lift and Drag Characteristics of an NACA 65A-008 Airfoil," M.S. Thesis, University of Notre Dame (1964).
3. Greenway, M.E. and C.J. Wood, "The Effect of a Beveled Trailing Edge on Vortex Shedding and Vibration," J. Fluid Mech., Vol. 61, pp. 322-335 (1975).
4. Bisplinghoff, R.L. et al., "Aeroelasticity," Addison-Wesley (1955).
5. Newman, J.N., "Marine Hydrodynamics," MIT Press (1977).
6. Powell, A., "On the Aerodynamic Noise of a Rigid Flat Plate Moving at Zero Incidence," J. Acoust. Soc. Am., Vol. 31, pp. 1649-1653 (1959).
7. Ffowcs Williams, J.E. and L.H. Hall, "Aerodynamics Sound Generation by Turbulent Flow in the Vicinity of a Scattering Half-Plane," J. Fluid Mech., Vol. 40, pp. 657-680 (1970).
8. Blake, W.K. et al., "Hydroelastic Variables Influencing Propeller and Hydrofoil Singing," ASME Symposium on Noise and Fluid Engineering, Winter Meeting (Nov 1977).
9. MacDonald, H.M., "A Class of Diffraction Problems," Proc. Lond. Math. Soc. (2), Vol. 14, pp. 410-427 (1915).
10. Crighton, D.G. and F.G. Leppington, "Scattering of Aerodynamic Noise by a Semi-Infinite Compliant Plate," J. Fluid Mech., Vol. 43, pp. 721-736 (1970).
11. Howe, M.S., "Contributions to the Theory of Aerodynamic Sound with Application to Excess Jet Noise and the Theory of the Flute," J. Fluid Mech., Vol. 71, pp. 625-673 (1975).
12. Bowman, J.J. et al., "Electromagnetic and Acoustic Scattering by Simple Shapes," North Holland (1969).
13. Hersh, A.S. and W.C. Meecham, "Sound Directivity Radiated from Small Airfoils," J. Acoust. Soc. Am., Vol. 53, pp. 602-606 (1973).

14. Siddon, T., "Surface Dipole Strength by Cross-Correlation Method," J. Acoust. Soc. Am., Vol. 53, pp. 619-633 (1973).
15. Clark, P.J.F. and H.S. Ribner, "Direct Correlation of Fluctuating Lift With Radiated Sound for an Airfoil in Turbulent Flow," J. Acoust. Soc. Am., Vol. 46, pp. 802-805 (1969).
16. Fink, M.R., "A Method for Calculating Externally Flown Flap Noise," NASA CR2954 (1978).
17. Sevik, M., "Lift in an Oscillating Body of Revolution," AIAA J., Vol. 2, pp. 302-305 (1964).
18. Theodorsen, T., "General Theory of Aerodynamic Instability and the Mechanism of Flutter," NACA Report 496 (1935).
19. Sears, W.R. and T. von Karman, "Airfoil Theory for Non-Uniform Motion," J. Aero. Sci., Vol. 5, pp. 379-390 (1938).
20. Horlock, J.H., "Fluctuating Lift Forces on Airfoils Moving Through Transverse and Chordwise Gusts," Trans. ASME, J. Basic Eng. Ser. D, Vol. 90, pp. 494-500 (1968).
21. Holmes, D.W., "Experimental Pressure Distributions on Airfoils in Transverse and Streamwise Gusts," University of Cambridge, Department of Engineering Report 8-181 CUED/A-Turbo/TR 21, Cambridge, England (1970).
22. Morfey, C.L., "Lift Fluctuations Associated with Unsteady Chordwise Flow Past an Airfoil," Trans. ASME, J. Basic Eng. Ser. D, Vol. 92, pp. 663-669 (1970).
23. Chu, S. and S. Widnall, "Lifting Surface Theory for a Semi-Infinite Wing in Oblique Gust," AIAA J., Vol. 12, pp. 1672-1678 (1974).
24. Howe, M.S., "The Influence of Vortex Shedding on the Generation of Sound by Convected Turbulence," J. Fluid Mech., Vol. 76, pp. 711-740 (1976).
25. Sears, W.R., "Some Aspects of Non-Stationary Airfoil Theory and its Practical Application," J. Aero. Sci., Vol. 18, pp. 104-108 (1940).
26. Abramowitz, M. and I.A. Stegun, "Handbook of Mathematical Functions," Dept. of Commerce, N.B.S. Publication No. 55 (1965).
27. Liepmann, H.W., "On the Application of Statistical Concepts to the Buffeting Problem," J. Aero. Sci., Vol. 19, pp. 793-801 (1952).

28. Reissner, E., "Effect of Finite Span on the Air Load Distribution for Oscillating Wings. I - Aerodynamic Theory of Oscillating Wings of Finite Span," NACA Tech Note 1194 (1947).
29. Reissner, E. and J.E. Stevens, "Effect of Finite Span on the Air Load Distributions for Oscillating Wings. II - Methods of Calculation and Examples of Application," NACA Tech Note 1195 (1947).
30. Mugridge, B.D., "The Generation and Radiation of Acoustic Energy by the Blades of a Subsonic Axial Flow Fan Due to Unsteady Flow Interaction," Ph.D. Thesis. Univ. of Southampton (Jan 1970).
31. Mugridge, B.D., "Sound Radiation from Airfoils in Turbulent Flow," J. Sound Vib., Vol. 13, pp. 362-363 (1970).
32. Filotas, L.T., "Response of an Infinite Wing to an Oblique Sinusoidal Gust: A Generalization of Sears' Problem," Conference on Basic Aerodynamic Noise Research, NASA SP-207, pp. 231-246 (1969).
33. Filotas, L.T., "Theory of Airfoil Response in a Gusty Atmosphere. Part I - Aerodynamic Transfer Function," UTIAS Report 139 (1969).
34. Filotas, L.T., "Theory of Airfoil Response in a Gusty Atmosphere. Part II - Response to Discrete Gusts or Continuous Turbulence," UTIAS Report 141 (1969).
35. Graham, J.M.R., "Lifting Surface Theory for the Problem of an Arbitrarily Yawed Sinusoidal Gust Incident on a Thin Aerofoil in Incompressible Flow," Aero. Quart., Vol. 21, pp. 182-198 (1969).
36. Graham, J.M.R., "Similarity Rules for Thin Aerofoils in Non-Stationary Subsonic Flows," J. Fluid Mech., Vol. 43, pp. 753-766 (1970).
37. Osborne, C., "Unsteady Thin Airfoil Theory for Subsonic Flow," AIAA J., Vol. 11, pp. 205-209 (1973).
38. Chu, S. and S.E. Widnall, "Prediction of Unsteady Airloads Oblique Blade-Gust Interaction in Compressible Flow," AIAA J., Vol. 12, pp. 1228-1235 (1974).
39. Amiet, R.K., "Compressibility Effects in Unsteady Thin Airfoil Theory," AIAA J., Vol. 12, pp. 252-255 (1974).

40. Amiet, R.K., "High Frequency Thin-Airfoil Theory for Subsonic Flow," AIAA J., Vol. 14, pp. 1076-1082 (1976).
41. Adamczyk, J.J., "Passage of a Swept Airfoil Through an Oblique Gust," J. Aircraft, Vol. 11, pp. 281-287 (1974).
42. Kemp, N.H. and G. Homicz, "Approximate Unsteady Thin-Airfoil Theory for Subsonic Flow," AIAA J., Vol. 14, pp. 1083-1089 (1976).
43. Miles, J.W., "On the Compressibility Correction for Subsonic Unsteady Flow," J. Aero. Sci., Vol. 17, p. 181 (1950).
44. Miles, J.W., "Quasi-Stationary Airfoil Theory in Subsonic Compressible Flow," Quart. Appl. Math., Vol. 8, pp. 350-358 (1950).
45. Amiet, R.K., "Airfoil Response to an Incompressible Skewed Gust of Small Spanwise Wave Number," AIAA J., Vol. 14, pp. 541-542 (1976).
46. Fujita, H. and L.S.G. Kovasznay, "Unsteady Lift and Radiated Sound from a Wake Cutting Airfoil," AIAA J., Vol. 12, pp. 1215-1221 (1974).
47. Diederich, F.W., "The Dynamic Response of a Large Airplane to Continuous Random Atmospheric Disturbance," J. Aero. Sci., Vol. 23, pp. 917-930 (1956).
48. Liepmann, H.W., "Extension of the Statistical Approach to Buffeting and Gust Response of Wings of Finite Span," J. Aero. Sci., Vol. 22, pp. 197-200 (1955).
49. Ribner, H.S., "Spectral Theory of Buffeting and Gust Response: Unification and Extension," J. Aero. Sci., Vol. 23, pp. 1075-1077 and 1118 (1956).
50. Miles, J.W., "The Aerodynamic Force on an Airfoil in a Moving Gust," J. Aero. Sci., Vol. 23, pp. 1044-1050 (1956).
51. Verdon, J.M. and R. Steiner, "Response of a Rigid Aircraft to Non-Stationary Atmospheric Turbulence," AIAA J., Vol. 17, pp. 1086-1092 (1973).
52. Jackson, R. et al., "The Lift on a Wing in a Turbulent Flow," Aero. Quart., Vol. 24, pp. 155-166 (1973).
53. McKeough, P.J. and J.M.R. Graham, "The Effect of Mean Loading on the Fluctuating Loads Induced on Airfoils by a Turbulent Stream," Aero. Quart., Vol. 31, pp. 56-69 (1930).

54. Paterson, R.W. and R.K. Amiet, "Noise and Surface Pressure Response of an Airfoil to Incident Turbulence," J. Aircraft, Vol. 14, pp. 729-736 (1977).
55. Paterson, R.W. and R.K. Amiet, "Acoustic Radiation and Surface Pressure Characteristics of an Airfoil Due to Incident Turbulence," NASA CR-2733 (1976).
56. Gradshteyn, I.S. and I.M. Ryzhik, "Table of Integrals Series and Products," Academic Press (1965).
57. Dean, L.W., "Broadband Noise Generation by Airfoils in Turbulent Flow," AIAA Paper 71-587, Palo Alto, Cal. (Jun 1971).
58. Fink, M.R., "Experimental Evaluation of Theories for Trailing Edge and Incidence Fluctuation Noise," AIAA J., Vol. 13, pp. 1472-1477 (1975).
59. Amiet, R.K., "Acoustic Radiation from an Airfoil in a Turbulent Stream," J. Sound Vib., Vol. 41, pp. 407-420 (1975).
60. Fink, M.R., "A Method for Calculating Strut and Splitter Plate Noise in Exit Ducts - Theory and Verification," NASA C.R. 2955 (Mar 1978).
61. Hayden, R.E., "Noise from Interaction of Flow with Rigid Surfaces: A Review of Current Statics of Prediction Techniques," NASA CR 2126 (Oct 1972).
62. Meyer, R.Y., "The Effect of Wakes on the Transient Pressure and Velocity Distribution in Turbomachines," Trans. ASME, Vol. 80, pp. 1544-1552 (1958).
63. Lefort, M.D., "An Investigation into Unsteady Blade Forces in Turbomachines," Trans. ASME, J. Eng. Power, Ser A, Vol. 87, pp. 345-354 (1965).
64. Schlichting, H., "Boundary Layer Theory," McGraw-Hill Book Co. (1979).
65. Abbott, I.H. and A.E. von Doenhoff, "Theory of Wing Selections," Dover (1959).
66. Gault, D.E., "Boundary and Stalling Characteristics of the NACA 63-009 Airfoil Section," NACA Tech Note 1894 (1949).
67. Peterson, R.F., "Boundary Layer and Stalling Characteristics of the NACA 64A-010 Airfoil Section," NACA Tech Note 2235 (1950).
68. von Doenhoff, A.E., "Investigation of the Boundary Layer About a Symmetrical Airfoil in a Wind Tunnel of Low Turbulence," NACA War-time Report L-507 (1940).

69. Huang, T.T. and F.B. Peterson, "Influence of Viscous Effects on Model/Full-Scale Cavitation Scaling," J. Ship Res., Vol. 20, pp. 215-223 (1976).
70. Leibbeck, R.H., "Optimization of Airfoils for Maximum Lift," Aircraft, Vol. 7, pp. 409-415 (1970).
71. Chu, W., "Unsteady Boundary Layer Flow Over an Oscillating Thin Foil," J. Hydronautics, Vol. 2, pp. 93-101 (1968).
72. Stuber, J., "Investigation of Boundary Layers on an Airplane Wing in Free Flight," NACA Tech Memo 751 (1934). Translation of "Untersuchung von Reibungsschichten am fliegenden Flugzeug," Luftfahrtforschung, Vol. 11, p. 26 (1934).
73. Sato, H. and K. Kuriki, "The Mechanism of Transition in the Wake of a Thin Flat Plate Placed Parallel to a Uniform Flow," J. Fluid Mech, Vol. 11, p. 321 (1961).
74. Mattingly, G.E. and W.O. Criminale, "The Stability of an Incompressible Two-Dimensional Wake," J. Fluid Mech., Vol. 51, pp. 233-272 (1972).
75. Chevray, R. and L.S.G. Kovasznay, "Turbulence Measurements in the Wake of a Thin Flat Plate," AIAA J., Vol. 7, pp. 1041-1043 (1969).
76. Paterson, R.W. et al., "Vortex Noise of Isolated Airfoils," J. Aircraft, Vol. 10, pp. 296-302 (1973).
77. Tam, C.K.W., "Discrete Tones of Isolated Airfoils," J. Acoust. Soc. Am., Vol. 55, pp. 1173-1177 (1974).
78. Longhouse, R.E., "Noise Mechanisms in Automotive Cooling Fans," Proc. ASME Symposium on Noise and Fluids Engineering (1977).
79. Archibald, F.S., "The Laminar Boundary Layer Instability Excitation of an Acoustic Resonance," J. Sound Vib., Vol. 38, pp. 387-402 (1975).
80. Fink, M.R., "Fine Structure of Airfoil Tone Frequency," Paper presented at the 95th Meeting of the Acoustical Society of America (1978).
81. Eagleson, P.S. et al., "Turbulence in the Early Wake of a Fixed Flat Plate," M.I.T. Hydrodynamics Laboratory Dept. of Civil Eng., Report 46 (1961).
82. Blake, W.K., "A Statistical Description of Pressure and Velocity Fields at the Trailing Edge of a Flat Strut," NSRDC Report 4241 (1975).

83. Blake, W.K., "Trailing Edge Flow and Aerodynamic Sound. I - Tonal Pressure and Velocity Fluctuations," DTNSRDC Report. 83/113, 1984.
84. Blake, W.K., "Trailing Edge Flow and Aerodynamic Sound. II - Random Disturbances," DTNSRDC Report. 83/113, 1984.
85. Bearman, P.W., "Investigation of the Flow Behind a Two-Dimensional Model with a Blunt Trailing Edge and Fitted with Splitter Plates," J. Fluid Mech., Vol. 21, pp. 241-255 (1965).
86. Seshagiri, B.V., "The Effect of Yaw on the Vortex Shedding Frequency of NACA 65A-008 Airfoil," M.S. Dissertation, Dept. of Aeronautical Engineering, University of Notre Dame (1964).
87. Wood, C.J., "The Effect of Lateral Vibrations on Vortex Shedding from Blunt-Based Aerofoils," J. Sound Vib., Vol. 14, pp. 91-102 (1971).
88. Brooks, T-F. and T.H. Hodgeson, "Trailing Edge Noise Prediction Using Measured Surface Pressures," J. Sound Vib., Vol. 78, pp. 69-117 (1981).
89. Abernathy, F.H. and R.E. Kronauer, "The Formation of Vortex Streets," J. Fluid Mech., Vol. 13, pp. 1-20 (1962).
90. Boldman, D.R. et al., "Vortex Shedding from a Blunt Trailing Edge with Equal and Unequal External Mean Velocities," J. Fluid Mech., Vol. 75, pp. 721-735 (1976).
91. von Karman, T. and H. Rubach, "Uber den Mechanismus des Fluessigkeits und Luftwiderstandes," Phys Ziet, Vol. 13, pp. 49-59 (1912).
92. Lamb, H., "Hydrodynamics," Dover (1945).
93. Cumming, R.A., "A Preliminary Study of Vortex-Induced Propeller Blade Vibrations and Singing," DTMB Report 1838 (Sep 1965).
94. Donaldson, R.M., "Hydraulic Turbine Runner Vibration," Trans. ASME Ser. A., J. Eng. Power, Vol. 78, pp. 1141-1147 (1956).
95. Heskestad, G. and D.R. Olberts, "Influence of Trailing Edge Geometry on Hydraulic-Turbine Blade Vibration," Trans. ASME Ser. A., J. Eng. Power, Vol. 82, pp. 103-110 (1960).
96. Ippen, A.T. et al., "The Hydroelastic Behavior of Flat Plates as Influenced by Trailing Edge Geometry," M.I.T. Hydrodynamics Laboratory, Dept. of Civil Eng., Report 36 (1960).

97. Toebs, G.H. and P.S. Eagleson, "Hydroelastic Vibrations of Flat Plates Related to Trailing Edge Geometry," Trans ASME, J. Basic Eng. Ser. D., Vol. 83, pp. 671-678 (1961).
98. Schaefer, J.W. and S. Eskinazi, "An Analysis of the Vortex Street Generated in a Viscous Fluid," J. Fluid Mech., Vol. 6, pp. 241-260 (1959).
99. Hansen, C.E., "An Investigation of the Near Wake Properties Associated with Periodic Vortex Shedding from Airfoils," M.I.T. Acoustics and Vibration Lab. Rep. 76234-5 (Sep 1970).
100. Mugridge, B.D., "The Generation and Radiation of Acoustic Energy by the Blades of a Subsonic Axial Flow Fan Due to Unsteady Flow Interaction," Ph.D. Thesis, Univ. of Southampton (Jan 1970).
101. Bauer, A.B., "Vortex Shedding from Thin Flat Plates Parallel to the Free Stream," J. Aero. Sci., Vol. 28, pp. 340-341 (1961).
102. Hersh, A.S. and R.E. Hayden, "Aerodynamic Sound Radiation from Lifting Surfaces with and without Leading-Edge Serration," NASA Contr. Rep. CR-114370 (1971).
103. Gongwer, C.A., "A Study of Vanes Singing in Water," Trans. ASME, J. Appl. Mech., Vol. 19, pp. 432-438 (1952).
104. Bearman, P.W., "The Effect of Base Bleed on the Flow Behind a Two-Dimensional Model with a Blunt Trailing Edge," Aero. Quart., Vol. 18, pp. 8-179, 207-224 (1967).
105. Bearman, P.W., "On the Vortex Street Wakes," J. Fluid Mech., Vol. 28, pp. 625-641 (1967).
106. Roshko, A., "On the Drag and Shedding Frequency of Two-Dimensional Bluff Bodies," NACA Tech Note 3969 (1954).
107. Davis, S., "Theory of Discrete Vortex Noise," AIAA J., Vol. 13, pp. 375-380 (1975).
108. Blake, W.K., "A Near-Wake Model for the Aerodynamic Pressures Exerted on Singing Trailing Edges," J. Acoust. Soc. Am., Vol. 60, pp. 594-598 (1976).
109. Howe, M.S., "Aerodynamic Sound Generated by a Slotted Trailing Edge," BBN Tech Memo AS6 (1979).

110. Milne-Thompson, L.M., "Theoretical Hydrodynamics," The Macmillan Co. (1960).
111. Blake, W.K., "Periodic and Random Excitations of Streamlined Structures by Trailing Edge Flows," Proc. 4th Biennial Symposium on Turbulence in Liquids, Rolla, Mo. (Sep 1975).
112. Graham, J.M.R., "The Effect of End Plates on the Two-Dimensionality of a Vortex Wake," Aeronaut. Quart., Vol. 20, pp. 237-247 (1969).
113. Howe, M.S., "The Generation of Sound by Aerodynamic Sources in an Inhomogeneous Steady Flow," J. Fluid Mech., Vol. 67, pp. 597-610 (1975).
114. Clark, L.T., "The Radiation of Sound from an Airfoil Immersed in a Laminar Flow," Trans. ASME, J. Eng. Power Ser. A, Vol. 93, pp. 366-376 (1971).
115. Clark, L.T. et al., "Wake Related Sound Generation from Isolated Airfoils," J. Acoust. Soc. Am., Vol. 59, pp. 24-30 (1976).
116. Kotake, S., "Random Vortex Shedding Noise of Airfoils," J. Sound Vib., Vol. 40, pp. 87-99 (1975).
117. Yudin, E.Y., "On the Vortex Sound from Rotating Rods," Zhurnal Tekhnicheskoi Fiziki, Vol. 14, p. 561 (1944). NACA Tech Memo 1136 (1947).
118. Sunyach, M. et al., "Correlations Between Far Field Acoustic Pressure and Flow Characteristics for a Single Airfoil," NATO AGARD Conference on Noise Mechanisms Paper No. 131.
119. Olsen, W. and A. Karchmer, "Lip Noise Generated by Flow Separation From Nozzle Surfaces," NASA TM-X71859 (1976).
120. Hayden, R.E., "Sound Generation by Turbulent Wall Jet Flow Over a Trailing Edge," M.S. Thesis, Purdue Univ. (1969).
121. Grosche, F.R., "On the Generation of Sound Resulting from the Passage of a Turbulent Air Jet Over a Flat Plate of Finite Dimensions," R.A.E. Library Translation No. 1460 (Oct 1970).
122. Hayden, R.E. et al., "Some Factors Influencing Radiation of Sound from Flow Interaction with Edges of Finite Surfaces," NASA CR-145073 (1976).

123. Scharton, T.D. et al., "A Study of Trailing Edge Blowing as a Means of Reducing Noise Generated by the Interaction of Flow with a Surface," NASA CR-132270 (1973).
124. Olsen, W.A. et al., "Noise Produced by a Small-Scale Externally Blown Flap," NASA TN D-6636 (1972).
125. Olsen, W.A. and D. Boldman, "Preliminary Study of the Effect of the Turbulent Flow Field Around Complex Surfaces on their Acoustic Characteristics," AIAA Paper 78-1123, 11th Fluid and Plasma Dynamics Conference, Seattle, Wash. (1978).
126. Tam, C.K.W. and N.N. Reddy, "Sound Generated in the Vicinity of the Trailing Edge of an Upper Surface Blown Flap," J. Sound Vib., Vol. 52, pp. 211-232 (1977).
127. Olsen, W. et al., "Flap Noise and Aerodynamic Results for Model QCSEE Over-The-Wing Configurations," NASA TM X-73588 (1977).
128. Goodykoontz, J.H. et al., "Effect of Simulated Forward Aerospeed on Small-Scale Model Externally Blown Flap Noise," NASA TN D-8305 (1976).
129. Yu, J.C. and C.K.W. Tam, "An Experimental Investigation of the Trailing-Edge Noise Mechanism," AIAA J., Vol. 16, pp. 1048-1052 (1978).
130. Joshi, M.C., "Acoustic Investigation of Upper Surface Blown Flaps," Ph.D. thesis, Univ. of Tenn. (1977).
131. Kendall, J.M., "Measurements of Noise Produced by Flow Past Lifting Surfaces," AIAA 16th Aerospace Sciences Meeting, paper 78-239 (Jan 1978).
132. Harden, J.C., "On Noise Radiation from the Side Edges of Flaps," AIAA J., Vol. 18, pp. 549-552 (1980).
133. Chase, D.M., "Sound Radiated by Turbulent Flow off a Rigid Half-Plane as Obtained from a Wave Vector Spectrum of Hydrodynamic Pressure," J. Acoust. Soc. Am., Vol. 52, pp. 1011-1023 (1972).
134. Chandiramani, K.L., "Diffraction of Evanescent Waves with Applications to Aerodynamically-Scattered Sound and Radiation from Unbaffled Plates," J. Acoust. Soc. Am., Vol. 55, pp. 19-29 (1974).
135. Chase, D.M., "Noise Radiated from an Edge in Turbulent Flow," AIAA J., Vol. 13, pp. 1041-1047 (1975).

136. Crighton, D.G., "Radiation Properties of the Semi-Infinite Vortex Sheet," Proc. Roy. Soc. Lon., Vol. A330, pp. 185-198 (1972).
137. Crighton, D.G., "Radiation from Vortex Filament Motion Near a Half-Plane," J. Fluid Mech., Vol. 51, pp. 357-362 (1972).
138. Jones, D.S., "Aerodynamic Sound Due to a Source Near a Half-Plane," J. Inst. Math. Appl., Vol. 9, pp. 114-122 (1972).
139. Crighton, D.G. and F.G. Leppington, "Radiation Properties of the Semi-Infinite Vortex Sheet: The Initial-Value Problem," J. Fluid Mech., Vol. 64, pp. 393-414 (1974).
140. Crighton, D.G. and F.G. Leppington, "On the Scattering of Aerodynamic Noise," J. Fluid Mech., Vol. 46, pp. 577-597 (1971).
141. Howe, M.S., "The Effect of Forward Flight on the Diffraction Radiation of a High Speed Jet," J. Sound Vib., Vol. 50, pp. 183-193 (1977).
142. Amiet, R.K., "Noise Due to Turbulent Flow Past a Trailing Edge," J. Sound Vib., Vol. 47, pp. 387-393 (1976).
143. Tam, C.K.W., "Intensity, Spectrum, and Directivity of Turbulent Boundary Layer Noise," J. Acoust. Soc. Am., Vol. 57, pp. 25-34 (1975).
144. Howe, M.S., "A Review of the Theory of Trailing Edge Noise," J. Sound Vib., Vol. 61, pp. 437-465 (1978).
145. Orsag, S.A. and S.C. Crow, "Instability of a Vortex Sheet Leaving a Semi-Infinite Plate," Studies Appl. Math., Vol. 44, pp. 167-181 (1970).
146. Brooks, T.F. and T.H. Hodgeson, "An Experimental Investigation of Trailing Edge Noise," Proc. IUTAM/ICA/AIAA Symposium on Mechanics of Sound Generation in Flows," Springer-Verlag (1979).
147. Schlinker, R.H., "Airfoil Trailing Edge Noise Measurements with a Directional Microphone," Paper 77-1269 AIAA 4th Aeroacoustics Conference, Atlanta, Ga. (1977).
148. Hinze, J.O., "Turbulence," McGraw-Hill Book Co., (1975).
149. Blake, W.K. and L.J. Maga, "On the Flow-Excited Vibrations of Cantilever Struts in Water. I - Flow-Induced Damping and Vibration," J. Acoust. Soc. Am., Vol. 57, pp. 610-625 (1975).

150. Blake, W.K. and L.J. Maga, "On the Flow-Excited Vibrations of Cantilever Struts in Water. II - Surface Pressure Fluctuations and Analytical Predictions," J. Acoust. Soc. Am., Vol. 57, pp. 1448-1464 (1975).
151. Leissa, A.Q., "Vibration of Plates," NACA Report SP-160 (1969).
152. Lawrence, H.R. and E.H. Gerber, "The Aerodynamic Forces on Low Aspect Ratio Wings Oscillating in an Incompressible Flow," J. Aero. Sci., Vol. 19, pp. 769-781 (1952).
153. Laidlaw, W.R. and R.L. Halfman, "Experimental Pressure Distributions in Oscillating Low Aspect Ratio Wings," J. Aero. Sci., Vol. 23, pp. 117-176 (1956).
154. Blake, W.K., "On the Damping of Transverse Motion of Free-Free Beams in Dense, Stagnant Fluids," Shock and Vibration Bulletin, No. 42, Part 4 (Jan 1972).
155. Baken, W.E. et al., "Air Internal Damping of Thin Cantilever Beams," Inst. J. Mech. Sci., Vol. 9, pp. 743-766 (1967).
156. Eagleson et al., "Turbulence in the Early Wake of a Fixed Flat Plate," MIT Hydrodynamics Laboratory Report No. 46 (Feb 1961).
157. Parker, R., "Resonance Effects in Wake Shedding from Parallel Plates: Some Experimental Observations," J. Sound Vib., Vol. 4, pp. 62-72 (1967).
158. Parker, R., "Resonance Effects in Wake Shedding from Parallel Plates: Calculation of Resonant Frequencies," J. Sound Vib., Vol. 5, pp. 330-343 (1967).
159. Parker, R., "Resonance Effects in Wake Shedding from Compressor Blading," J. Sound Vib., Vol. 6, pp. 302-309 (1967).
160. Archibald, F.S., "Self-Excitation of an Acoustic Resonance by Vortex Shedding," J. Sound Vib., Vol. 38 pp. 81-103 (1975).
161. Cumsty, N.A. and D.S. Whitehead, "The Excitation of Acoustic Resonances by Vortex Shedding," J. Sound Vib., Vol. 18, pp. 353-369 (1971).
162. Parker, R. and D. Lhewelyn, "Flow Induced Vibration of Cantilever Mounted Flat Plates in an Enclosed Passage: An Experimental Investigation," J. Sound Vib., Vol. 25, pp. 451-463, (1972).
163. Skop, R.A. and O.M. Griffin, "A Model for the Vortex Excited Resonant Response of Bluff Cylinders," J. Sound Vib., Vol. 27, pp. 225-233 (1973).

164. Jones, G.W., "Unsteady Forces Generated by Vortex Shedding about a Large Stationary and Oscillating Cylinder at High Reynolds Numbers," ASME Paper 68-FE-36 (1968).
165. Bishop, R.E.D. and A.Y. Hassan, "The Lift and Drag Forces on a Circular Cylinder in a Flowing Fluid," Proc. Roy. Soc., Vol. A277, pp. 32-50 (1964).
166. Bishop, R.E.D. and A.Y. Hassan, "The Lift and Drag Forces on a Circular Cylinder in a Flowing Fluid," Proc. Roy. Soc., Vol. A277, pp. 51-75 (1964).
167. Griffin, O.M., "Vortex-Excited Unsteady Forces on Resonantly Vibrating, Bluff Structures," Nav. Res. Lab. Memo 3820 (1978).
168. Toebs, G.H., "The Unsteady Flow and Wake Near an Oscillating Cylinder," Trans. ASME, J. Basic Eng., Vol. 91, pp. 493-505 (1969).
169. Leehy, P. and C.E. Hanson, "Aeolian Tones Associated with Resonant Vibration," J. Sound Vib., Vol. 13, pp. 465-483 (1971).
170. Vickery, B.J. and R.D. Watkins, "Flow Induced Vibrations of Cylindrical Structures," Proc. First Australian Conference on Hydraulics and Fluid Mechanics (1962).
171. Hartlen, R.T. et al., "Vortex Excited Oscillating of a Circular Cylinder," Univ. of Toronto Report UTME-Tr 6809 (Nov 1968).
172. Blevins, R.D. and T.E. Burton, "Fluid Forces Induced by Vortex Shedding," Trans. ASME, J. Fluid Eng., Vol. 98, pp. 19-26 (1976).
173. Burton, T.E. and R.D. Blevins, "Vortex-Shedding Noise from Oscillating Cylinders," Vol. 60, pp. 599-606 (1976).
174. Griffin, O.M. and S.E. Ramberg, "The Effects of Vortex Coherence, Spacing, and Circulation on the Flow-Induced Forces on Vibrating Cables and Bluff Structures," Nav. Res. Lab. Rep. 7945 (1976).
175. Blake, W.K. and L.J. Maga, "Near Wake Structure and Unsteady Pressures at Trailing Edges of Airfoils," Proc. IUTAM/ICA/AIAA Symposium on Mechanics of Sound Generation in Flows, Springer-Verlag (1979).
176. Graham, J.M.R. and D.J. Maull, "The Effects of an Oscillating Flap and an Acoustic Resonance on Vortex Shedding," J. Sound Vib., Vol. 18, pp. 371-380 (1971).

177. Wood, C.S. and S.F.A. Kirmani, "Visualization of Heaving Aerofoil Wakes Including the Effect of Jet Flap," J. Fluid Mech., Vol. 41, pp. 627-640 (1970).
178. Shioiri, J., "An Aspect of the Propeller-Singing Phenomenon as a Self-Excited Oscillation," Stevens Inst. of Tech., Davidson Lab Report R-1059 (1965).
179. Tsakonas, S. and W.R. Jacobs, "Propeller Singing," Stevens Inst. of Tech., Davidson Lab Report R-1353 (1969).
180. Arnold, L. et al., "Propeller Singing Analysis," General Applied Science Laboratories Report No. 221 (1961).
181. Hartlen, R.T. and I.G. Currie, "Lift-Oscillator Model of Vortex Induced Vibration," J. Am. Soc. Civil Eng., J. Eng. Mech. Div. No. EM5, pp. 577-591 (1970).
182. Skop, R.A. and O.M. Griffin, "On a Theory for the Vortex-Excited Oscillations of Flexible Cylindrical Structures," J. Sound Vib., Vol. 41, pp. 263-274 (1975).
183. Griffin, O.M. et al., "The Resonant, Vortex-Excited Vibrations of Structures and Cable Systems," Offshore Technology Conference Paper No. OTC 2319 (May 1975).
184. Griffin, O.M. et al., "The Vortex-Excited Resonant Vibrations of Circular Cylinders," J. Sound Vib., Vol. 31, pp. 235-249 (1973).
185. Iwan, W.D. and R.D. Blevins, "A Model for Vortex-Induced Oscillation of Structures," Trans. ASME, J. Appl. Mech., Vol. 41, pp. 581-586 (1974).
186. Iwan, W.D., "The Vortex Induced Oscillation of Elastic Structural Elements," Trans. ASME, J. Eng. Ind., Ser. B., Vol. 97, pp. 1378-1382 (1975).

CHAPTER 10

NOISE FROM AXIAL-FLOW MACHINERY

10.1 INTRODUCTION

The flow-induced noise sources in turbomachinery are virtually the same as those discussed in previous chapters. The acoustics of rotating machinery are interesting enough to warrant a separate chapter because of the special acoustical considerations brought about by the rotational motion of the blades relative to the acoustic medium; that causes periodic Doppler shifting of far field pressures; the fact that multiple flow excitations may coexist, providing varied spectral quality in different frequency ranges; modifications of blade forces due to interactions of blades in the rotor with each other and with other blade rows; and frequency/wave number matching of the rotor with ingested disturbances and with acoustical modes of enclosures. As pointed out in the introduction to the preceding chapter, noises from rotating vanes can often dominate sound generated by other components of the machine because the vane tips rotate at larger velocities relative to the fluid than any other component. The machinery to which this chapter applies ranges from helicopter blades to automotive cooling fans. Although we discuss specifically axial flow machinery, many of the noise abatement measures are qualitatively applicable to centrifugal machines.

This chapter is limited to noncavitating, subsonic rotor noise. Cavitation noise of propellers is discussed in Chapter 4; noise from supersonic tips is beyond the scope of this book. The restriction to subsonic tip speeds greatly simplifies the mathematical treatment of rotor noise, but it does not severely restrict either the fundamentals of the subject or many of its practical applications. In this chapter we examine the important acoustic particulars of rotor systems and then apply various elements of the preceding chapters to facilitate estimates of radiated sound. Here, as before, we shall in due course distinguish between the outright prediction of levels and the development of a methodology for test planning and model scaling.

Survey papers on noise from turbomachinery appear from time to time; among the most notable are those of Sharland,¹ Mugridge and Morfey,² Morfey,^{3,4} Cumpsty,⁵ Wright,⁶ and Niese,⁷ with that of Cumpsty being particularly incisive. Extensive treatments of the theoretical acoustics of fans either in ducts or in the free field have been given by Morse and Ingard⁸ and by Goldstein.⁹ A recent review of broad band noise sources of rotor blades has been published by Schlinker and Brooks.¹⁵¹

This chapter first examines the fundamental characteristics of unsteady loads and the noise of rotating vanes that arises by virtue of geometry and rotational symmetry. Section 10.3 discusses the important performance features of rotating machinery, for these must occasionally compete with noise control measures. The theoretical aspects of free-field rotor noise are discussed in Section 10.4; examples of measured noises and schemes for their prediction or control are given in Section 10.5. Section 10.6 covers the methodology for estimating unsteady interaction forces, and section 10.7 examines the fundamental acoustics of ducted rotors.

This chapter does not consider separately noises from propellers, fans, helicopters, etc. Rather, it is organized phenomenologically to consider the general lifting surface powering, blade (vane) interactions, and viscous flow (self) noise. Application of each noise-producing phenomenon is made by drawing on available noise data for one rotor configuration or another.

10.2 ELEMENTARY ACOUSTICS OF ROTATING MACHINERY

10.2.1 Sources of Noise

The sources of sounds from rotors, either used as single elements (propellers, fans, and helicopters) or in combination with other fixed or moving vane arrangements in compound machinery (turbines, turbofans, and the like), may be usefully separated into two classes: interaction noise and self-noise. Interaction noise refers to all sounds that result from the encounter of a rotating blade by a time-varying disturbance in a frame of reference moving with the blade element. For purposes of clarity, note that two frames of reference may be profitably identified, one moving with the blades, the other moving with the axial flow machine (i.e., fixed with stators, guide vanes).^{*} Recall, for example, Figure 9.16, which shows the time-varying loads and noise from a lifting surface as induced by an incident wake.

Self-noise refers to sounds resulting from the flow over the blades themselves and requiring no unsteady inflow. Self-noise is generally due to viscous flow over the blades, while interaction noise is generally regarded as due to the potential reaction of the blades to local alternating angle of attack. The two types of noise

^{*}A third frame of reference fixed with the acoustic medium can also be important in cases involving high-speed flight.

are often mutually independent, although some changes in viscous flow can be effected by inflow unsteadiness. A form of self-noise arising from potential blade flow is so-called Gutin noise (named for the first investigator who quantified its level),¹⁰ which occurs at multiples of the blade passage frequency. Gutin noise, which is proportional to the steady loading on the rotor, is generally important at nearly sonic tip speeds and small blade numbers. This noise results from the fact that although the forces on blade elements are steady in a frame of reference moving with the blade, the force is unsteady with respect to the acoustic medium because of the rotation of the blades. The measure of acoustic radiation efficiency for this source is the ratio of the acoustic propagation time between blades to the rotation time between blades, which is the rotational Mach number.

Important causes of interaction noise are

1. rotor-stator interaction in compound turbomachinery,
2. blade-to-blade tip vortex interaction (blade slap in helicopter acoustics) caused by flow across the rotor axis that forces a tip vortex of a forward blade to be overtaken by a following blade,
3. inlet flow disturbances caused by secondary vortical flows and large scale turbulence of forward stators, rotors, and grilles,
4. interaction of rotor blading with annular boundary layers as in ducted rotors.

The causes of self-noise are

1. the passage of blade boundary layer turbulence past trailing edge,
2. laminar separation at any point on the rotor causing unsteady blade pressures and, in aggravated state, lift breakdown,
3. laminar vortex development in the trailing edge wake,
4. periodic vortex development in wakes of blunt trailing edges,
5. rotation (Gutin) noise due to steady thrust and torque,
6. noise due to the finite thickness of the blade section (high speed only $M > 1$).

In all types of flow excitation, the elasticity of the blades can be important. Especially where trailing edge vortex shedding is concerned (laminar or turbulent types), hydroelastic interaction will give rise to rotor blade singing, and all the principles of Chapter 9 apply. The resulting acoustical tone will often appear at a fundamental frequency of the shedding, $f_s \gg \Omega B$, with side bands spaced around $f = f_s$ at intervals of ΩB .

Figure 10.1 shows many characteristics of rotor noise for the case of a helicopter rotor developing varying thrust magnitudes. The data are those of Leverton,¹¹ and the illustration is taken from Wright.⁶ At low frequencies are tones at multiples (m) of the blade passage frequency; these are identifiable in Figure 10.1d to the $m = 25$ harmonic. Expected levels of Gutin sound, caused by the rotation of the lift vector on the blades, would occur at the levels denoted by the envelopes $s = 0$. Observed noise levels in this frequency range exceed the expected rotational noise, especially at higher harmonics and negligible thrust. Interaction noise, indicated by the scalloped envelopes, is due to the transient interaction of the blade with the tip vortices of adjacent blades. This interaction is most prominent when there is no thrust and therefore little axial mean flow through the rotor disk. This axial flow will force the tip vortices into a helix (see Figure 4.44b) away from the rotor. It should be noted that the rotor in this case is held

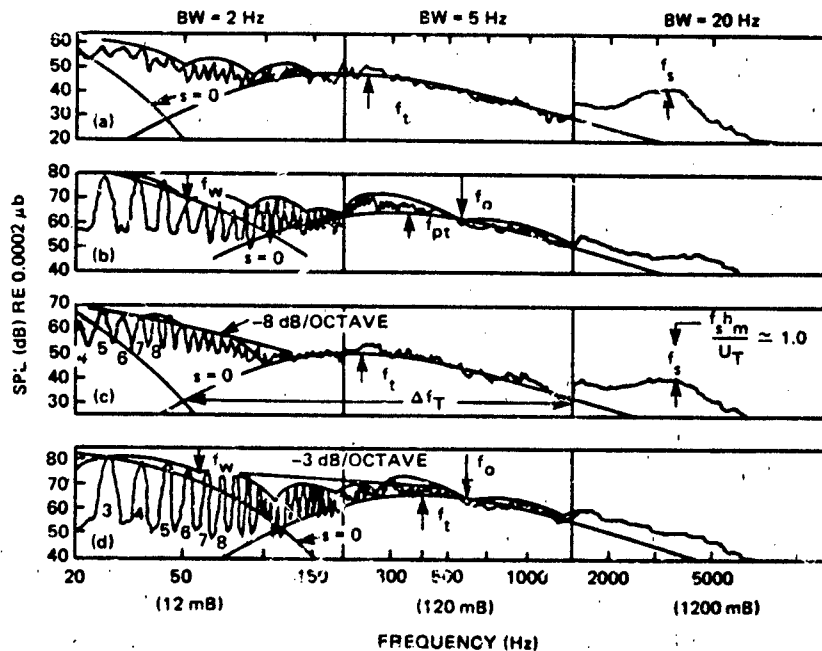


Figure 10.1 - Noise from a 55-ft Helicopter Rotor on a Whirl Tower
(Adopted by Wright⁶ from Measurements of Leverton.¹¹)
Rotor Type: S 55, NACA 0012 Section, $C = 16$ in, $R = 250$ ft, $B = 2$,
Measurement Position 11.5 deg Off Rotor Plane.
(a) $U_T = 465$ ft/sec, $n_s = 2.6$ rps, $T = 0$ lbf; (b) $U_T = 760$ ft/sec,
 $n_s = 4.3$ rps, $T = 0$ lbf; (c) $U_T = 465$ ft/sec, $n_s = 2.6$ rps,
 $T = 3000$ lbf; (d) $U_T = 760$ ft/sec, $n_s = 4.3$ rps, $T = 5000$ lbf.
 $f_{3h_m}/U_T \approx 1.0$, $f_t C/U_T \approx 0.7$, $\Delta f_T/f_t \approx 6$, BW = Filter Bandwidth
(Copyright Academic Press)

in a whirl tower. The blade interactions resemble those of hovering rather than translating craft. The level and general frequency dependence of the scalloped envelope of the interaction noise is determined by the impulsive nature of the interaction, while the frequency interval between scallops is determined by the fraction of the circumference $2\pi R$ during which the impulse occurs. This type of noise is discussed in Section 10.5.

Two forms of broadband noise are visible. The broad hump centered on $f = f_t$ occurs in many rotor signatures, and it has been attributed to turbulent flow over the blades^{6,11-13}; it has also been attributed to interaction of blades with turbulent wakes of other blades.¹⁴ Elsewhere⁴ noise in this frequency range has been attributed to some stalling of blade sections. Competing empirical correlations of this noise with performance parameters of rotors for a wide variety of axial flow machinery,⁶ and for helicopters specifically,¹² have shown a general increase in these broadband noise levels as either the total thrust or the effective blade pitch increases. This correlation would seem to be at least in line with Morfey's¹⁴ suggestion that blade stalling or some other form of turbulent boundary-layer thickening on the blades could enhance these levels. At much larger frequencies, near f_s , both broadband noise and tones have been observed. These noises are trailing-edge flow noises, much like those discussed in Chapter 9, Sections 9.5 and 9.6.2. Both sources of broadband noise are more fully discussed in Section 10.5.

10.2.2 The Tonal Spectrum of Compressor Noise

Many of the important characteristics of the tonal quality of noises from rotating machinery can be determined simply from the kinematics of the blade interactions. Such qualitative arguments were applied in many of the earlier analyses of noise spectra, e.g., by Griffiths¹⁵ and Cumsty.¹⁶ The general qualities of rotor-stator (or of rotor-rotor) interaction noises may be regarded as a circumferential spatial filtering in which samples of wake harmonics from the upstream components are made at integer multiples of the downstream blade number. Readers already familiar with Chapter 7 will recognize this behavior as much like the sampling of turbulent pressures by a wave vector filter. We consider here only the generalities; in Section 10.6 the details are developed. In the frame of reference rotating with the rotor blades, the inflow is viewed as spinning at the rotational speed of the rotor. The response of each blade to the unsteadiness is given by the airfoil admittance function times the intensity of the incident disturbance. The

discrete spatial filtering comes about from the scanning of the inflow by the blade array, as illustrated in Figure 10.2. At low tip Mach numbers, the acoustic signal emitted will be proportional to a summation of the responses of the individual blades with time delays (or relative phases) given by the ratio of the blade spacing to the wavelength of the sound emitted. At low enough Mach numbers the wavelength of the sound is larger than the rotor circumference; then the rotor acts simply as a summing device which gives the resultant sound proportional to the force components (thrust and torque) induced on the rotor. From the theory of the wave vector filter, we expect a maximum summed response to all circumferential wavelengths which are integral numbers of the blade spacing; the wave number filtering bandwidth for a fixed filter wavelength of $2\pi R/B$ will be inversely proportional to the radius of the rotor (i.e., to the total length of the "array" of sensing elements). Because the disturbances are convected past the blade array at speeds of the same order as the tangential velocity of the blades, the frequency spectrum of the resultant response of the rotor blade system (i.e., the summed blade forces) will display humps at frequencies coincident with the peripheral acceptance wave numbers of the blading times the circumferential velocity of the blades.

Figure 10.2 illustrates the response of an eight-bladed rotor to an inflow composed of a steady (16 cycle) wake on which is superimposed a continuous random velocity component. For now, we consider only the velocity in the direction normal to the blade surface, i.e., nearly axial. The linear blade response, which is directly proportional to the magnitude of this nonuniform axial velocity, is as shown in Figure 10.2a. The dotted line for blade response qualitatively expresses an averaging of the peripheral wave over a blade chord. Thus the sum response of all B blades will be important only at nearly discrete values of $k_0 R = mB$. Note that there will be a similar response function at all radii; however, if C is proportional to the radius and the blades are radial, then the rotor acceptance function will be in phase and of the same dimensionless magnitude at all radii. The inflow spins at a peripheral velocity $U_c = \Omega R$ relative to the blades. This is illustrated in both the wave number frequency domain and the space-time domain in Figure 10.2b. If the spatial pattern does not change during the rotation of one circumference, then the spectrum function has values only on the line $\omega = U_c k$. Any change in the spatial pattern will cause this function to be less concentrated,

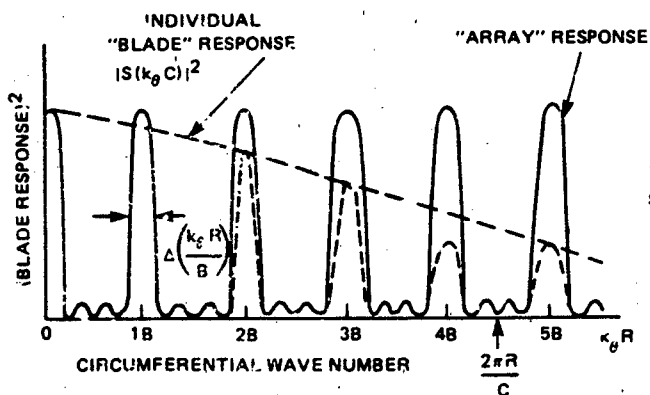


Figure 10.2a - Rotor Acceptance Function
 $\Delta(k_0 R/B) = YB$

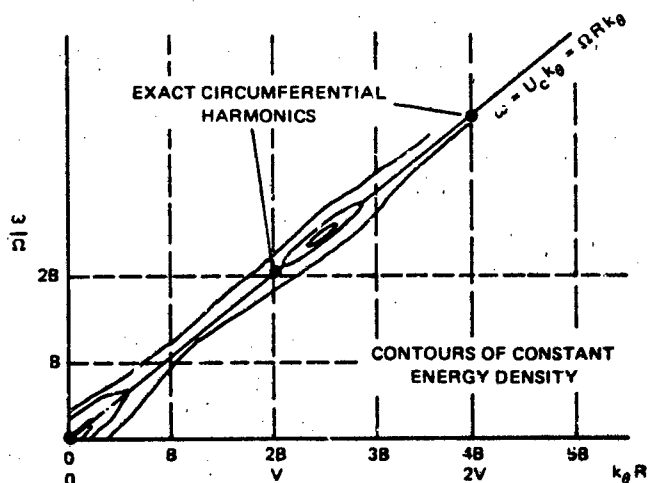


Figure 10.2b - Energy Density of Inflow

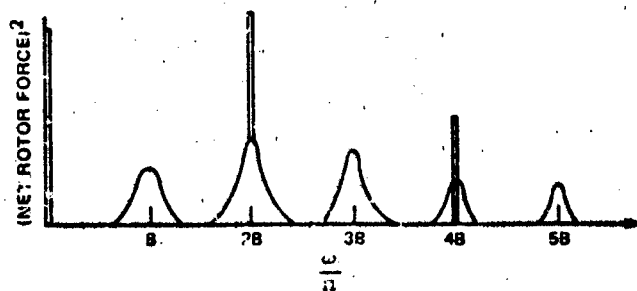
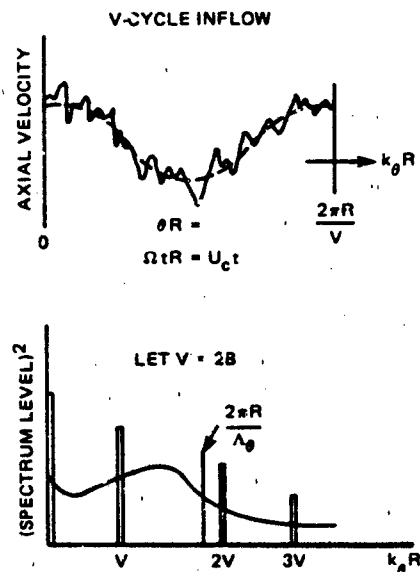


Figure 10.2c - Force Response of Blade Array

Figure 10.2 - Interpretation of a Rotor Response to Inflow Nonuniformity as a Filter Responding to a Signal Plus Noise. Turbulence Acts As Noise Because It Is Broadband and Because Its Macroscale Is Larger Than a Blade Spacing

as shown. At the right is illustrated the variation of axial velocity around that portion of the rotor circumference between adjacent blade centers. The periodic component repeats for V successive intervals around the circumference $2\pi R$, but the superimposed random component does not. Because of the relative rotational motion, the pattern convects past the blades at speed ΩR . The energy density, distributed over both wave number and frequency, is shown at the left and lower right of Figure 10.2b. Because of the rotation, contours of constant energy density are rotated on to the "convection" line, $\omega = (\Omega R)k_\theta$.^{*} In correspondence with the pattern on the right, the discrete energy is concentrated near $Rk_\theta = 0$ (the steady flow component) and near $Rk_\theta = 2B, 4B$, etc. (for a $V=2B$ -cycle component). These two components are essentially delta functions at the respective wave numbers. In the case of two interacting rotors (reference 16), the interaction tones for the unsteady axial shaft loads will occur at frequencies $\omega = n_1 B_1 \Omega_1 \pm n_2 B_2 \Omega_2$ where subscripts 1 and 2 refer to the upstream and downstream rotors, and n_1 and n_2 are the respective circumferential mode orders 0,1,2,3...etc.

As in other areas of turbulence theory (Chapters 3 and 7), the random inflow velocity intensity is continuously distributed along the $\omega = (\Omega R)k_\theta$ line out to wave number $k_\theta R = 2\pi R/\Lambda_\theta$, where Λ_θ is the circumferential macroscale of the ingested turbulence. For fixed frequency and varying wave number, the spectrum drops off rapidly because of the nearly frozen convection. At a given frequency, the force output of the rotor is the sum of responses of the individual $k_\theta R = B, 2B, 3B$, etc., lobes of the spatial filtering. The net force squared, however, is an arithmetic sum of the individual contributions squared of each mB lobe. A frequency spectrum of the total mean-square force on the rotor will reflect these separate lobes if the bandwidth of the exciting spectrum $(\Delta k_\theta)R$, is less than the response lobe spacing B . In this case Λ_θ must exceed $2\pi R/B$. Assuming that this is the case, the frequency spectrum will display humps corresponding to the continuous wave number spectrum of the inflow intersecting with the humps of the wave number acceptances of the rotor around $Rk_\theta = \omega/\Omega$. In other words,

(Mean-square force at ω) =

$$\int_{-\infty}^{\infty} (\text{Wave number spectrum of intensity component at } k_\theta) \cdot (\text{Response of rotor at } k_\theta) \cdot \delta(\omega - \Omega R k_\theta) dk_\theta$$

^{*}Here and in the following, θ ideally lies in the flow helix of the blades, but for low-pitch devices it may be approximated to lie in the plane of the rotor.

where $\delta(\omega - \Omega R k_\theta)$ expresses the frozen convection of the turbulence over a blade element. Tones appear in the force spectrum when the wavelength of a periodic component corresponds with a rotor acceptance wave number $Rk_\theta = mB$. The shapes of the humps in response to turbulence will be determined by the rotor filtering function if $k_\theta R < 1/E$ (or $\Lambda_\theta > 2\pi BR$). On the other hand, if the turbulent excitation is such that it is not convected in nearly frozen pattern across the blades (i.e., the blades respond nearly independently), then the spectrum will be not so well concentrated along $k_\theta R = \omega/\Omega$ and individual lobes of the spatial response will be less distinguishable. The summed response will then yield a frequency spectrum of the force which will be more or less broadband. That is, each blade will respond independently of adjacent blades. This, of course, is also the case in the general class of viscous-flow-induced self-noise in which the blades are excited separately.

The translation of these notions to the problem of acoustic radiation is trivial only in the case of compact rotors, i.e., at those frequencies for which $\omega(2\pi R_T)/c_0 \ll 1$. As stated above, the radiated sound then emanates directly from the resultant alternating rotor force acting on the fluid in exactly the same fashion as that considered in Chapter 5 leading to Equation (5.51). At higher frequencies or tip Mach numbers, since $\omega R_T/c_0 = mB\Omega R_T/c_0 = mBU_T/c_0$, the blades around the rotor circumference are not in the same acoustic phase and the resulting radiated sound will occur at successive blade harmonics because of the relative motion of forces on each blade with respect to the acoustic medium. In fact, even in the absence of inflow nonuniformity, we have already stated that the steady force rotating in the acoustic medium will radiate Guitin sound (see also Section 10.4). For the discussion below, we continue to consider the blade tip Mach number as small enough to validly restrict considerations only to the resultant rotor force.

10.2.3 Elementary Considerations for the Control of Interaction Noise

Many characteristics of interaction noise have little to do with blade design, but rather with spatial matching of the rotor geometry and the inflow geometry. Several of these characteristics and the implications they bear on noise abatement are now examined briefly using the notions of Figure 10.2 at least for the lower-order blade harmonics for which we have both $nBC/R \ll 2\pi$ (according to Figure 10.2a) and $nBC/R \ll 1/M_T$ (ensuring linear, incompressible blade response to inflow disturbances) as well as $M_T \ll 1$. The response of any rotor will involve the relationship between its acceptance function (already described) and the circumferential

de decomposition of the inflow, discussed below. Although the general comments low are directed at axial flow machinery, many concepts can be applied to centrifugal fans. Figure 10.3 illustrates several spatial patterns as well as their associated circumferential wave number decompositions.* If, as presumed, the chord the blade is much smaller than the blade spacing for the first n harmonics, i.e., $< 2 R/C$, then the rotor acoustic response simply matches the array response. Since the array response is itself only a function of the rotor geometry, the response of the rotor comes down to evaluating the geometrical similarities between the rotor and the inflow as manifested in the respective circumferential wave number spectra.

The four wave number spectra shown in Figure 10.3 illustrate some important general characteristics of circumferentially varying inflows. Figures 10.3a and b apply to V identical periodic pulses around the circumference. These cause a series of discrete tones at wave numbers nV whose amplitudes are determined by the shape of the pulse. The more narrow the pulse, the more high wave number tones. Whenever there is an overlap of any mB response lobe with an nV inflow harmonic there will be a resultant force tone at frequency $\omega = mB\Omega$. Figure 10.3c shows that circumferential amplitude modulation of the fundamental V cycle pulse train results in side-band harmonics at intervals S about each nV tone. The envelope of the tone levels is still governed by the pulse shape, but the amplitude of each side band bears a ratio α_m with the fundamental, where $\alpha_s \cos s\theta$ ($\alpha_s < 1, \alpha_0 = 1$) describes the s th circumferential modulation mode. Figure 10.3d is a gated noise so that a random noise is generated V times per revolution. As long as the wave number spectrum of the individual noise pulse, $F_0(k_\theta)$, is narrower than V , the noise pulse can be seen to repeat every $\Delta k_\theta = V$. The envelope of the repetition is determined by the gating function. In the example, this gating function is a rectangular pulse. For larger bandwidths of $F_0(k_\theta)$, the repeated wave number spectra overlap so that the resultant spectrum is broadband. A further point to be noted from Figure 10.3 is that the first three examples show deterministic variations which give rise to discrete wave numbers nV , while the fourth example involves random variation for which the spectrum is continuous. In the last case the phases between successive pulses are

*The analytical methods for making this decomposition, as well as the formal applications for blade response, are examined in Sections 10.4 and 10.6.

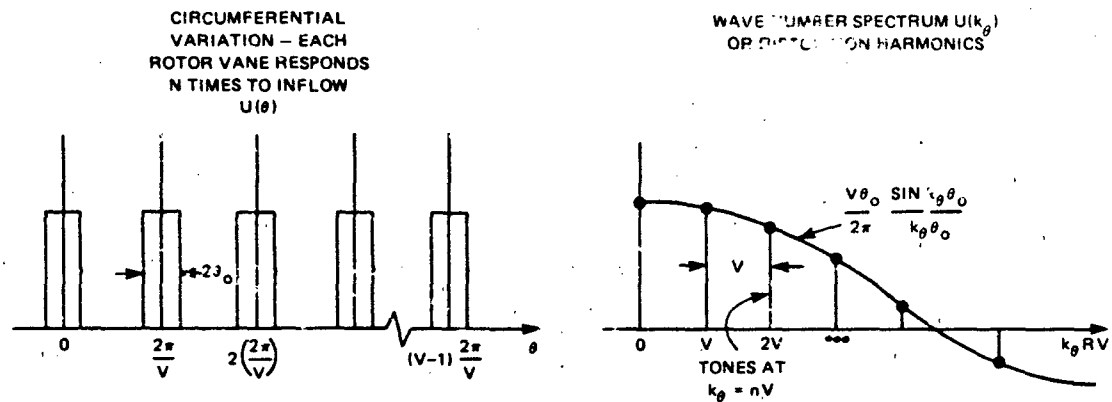


Figure 10.3a - Pulse Train

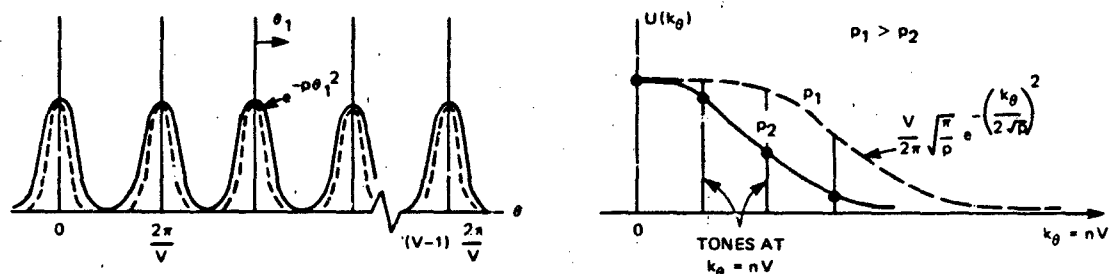


Figure 10.3b - Train of Wave Defects

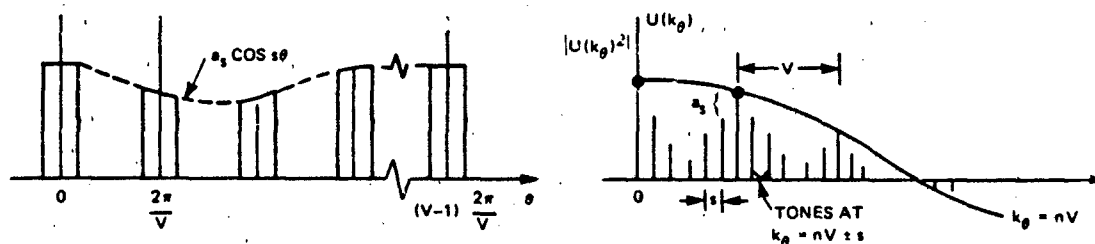


Figure 10.3c - Modulated Pulse Train

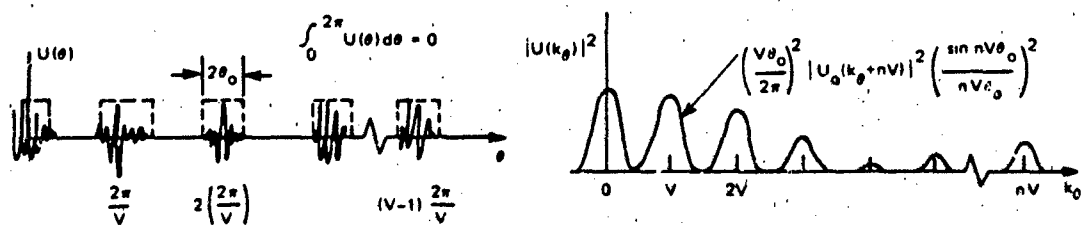


Figure 10.3d - Gated Noise

Figure 10.3 - Illustrations of Circumferential Wave Number Spectra for Repeated Signals. Angles θ Run from 0 to 2π ; Wave Numbers k_θ and Indices n Run from $-\infty$ to ∞

random so that it makes sense only to represent the amplitude squared of the spectrum function.

The most basic noise control prospect for axial flow fans to be seen from Figure 10.3 is that it is well to mismatch the number of rotor blades B and the number of inflow pulses V because a net axial force can only be generated when $mB = nV$. When circumferential modulation occurs, correspondence between mB and modes $nV \pm s$ is possible even though $nV \neq mB$. Any randomization of the pulses, for example, because of stator wake turbulence, will cause broadening of the circumferential spectrum, and overlap between mB acceptance regions and nN spectra is possible.

We have suggested that the envelope of the resultant force spectrum (at low Mach numbers so we can ignore acoustical complications) reflects the inflow circumferential wave number spectrum. Thus scalloped envelopes have been drawn over the low-frequency parts of the spectra in Figure 10.1 following an assumption that the circumferential blade loading occurs from nearly step-like pulses on each blade once per revolution; the loading has a characteristic frequency f_w corresponding to

$$2\pi f_w = mB\Omega = nV\Omega = \frac{\pi}{\theta_w} \Omega$$

where θ_w is the apparent angular width of the pulse ($\theta_w \approx 0.07(2\pi)$). Even though the frequencies f_w are not known a priori, the envelope is cusped in intervals f_w to match the apparent pattern of the blade passage harmonics at $\omega = mB\Omega$. Otherwise the magnitude of the envelope is just drawn to match the spectrum.

A second technique of noise control utilizes the fact that the net rotor force (and low Mach number noise) depends on the superposition of net circumferential loads at various radial elements. It has been assumed here that both the inflow and the blades are co-linear, as illustrated in Figure 10.4. As shown, the blades intersect the inflow disturbance in phase along the leading edge. In Figure 10.4b the blades are shown swept compared with the inflow disturbances so that, relative to the blade, the disturbance appears as an oblique gust. As given by linear unsteady airfoil theory (Equation (9.44)), the pressure response of a blade section at radius R to an oblique gust relative to a normal gust is in the ratio of

$$e^{ik_0^R \cos \theta_s}$$

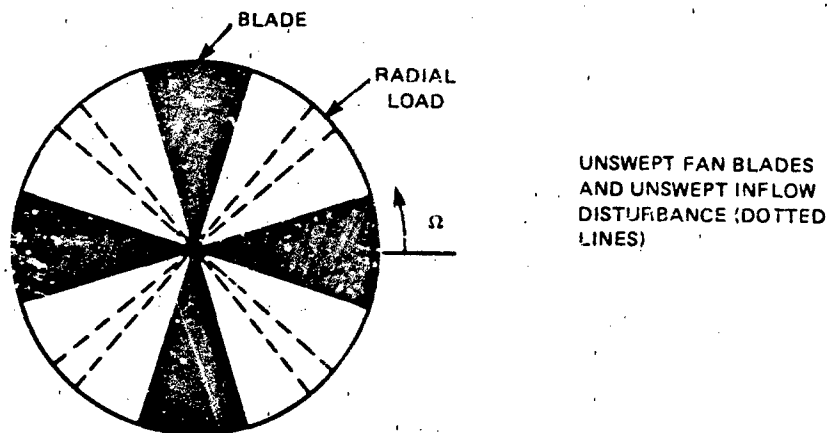


Figure 10.4a - Unswept Blades

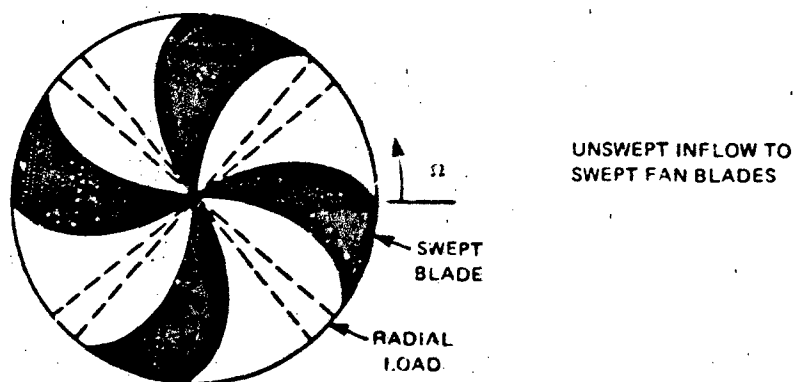


Figure 10.4b - Swept Blades

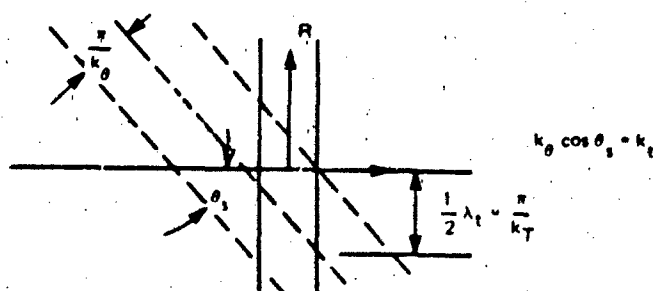


Figure 10.4c - Trace Wave Number

Figure 10.4 - The Geometries of Swept and Unswept Rotor Vanes

where k_θ is the circumferential wave number of the incident gust, R is the radius corresponding to the spanwise coordinate, and θ_s is the sweep (or yaw) angle. Therefore the total unsteady load response L_T of the swept blade relative to the radial blade will be

$$L_T = \int_{R_H}^{R_T} \left(\frac{dL}{dR} \right)_s \cdot e^{ik_\theta R \cos \theta_s(R)} dR$$

versus

$$L_T = \int_{R_H}^{R_T} \left(\frac{dL}{dR} \right) dR$$

where dL/dR and $(dL/dR)_s$ are the radial unsteady load distribution for the unswept and swept blades and R_H and R_T are the hub and tip radii, respectively. Since dL/dR generally increases as the local tangential velocity (ΩR) times the disturbance u

$$\frac{dL}{dR} \approx \rho_o (\Omega R) u C S_{2D}(k_\theta R \cos \theta_s, k_\theta R \sin \theta_s)$$

(where ρ_o is the fluid density and C is the local chord), and $S_{2D}(k_1, k_3)$ is the surface response function. For the current qualitative discussion, for small sweep we may consider $|S_{2D}(k_1, k_3)| \leq S_e |(k_1, 0)|$. The above integrals are weighted to the tips of the rotors due to the ΩR factor. Thus sweep at the tips of rotors has traditionally been an effective noise control measure (e.g., references 17 and 18) in axial flow machines. (In centrifugal fans dL/dR is roughly constant along the vanes so that constant sweep angles have been found effective.⁷)

A third noise control measure, effective in quieting automotive fans, utilizes unequal blade spacings. By this measure the array response in Figure 10.2c smooths out for $k_\theta R > 0$. Thus the annoying tones at harmonics of blade passage frequency are replaced by a more broadband noise because of the smoothing of the response lobes. Unequal spacing will result in broader, lower level admittance humps spaced at integral multiples of the average blade spacing.

A fourth noise control measure, not obvious from Figure 10.2, is to reduce the individual gust response of the blade section. This has been done by allowing fluid bleeding from one side of the blade to the other through the use of porous blade materials. Unfortunately, however, the reduction of unsteady lift that results also effects a reduction in steady lift. Since the steady performance of rotors depends on the steady lift they produce, such quieting measures have associated degradations in performance.

A fifth basic noise control measure is to reduce the intensity of ingested disturbances. This can be done in axial flow fans by displacing the rotor vanes axially relative to the source of disturbance and in centrifugal fans by displacing the outlet port radially. When the unsteady force results from a potential interaction, great benefits may result from relatively modest increases in blade clearances. There is, however, an offsetting performance penalty due to increased clearance leakages. Somewhat reduced benefits of increased clearance may result when the interaction occurs with a viscous wake because velocity defects of viscous wakes generally persist downstream of lifting surfaces farther than those due to potential disturbances.

10.3 DESIGN PARAMETERS OF ROTORS AS LIFTING SURFACES

In order to cast noise-controlling parameters within the context of other performance requirements, it is necessary to appreciate the fundamentals of rotor powering. There are available many publications that deal with either the basic or the advanced aspects of design. We adopt here a method that relates to elements of the approach known as lifting line theory in order to keep discussions basic. Relationships are derived for rotor performance, ignoring interblade coupling. The validity of this assumption is then tested for the special case of marine propellers. This section defines terms, identifies the limitations associated with treating the rotor as an array of independently responding blades, and familiarizes the reader with general performance qualities.

Much has been written about both the general and the detailed theory of design of marine propellers; much of the instructional material on powering and similitude can be found in the naval architecture monographs,^{19,20} as well as in von Mises "Theory of Flight."²¹ Design methods for axial flow machinery (pump jets, compressors, etc.), in which a rotor is enshrouded in a duct and is perhaps used in

conjunction with other stationary or rotating stages, have been outlined in other texts.²²⁻²⁴ Traditionally, the performance estimates of turbomachines of all types were strongly based on empirical data developed over long periods of time, often utilizing systematically designed families of blading for rotors and cascades. Notable in this regard are the Wageningen-B^{25,26} propeller series, and the NACA-65 series cascade tests.²⁷ The powering estimates were often based on momentum and energy balances across the machine and did not specifically account for details in blade fluid dynamics.

More recently, however, blading details have become of interest in order to further improve efficiency at the design condition, to maintain adequate efficiency at conditions off the design point, and to promote various types of noise abatement. All these objectives require design methodology that incorporates a consideration of the details of fluid mechanics of blades as lifting surfaces, even though preliminary design may still involve the more traditional role of series data and power balances. The importance to noise control of considering blade detail can be realized by reviewing the preceding chapter, in which noise radiation and vibration were shown to be controlled by such details as surface condition, sweep, and edge geometry. We now review the basic performance parameters for axial flow machines and then examine some fundamentals of lifting surface flow; at least a superficial knowledge of performance parameters is essential because they may either reinforce or compete with reasonable noise abatement procedures.

10.3.1 Similitude of Turbomachines

Figure 10.5 illustrates two powering concepts of propellers: the general performance as an actuator disk (a) and the resolution of blade flow (b). Overall, in the steady state operation of the propeller the flow enclosed in the dotted streamlines (a) is accelerated a velocity increment v_a due to an applied thrust T that is assumed to be applied uniformly over the disk. The application of the thrust is assumed to be frictionless, and it is also assumed that no rotation or motion is imparted to the downstream fluid. Under these circumstances momentum and continuity balances across the actuator disk* yield an ideal propulsive efficiency for the device which is defined as

*See References 14-20 or any basic fluid dynamics text.

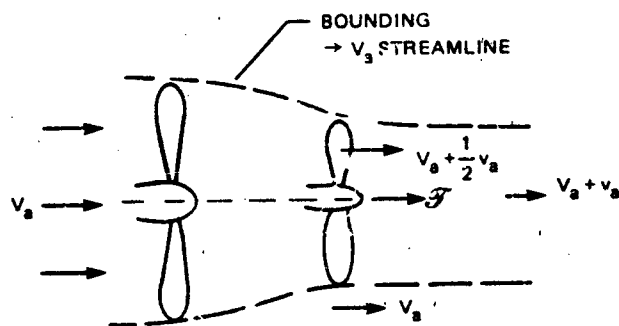


Figure 10.5a - Actuator Disk Model of a Propeller, Useful for Power and Momentum Balances

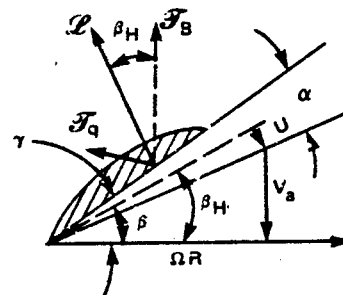


Figure 10.5b - Resolution of Kinematics of Blade Section

Figure 10.5 - Actuator Disk and Lifting Surface Analogies for Rotor Kinematics

$$\begin{aligned} \eta_i &= \frac{\text{Effective work}}{\text{Actual work on the fluid}} = \frac{T \cdot V_a}{T \cdot V_p} \\ &= \frac{V_a}{V_p} = \frac{V_a}{V_a + \frac{V_a}{2}} \\ &= \frac{2}{1 + (1+C_T)^{1/2}} \end{aligned} \quad (10.1)$$

where C_T is a dimensionless thrust coefficient

$$C_T = \frac{T}{\frac{1}{2} \rho \frac{\pi D^2}{4} U_a^2} = \frac{T}{\frac{1}{2} \rho U_a^2 (\text{disk area})} \quad (10.2)$$

The velocity V_p is the axial velocity at the propeller disk; the momentum balance gives this as $V_a + (1/2)V_a$. The useful, or effective, work done on the fluid is that required to move the inflow at a speed V_a with a thrust T ; the work actually done is the product of T and the actual velocity at the disk, V_p .

As seen in the force diagram of Figure 10.5b, the mechanics of transmitting rotational power in the shaft to translational energy to the fluid is somewhat more complicated. The thrust is accompanied by a drag in the direction of rotation; this drag is partly viscous, partly form drag, and partly lift-induced due to the finite blade angle that is necessary to propel the fluid. Therefore the parameters of thrust and axial velocity are, in reality, associated with a torque and a shaft speed, which provide a hydrodynamic efficiency that relates the shaft power into thrusting power.

In aircraft and marine propeller technology it has become accepted practice to regard propulsor diameter D and shaft speed n as independent nondimensionalizing parameters and thrust T and torque Q as dependent performance variables. The resultant tip speed of the propeller is just

$$U_T(R) = \left((\Omega R_T)^2 + v_a^2 \right)^{1/2} \quad (10.3)$$

where $\Omega = 2\pi n_s$ is the angular velocity of the blade and R_T is the tip radius. The secant of the angle β in Figure 10.5b is

$$\begin{aligned} \sec \beta &= \frac{U_T}{\Omega R_T} \left[1 + \frac{1}{\pi^2} \left(\frac{v_a}{n_s D} \right)^2 \right]^{1/2} \\ &= \left(1 + \frac{1}{\pi^2} J^2 \right)^{1/2} \end{aligned}$$

where

$$J = \frac{v_a}{n_s D} \quad (10.4)$$

is called the, advance coefficient of the propeller. For a propeller operating at a given advance coefficient there is a nondimensional thrust, called "thrust coefficient"

$$k_T = \frac{T}{\rho n_s^2 D^4} \quad (10.5)$$

and a nondimensional torque, called "torque coefficient"

$$k_Q = \frac{Q}{\rho n_s^2 D^5} \quad (10.6)$$

The thrust coefficient k_T is related to the coefficient in the actuator disk formula by

$$C_T = \frac{8}{\pi} \frac{k_T}{J^2} \quad (10.7)$$

so that the ideal (actuator disk) efficiency is rewritten

$$\eta_i = \frac{2J}{J + \left(J^2 + \frac{8}{\pi} k_T\right)^{1/2}} \quad (10.8)$$

To deduce the dependence of η_i on advance coefficient, we must inquire about the dependence of k_T on J . Figure 10.6 shows a propeller diagram²⁸ for a model marine propeller, whose projected view (plan form) is shown as the silhouette in the upper right. The operating advance coefficient is indicated by the arrow on the abscissa. The thrust coefficient increases nearly linearly with decreasing J . Referring to Figure 10.5b we see that as J decreases, the angle β decreases, but the angle of attack α increases. Assuming for now that the propeller blade has a linear lift coefficient-angle of attack characteristic, then, approximately, the lift (or the thrust) increases as $\alpha = (\gamma - \beta)$ increases. This accounts for the $k_T - J$ dependence shown. Equation (10.8) therefore shows that $\eta_p \rightarrow 0$ as $J \rightarrow 0$. As J increases, β increases, so that the angle of attack decreases until some point is reached for which $k_T = 0$ at J_o , for example. At this point Equation (10.8) shows that $\eta_p = 1$. Figure 10.6, on the other hand, shows that when $J = J_o$ both $k_T = 0$ and $\eta = 0$. A maximum efficiency is reached, however, when J is just less than J_o . In fact, up to this point of maximum efficiency Equation (10.8) crudely approximates the actual efficiency, η_p . The discrepancy between the actual and ideal efficiencies is due to the viscous section drag; thus, even though the thrust is zero, a finite torque is required just to overcome friction.

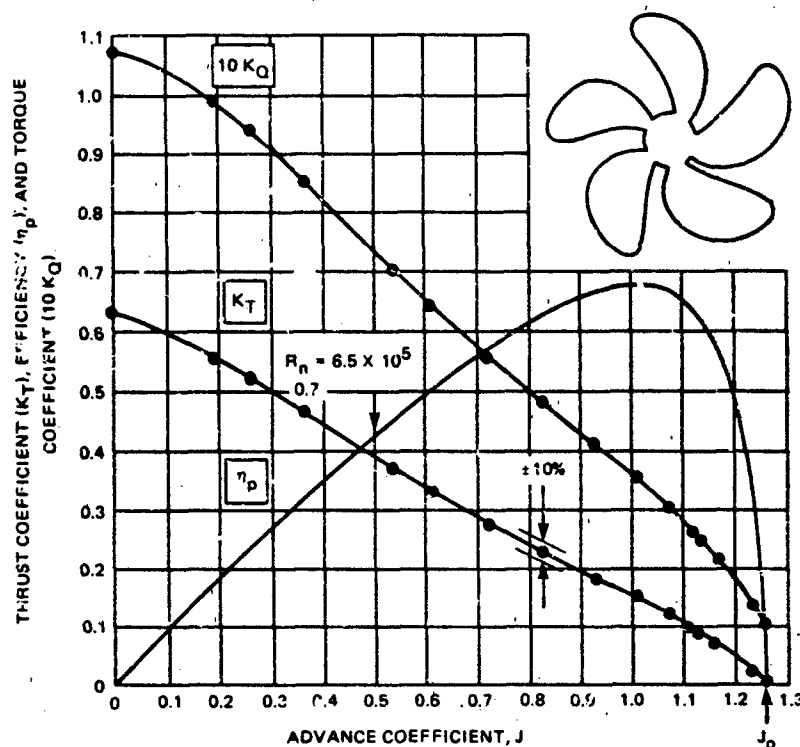


Figure 10.6 - Open Water Characteristics of a Propeller
with 36 deg Sweep (R_n)_{0.7} = 7×10^5

10.3.2 Propeller Blades as Lifting Surfaces

The propeller blade diagram in Figure 10.5b is expanded in Figure 10.7 to show the force diagram for a section at a distance R from the hub more clearly. In addition to the thrust and lift vectors, there is a force T_θ in the direction opposite to the rotation. This force is controlled by both the section drag and the lift-induced drag. The torque applied to the shaft due to forces at the blade section is given by $T_\theta \cdot R$. Associated with any lifting surface of finite aspect ratio is an induced velocity that is directed normal to the inflow vector. This is shown in Figure 10.7 as u , and it causes the actual angle of attack to be smaller than the geometric angle of attack. The angle between the rotational velocity ΩR ($\Omega = 2\pi n_s$) and the total velocity $V_a + v_a$ (where $v_a = u \cos \beta_H$) is called the "hydrodynamic pitch angle" β_H . The lift vector is directed normal to this velocity; the lift-induced drag is parallel to this velocity, and the viscous section drag is parallel to the body. For simplicity we take both components of drag to be parallel to the actual inflow vector. The forces on the blade section then resolve to

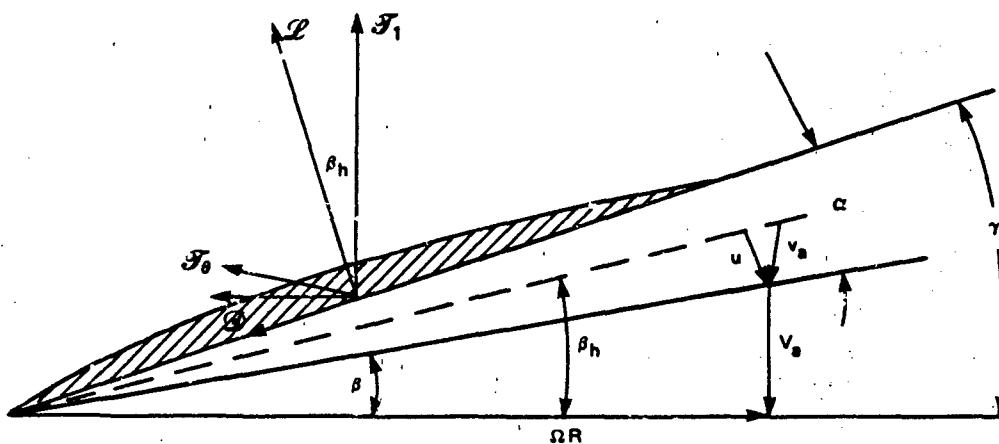


Figure 10.7 - Force Diagram for a Propeller Blade Section

$$T_1(R) = L(R) \cos \beta_h - D(R) \sin \beta_h \quad (10.9)$$

and

$$T_\theta(R) = L(R) \sin \beta_h + D(R) \cos \beta_h \quad (10.10)$$

where we can write the lift in terms of the resultant velocity $U(R)$, a lift coefficient, and a chord C ; i.e.,

$$L(R) = L'(R) dR = \frac{1}{2} \rho_o U^2(R) C_L \cdot C \cdot dR \quad (10.11)$$

The total lift L on the blade is just

$$\int_{R_H}^{R_T} L'(R) dR = L$$

Several factors contribute to a complication of the analysis from this point. The blade has a varying chord, the flow lines lie on a helicoidal surface, the blade surface is of finite aspect ratio, and the circulation on each point of a given blade is influenced by the velocities induced by adjacent blades. For these reasons,

involved computer programs²⁹⁻³¹ have been developed to accurately calculate and refine loading on highly swept propeller blades. For our purposes, such extremes are not necessary and we resort to a more rudimentary treatment more akin to the older lifting line theory.^{21,32,33} Rather than be concerned with the detailed surface distribution of lift-producing blade vorticity, we regard the blade as a system of strips each with a geometric angle of attack

$$\alpha = \gamma - \beta$$

or

$$\alpha = \tan^{-1} \left(\frac{P_i}{2\pi R} \right) - \tan^{-1} \left(\frac{U_a}{2\pi \omega_s R} \right) \quad (10.12)$$

where P_i is the pitch of the blade section. The pitch is the forward distance moved by the blade section in one complete rotation. If the section is cambered, there is a finite lift C_{L_0} when $\alpha = 0$. Furthermore, because of the finite aspect ratio AR of the propeller blade, the lift angle of attack slope is reduced from the value for two-dimensional flow (which is 2π) by a factor²¹

$$\frac{1}{1 + \frac{2}{AR}} \quad (10.13)$$

The average aspect ratio of the propeller blade is the hub-to-tip distance divided by the average blade chord \bar{C} . The total area of B blades is

$$\text{Blade area} = B \cdot \bar{C} (R_T - R_H) \approx \text{EAR} \cdot \pi R_T^2$$

where EAR is the "expanded area ratio." Therefore the aspect ratio

$$AR = \frac{R_T - R_H}{\bar{C}} \approx 0.8 \frac{R_T}{\bar{C}}$$

is approximated by

$$AR = \frac{2B}{3\pi \text{EAR}} \quad (10.14)$$

To retain analytical simplicity, assume that the lift coefficient is typified by that at a standard radius $R = 0.7R_T$ and that angles γ and β remain small, so that

$$C_L = C_{L_o} + \frac{dC_L}{d\alpha} \cdot \frac{1}{0.7\pi} \cdot \left(\frac{P_1}{D} - J \right) \quad (10.15)$$

$$= \frac{dC_L}{d\alpha} \left[\alpha_o + \frac{1}{0.7\pi} \left(\frac{P_1}{D} - J \right) \right]$$

$$C_L = \frac{2\pi}{1 + \frac{3\pi EAR}{B}} \left[C_c + \frac{1}{0.7\pi} \left(\frac{P_1}{D} - J \right) \right] \quad (10.16)$$

where α_o accounts for the fact that the blade section has a finite camber. This is not strictly true at all radii because properly designed propellers are unloaded at the tips, requiring that C_L approach 0 as R approaches R_T . Since

$$U^2(R) = \Omega^2 R^2 \left[1 + \left(\frac{V_a}{\Omega R} \right)^2 \right] \quad (10.17)$$

at any radius, then approximately

$$\cos \beta_H = \frac{1}{\left[1 + \left(\frac{J}{0.7\pi} \right)^2 \right]^{1/2}} \quad (10.18)$$

at the standard radius ($0.7 R_T$). Integration of Equations (10.9) and (10.11) with varying $(\Omega R)^2$, but with representative values of C_L , J , and β_H , we find (with

$T = B \cdot \int_0^{R_T} T'(R) dR$) that

$$k_T = \frac{\pi^3}{24} \cdot EAR \left(1 + \frac{J^2}{\pi^2} \right) \left\{ \frac{\left(C_{L_o} \right)_{2D} + \frac{2\pi}{0.7\pi} \left[\left(\frac{P_1}{D} \right)_{0.7} - J \right]}{1 + \frac{3\pi EAR}{B}} \right\} \cos \left(\frac{J + \frac{P_1}{D}}{0.7\pi} \right) \quad (10.19)$$

where $(C_{L_o})_{2D}$ is the two-dimensional lift coefficient of the cambered section at $\alpha = 0$. Equation (10.19) expresses many of the important features of the propeller

thrust: The thrust vanishes nearly linearly when J is slightly larger than $\left(\frac{P_i}{D}\right)_{0.7}$ at given value of J ; k_T increases as P_i/D , but the slope $\Delta k_T/\Delta J$ is not sensitive to changes in P_i/D . For small values of EAR/B , Equation (10.19) suggests that k_T increases with EAR ; i.e., for long slender blades the thrust increases with blade area. This is only partly true because as the number of blades increases, the blades get closer together, promoting blade-to-blade interference that will be evaluated below.

Equation (10.19) was derived ignoring this interference which is a function of both the geometry and the loading. The important geometrical variable is the chord-to-spacing ratio, solidity, C/S , shown in Figure 10.8. In terms of the propeller parameters introduced above, the ratio of average values is ($A_B = EAR \pi R^2 = BCR$)

$$\frac{\bar{C}}{\bar{S}} \approx \frac{\pi k \frac{EAR}{B}}{2(0.7) \frac{\pi R}{B}} = \frac{EAR}{1.4} \quad (10.20)$$

where the mean spacing is taken at the $0.7R$ radius. The behavior in Figure 10.8 shows that an additional dependence on expanded area ratio exists beyond that given by Equation (10.19). This dependence will apply to both steady and unsteady forces on the propeller only at low frequencies (Section 10.6.1.2). To illustrate this additional behavior, a selection of propeller data has been reduced for pitch to diameter ratios ranging from 1.0 to 1.2 at values of $J - J_0 = 0.26$. Measured^{25,28,34} values of k_T normalized on the functions of EAR that appear in Equation (10.19) are shown in Figure 10.9 to be nearly universally described as a function of EAR regardless of the number of blades or the angle of sweep (skew). The dashed line is extracted from calculations made by Thompson³⁵ using experimental cascade data,²⁷ and it demonstrates the order of magnitude of blade interference that is to be expected.

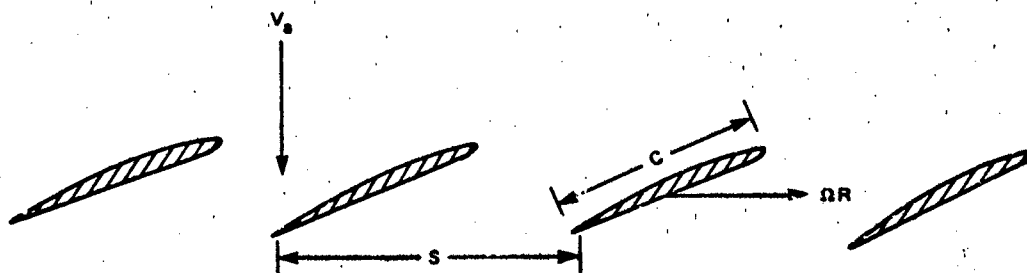


Figure 10.8 - Flow Diagram of a Blade Row

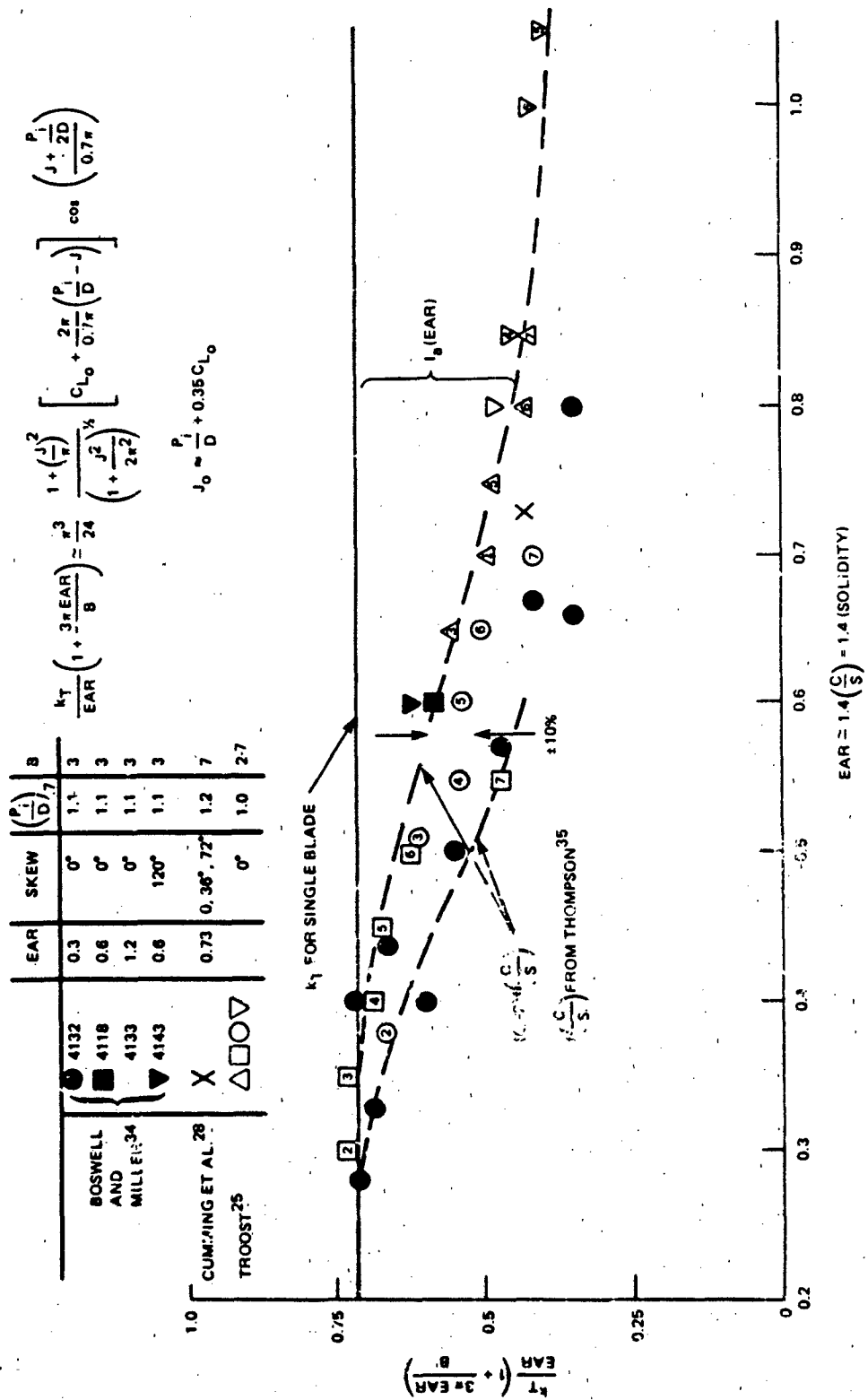


Figure 10.9 - Interaction (Cascade) Effect on Thrust Coefficients of Marine Propellers Deduced From Open Water Tests for $P_i/D = 1.0$ to 1.2 at $J - J_0 = 0.26$. Points Δ , \circ , ∇ , \square Pertain to Wageningen-B Series Propellers; Numbers in Symbols Denote Blade Nos. B

Equation (10.19), with Figure 10.9, gives approximate thrust design characteristics for propellers of varying pitch, area, and advance coefficient. Now we examine the effects of such parameters on efficiency. The efficiency of the propeller η_p is defined as

$$\eta_p = \frac{\text{Effective power imparted to fluid}}{\text{Shaft horsepower}}$$

$$= \frac{TV_J}{2\pi Q n_s} \quad (10.21a)$$

$$= \frac{k_T}{k_Q} \frac{J}{2\pi} \quad (10.21b)$$

As previously, we evaluate β_h , C_L , and pitch at the standard section ($R=0.7R_T$), but weight the $(\Omega R)^2$ from $R=0$ to $R=R_T$. Equations (10.9) and (10.10) can then be rewritten in approximate form

$$(\tau_l)_{0.7} = L \cos \beta_h - D \sin \beta_h \quad (10.22a)$$

$$(\tau_e)_{0.7} \cdot R_T \approx Q = R_T (L \sin \beta_h + D \cos \beta_h) \quad (10.22b)$$

where the viscous drag is

$$D_v \approx B \int_0^{R_T} \frac{1}{2} \rho_o U^2(R) C_D \cdot C \, dR$$

$$\approx \frac{\pi^2}{6} \rho_o \cdot AB (n_s D)^2 \left[1 + \left(\frac{J}{\pi} \right)^2 \right] (C_D)_{0.7} \quad (10.23)$$

$$\approx \frac{\pi^3}{24} \rho_o n_s^2 D^4 E A R \left[1 + \left(\frac{J}{\pi} \right)^2 \right] (C_D)_{0.7}$$

For comparison we write explicitly the expression for L :

$$L = \frac{\pi^3}{24} \text{EAR} \left(1 + \frac{J^2}{\pi^2}\right) \left\{ \frac{(C_{L_o})_{2D} + \frac{2\pi}{0.7\pi} \left[\left(\frac{P_i}{D}\right)_{0.7} - J \right]}{1 + \frac{3\pi \text{EAR}}{B}} \right\} I(\text{EAR}) \quad (10.23a)$$

where $I(\text{EAR})$ is the interference function shown in Figure 10.9. As a practical matter, L is only a weak function of EAR , so we may write

$$L \approx L' \left(1 + \frac{J^2}{\pi^2}\right) (J_o - J) \quad (10.23b)$$

Substitution of Equations (10.22) into (10.21a) gives the efficiency in the particularly simple form

$$\eta_p = \left(\frac{\tan \beta}{\tan \beta_h} \right) \left(\frac{1 - \frac{D}{L} \tan \beta_h}{1 + \frac{D}{L} \cotan \beta_h} \right) \quad (10.24)$$

Inspection of Figure 10.7 will show that the first term in Equation (10.24) is the ratio of V_a to $V_a + v_a$, which is the same as the ideal efficiency of the actuator disk. The second term is due to the viscous plus induced drag of the surface. As J approaches J_o , k_T and L also approach zero (Equation (10.23b)) so that the behavior of $(D/L) \tan \beta_h$ in relation to unity will determine the change in η_p with advance coefficient and in fact the efficiency must pass through zero with increasing D/L . Since the distribution $D(R)$ is partly dependent on $L(R)$ and partly dependent on details of blade geometry and blade finish, it is difficult within the constraints of the simple theory above to set down a general rule for the actual behavior of efficiency. As a practical matter it tends toward a maximum when J is approximately equal to $(P_i/D)_{0.7}$.

Detailed lifting surface calculations or a careful examination of the characteristics of propeller series data must be used³³ to examine the behavior of maximum propeller efficiency as a function of design parameters. However, a few general statements can be made from series data.³³ Such variables as diameter, expanded area ratio, and blade thickness must often be determined when the prime mover is torque limited, i.e., for a prescribed shaft horsepower and shaft speed. Of these parameters, the efficiency is most sensitive to propeller diameter; an optimum value

can be found, and designers generally design for the optimum or the largest that can be accommodated by the geometry of the ship. Conversely, if diameter is fixed, then there can be found an optimum shaft speed. For a given diameter, the optimum efficiency is generally reduced by increasing the expanded area ratio (EAR) because greater friction losses occur with larger blade areas. This can be deduced by noting the ratio of Equations (10.23) and (10.23b) to be proportional to EAR. Larger blade areas, however, tend to reduce the possibility of cavitation by increasing the average pressure on the blade surface. The optimum efficiency is also reduced by increasing the blade thickness because larger thickness - chord ratios increase form drag (C_D in Equation (10.23)). This is also true for sections near the tip.³⁶

Examples of tradeoffs among propeller efficiency, shaft speed, diameter, and radiated sound are shown in Figure 10.10. The propulsion properties were taken from Troost.²⁵ One of the two tradeoffs shows effects of varying diameter for a given shaft speed with the reference diameter being the one required for maximum efficiency. The second tradeoff is a variation of maximum shaft speed and the diameter selection is constrained by a requirement that the propeller efficiency must be maintained at its maximum possible values. The slopes of the lines ΔL_N vs. D/D_{OPT} or ΔL_N vs. N/N_0 are dependent* on the exact point on the propeller operating curve. The sound pressure level is presumed to vary as $60 \log U_T \propto 60 \log (ND)$ neglecting any dependence on blade area as being secondary to dependence on tip speed. The maximum possible propeller efficiency increases somewhat as the number of blades decreases for a given P_i , D , EAR, and τ . Furthermore, as the number of blades decreases, the optimum diameter increases. Blade sweep, when properly applied, does not strongly influence propeller efficiency.²⁸

The increased maximum thickness h_m influences the strength of the propeller, because the blade stresses τ_b decrease as h_m^{-2} ; the appropriate similarity formula for blade stresses is

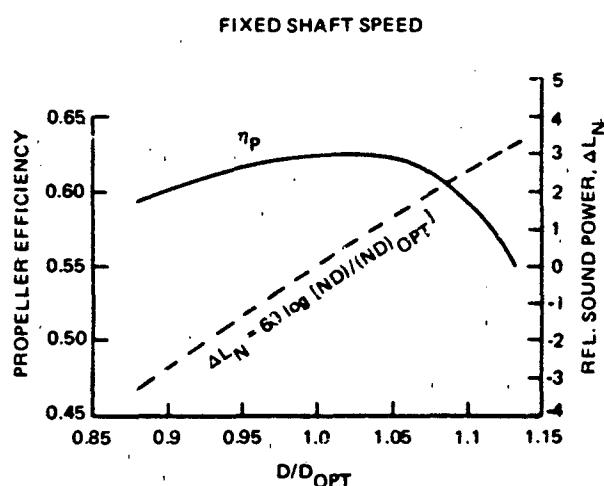
$$\tau_b \propto \frac{T}{B} \frac{1}{h_m^2} \frac{D}{C}$$

or

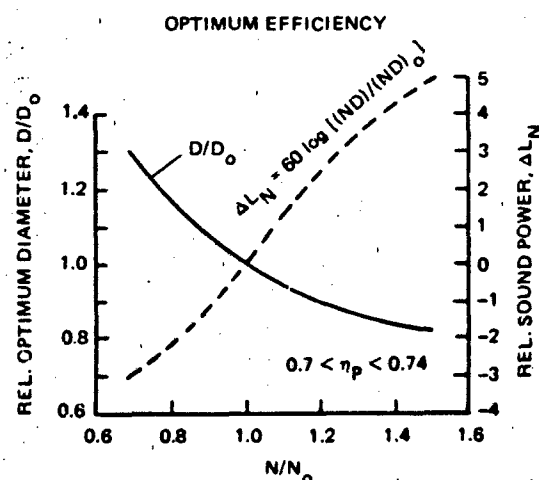
$$\tau_b \propto \frac{T}{EAR h_m^2}$$

* $N = 2\pi n_s$

Blades with larger h_m/C may have larger local minimum pressures and therefore may have pressure minima whose magnitudes are less susceptible to the changes in variations in local angles of attack due to inflow disturbances. The above similarity rule applies only between propellers for which the distribution of load over the blades remains similar.



(a) FIXED SHAFT SPEED AND POWER NON-OPTIMAL DIAMETER SELECTION



(b) FIXED POWER AND SHIP SPEED OPTIMUM DIAMETER FOR VARIOUS MAXIMUM SHAFT SPEED

Figure 10.10. Examples of Performance Tradeoffs Between Overall Sound Power and Powering Performance for Various Diameter and Shaft Speed Changes

10.4 THEORETICAL FREE-FIELD ACOUSTICS OF ROTORS

10.4.1 Fundamental Analysis

The discussion in Section 10.2 is now given theoretical foundation in terms of parameters common to both the acoustic and powering performance. Specifically, rotational effects on radiation from blade forces as well as noises from blade flow interactions are formulated. Figure 10.11 illustrates the geometry. The acoustic problem consists of evaluating the far-field sound pressure from a rotating source (dipole or monopole) whose space-time behavior is prescribed in a frame of reference

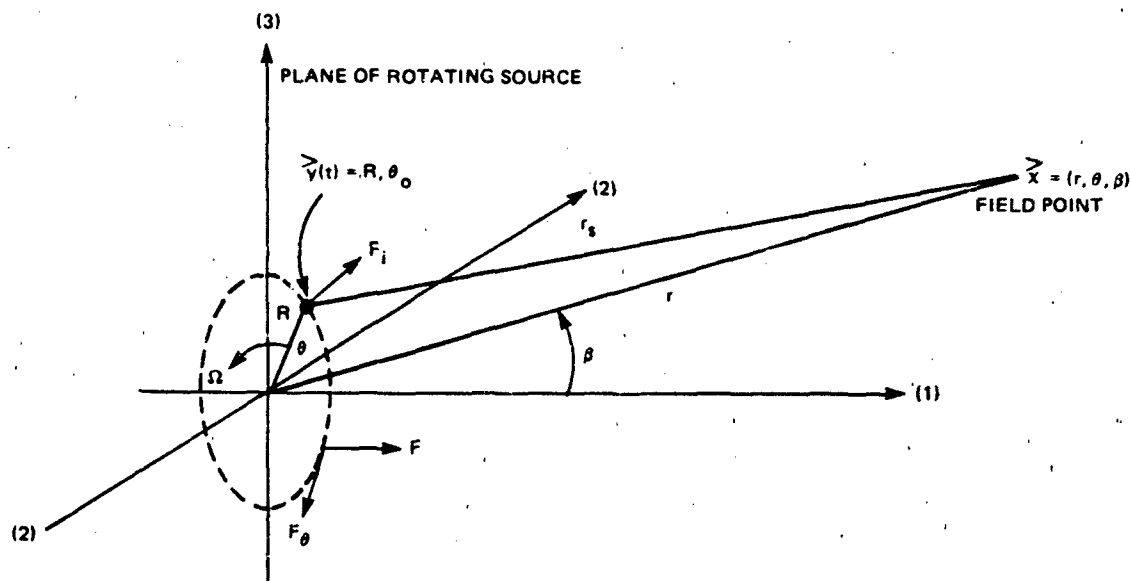


Figure 10.11 - Geometry of Rotating Source and Acoustic Field

moving with the source.* The time-dependent forces and volume velocities are the result of the steady loads (thrust and torque) on the blades as well as unsteady loads due to spatial and temporal nonuniformities in the inflow to the propeller disk. The results derived here apply to any isolated rotor; they also apply approximately to components in compound machinery consisting of multiple stages of rotors and stators except that for multistage compound machinery with very high solidity (small spacing to chord ratios) in which propagation of sound is disrupted by reflections from blade rows of adjacent stages.

The elementary acoustics of the problem have been given in Chapters 2 and 3. From Equations (2.44), (2.47), (2.48a) and (2.62a), the acoustic pressure $p(\vec{x}, t)$ from a region of forces F_i and volume sources \dot{q} is

$$p(\vec{x}, t) = \frac{1}{4\pi} \iiint \left[\frac{\partial \dot{q}}{\partial t} \right] \frac{dV(\vec{y})}{r_s} - \frac{1}{4\pi} \frac{\partial}{\partial x_i} \iiint [F_i] \frac{dV(\vec{y})}{r_s} \quad (10.25)$$

*Technically, quadruple sources may also be treated in this manner, but as we have seen repeatedly, these sources are dominated by lower-order sources at low subsonic speeds.

The source point $y(t)$ rotates with angular velocity Ω , at a radius R , as shown in Figure 10.11. Recall that the terms in brackets, e.g., $[F_i]$, denote quantities evaluated at retarded times, e.g., $F_i(\vec{y}, t - r_s/c_0)$. Even if, in the frame of reference rotating with the blade, F_i is constant, the variation of r_s with time due to the $\vec{y}(t)$ will cause oscillating far-field sound. The two terms in Equation (10.25) have in common the volume integral

$$I_i(\vec{x}, t) = \frac{1}{4\pi} \iiint_V [a_i] \frac{dV(\vec{y}(t))}{r_s} \quad i = 0, 1, 2, 3 \quad (10.26)$$

where $i = 0$ refers to the volume source, $i = 1$ to the axially directed forces, and $i = 2, 3$ to the transversely directed force.

The first stage in the evaluating Equation (10.26) for the rotating system is to rewrite $a_i(\vec{y}, t)$ in terms of its Fourier transform $a(\vec{y}, \omega')$ of the sources in the frame of reference fixed with rotating source

$$a(\vec{y}, t) = \int_{-\infty}^{\infty} a(\vec{y}, \omega') e^{-i\omega' t} d\omega' \quad (10.27)$$

so that the retarded source function is

$$[a(\vec{y}, t)] = \int_{-\infty}^{\infty} a(\vec{y}, \omega') e^{-i\omega' (t - r_s/c_0)} d\omega' \quad (10.28)$$

According to the notation of Figure 10.11. the source-field range is

$$r_s = \left[r^2 + R^2 - 2Rr \sin \beta \cos (\theta - \theta_0) \right]^{1/2} \quad (10.29)$$

which reduces to

$$r_s = r - R \sin \beta \cos (\theta - \theta_0) \quad (10.30)$$

when $r \gg R$, i.e., in the far field. Substitution of Equation (10.30) into Equation (10.28) gives

$$[a(\vec{y}, t)] = \int_{-\infty}^{\infty} a(\vec{y}, \omega') e^{-i\omega' t} e^{ik'_0 r} e^{-ik'_0 R \sin \beta \cos(\theta - \theta_0)} d\omega' \quad (10.31)$$

where $k'_0 = \omega'/c_0$. The identity³⁷

$$e^{-ik'_0 R \cos(\theta - \theta_0) \sin \beta} = \sum_{n=-\infty}^{\infty} (-i)^n e^{+in(\theta - \theta_0)} J_n(k'_0 R \sin \beta) \quad (10.32)$$

is substituted into Equation (10.31) to give

$$[a(\vec{y}, t)] = \sum_{n=-\infty}^{\infty} (-i)^n \int_{-\infty}^{\infty} a(\vec{y}, \omega') e^{i\omega' t} J_n(k'_0 R \sin \beta) e^{+ik'_0 r} e^{+in(\theta - \theta_0)} d\omega' \quad (10.33)$$

The angle θ_0 is time varying due to steady rotation such that $\theta_0 = \theta_b + \Omega t$. We assume that source distribution $a(\vec{y}, t)$ is concentrated in the $y_1 = \text{plane}$,

$$a(\vec{y}, t) = a(\vec{y}_{2,3}, t) \delta(y_1) \quad (10.34)$$

as long as the axial dimension of the rotor, say, $C \sin \gamma$, where γ is the pitch angle and C is the blade chord, is smaller than an acoustic wavelength.

The resulting value of $I_1(\vec{x}, \omega)$ is

$$I_1(\vec{x}, \omega) = \sum_{n=-\infty}^{\infty} \frac{e^{+ik'_0 r}}{4\pi r} \cdot \int_0^{2\pi} \int_{R_H}^{R_T} a_1(R, \theta_b, \omega = n\Omega) J_n(k'_0 R \sin \beta) \times e^{in(\theta - \theta_b - \pi/2)} R dR d\theta_b \quad (10.35)$$

where $\vec{x} = r_0, \theta, \beta$, and $a_1(R, \theta_b, t)$ moves with the rotor blade, the integration extends over the entire propeller disk, and approximations of Equations (10.30) and (10.34) are assumed. If the source density $a(R, \theta, \omega)$ represents effects of multiple compact

blades, then the exponential factor $\exp(-in\theta_b)$ indexes the blades sequentially around the rotor disk at multiples of $2\pi/B$. Equation (10.35) may be used to evaluate the acoustic pressure transform, $p(\vec{x}, \omega)$ resulting from Equation (10.25) by taking the appropriate derivatives as in Equation (10.36). For cavitation noise, $a(\vec{z}, \omega)$ represents the volume acceleration of the fluid.

The cylindrical Bessel function $J_n(\xi)$ has the following asymptotic formulae³⁷ that will be used later:

$$\lim_{\xi \rightarrow 0} J_n(\xi) = \frac{\left(\frac{1}{2}\xi\right)^n}{\Gamma(n+1)} \quad (10.35a)$$

which really applies when $\xi < 1$ and where

$$\begin{aligned} \Gamma(n+1) &= 1 \cdot 2 \cdot 3 \dots (n-1)n = n! \\ &= \left(\frac{2\pi}{n+1}\right)^{1/2} (n+1)^{n+1} e^{-(n+1)}, \quad (n+1) > 1 \end{aligned} \quad (10.35b)$$

$$\Gamma(1) = 1$$

For large arguments,

$$\lim_{\xi \rightarrow \infty} J_n(\xi) = \left(\frac{2}{\pi\xi}\right)^{1/2} \cos\left(\xi - \frac{n\pi}{2} - \frac{\pi}{4}\right) \quad (10.35c)$$

which really applies when $\xi > n$.

Without referring explicitly to a particular source type (dipole, monopole, etc.), we note that two important limiting forms of Equation (10.35) can be written immediately. These forms are consequences of the frequency characteristics of the sources on the blades.

If the source is broadband, i.e., $a(\vec{z}, \omega - n\Omega) = a(\vec{z})$ over many harmonics of n , then

$$I_1(\vec{x}, \omega) = \frac{e^{ik_0 r}}{4\pi r} \int_{R_H}^{R_T} \int_C^{2\pi} a_1(R, \theta_b) \sum_{n=-\infty}^{\infty} J_n(k_0 R \sin \beta) e^{+in(\theta - \theta_b - \pi/2)} R dR d\theta_b$$

Since³⁷

$$\sum_{n=-\infty}^{\infty} J_n^2(\xi) = 1$$

the sound pressure spectrum is proportional to the magnitude $|I(\vec{x}, \omega)|^2$, i.e.,

$$\phi_{\text{p rad}}(\vec{x}, \omega) = \frac{1}{16\pi^2 r^2} \phi_{\text{aa}}(\omega)$$

where it is necessary to assume that the source is at a point with a spectrum of the form

$$\phi_{\text{aa}}(R, \theta_b, \omega) = |a_i(R, \theta_b, \omega)|^2 \delta(R - R') \delta(\theta_b - \theta'_b) \delta(\omega - \omega')$$

with an integral over R and θ_b expressed as

$$\phi_{\text{aa}}(\omega) = \int_0^{2\pi} \int_{R_\omega}^{R_T} \phi_{\text{aa}}(R, \theta_b, \omega) R dR d\theta_b$$

This shows that the radiated sound spectrum of a rotating broadband source is unaffected by rotation.

If the source is a tone at frequency ω_t , situated at radius R_1

$$a(\vec{z}, \omega - n\Omega) = a(R_1) \delta(\omega - n\Omega \pm \omega_t)$$

and the spectrum will be of the form

$$\phi_{\text{aa}}(R, \theta_b, \omega) = \phi_{\text{aa}}(R, \theta_b) \delta(\omega - n\Omega \pm \omega_t)$$

so that the sound spectrum in the far field will give a series of lines at frequencies $\omega = \omega_t \pm n\Omega$, with the maximum intensity occurring at $\omega = \omega_t$. The function

$$J_n(k_o R_1 \sin \beta) = J_n\left(\frac{\omega_t \pm n\Omega}{c_o} R_1 \sin \beta\right)$$

forms an envelope around the tone amplitudes. Thus the spectrum of radiated sound from a point source at R_1 will then be of the form

$$\phi_{p_{rad}}(x, \omega) = \frac{1}{16\pi^2 r^2} \sum_{n=-\infty}^{\infty} \phi_{aa}(\omega_t \pm n\Omega) \left| J_n \left(\frac{\omega_t \pm n\Omega}{C_o} R_1 \sin \beta \right) \right|^2 \delta(\omega - \omega_t \pm n\Omega)$$

Furthermore, the amplitude of the envelope will depend on the angle β . On the axis of the rotation, i.e., when $\beta = 0$, only the fundamental will be heard, while at larger angles many harmonics will be audible as $\sin \beta$ increases. This is illustrated in Figure 10.12.

The spectrum of noise from each i-th directional component of the rotating forces is found by combining Equation (10.25) and (10.35) to give in the far field (letting $F''_i(R, \theta_o, \omega)$ be the frequency spectrum of force per unit area)

$$p_i(\vec{x}, \omega) = \sum_{n=-\infty}^{\infty} - \frac{\partial}{\partial x_i} \left(\frac{e^{ik_o r}}{4\pi r} \right) e^{+in(\theta - \pi/2)}$$

$$\int_{R_H}^{R_T} \int_0^{2\pi} [F''_i(R, \theta_b, \omega - n\Omega)] e^{-in\theta_b} J_n(k_o R \sin \beta) R dR d\theta_b$$

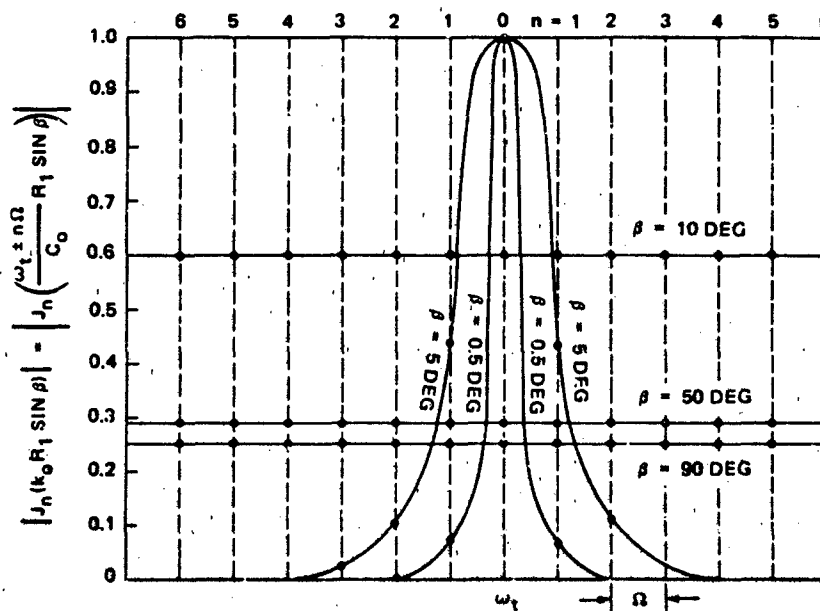


Figure 10.12 - Relative Levels of Far-Field Acoustic Line Components for a Spinning Tone of Frequency $\omega_t R_1 / C_o = 10$ and Rotation Rate $\Omega R_1 / C_o = 1.0$ (See Equation (10.35)), β is the Angle of Observation Measured from the Spin Axis

in the axial direction, $\partial/\partial x_i = \partial/\partial x_1$,

$$p_1(\vec{x}, \omega) = \sum_{n=-\infty}^{\infty} \frac{-ik_o \cos \beta e^{ik_o r}}{4\pi r} e^{-in(\pi/2-\theta)} \cdot [F_1(\omega)]_n$$

here

$$[F_1(\omega)]_n = \int_{R_H}^{R_T} \int_0^{2\pi} F_1''(R, \theta_b, \omega - n\Omega) e^{-in\theta_b} J_n(k_o R \sin \beta) R dR d\theta_b \quad (10.36a)$$

for tangential forces, those in the θ direction, $\partial/\partial x_i = 1/R(\partial/\partial \theta)$,

$$p_\theta(\vec{x}, \omega) = \sum_{n=-\infty}^{\infty} - \left(\frac{e^{ik_o r}}{4\pi r} \right) e^{-in(\pi/2-\theta)} \int_{R_H}^{R_T} \int_0^{2\pi} \frac{1}{R} F_\theta''(R, \theta_b, \omega - n\Omega) e^{-in\theta_b} [n J_n(k_o R \sin \beta)] \cdot R dR d\theta_b \quad (10.36b)$$

The net sound pressure from both components is

$$p(\vec{x}, \omega) = p_1(\vec{x}, \omega) + p_\theta(\vec{x}, \omega) \quad (10.36c)$$

The integrals over angle θ_b of the force components appearing in Equations (10.36) are really the circumferential wave number spectra of the force array around the rotor disk, but referred to a reference frame rotating with the propeller.

10.4.2 Interaction Tones from Rotating Blade Forces

The general representation of blade forces as a discrete circular array of lifting surfaces follows from the principles of Chapter 7 (array response) and Chapter 9 (gust response). It is easiest to derive the force spectrum by "unrolling" the blade sections, as illustrated in Figure 10.13. The blade row, considered stationary with respect to the gust, is shown as an array of lifting surfaces spaced $b = 2\pi R/B$ apart. The incident gust has a wavelength $2\pi R/w$ and it advances through the blade row at speed $U(R)$ (in the context of Section 10.2 for circumferential

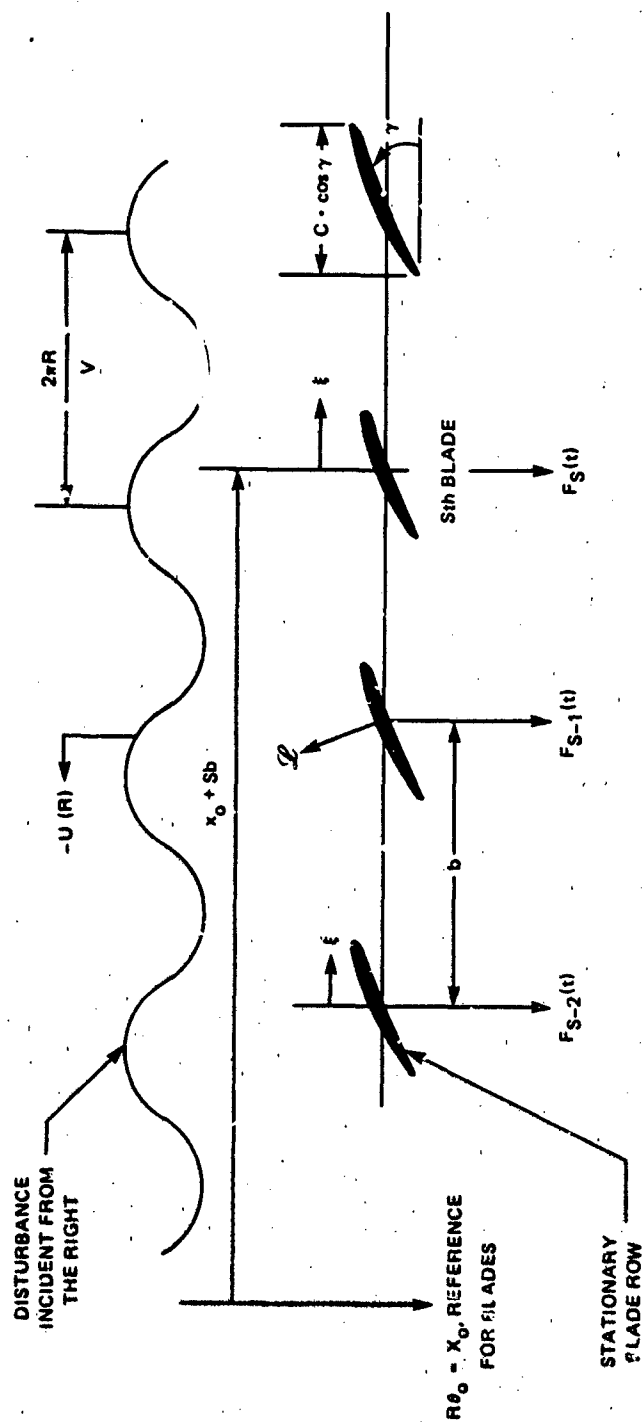


Figure 10.13 - Geometry of an Array of Lifting Sections Responding to a Sinusoidal Incident Gust

monics $\omega = nV$). In general, this incident flow will consist of a steady component on which is superimposed both periodic (deterministic) and stochastic (turbulent) components. The problem is to determine the expression for the blade forces as functions of time and position in the disk. We do that now for the case of a deterministic inflow perturbation to which the blades each respond linearly and independently. Later the result is generalized (Section 10.5.2.3) for turbulent flow, and the assumption of independent blade response is explored (Section 10.6.1.3). Following Section 9.3.1 the lift response of each surface is

$$\frac{dL_{s,w}}{dR} = \rho_o \pi |u(w)| U(R) C S_{2D} \left(k_R, \frac{wC}{R} \right) e^{i w \left(\theta_w - \frac{U(R)}{R} t + \frac{sb}{R} \right)} \quad (10.37)$$

where $dL_{s,w}(R,t)/dR$ represents the local force per unit radius on the sth blade, and the inflow disturbance is represented as in Chapter 9, Equation (9.34) (the wave number k_1 is replaced by $k_\theta = w/R$, k_3 is replaced by k_R),

$$u(w) e^{i \frac{w}{R} [x - U(R)t]} = |u(w)| e^{i w \left[\left(\theta_w + s \frac{b}{R} + \frac{\xi}{R} \right) - \frac{U(R)t}{R} \right]} \quad (10.38)$$

where $w\theta_w$ is the phase of the w wave number of the wake at radius R and includes all radial variations of gust phase. The generalized aerodynamic response function introduced in Chapter 9 is also formally included,

$$S_{2D}(k_1 C, k_3 C) = S_{2D} \left(\frac{wC}{R}, \frac{C}{R} \right)$$

The net lift response per unit span of the sth blade is conveniently expressed as

$$\frac{dL_{s,w}}{dR} = L'_w \left(R, \frac{wC}{R} \right) e^{i w \theta_w} e^{i w \left(\frac{sb}{R} - \frac{U(R)}{R} t \right)} \quad (10.39)$$

where the amplitude of the net lift per unit span from the w th gust harmonic is

$$L'_w \left(R, \frac{wC}{R} \right) = \rho_o \pi |u(w)| U(R) C S_{2D} \left(\frac{C}{R}, \frac{wC}{R} \right) \quad (10.40)$$

and θ_w accounts for the possibility of a radially varying sweep angle. Equation (10.40) is just the linear gust response of the lifting surface to the $2\pi R/w$ wavelength of the incident gust. The response of surface will be a function of radius and of wC/R , because the frequency of gust encounter is

$$\omega_e = 2\pi \left[\frac{U(R)}{\frac{2\pi R}{w}} \right] = w\Omega \quad (10.41)$$

so that the reduced frequency on which the admittance function depends is

$$\frac{\omega_e C}{2U(R)} = \frac{wC}{2R}$$

The index w is the circumferential mode order of the incident disturbance field so that $\omega_e C/2U(R)$ will increase as the radius decreases from the tip to the hub. Therefore the relative phases of the response of different blade sections will depend on radius.

The general equation for the circumferential radial distribution of fluctuating lift on the blades, in a frame rotating with the rotor, for the summation over w wake components is, from Equation (10.37),

$$\frac{dL(R, \theta_b, t)}{dR} = \sum_{s=0}^{B-1} \sum_{w=-\infty}^{\infty} L'_w \left(R, \frac{wC}{R} \right) e^{-i\omega\Omega t} e^{iw(\theta_b + \theta_w)} \delta \left(\theta_b - s \frac{2\pi}{B} \right) \quad (10.42a)$$

This represents a series of B line forces located at regular intervals $2\pi/B$ around the periphery and directed perpendicular to the resultant inflow velocity. The relative phase of L'_w at each radius, given above by $w\theta_w(R)$, accounts for the effects of sweep in either the blade or the incident gust. A similar expression could be written for tangential forces with $\sin \gamma$ replacing $\cos \gamma$. In parallel fashion to Equations (9.38 and 9.40), we can now write, instead of Equation (10.40), the familiar relationship for the lift per unit span on each blade

$$L'_w \left(R, \frac{wC}{R} \right) = \rho_0 \pi C |u(w, k_3)| U(R) S_{2D} \left(\frac{wC}{2R}, \frac{k_3 C}{2} \right) \quad (10.42b)$$

where $k_3 C/2$ is the radial wave number of the inhomogeneity which in general may have some radial variation. It is assumed that both the blade angle and the

hydrodynamic pitch angle are equal to γ as long as the rotor blades are designed for negligible angle of attack. The force distribution defined by Equation (10.42a) is analogous to those used in Equations (10.36), i.e., with a partial integration over the individual blade chord

$$\int_{\xi/R} F_i''(R, \theta_b, \omega) R d\theta_b = \left[\frac{dL(R, \theta_b, \omega)}{dR} \right] n_i(\gamma) = F_i'(R, \theta_b, \omega) \quad (10.43)$$

which represents a series of line forces per unit span located at angles θ_b and $n_i(\gamma)$ is the direction cosine of the pitch angle. The net thrust per unit radius imparted to the fluid by the w component of the ingested disturbance is

$$\left[F_1(t) \right]_w = \int_{\text{rotor disk}} \left[\frac{dL(R, \theta_b, t)}{dR} \right]_w \cos \gamma \, dR d\theta_b \quad (10.44)$$

where the subscript w indicates only one w component of Equation (10.42a) summed over the entire number of blades B . The net axial force on the rotor due to all the w order disturbances is

$$F_1(t) = \sum_{w=-\infty}^{\infty} \int_{R_H}^{R_T} L'_w \left(R, \frac{wC}{2R} \right) \cos \gamma \cdot \sum_{s=1}^{B-1} e^{i w (\theta_w + s(2\pi/B) - \Omega t)} \cdot dR \quad (10.45)$$

letting $b = 2\pi R/B$ be the spacing between the blades. In Equation (10.45), the integration over R of $L'_w(R, wC/R) \exp(iw\theta_w)$ accounts for variation in the phases of both the aerodynamic response function and any radial variation of sweep angle of the flow θ_w along the radius. The angle $w\theta_w$ replaces the phase $k_3 y_3$ in Equation (9.44).

The summation over s involves only the $\exp [iws(2\pi/B)]^1$, which is a partial sum of a geometric progression $a_0 + a_1^2 + a_2^3 + \dots + a_s^s$, which has the value B only when $w = \pm mB$, where m is an integer and it is zero otherwise. Formally this is

$$\sum_{s=0}^{B-1} e^{i w (2\pi/B) s} = B \delta(w \pm mB) \quad (10.46)$$

Therefore the total steady-plus-unsteady thrust is

$$F_1(t) = \sum_{m=-\infty}^{\infty} B \int_{R_H}^{R_T} L'_{mB} \left(R, \frac{mBC}{2R} \right) \cos \gamma \, e^{i \left[\frac{mB\theta}{mB} \right]} dR \, e^{-imB\Omega t} \quad (10.47)$$

This result shows that the $m = 0$ contribution is due to the rotation of the steady blade forces, while the $m \neq 0$ components are due to responses to inflow disturbances $u(w) = u(mB)$. This means that if there are inflow nonuniformities of circumferential wavelength $2\pi R/mB$, the rotor selects only these disturbances to generate time-dependent thrust; all blade responses to other harmonics cancel. This brings us back to the point of Figure 10.2, which illustrates the analogy of the rotor as a spatial filter.

The orientation of forces in the 2, 3 plane with respect to the fixed 2, 3 axes oscillates as each blade rotates. The elemental force along the 2-axis is in the form of Equation (10.42a)

$$\frac{dL_{s,w}}{dR} \cos \theta_f =$$

$$L'_w \left(R, \frac{wC}{R} \right) e^{-i\omega\Omega t} e^{i\omega(\theta_b + \theta_w)} \delta \left(\theta_b - s \frac{2\pi}{B} \right) \cos (\theta_b + \Omega t)$$

where the time-varying angle $\theta_f = \theta_b + \Omega t$. For the component of the tangential force directed along the 3-axis, replace $\cos \theta_f$ with $\sin \theta_f$. The side force components $F_2(t)$ and $F_3(t)$ can be found by summing over all s and w and integrating over the radius. For example the $F_2(t)$ is

$$F_2(t) = \sum_{s=0}^{B-1} \sum_{w=-\infty}^{\infty} \int_{R_H}^{R_T} \sin \gamma L'_w \left(R, \frac{wC}{R} \right) e^{-i\omega\Omega t} e^{i(\omega\theta_b + \omega\theta_w)} \frac{e^{i(\theta_b + \Omega t)} + e^{-i(\theta_b + \Omega t)}}{2} \delta \left(\theta_b - \frac{s2\pi}{B} \right) dR$$

which becomes, with Equation (10.46),

$$F_2(t) = \sum_m \frac{B}{2} \int_{R_H}^{R_T} \sin \gamma B L'_{mB \pm 1} \left(R, \frac{(mB \pm 1)C}{R} \right) e^{-imB\Omega t} e^{i(mB \pm 1)\theta} dR \quad (10.47a)$$

In contrast to the axial force, the transverse force of the mB blade-frequency harmonic arises from the $w = mB \pm 1$ inflow harmonic.

In order to determine the acoustic radiation using Equation (10.36a), we must determine a function equivalent to $F_1''(R, \theta_o, \omega)$ in the terms of Equation (10.37) or (10.42a). Recall our initial premise that each blade chord is acoustically compact, but the overall rotor size is not necessarily so. Therefore the n harmonic decomposition of the dipole source strength in Equation (10.36a) can be found by replacing $F''(R, \theta_o, \omega)$ as described by Equation (10.43). Therefore, in the case of the unsteady axial force, the circumferential Fourier harmonic of the w th wake mode given by the integral in Equation (10.36a) requires a coefficient

$$[F_1(R, \omega)]_n = \int_0^{2\pi} \left[\frac{1}{2\pi} \int_{-\infty}^{\infty} e^{i\omega t} F_1(R, \theta, t) dt \right] e^{-in\theta} d\theta$$

Introducing Equation (10.42a), we have for each w component

$$[F_1(R, \omega)]_{n,w} = \sum_{s=0}^{B-1} \int_{-\infty}^{\infty} dt \int_0^{2\pi} d\theta_b \frac{L'_w(R, \frac{wC}{R})}{(2\pi)} (\cos \gamma J_n(k_o R \sin \beta))$$

$$e^{i(-w\Omega + \omega)t} e^{i(w-n)\theta_b} e^{i\omega\theta_w} \delta\left(\theta_b - \frac{s2\pi}{B}\right) \quad (10.48)$$

The integral in Equation (10.48) will be recognized as the circumferential wave number spectrum* of the blade circumferential distribution of forces at a radius R since $n\theta$ is analogous to, say, $k_\theta \xi_\theta$ where $k_\theta = n/R$ is the circumferential wave number and ξ_θ is the circumferential coordinate.

Now, using Equation (10.48), the desired coefficient is

$$[F_1(\omega)]_{n,w} = \sum_{s=0}^{B-1} \frac{1}{2\pi} \int_{-\infty}^{\infty} dt \int_{R_H}^{R_T} L'_w\left(R, \frac{wC}{2R}\right) \cos \gamma J_n(k_o R \sin \beta)$$

$$\cdot e^{i\omega(\theta_w + s2\pi/B - \Omega t)} \cdot e^{-ins \frac{2\pi}{B}} e^{i\omega t} dR \quad (10.49)$$

Carrying out the time integration yields

$$2\pi \delta(\omega + w\Omega)$$

*Note that the circumferential Fourier coefficient would be $a_n = (1/2\pi) \int_0^{2\pi} a(\theta) e^{-in\theta} d\theta$.

and the summation over s yields, as in Equation (10.46),

$$B \delta(\omega - n + mB)$$

so that the Fourier amplitude of the n th harmonic axial force response to the w th wave harmonic of the inflow is

$$\begin{aligned} [F_1(\omega)]_{n,w} = B \cdot \int_{R_H}^{R_T} J_n(k_0 R \sin \beta) L_w\left(R, \frac{wC}{2R}\right) \cos \gamma e^{i w \theta} dR \\ \cdot \delta(\omega - n + mB) \delta(\omega + w\Omega) \end{aligned} \quad (10.50)$$

in the rotating frame.

Analogously, the coefficients of forces $[F_\theta(\omega)]_{n,w}$ can be determined and inserted into Equations (10.36) to yield an expression for the sound pressure due to a rotor operating in a deterministic nonaxisymmetric flow field. Thus at $\vec{x} = (r, \theta, \beta)$

$$\begin{aligned} p_{w,m}(\vec{x}, t) = \frac{-iB}{4\pi r} \left(f_{1,w} k_0 \cos \beta + \frac{mB-w}{R_1} f_{\theta,w} \right) \cdot \\ \cdot J_{mB-w}(k_0 R_1 \sin \beta) \exp \left[i \left(k_0 r + (mB-w) \left(\theta - \frac{\pi}{2} - mB\Omega t \right) \right) \right] \end{aligned} \quad (10.51)$$

where $k_0 = \omega/c_0 = mB\Omega/c_0$. The total pressure from all blade harmonics m and all wake harmonics w is a summation over all combinations

$$p(\vec{x}, t) = \sum_{m=-\infty}^{\infty} \sum_{w=-\infty}^{\infty} p_{w,m}(\vec{x}, t) \quad (10.52)$$

The functions $f_{1,w}$ and $f_{\theta,w}$ are

$$f_{1,w} = \int_{R_H}^{R_T} L_w\left(R, \frac{wC}{R}\right) \cos \gamma J_{mB-w}(k_0 R \sin \beta) e^{i w \theta} dR \quad (10.53a)$$

and

$$f_{\theta, w} = \int_{R_H}^{R_T} L'_w \left(R, \frac{wC}{R} \right) \sin \gamma J_{mB-w} (k_O R \sin \beta) e^{i w \theta} dR \quad (10.53b)$$

where the $L'_w(R, wC/R)$ is given by Equation (10.42b). These functions are the axial and tangential force response coefficients on a blade to the w th wake component; they contain no blade-to-blade phase information since that has already been expressed by the summations.

Equation (10.51) is the fundamental analytical result of this chapter; it gives the complete sound field emanated by a rigid propeller in a uniform or non-uniform inflow. The result is not strictly dependent on Mach number; however, the forward speed Mach number must be very much less than unity and the observation point must be in the far field, $r \gg R_T$. The expression was derived originally by Ffowcs Williams and Hawkings,³⁸ along the same lines as above, and an expression that differs in derivation and in some details can be found in Morse and Ingard.⁸ Before Ffowcs Williams and Hawkings, similar results were also obtained by Lowson,³⁹⁻⁴¹ Lowson and Ollerhead,⁴² and Hanson.⁴³ Similar analysis applied to localized sources has been given by Morfey and Tanna,⁴⁴ while Wright^{6,45,46} and Morfey³ have used variations of Equations (10.51) to deduce the spectral forms of rotor noise for a variety of inflow disturbances. Application of Equation (10.51) to a design scenario has been given by Hanson,⁴⁷ who also included the effects of forward flight. Extensions of the analysis to supersonic and transonic tip speeds have been given by Hawkings and Lowson⁴⁸ and by Hanson and Fink.⁴⁹ Analysis of the alternative problem of radiation from stators downstream of a rotating disturbance field has been given by Lowson⁴¹ and Hanson.⁵⁰ The method follows closely that shown here; Equation (10.37) is substituted into Equation (10.34) using Equation (10.34a) with $\Omega = 0$ for the stator coordinate.

An interesting comparison can be drawn between Equations (10.37) and (10.51). For an inflow of w circumferential cycles, the force on each blade occurs at a frequency $w\Omega$, which is the encounter frequency of the blade with the gust. The sound pressure and the axial force, however, generate tones only when inflow harmonics are multiples of the blade number. All other inflow responses by the blades cancel. At small tip speed Mach numbers, $M_T = \Omega R_T / c_O = k_O R_T / m < 1$,

Equation (10.35) shows that the smallest order $n = mB - w$ Bessel function will generate the most noise, since $\xi_0 = k_0 R_T$ is less than unity. A nice experimental example of this matching of inflow and blade multiples has been provided by Heller and Widnall⁵¹ and is shown in Figure 10.14. Here a 10-bladed ($B=10$) rotor operated downstream of a 9-bladed stator $V = 9$, $w = kV$. One of the blades of the rotor was instrumented to give the alternating differential pressure across the blade surface while a microphone picked up the far field sound. The radiating mode order is then

$$n = mB - kV = 10m - 9k$$

The radiation tone occurs at

$$\omega = n(10\Omega)$$

but the encounter frequency of the blade is

$$\omega_e = k \cdot 9\Omega$$

The radiating "acoustic modes" from the rotor-stator interaction occur at $n=1,2,3\dots$ as shown and have spiral phase fronts of $n\theta - 10m\Omega t$. Such spiral wave fronts are called "spinning modes."

Another behavior indicated by Equation (10.51) is that radiation from the tangential forces will be zero whenever $mB = w$, because of the coefficient on $f_{\theta,w}$ in Equation (10.51). Therefore the strongest radiating tangential mode will occur when $mB = w \pm 1$ in compliance with the expression for the in-plane force (Equation (10.47a)). The directivity of the dipole sound will differ for the two force components. The axial force dipole will be zero in the plane of the rotor, because of the $\cos \beta$ directivity, while the tangential dipole will be finite in that plane. At other angles the relative magnitudes of the axial to tangential dipole strengths should be (crudely, at least for the same disturbance magnitudes at the respective inflow harmonics) in proportion to the steady thrust relative to the steady torque divided by radius; using Equations (10.22) this ratio is

$$\frac{F_1}{F_\theta} = \frac{TR_T}{Q} = \cot \beta_H = \cot \gamma$$

which is roughly 3 for a pitch to diameter ratio of unity.

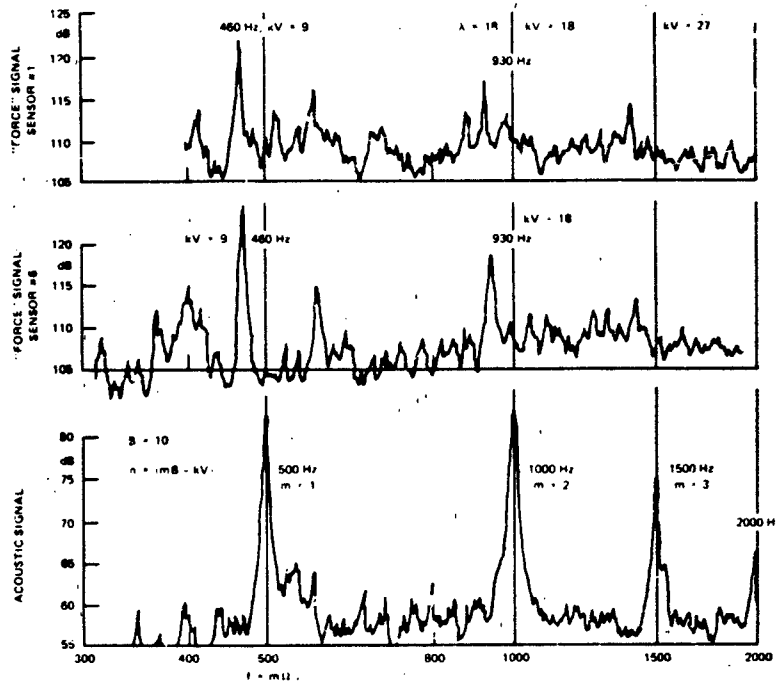


Figure 10.14 - Measured Forces on Rotating Blades and Sound Spectrum for a 10-Bladed Rotor Behind a 9-Bladed Stator Row (From Reference 51)

A final point to be made is that the direct dipole radiation from an acoustically compact rotor ($k_0 R \rightarrow 0$) may be written from Equation (10.51). In the limit of $k_0 R \rightarrow 0$, the limits of $J_n(\xi)$ (see Equation (10.35a)) give the acoustic pressure from the m th blade harmonic to the w th inflow distortion to first order

$$P_{w,m}(\vec{x}, t) \approx \frac{-iBk_0 \cos \beta}{4\pi R} \left\{ \int_{R_H}^{R_T} L'_w \left(R, \frac{wC}{R} \right) \cos \gamma e^{i w \theta_w} dR \right\} \times e^{i(k_0 R - mB\Omega t)}$$

for $w = mB$ only and $k_0 R \ll 1$. The term in brackets is simply the axial component of force on each blade due to the $w = mB$ inflow distortion. A second order term, proportional to $(k_0 R)^{w-mB}$, and due to the side forces is not dipole, but higher order, and is important only in the plane of the rotor. Its magnitude is much less than that of the dipole sound evaluated on axis. The above result could have been obtained through the combination of Equations (2.77) and (10.47).

10.5 SELF-NOISE FROM ROTATING MACHINERY

Although there has been extensive work on Gutf and thickness noise, very little work has been done on the viscous sources of self-noise. The work that has been done is so fragmented that a clear picture of all the dominant physical variables cannot be given. However, the results of previous chapters will be drawn on to give the best possible explanation of observed self-noises from isolated rotors.

10.5.1 Sounds from Steady Loading: Gutf Sound

When $w = 0$, the inlet flow is uniform, so $L_{s,w} = L_{s,0}$ in Equation (10.37) which reduces to just the steady loading on the blades (Equations (10.9) and (10.10)). The Fourier amplitude of the harmonic force given by Equations (10.50) and (10.53) becomes for the axial force

$$Bf_{1,0} = T$$

and

$$Bf_{\theta,0} = T_{\theta} = \frac{Q}{R_T}$$

for the tangential force. These are the force components, steady in the rotating frame, but transiently applied at a frequency $B\Omega$ to fluid particles passing through the rotor disk, which make sounds. Equation (10.51), evaluated for $w = 0$, gives each harmonic $p_{o,m}(\vec{x}, t)$ (normalized on the dynamic pressure based on rotational speed).

$$\begin{aligned} \frac{p_{o,m}(\vec{x}, t)}{q_T} = & \frac{-1}{\pi^3} k_T \frac{mB\Omega T}{1 + \left(\frac{J}{h}\right)^2} \left(\frac{D}{r_o}\right) \left[\cos \beta + 2 \left(\frac{\Omega(0.35\eta)}{c_o} \right)^{-1} \frac{k_Q}{k_T} \right] \\ & \cdot J_{mB} \left[\frac{mB\Omega(0.35D)}{c_o} \sin \beta \right] \exp i \left[\frac{mB\Omega r_o}{c_o} + mB \left(\theta - \frac{\pi}{2} \right) - mB\Omega t \right] \end{aligned} \quad (10.54)$$

$$-\infty < m < \infty$$

where $M_T = \Omega R_T / c_o$, and

$$q_T = \frac{1}{2} \rho_o \left(\Omega^2 R_T^2 + v_a^2 \right)$$

and k_T, k_Q , and J are the propeller parameters introduced in Section 10.2. Since propellers are designed so that the maximum value of $L(R)$ occurs near the midspan ($0.7R_T$), we have let $R_1 = 0.7R_T = 0.35D$. The total pressure is a summation over all modes $-\infty < m < \infty$. Equation (10.54) is a classical result that was first derived by Gutin¹⁰ in 1936. Later elaboration of the theory to account more precisely for propeller design parameters was given by Merbt and Billing,⁵² who also considered the effects of forward flight. Experimental verification of Equation (10.54) was first provided by Ernsthausen⁵³ ($0.6 < M_T < 0.9$) and Deming⁵⁴ ($0.7 < M_T < 0.9$) and later by Hubbard and Lassiter,⁵⁵ covering the range $0.75 \leq M_T \leq 1.3$, as shown in Figure 10.15.

The first nontrivial mode of Equation (10.54) is $m = 1$, i.e., a tone at $\omega = B\Omega$. Using Equations (10.35a) and (10.35b), Equation (10.54) can be simplified. A spectral density function can be created from the amplitudes of $p_{o,m}$, so that the autospectral density of the radiated sound pressure is

$$\phi_{p_{rad}}(\vec{x}, \omega) = \frac{1}{4} |p_{o,m}(\vec{x}, MB)|^2 [\delta(\omega \pm mB\Omega)]$$

$$\begin{aligned} \frac{\phi_{p_{rad}}(\vec{x}, \omega)}{q_T^2} &= \frac{1}{\pi^6} \frac{k_T^2 (mB) M_T^2}{\left(1 + \left(\frac{J}{\pi}\right)^2\right)^2} \left[\frac{e}{(2\pi)^{1/2}} \left(\frac{mB}{mB+1}\right)^{mB+1/2} \right]^2 \cdot \left(\frac{R}{r_o}\right)^2 \\ &\cdot \left[\frac{1}{2}(0.7)e M_T \sin \beta \right]^{2mB} \left[\cos \beta + \frac{2(0.7)}{M_T} \frac{k_0}{k_T} \right]^2 [\delta(\omega \pm mB\Omega)] \end{aligned} \quad (10.55)$$

or $m > 0$

where $(e/2)(0.7) M_T < 1$ and $e = 2.71828$. This expression is easily interpreted to give five general features of Mach number dependence, blade number dependence, and directivity. The function involving $mB/(mB+1)$ in the brackets is nearly unity

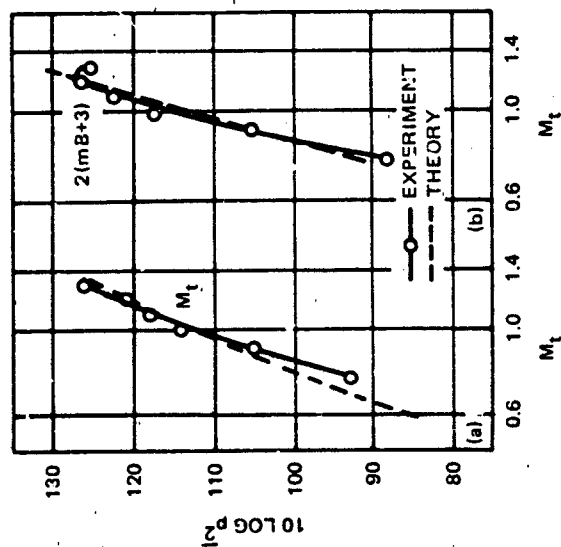
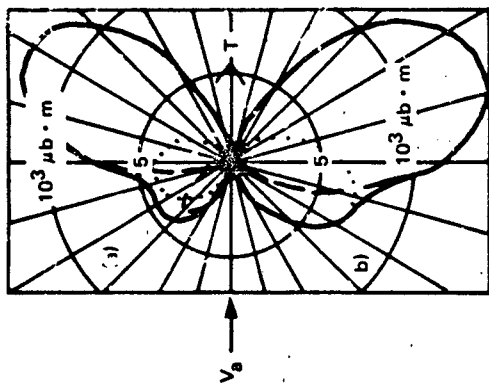


Figure 10.15a - Measurements by Hubbard and Lassiter, 55
 $B = 2$, $D/R = 0.13$, $k_T \approx 0.09$, $k_Q \approx 0.01$,
 $\gamma = 15$ deg, $D = 2$ ft

--- Gutin Sound
 Thickness Sound
 $mB = B = 2$, $M_T = 0.8$

Figure 10.15 - Illustration of Rotation Sound from Steady Loading (Gutin) and Thickness

for large numbers of blades and may be ignored. The first observation is that the absolute value of the spectrum consists as a series of discrete tones whose level increases as $U_T^{(2mB+6)}$, accounting for the fact that rotation sound is mainly a high-speed source. See, for example, Figures 10.1 and 10.15. Furthermore, since M_T is less than unity, the $M_T^{(2mB)}$ behavior shows that at a given shaft speed the propeller with larger blade number will generate less sound; the sound levels fall off rapidly as the harmonic order m increases as long as tip velocities remain subsonic. The noise is also directive (Figure 10.15), being zero on the axis of the propeller and relatively small (except at very low Mach numbers) in the plane of the propeller. The sound is directed at intermediate angles that approach the plane of the propeller as mB increases.

5.2 Laminar Flow Surfaces

At Reynolds numbers, based on chord, that are less than 10^6 to 2×10^6 , vortex shedding tones occur at the trailing sharp edges of translating airfoils. The frequencies of the tones increase roughly as $U^{1.5}$. This behavior was discussed in Section 9.4.4.1 and Figure 9.37, and one would expect it to occur in a similar fashion on propellers. In terms of the analysis of Section 10.4, the vortex dipole force, for example, F_v , should occur normal to the blade so that the axially directed component will be $F_v \cos \gamma$ and the tangential component will be $F_v \sin \gamma$. The frequency and strength of F_v would increase with radius because the velocity inflow to each blade section increases with the radius of the section. The frequency of "laminar" shedding increases with radius roughly as $r^{1.5}$. The analytical modeling of this noise can follow along the lines of Section 5.7, where the vortex sound spectrum was shown to be continuous even though the vortex shedding is locally discrete. A precise reanalysis for "laminar" shedding along those lines would differ slightly to account for the $U^{1.5}$ dependence of frequency on speed. In order to make use of the results of Chapter 5 we ignore this effect; to include it would serve only to change slightly the noise spectrum shape at frequencies less than $f/U_T = 1$, where y_f is the vortex shedding length scale that is implied by Equations (9.64) and (9.67) for airfoils with sharp trailing edges. Using Equations (9.64) and (9.67)

$$\frac{\omega_s y_f}{U_s} \approx \frac{\omega_s y_f}{U_\infty} \approx 1$$

$$\frac{2\pi f_s \delta}{U_\infty} = \frac{\omega_s \delta}{U_\infty} \approx 0.11\pi$$

which implies that

$$y_f \approx 2\delta \text{ to } 3\delta$$

where δ is the laminar boundary layer thickness estimated in Section 7.5.1. The sound spectrum may then be approximated by Equation (5.60), but with $y_f \approx 2\delta$ replacing the cylinder diameter, $\overline{C_L^2} = 2C_L(\omega)\Delta\omega$, as in Figure 9.37, and $2L$ represents the diameter of the rotor. To account for the number of blades, Equation (5.60) must be multiplied by a factor $B/2$.

The rotation effects introduced in Section 10.4 are not important because of the distributed nature of the sound spectrum of Figure 5.27a caused by the continuous increase of shedding frequency with radius. This distribution applies equally to the force function $F_1(R, \theta_o, \omega)$ appearing in Equation (10.36a) that is integrated along the radius, thus distributing the spectrum in much the same way as Equation (5.58) yielded Equation (5.60). Since the maximum value of the integrated force spectrum will occur at $\omega = U_T/y_f$, and since harmonics of the type shown in Figure 10.12 occur at intervals $\Omega \ll U_T/y_f$, it is clear that the noise source that consists of a continuous vortex shedding along the radius will be essentially broadband, and the direct application of the results of Section 5.7 is appropriate.

Measurement of the sounds of "laminar" shedding from propellers has been provided by Grosche and Stiewitt⁵⁶ and by Hersh and Hayden.⁵⁷ Figure 10.16 shows an example of a measured dimensionless sound pressure spectral density. The sound was generated by a propeller with two blades which were NACA 0012 sections with a 22.5 deg constant blade (pitch) angle. Throughout most of the frequency range of measurement, $\omega C/c_o$ exceeded π ; therefore a single power of Mach number was used in the normalization (see Section 9.2.3). Figure 10.17 also shows a broad hump at $f = f_s$ where $f_s \propto n_s^{1.5}$, which suggests that y_f behaves as a laminar thickness scale. However, we find that in this case $2f_s \delta/U_T \approx 0.57$. This result is included to

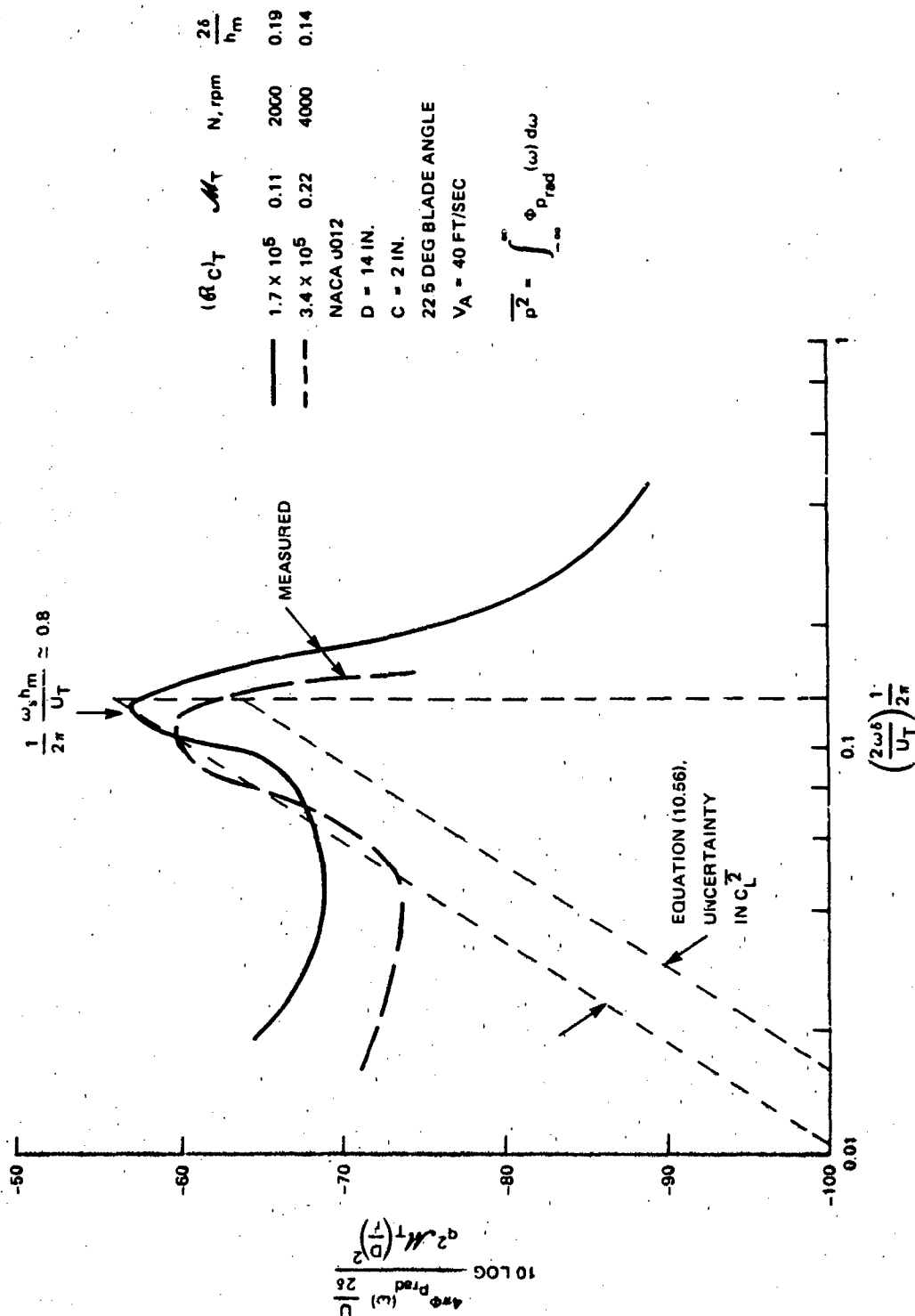


Figure 10.16 - "Laminar" Vortex Shedding Noise from Two-Bladed Propeller
 Measured by Hersh and Hayden⁵⁷ and Computed Using Equation (10.56)
 with Parameters from Chapter 9. δ is the Estimated Laminar
 Boundary Layer Thickness at the Tips

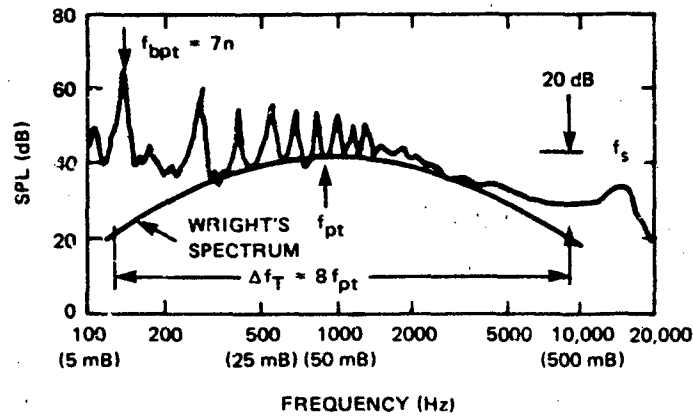


Figure 10.17 - Acoustic Spectrum of an Open Fan.

$U_T = 140$ ft/sec, $B = 7$, $D = 2.25$ ft,

$h_m = 0.13$ in, $C = 2.6$ in, $r = 7.5$ ft,

$\beta = 0$ deg, $\Delta f = 3.16$ Hz; $f_{pt} C/U_T = 1.0$,

$f_s h_m/U_T \approx 1$, $R_{c_T} = 1.5 \times 10^5$

(From Ref. 6, Copyright Academic Press)

suggest that the estimation of these noises is at best crude for many practical situations for which the flow conditions may not be closely controlled. It is clear that further work must be done.

When Equation (5.60) is used to predict the sound pressure spectrum, it must be multiplied by the diffraction factor $\mathcal{D}(\omega c/c_0)$, plotted in Figure 9.15. The appropriate equation for the spectral density is $\phi_{p_{rad}}(r, \omega)$ following the scheme outlined above (with $\omega_s \propto R$ rather than $\omega_s \propto R^{1.5}$):

$$\frac{\phi_{p_{rad}}(r, \omega) \frac{U_T}{2\delta}}{q_{T M_T}^2 \left(\frac{D}{r}\right)^2} = \frac{B}{2} \frac{\cos^2 \beta}{32\pi^3} \left(\frac{8}{\pi}\right) \left(\frac{2\delta}{C}\right) \left(\frac{2\omega\delta}{2\pi U_T}\right) \cdot \left[\left(\frac{\omega C}{U_T}\right)^2 \frac{2\Lambda_3}{2\delta} \frac{C_L^2}{C_L^2} \right]$$

$$\begin{cases} \frac{1}{2} \left(\frac{1}{2\pi S}\right) \left(\frac{2\omega\delta}{2\pi U_T}\right)^4, & \frac{2\omega\delta}{U_T} < 2\pi S \approx 1 \\ 0 & \frac{2\omega\delta}{U_T} > 2\pi S \end{cases} \quad (10.56)$$

A few comments of explanation regarding Equation (10.56) are in order. The $8/\pi$ factor results from the linear approximation for $\mathcal{D}(\omega c/c_0)$ shown in Figure 9.15. The value of the $\overline{C_L^2}$ term in brackets can be taken directly from Figure 9.37 for the appropriate values of the tip Reynolds number. The two values measured by Hersh and Hayden shown in Figure 9.37 were used in the calculation. The values of δ were computed for the tip velocity and S is the Strouhal number definition (Equation 9.64) of Paterson et al.⁵⁸ The experimental results shown in Figure 10.16 are consistent with those of Grosche and Stiewitt.⁵⁶ Discrepancies between measured and theoretical spectra for cylinders were discussed in Section 5.7; they apply to this case.

10.5.3 Turbulent Trailing-Edge Noise

Noise arising from the convection of turbulent flow past sharp trailing edges was discussed at length in Chapter 9, particularly Sections 9.6.3.4 and 9.6.3.5. In the case of propellers the physical processes are expected to be identical. Since the spanwise correlation length of the largest of eddies causing the noise is only on the order of the local boundary layer thickness, the noise is locally generated at each radius section. In Chapter 9, this noise was shown for a given type of flow (wall jet, boundary layer, etc.) to be a function of flow and geometry parameters. Drawing on those results, the one-third octave band levels of sound pressure radiated to the field point r on the axis of the propeller by an element of the span dR is given by

$$d \left[\overline{p^2} (r, \omega; \Delta \omega) \right] = q_T^2 M_T \left(\frac{R}{R_T} \right)^5 \frac{\delta \cdot dR}{r^2} f \left(\frac{\omega \delta^*}{U(R)} \right) \Delta \left(\frac{\omega \delta^*}{U(R)} \right) \quad (10.57)$$

where $f(\omega \delta^*/U)$ is a dimensionless spectrum function expected to be much like those shown in Figures 9.38 and 9.41. The sound will be roughly dipole-like, with a maximum intensity on the propeller axis; for small blade angles there should be little sound in the plane of the propeller. The spectrum function $f(\omega \delta^*/U)$ will depend on the details of flow; it is a smooth function of its argument and for simplicity may be regarded as having a power form such as

$$f(\Omega) = A \Omega^{-\alpha} \quad (10.57a)$$

$\delta \omega = a \omega$ for proportional bands, where α may have values from 0 to roughly 2 as indicated by the measurements and theory that are given in Section 9.6.3.

The total sound pressure from B blades can be found approximately by integrating over $0 < R/R_T < 1$:

$$\overline{p^2}(r, \omega; \Delta\omega) = 2 \phi_p(r, \omega) \Delta\omega \approx \frac{B}{5+\alpha} q_T^2 M_T \frac{\delta^* R_T}{r^2} f\left(\frac{\omega \delta^*}{U_T}\right) \left[\frac{(\Delta\omega) \delta^*}{U_T}\right] \quad (10.58)$$

This form is obtained by integrating the algebraic approximations introduced above, Equation (10.57a), regrouping terms, and finally reinstating the original functional representations. The function $f(\omega \delta^*/U_T)$ is still the dimensionless spectrum function, dependent on flow details and therefore sensitive to the surface profile. Depending on the specific nondimensionalization used δ^* may be replaced by alternative length scales as discussed in Section 9.6.3. Figure 9.38, for example, shows measurements by Schlinker⁵⁹ of noise from two NACA profiles with sharp trailing edges compared with estimates made using Equation (9.114) and it represents $f(\omega \delta^*/U_T)$ for sharp-edged blade sections. For sections other than the NACA sections the δ^*/h_m will fall approximately within the bounds given in that Figure. For edges which are other than sharp, the continuous spectrum function may be formed by using Equations (9.111) or (9.112) and spectra such as shown in Figures 9.33 and 9.34 and integral lengths such as those given in Section 9.34. It is to be stressed, however that such estimates are without real current experimental validation.

Available measurements of sound radiated from airborne fans and propellers substantially corroborate the validity of Equation (10.58). These measurements are shown in normalized fashion, using the maximum blade thickness h_m at $R = 0.7 R_T$, in Figure 10.18. Shown are spectra obtained from two propellers (of 2 blades each), a ventilation fan,⁷⁰ and a two bladed helicopter rotor in a whirl tower.⁶¹ Of the two bladed propellers, that of Hersh and Hayden⁵⁷ is identical to that discussed in connection with Figure 10.16 but with tripped boundary layers. The second of the spectra from a two blade propeller is previously unpublished and it was generated with constant-pitch blades having an NACA 66 section ($h_m/c = 0.1$) modified with an elliptical trailing edge,^{70a} but beveled as edge 9 in Table 9.3. For $fh_m/U_T > 0.3$ all spectra collapse into a reasonable band. The broad humping of the helicopter and fan rotors may be due to a broad band vortex shedding such as described in Chapter 9. At low frequencies, $fh_m/U_T \sim 0.05$, a second broad hump is also apparent, this will be discussed in Section 10.5.4.

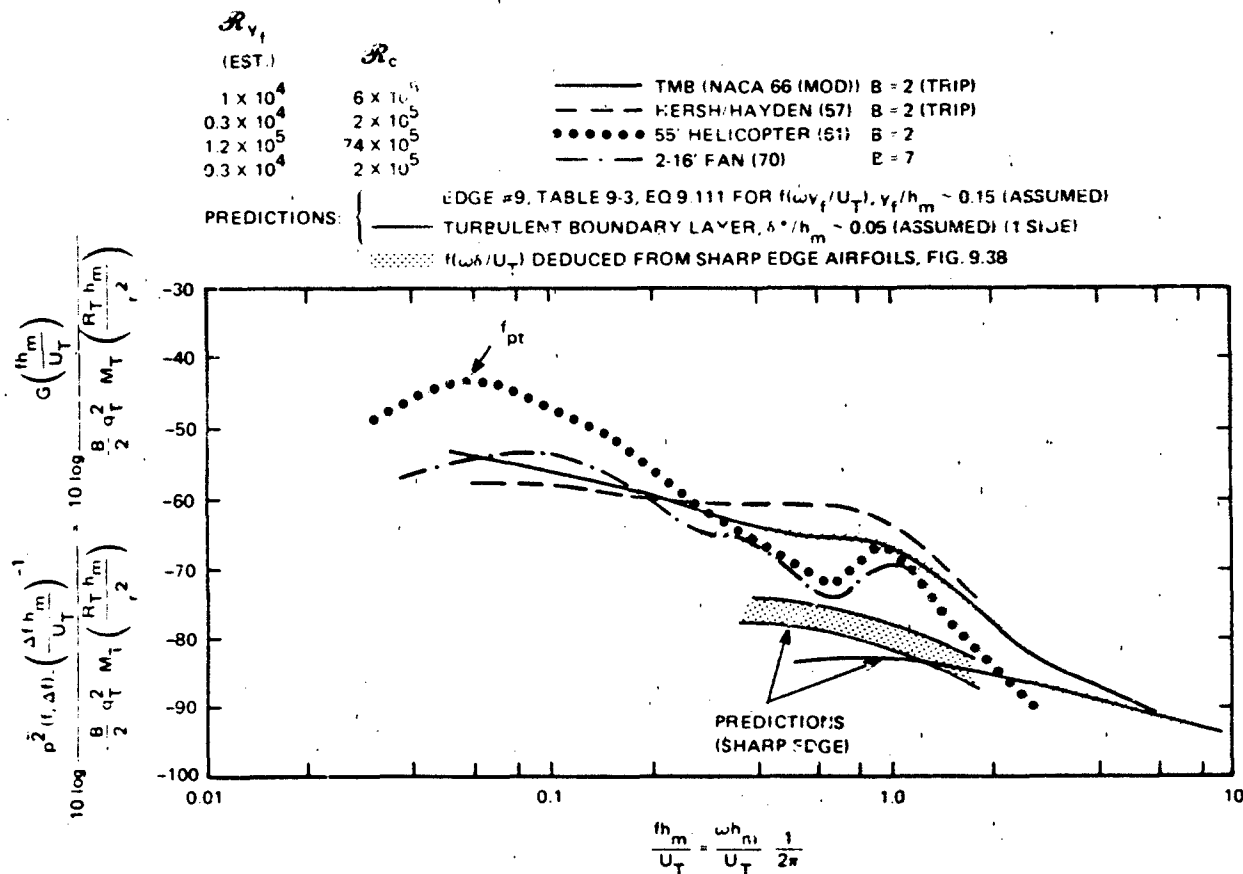


Figure 10.18 - Comparison of Nondimensional Sound Spectra for Various Fans and Rotors with Known or Suspected Turbulent Flow

Some rough theoretical estimates, obtained using the methods described above are also shown in Figure 10.18. Separated flow such as discussed in Chapter 9 is assumed on one side of the blades while attached turbulent flow is assumed on the other. The ordinate, expressed in terms of Equations (9.111 and 10.58) is for the curved or beveled

$$\begin{aligned}
 \frac{\overline{p^2(f, \Delta f)} \left(\frac{\Delta f h_m}{U_T} \right)^{-1}}{\frac{B}{2} q_T^2 M_T \left(\frac{R_T h_m}{r^2} \right)} &= \frac{G \left(\frac{f h_m}{U_T} \right)}{\frac{B}{2} q_T^2 M_T \left(\frac{R_T h_m}{r^2} \right)} \\
 &= \frac{4}{7\pi} \frac{\Lambda_3}{h_m} \frac{y_f}{h_m} \left(\frac{\phi_{pp}(\omega)}{q_\infty^2} \right) \frac{U_T}{y_f} \quad \omega = 2\pi f
 \end{aligned}$$

where $\alpha = 2$ has been taken as an average over the frequency range and where the spectrum function for edge 9 is shown in Figure 9.32 and Λ_3/y_f is given by Equation (9.85). Also shown is the estimate for the case of turbulent flow past the sharp edge. These estimates are given assuming that one flow type exists on each side of the surface in accordance with the known geometric form of the NACA 66 (MOD) sections used for one of the propellers and this estimate should at least match measured levels for that propeller. Clearly, the separated flow on the beveled side dominates the radiated sound, and if the section had cusped edges, then one would expect the roughly 3 dB greater values than those indicated for the boundary layer turbulence. Both the helicopter and the fan levels begin to approach this latter estimate on either side of the $fh_m/U_T \approx 1$ hump. It is to be noted that utilization of nondimensional levels for the NACA0012 section in Figure 9.2 for $f(\omega\delta^*/U_T)$ gives estimates that are shown as the shaded area. Any vortex shedding induced by bluntness and that is superimposed on the flow would create an additional concentration of sound energy near $fh_m/U_T \approx 1$. Thus it is apparent that sound from rotating blades will be dependent on both the type of flow (compare Figures 10.16 and 10.18), Reynolds number, and edge geometry as suggested by the range of measured sound levels shown. A further systematic study focussed on this matter is clearly needed, however, such as those offered recently by Schlenker and Amiet¹⁵² and by Kim and George.¹⁵³

10.5.4 Broadband Noise Related to Loading

In a substantially lower frequency range than $f \approx h_m/U_T$, there is a broadband noise for which there are conflicting hypotheses.⁶ This noise has a spectrum centered on the frequency f_t , as illustrated in Figures 10.1 and 10.18. The 20 dB-down bandwidth of this spectrum Δf_t is of order

$$\Delta f_t \approx 8 f_t$$

and the center frequency appears to vary as

$$\frac{f_t C}{U_T} \approx 0.8 \text{ to } 1.0 \quad (10.59a)$$

according to Wright⁶ who examined the large body of data or in some cases at a slightly lower frequency

$$\frac{f_t C}{U_T} \approx 0.45 \quad (10.59b)$$

according to Stuckey and Goddard¹³ for their own data. Widnall¹² and Wright⁶ have proposed competing empirical correlations for this noise that are based on the idea of a vortex-dipole mechanism. Widnall addressed only the question of the total sound pressures of helicopter rotor noise in the hovering (or whirl tower) condition, while Wright examined the 1-Hz band levels at the peak of the spectrum, i.e., at the dimensionless frequency of Equation (10.59a). He performed the data analysis for 12 samples of single-stage axial-flow machinery including helicopter rotor, propellers, and automobile cooling fans (Table 10.1). Although Wright's analysis was strictly empirical (Widnall's was couched in dimensional arguments based on vortex noise (Section 5.7)), he was able to collapse various measurements rather well.

Figure 10.19 shows Widnall's correlation with a few additional points that have become available since the original analysis. It is not a dimensionless representation, but it can be interpreted as a function of tip speed, Mach number, blade area, and thrust coefficient k_T

$$\overline{p}_{TOT}^2 = c_T^2 \frac{A_B}{r_o^2} M_T^2 f \left(\frac{T}{\rho_o A_B U_T^2} = \frac{k_T}{EAR} \right) \quad (10.60)$$

where the function of k_T/EAR , given by the normalization, is shown as the shaded region in Figure 10.19. For thrust-independent noises (which the high-frequency trailing-edge noise is expected to be) $f(k_T/EAR)$ should be a constant. Widnall's analysis shows this to be true for this low-frequency noise at low thrust coefficients, but for larger loading on the rotor the normalized sound pressure increases roughly as $(k_T/EAR)^2$.

Wright⁶ also accounted for variations of noise with changes in the steady load by including a function of blade angle whose form was selected on no other basis than to collapse the data. Figure 10.20 shows the peak 1-Hz band levels reduced to a "standard" rotor with the parameters indicated in the caption.

TABLE 10.1
SUMMARY OF ROTOR PARAMETERS⁶ FOR SPL_{sb} IN FIGURE 10.19

Rotor(ref.)	U_t (ft/s)	β°	B	D(ft)	C(in)	R(ft)	BW(Hz)	SPL rotor	SPL std. bld	f_t (Hz)	$\frac{f_t}{U_t}$	$\frac{f_t}{C}$	$\frac{f_t}{R}$	f_{bpf} (Hz)
4 ft VGR	210	$\beta = 5$	2	4	3.15	10	1	33	-9	600	0.7	10	10	32
19.5 in Auto fan (60)	228	$\alpha = 4^*$	20	1.6	2.4	5	300	68	-6	1.2k*	1.1	12	12	870
9 ft Hel (61)	284	$\beta = 6$	2	9	4	28	5	45	-4	500	0.6	11	11	30
24 in Auto fan (60)	345	$\alpha = 4^*$	9	2	5	6	300	78	3	800	1.0	8	8	495
4 ft Prop (62)	450	$\beta = 16$	2	4	3	12	25	68	6	1.5k	0.8	7	7	70
55 ft Hel (63)	465	$\beta = 6$	2	55	16	250	5	54	5	250	0.7	6	6	5.4
1.5 ft Aero fan (64)	599	$\alpha = 3$	12	1.5	2.86	25	100	69	17	2.8k*	1.1	8	8	1.5k
1.75 ft Aero fan (65)	700	$\alpha = 6$	12	1.75	2.8	10	100	86	19	3k	1.0	9	9	1.5k
60 ft Hel (66)	850	$\beta = 7$	3	60	25	60	1	90	28	300	0.7	6	6	15
7.2 ft Fan jet (67)	900	$\alpha = 4$	33	7.2	10	140	16	85	32	1.4k	1.0	10	10	1.4k
7 ft Prop (68)	910	$\beta = 8$	2	7	6	100	121	80	29	1.5k	0.8	6	6	84
3 ft Lift fan (69)	950	$\alpha = 4^*$	42	3	2.5	250	50	71	30	4k*	0.9	6	6	4.2k

*Estimated.

β is blade pitch angle not effective force angle; S_t is referred to the rotor tip speed not effective rotor speed.

$\frac{l}{Q} = \Delta f_t / f_{pt}$, a = chord, BW = bandwidth of sound measurement, SPL ref 1 μ b.

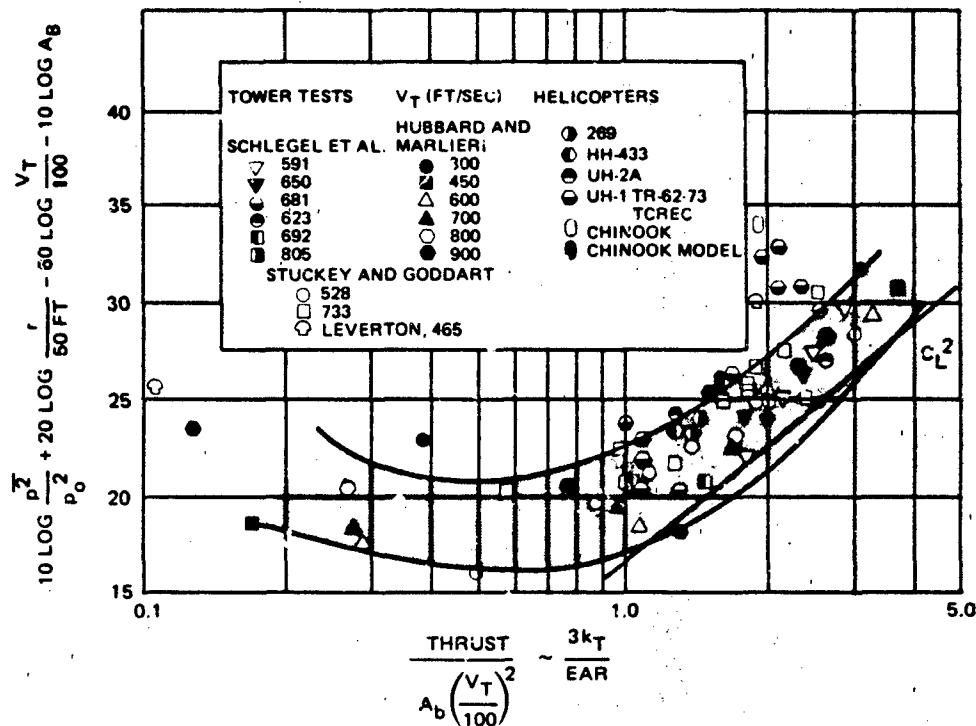


Figure 10.19 - Low-Frequency Broadband Noise of Helicopter Rotors from Whirl Tower and Helicopter Noise Measurements. Levels are OASPL re $p_0 = 20 \times 10^{-6} \text{ n/m}^2$ Reduced on Rotor Parameters by Windnall.¹² T , lbf; U_T , ft/sec; A_B , ft^2

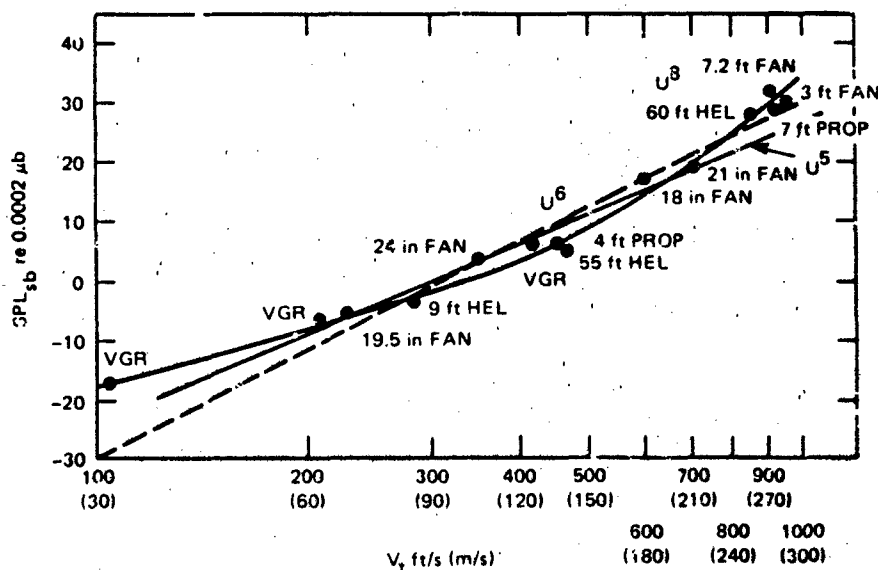


Figure 10.20 - Reduced Sound Pressure Levels (see Equation (10.61)) of Various Axial Flow Fans, Propellers, and Helicopters.

$D_{sb} = 1 \text{ ft}$, $B_{sb} = 1$, $C_{sb} = 1/3 \text{ ft}$, $r_{sb} = 100 \text{ ft}$.⁶
The U^5 Line Applies to $10 \log G(1) = -88$

The SPL_{sb} is just

$$10 \log \left\{ \frac{\overline{p^2}(f_{pt}, \Delta f)}{\Delta f} \left(\frac{r}{r_{sb}} \right)^2 \left(\frac{D_{sb}}{D} \right)^2 \frac{B_{sb}}{B} \frac{C_{sb}}{C} \right\} - 2\alpha = SPL_{SB} \quad (10.61)$$

where f_{pt} is the frequency of the peak level (Equation (10.59a)) and α is the blade angle of attack in degrees. The blade angles used varied from 3 to 3 deg (average of 5 deg) for 11 of the samples; it was 16 deg for the 4-ft propeller. Therefore generally the variation in the corrections for α from case to case amounted to no more than ± 5 dB. This is significant only in that the introduction of α in the normalization is an attempt to account for possible load variations. Table 10.1 shows the remainder of the rotor parameters. Figures 10.1 and 10.17 (data from Reference 70) show examples of the agreement of Wright's correlation and measured sound levels.

The normalization of Equation (10.61) can be put on more theoretical grounds by the following argument. The dipole-induced sound pressure can be written in terms of a general dimensionless spectral density, for example, $G(fC/U_T)$, a loading function, for example, $P(\alpha)$ or $P(EAR/k_T)$, and the other familiar parameters, i.e.,

$$\begin{aligned} \overline{p^2}(f, \Delta f) &= B q_T^2 \left(\frac{D}{r} \right)^2 M_T^2 G \left(\frac{fC}{U_T} \right) P(\alpha) \frac{\Delta f C}{U_T} \\ &= \overline{p^2}(\omega, \Delta \omega) \end{aligned} \quad (10.62)$$

The function $G(fC/U_T)$ is just the spectrum shape which is maximum at $G(1)$ and which appears as an arc-shaped curve with 20 dB down points indicated in Figure 10.1.

$G(f_t C/U_T)$ and the sound pressure levels in a 1-Hz band for the standard blade SPL_{sb} are related by $SPL_{sb} = 10 \log G(1) + 20 \log q_T + 10 \log M_T - 75$ at $f_t C/U_T = 1$; $10 \log G(1) = -88$. A function $P(\alpha)$ was derived by Wright by the identify

$$2\alpha = 10 \log e^{0.46\alpha}$$

making $P(\alpha) = \exp(0.46 \alpha)$. For a given value of α and Δf , the peak sound pressure $\overline{p^2}(f=f_t=U_T/C, \Delta f)$ will be given by Equation (10.62) to increase as U_T^5, C, D^2, r^{-2} ,

d B in accordance with the form used by Wright (Equation (10.61)). The U_T^5 speed dependence is evidently displayed by a range of reduced values shown in Figure 10.20. From Equation (10.62), it is also possible to deduce Widnall's form. The total mean-square sound pressure is the integral over the dimensionless frequency. The thrust of the device is proportional to a lift coefficient times blade angle; i.e., we let

$$\overline{p^2} = \int_0^\infty \left[\overline{p^2}(f, \Delta f) / \Delta f \right] df$$

d

$$T \propto \frac{1}{2} \rho_o U_T^2 A_B C_L \alpha$$

where C_L is a lift coefficient. Making these substitutions, the total mean-square pressure $\overline{p^2}$ may be seen to depend on the proportionality

$$\frac{\overline{p^2} r^2}{A_B U_T^6} \propto \frac{1}{B} \left(\frac{T}{\rho_o A_B U_T^2} \right) \frac{1}{C_L^2} \left(\frac{D^2}{A_B} \right) \frac{P(\alpha)}{\alpha^2} \quad (10.63)$$

This shows a general behavior that is consistent with Figure 10.19, at least for the larger values of thrust. Note that for the range of α (3 to 8 deg) covered by most of the cases in Table 10.1, $P(\alpha)/\alpha^2$ shows remarkable constancy, varying by less than ± 0.5 dB. Therefore, within the scatter band of both Widnall's and Wright's correlation, the two approaches appear to be equivalent, and both suggest a direct relationship between the moderate-frequency noise and loading. As the thrust loading on the rotor increases, so does the radiated noise. For marine and air screws that operate at small flow angles of attack, k_T does not generally exceed 0.2. This value seems to be equivalent to a normalized thrust in Widnall's curve of approximately 1.2 or less. Therefore the load-dependent noise is perhaps of less importance on propellers compared to such noise from hovering helicopters, fans, and other stationary low-J (high k_T /EAR) devices due to the large flow angles in such machinery. These larger flow angles may cause thicker blade boundary layers and large-scale turbulence than on the higher-J devices.

10.5.5 Propeller Singing

Propeller singing due to trailing-edge vortex shedding is phenomenologically so similar to hydrofoil singing (Section 9.6), that the parameters governing both occurrences are the same. Remarks here are therefore limited to additional published experience with propellers specifically. The reader is referred to Section 9.7 for the basics. Furthermore, since singing is the result of the strong tonal excitation of a specific rotating blade mode, a narrow-band spectrum of the sound will appear as a series of lines as illustrated in Figure 10.12 due to periodic Doppler shifting.

The source of propeller singing is here regarded as trailing-edge vortex formation; however, in the early literature it was not known whether leading- or trailing-edge flow was responsible for the tones. In an early paper Hunter⁷¹ presented a series of full-scale "case" studies from which he concluded that the hydrodynamic cause of leading-edge surface pitting (due to cavitation) on some propellers was the same as that which caused "humming," "clapping," and "singing" sounds. He also recognized that such noises could be related to the structural resonances of the blades and that cast iron propellers were less apt to cause "singing" tones than bronze ones because of higher damping in the former. In subsequent papers on the subject⁷²⁻⁷⁴ the notion of leading-edge excitation persisted because of the continuing experience that thickening leading edges often alleviated the problem. There was, nonetheless,^{75,76} growing evidence of a trailing-edge source. Also, the notion of increased structural damping as a remedy continued to be recommended.⁷³ The idea of leading-edge excitation seems to have persisted at least until 1951,⁷⁵ although there was growing sentiment toward the importance of trailing-edge flow. The problem was that most reasoning was based on supposition and conjecture; observations were exclusively full scale.

Following Gongwer's⁷⁷ classic experiments in 1952, Lankester and Wallace⁷⁸ performed a series of model and full-scale propeller experiments that showed irrefutably the importance of trailing-edge thickness and form in controlling singing. Furthermore, they elucidated the importance of trailing-edge sweep and trailing-edge thickness in controlling the singing frequency by successfully applying Equation (9.27) to predict the singing frequencies of propellers. They observed amplitude modulation of the tone signal as the blades passed through the ships' wake, and they suggested that manufacturing variations in surface finish and edge detail were responsible for some propellers singing and others not. The notion of leading-edge flow as a source of noise and vibration has apparently vanished from the

terature; however, in retrospect it is easy to conceive that certain separating leading-edge flows could excite blade vibration just as they influence cavitation inception.

Subsequent experimental work by Krivtsov and Pernik⁷⁹ and later by Cumming⁸⁰ determined that propellers were most likely to sing when the blade sections operate at their (small) design angle of attack, or advance coefficient, and that a hysteresis effect⁸⁰ could occur in the singing frequency - shaft speed relationship when the "lock-in" was most pronounced. The use of a wedge-like trailing edge to reduce the tendency of propellers to sing was examined by van de Voorde,⁸¹ who concluded that wedge angles less than 25 deg were required to prevent singing. This behavior is discussed extensively in Chapter 9. A review of this and other work prior to 1964 has been provided by Ross.⁸²

Examination of blade vibration modes exclusively was made by Burrill,^{83,84} who determined mode shapes and resonance frequencies in air and in water.⁸⁴ The modes observed in air and water often differed in detail, and the added masses indicated from the resonance frequencies were within a factor of two of those estimated with equation (6.91).

1.5.6 Thickness Noise

As a rotor blade of finite thickness passes through the fluid particles close to the fluid, the blade surface is accelerated around the contour of the blade. It is the motion of these fluid particles that causes sound known as thickness noise. In a sense, because fluid in a fixed control volume is made to compress and expand as the penetrating blade displaces fluid, this acoustic source is a volume source. One of the earliest analyses of the problem was that of Deming⁸⁵; later analysis was done by Merbt and Billing.⁵² More recently the systematic control of this noise by proper choice of blade thickness and profile has been examined by Lyon^{86,87} and by Hanson.⁴⁷ Since this noise is not important for low subsonic speed rotor flow, no quantitative analysis of the problem is given; interested readers should consult the references cited.

Figure 10.14b, due to Merbt and Billing,⁵¹ shows the relative magnitudes of thickness and Gurney sound for $M_T = 0.8$. It is to be noted that, although thickness noise does not dominate the sound power, it does fill in the directivity of the sound. Control of thickness noise is generally accomplished by selecting rotor

blade sections that minimize fluid accelerations near the leading-edge. Lyon⁸⁶ and Hanson⁴⁷ show examples of some leading-edge shapes that have been designed for low noise.

10.6 INTERACTION NOISE IN AXIAL FLOW MACHINES

10.6.1 Deterministic Unsteady Loading

For subsonic tip speeds, the Gutin sound (Section 10.5.1) is nearly always exceeded by sounds resulting from blade forces that result from circumferentially nonuniform inflows. Such unsteady loads occur in multistage axial-flow machines due to upstream rotors or stationary inlet guide vanes that (due to their own lifting characteristics) create a potential down wash and (due to their drag) create a wake velocity defect that leaves an imprint on the downstream flow ingested by the rotor. Such loading also occurs in single-stage machines, fans, propellers, and the like, due to the wakes produced by upstream grilles and wing surfaces, and in helicopters in forward flight due to interaction of blades with the tip vortices "washed" back into the rotor disk. The mathematical analysis of these sounds has, generally speaking, involved the following broad classes of predictions:

- a. Single unsteady blade loads due to a prescribed velocity defect; such predictions can be cast into the form of Equation (10.50) for acoustic predictions.
- b. Blade row responses to potential and viscous interaction with adjacent rows and including blade-blade interferences in the responding row.
- c. Acoustic emissions from potential and viscous interactions of blade rows in free acoustic fields or in enclosures using a complete formulation of both the blade forces and field pressures.

In the first two classes of problems, the results can be interpreted to give angular expansions of the acoustic dipole source strength, but such techniques will be most powerful when each blade is acoustically compact. For high frequencies, and high axial flow and tip Mach numbers, the numerical solutions resulting along the lines of the third classification will be most powerful. A recent review of the available analytical approaches has been given by Cumsty.⁵ Somewhat different analytical approaches than that used here have been adopted by Morfey⁸⁸ and by Mani,⁸⁹ as well as others concerned with propagation generated sound through blade rows (Section 10.6.1.4).

1.1.1 Single Blade Element Analysis of Cascades: First-Order Estimate of Sound

sure. For frequencies low enough that the individual blades may be considered statically compact, the first-order estimate of blade forces in a cascade considers each blade in a responding row as separate from adjacent blades. The classical Kemp-Sears analysis⁹⁰⁻⁹² determines the fluctuating loading on a stationary row downstream of a moving blade row and on a moving blade downstream of a fixed row. The upstream lifting surfaces were modeled as a cascade of flat-plate lifting surfaces; the downstream responding blade was also modeled as a flat two-dimensional surface. Figure 10.21 shows the geometry of a cascade consisting of a rotor following a stator row. The advancing flow V_a is turned in the first stage so that the effective advance flow into the second stage is V_{a1} . The potential reaction was found⁹¹ by approximating the field induced at the isolated responding blade due to the passing bound circulation Γ_s in the case of the stator, or Γ_r in the case of the rotor. The array of local point circulations causes a summation of circumferential modes (analogous to w in Equation (10.37)) to which the blade responds according to linear unsteady two-dimensional lifting theory. The lift on a rotor blade to the w th mode of the incident potential stator row disturbance depends on row geometry according to the proportionality

$$\left(\frac{L_r^s}{p} \right) \propto \exp \left\{ -\pi \sigma_{rs} \left[\frac{S_r}{S_s} \left(\frac{2d'}{c_r} + \frac{1}{2} \left(1 + \frac{c_s}{c_r} \right) \right) \right] \right\} \quad (10.64)$$

where $\sigma_{rs} = c_r/S_r$ is called the "solidity" of the rotor; in Figure 10.9 it is approximated by the expanded area ratio. The proportionality constant in Equation (10.64) is analogous to the Sears function of unsteady airfoil theory. The equation shows that for a given rotor/stator geometry the unsteady lift decays exponentially with row spacing d' . The major effect occurs as the spacing increases from negligible to the same order as the semichord of the rotor, $d' = C_r/2$. A similar result that applied to the mean-square rotor force was obtained by Heatherington.⁹³

The viscous interaction occurs because of the "gust" response of the downstream blade to an incident velocity defect in exactly the same manner as determined in Section 9.4 (see also Equation (10.37)) when the cascade effects in the responding row are ignored. The perturbation velocity superimposed on V_a , induced at the rotor,

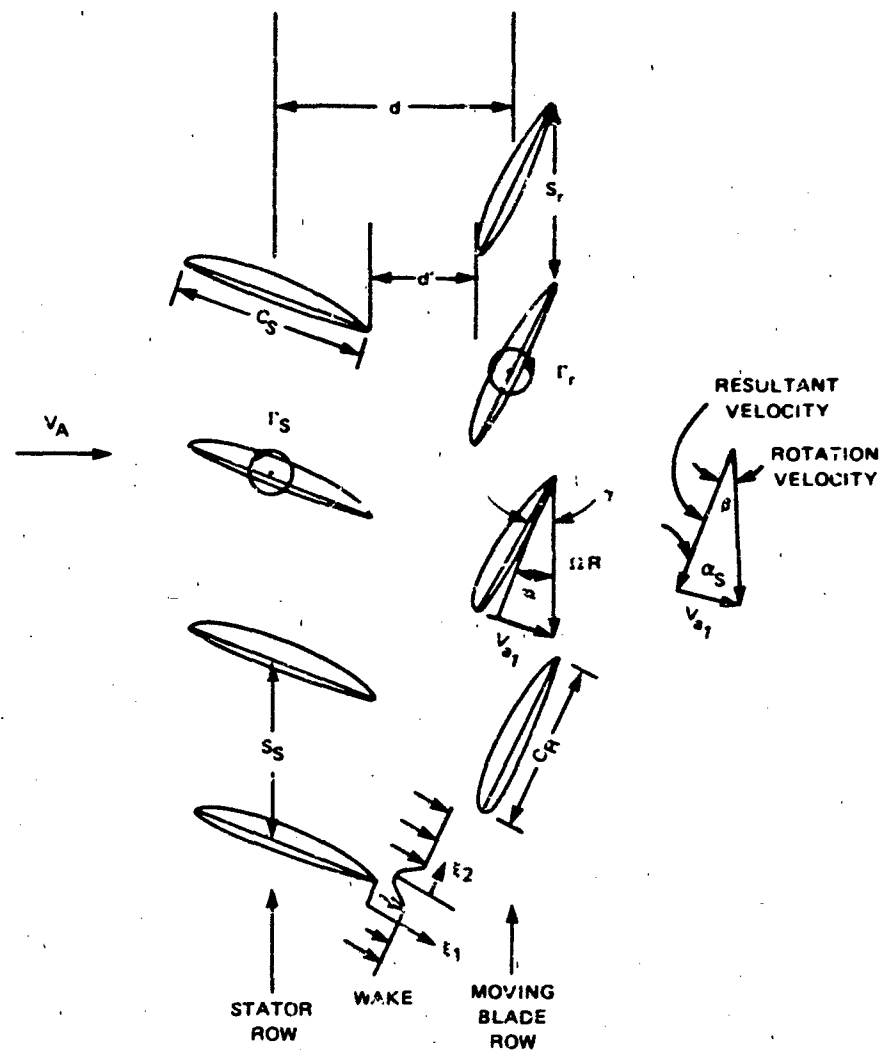


Figure 10.21 - Geometry of a Two-Stage Cascade. Γ_s and Γ_r are Bound Circulation of Stator and Rotor Blades, ΩR is the Rotational Velocity of Rotor Row, S_s and S_r are the Blade Spacing in the Respective Rows. β is the hydrodynamic pitch angle, α_s is the stagger angle, and γ is the blade pitch angle

$u(R, \theta)$, is circumferentially decomposed so that, relative to the rotating blade, with $\theta_f = \theta_w + \theta + \Omega t$

$$u(R, \theta(t)) = u(R, t) = \sum_{w=-\infty}^{\infty} u_w(R) e^{i w [6_w(R) + \theta - \Omega t]} \quad (10.65)$$

where

$$u_w(R) = \frac{1}{2\pi} \int_0^{2\pi} e^{-i w \theta} u(R, \theta) d\theta \quad (10.66)$$

and the phase angle $\theta_w(R)$ accounts for the possibility that the velocity defects are not all aligned radially. The $u_w(R) e^{i \theta_w(R)}$ are then fed directly into Equations (10.37), (10.42a) or (10.42b).

Kemp and Sears,⁹² as well as others, e.g., Morfey,⁹⁴ and Kaji and Okazaki,⁹⁵ have approximated each of the individual wakes as

$$u(\xi_1, \xi_2) = u_m(\xi_1) \exp \left[-\left(\frac{\xi_2}{y_w} \right)^2 \right] \quad (10.67)$$

where⁹⁶ the centerline velocity perturbation is

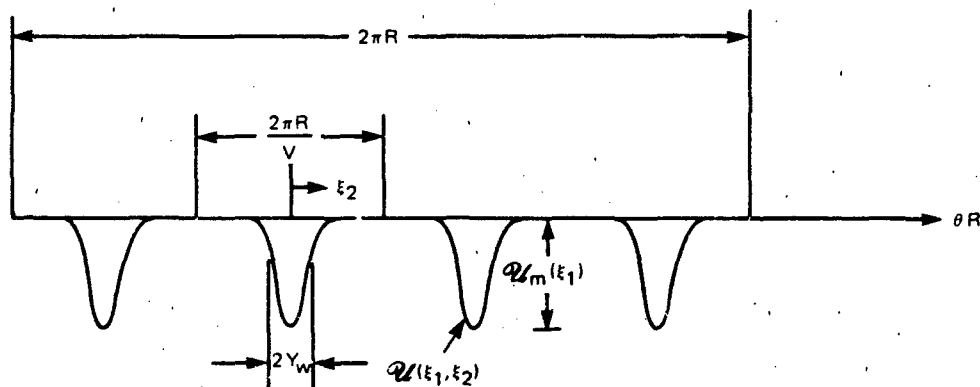
$$\frac{u_m(\xi_1)}{v_{a1}} = \frac{-(1.21 C_{Ds}^{1/2})}{\left(\frac{2\xi_1}{C_s} + 0.3 \right)} \quad (10.68)$$

and the characteristic wake width is

$$\frac{2y_w}{C_s} = 0.68 \left[C_{Ds} \left(\frac{2\xi_1}{C_s} + 0.15 \right)^{1/2} \right] \quad (10.69)$$

where C_{Ds} is the drag coefficient of the stator.* As illustrated in Figure 10.22, the pulse train of wakes causing a continuous perturbation velocity function around the disk is

*More recent wake measurements^{97,98} behind airfoils in cascades have indicated that Equations (10.67) to (10.69) are substantially valid for blade rows.



$$u(\theta R, R) = \sum_{k=1}^{V-1} u\left[\xi_1, R\left(\theta - \frac{k2\pi}{V}\right)\right] \delta\left(\theta - \frac{k2\pi}{V} - \xi_2\right)$$

Figure 10.22 - Illustration of a Circumferentially Periodic Wake Defect

$$u(R, \theta) = u_m(\xi_1) \sum_{\ell=1}^{V-1} \exp \left\{ - \left[\frac{R(\theta - \theta_w - \ell(\frac{2\pi R}{V}))}{Y_w} \right]^2 \right\} \cdot \delta \left[R(\theta - \theta_w) - \ell \left(\frac{2\pi R}{V} \right) - \xi_2 \right] \quad (10.70)$$

where θ_w is the (radially varying) sweep angle of the wakes. Substituting it into Equation (10.66), we have for the w th wake harmonic appearing in Equation (10.67)

$$\begin{aligned} u_w(R) &= \frac{1}{2\pi} \sum_{\ell=1}^{V-1} e^{i w [\theta_w + \ell(2\pi/V)]} \frac{1}{R} \int_{\xi_w} u_m(\xi_1) e^{-(\xi_2/Y_w)^2} e^{-i \frac{w}{R} \xi_2} d\xi_2 \\ &= u_m(\xi_1) e^{i w \theta_w} \cdot \frac{V}{2\pi R} \int_{-\infty}^{\infty} e^{-(\xi_2/Y_w)^2} e^{-i \frac{w}{R} \xi_2} d\xi_2 \cdot \delta(kV \pm w) \end{aligned} \quad (10.71)$$

The limits on the integral over the velocity defect have been changed from the total width ξ_w to infinity so that closed-form integrations can be used. This is formally correct as long as the wake is thin, i.e., $2Y_w < S_s$. The evaluation gives (Reference 99, p. 480) the distribution of distortion harmonics

$$u_w(R) = u_m(\xi_1) e^{i\omega\theta_w} \cdot \pi^{\frac{1}{2}} \left(\frac{VY_w}{2\pi R} \right) \exp \left[- \left(\frac{1}{2} \frac{wY_w}{R} \right)^2 \right] \cdot \delta(kV \pm w) \quad (10.72)$$

This relationship, illustrated in Figure 10.3(b), shows that as the wake becomes thinner, Y_w/R decreasing, the higher-order harmonics will be enhanced. From Equation (10.69), Y_w^2 will decrease in proportion to a decrease in the stator drag coefficient. This implies a strong (nearly exponential) dependence of radiated sound on C_D .

The functions $L_v^s(R, wC/R)$ that appear in the $f_{1,w}$ and $f_{\theta,w}$ of Equations (10.51) and (10.53) are, from Equation (10.42b),

$$L_w^s \left(R, \frac{wC}{R} \right) = \rho_c \pi C(\Omega R) u_m(d') w(w) \omega(kV \pm w) S_{2D} \left(\frac{wC}{R} \right) \quad (10.73)$$

$$-\infty < k < \infty \text{ and } -\infty < w < \infty$$

where $S_{2D}(wC/R)$ is the general lifting response function (Sears' in infinite R) and

$$w \left(\frac{Y_w}{R} \right) = (\pi)^{\frac{1}{2}} \frac{VY_w}{2\pi R} \exp \left[- \left(\frac{1}{2} \frac{wY_w}{R} \right)^2 \right] \quad (10.74)$$

is the wave number spectrum of the wake defect. If, for simplicity, we let the blade angle γ be small so that the tangential force can be ignored, then we can approximate the dipole sound pressure from the w th inflow harmonic as

$$\begin{aligned} p_{w,m}(\vec{x}, \omega) &= \frac{-iB}{4\pi r} J_{mB-w}(k_o R \sin \beta) \exp \left[i(k_o r + (mB-w) \left(\theta - \frac{\pi}{2} \right)) \right] \\ &\cdot k_o \left[\rho_o u_m(d') \Omega R_T C R_T \pi \right] e^{i\omega\theta_w(R_1)} w \left(\frac{Y_w}{R} \right) S_{2D} \left(\frac{wC}{R_1} \right) \\ &\cdot \delta(\omega - mb\Omega) \cdot \delta(kV \pm w) \end{aligned} \quad (10.75)$$

where the p is summed over $-\infty < m < \infty$ and $-\infty < k < \infty$ and where the circumferential velocity and the integrals over radius have been replaced by the integrand evaluated at the typical radius (usually taken as $R_1 = 0.7 R_T$). The function $W(kVY_w/R_1)$ is given by Equation (10.74) or an equivalent relationship if a wake defect alternative to Equation (10.67), is used.

In terms of the parameters of Equation (10.69), Equation (10.75) shows that the lowest-order sound pressure, $k = mB$, could depend on the stator drag coefficient and spacing-chord ratio as

$$p_{mB,m}(x,\omega) \sim C_D \left(\frac{\frac{2d'}{C_s} + 0.15}{\frac{2d'}{C_s} + 0.3} \right)^{1/2} \cdot \exp \left[- \left(\frac{0.16C_s}{R_T} \right)^2 C_D \left(\frac{2d'}{C_s} + 0.15 \right) (mB)^2 \right] \quad (10.76)$$

which shows a direct reduction of $p_{mB,m}$ with decreasing drag coefficient of upstream vanes and a slightly weaker dependence on spacing, d'/C_s . A comparison with Equation (10.64) in Figure 10.23 shows that, due to the smaller coefficient $(0.16)B C_s/R_T (C_{Ds}^{1/2}) < 1$ in Equation (10.76) compared with $\pi\sigma_{rs} \approx \pi$, and $S_r \approx S_s$ in Equation (10.64), the dependence on axial spacing is stronger for the potential interaction; for $d' > C_r/2$, the sounds from viscous interaction generally will be controlling. This result is borne out in the results of a numerical analysis, shown in Figure 10.24 and done by Kaji and Okazaki.⁹⁵ They computed the far field sound pressure radiated both upstream and downstream of a two-dimensional rotor/stator combination and accounted for both the aerodynamic and acoustic interferences between the dipoles and surfaces on the rotor and stator blading. Note that upstream and downstream radiation is different because of the partial interferences of rotor-stator force components. A similar distinction between upstream and downstream net forces on the fluid was calculated by Heatherington.⁹³

As Equation (10.75) shows, the most important contribution to the sound field arises from all acoustic modes for which $n = mb - kV = 0$, especially at low tip

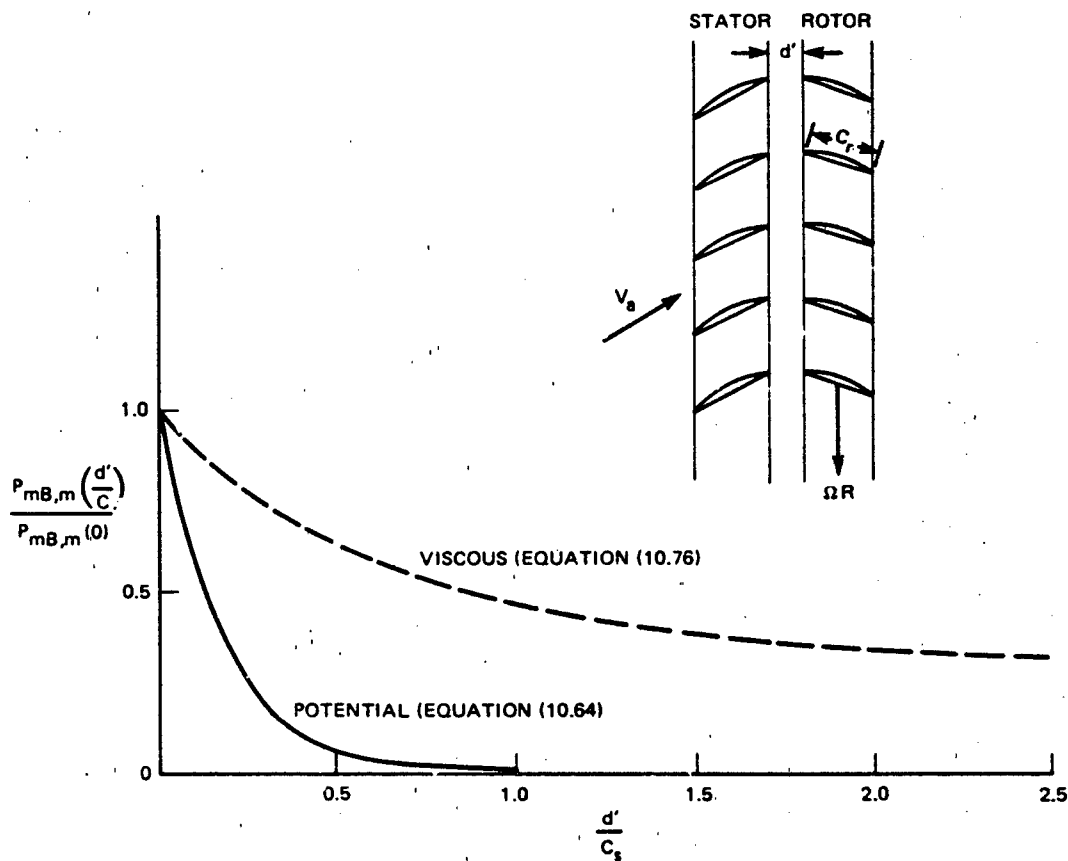


Figure 10.23 - Relative Reductions of Rotor Blade Lift at Blade Passage Frequency as a Function of Stator-Rotor Spacing, for Potential and Viscous Interactions of Blade Rows.

$$C_s = C_r = S_r = S_s, m = 1, B = 10, \\ C_{D_s} = 0.02, C = R_T/6$$

Mach numbers. Even when $\mu = mB - kV \neq 0$, as Figure 10.13 clearly shows, there can be substantial radiation. However, this radiation will decrease as

$$|k_o R_1 \sin \beta|^{(mB-k)} = |m \frac{R_1}{R_T} M_T \sin \beta|^{(mB-k)}$$

when $k_o R_T < 1$.

Another point to be recognized is that the temporal variation of the sound pressure of each mode, for example, $p_{mB,k}(\vec{x}, t)$ will behave as two angular rotating modes; these are "spinning modes" of the acoustic radiation. To see this, note that

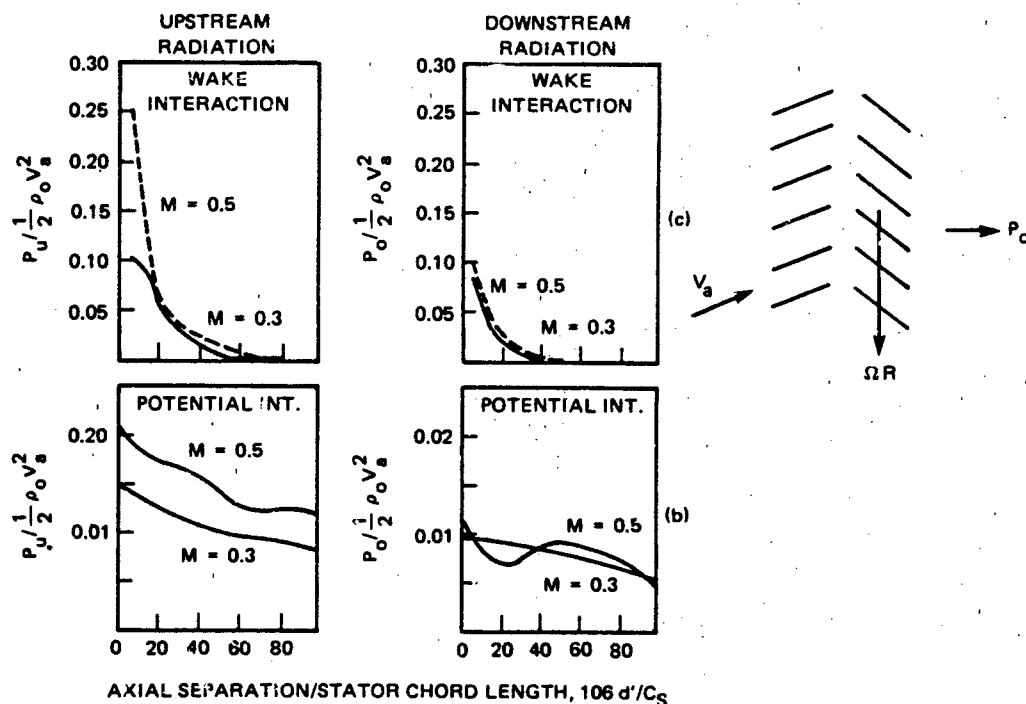


Figure 10.24 - Effect of Axial Separation. $s_s = s_R = 1.0$, $m = n = 1$,
 $C_s = 0.02$. $\theta = 30$ deg from Kaji and Okazaki⁹⁵
 (Copyright Academic Press)

$J_n(\xi) = J_{-n}(-\xi)$, Equation (10.75) can be rearranged to combine terms with $m, w > 0$ and $m, w < 0$ separately from those with m and w of opposite sign. This allows a rearrangement of the equation, giving the total sound pressure as

$$\frac{P(\vec{x}, t)}{\rho_o (\Omega R_T)^2 R_T^2} = \sum_{m=1}^{\infty} \frac{BR_T}{2\pi r} \left(\frac{u_m(d')}{\Omega R_T} \right) \left(\frac{R_I}{R_T} \right)^2 \frac{C}{R_T} mBM_T$$

$$\cdot \sum_{k=0}^{\infty} \omega \left(\frac{kV Y_w}{R_I} \right) S \left(\frac{kV C}{R_I} \right) \left\{ \sin \left[k_o r + (mB - kV) \left(\theta - \frac{\pi}{2} \right) - mB\Omega t + k\theta_k \right] J_{mB-kV}^{(mBM_1 \sin \beta)} \right.$$

$$\left. + \sin \left[k_o r + (mB + kV) \left(\theta - \frac{\pi}{2} \right) - mB\Omega t + k\theta_k \right] J_{mB+kV}^{(mBM_1 \sin \beta)} \right\} \quad (10.77)$$

s result shows two rotating acoustic waves, one behaving as

$$\sin \left[(mB - kV) \left(\theta - \frac{\pi}{2} \right) - \omega t \right]$$

the other as

$$\sin \left[(mB + kV) \left(\theta - \frac{\pi}{2} \right) - \omega t \right]$$

are $\omega - mB\Omega$. The respective angular velocities of the two propagative waves will be

$$\frac{mB\Omega}{mB - kV}$$

1

$$\frac{mB\Omega}{mB + kV}$$

a wave will therefore spin faster than Ω ; the other will spin slower. Depending the numbers mB and $kV = w$, the faster-spinning mode $mB\Omega(mB - kV)^{-1}$ could rotate the opposite direction of the rotor. The properties of the Bessel function are such that higher order radiating modes $mB - kV$ do not radiate appreciably unless $-kV > mBR_1 \sin \beta$. This behavior is known as a cut-off condition for high order for a given kV because of a relatively small increase in M_T required for the onset of radiation.

6.1.2 Blade/Vortex Interactions in Helicopter Noise. The related blade "slapping" or "chopping" occurs in forward flight when a blade passes close to the tip vortex of a leading blade, as illustrated in Figure 10.25a. The gust is caused by the induction field of the proximate vortex and appears as illustrated in Figure 10.25b. At a given radius of the rotor, the incident gust occurs in short, well-defined time intervals as a series of pulses, which give rise to harmonic content in the circumferential wave number spectrum (Figure 10.26). The response to this disturbance field $L'_w(R, \omega C/R)$ may be determined as in the preceding section. Analyses that utilize circumferential mode analysis as a starting point have been done, with varying degrees of complexity, by, e.g., Leverton and Taylor,¹⁰⁰ Widnall,¹⁰¹ and Alotas.¹⁰² Widnall's analysis further includes the effects of finite blade Mach number as well as determining sound directivity and power, but it does not include

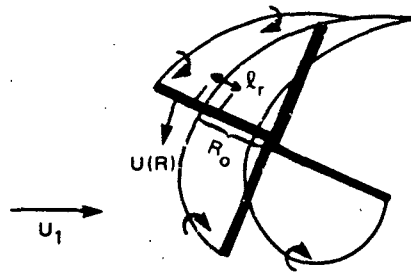


Figure 10.25a - Blade-Vortex Interaction
for Blade Slap

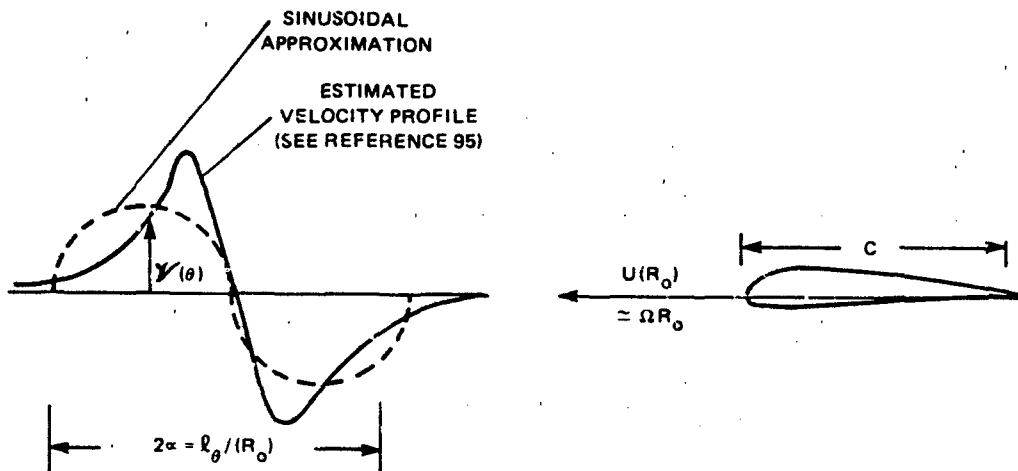


Figure 10.25b - Vortex-Induced Gust Incident
on the Blade Section

Figure 10.25 - Idealizations of the Blade-Vortex Interaction
That Gives Rise to Impulse Loading of Rotor Blades

effects of the finite aspect ratio of the blade. Filotas¹⁰² includes these effects and finds them relatively small compared with the influence of the inclination of the vortex relative to the chord of the blade. The blade loadings may be considered separately for each blade because of the low solidity of the helicopter. Vortex-blade viscous interactions have been isolated as noise sources when both the vortex and the lifting surface are stationary by Paterson et al.⁵⁸

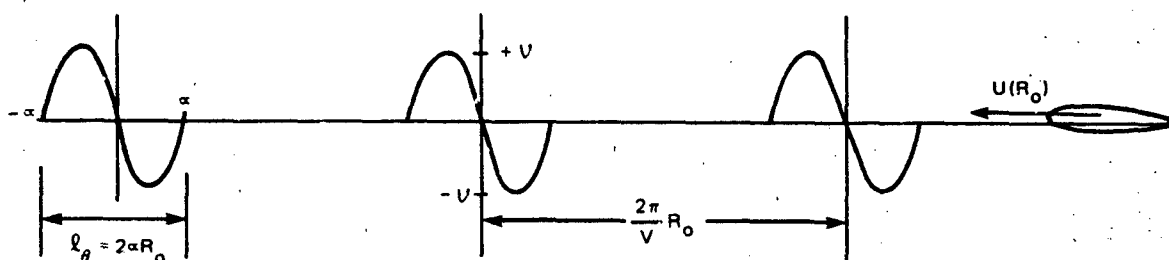


Figure 26a - Gust Configuration for Loading by Single-Cycle Sinuous Disturbance of $\pm V$

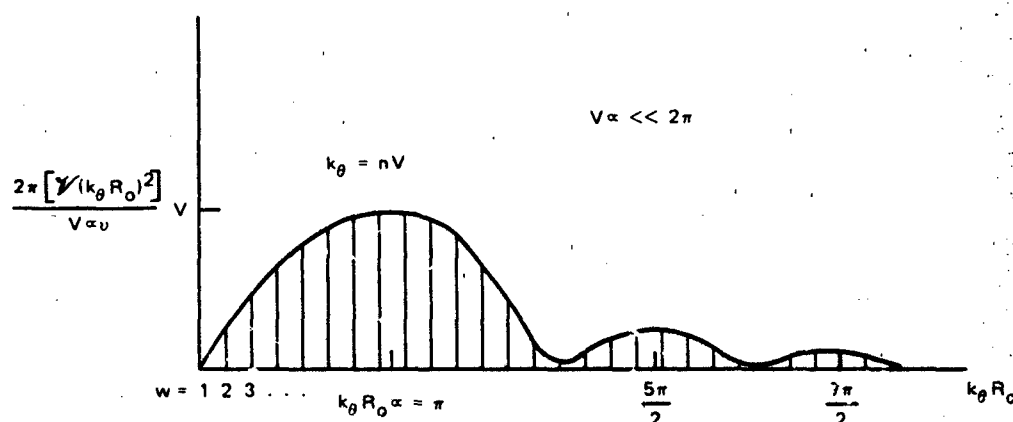


Figure 10.26b - Circumferential Wave Number Spectrum for Above Disturbance

Figure 10.26 - Circumferential Harmonics of the Incident Velocity Field of Isolated Sinusoid Pulses

Leverton and Taylor¹⁰⁰ measured blade slap noise in a whirl tower for which a down wash of a vortex was simulated by the velocity fields of two parallel air jets in opposite directions and oriented perpendicular to the plane of the rotor. The blade, in passing through the steady velocity defect, experienced a once-per-revolution transient loading and produced a slapping sound that closely simulated that made by a helicopter. The chord-wise variation of the gust resembled a single sine wave, as illustrated in Figure 10.26. The measured noise spectra are shown in Figure 10.27.

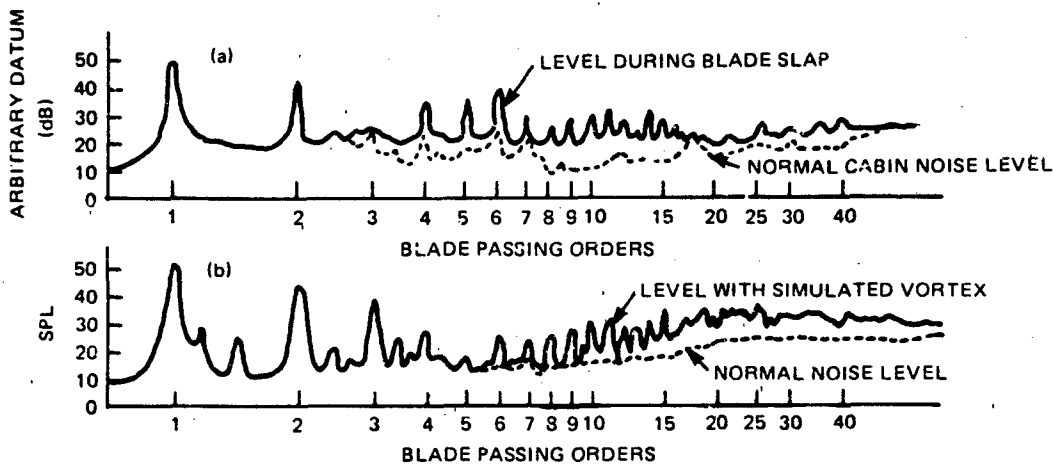


Figure 10.27 - Comparison of Helicopter and Simulated Blade Slap, Narrow Band Analysis (1.5%). (a) Belvedere Helicopter (Two 4-Bladed Rotors—250 rev/min); (b) Simulated Blade Slap (3-Bladed Rotor—600 rev/min)¹⁰⁰
(Copyright Academic Press)

To indicate the salient features of this type of noise, we adopt this simplified notion of the incident flow, even though a more accurate analysis would have to account for forward speed and the actual inclination of vortex with respect to the advancing blade. The circumferential wave number transform of the incident periodic gust field is a series of pulses separated in angle $(2\pi/V)$ per revolution; V will subsequently be let equal to unity,

$$V(k_{\theta} R_0) = \frac{1}{2\pi} \int_{-\pi}^{\pi} e^{ik_{\theta} R_0 \theta} v(\theta R_0) d(\theta R_0)$$

where, instead of Equation (10.70), we write for the pulses shown in Figure 10.26.

$$V(\theta R_0) = \sum_{l=-\infty}^{\infty} v \sin\left(\frac{\pi}{\alpha} \theta'\right) \delta\left(\theta - l \frac{2\pi}{V} - \theta'\right) \cdot -\alpha < \theta' < \alpha \quad (10.77a)$$

The gust field is localized at a radius R_0 and over an increment of radius, l_r . The resulting wave number spectrum that replaces Equation (10.72) is

$$V(k_{\theta} R_0) = \sum_{\ell=-\infty}^{\ell=\infty} \frac{V_{\alpha} v}{2\pi} \delta(k_{\theta} R_0 - \ell v) \left[\frac{\sin(k_{\theta} R_0 \alpha - \pi)}{k_{\theta} R_0 \alpha - \pi} - \frac{\sin(k_{\theta} R_0 \alpha + \pi)}{k_{\theta} R_0 \alpha + \pi} \right] \quad (10.77b)$$

which is shown in Figure 10.26; the average upwash is zero, which accounts for a missing pulse at $k_{\theta} R_0 = \ell v = 0$.

Letting $\ell v = w$, Equation (10.77b) may be substituted for $u(w)$ in Equation 10.42b) to give the associated lift per unit span on the blade. If the spanwise extent of the blade that chops the vortex is $L_r \ll R_0$ (Figure 10.25), then we can approximate the integral in Equation (10.50) by the value of the integrand at $R = R_0$ multiplied by the interval $dR = L_r$. To be precise, the associated sound field is given by Equation (10.51), but to retain simplicity we will examine the on-axis ($\theta = 0$) radiation far away from the center of the helicopter $r_0 \gg R_0$, when B blades counter one vortex per revolution ($V=1$). Therefore we are only interested in the $\ell = w$ component, for which the acoustic intensity of the mB harmonic is (Equation 10.15))

$$I(r_0, mB) = \frac{(mB)^2}{16} \rho_0 \left(\frac{C}{r} \right)^2 \left(\frac{L_r}{R_0} \right)^2 \frac{U^4 v^2}{c_0^3} \left| \frac{V(mB)}{v} \right|^2, \quad (10.77c)$$

which occurs at frequencies $\omega = mB$. The reduced frequency $k_1 C = mBC/2R_0$ has been taken as much less than unity so that the Sears function could be given the value unity.

Equation (10.77c) and Figure 10.26b show that intensity will be pronounced at high frequencies, $mB \gg 1$, because of the transient behavior with durations that are short compared with the period of rotation, Ω^{-1} . Using typical values, let $\ell = 2\pi/20$ ($V=1$); therefore $R_0 k_{\theta} \alpha = 2\pi(\ell/20) = \pi\ell/10$. The peak sound level will then be in the vicinity of $\ell = 10$. In Figures 10.1 and 10.27 we see sound levels at high-order blade-frequency harmonics that exceed the rotation noise (Gutin sound) in increasing amounts as the harmonic order increases.

If the perturbation velocity v increases with velocity $U(R_0)$, then Equation (10.77c) shows the well-known $[U(R_0)]^6$ speed dependence for dipole sound for a given harmonic order. The sound levels decrease as either the chord of the blade or the span-wise extent of the vortex (L_r) is reduced. For a given rotation velocity $U(R_0)$, the sound can be reduced by decreasing v , or the product va . This latter

noise control parameter is the same as the varying strength of the tip vortex since the circulation is proportional to $v \cdot l_\theta$.

10.6.1.3 Influence of Adjacent Blades and Incompressible Cascade Effects. Although the above analysis gives many of the salient features of the interaction tones emanating from stages of blade rows, many details have been overlooked. As already stated, acoustic and aerodynamic interferences between blades in a row and between adjacent rows can occur. A number of numerical methods have been developed to handle these interactions. The analytics involved are well outside the scope of this text; thus only a few notes of description will be offered here. Almost all these methods involve two-dimensional cascade models, with work done largely by members of the aeroacoustic community because of their interest in multistage axial flow machines.

The first refinement to the incompressible theory involves accounting for the influence of the induced unsteady velocity field on a blade due to the unsteady loads on adjacent blades in two-dimensional cascades. The earliest work of Sisto¹⁰³ and Whitehead^{104,105} was applied to the vibration and flutter problems. The flow was considered two dimensional, and blades were considered as uncambered flat plates at zero angle of attack and of zero thickness; effects of adjacent blades were modeled as velocities induced on the control blade due to an array of line vortices representing the adjacent blades. The approach was later applied to the problems of gust response by Henderson and Daneshyar¹⁰⁶ who also considered effects of camber on thin airfoils at small angles of attack. Comparisons of various cascade prediction methods at low frequencies have been given by Horlock, Greitzer, and Henderson.¹⁰⁷

Subsequent experimental validation of the computed gust response was obtained for a rotor downstream of a circumferentially periodic disturbance generated by wake screens.¹⁰⁸⁻¹¹⁰ The first confirmation¹⁰⁸ was made indirectly by deducing blade circulation using measurements of downstream mean total pressure, while in subsequent measurements^{109,110} the total mean fluctuating lift and moments on a rotor blade were determined. The important features of the blade interference can be seen in Figure 10.28 (reference 110). The first effect occurs near zero reduced frequency, $\omega C_r / 2U_r \rightarrow 0$ (where U_r is the mean velocity of the blade). As spacing to chord, S_r / C_r , decreases, the unsteady lift coefficient is less than that predicted

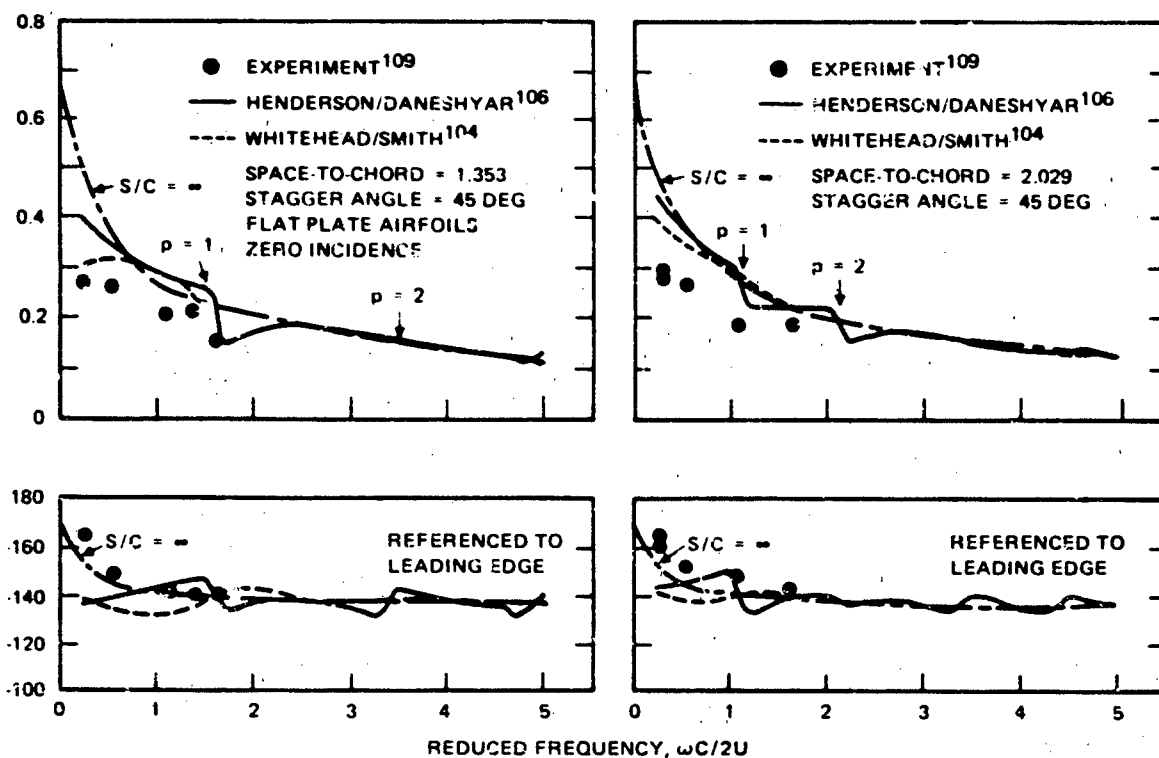


Figure 10.28 - Unsteady Lift Coefficient Versus Reduced Frequency, Predicted and Experimental.¹¹⁰ Phases with Respect to the Upwash.

In the case of isolated surfaces. In terms of Figure 10.9, $S_r/C_r = 1.35$ corresponds roughly to $EAR \approx (1.35)^{-1} = 0.74$. A corresponding reduction in lift is $|C_r/C_r=1.35| \approx 0.5 |C_L(S_r/C_r=\infty)|$ and this is just about the value indicated in Figure 10.9, i.e., $k_T \approx 0.5(k_T)_\infty$. Thus it appears that observed and calculated interferences are consistent with independently observed propeller loading. For $\omega C/2U_r > 1$, the isolated surface response is apparently a reasonable rough approximation of the cascade response.

An exception to this independence can occur at coincidence of the blade rows, when an integral number of disturbance wavelengths λ_s becomes equal to the spacing row blade spacing; i.e., in the terminology of Figure 10.21

$$p\lambda_s = S_r$$

The encounter frequency is equal to the resultant blade velocity U_T divided by the trace wavelength along the chord λ_{sc} and

$$\lambda_{sc} \sin \alpha_s = \lambda_s$$

where α_s is the stagger angle. Therefore the reduced frequency of coincidence is

$$\begin{aligned} \frac{\omega C}{2U_r} &= \frac{\omega C}{2\Omega R} \\ &\approx p \frac{C}{2\Omega R} \cdot 2\pi \cdot \frac{\Omega R}{\lambda_{sc}} \\ &\approx \pi p \frac{C}{S_r} \sin \alpha_s \end{aligned}$$

These frequencies correspond to the arrows $p = 1, 2$ in Figure 10.28 at which points there is a perturbation of the magnitude and phase of the lift that is not estimated by the Kemp-Sears theory. The lifting surfaces in the cascade therefore cease to respond separately (as assumed in all preceding sections). Instead, they become slightly coupled. The effect will, however, be most important when $\omega C/2U_r < 1$.

Additional refinements to the theory have recently been made by Goldstein and Atassi,^{111,112} who accounted for effects of finite thickness and camber, and by Atassi and Akai,^{113,114} who included the effects of heavy loading, finite angle of attack.

10.6.1.4 Acoustic Interference in Blade Rows. The above investigations considered only incompressible coupling among blades and rows. As mentioned above, Kaji and Okazaki⁹⁵ considered both aerodynamic and acoustic coupling. Later work by Smith¹¹⁵ and Whitehead¹¹⁶ has also included both acoustic and aerodynamic coupling, as well as providing for the acoustic reflections at blade rows. Specific treatment of acoustic reflections by blade rows without consideration of aerodynamic effects has been given by Mani and Horvay,¹¹⁷ Kaji and Okazaki,^{118,119} and Amiet.^{120,121}

10.6.1.5 Recent Developments in Unsteady Lifting-Surface Theory. In the marine propeller community, a different line of theoretical development has been undertaken by both the Stevens and M.I.T. groups, among others. These methods have been developed for the single-stage propulsor, and they have, over the years, come to include effects of blade number, finite camber, thickness, and angle of attack. Furthermore, the work has been concerned with the calculations of unsteady load coefficients F_1 and F_0 , rather than with acoustic effects.

The computational procedure developed in the 1960s at Stevens Institute of Technology by Tsakonas and his co-workers¹²²⁻¹²⁴ allows a calculation of blade lifts and moments to a prescribed velocity inflow. The method involves a three-dimensional gust response of the blades under the influences of the adjacent blades in the propeller disk. The method has shown good agreement to measured thrust and transverse forces for a range of reduced frequencies ($\omega C_{0.75}/2\Omega R_{0.75}$ where $C_{0.75}$ and $R_{0.75}$ are the propeller blade chord and radius at $0.75 R_T$) and for expanded area ratios up to 0.6. The experiments of Boswell³⁴ were conducted for three-bladed propellers behind three- and four-cycle wake screens. Also conducted were measurements of Brown¹²⁵ using a four-cycle inflow to a four-bladed propeller. The inflow harmonic was created with a special flow regulator.

More recently, an alternative numerical method has been designed by Frydenlund and Kerwin¹²⁶ and Kerwin and Lee¹²⁷ to calculate unsteady pressure distributions on propeller blades. The method is an extension of numerical techniques that were developed by Kerwin and co-workers^{30,128-130} in the 1960s. These lifting-surface calculations included effects of finite camber and thickness in three-dimensional flows.

10.6.1.6 An Approximate Similarity Relationship for Unsteady Thrust in Propeller Fans. In order to fix ideas to illustrate the major points of Sections 10.6.1.2 through 10.6.1.4, and to indicate the magnitude of error that may occur in some cases, an approximate expression for the unsteady axial force in a disturbed inflow will be derived. First the unsteady lift on an individual isolated blade will be estimated from Equation (10.37). The intent here is to indicate the important variables as well as the general dependence on each, rather than to reach precise quantitative evaluations. The approach used here is formally similar to that used by Lewis¹³¹ and by Tsakonas et al.¹²³; it is an extension of the results of Section 10.6.1.1.

The total axial force on the blades can be written from Equations (10.45a), (10.46), and (10.73)

$$T(t) = \sum_{m=-\infty}^{\infty} B \pi \rho_0 \int_{R_H}^{R_T} C \Omega R u_{mB}(R) S_{2D} \left(\frac{mBC}{2R}, \frac{C}{R} \right) \cos \gamma e^{imB\theta} mB dR \cdot e^{-imB\Omega t} \quad (10.78)$$

where $U(R)$ has been approximated by ΩR , and we assume that the inflow harmonic is a function of radius. Rather than invoke the three dimensionality of the problem, we note that the presence of the ΩR term as well as the reduced frequency mBC/R weights the integral toward the tips of the fan. To see this, recall that the amplitude of the two-dimensional Sears function (Equation (9.57)) will approach unity as $\pi k_1 C = \pi mBC/R$ approaches zero. Therefore near the tips of the blades, if mBC/R_T is small enough (Figures 9.28 and 9.30 suggest that unity is small enough to avoid rapid phase variations) Equation (10.78) gives (using $S(mBC/2R_T, C/R_T) = S_e(mBC/2R_T)$ and Equation (9.57))

$$T(t) = \frac{1}{2} \sum_{m=-\infty}^{\infty} B \pi \rho_0 C R_T \Omega R_T \frac{u_{mB}(mB, R_T) \cos \gamma_T}{\left(1 + \pi \left| \frac{mBC}{R_T} \right| \right)^{1/2}} e^{imB\theta} w_T e^{-imB\Omega t} \quad (10.79)$$

The $1/2$ in front arises from $\int_0^1 R dR$. Equation (10.79) ignores the finite aspect ratio on the lift response, the variation response phase with radius, and the variation of chord with radius. However, the effect of finite R will be heuristically accounted for just as in Section 10.3, Equation (10.16). The factor C/R_T is given approximately in terms of blade number and expanded area ratio by $\pi EAR/B$. Therefore the m th component of the force can be very crudely approximated as

$$T_m(t) = \pi \rho_0 \Omega R_T u_{mB}(R_T, mB) R_T^2 \cos \gamma_T \cos \left[mB(\theta - \omega_T t) \right] \cdot \frac{EAR}{\left(1 + mB \frac{\pi^2 EAR}{B} \right)^{1/2}} \cdot \frac{1}{1 + \frac{3\pi EAR}{B}} \cdot I_A \left(EAR, \frac{mBC}{2R_T} \right) \quad (10.80)$$

here $I_A(EAR, mBC/2R_T)$ is the cascade effect that accounts for a reduction in blade forces due to interaction (Figures 10.9 and 10.28). In most practical cases that involve wide swept blades in which θ_w and $mBC/\Omega R$ varies significantly over the radius, the above relationships are only useful in crudely approximating the forces.

Equation (10.80) illustrates all the main features that control the forces. $\tilde{T}_m(t)$ is proportional to the strength of the mB harmonic of the disturbance; it is proportional to $\cos mB\theta_{wT}$ where θ_{wT} is the relative angle between the blade leading edge and the inflow wave front (relative sweep angle). To compare Equation (10.80) with Boswell's propeller force measurements we form

$$\tilde{k}_T = \frac{|\tilde{T}_m(t)|}{\rho_o n_s^2 D^4}$$

or

$$(\tilde{k}_T)_m \approx \frac{\pi^2}{4} J \cdot \left(\frac{u_{mB}}{V_a} \right) \cdot \frac{EAR}{\left(1 + mB \frac{\pi^2 EAR}{B} \right)^{1/2}} \frac{I_A(EAR, mB)}{1 + \frac{3\pi EAR}{B}} \quad (10.81)$$

for $mBC/R_T < 1$.

We see from Equation (10.81) a linear increase of \tilde{k}_T with both J and harmonic amplitude that has been verified by both Brown¹²⁵ and Boswell and Miller.³⁴ The dependence on EAR is more complicated and is illustrated in Figure 10.29 together with measured values of $(\tilde{k}_T)_{m=1}$ and values calculated by Tsakonas¹²³ that were numerically obtained using a three-dimensional lifting-surface theory being developed at that time (1968). The comparison shows that the two-dimensional lifting-surface theory, corrected for the effect of aspect ratio as if for steady lift, but not corrected for those effects on the aerodynamic response function, closely approximates the actual values. When the effect of finite aspect ratio is modest or less, i.e., when $3\pi EAR/B < 1$ which for this case occurs when $EAR = 1/\pi$. Other simple modified forms of the two-dimensional theory can overestimate the axial forces. This was shown by Schwanecke¹³² (see also Kerwin and Lee¹²⁷), who reviewed the available methods of calculating wake-induced forces and compared the results of a series of measurements and calculations by different means. Generally, three-dimensional calculations, e.g., using the methods of the Stevens group^{123,124} and

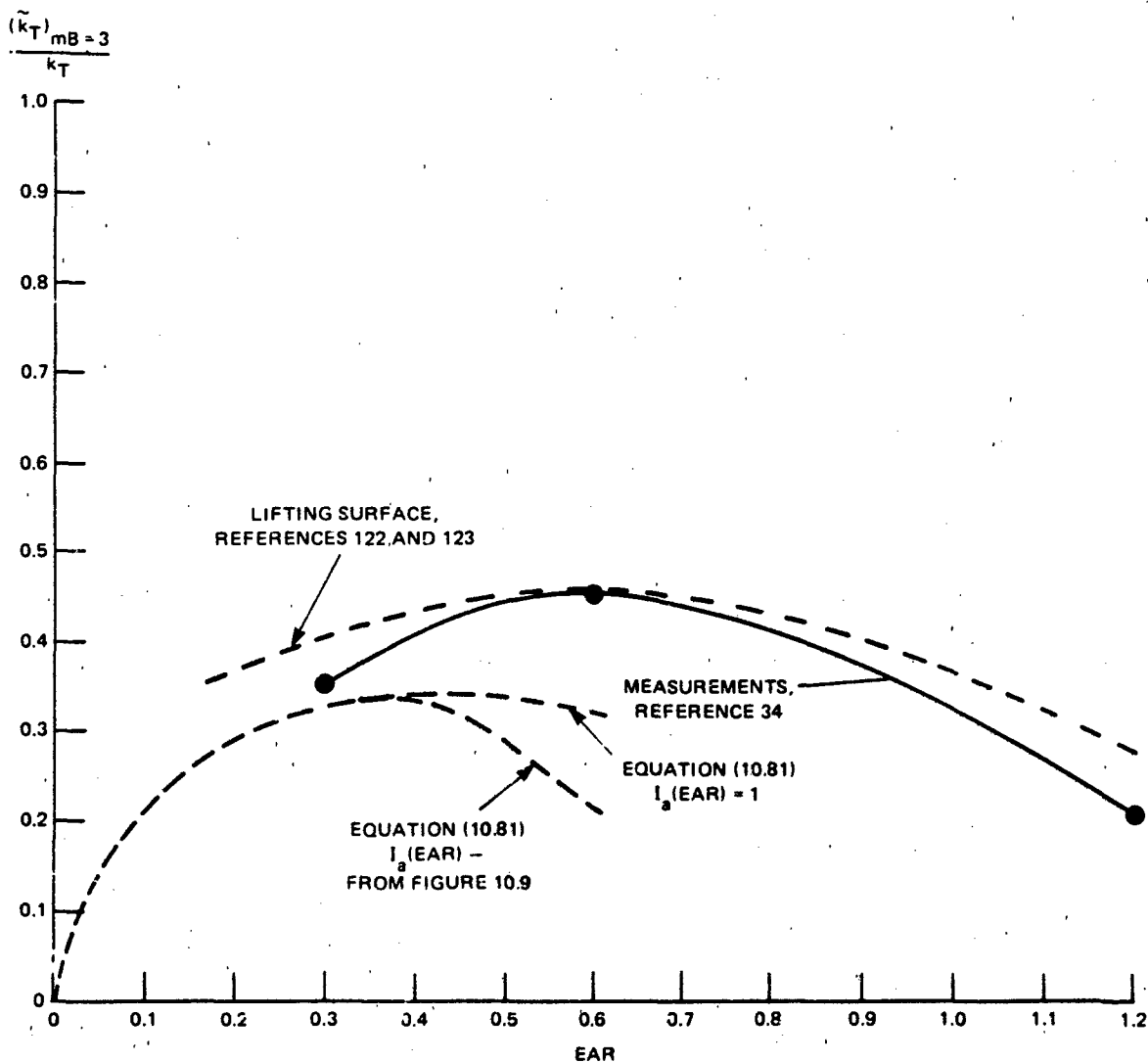


Figure 10.29 - Unsteady Thrust ($m=1$) on Three-Blade Propellers Calculated from Approximate Two-Dimensional Unsteady Theory with Calculated from Three-Dimensional Lifting Surface Theory, Measured Behind Three-Cycle Wake. $J = 0.89$, $u_3/V_a = 0.24$, $k_T = 0.13$

Kerwin and L  e¹²⁷ more successfully predict axial forces. It is noteworthy that even though Equation (10.81) does not correctly predict the magnitude of the forces, throughout the entire range of EAR it does predict the qualitative dependence on expanded area ratio. This had been found earlier by Boswell.³⁴

10.6.2 Turbulent Inflows

In comparison to the work done on the deterministic aspects of nonuniform inflows, less work has been done on the response of rotors to turbulence. However, the analytical treatments of deterministic loading may be extended to examine the response to a turbulent field. Fairly adequate predictions can also be made with more or less straightforward application of the results of Section 9.4.1. Such an application has been used in the past by Sevik,¹³³ who considered the case of turbulent scales smaller than a blade spacing and therefore regarded the blades as responding individually to the turbulence and Chandrashekhara,¹³⁴ who examined only those cases for which the circumferential correlation length was larger than a blade spacing. Mani,¹³⁵ Homicz and George,¹³⁶ and Amiet¹³⁷ all considered rotor forces and sounds radiated by a spectrum of turbulent wave numbers.

The analytical formulation for rotor response follows from the above if, rather than the discrete summation of Equation (10.65), we consider a continuum of turbulence wave numbers so that

$$u(R, \theta, t) = \iiint_{-\infty}^{\infty} U(k_R, k_\theta, \omega) e^{i[k_\theta(\theta R) + k_R R] - \omega t} dk_\theta dk_R d\omega$$

In a special case to be considered below the disturbance is assumed to have spatially and temporally stationary statistics and to be convected in frozen fashion so

$$U(k_R, k_\theta, \omega) = U(k_R, k_\theta) \delta[\omega - k \cdot U(R)]$$

is the (complex) Fourier amplitude of the $u(r, \theta)$ contribution at wave numbers k_R, k_θ . $U(k_R, k_\theta, \omega)$ is a stochastic variable in the sense employed in Chapters 3, 7, and 9. The response of the s th blade to each general wave harmonic $U(\vec{k}, \omega)$ is written analogously to Equation (10.37), but in a slightly generalized form

$$dF_s(R, \xi, t; k_\theta, k_R, \omega) = \rho_o \pi |U(k_R, k_\theta, \omega)| S_{2D}\left(\frac{\omega C}{U(R)}, \frac{\xi}{C}, k_\theta C\right) U(R) \cdot e^{ik_\theta \left[\theta_k(k_\theta) - U(R)t + \theta R \right]} \delta\left(\theta - \frac{sb}{R} - \frac{\xi}{R}\right) \cdot dC dR dk_\theta dk_R \quad (10.82)$$

where $k_\theta R$ is now continuous rather than the discrete w appearing in Equation (10.65). $S_{2D}(\omega C/U(R), \xi/C; k_\theta C)$ is a generalized function representing the pressure response of the blade, integration over the chord $-C/2 < \xi < C/2$ will yield the aerodynamic influence function (Sears' for infinite R). We will be interested in the summed force on all B blades. This will involve the summation

$$A_s(k_\theta R) = \sum_{s=0}^{B-1} e^{ik_\theta (sb)} = \sum_{s=0}^{B-1} e^{ik_\theta R \left(\frac{s2\pi}{B}\right)}$$

$$A_s(k_\theta R) = \frac{\sin\left[\frac{B}{2}\left(k_\theta R \frac{2\pi}{B}\right)\right] e^{i(B-1)\left(k_\theta R \frac{\pi}{B}\right)}}{\sin\left[\frac{1}{2}\left(k_\theta R \frac{2\pi}{B}\right)\right]} \quad (10.83)$$

by Equation (7.164b), which is diagrammed in Figures 7.45 and 10.1. Due to the continuous nature of k_θ , $A_s(k_\theta R)$ is a continuous spectrum with peaks at $k_\theta R = mB$. When $k_\theta R = w$, Equation (10.83) reverts to Equation (10.46). Letting the net lift on the s th blade be

$$L_s(t) = \iiint_{A_B} dF_s(\xi, t) d\xi dR dk_\theta dk_R \quad (10.84)$$

where $L_s(t)$ is a temporally random variable of time due to the stochastic nature of $U(k_R, k_\theta)$, the total lift on the rotor is

$$L(t) = \sum_{s=0}^{B-1} L_s(t) \quad (10.85)$$

and the mean square lift is

$$\begin{aligned} \overline{L(t) L(t)}^t &= \overline{\left[\sum_{s=0}^{B-1} L_s(t) \sum_{p=0}^{B-1} L_p(t) \right]^t} \\ &= \sum_{s=0}^{B-1} \sum_{p=0}^{B-1} \overline{L_s(t) L_p(t)}^t \end{aligned} \quad (10.86)$$

Making the required substitutions and letting

$$L_a(\xi) = \rho_o \pi S_{2D} \left(\frac{\omega C}{U(R)}, \frac{\xi}{C}, k_\theta C \right)$$

represent the aerodynamic response function, we find (using the methods of Section 2.6.2), an expression for the mean-square unsteady loading

$$\overline{L^2(t)}^t = \iiint \iiint |A_s(k_\theta R)|^2 \overline{u^2} \phi_{u_\theta}(k_\theta) \phi_1(k_1) \phi_m[\omega - k \cdot U(R)] \quad (10.87)$$

$$U(R_1) U(R_2) R_r(R_2 - R_1) |L_a(k_\theta)|^2 d\omega d^2 \vec{k} dR_1 dR_2$$

In Equation (10.87), the wave vector properties are represented in the forms used in Chapter 3. The function $L_a(k_\theta)$ is the wave number transform of $L_a(\xi)$ over the chord dimension; it will be related to the familiar lift response function below. In the above equation all the blade coupling is contained in the functions $A_s(k_\theta R)$; no mutual induction effects are assumed in the $L_a(k_\theta)$. This is consistent with Figure 10.28, which indicates that cascade effects are relatively small at reduced frequencies $\omega C/2U$ greater than 0.5. The turbulence field, as illustrated in Figure 10.30, has correlation characteristics which we assume in the conventional manner to be separable (Chapters 3 and 7).

$$R(\vec{r}, \tau) = R_M(\tau) R_1(r_1) R_\theta(r_\theta) R_R(r_R)$$

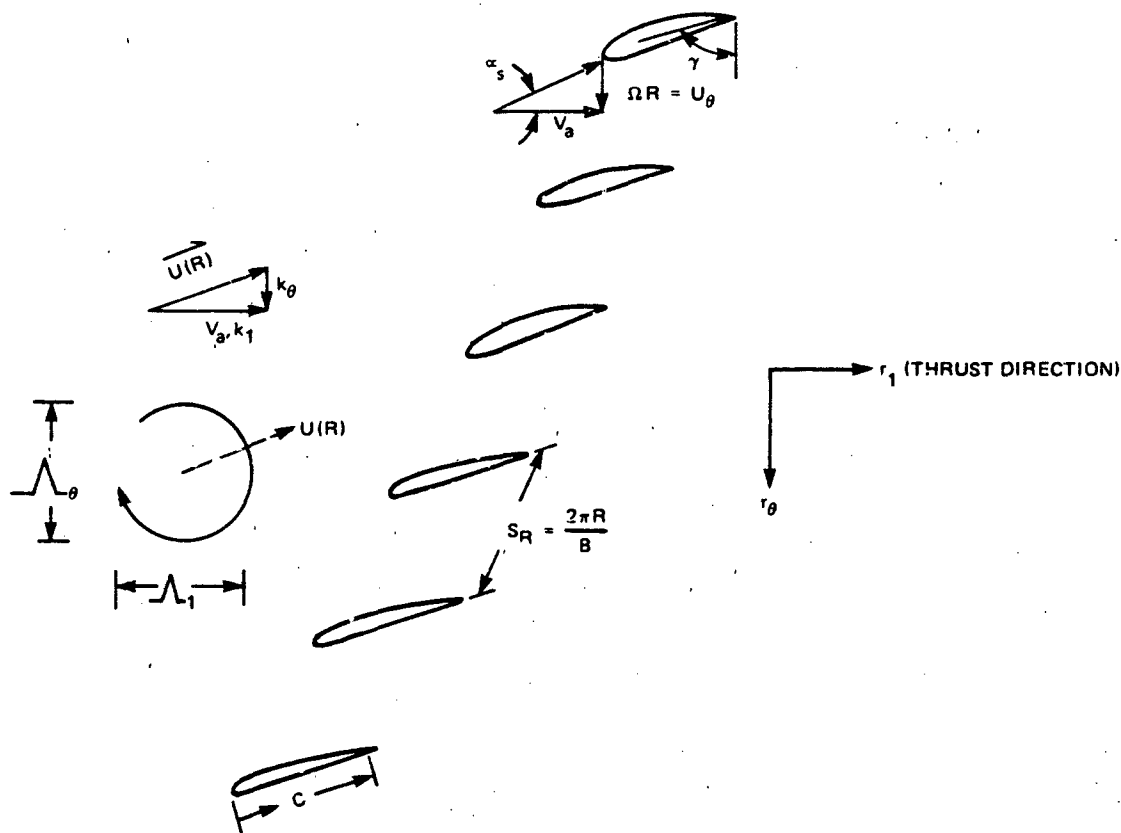


Figure 10.30 - Idealization of a Vortex Ingested into a Moving Blade Row
Statistical Properties of the Turbulence Are Defined in the
I, θ Directions; the Resultant Encounter Velocity of the
Turbulence with the Blade Row Is $U(R)$. γ is the Blade
Pitch Angle and α_s is the Hydrodynamic Stagger Angle,
 $\alpha_s = \pi/2 - \beta$.

where r_θ, r_1, r_R are separation coordinates in the tangential, axial, and radial directions and $R_M(\tau)$ is the moving axis correlation of the turbulence. The mean-square turbulence intensity is $\overline{u^2}$. The associated (normalized on $\overline{u^2}$) wave number spectrum is

$$\phi(\vec{k}, \omega) = \phi_M(\omega - U_c k_1) \phi_1(k_1) \phi_\theta(k_\theta) \phi_R(k_R)$$

where the corresponding wave spectra and correlations are denoted by subscripts. Since the blades are not moving radially, we simply retain the radial correlation function in the form

$$R_R(r_R) = R_R(R_2 - R_1)$$

Since the relative velocity of the turbulence to the blades is $\vec{U}(R)$ with

$$U_1(R) = U(R) \cos \alpha_s + U_c$$

$$U_\theta(R) = U(R) \sin \alpha_s$$

we rewrite the spectrum as

$$\phi(k_1, \theta, \omega; r_R) = \phi_m(\omega - \vec{U} \cdot \vec{k}) \phi_1(k_1) \phi_\theta(k_\theta) R_R(R_2 - R_1)$$

where

$$\vec{U} \cdot \vec{k} = U_\theta(R) k_\theta + U_1(R) k_1$$

The integral length scales in the R, θ, y_1 direction are $\Lambda_R, \Lambda_\theta$, and Λ_1 , respectively. The wave number spectra will be assumed to have the form of Equation (3.101) which implies an integral correlation length of $2\Lambda_1$.

We now find an equation for the blade response function $L_a(k_\theta)$ in terms of more familiar functions. The mean-square lift on a given single blade is

$$\overline{L_s^2(t)} = \iint_{R_H}^{R_T} \overline{u^2} \phi_\theta(k_\theta) \phi_1(k_1) R_{uu}(R_2 - R_1) |L_a(k_\theta)|^2 U(R_1) U(R_2)$$

$$\phi_m[\omega - \vec{k} \cdot \vec{U}(R)] d\omega dk_\theta dR_1 dR_2 dk_1$$

For a two-dimensional wing for which $U(R_1) = U(R_2)$, Equation (9.68) gives an analogous relationship

$$\overline{L^2} = \iiint_{-\infty}^{\infty} \iiint_{R_H}^{R_T} \pi^2 \rho_o^2 U^2(R) \overline{u^2} 2\Lambda_R |S_e(\frac{c}{2})|^2 \cdot \phi_1(k_1) \phi_\theta(k_\theta) \phi_m[\omega - \vec{k} \cdot \vec{U}(R)] dk_\theta dk_1 d\omega dR$$

which can be expressed in the above terminology as

$$\overline{L}_S(t) = \iiint_{-\infty}^{\infty} \int_{R_H}^{R_T} \overline{u^2} \phi_\theta(k_\theta) \phi_1(k_1) \phi_m[\omega - \vec{k} \cdot \vec{U}(R)] |L_a(k_\theta)|^2 U^2(R) \left[\int_{R_{uu}}(\xi_R) d\xi_R \right] dR dk_\theta dk_1 d\omega$$

The integral of $R_{uu}(R_2 - R_1)$ over $R_H < R_1, R_2 < R_T$ is therefore approximated by $2\Lambda_3$. The correspondence between $L_a(k_\theta)$ and $S_e(k_\theta C/2)$ can be seen by comparing the two equations, i.e., $L_a(k_\theta) = \rho_o \pi C S_e(k_\theta C/2)$. Of course, in the case of rotor blades, due to the $[U(R)]^2 = \Omega^2 R^2$ dependence on radius, the integrals are weighted to the tips. To approximately evaluate Equation (10.87), values of $A_s(k_\theta R)$, $S_e(k_\theta C/2)$, and Λ_3 are replaced by values at the tip, which leaves an integral over $R^2 dR$ that has the value $(1/3)R_T^3$. The mean-square axial thrust spectrum from the inflow turbulence is with $T = L \cos \gamma \approx L \sin \alpha_s$ where γ is the blade pitch angle

$$\begin{aligned} \phi_t(\omega) &= \frac{\pi^2}{3} \left[\rho_o (\Omega R_T)^2 \right]^2 (C R_T)^2 \frac{\overline{u^2}}{(\Omega R_T)^2} \left| S_e \left(\frac{\omega C}{2U} \right) \right|^2 \cos^2 \gamma \\ &\cdot \left(\frac{2\Lambda_3}{R_T} \right) \cdot \int_{-\infty}^{\infty} |A_s(k_\theta R)|^2 \phi_1(k_1) \phi_\theta(k_\theta) \phi_m[\omega - \vec{k} \cdot \vec{U}(R_T)] dk_\theta dk_1 \quad (10.88) \end{aligned}$$

An important distinction must be emphasized here between response to turbulence and response to nonuniform mean velocity. In the present case we assume $\Lambda_3 \ll R_T - R_H$ and further that the loading functions on the blades are uncoupled. This may not be done in the case of nonuniform mean velocity, since the assumption on the radial correlation is rendered invalid. This means that response depends on the phasing of the nonuniformity, of the response function, and of adjacent blades as a function of radius. For frozen convection of the turbulence past blades with large stagger angle α_s or, equivalently, small pitch $\approx \gamma$, the effective form of the moving axis spectrum is the delta function, i.e.,

$$\phi_m[\omega - \vec{k} \cdot \vec{U}(R)] = \delta[\omega - U(R_T) k_1 \sin \gamma - U(R_T) k_\theta \cos \gamma]$$

Therefore for this case the spectrum of the load may be written

$$\phi_t(\omega) = \frac{\pi^2}{3} \left[\rho_o (\Omega R_T)^2 \right]^2 (C R_T)^2 \frac{\overline{u^2}}{(\Omega R_T)^2} \cos^2 \gamma \left(\frac{2\Lambda_R}{R_T} \right) \cdot \left| S_e \left(\frac{\omega C}{2U_T} \right) \right|^2 \cdot \left[\frac{1}{U_T} \phi_\theta \left(k_\theta = \frac{\omega}{U_T} \right) \right] \int_{-\infty}^{\infty} \phi_1(k_1) \left| A_s \left(\left| \frac{\omega}{U} - k_1 \sin \gamma \right| b \right) \right|^2 dk_1 \quad (10.89)$$

and $-\infty < \omega < \infty$. For small values of γ , $\cos \gamma = 1$ and accordingly k_θ has been approximated by $(\omega/U_T) - k_1 \sin \gamma$. Equation (10.89) shows that the correlation in the axial direction, k_1 , controls the spectrum of the unsteady thrust for small pitch angles. For sufficiently narrow $\phi_1(k_1)$ compared to $|A_s|^2$ the integral in Equation (10.89) will have a dependence on frequency with peaks at all $\omega/U = mB/R_T$ or $\omega/\Omega = mB$. For a sufficiently broad $\phi_1(k_1)$ compared to $|A_s|^2$ the peaks in $|A_s|^2$ will be homogenized and no such frequency dependence will result.

An expression for the unsteady thrust for the case of narrow $\phi_1(k_1)$ can be derived by noting that, according to Equation (3.101), $\phi_1(k_1)$ is limited to wave numbers in the range $-\pi/\Lambda_1 < k_1 < \pi/\Lambda_1$. Peaks in $|A_s|^2$ are not coupled by $\phi_1(k_1)$ if the spacing of these peaks $\Delta k_1 = B/R_T$ is greater than the wave number band $-\pi/\Lambda_1 < k_1 < \pi/\Lambda_1$ or $\Delta k_1 \sin \gamma < B/R_T$. Letting $\Delta k_1 = 2\pi/\Lambda_1$ represent the effective k_1 range of $\phi_1(k_1)$, the condition becomes $\sin \gamma < B\Lambda_1/2\pi R_T$. This condition is illustrated in the upper part of Figure 10.31. Since, for small pitch, $\sin \gamma = \gamma$, this condition states that the unsteady rotor forces will peak at $\omega = mB\Omega$ as long as the integral correlation length of the turbulence in the axial direction is larger than the blade spacing in that direction. The spectrum shape of the unsteady force will mirror that of $|A_s|^2$ as long as $\Delta k_1 \sin \gamma$ is less than a peak in $|A_s|^2$, or

$$\Delta k_1 \sin \gamma = \frac{2\pi}{\Lambda_1} \sin \gamma < \frac{1}{R_T}$$

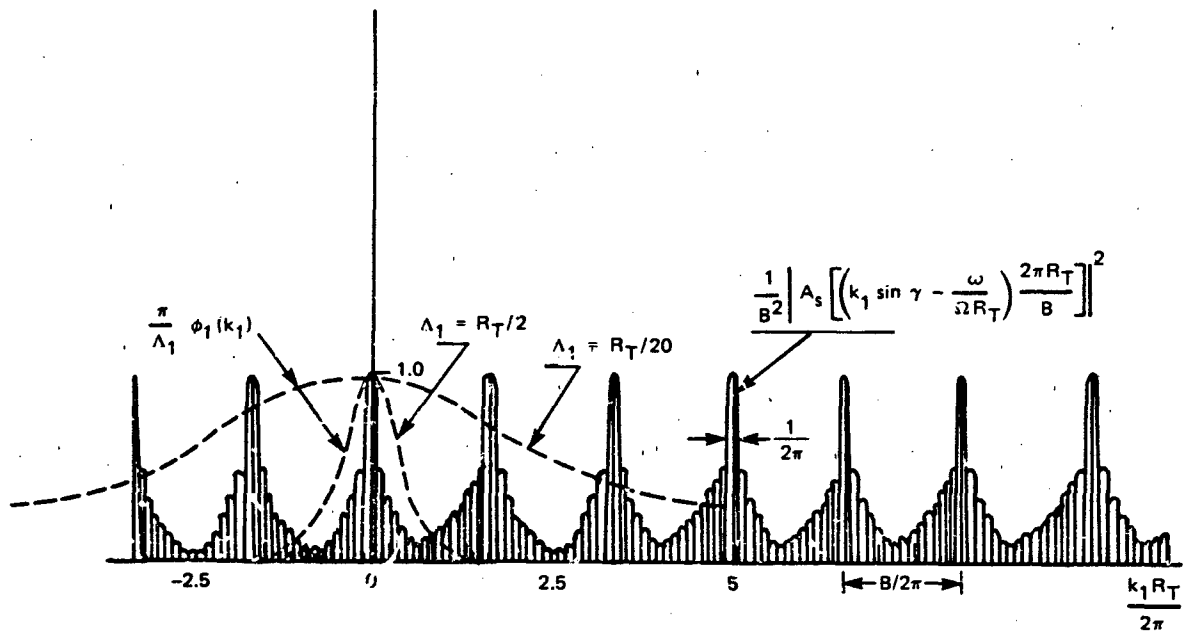


Figure 10.31a - Schematic of the Terms in the Integral of Equation (10.89) for $B = 10$, $\sin \gamma = 1/3$ ($J=1.1$), and Two Values of Λ_1

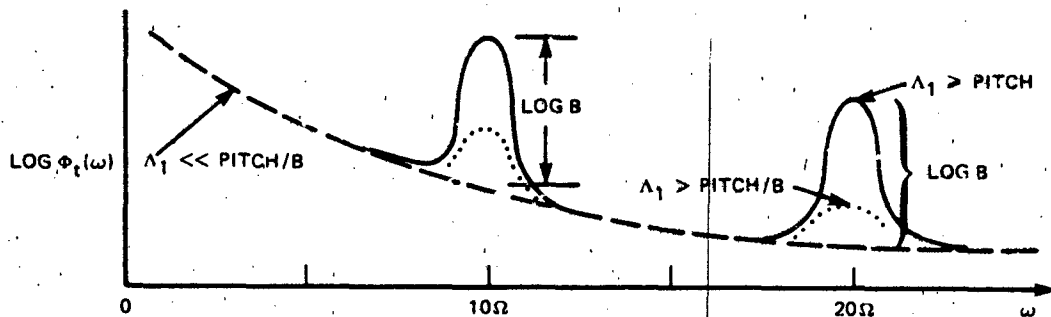


Figure 10.31b - Schematic of the Types of Spectra of Rotor Thrust Fluctuations Due to Turbulence of Different Axial Correlation Lengths. $B = 10$; $\sin \gamma = 1/3$ so Pitch $\approx 2R_T$ and (Pitch)/ $B = R_T/5$

Figure 10.31 - Illustration of Limiting Forms of $\phi_1(k_1)$ and Effects on $\phi_t(\omega)$

so that

$$\sin \gamma < \frac{\Lambda_1}{2\pi R_T}$$

or that Λ_1 is greater than the pitch of the rotor. In this case the $|A_s|^2$ comes outside the integral in Equation (10.45), giving

$$\begin{aligned} \phi_t(\omega) &= \frac{\pi^2}{3} \left[\phi_o(\Omega R_T)^2 \right]^2 (C R_T)^2 \frac{u^2}{(\Omega R_T)^2} \left| S_e \left(\frac{\omega C}{2U_T} \right) \right|^2 \\ &\quad \left(\frac{2\Lambda_R}{R_T} \right) |A_s(\frac{\omega}{\Omega})|^2 \left[\frac{1}{\pi} \frac{\frac{\Lambda_\theta}{U_T}}{1 + \left(\frac{\omega \Lambda_\theta}{U_T} \right)^2} \right] \end{aligned} \quad (10.90)$$

where $U_T = \Omega R_T$, and Equation (3.101) has been used to describe $\phi_\theta(k_\theta)$. The load spectrum for the rotor will resemble that shown in Figure 10.31.

In the alternative limit of $\Delta k_1 \sin \gamma > B/R_T$, or

$$\sin \gamma > \frac{B\Lambda_1}{2\pi R_T}$$

the integral scale is smaller than an axial blade spacing so that the blades are essentially independently excited by the turbulence. While the lift response can be derived from B times Equation (9.68b), it can also be deduced from Equation (10.89). Thus

$$\begin{aligned} &\int_{-\infty}^{\infty} \phi_1(k_1) \left| A_s \left(\left| \frac{\omega}{U} - k_1 \sin \gamma \right| \frac{2\pi R_T}{B} \right) \right|^2 dk_1 \\ &= \left[\text{Magnitude of } \phi_1 \left(k_1 < \frac{\pi}{\Lambda_1} \right) \right] \times \left[\text{Maximum value of } |A_s|^2 \right] \times \end{aligned}$$

$$\left[\text{Bandwidth of } |A_s|^2 \right] \times \left[\text{Number of peaks of } |A_s|^2 \text{ inside } \frac{\pi}{\Lambda_1} \right]$$

$$= \left[\frac{\Lambda_1}{\pi} \right] \times [B^2] \times \left[\frac{1}{R_T} \right] \times \left[\frac{\frac{\pi}{\Lambda_1}}{\frac{B}{R_T}} \right] = B$$

so that the frequency spectrum of unsteady thrust is

$$\Phi_t(\omega) = B \frac{\pi^2}{3} \left[\rho_o (\Omega R_T)^2 \right]^2 (C R_T)^2 \frac{\overline{u^2}}{(\Omega R_T)^2} \left| s_e \left(\frac{\omega C}{2U} \right) \right|^2 \cdot$$

$$\cdot \left(\frac{2\Lambda_R}{R_T} \right) \left(\frac{1}{\pi} \frac{\frac{\Lambda_\theta}{U_T}}{1 + \left(\frac{\omega \Lambda_\theta}{U_T} \right)^2} \right) \quad (10.91)$$

Equations (10.90) and (10.91) are compared in Figure 10.31, which shows that the load response of the rotor to fine scale turbulence will be devoid of bumps at multiples of the blade passage frequency, while response to turbulence of long axial scale will be a factor of B larger. This behavior is analogous to an array gain of acoustic arrays. For the intermediate scales of turbulence

$$\frac{(\text{Rotor pitch})}{B} < \Lambda_1 < \text{Rotor pitch}$$

broader, lower level bumps will appear.

For a compact subsonic rotor, on-axis sound is given by either the limiting form Equation (10.51) for $k_o R_1 \rightarrow 0$ or the standard relation for dipole sound. As indicated on p. 1141 this will give the sound pressure spectrum:

$$\Phi_{p_{\text{rad}}}(r, \omega) = \frac{k_o^2 \cos^2 \beta}{16\pi^2 r^2} \Phi_t(\omega) \quad (10.92)$$

or the sound power spectrum*:

$$\begin{aligned}\pi(\omega) &\approx \frac{k_o^2 \phi_t(\omega) (4\pi)}{\rho_o c_o (16\pi^2) 3} \approx 4\pi r^2 \frac{\left(\frac{1}{3}\right) \phi_{p_{rad}}(R_o, \beta=0, \omega)}{\rho_o c_o} \\ &= \frac{1}{3} \frac{k_o^2 \phi_t(\omega)}{\rho_o c_o 4\pi}\end{aligned}\quad (10.93)$$

when $\phi_t(\omega)$ is given by Equation (10.90) or (10.91).

As an example of the above relationships we compare estimated lift fluctuations from both the coupled blade, Equation (10.90), and the power-summed isolated blades, Equation (10.91), for a rotor in homogeneous turbulence. Letting $\gamma \rightarrow 0$,

$$\Lambda_r = \Lambda_\theta = \Lambda_1 = \Lambda$$

and

$$\overline{T^2} = \overline{L^2} = 2 \int_{\Delta\omega} \phi_L(\omega) d\omega$$

find for the correlated thrust response from Equations (10.90) and (10.91) (using the approximation for the Sears function)

$$\begin{aligned}\overline{T^2}(f, \Delta f) &\approx \frac{8\pi^2}{3} \frac{\Delta f}{n_s} \cdot q_A^2 R_T^4 \left(\frac{C}{R_T}\right)^2 \left(\frac{\pi}{J}\right)^2 \frac{u^2}{v_a^2} \left(\frac{2\Lambda}{R_T}\right) \\ &\cdot \frac{\frac{\Lambda}{\pi} R_T}{1 + \frac{\Lambda m B}{R_T}} \cdot \frac{\left|A_s\left(\frac{f}{n_s}\right)\right|^2}{1 + \frac{\pi m B c}{R_T}}\end{aligned}\quad (10.94)$$

*The factor 1/3 is deduced from the expression for \overline{P}_D resulting from Equation (2.37) and noting that the surface-averaged mean-square sound pressure of a dipole is 1/3 the peak pressure amplitude squared.

where $q_A = 1/2 \rho_o V_a^2 n_s$ is the shaft rotation velocity, $2\pi\Omega$, and $|A_s(f/n_s)|^2 = B^2$ for $f/n_s = mB$ with a bandwidth $\Delta f = n_s$, and for the uncorrelated response

$$\overline{T^2}(f, \Delta f) = \frac{B8\pi^2}{3} \frac{\Delta f}{n_s} q_A^2 R_T^2 \left(\frac{C}{R_T}\right)^2 \left(\frac{\pi}{J}\right)^2 \frac{u^2}{V_a^2} \left(\frac{2\Lambda}{R_T}\right) \cdot \frac{\Lambda_\theta / \pi R_T}{1 + \left(\frac{\Lambda_\theta mB}{R_T}\right)^2} \frac{1}{1 + \frac{\pi mBC}{R_T}} \quad (10.95)$$

Equation (10.95) should apply when $f/n_s \neq mB \pm n$, or when $2\Lambda_\theta \ll 2\pi R/B$; Equation (10.96) should apply otherwise. These relationships are compared to each other and to Sevik's¹³³ measurements in Figure 10.32. The measurements were conducted by measuring the unsteady thrust on a 10-blade rotor operating downstream of a turbulence-producing screen in a water tunnel.

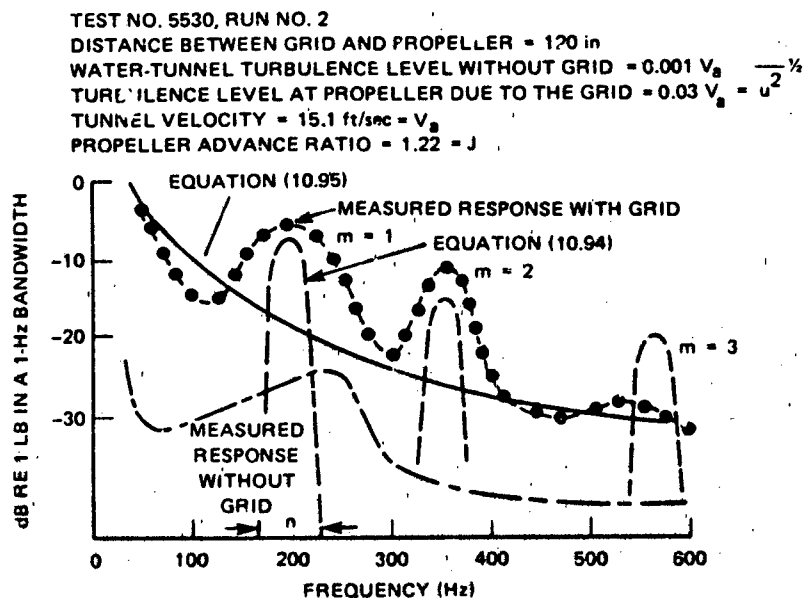


Figure 10.32 - Spectrum ($\Delta f=1$ Hz Band) of Unsteady Thrust on a 10-Bladed Rotor Downstream of a 6-in Grid Wire

Screen¹³³ for which the Measured $\Lambda_\theta = 0.5 R_T$.

$R_T = 4$ in, $n_s = 19$ rev/sec

The above theory has been applied to helicopter rotor noise by Homicz and George,¹³⁶ and George and Kim.¹³⁸ The question of noise from atmospheric turbulence injection to turbo-fans and inlet distortions has been approached in the above manner by Pickett,¹³⁹ Hanson¹⁴⁰ and Clark.¹⁴¹ Noise from rotor interaction with secondary inlet flow disturbances^{142,143} and duct, wall boundary layers^{142,144} can also be examined in this manner. Notable noise reduction of both discrete and stochastic levels has been effected in ducted rotors by boundary layer removal.¹⁴⁴

10.7 ROTATING MACHINERY IN ENCLOSURES

When rotors generate sound in acoustic enclosures, the radiated sound intensity depends on the coupling of the acoustic modes of the enclosure and the rotating dipole modes. The first studies of this coupling were by Tyler and Sofrin,^{145,146} with follow-on work and additional sophistication by Morfey,^{147,148} Mugridge,¹⁴⁹ and Wright.¹⁵⁰ Description of other work has been given by Cumpsty.⁵ In this section only the elementary considerations of ducted rotor noise are given.

10.7.1 Elementary Duct Acoustics

Acoustic sound propagation in ducts is complicated by the finite cross section that forces the sound to exist as standing waves across the duct cross section. Only certain of these modes produce propagating waves along the axis; pressures of other modes decay exponentially with axial distance from the source. To illustrate this effect, consider the sound pressure that can exist inside the hard-walled rectangular duct illustrated in Figure 10.33. The sound pressure of a wave of frequency ω is $p(\vec{x}, \omega)$ caused by a unit source at \vec{x}_0 in the duct is just the Green's function satisfying Equation (2.106). The pressure dependence in the x_2 , x_1 direction that satisfies the condition of zero velocity at the wall, i.e.,

$$\frac{\partial p}{\partial x_1} = \frac{\partial p}{\partial x_2} = 0 \quad \text{on } x_1 = \pm \frac{L_1}{2} \text{ and } x_2 = \pm \frac{L_2}{2}$$

is

$$p(\vec{x}, \omega) = \sum_{mn} A_{mn} \sin k_m x_1 \sin k_n x_2 e^{ik_3(x_3)} \quad (10.96)$$

where

$$k_m = \frac{m\pi}{L_1} \quad k_n = \frac{n\pi}{L_2} \quad -\infty < m, n < \infty$$

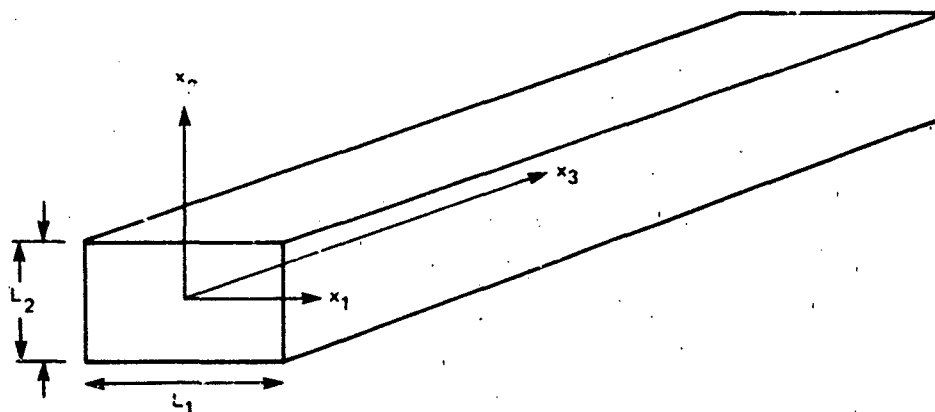


Figure 10.33 - Geometry of a Rectangular Duct

by substituting into the homogeneous form of Equation (2.106), and we find for the k_3 wave number of the propagating wave,

$$k_m^2 + k_n^2 + k_3^2 - k_o^2 = 0$$

$$k_3 = \left(k_o^2 - k_{mn}^2 \right)^{1/2} \quad (10.97)$$

where

$$k_{mn}^2 = k_m^2 + k_n^2$$

As long as k_{mn} is less than k_o , the wave number k_3 is real and the waves propagate unattenuated. However, if k_o is less than k_{mn} , then k_3 is imaginary so that

$$\begin{aligned} k_3 &= +i \left(k_{mn}^2 - k_o^2 \right)^{1/2} \quad \text{for } x_3 > 0 \\ &= -i \left(k_{mn}^2 - k_o^2 \right)^{1/2} \quad \text{for } x_3 < 0 \end{aligned}$$

This result shows that for a given excitation wave number $(k_{1,2})_e$, if the frequency is so low that $k_o < (k_{1,2})_e = k_e$, then the sound will not propagate along the duct. The frequency ω_c for which

$$k_e = k_o = \frac{\omega_c}{c_o} \quad (10.98)$$

is called the cut off frequency of the mode. There is an exceptional mode, however, for which propagation always occurs. When $m = n = 0$, i.e., when the propagating wave is a plane wave across the duct, then $k_3 = k_o$ and no attenuation occurs. Thus plane waves always propagate in ducts.

For a monopole source of unit strength set at position x_{10}, x_{20}, x_{30} , substituting into Equation (2.106) we find (following the methods of Chapter 6)

$$A_{mn} \left[\left(\frac{d^2 Z}{dz^2} \right) + k_3^2 Z \right] = \frac{-4}{L_1 L_2} S_{mn}(x_1, x_2)_0^0 \delta(x_3 - x_{30})$$

where

$$Z = e^{ik_3 |x_3 - x_{30}|}$$

$$S_{mn}(x_1, x_2)_0^0 = \sin k_m x_1 \sin k_n x_2$$

To find A_{mn} we integrate from $x_3 \rightarrow -\infty$ to x_{30} and from x_{30} to $x_3 \rightarrow \infty$ to obtain

$$\lim_{|\xi| \rightarrow 0} \left[A_{mn} \left(\frac{dZ}{dz} \right)_{-\xi}^{\xi} \right] = A_{mn} 2ik_3 = \frac{-4}{L_1 L_2} S_{mn}(x_1, x_2)_0^0$$

so that the Green's function for the sound pressure is

$$p_m(\vec{x}, \vec{x}_o, \omega) = \frac{2i}{L_1 L_2} \sum_{mn} \frac{S_{mn}(x_1, x_2)_0^0 S_{mn}(x_1, x_2)_0^0}{(k_o^2 - k_{mn}^2)^{1/2}} e^{ik_3 |x_3 - x_{30}|} \quad (10.99)$$

In like manner, for the dipole aligned with the duct axis, say of strength $\partial F / \partial x_3$, the Green's function will be

$$p_{d_3}(x, \omega) = \frac{\partial}{\partial x_3} (\text{monopole function})$$

or

$$p_{d_3}(\vec{x}, \vec{x}_0, \omega) = \frac{-2}{L_1 L_2} \sum_{mn} S_{mn}(x_1, x_2) S_{mn}(x_1, x_2) e^{ik_3 |x_3 - x_{30}|} \quad (10.100)$$

The propagation of sound therefore not only depends on the wave number of the mode excited relative to the acoustic wave number, but also on the local admittance of the duct, which is expressed by the mode shape evaluated at the source location: $S_{mn}(x_1, x_2)$. Other, more advanced concepts of duct acoustics can be found in Morse and Ingard.⁸

The sound pressure from a distributed dipole force $f_3(x_0, x_0, \omega)$ axially concentrated located at the location x_3 is

$$p(x, \omega) = \iint_{A_p} p_{d_3}(\vec{x}_0, \vec{x}, \omega) f_3(\vec{x}_0, \omega) d\vec{x}_0 \quad (10.101)$$

where A_p is the disk surface area of the dipole or the projected area of the surface in the axial direction.

10.7.2 Propagating Modes of a Ducted Rotor

Using the same approach as above, the dipole Green's function of an infinitely long circular duct illustrated in Figure 10.34 is⁸

$$p_{d_3}(r, \theta; r_0, \theta_0) = \sum_{mn} \pi \frac{1}{a^2 \Lambda_{mn}} J_m(k_{mn} a) J_m(k_{mn} r) e^{im(\theta - \theta_0)} e^{ik_3 |x_3 - x_{30}|} \quad (10.102)$$

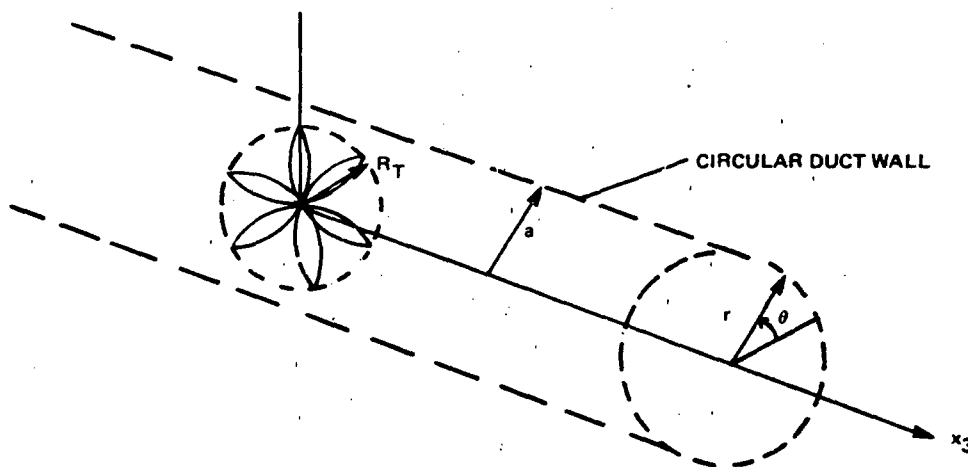


Figure 10.34 - Geometry of a Rotor in a Circular Duct

where

$$\Lambda_{mn} = \frac{1}{2} \left(1 - \frac{m^2}{\kappa_{mn}^2 a^2} \right) J_m^2(\kappa_{mn} a)$$

$$k_3^2 = k_o^2 - \kappa_{mn}^2 \quad (10.103)$$

The wave number k_{mn} is a parameter of the wave equation for the m th circumferential mode of the duct, i.e., m node lines around the circumference. For the general pressure

$$p(r, \theta, z, \omega) = J_m(\kappa_m r) e^{im\theta} e^{ik_3 z}$$

the homogeneous wave equation gives

$$\frac{1}{r} \frac{\partial}{\partial r} \left(r \frac{\partial p}{\partial r} \right) + \frac{1}{r^2} \frac{\partial^2 p}{\partial \theta^2} + \frac{\partial^2 p}{\partial z^2} + k_o^2 p = 0$$

from which emerges

$$r^2 \left(\frac{\partial J_m(\kappa_m r)}{\partial r} \right) + r \frac{\partial J_m(\kappa_m r)}{\partial r} + \left[(\kappa_m r)^2 - m^2 \right] J_m(\kappa_m r) = 0$$

The specific values of $\kappa_m = \kappa_{mn}$ for the hard-walled duct result from the boundary condition of zero radial gradient of the pressure at the wall which gives

$$\kappa_{mn} J'_m(\kappa_{mn} a) = 0$$

for which the n th zero of the derivative of the m th order Bessel's function, f_{mn} , say

$$\kappa_m a = f_{mn} = \kappa_{mn} a \quad (10.104)$$

i.e., f_{mn} is the n th zero ($n=1,2,3,\dots$) of the J'_m ; the approximate values are³⁷

$$f_{mn} \approx \left(n + \frac{1}{2}m - \frac{3}{4} \right) \pi - \frac{4m^2 + 1}{8 \left(n + \frac{m}{2} - \frac{3}{4} \right) \pi} \quad n \gg m \quad (10.105)$$

$$f_{mn} \approx n\pi$$

with specific values

$$f_{1,1} = 0.59\pi, f_{2,1} = 0.97\pi, f_{0,1} = 1.2\pi, f_{0,2} = 2.2\pi, f_{1,2} = 1.7\pi, \text{ and } f_{2,2} = 2.2\pi \quad (10.106)$$

To find an expression for the radiating pressure, the dipole source strength of a rotor with small pitch ($\gamma \ll 1$) in a frame of reference fixed with the duct is first found by substituting $\theta = \theta_f - \Omega t$ into Equation (10.42a) and summing over B blades. The result is of the form

$$f_3(r_o, \theta_o) = \sum_w \sum_{s=0}^{B-1} BL_w \left(R, \frac{wC}{R} \right) e^{i(w+sB)\theta_f} e^{-isB\Omega t} \quad (10.107)$$

Equation (10.107) is the result of first writing the force in Equations (10.42a) and (10.43) for $\gamma \ll 1$ as

$$\frac{dT_3(r, \theta, t)}{dR} = \sum_q \left[f_w(R, T) \right]_q e^{iq\theta}$$

in a frame of reference fixed with the rotor, where we define

$$\begin{aligned} \left[f_w(R, t) \right]_q &\equiv \frac{1}{2\pi} \int_0^{2\pi} \frac{dT_3}{dR}(R, \theta, t) e^{-iq\theta} d\theta \\ &= \frac{B}{2\pi} L_w \left(R, \frac{wC}{R} \right) e^{i\omega\Omega t} \delta(q - w - sB) \end{aligned}$$

as can be determined through the use of Equation (10.46). Equation (10.107) gives the total force distribution for all w harmonics of the inflow in a frame of reference fixed with the duct.

Substitution of Equation (10.107) into Equation (10.102) and integration over θ_f yields the radiated sound pressure due to the w th inflow mode

$$\begin{aligned} p_w(r, \theta, z, t) &= \sum_m \sum_n \sum_{S=0}^{B-1} \frac{B}{\pi a^2 \lambda_{mn}} J_{mn}(\kappa_{mn} a) J_{mn}(R_{mn} r) L_w \left(R, \frac{wC}{R} \right) \\ &\quad \delta(w + sB - m) e^{im\theta} e^{ik_3 |x_3 - x_{30}|} e^{-i\omega B \Omega t} r dr \end{aligned} \quad (10.108)$$

where only values $m = w + sB$ are allowed and s may take on positive and negative values.

Our condition for radiating modes becomes (from Equation (10.103)),

$$\kappa_{mn} = \frac{a}{f_{mn}} < k_0$$

or

$$k_{w+sB,n} = \frac{a}{f_{w+sB,n}} < k_o$$

For large-enough orders of the Bessel's function. Thus Equation (10.106) holds, i.e.,

$$w + sB < m$$

We have from Equation (10.105)

$$k_{mn} = \frac{m}{a} = \frac{w + sB}{a}$$

Since

$$k_o = \frac{\omega}{c_o} = \frac{sB\Omega}{c_o}$$

our condition for radiating modes becomes

$$\frac{\Omega a}{c_o} > \frac{w + sB}{sB}$$

Assuming that the rotor radius is nearly equal to the radius of the duct, $R_T = a$, then we have as a requirement

$$M_T > \frac{w \pm sB}{sB} \quad (10.109)$$

What the condition of Equation (10.109) means is that two modes are possible. One, requiring supersonic tip speeds, occurs for $sB + w$; the other, requiring subsonic tip speeds, is for $sB - w$. Furthermore for blade frequency forces such that $sB = w$, the rotor will always radiate sound; once $m = w - sB = 0$, so that the sound is plane wave across the duct. If the inflow to the rotor is homogeneous and steady,

i.e., $w = 0$, then only Gutin sound could be produced, but, by Equation (10.109), it will only propagate when the tip speeds are supersonic; i.e., the condition for propagating Gutin sound in the duct is $M_T > 1$.

Finally, Equation (10.108) shows that the θ, t phase combination gives spiral wave fronts:

$$m\theta - sB\Omega t = (sB + w)\theta - sB\Omega t$$

This shows the existence of two rotating waves—one spinning faster than Ω , the other spinning slower. The rotational speed of the spinning modes is

$$\frac{\Omega_r}{\Omega} = \frac{sB}{sB + w}$$

Together with Equation (10.109), this expression means that the radiating modes are those for which Ω (the shaft rate) is faster than the spinning rate of the acoustic modes. Such modes are called spinning modes.

10.8 REFERENCES

1. Sharland, I.J., "Sources of Noise In Axial Flow Fans," J. Sound Vib., Vol. 1, pp. 302-322 (1964).
2. Mugridge, B.D. and C.L. Morfey, "Sources of Noise in Axial Flow Fans," J. Acoust. Soc., Vol. 51, pp. 1411-1462 (1972).
3. Morfey, C.L., "The Acoustics of Axial Flow Machines," J. Sound Vib., Vol. 22, pp. 445-466 (1972).
4. Morfey, C.L., "Rotating Blades and Aerodynamic Sound," J. Sound Vib., Vol. 28, pp. 587-617 (1973).
5. Cumpsty, N.A., "A Critical Review of Turbo Machinery Noise," ASME J. Fluid Eng., Vol. 99, pp. 278-293 (1977).
6. Wright, S.E., "The Acoustic Spectrum of Axial Flow Machines," J. Sound Vib., Vol. 45, pp. 165-223 (1976).
7. Niese, W., "Noise Reduction in Centrifugal Fans: A Literature Survey," J. Sound Vib., Vol. 45, pp. 375-403 (1976).
8. Morse, P.M. and K.U. Ingard, "Theoretical Acoustics," McGraw-Hill Book Co. (1968).
9. Goldstein, M.E., "Aeroacoustics," McGraw-Hill Book Co. (1976).
10. Gutin, L., "On the Sound Field of a Rotating Propeller," NACA TM 1195 (1948). Translation of "Über das Schallfeld einer rotierenden Luftschraube," Physikalische Zeitschrift der Sowjetunion, Vol. 9 (1936).
11. Leverton, J.W., "The Noise Characteristics of a Large 'Clean' Rotor," J. Sound Vib., Vol. 27, pp. 357-376 (1973).
12. Widnall, S.E., "A Correlation of Vortex Noise Data from Helicopter Main Rotors," J. Aircraft, Vol. 6, pp. 279-281 (1969).
13. Stuckey, T.J. and J.O. Goddard, "Investigation and Prediction of Helicopter Rotor Noise, Part I, Wessex Whirl Tower Results," J. Sound Vib., Vol. 5, pp. 50-80 (1967).
14. Morfey, C.L., "Broadband Sound Radiated from Subsonic Rotors," International Symposium on the Fluid Mechanics and Design of Turbomachinery, Penn State University, NASA SP-304 Part II (1974).

15. Griffiths, J.W.R., "The Spectrum of Compressor Noise of a Jet Engine," J. Sound Vib., Vol. 1, pp. 127-140 (1964).
16. Cumsty, N.A., "Sum and Difference Tones from Turbomachines," J. Sound Vib., Vol. 32, pp. 383-386 (1974).
17. Nemec, J., "Noise of Axial Flow Fans and Compressors: Study of its Radiation and Reduction," J. Sound Vib., Vol. 6, pp. 230-236 (1967).
18. Brown, N.A., "The Use of Skewed Blades for Ship Propellers and Truck Fans," Proc. ASME Symposium on Noise and Fluids Engineering, Atlanta, Ga. (1977).
19. Barnaby, K.C., "Basic Naval Architecture," Hutchinson and Co. (1963).
20. Rossell, H.E. and L.B. Chapman, "Principles of Naval Architecture," Soc. Naval Architects and Marine Engineers, N.Y. (1939).
21. Von Mises, "Theory of Flight," Dover (1959).
22. Dixon, S.L., "Thermodynamics and Mechanics of Turbomachinery," 3rd Ed., Pergamon Press (1978).
23. Horlock, J.H., "Axial Flow Turbomachines," Butterworth (1966).
24. Wislicenus, G.F., "Fluid Mechanics of Turbomachinery," Vols. 1 and 2, Dover (1965).
25. Troost, I.L., "Open Water Test Series with Modern Propeller Forms," N.E. Coast Inst., Eng. Shipbuilders, Vol. 67 (1938, 1940, 1951).
26. van Lammeren, W.P.A. et al., "The Wageningen-B Screw Series," Trans. SNAME, Vol. 77, pp. 269-343 (1969).
27. Emery, J.C. et al., "Systematic Two-Dimensional Cascade Tests of NACA-65 Series Compressor Blades at Low Speeds," NACA TN-1368 ().
28. Cumming, R.A. et al., "Highly Skewed Propellers," Trans. Soc. Nav. Arch. Marine Eng., Vol. 80, pp. 98-135 (1972).
29. Kerwin, J.E. and R. Leopold, "Propeller-Incidence Correction Due to Blade Thickness," J. Ship Res., Vol. 7, pp. 1-6 (1963).
30. Kerwin, J.E. and R. Leopold, "A Design Theory for Sub-cavitating Propellers," Trans. Soc. Nav. Arch. Marine Eng., Vol. 72, pp. 294-335 (1964).

31. Morgan, W.B. et al., "Propeller Lifting Surface Corrections," Trans. SNAME, Vol. 76, pp. 309-347 (1968).
32. Eckhardt, M.R. and W.B. Morgan, "A Propeller Design Method," Trans. SNAME, Vol. 63, pp. 325-374 (1955).
33. van Manen, J.D., "Fundamentals of Ship Resistance and Propulsion," Int. Shipbuilding Progress, Vol. 4, pp. 107-124, 155-183, 229-238, 271-288, 317-391, 436-452, 495-502 (1957).
34. Boswell, R.J. and M.L. Miller, "Unsteady Propeller Loading-Measurement Correlation with Theory, and Parametric Study," Naval Ship R&D Center Rep 2625 (1968).
35. Thompson, D.E., "Propeller Time-Dependent Forces Due to Non-Uniform Flow," ARL-PSU Tech. Memo. 76-48 (Mar 1976).
36. Denney, S.B. et al., "Hydrodynamic Design Considerations for the Controlable-Pitch Propeller for the Guided Missile Frigate," Nav. Eng. J., Vol. I, pp. 72-81 (Apr 1975).
37. Abramowitz, M. and L.A. Stegun, "Handbook of Mathematical Functions with Formulas, Graphs, and Mathematical Tables," N.B.S. Pub. No. 55 (1964).
38. Ffowcs Williams, J.E. and D.L. Hawkings, "Theory Relating to the Noise of Rotating Machinery," J. Sound Vib., Vol. 10, pp. 10-21 (1969).
39. Lowson, M.V., "The Sound Field for Singularities in Motion," Proc. Roy. Soc., Ser A286, pp. 559-572 (1965).
40. Lowson, M.V., "Basic Mechanisms of Noise Generation by Helicopters, V/Stol Aircraft and Ground Effect Machines," J. Sound Vib., Vol. 3, pp. 454-466 (1966).
41. Lowson, M.V., "Theoretical Analysis of Compressor Noise," J. Acoust. Soc. Am., Vol. 47, pp. 371-385 (1970).
42. Lowson, M.V. and J.B. Ollerhead, "A Theoretical Study of Helicopter Rotor Noise," J. Sound Vib., Vol. 9, pp. 197-222 (1969).
43. Hanson, D.B., "Spectrum of Rotor Noise Caused By Inlet Guide Vane Wakes," J. Acoust. Soc. Am., Vol. 55, pp. 1247-1251 (1974).
44. Morfey, C.L. and H.K. Tanna, "Sound Radiation from a Point Force in Circular Motion," J. Sound Vib., Vol. 13, pp. 325-351 (1971).

45. Wright, S.E., "Sound Radiation from a Lifting Rotor Generated by Asymmetric Disk Loading," J. Sound Vib., Vol. 9, pp. 223-240 (1969).
46. Wright, S.E., "Discrete Radiation from Rotating Periodic Sources," J. Sound Vib., Vol. 17, pp. 437-498 (1971).
47. Hanson, D.B., "The Influence of Propeller Design Parameters on Far Field Harmonic Noise in Forward Flight," AIAA 5th Aeroacoustics Conference, Seattle, Wash. (1979).
48. Hawkings, D.L. and M.V. Lowson, "Theory of Open Supersonic Rotor Noise," J. Sound Vib., Vol. 36, pp. 1-20 (1974).
49. Hanson, D.B. and M.R. Fink, "The Importance of Quadrupole Sources in Prediction of Transonic Tip Speed Propeller Noise," J. Sound Vib., Vol. 62, pp. 19-38 (1979).
50. Hanson, D.L., "Unified Analysis of Fan Stator Noise," J. Acoust. Soc. Am., Vol. 54, pp. 1571-1591 (1973).
51. Heller, H.H. and S.E. Widnall, "The Role of Fluctuating Forces in the Generation of Compressor Noise," NASA CR-2012 (1972).
52. Merbt, H. and H. Billing, "Der Propeller als rotierende Schallquelle," Zeitschrift für angewandte Mathematik und Mechanik (ZAMM), Vol. 29, pp. 301-311 (1949).
53. Ernsthausen, W., "Der Einfluss aerodynamischer Eigenschaften auf Schallfeld und Strahlungsleistung einer Luftschraube," Akust. Zeitschr., Vol. 6, p. 245 (1941).
54. Deming, A.F., "Propeller Rotation Noise Due to Torque and Thrust," J. Acoust. Soc. Am., Vol. 12, pp. 173-181 (1940).
55. Hubbard, H.H. and L.W. Lassiter, "Sound from a Two Blade Propeller at Supersonic Tip Speeds," NACA Report 1079 (1932).
56. Grosche, F.R. and H. Stiewitt, "Investigation of Rotor Noise Source Mechanisms with Forward Speed Simulation," AIAA Journal, Vol. 16, pp. 1255-1261 (1978).
57. Hersh, A.S. and R.E. Hayden, "Aerodynamic Sound Radiation with and without Leading Edge Serrations," NASA CR-114370 (1971).
58. Paterson, R.W. et al., "Isolated Airfoil-Tip Vortex Interaction Noise," J. Aircraft, Vol. 12, pp. 34-40 (1975).

59. Schlinker, R.H., "Airfoil Trailing Edge Noise Measurements with a Directional Microphone," Paper 77-1269, AIAA 4th Aeroacoustics Conference, Atlanta, Ga. (1977).

60. N. Le S. Filleul, "An Investigation of Noise in Axial Flow Fans," Ph.D. Thesis, London University (1966).

61. Leverton, J.W. and J.S. Pollard, "A Comparison of the Noise Characteristics of Full Scale and Model Helicopter Rotors," Westland Helicopters Limited, Research Paper 428 (1972).

62. Brown, D. and J.B. Ollerhead, "Propeller Noise at Low Tip Speeds," Wyle Laboratories Technical Report AFAPL-TR-71-55 (1971).

63. Stowell, E.Z. and A.F. Deming, "Vortex Noise from Rotating Cylindrical Rods," J. Acoust. Soc. Am., Vol. 7, pp. 190-198 (1936).

64. Metzger, F.B., Private communication to S.E. Wright, of Hamilton Standard Company, Windsor Locks, Connecticut (1974).

65. Metzger, F.B. et al., "Analytical Parametric Investigation of Low Pressure Ratio Fan Noise," NASA CR-2188 (1973).

66. Sternfeld, H. et al., "An Investigation of Noise Generation on a Hovering Rotor - Part I and II," Boeing Vertol Report for U.S. Army Research Office Contract DAHCO4-69-C-0087 (1973).

67. Lowrie, B., Private communication to S.E. Wright of Rolls-Royce (1971) Limited, Derby (1974).

68. Trillo, R.L., "An Empirical Study of Hovercraft Propeller Noise," J. Sound Vib., Vol. 3, pp. 476-509 (1966).

69. Kazin, S.B. and L.J. Volk, "Lift Fan Modification and Acoustic Test Program," NASA CR-1934 LF 336 (1971).

70. Lowson, M.V. et al., "Source Mechanisms for Rotor Noise Radiation," NASA CR-2077 (1973).

70a. Brockett, T. "Minimum Pressure Envelopes for Modified NACA-66 Section with NACA $a = 0.8$ Camber and BuShips Type I and Type II Sections," DTMB Report 1780, 1966.

71. Hunter, H., "Singing Propeller," Trans., N.E. Coast Inst. Eng. Shipbuilders, Vol. 53, pp. 189-222 (1936-37).

72. Shannon, J.F., "Statistical and Experimental Investigations of the Singing Propeller Problem," Trans. Inst. Eng. Shipbuilders Scotland, Vol. 82, pp. 256-289 (1939).
73. Hughes, G., "On Singing Propellers," Trans. Inst. Nav. Arch., Vol. 87, pp. 185-216 (1945).
74. Work, C.E., "Singing Propellers," J. Soc. Nav. Eng., Vol. 63, pp. 319-331 (1951).
75. Kerr, W. et al., "The Problems of the Singing Propeller," Proc. Inst. Mech. Eng., Vol. 144, pp. 54-90 (1940).
76. Conn, J.F.C., "Marine Propeller Blade Vibration," Trans. Inst. Eng. Shipbuilders Scotland, Vol. 83, pp. 225-255 (1939).
77. Gongwer, C.A., "A Study of Vanes Singing in Water," J. Appl. Mech., Vol. 19, pp. 432-438 (1952).
78. Lankester, S.G. and W.D. Wallace, "Some Investigations into Singing Propellers," Trans. N.E. Coast Inst. Eng. Shipbuilders, Vol. 71, pp. 291-318 (1954-1955).
79. Krivtsov, Y.V. and A.J. Pernik, "The Singing of Propellers," DTMB Translation 281 (1958).
80. Cumming, R.A., "A Preliminary Study of Vortex-Induced Propeller Blade Vibrations and Singing," DTMB Report 1838 (1965).
81. van de Voorde, C.B., "The Singing of Ship Propellers," Int. Shipbuilding Prog., Vol. 7, pp. 451-455 (1969).
82. Ross, D., "Vortex Shedding Sounds of Propellers," Bolt Beranek and Newman Report 1115 (1964).
83. Burrill, L.C., "Marine Propeller Blade Vibrations: Full Scale Tests," Proc. N.E. Coast Inst. Eng. Shipbuilders, Vol. 62, pp. 249-270 (1945).
84. Burrill, L.C., "Underwater Propeller Vibration Tests," Proc. N.E. Coast Inst. Eng. Shipbuilders, Vol. 65, pp. 301-314 (1949).
85. Deming, A.F., "Noise from Propellers with Symmetrical Sections at Zero Blade Angle II," NACA TN 679 (1938).

86. Lyon, R.H., "Radiation of Sound by Airfoils that Accelerate Near the Speed of Sound," J. Acoust. Soc. Am., Vol. 3, pp. 894-905 (1971).
87. Lyon, R.H. et al., "Synthesis of Helicopter Rotor Tips for Less Noise," J. Acoust. Soc. Am., Vol. 53, pp. 607-618 (1973).
88. Morfey, C.L., "Sound Generation in Subsonic Turbomachinery," Trans. ASME Ser D, J. Basic Eng., Vol. 92, pp. 450-458 (1970).
89. Mani, R., "Discrete Frequency Noise Generation from an Axial Flow Fan Blade Row," Trans ASME Ser D, J. Basic Eng., Vol. 92, pp. 37-43 (1970).
90. Kemp, N.H., "On the Lift and Circulation of Airfoils in Some Unsteady-Flow Problem," J. Aero. Sci., Vol. 3, pp. 713-714 (1952).
91. Kemp, N.H. and W.R. Sears, "Aerodynamic Interference between Moving Blade Rows," J. Aero. Sci., Vol. 20, pp. 585-597, 612 (1953).
92. Kemp, N.H. and W.R. Sears, "The Unsteady Forces Due to Viscous Wakes in Turbomachines," J. Aero. Sci., Vol. 22, pp. 478-483 (1955).
93. Heatherington, R., "Compression Noise Generated by Fluctuating Lift Resulting from Rotor Stator Interaction," AIAA Journal, Vol. 1, pp. 473-474 (1963).
94. Morfey, C.L., "Sound Generation in Subsonic Turbomachinery," Trans. ASME, Ser D., J. Basic Eng., Vol. 92, pp. 450-458 (1970).
95. Kaji, S. and T. Okczaki, "Generation of Sound by Rotor-Stator Interaction," J. Sound Vib., Vol. 13, pp. 281-307 (1970).
96. Silverstein, A. et al., "Downwash and Wake Behind Plain and Flapped Airfoils," NACA Report 651 (1939).
97. Raj, R. and B. Lakshminarayana, "Characteristics of the Wake Behind a Cascade of Airfoils," J. Fluid Mech., Vol. 61, pp. 707-730 (1973).
98. Satyanarayana, B., "Unsteady Wake Measurements of Airfoils and Cascades," AIAA Journal, Vol. 15, pp. 613-618 (1977).
99. Gradshteyn, I.S. and I.M. Ryzhik, "Table of Integrals Series and Products," Academic Press (1965).
100. Leverton, J.W. and F.W. Taylor, "Helicopter Blade Slap," J. Sound Vib., Vol. 4, pp. 345-357 (1966).

101. Widnall, S., "Helicopter Noise Due to Blade Vortex Interaction," J. Acoust. Soc. Am., Vol. 50, pp. 354-365 (1971).
102. Filotas, L.T., "Vortex-Induced Helicopter Blade Loads and Noise," J. Sound Vib., Vol. 27, pp. 387-398 (1973).
103. Sisto, F., "Unsteady Aerodynamic Reactions on Airfoils in a Cascade," J. Aero. Sci., Vol. 22, pp. 297-302 (1955).
104. Whitehead, M.A., "Force and Moment Coefficients for Vibrating Aerofoils in Cascade," ARC R&M No. 3254 (1962).
105. Whitehead, M.A., "Bending Flutter of Unstalled Cascade Blades at Finite Deflection," ARC R&M 3386 (1965).
106. Henderson, R.E. and H. Daneshyar, "Theoretical Analysis of Fluctuating Lift on the Rotor of an Axial Turbomachine," ARL R&M 3684 (1972).
107. Horlock, J.H. et al., "The Response of Turbomachine Blades to Low Frequency Inlet Distortions," ASME J. Eng. Power, Vol. 99, pp. 195-203 (1977).
108. Henderson, R.E., "The Unsteady Response of an Axial Flow Turbomachine to an Upstream Disturbance," Ph.D. Thesis, Churchill College, Cambridge Univ. (1973).
109. Bruce, E.P. and R.E. Henderson, "Axial Flow Rotor Unsteady Response to Circumferential Inflow Distortions," Project Squid Technical Report PSU-13-P, Project Squid Headqts., Thermal Science and Propulsion Center, Purdue Univ. (1975).
110. Henderson, R.E., "The Unsteady Design of Axial Flow Turbomachines," ASCE, IAHR/AIAR, ASME Joint Symposium on Design and Operating Fluid Machinery, June 1978, Ft. Collins, Co.
111. Atassi, H. and M.E. Goldstein, "Unsteady Lift Forces on Highly Cambered Airfoils Moving through a Gust," AIAA 12th Aerospace Sciences Mtg. Paper 74-88 (1974).
112. Goldstein, M.E. and H. Atassi, "A Complete Second-Order Theory for the Unsteady Flow about an Airfoil Due to a Periodic Gust," J. Fluid Mech., Vol. 74, pp. 741-765 (1976).
113. Atassi, H. and T.J. Akai, "Effect of Blade Loading and Thickness on the Aerodynamics of Oscillating Cascades," AIAA 16th Aerospace Sciences Mtg. Paper 78-227 (1978).

114. Atassi, H. and T.J. Akai, "Aerodynamic Force and Moment on Oscillating Airfoils in Cascade," AIAA Paper 78-GT-181 (1979).

115. Smith, S.N., "Discrete Frequency Sound Generation in Axial Flow Turbomachines," ARC R&M 3709 (1973).

116. Whitehead, D.S., "Vibration and Sound Generation in a Cascade of Flat Plates in Subsonic Flow," ARC R&M 3685 (1972).

117. Mani, R., G. Horvay, "Sound Transmission through Blade Rows," J. Sound Vib., Vol. 12, pp. 59-83 (1970).

118. Kaji, S. and T. Okazaki, "Propagation of Sound Waves through a Blade Row, I. Analysis Based on the Semi-Actuator Disk Theory," J. Sound Vib., Vol. 11, pp. 339-353 (1970).

119. Kaji, S. and T. Okazaki, "Propagation of Sound Waves through a Blade Row, II. Analysis Based on the Acceleration Potential Method," J. Sound Vib., Vol. 11, pp. 355-375 (1970).

120. Amiet, R., "Transmission and Reflection of Sound by a Blade Row," AIAA Journal, Vol. 9, pp. 1893-1894 (1971).

121. Amiet, R., "Transmission and Reflection of Sound by Two Blade Rows," J. Sound Vib., Vol. 74, pp. 399-412 (1974).

122. Tsakonas, S. and W.R. Jacobs, "Unsteady Lifting Surface Theory for a Marine Propeller of Low Pitch Angle with Chordwise Loading Distribution," J. Ship Res., Vol. 8, pp. 79-101 (1965).

123. Tsakonas, S. et al., "Correlation and Application of an Unsteady Flow Theory for Propeller Forces," Trans SNAME, pp. 158-193 (1967).

124. Tsakonas, S. et al., "Unsteady Propeller Lifting-Surface Theory with Finite Number of Chordwise Modes," J. Ship Res., Vol. 12, pp. 14-46 (1968).

125. Brown, N.A., "Periodic Propeller Forces in Non-Uniform Flow," MIT Dept. of Naval Architecture and Marine Engineering Report 64-7 (1964).

126. Frydenlund, O. and J.E. Kerwin, "The Development of Numerical Methods for the Computation of Unsteady Propeller Forces," Norwegian Maritime Research, Vol. 5, pp. 17-28 (1977).

127. Kerwin, J.E. and C. Lee, "Prediction of Steady and Unsteady Marine Propeller Performance by Numerical Lifting-Surface Theory" SNAME Trans., Vol. 86, pp. 218-253 (1978).
128. Kerwin, J.E. and R. Leopold, "Propeller-Incidence Correction Due to Blade Thickness," J. Ship Res., Vol. 7, No. 2, pp. 1-6 (1963).
129. Cumming, D.E., "Numerical Prediction of Propeller Characteristics," J. Ship Res., Vol. 17, pp. 12-18 (1973).
130. Kerwin, J.E., "Computer Techniques for Propeller Blade Section Design," Int. Shipbldg. Prog., Vol. 20, pp. 227-251 (1973).
131. Lewis, F.M., "Propeller Vibration Forces," Trans SNAME, Vol. 71, pp. 293-326 (1963).
132. Schwanecke, H., "Comparison of Methods for the Calculation of Wake Induced Propeller Blade Exciting Forces," Proc. Symposium on High Powered Propulsion of Large Ships, Part I., Paper XIII, Netherlands Ship Model Basin, Pub. 490 (1974).
133. Sevik, M., "Sound Radiation from a Subsonic Rotor Subjected to Turbulence," Int. Symposium on the Fluid Mechanics and Design of Turbomachinery, Penn State Univ., NASA SP-304, Part II (1974).
134. Chandrashekhara, N., "Tone Radiation from Axial Flow Fans Running in Turbulent Flow," J. Sound Vib., Vol. 18, pp. 533-543 (1971).
135. Mani, R., "Noise Due to Interaction of Inlet Turbulence with Isolated Stators and Rotors," J. Sound Vib., Vol. 17, pp. 251-260 (1971).
136. Homicz, G.F. and A.R. George, "Broadband and Discrete Frequency Radiation from Subsonic Rotors," J. Sound Vib., Vol. 36, pp. 151-177 (1974).
137. Amiet, R., "Noise Produced by Turbulent Flow into a Propeller or Helicopter Rotor," AIAA Journal, Vol. 15, pp. 307-308 (1977).
138. George, A.R. and Y.M. Kim, "High Frequency Broadband Rotor Noise," AIAA Journal, Vol. 15, pp. 538-545 (1977).
139. Pickett, G.F., "Effects of Non-Uniform Inflow on Fan Noise," United Aircraft Corporation Publication Paper Presented at 9th Meeting Acoust. Soc. Am. (April 1974).

140. Hanson, D.B., "The Spectrum of Rotor Noise Caused by Atmospheric Turbulence," J. Acoust. Soc. Am., Vol. 56, pp. 110-126 (1974).
141. Clark, L.T., "Sources of Unsteady Flow in Subsonic Aircraft Inlets," Boeing Airplane Co., Publication, Paper presented at 97th Meeting of Acoust. Soc. Am. (April 1974).
142. Moiseev, N. et al., "Noise Due to Interaction of Boundary-Layer Turbulence with a Compressor Rotor," J. Aircraft, Vol. 15, pp. 53-61 (1978).
143. Trunzo, R. et al., "The Effect of Inlet Guide Vane Disturbances on Turbomachinery Noise," AIAA 5th Aeroacoustics Conf., Seattle, Wash. (1979).
144. Moore, C.J., "Reduction of Fan Noise by Annulus Boundary Layer Removal," J. Sound Vib., Vol. 43, pp. 671-681 (1975).
145. Tyler J.M. and T.G. Sofrin, "Axial Flow Compressor Noise Studies," Trans. SAE, Vol. 70, pp. 60-37 (1962).
146. Tyler, J.M. and T.G. Sofrin, "Stop Compressor Noise Before It Starts," SAE Journal, pp. 54-60 (1962).
147. Morfey, C.L., "Rotating Pressure Patterns in Ducts Their Generation and Transmission," J. Sound Vib., Vol. 1, pp. 60-87 (1964).
148. Morfey, C.L., "Sound Transmission and Generation in Ducts with Flow," J. Sound Vib., Vol. 14, pp. 37-55 (1971).
149. Mugridge, B.D., "The Measurement of Spinning Acoustic Modes Generated in an Axial Flow Fan," J. Sound Vib., Vol. 10, pp. 227-246 (1969).
150. Wright, S.E., "Wave Guides and Rotating Sources," J. Sound Vib. Vol. 25, pp. 163-178 (1972).
151. Schlinker, R.H. and T.F. Brooks, "Progress in Rotor Broadband Noise Research," 38th Annual Forum of The American Helicopter Society, Anaheim, CA (1982).
152. Schlinker, R.H. and R.K. Amiet, "Helicopter Rotor Trailing Edge Noise," AIAA 7th Aeroacoustics Conference, Paper AIAA-81-2001, Palo Alto, CA (1981).
153. Kim, Y.N. and A.R. George, "Trailing Edge Noise from Hovering Rotors," AIAA Journal, Vol. 20, pp. 1167-1174 (1982).

INDEX

Acoustic coincidence frequency, 582
 Acoustic compactness, 497
 and lifting surface noise, 908
 Acoustic impedance, specific, 39
 Acoustic intensity, 17, 39
 Aeolian tone, 504
 far field, definition, 38
 jet noise, 166
 rotating rod, 514
 Acoustic power, 40
 and input power, 50
 dipole, 49
 effect of reflecting surface on, 48
 free jet, 169
 monopole, 48
 rectangular plate, 579-581
 Acoustic radiation:
 point force on infinite plate, 594-597
 rectangular panel:
 example, 604-609
 formulation, 571-575
 Acoustic radiation damping, 598
 Acoustic radiation efficiency, 8
 baffled beam, 587
 definition, 8, 581
 measurements, 587, 590-593
 modal average, 588-590
 mode classifications of
 rectangular plate, 583, 602
 numerical example, 615
 unbaffled beam, 586
 unbaffled plates, 585
 Acoustic radiation efficiency,
 rectangular plate:
 corner mode, 584
 edge mode, 584
 surface mode, 585
 Acoustic radiation loss factor, 247, 553, 615
 Acoustic radiation resistance, 579
 (see also acoustic radiation efficiency)
 Actuator disc, propeller, 1112
 Added mass, 593
 and fluid loading, 597-598
 Adiabatic, 35, 55
 expansions, 36, 240
 oscillations, 245
 Advance coefficient, 428, 1113
 nomographs, 33, 429
 Aeolian tone, 89, 449, 507
 intensity of, 504-507
 (see also vortex shedding, cylinder, airfoil)

Aerodynamic Influence Functions
 (see lift, fluctuating on airfoils)
 Air, physical properties of, 427
 Airfoils, summary of noise source (table), 903-904
 Array, as a spatial filter, 760
 Average:
 in space, 154, 555
 in time, 17, 153, 543
 over resonant modes, 562-563
 Axial flow fan noise:
 basic equation for blade rate tones, 1131
 broadband related to loading, 1152-1159
 ducted rotor, basic equation, 1199
 general equation for, 1124-1128
 Gutin Sound, 1142
 laminar flow tones, 1145
 table of rotor parameters, 1154
 thickness noise, 1159
 turbulence induced, 1190
 Barotropic fluid, definition, 35
 Beam, mode density, 560
 Beam, radiation efficiency, 587
 Bending waves, phase speed of, 549
 Bernoulli's equation, 82, 233
 Bernoulli-Euler equation, 546
 Bessel's functions, 1128
 Blade element analysis:
 turbulent inflow, 1181-1185
 Blade rate forces:
 acoustic radiation from, 1136-1147
 blade element analysis, 1130-1136
 (see also lift, fluctuating on airfoils)
 induced by turbulence, 1186
 example, 1192
 limiting equations, 1189-1190
 influence of expanded area ratio, 1130
 measurement example, 1141
 Blade rate noise:
 from compact rotor, 1141
 general behavior, 1100-1103
 general equations, 1131, 1138
 Blade row:
 acoustic blade interactions, 1176
 and unsteady lifting and surface theory, 1177
 aerodynamic blade interactions, 1174
 as spatial filter, 1100-1101, 1187
 basic equation of interaction tones, 1164
 harmonic analysis of wake defects, 1161
 Kemp-Sears theory, 1161, 1166-1168
 thrust coefficient, influence of blade interaction, 1120
 viscous and potential interactions, 1167

Blade slap, 1169-1172
 Blade stresses, 1123
 Blade thickness noise, 1159
 Blade turbulence interaction, 1103
 Blade vortex interactions, 1097, 1169-1173
 (see also Blade slap)
 Boundary layers:
 equilibrium, 624
 self-preserving, 624, 629
 Bubbles, collapse of cavitation, 283
 adiabatic gas law, 292
 and presence of walls, 301
 collapse time, 285
 details of final stage, illustration, 293
 effect of internal pressure on, 291
 (see also diffusion and vaporous cavitation)
 effects of viscosity, 300
 empty bubbles, 294
 illustrations, 286-287
 limiting functions, 295-299
 limiting velocities of bubble wall, 288, 297
 minimum radius, 291-292
 non-spherical bubbles, 300
 Rayleigh's equation, 383-385
 Bubbles, formation of, 413-423
 and noise, 413
 (see also bubbles, linear oscillations)
 by diffusion, 267-272
 in turbulence, 312-316, 422-423
 jet break-up, 417-421
 jet break-up in cross flow, 408-411
 periodic, 409, 414
 sizes and sounds (table), 412
 splitting, 422
 Bubbles, linear oscillations, 244-258
 amplification factors, 266
 damping, 243-247
 noises emitted from, 397-412
 observed, 407-411
 sound pulse illustration, 398
 speed dependence, 404, 406, 411, 412
 resonance frequency, 243, 245
 simple harmonic motion, 243-248
 Bubbles, non-linear motion, 259ff
 critical pressure, 260-262
 critical pressure illustration, 262
 critical radius, 261
 limiting radius, 265
 onset of, 259
 radius time curve illustration, 259
 radius time dependence in turbulent layer, 326
 radius time formula, 264

Bubble distribution:
 definition of, 250
 in mixtures, 252
 (see also nucleus distribution)
 Bubble dynamics, basic equation of, 238-242
 Bubble equation, linearization, 243
 Bubble rebounds, 287, 335
 Bubbly mixture:
 sound propagation, 248-259
 speed of sound, 251
 transmission in, 251
 Cascade (see Blade row)
 Cavitation:
 and nucleus distribution, 381-383, 386-390
 and turbulence structure, 386
 behind disk, 321
 behind orifice plate, 321
 bubble screening, 387-388
 event rates, 384-390
 free jet, 322
 in periodic vortex street, 320
 mass of gas diffused during, 271
 propeller noise, bubble model, 394-397
 propellers, 365
 (see also propeller cavitation)
 separating laminar boundary layers, 327
 tip vortex, 319, 368
 photograph, 368
 turbulent boundary layer, 324
 Cavitation, bubble:
 photographs on hydrofoil, 358
 photographs on propeller, 367
 Cavitation inception:
 bubble equation, 306-310
 critical pressures for, 260, 308
 diffusion influences, 268
 disk, sharp edged, 321
 hydrofoil, 303, 312
 influence of dissolved gas, 272, 310
 in turbulent boundary layer, 324
 isolated roughness, 331-333
 orifice plates, 321
 scale effects, 302-306, 327-331
 separated laminar boundary layer, 327-330
 thresholds for gaseous type equation, 311, 315
 turbulent jets, 322
 vortex cavitation, 316
 vortex streets, 320
 Cavitation index, 17, 234, 302-333
 nomograph, 429

cavitation noise:

- alternative length and time scales, 346, 348-350, 370
- dependence on hydrostatic pressure, 347-352, 370
- free jet observation, 353
- hydrofoil cavitation observation, 357-365
- hydrofoil noise from, 357
- rotating blade, 376
 - (see also propeller cavitation)
- rotating rod, 345
- rules of similitude, 344-352
 - with shock formation, 350-352
 - with unequal cavitation indices, 348-349
- single bubbles:
 - and liquid compressibility (shocks), 341
 - and liquid compressibility (shocks)
 - effect on spectrum, 343
 - and stages in bubble history, 338
 - ideal spectrum function, 337-341
 - time trace, 335
- stochastic models:
 - and statistics of turbulence, 383
 - and bubble statistics, 386
 - prediction and scaling rules, 374-380, 390-397
- cavitation noise modeling:
 - and hydrofoil cavitation, 360-361, 378-379
 - and jet cavitation, 354-355
 - propeller cavitation, 394-397
 - stochastic theories of, 381-397
- cavitation nuclei,
 - (see Nucleus distribution)
- cavitation number,
 - (see Cavitation index)
- cavitation sheet, 367
 - photograph on hydrofoil, 364
- cavitation thresholds, 272
 - (see also nucleus distribution, critical pressure)
 - acoustic methods of measurement, 281
 - (see also bubbly mixture, transmission of sound in)
 - event counting, 281
 - influence of gas content, 272
 - measurements, 273, 274
 - stabilized cavitation nuclei, 275
- cavitation types:
 - photograph on headform, 305
 - photograph on propeller, 367, 368
- cavity resonance, 125
- cavity tones, 129, 130
 - sound radiation from, 133
 - Strouhal number illustration, 130
- circulation, definition, 84
- circulation of Vortex Streets, 320, 988, 992
- clamped beam, 565

Coincidence frequency:

- acoustic, 582
- hydrodynamic, 842-844
- Coaxial nozzle, vortex shedding, 1011
- Compressor noise:
 - overview of sources, 1097-1100
- Continuity equation, 34, 52, 82
- Convection velocity of turbulence, 177, 665
- Corner (acoustic) mode, 583
- Correlation area, 189, 669, 868
 - definition, 669
- Correlation functions:
 - and statistical probability, 153
 - and Taylor's hypothesis, 183
 - centroid, 504
 - Fourier transform of, 155-160
 - illustrations of, 216, 480, 656, 658, 738, 999, 1059
 - inequalities, 659
 - separable representations of, 182, 184
- Correlation length, 64, 180, 672
 - relationship to wave number spectrum, 180
- Correlation volume, 189
- Covariance (see also correlation functions)
 - spatial, 64
- Critical pressures, 234
 - cavitation inception, 260-262
 - crevices in hydrophobic particles, 276
- Cross spectral density:
 - determination from filtered signals, 213
 - measurement, 208
 - physical interpretation of, 208-209
 - spatial, 155, 158
- Curle of vector, 82
- Curle's equation, 69, 497
- Cut-off, (cut-on) frequency, 1169, 1200
- Cylinder:
 - drag coefficients of, 464
 - pressure distribution, 464
- Cylinders, noncircular cross section, 519
- Cylindrical coordinate system, 41
- Damping:
 - acoustic radiation, 598
 - bubbles, 244-246
 - control of hydroelastic vibrations, 1055-1056
 - hydrodynamic, 1044
 - in presence of vortex shedding, 1050
 - in simple harmonic oscillator, 542, 533
 - vibration decay, 544
 - viscous, 1046
 - with fluid loading, 599

- Decibel, 18
- Delta function, 99
 - as Fourier transform of exponential, 99, 156
- Diffusion of Gas:
 - and gaseous cavitation, 267
 - and vaporous cavitation, 270
 - coefficient, 269
 - convective, 268-270
 - critical pressure for, 262
 - rectified, 270
- Diffusivity, (diffusion coefficient), 269, 427
- Dipole, 2, 44, 69, 91
 - directivity, 48, 518, 917
 - enhancement to jet noise, 1011, 1034
 - force, 46, 73-74
 - heaving sphere, 71-73
 - near a half-plane, 914
 - sound in free space, 44, 914
 - sound in two phase flow, 203-204
- Directivity patterns:
 - compact dipole, 48
 - edge noise, 916-917
 - jet noise, 167
 - point force on infinite plate, 595-596
 - propeller noise, 1144
 - quadrupole, 50
 - rotating rod noise, 518
- Displacement thickness, 642
- Distortion harmonics,
 - (see also axial flow fan)
 - general description, 953, 1101
 - formulation of unsteady loads, 1132-1135
 - rotor-stator interaction, 1162-1165
- Divergence operator, 35
- Divergence theorem (see Gauss' theorem)
- Drag coefficient, cylinders:
 - definition, 462
 - fluctuating, 472, 477
 - oscillatory, 473
- Duct acoustics, 1193-1196
- Eddy (see vortex)
- Edge (acoustic) mode, 582-583
- Edge tone, 140, 143-148
 - effective dipole force, 148
 - Strouhal number, illustration, 146
- Efficiency, Propeller, 1121
- Eigenfunctions, 547
- Epstein-Plesset theory, 269
- Ergodic process, 154
- Error Function, 985
- Euler's equation, 52
 - (see also momentum equation)
- Expanded area ratio, 1117
- Fan (see axial flow fan)
- Feedback:
 - in self excited flows, 144
 - vortex shedding
 - cylinder wakes, 484, 1056, 1057
 - trailing edge flow, 1057-1062
- Filter:
 - electronic, 18
 - one-third octave, 22
- Flexural waves, 549-551
 - matching with acoustic waves, 578
 - matching with hydrodynamic waves, 851
- Flow induced vibrations:
 - by convected pressure fields, 834-844
 - cavitation induced, 363-365
 - hydroacoustic mode classification, 858
 - mode classifications, 851
 - noise control principles, 861-868
- Fluctuations, stochastic, 97
- Fluid loading, 553, 566-579, 594-599
- Force dipole, 73-74
- Fourier transform, 24, 92, 98, 158-160
 - relationships, 155-160
 - spatial, 102
- Free surface boundary, 48
- Frequency, 19
- Frequency filter function, 211
- Friction velocity, 628
- Froude number, 17, 237, 414
- Gaseous cavitation, 231, 267-272
- Gauss' theorem, 62, 68
- Gradient operator, 35
- Green function:
 - free space, 93
 - half-plane, 912
 - opening in rigid wall, 133
 - rigid plane, 95
 - separable, 102
 - sources in ducts, 1195-1196
- Gutin sound, 1142
 - in duct, 1201
- Half-plane (see trailing edge)
- Helicopter rotor noise, 1153, 1172
 - (see also blade vortex interactions)

Helmholtz integral equation, 92
 trailing edge noise, 919
 Helmholtz (cavity) resonance, 132, 135
 Henry's law, 268, 427
 Hole tones, 139, 143
 Hydrodynamic coincidence, 834-840
 frequency, 837, 839, 842, 844
 Hydrodynamic instability, 118-121, 135-149
 amplification by sound, 142-144
 amplification by vibration, 1057-1060
 free shear layer, 121, 963
 in wake of airfoil, 963-969
 in wake of cylinder, 457-459
 Hydrophobic particles, 275

 Impedance, definition, 538
 Impedance:
 acoustic, 39
 infinite plate to point force, 564
 Inlet flow distortion (see Distortion Harmonics)
 Intensity (see acoustic intensity)
 Intermittency, 795
 Isothermal motion, 240

 Jets, turbulent:
 noise, 61
 axisymmetric disturbances, 196
 enhancement by proximate edge, 1034
 formal analysis, 160-166, 189
 frequency dependence, 169, 192
 measurements, 166-170
 subsonic noise, 160-170
 turbulent velocity:
 covariances, 177
 cross spectral densities in, 187
 dimensional analysis, 192-195
 integral scales, 180
 turbulence levels, 174, 179
 vortex structures, 141
 wave number spectrum, 182
 two-phase, 197-207
 bubble noise from, 206-207
 dipole sound from, 201, 203
 monopole sound from, 203
 Jet laminar, 118, 121-122, 135-149
 Jet stability, 135-149
 Jet tones, Strouhal number illustration, 139

 Karman vortex street, 486, 906
 Kirchhoff's equation, 56-60
 Kutta condition, steady flow, 929
 importance in analysis of trailing edge noise, 1016

Laminar boundary layer, 118, 121, 327, 790, 971,
 1007-1010, 1145-1149
 Laplacian operator, definition, 37
 Law of the wake, 636
 Law of the wall, 633
 Leading edge noise (see Lift, fluctuating on airfoils)
 Lift, fluctuating on airfoils:
 aerodynamic influence functions, 933, 939-942
 differential pressures due to, 935, 943-946, 952
 due to gusts, 932, 939-942
 due to upstream wakes, 951-954
 due to vortex shedding, 1001
 sound radiation in turbulence, 946-950
 surface pressures due to, 943-945
 Lift, fluctuating on cylinders:
 correlation function for, 479
 correlation length, definition, 479
 measurement illustration, 474
 sound radiation from, 502-508
 theory versus measurement, 495
 two-dimensional vortex model, 486-495
 Lifting surface theory, 1177
 Lighthill's equation, 52, 60
 free-space form, 62
 Loss factor, definition, 541
 (see also damping)

 Mach number, 5, 14, 31
 Matched asymptotic expansion, 109
 Mean square, 18, 152
 Membrane waves, 551
 Micropascal, 18
 Microscale, turbulence, 180
 Modal density, 559, 615
 Modal force (see modal pressure)
 Modal Pressure:
 definitions for random excitation, 548, 554
 from turbulent boundary layer, 840
 from point force, 604, 606, 611
 random excitation of single mode, 554
 vibration of hydrofoils, 1039
 Modal shape functions:
 asymptotic forms of, 570
 cantilever plates, 1042
 ducts, 1195-1196
 even-order mode shape, 568
 for simple structures, 565-571
 normalization, 566
 simply-supported membrane, 566
 simply-supported plates, 565
 Mode count:
 hydrodynamically coincident modes, 852
 Momentum equation, 34, 82

- Momentum integral equation, 642
- Momentum thickness, 642
- Monopole, 2, 42
 - and cavitation, 334
 - sound in inhomogeneous discharge, 203
- Moving axis correlation, 185, 660, 1184
- Newmann boundary condition, 95
- Nomographs:
 - advance coefficients, 33
 - bubble resonance frequencies, 245
 - cavitation indices, 429
 - decibel addition chart, 24
 - dynamic pressure, 31
 - hydrodynamic coincidence frequencies, 844
 - radiation efficiencies of plates, 615
 - tip velocities of propellers, 33
 - vibration and noise control, 863
- Nozzles, 135-137
- Nucleation, cavitation, 275
 - wetting, 275-277
- Nucleus distribution:
 - illustration, 279, 280
 - measurement of, 278
 - event counting, 281
 - acoustic absorption, 281
 - optical methods, 283
- Orifices, 149
- Orifice tones, 141
 - Strouhal numbers, illustration, 142
- Orr-Sommerfeld equation, 120
 - (see also hydrodynamic instability)
- Orthogonal functions, 547
- Pascal, 18
- Peclet number, 270
- Pipe flow, 783
- Pitch, 1186
- Pitch angle, 1115
- Plane boundary, sound from turbulence near, 76-79
- Powell's reflection theorem, 74-79
- Powell's theory of vortex sound, 80-90
- Power dissipated, 543
- Power, input:
 - simple harmonic oscillator, 544
- Power:
 - and modal pressure, 563
 - input to flexural waves, 555, 563-565
 - net of many modes, 563, 565
- Power spectral density (see spectral density)
- Pressure, acoustic, 18, 35-39
- Pressure, dynamic, 27, 30
- Pressure release boundary (see free-surface boundary)
- Propeller cavitation, 365-376
 - blade analyses, 390-397
 - blade passage frequency, 366
 - noise, 369, 372
 - noise, dependence on speed, 374-378
 - noise scaling, 370, 373, 375
 - photographs, 367-368
 - tip vortex, illustration, 368
 - velocity dependence, 376
- Propeller diagram, 1115
- Propeller noise control tradeoff example, 1124
- Propeller singing, 1158-1159
- Propulsive efficiency, 1112
- Quadrupole, sound, 2, 49-51, 61
 - importance to Aeolian tone, 500-502
 - lateral, 49
 - longitudinal, 49
 - Reynolds stresses as sources of, 66
 - sources, 49-51
 - jet noise, 66, 167
- Quality factor, 542
 - (see also damping)
- Radiation:
 - condition, 51-52, 94
 - loss factor (see acoustic radiation loss factor)
 - resistance (see acoustic radiation efficiency)
- Radius of gyration, plate, 546
- Random variable:
 - homogeneous, 153-159
 - spatially homogeneous, 103, 153
 - temporally homogeneous, 153
- Random vibration:
 - (see also power, input and modal pressure)
 - multi-mode oscillators, 556-564
 - simple harmonic oscillator, 541
 - two-dimensional structures, formulation, 552-565
- Rectangular plate:
 - flexural modes, 556
 - mode density, 559
- Reduced wave equation, 92
- Retarded time, 61
- Reynolds number, 13, 235, 236
- Reynolds stress, 54, 55
 - fluctuating, 63
 - near a half plane, 919
- Ring frequency, cylinder, 593

- Ring tone, 143-144
- Rotating cylinder, geometry, 498
- Rotating rods:
 - directivity patterns, 518
 - measured, 515-518
 - radiation, 511-517
 - spectral density of noise from, 516
- Rotor-Stator Interactions (see distortion harmonics)
- Rough surfaces:
 - cavitation inception, 331
 - turbulent boundary layer, 637-641, 647, 654, 679, 727, 734, 742-744, 770-772, 804
- Sears function, 931
- Self-sustained tone, 144, 1046-1056
 - (see also Feedback)
- Shape factor, 642
- Shape functions, modal, 554
- Shear Layer, examples, 117
 - and jet tones, 122, 142-148
 - and sound radiation, 124
 - behind cylinders, 457-458
 - instability at trailing edges, 962-963
 - linear stability analysis, 118-123
 - shear noise, 172
- Similitude, 12
 - of turbomachines, 1111
- Simple harmonic oscillator:
 - linear response formula, 541
 - mass controlled motion, 542
 - power relationships, 543
 - resonance frequency, 541
 - stiffness controlled motion, 542
- Singing, hydrofoil (see vortex shedding hydrofoil)
- Solubility of air in water, 268, 427
- Solidity of rotors blading, 1119
- Sommerfeld's radiation condition, 51
- Sound, dipole:
 - from compact body, 509
 - from compact force, 503
 - from rigid cylinder, 504
 - (see also vortex shedding, cylinder)
- Sound pressure level, definition, 16
 - combination, 23
 - overall, 20
- Sound pressure spectrum, 18
- Source levels, superposition, 70-71
- Spectral density, 21, 25
 - cross, 100-101
 - dimensionless, 24
 - frequency, 155-160
- Spectral density, (continued)
 - intensity, 217
 - measurement, 20, 213
 - power, 4, 217
 - pressure, 4, 100, 217
 - wave number, 105, 155-160
- Speed of sound, 36
- Sphere:
 - heaving, 71-73, 107
 - volume source, 42
- Spherical coordinates, 41
- Spinning modes, 1140, 1200-1201
 - condition for propagation in ducts, 1200
- Stability (see hydrodynamic instability)
- Stagger angle, 1162, 1176, 1186
- Stationary phase, method of, 574-575
- Statistical energy analysis, 539, 544
- Stiffness, bending of plate, 546
- Stokes' theorem, 85
- Stress tensor, 96
 - Lighthill's, 53
 - Stokes', 53, 82
- Strip theory, 939
- Strouhal number, 466-468
 - definition, 127
 - lifting surfaces, 969-978
 - table, 974
 - vortex shedding cylinder, illustration, 467-468
- Surface, acoustic influence on sound generation, 67, 74-80, 915-917
- Surface tension, 238, 427
- Taylor's hypothesis, 174
- Tensile strength of water, 231
 - (see also cavitation thresholds)
- Third-octave-band spectrum, 21, 218
- Thrust coefficient, propeller, 1112, 1114
- Time average, 17
- Torque coefficient, 1114
- Total loss factor, 247, 553
 - (see also damping)
- Trailing edge noise:
 - (see also vortex shedding, airfoils)
 - aeroacoustic scattering theory, 1012-1018
 - and surface pressures, 1018
 - axial flow fans, 1148-1152
 - blown flaps and impinging jets, 1027-1033
 - compared to boundary layer noise, 889, 891, 1016
 - compactness arguments, 908-917
 - dipole near half plane, 909-915
 - evanescent wave theories of, 1023

Trailing edge noise: (continued)

- from flexible surfaces, 1035
- from wedges, 1036
- from turbulent flow past edge, 918-924
- general scaling relationship, 923, 1022
- influence of yaw, 923
- measurements, 1031, 1032, 1034
- measurements on propeller fan, 1151
- relationship to surface pressures, 1018-1023

Transition to turbulence:

- body of revolution, 790
- condition for in boundary layer, 787-790
- intermittency, 795

Tube bundles, 521

- fluctuating lift, 525
- Strouhal numbers, 524
- vibration in, 525
- whirling parameters, 526

Turbulence:

- correlation functions, 158
- expectation, 151
- mean square, 152
- probability, 151
- sound from free, dimensional analysis, 61-66
- variance, 152
- wave number spectrum and Fourier transform, 156
- in axial flow fan inlet, 1181-1193
- interaction with airfoil, 904-907, 936-943

Turbulence microscale, 970

Turbulent boundary layer:

- axisymmetric on cylinders, 807
- body of revolution, 790-795
- bursting events, 680
- convection velocities, turbulence, 665
- law of the wake, 636
- law of the wall, 633
 - on circular cylinders, 809
- logarithmic region, 636, 637
- on NACA 0012 airfoil, 962
- on NACA 63-009 airfoil, 964
- parameter estimation formula, 645
- Reynolds stresses, 654, 673-675
- roughness height, 638
- streamwise vortex, structures in, 675
- surface roughness, table, 647
- turbulence intensities, 649-653
- turbulence spectra, 661-663
- turbulence statistics, 655
- von Karman constant, 637
- with pressure gradients, 800
- with pressure gradients, wall pressures in, 801-805
- wall shear coefficient, 631
- in transitional flow, 793-795

Turbulent boundary layer, induced vibrations:

- Dyer's criteria for spatially homogeneous excitation, 838-840, 856
- hydrodynamic coincidence, 842
 - of hydrofoils, 1039-1040
- measurements, 847-848
- modal pressure, 841, 843
- mode classifications, 845
- multi-modal estimates, 849
- parametric dependences, 864-865
- sound from, 856-861
- speed dependence, 855

Turbulent boundary layers, sound radiation from:

- (see also trailing edge noise)
- boundary layers on flexible surfaces, 878
- comparisons with other mechanisms, 889, 891
- dipole sound, 871-873
- efforts at measuring, 873
- formulas for, 878, 880, 883, 885

Turbulent boundary layer, wall pressure:

- and quadrupole sound, 885
- at low wave number, measurements, 863
- at sonic wave numbers, measurements, 766
- at sonic wave numbers theory, 878
- attenuation by elastomer layers, 783
- circular cylinders, 810
- covariances on trailing edges, 998-1000
- convection velocities, 744
- influences of surface impedance, 878-881
- influences of viscous absorption, 881
- in transitional flow, 797
- measured frequency spectrum, 731-735
- on trailing edges, 993-998
- outer-inner variable scaling, 734
- rough walls, 770
- separated flow, 806
- space-time statistics, 737
- spatial resolution, 772, 777
- theoretical frequency spectrum, 709

Unsteady airfoil theory, 926-931

- (see also lift, fluctuating on airfoils)

Viscosity, kinematic of water, 427

Viscous sublayer, 633

Vortex, 1, 80, 81

- sound 87-89, 124, 497-508
- sound from half plane, 1004

Vortex formation lengths, 461, 962

- Vortex shedding, airfoils (see also Vortex shedding, cylinders, hydrofoils)**
 - acoustic radiation formula, 1007
 - blunt edges, 1011

Vortex shedding, airfoils, (continued)
and turbulent flow structures, 967-970
at blunt trailing edge, 961-962, 966-969
at sharp trailing edge, 959-960, 971
effects of edge vibration, 1058-1060
fluctuating forces, 1001
frequency of, 971-978, 974 (table)
laminar flow tones, 1007
relationship to other sources, 903-905
rotating blade with laminar flow, 1145
suppression with splitter plates, 964
tonal pressures due to, 985-987, 990, 992, 1008,
1010-1011
wake strengths, 992

Vortex shedding, cylinder:
acoustic intensity, 505-511
acoustic intensity, effect of yaw, 510
and Orr-Sommerfeld's equation, 453-459
effects of cylinder vibration on, 483, 509, 1057-1058
effects of free stream turbulence on, 483
effect of splitter plates on, 485
fluctuating velocities in wake, 456
formation zone, 459-462
frequency of, 465, 467-469
mean velocity in wake, 455
photograph, 451
vibration control, 526-528, 1056
vibration modeling, 1066

Vortex shedding, hydrofoils:
(see also vortex shedding, airfoils, cylinders)
analytical modeling techniques, 1042, 1061-1067
control by hysteretic damping, 1051-1056
vibration, 1037-1041, 1046-1049
wake-vibration coupling, 1057-1061

Vortex shedding frequency, 466
Vortex sheet, 118, 121
Vortex spacing ratio, 471
Vorticity vector, 82

Wall shear stress, 631
Wall pressure fluctuations (see turbulent boundary layer,
wall pressure)

Water, physical properties, 427

Wave equation, 37

Wave number:

acoustic, 43
free flexural waves, 549
lattice, 557
mode density, 559-560
on resonant rectangular plate, 566
trace, 164, 575

Wave speed, longitudinal, 559

Wave vector filter:

analogy to rotor response, 1101-1104, 1182, 1186-1190
as measurement tool, 760
formulae, 755

Weber No., 17, 413

Wedge, scattering, 1036

Wiener-Hopf technique, 912

Young's modulus, 546

END

FILMED

4-85

DTIC